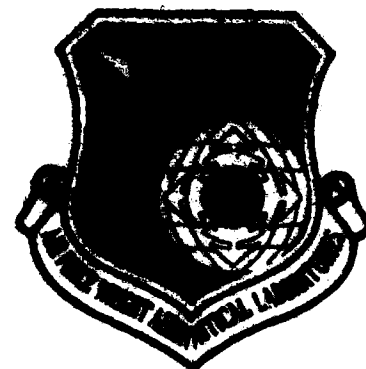




AFWAL - TR - 88 - 3034



AD-A197 808

PROCEEDINGS OF THE
THIRD INTERNATIONAL CONFERENCE
ON

RECENT ADVANCES

IN

STRUCTURAL DYNAMICS

VOLUME II

DTIC
ELECTE
JUL 22 1988
S 9 E D

UNCLASSIFIED PUBLIC RELEASE; DISTRIBUTION UNLIMITED

88 7 21 054

AIR FORCE RESEARCH LABORATORY
WRIGHT PATTISON AFB, OH 45433

NOTICE

When Government drawings, specifications, or other data are used for any purpose other than in connection with a definitely related Government procurement operation, the United States Government thereby incurs no responsibility nor any obligation whatsoever; and the fact that the Government may have formulated, furnished, or in any way supplied the said drawings, specifications, or other data, is not to be regarded by implication or otherwise as in any manner licensing the holder or any other person or corporation, or conveying any rights or permission to manufacture, use or sell any patented invention that may in any way be related thereto.

This report has been reviewed by the Information Office (OI) and is releasable to the National Technical Information Service (NTIS). At NTIS, it will be available to the general public, including foreign nations.

This technical report has been reviewed and is approved for publication.

Howard F. Wolfe
HOWARD F. WOLFE, Tech Mgr
Acoustics and Sonic Fatigue Group
Structural Dynamics Branch
Structures Division

Jean Pearson
JEAN PEARSON, Chief
Structural Dynamics Branch
Structures Division

FOR THE COMMANDER

RM Bader
ROBERT M. BADER, Asst Chief
Structures Division

If you address has changed, if you wish to be removed from our mailing list, or if the information is no longer employed by your organization please notify the National Council, 600 N. 4th St. to help us maintain a current mailing list.

Content of this report shall not be disclosed or released in any form or by any means, electronic or mechanical, including photocopying, recording, or by any information storage and retrieval system, except as may be required in writing by a court of law or by a specific statute.

AD A-1

REPORT DOCUMENTATION PAGE				Form Approved OMB No. 0704-0188	
1a. REPORT SECURITY CLASSIFICATION UNCLASSIFIED			1b. RESTRICTIVE MARKINGS		
2a. SECURITY CLASSIFICATION AUTHORITY			3. DISTRIBUTION/AVAILABILITY OF REPORT Approved for public release; distribution unlimited		
2b. DECLASSIFICATION/DOWNGRADING SCHEDULE					
4. PERFORMING ORGANIZATION REPORT NUMBER(S) AFWAL-TR-88- 3034			5. MONITORING ORGANIZATION REPORT NUMBER(S)		
6a. NAME OF PERFORMING ORGANIZATION Acoustics & Sonic Fatigue Group		6b. OFFICE SYMBOL (if applicable) AFWAL/FIBGD	7a. NAME OF MONITORING ORGANIZATION		
6c. ADDRESS (City, State, and ZIP Code) Wright-Patterson Air Force Base, OH 45433			7b. ADDRESS (City, State, and ZIP Code)		
8a. NAME OF FUNDING / SPONSORING ORGANIZATION		8b. OFFICE SYMBOL (if applicable)	9. PROCUREMENT INSTRUMENT IDENTIFICATION NUMBER		
8c. ADDRESS (City, State, and ZIP Code)					
			10. SOURCE OF FUNDING NUMBERS		
			PROGRAM ELEMENT NO. 62201F	PROJECT NO. 2401	TASK NO. 04
11. TITLE (Include Security Classification) Third International Conference on Recent Advances in Structural Dynamics (Unclassified)					
12. PERSONAL AUTHOR(S)					
13a. TYPE OF REPORT Conference Proceedings		13b. TIME COVERED FROM 84 TO 88		14. DATE OF REPORT (Year, Month, Day) 1988 July	
15. PAGE COUNT					
16. SUPPLEMENTARY NOTATION					
17. COSATI CODES			18. SUBJECT TERMS (Continue on reverse if necessary and identify by block number)		
FIELD	GROUP	SUB-GROUP			
19. ABSTRACT (Continue on reverse if necessary and identify by block number) Individual papers of the Third International Conference on Recent Advances in Structural Dynamics to be held 18-22 July 1988 at the Institute of Sound and Vibration Research in Southampton, England are presented. The subjects include: Analytical methods, finite element methods, testing techniques and correlation, shock, failure and fatigue, vibration control and damping, nonlinear techniques, random vibration of nonlinear systems, parameter excitation, composites, large space structures, structural/acoustic interaction, civil engineering.					
20. DISTRIBUTION/AVAILABILITY OF ABSTRACT <input checked="" type="checkbox"/> UNCLASSIFIED/UNLIMITED <input type="checkbox"/> SAME AS RPT. <input type="checkbox"/> DTIC USERS			21. ABSTRACT SECURITY CLASSIFICATION UNCLASSIFIED		
22a. NAME OF RESPONSIBLE INDIVIDUAL HOWARD F. WOLFE			22b. TELEPHONE (Include Area Code) 513-255-5229		22c. OFFICE SYMBOL AFWAL/FIBGD

PROCEEDINGS OF THE
THIRD INTERNATIONAL CONFERENCE
ON

RECENT ADVANCES
IN
STRUCTURAL DYNAMICS

18-22 JULY 1988

University of Southampton, England

Edited by

M. Petyt , H.F. Wolfe and C. Mei

VOLUME II

Accession For	
NTIS GRA&I	<input checked="checked" type="checkbox"/>
DTIC TAB	<input type="checkbox"/>
Unannounced	<input type="checkbox"/>
Justification	
By _____	
Distribution/	
Availability Codes	
Dist	Avail and/or Special
A-1	

ORGANISATION

The Conference was organised by the

Institute of Sound and Vibration Research

with the support of the following bodies:

Air Force Wright Aeronautical Laboratories

Wright Patterson Air Force Base

European Office of Aerospace Research and Development

Institute of Mechanical Engineers

Institute of Civil Engineers

The Society for Earthquake and Civil Engineering Dynamics

ORGANISING COMMITTEE

Dr. M. Petyt

Professor R.G. White

Dr. F.J. Fahy

Mr. R.C. Drew

Mr. M.J.B. Shelton

Mr. H.F. Wolfe

Lt.Col. J.G.R. Hansen

Dr. R.J. Pinnington

Mr. S.C.P. Galea

Mrs. M.Z. Strickland

Dr. C. Mei

Professor H. Tottenham

Mr. N.S. Ferguson

Miss J.L. Horner

CONTENTS

Page No.

1. ANALYTICAL METHODS

1. D.J. GORMAN 3
A general computational technique for the free vibration analysis of rectangular plates with classical edge support based on the superposition method
2. P. HAMMER and B. PETERSSON 13
Minimised input power by line force excitation
3. O.A. FETTAHLIOGLU 21
Exact solutions for wave propagation in rings and arches on elastic foundations
4. D.J. MEAD and Y. YAMAN 35
Vibration analysis of finite uniform structures using the harmonic response functions of the infinite structure
5. G.J. KISSEL 45
Randomly disordered periodic structures
6. J. WEI and M. PETYT 55
Free vibration of ring stiffened cylindrical shells
7. T.N. SHIAU and C.C. PAN 65
Sensitivity analysis and dynamic behaviors of rotating pretwisted tapered blade
8. I. ELISHAKOFF, C.D. HETTEMA and E.L. WILSON 75
Direct superposition of Wilson trial functions by computerized symbolic algebra
9. I-CHEN CHANG 87
Problems of structural dynamics solved by Chinese remainder algorithm

2. FINITE ELEMENT METHODS

10. E. HINTON and B. AL JANABI 101
Vibration of plates with concentrated masses and plates with point supports
11. D.J. MEAD, D.C. ZHU and N.S. BARDELL 111
Free vibration of an orthogonally stiffened flat plate
12. R.P. LEAL and C.A. MOTA SOARES 123
Mixed elements in design sensitivity analysis of plates with dynamic and stability constraints
13. A. POTIRON 133
A new finite element for the dynamical study of pretwisted beams

- | | | |
|-----|---|-----|
| 14. | S.S. GUPTA | 147 |
| | A complex vibration analysis of a three-shaft geared, compressor set mounted on a steel entablature | |
| 15. | Y.A. KHULIEF and H.T. CHIU | 159 |
| | Transient dynamics of rotating flexible bodies with base motion excitations | |

3. COMPOSITES

- | | | |
|-----|---|-----|
| 16. | E.R. BAYLIS and W.A. GREEN | 171 |
| | Impact stress waves in fibre reinforced laminated plates | |
| 17. | W.A. GREEN and E.R. BAYLIS | 185 |
| | The contribution of high-harmonics to transient waves in plates and laminates | |
| 18. | G. CEDERBAUM, L. LIBRESCU and I. ELISHAKOFF | 199 |
| | Response of laminated composite plates to non-stationary random excitation | |
| 19. | S.P. LIM, K.H. LEE and N.R. SENTHILNATHAN | 211 |
| | Nonlinear vibrations of antisymmetric angle-ply laminates using a simple higher-order theory | |
| 20. | MALLIKARJUNA and T. KANT | 219 |
| | On transient response of laminated composite plates based on higher-order theory | |
| 21. | L. LIBRESCU, A.A. KHDEIR and D. FREDERICK | 229 |
| | Free vibration and buckling of cross-ply laminated shear deformable shallow shell-type panels | |
| 22. | N. SANKARANARAYANAN, K. CHANDRASEKARAN and G. RAMAIYAN | 241 |
| | On the free vibrations of laminated conical shells of variable thickness | |

4. TESTING TECHNIQUES AND CORRELATION

- | | | |
|-----|--|-----|
| 23. | D.L. BROWN | 253 |
| | Invited Paper - Future trends in modal analysis | |
| 24. | G.R. TOMLINSON and P. MILAS | 265 |
| | Impulse testing techniques applied to large vibration isolators | |
| 25. | H.G.D. GOYDER | 279 |
| | Three methods for determining natural frequencies and damping ratios from vibration spectra | |
| 26. | T.K. TEE, J.E. MOTTERSHEAD, R. STANWAY, and D.J. BROOKFIELD | 289 |
| | Application of filtering techniques for system identification of vibrating structures | |
| 27. | K. WORDEN and G.R. TOMLINSON | 299 |
| | Identification of linear/nonlinear restoring force surfaces in single and multi-mode nonlinear systems | |

28.	F. BENEDETTINI, D. CAPECCHI and F. VESTRONI On identification of linear and nonlinear structural systems	309
29.	J. BRANDON On the use of oversized models for modal identification in structural dynamics	319
30.	H.G.D. GOYDER and A.P. LINCOLN An experimental technique for investigating nonlinear structures	329
31.	H.R. LO and J.K. HAMMOND Nonlinear system identification using the surface of nonlinearities form: discussion on parameter estimation and some related problems	339
32.	L. GAZDAG and G.T. ENDKOCZI Multilevel substructuring and mode superposition for complex structures	349
33.	P.O. LARSSON Methods using frequency-response functions for the analysis of assembled structures	363
34.	J. ZEISCHKA, M. BRUGHMANS and O. STORRER LMS/LINK correlating and validating Finite Element Analysis (FEA) for dynamic structure behaviour with experimental modal analysis	377
35.	J.L. HORNER and R.G. WHITE Vibrational power transmission through discontinuities	387
36.	B.A.T. PETERSSON Giant magnetostrictive devices in structural acoustics	397

5. VIBRATION CONTROL AND DAMPING

37.	D.I.G. JONES Invited Paper - Recent advances in structural damping	409
38.	C.U. BRUER and J.S. BOLTON Damping of continuous structures by the use of elastic porous materials	429
39.	S.N. SHOUKRY Assessment of frictional damping in tangentially loaded metallic interfaces	437
40.	J.M. CUSCHIERI and V.R. DESAI Friction damping due to interfacial slip	449
41.	E. SEMERCIGIL and N. POPPLEWELL The bean bag impact damper	459
42.	M.A. CATCHINS, J.E. COCHRAN, P. KUMAR, N.G. FITZ-COY, and M.L. TINKER Analysis of coils of wire rope arranged for passive damping	469

- | | | |
|-----|--|-----|
| 43. | A. PREUMONT, E. CZAJKOWSKI, and R.T. HAFTKA
Stabilizing the neglected dynamics in active control of vibration | 481 |
| 44. | R. UHRIG
Vibration problems in coalmine hauling systems | 491 |
| 45. | W. D'AMBROGIO and A. SESTIERI
Altering the vibrational behavior of an I.E. engine as a preliminary step for noise reduction | 499 |

6. SHOCK

- | | | |
|-----|---|-----|
| 46. | D.L. ANDERSON and M.D. OLSON
Recent progress in analyzing the nonlinear response of beams and stiffened plates | 511 |
| 47. | XI DECHANG and PEN NANLING
Nonlinear responses of a rigid block with a simply supported beam subjected to shock excitation | 521 |
| 48. | W.P. SCHONBERG
Dynamic impact of beams - a correlation of experimental and theoretical results | 527 |
| 49. | D.H. TREPESS and R.G. WHITE
Shock testing with electrodynamic exciters using oscillatory transient excitation | 537 |
| 50. | S.J.C. DYNE, J.K. HAMMOND and P. DAVIES
A method for finding an upper bound for the response of structures to blast waves | 551 |
| 51. | D.K. ANDERSON
Impact coupled oscillator systems | 561 |

7. FAILURE AND FATIGUE

- | | | |
|-----|--|-----|
| 52. | J.S. MIXSON
Invited Paper - Overview of acoustic fatigue activities at NASA Langley Research Center | 573 |
| 53. | R. VAICAITIS and S.T. CHOI
Acoustic fatigue of stiffened structures | 593 |
| 54. | N.S. FERGUSON
An analytical investigation into the behaviour of composites | 605 |
| 55. | C.F. NG
The influence of snap-through motion on the random response of curved panels to intense acoustic excitation | 617 |
| 56. | S.C. GALEA and R.G. WHITE
Effect of temperature on acoustically induced stresses in some CFRP plates | 629 |
| 57. | P. DAVIES and J.K. HAMMOND
Two methods for the detection of failure in mechanical systems | 641 |

8. NONLINEAR TECHNIQUES

- | | |
|--|-----|
| 58. A.H. NAYFEH
Invited Paper - Modal interactions in the nonlinear response
of structural elements - theory and experiment | 653 |
| 59. C. HOFF
Dissipative step by step integration methods in nonlinear
structural dynamics | 671 |
| 60. F. BRANCALEONI and C. VALENTE
On some aspects of operational error distribution and
propagation in direct integration for nonlinear dynamics | 683 |
| 61. C.E. TEH and H.G.D. GOYDER
Nonlinear vibration of a loosely supported beam | 693 |
| 62. P.B. GONCALVES and R.C. BATISTA
Nonlinear vibrations of fluid loaded cylindrical shells | 705 |

9. RANDOM VIBRATION OF NONLINEAR SYSTEMS

- | | |
|---|-----|
| 63. Y.K. LIN
Invited Paper - Recent advances in nonlinear random vibration | 717 |
| 64. H.J. PRADLWARTER, G.I. SCHUELLER and X.-W. CHEN
Consideration of non-Gaussian response properties by use
of stochastic equivalent linearization | 737 |
| 65. G. TSIATAS and H. SADID
Random vibration of hysteretic systems | 753 |
| 66. M.J.H. FOX
A method for the dynamic analysis of randomly excited
structures with frictional constraints | 759 |
| 67. C.K. CHIANG and CHUH MEI
A finite element large deflection multiple-mode random
response analysis of beams subjected to acoustic loading | 769 |
| 68. F. CASCIATI, L. FARAVELLI
Non linear stochastic dynamics of frames | 781 |

10. PARAMETRIC EXCITATION

- | | |
|--|-----|
| 69. C.W.S. TO
Recent advances in vibration analysis of systems with
parametric random excitations | 793 |
| 70. D.A. STREIT, A.K. BAJAJ and C.M. KROUSGRILL
Parametric instabilities and chaotic amplitude modulations in
a system with two degrees of freedom | 809 |
| 71. G. OSTIGUY and H. NGUYEN
Combination resonances of parametrically excited rectangular
plates | 819 |

11. STRUCTURAL/ACOUSTIC INTERACTION

- | | | |
|-----|--|-----|
| 72. | A. FRID | 833 |
| | Fluid vibration in piping systems - a structural mechanics approach | |
| 73. | J.S. POLLARD | 845 |
| | Application of statistical energy analysis to helicopter cabin type structures | |
| 74. | H. CARLSSON and G. SANDBERG | 857 |
| | Finite element analysis of structure acoustic interaction | |
| 75. | P. GORANSSON | 869 |
| | Analysis of the transmission of sound into the passenger compartment of a propeller aircraft using the Finite Element Method | |

12. LARGE SPACE STRUCTURES

- | | | |
|-----|--|-----|
| 76. | S. ABRATE | 881 |
| | Modelling of latticed structures for dynamic analyses | |
| 77. | H.V. PANOSSIAN | 891 |
| | An assessment of model order reduction techniques | |
| 78. | G.A. BECUS and C.W. CHENG | 901 |
| | Energy methods for model reduction in the dynamics and control of large structural systems | |
| 79. | S.E. LAMBERSON and C.A. FISHER | 911 |
| | Structural dynamic analysis and tests of a planar large space truss subcomponent | |
| 80. | S. MAHANIAN | 921 |
| | The effects of cable suspension on bending vibration of large beams | |
| 81. | G.L. SLATER, M.D. MCLAREN, V.B. VENKAYYA and V.B. TISCHLER | 933 |
| | Robustness and positive real control design for large space structures | |

13 CIVIL ENGINEERING

- | | | |
|-----|---|-----|
| 82. | L. FRYBA | 945 |
| | Invited Paper - Dynamics of bridges | |
| 83. | J. RAVINGER | 963 |
| | Dynamic post-buckling of slender webs | |
| 84. | H-J ZHOU | 973 |
| | Determination of dynamic behavior of thin arch dams using spline semi-analytic method | |
| 85. | L.A. DE BEJAR | 981 |
| | Effect of the gradient of elastic eccentricity on the lateral-torsional effective earthquake forces on building systems | |

86.	R.K.N.D. RAJAPAKSE and A.H. SHAH Torsional oscillations of flexible inclusions in a layered elastic half-space	993
87.	J.R. MAGUIRE A frequency/damping database for tall chimneys	1003
88.	S. TSANG and C. WILLIAMS Application of experimental modal analysis to full scale civil engineering structures	1009
89.	L. FARAVELLI Source-to-site seismic models in structural dynamics	1021
90.	F. LOPEZ-ALMANSA, J. RODELLAR, A.H. BARBAT and J.A. CANAS An assessment of digital active tendon control of building structures	1033
91.	G. HIRSCH and A. KLEINE-TEBBE Semi-active control of earthquake induced oscillations in structures - mechanical qualification by means of the SAMSON shaking table.	1043

6. SHOCK

RECENT PROGRESS IN ANALYZING THE NONLINEAR RESPONSE OF BEAMS AND STIFFENED PLATES

D.L. Anderson and M.D. Olson
Department of Civil Engineering
University of British Columbia
Vancouver, B.C., Canada, V6T 1W5

1. INTRODUCTION

The response of structures to air blast has for many years been the subject of numerous studies, some of which were reviewed in [1]. The difficulties that arise from the complexity of the problem, which involves time dependent finite deformations, high strain rates and nonlinear inelastic material behaviour, have motivated various assumptions and approximations to simplify the models. These models span the full range of sophistication from simple one degree of freedom representations to general purpose finite element programs such as ADINA.

At the time of the aforementioned review, it appeared that there was a need for further analytical work on even such simple configurations as a rectangular cross section beam with constrained ends. That is, while the impulsive response of such a beam was known, there was no solution for a general load shape in the dynamic range and hence it was not possible to draw an iso-response curve for such a problem. At the other extreme, it appeared that although very complex structures could be modelled with available finite element codes, they are extremely complicated and expensive to run and all but impractical for design purposes. Hence we decided to work on the problem from both ends, that is, to extend the analytical work on simple structures as well as try to simplify the computer modelling for more complex structures. In this paper, we present a brief review of the progress made by our group over the last few years.

2. BEAM STRUCTURES

It was clear from the literature survey that there were very few "exact" rigid-plastic solutions of beams which retained the influence of finite deflections and also accounted for the time distribution of the dynamic loading. In his MSc thesis [2], Vaziri analysed a rigid-perfectly plastic rectangular beam with constrained ends subjected to a pressure pulse of finite duration. The deformation proceeds under two distinct mechanisms depending on the level of the peak pressure. Although the governing equations were derived for a general pressure-time relationship, they were only solved for the particular case of a rectangular pulse. Closed form expressions were developed for the prediction of the maximum permanent deflection. Finally the dependence of the permanent deflection on the applied pressure and impulse was obtained for a family of rectangular pulses, and the results were represented by iso-response curves in a form convenient for direct engineering use [3].

The above work has been further extended by Schubak [4]. He solved the static problem exactly and then showed that the exact solution differed very little from an approximate analysis that assumed a single central hinge and a linear moment-axial force interaction diagram [5]. He then applied the same approximations to the dynamic case. Comparisons of the results with those of Vaziri showed close agreement for the final permanent deformation. The advantage of using the linear interaction relation is that the resulting governing equations are linear. Thus it is possible to solve the beam problem for pressure pulses that more closely resemble the blast pressure pulse.

Using the above approximations, Schubak was able to solve a number of previously unmanageable problems, such as a general blast load shape on an I-beam. An example is shown in the following. He was also able to solve for the effect of the rise time in a triangular pulse shape on the permanent deflection [6]. As expected its greatest influence comes when the peak pressure is low and the pulse duration is large. For high pressure nearly impulsive loads, it has no influence. In general, the effect is small and for pressures greater than twice the static collapse pressure it can be ignored.

Folz [7] has developed a finite element code (FENTAB) based on Euler-Bernoulli beam theory to augment the above work. The program includes large deflections, elastic-plastic strain hardening and strain rate sensitive material and calculates transient response using central difference time stepping with a diagonalized mass matrix.

Figure 1 shows the particulars of an example symmetric I-beam subjected to a rectangular pulse of short duration. Fig. 2 shows the midspan displacement response as predicted by this program and as predicted by the simple rigid-plastic theory developed by Schubak. Note that the deflections are well into the nonlinear geometry and yielding range. The agreement is very encouraging, especially with respect to the predicted permanent deflection.

This analysis has also been applied to an asymmetric I-beam with clamped ends and the response results are shown in Figure 3. The beam represents one stiffener and its tributary plating from the DRES panel (Sec. 3.2.4), and the load was a rectangular pressure pulse of magnitude 4635 lb/in (or 129 psi on the panel) and duration 2 msec. The agreement between the FENTAB program and the simple rigid-plastic theory is remarkably good up to the maximum displacement but then the latter overpredicts the permanent displacement by about 10%. This is obviously due to the neglecting of elastic effects and its importance decreases as the load intensity increases. The foregoing may be thought of as a reasonable approximation of the response of one-way stiffened panels to intense blast loads.

3. PLATE STRUCTURES

As mentioned in the introduction, the numerical analysis of complex plate structures such as stiffened plates is prohibitively expensive especially for preliminary design work. Hence there appeared to be a need for a more economical but perhaps less accurate approach. Exploratory work by Mofflin, et al. [8] showed that using the finite strip method had the potential of considerable savings in computer costs over finite elements.

A complete finite strip program has now been developed for the large deflection, elastic-plastic static and dynamic response of plate structures [9-12]. In the following, we present a brief description of the method and some example results.

3.1 Finite Strip Formulation

Finite strip displacement functions vary across the strip in the same manner as finite elements, but the variation along the length is given by continuous functions selected to satisfy the boundary conditions at the ends of the strips as well as provide a reasonable approximation of the displacement distribution. Letting the degrees of freedom be the u, v, w displacements and the rotation (θ) about the x axis (i.e. $\theta = \partial w / \partial y$) at each of the two nodal lines (Figs. 4(a) and (b)), the displacements for a strip are given by

$$u = \sum_m [(1-\eta)u_{1m} + \eta u_{2m}] g_m^u(\xi), \quad v = \sum_n [(1-\eta)v_{1n} + \eta v_{2n}] g_n^v(\xi), \quad (1)$$

$$w = \sum_p [(1-3\eta^2+2\eta^3)w_{1p} + (\eta-2\eta^2+\eta^3)b\theta_{1p} + (3\eta^2-2\eta^3)w_{2p} + (\eta^3-\eta^2)b\theta_{2p}] g_p^w(\xi)$$

where $\eta = y/b$, $\xi = x/a$, $u_1 = \sum_n u_{1n}$, $v_2 = \sum_m v_{2m}$, etc. In the strip direction, the displacements vary according to the g_m^u, g_n^v, g_p^w functions, which for different boundary conditions are as follows:

- (i) Members without stiffeners (axially constrained):
a. Simply supported ends: b. Clamped ends:

$$\begin{aligned} g_m^u(\xi) &= \sin m\pi\xi &= \sin m\pi\xi & ; m = 2, 4, 6... \\ g_n^v(\xi) &= \begin{cases} \sin n\pi\xi \\ \cos n\pi\xi \end{cases} &= \begin{cases} \sin n\pi\xi \\ \cos n\pi\xi \end{cases} & ; \begin{matrix} n = 1, 3, 5... \\ n = 2, 4, 6... \end{matrix} \\ g_p^w(\xi) &= \sin p\pi\xi &= \phi_p(\xi) & ; p = 1, 3, 5... \end{aligned} \quad (2)$$

where the ϕ_p are the clamped beam vibration modes.

- (ii) Members with stiffeners (I-beams or stiffened plates):
a. Simply supported ends: b. Clamped ends:

$$\begin{aligned} g_m^u(\xi) &= \cos m\pi\xi &= \frac{\partial \phi_m(\xi)}{\partial x} & ; m = 1, 3, 5... \\ g_n^v(\xi) &= \sin n\pi\xi &= \phi_n(\xi) & ; n = 1, 3, 5... \\ g_p^w(\xi) &= \sin p\pi\xi &= \phi_p(\xi) & ; p = 1, 3, 5... \end{aligned} \quad (3)$$

For large deflections, a second u-mode was found necessary for each case, namely $\sin 2\pi\xi$ and $\sin 4\pi\xi$ for simply supported and clamped ends, respectively.

Stiffeners can be modelled by considering the strip turned on its edge. In the same way I beams can be built up using a series of strips as shown later. For these cases, the v displacement in the web stiffener must match the w displacement in the other strips, and thus they must have the same functional form and magnitude.

The derivation of the matrix equations for a strip follows that for finite elements and only some of the pertinent points are discussed in the following. The nonlinear strain displacement equations of von Karman type are used. These include quadratic terms in both v and w. The material is assumed to follow a bilinear elastic-plastic law, with a strain rate sensitive yield stress. The von-Mises yield criteria and an associated hardening flow rule are used.

The equilibrium equations for one strip are obtained via the principle of virtual work in the form

$$\int_V [\underline{B} + \underline{C}]^T \underline{\sigma} dV = \underline{p} \quad (4)$$

where B and C are the linear and nonlinear strain-displacement matrices, respectively, $\underline{\sigma}$ is the stress vector, and \underline{p} is the consistent load vector.

The volume integrals are evaluated numerically using a Gauss integration scheme. The number of integration points depends on the mode shape and whether the material behaviour is plastic or remains elastic. For the simplest elastic problem with a single half sine wave displacement, a scheme with 5-2-2 integration points in the x-y-z directions was found to be adequate.

Static problems are solved by the Newton-Raphson method applied to Eq. (4) to yield the standard stiffness matrix representation. Dynamic solutions on the other hand are obtained by assembling a generalized force vector for a complete structure directly from Eq. (4) (including damping and inertia forces) and integrating with a finite difference time stepping procedure with a diagonalized mass matrix.

3.2 Numerical Results

Several beam and plate examples have been solved to test the accuracy of the finite strip method. The central deflections predicted for linear elastic rectangular beams subjected to static uniform loads are very good. A one mode solution for the simply supported case is nearly exact, while the clamped case is in error by about 4%.

For large deflections, the results are highly dependent on the mode shape used for the u displacement. As a general rule if w is represented by a mode shape given by $\cos p\pi\xi$, then u should have a shape of $\sin 2p\pi\xi$ to give the best approximation of axial equilibrium. Good static results were obtained for the large deflection, elastic-plastic response of both simply supported and clamped rectangular beams using $(m,n,p) = (2,1,1)$ and $(4,1,1)$, respectively [9].

3.2.1 Simply Supported I Beam - Uniform Static Load

Elastic large deflection results of a simply supported I beam are presented in Figure 5, along with the section dimensions and material properties. Finite strip results were obtained by employing six finite strips, two each in the top flange, bottom flange, and the web. In this case two modes are needed to represent the u displacement, even though only one w mode is used. One u mode accounts for the bending strains, and so should have the shape given by $\partial w / \partial x$, or $\cos 2\pi\xi$ in this case, while the other u mode accounts for the axial forces in the large displacement region of the response as discussed above. It is clear from Figure 5 that the central deflections are in very good agreement with finite element results obtained by FENTAB.

The comparison of predicted central deflections with FENTAB for an elastic-perfectly plastic material, including large deflections, is presented in Figure 6, where it is seen that the agreement is excellent. When the central deflection approaches twice the beam depth, the FENTAB solution runs asymptotic to the plastic string limit. The finite strip solution, on the other hand, agrees with the solution obtained using a one mode Galerkin procedure on the governing differential equation for a plastic string. This is expected as the assumed displacement variation in the Galerkin analysis is the same as in the finite strip, namely $\sin \pi\xi$.

3.2.2 Clamped I-Beam - Uniform Step Load

The dynamic response of the same I-beam with clamped ends was obtained for a step load in time of magnitude 495 lb/in assuming elastic-perfectly plastic material behaviour and nonlinear geometry. The central displacement history is shown in Figure 7 along with that from FENTAB. The second u mode referred to in the figure was $\sin 4\pi\xi$. The lumped mass matrix was used, and the time step was 0.02 msec. The two results compare quite well for most of the response, but the finite strip model is stiff compared to the FENTAB model as the deflections are less and the peak displacement is reached sooner. However the displacement levels predicted here are very extreme, being about 4 times the beam depth. At these levels, the beam is acting essentially as a plastic string and the clamped beam mode used herein is not optimum for this case. Hence considering all this, an error of only 15 per cent in the maximum displacement is really exceptionally good.

3.2.3 Simply Supported Square Plate - Dynamic Load

Figure 8 shows a comparison of the finite strip results with other numerical results [13] for a nonlinear, elastic-plastic response of a simply supported square plate with edges constrained against in-plane motion subjected to a transient uniform pressure. This example is one of very large deflections with a central deflection of approximately 25 thicknesses or 0.12 times the span. Increasing the number of strips, and using 2 modes instead of one for each of the displacement functions reduced the stiffness of the finite strip model and made it closer to the other predicted results shown in Figure 8.

3.2.4 DRES Stiffened Panel - Air Blast Test

An 8'x15' T-beam stiffened steel panel with 1/4" plating and 3"x6" T-beam stiffeners was tested at the Defence Research Establishment, Suffield, Alberta (DRES) [14]. Figure 9 shows the details for one half of this panel. The panel was embedded in a reinforced concrete foundation to simulate clamped boundary conditions, and was subjected to an air blast load from a ground explosion. The pressure time history shown in Figure 10 was obtained by averaging the measurements of several pressure transducers after synchronizing the rise times. The following analysis was simplified by ignoring the transient time (about 3 msec) of the shock front over the panel (parallel to the stiffeners), and assuming the pressure loading to be spatially uniform over the panel surface.

The half-panel was modelled with 16 finite strips, 4 between stiffeners, 1 for each web and 2 for each bottom flange, and a time step of 20 microseconds was used for the calculations. The predicted responses of points D12 and D13 (Figure 9) are shown in Figures 11(a) and (b), respectively, along with the experimental results for the first 50 msec. The essential features of the response seem to be well represented by this relatively simple model. That is, the predicted and measured transient deflections which are well into large deflection-yielding levels are reasonably close and, although not shown here the final permanent deflections predicted by the model are close to the experimentally observed ones of 0.6 and 1.0 inches for the stiffener and central panel, respectively.

The foregoing calculations used about 14 minutes of CPU time on an AMDAHL 580 Computer, which is one order of magnitude less than that required for a comparable calculation using ADINA.

4. CONCLUSIONS

A review has been presented of recent progress in modelling the large deflection, elastic-plastic dynamic response of beam and plate structures to air-blast pressure loads. Simple beams with constrained ends were considered first and some new important solutions for this case were discussed. In particular, it was noted that closed form solutions could be obtained for rigid-plastic beams of general cross-section using simple hinge mechanisms and a linear representation of the appropriate interaction diagram.

For plate structures, a new finite strip formulation which includes the effects of large deflections, yielding, strain hardening and high strain rates was briefly reviewed. The results reported herein are very encouraging. It appears that reasonable engineering accuracy is achievable with modelling involving only a few modes and a few finite strips. The number of variables and the computer times are typically an order of magnitude less than those required by corresponding finite element codes. Thus considerable savings in cost are possible for certain problems with only a minimal loss in accuracy.

Work is currently underway to extend the finite strip analysis to composite, laminated structures.

5. ACKNOWLEDGEMENT

This research was supported by the Canadian Department of National Defence through a series of contracts from the Defence Research Establishment, Suffield, Alberta.

6. REFERENCES

1. J. ARI-GUR, D.L. ANDERSON and M.D. OLSON 1984 Procs. 2nd Int. Conf. on Recent Advances in Structural Dynamics, U. of Southampton, Southampton, England, April 8-13, 383-392. Review of Air-Blast Response of Beams and Plates.
2. R. VAZIRI 1985 M.A.Sc. Thesis, Department of Civil Engineering, University of B.C., Vancouver, Canada. Finite Deflection Dynamic Analysis of Rigid-Plastic Beams.
3. R. VAZIRI, M.D. OLSON and D.L. ANDERSON 1987 Int. J. Solids and Structures, Vol. 23, No. 1, 153-174. Dynamic Response of Axially Constrained Plastic Beams to Blast Loads.
4. R.B. SCHUBAK 1986 M.A.Sc. Thesis, Department of Civil Engineering, University of B.C., Vancouver, Canada. Finite Deflection Dynamic Response of Axially Restrained Beams.
5. R.B. SCHUBAK, M.D. OLSON and D.L. ANDERSON 1987 J. Applied Mechanics, Vol. 54, No. 3, 720-723. Simplified Rigid-Plastic Beam Analysis.
6. R.B. SCHUBAK, D.L. ANDERSON and M.D. OLSON 1987 I.J. Impact Engineering (in press). Simplified Dynamic Analysis of Rigid-Plastic Beams.
7. B.R. FOLZ 1986 M.A.Sc. Thesis, Department of Civil Engineering, University of B.C., Vancouver, Canada. Numerical Simulation of the Non-Linear Transient Response of Slender Beams.

8. D.S. MOFFLIN, M.D. OLSON and D.L. ANDERSON 1986 Finite Element Methods for Nonlinear Problems, Eds., P.C. Bergan, et al., Springer-Verlag, 539-554. Finite Strip Analysis of Blast Loaded Plates.
9. S.B.S. ABAYAKOON, M.D. OLSON and D.L. ANDERSON 1987 Submitted to I.J. Num. Meths. Engineering. Large Deflection Elastic-Plastic Analysis of Plate Structures by the Finite Strip Method.
10. S. ABAYAKOON 1987 Ph.D. Thesis, Dept. of Civil Engineering, Univeristy of British Columbia, Vancouver, B.C. Large Deflection, Elastic-Plastic Analysis of Plate Structures by the Finite Strip Method.
11. M.R. KHALIL, M.D. OLSON and D.L. ANDERSON 1988 J. Computers Structures, (in press). Nonlinear Dynamic Analysis of Stiffened Plates.
12. R. KHALIL, M.D. OLSON and D.L. ANDERSON 1987 Struc. Series Report No. 33, Department of Civil Engineering, University of British Columbia, Vancouver, B.C., March. Large Deflection, Elastic-Plastic Dynamic Response of Air-Blast Loaded Plate Structures by the Finite Strip Method.
13. T.R. STAGLIANO and L.J. MENTE 1979 Finite Difference and Modal Solutions, Nonlinear Finite Element Analysis and Adina, Proc. ADINA Conference. Large Deflection, Elastic-Plastic Dynamic Structural Response of Beams and Stiffened or Unstiffened Panels - A Comparison of Finite Element.
14. J.E. SLATER and R. HOULSTON 1987 Defence Research Establishment Research Memorandum (in preparation), Suffield, Ralston, Alberta. Air-Blast Experiments on Stiffened Ship Panels.

7. CONVERSION UNITS

Most of the results shown in the figures are presented in English units which may easily be converted to SI units as follows: 1 psi = 6.895 kPa, 1 lb/in = 0.175 kN/m, 1 in = 25.4 mm, density $\rho = 0.25 \times 10^{-3}$ lbsec²/in⁴ = 2670 kg/m³.

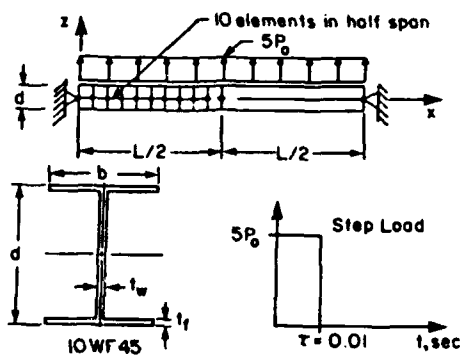


Fig. 1. Simply supported I-beam;
(dimensions as in Fig. 5,
 $5P_0 = 495$ lb/in,
 $\sigma_0 = 36,000$ psi)

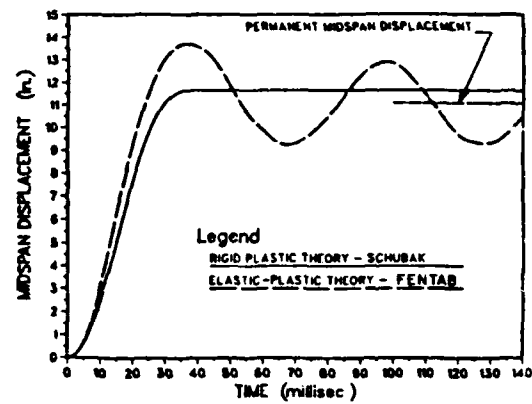
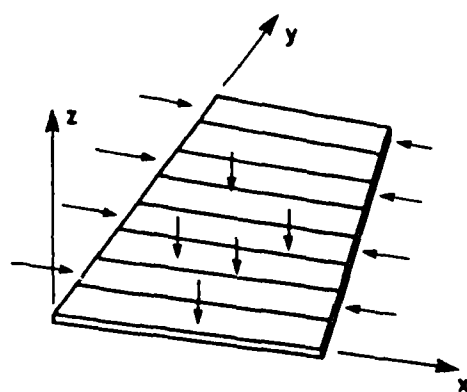
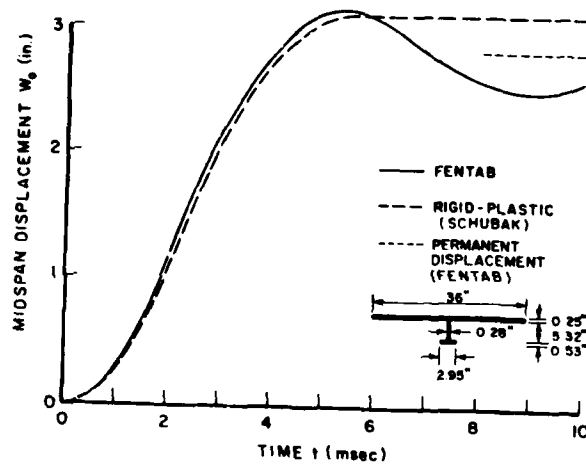
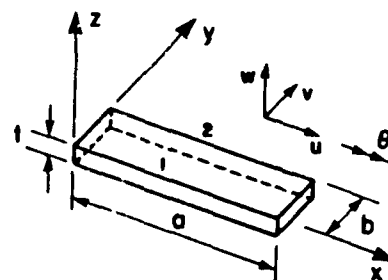


Fig. 2. Dynamic response of axially
restrained S.S. I-beam

Fig. 3. Dynamic response of
clamped asymmetric
I-beam.



(a) Typical Strip Division for a Plate



(b) Strip Parameters

Fig. 4. Finite strip definitions.

Fig. 5. Static deflection of S.S. I-beam - elastic case

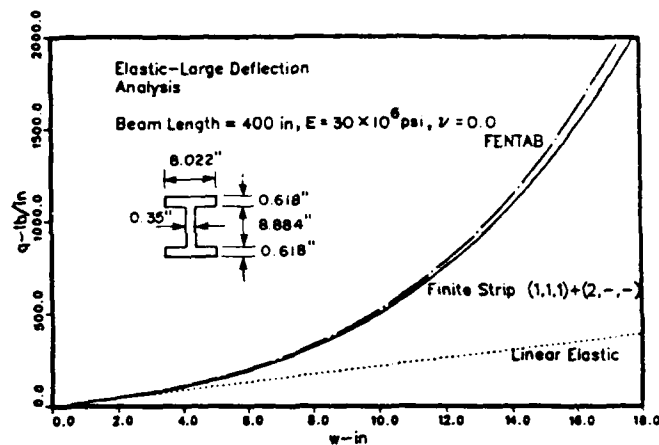


Fig. 6. Static deflection of S.S. I-beam - elastic, plastic case, $\sigma_0 = 36,000$ psi

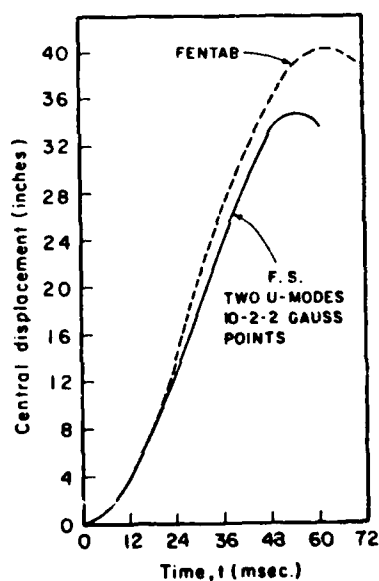
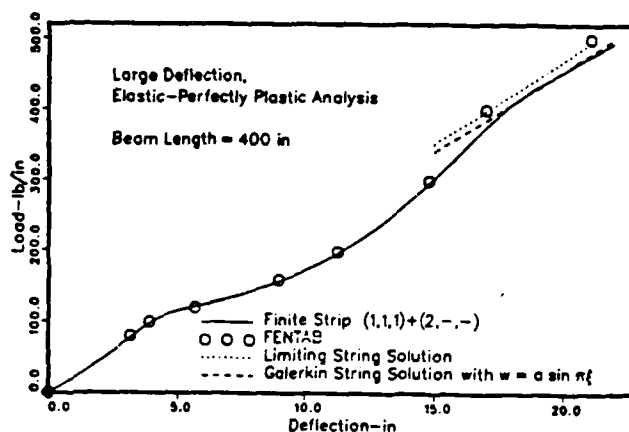


Fig. 7. Clamped I-beam response to step load, $\sigma_0 = 36,000$ psi

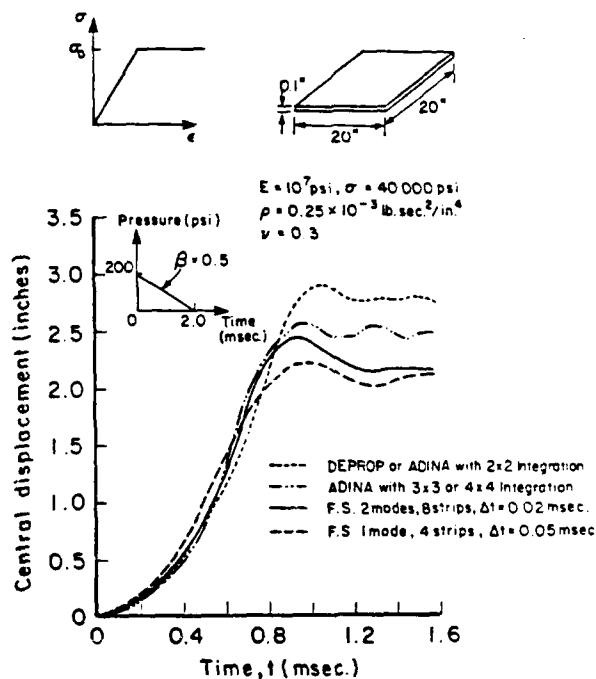


Fig. 8. Response of S.S. square plate to triangular blast load

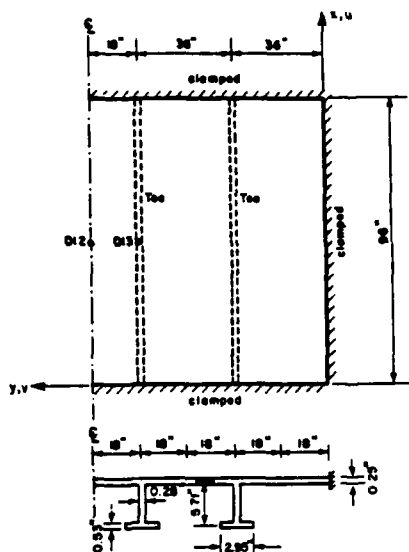


Fig. 9. DRES stiffened panel geometry,
 $\sigma_o = 54,000$ psi, $E_T = 178,000$
 psi, $\Delta t = 5$ μ sec

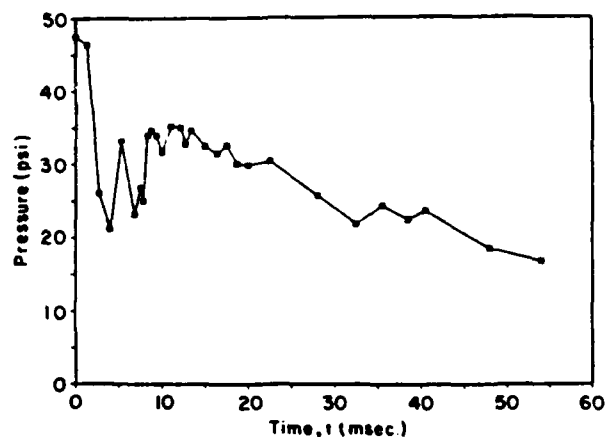


Fig. 10. Pressure time history
 on DRES panel

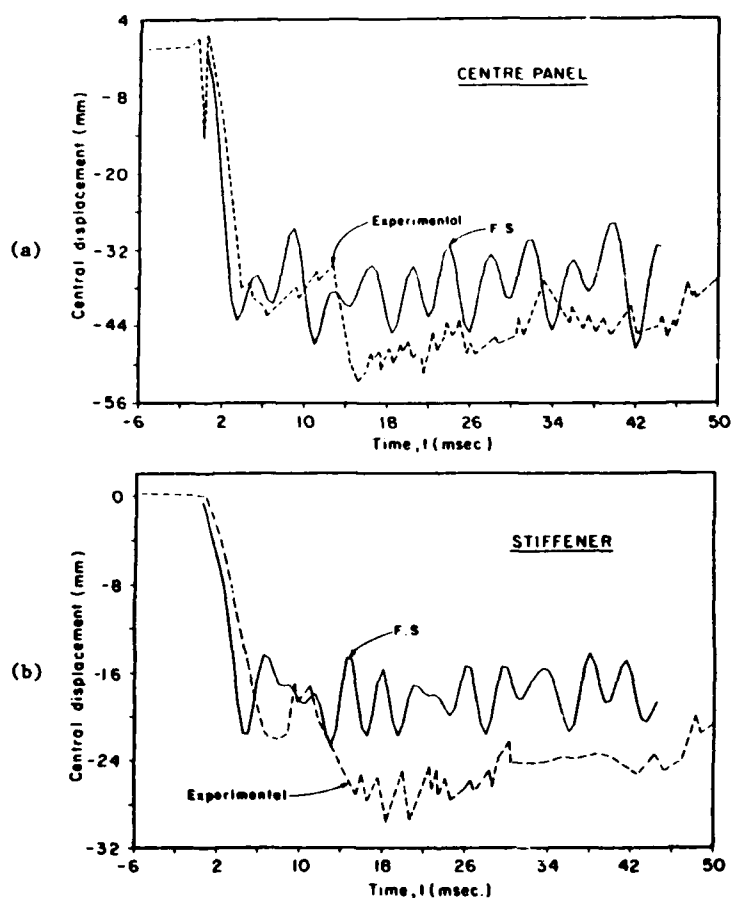


Fig. 11. Dynamic response of DRES panel

NONLINEAR RESPONSES OF A RIGID BLOCK WITH A SIMPLY SUPPORTED BEAM SUBJECTED TO SHOCK EXCITATION

Xi Dechang* and Pen Nanling

Zhejiang University, China

1. ABSTRACT

In this paper, the responses of a rigid block-simply supported beam system with nonlinear elastic material at the block's bottom subjected to shock excitation are discussed, and the nonlinear differential-integral equation which governs the motion of the system is deduced. Numerical solution of this equation is obtained by using Spline Functions in the paper. Through computation, the influence of different variables on the acceleration of the rigid block and the stress in the beam is analysed. Some measurements have been presented to decrease the response value.

2. NOTATIONS

x	axial coordinate of beam
t	time
m_1	mass of rigid block
l	length of beam
ρA	mass per unit length of beam
EJ	bending stiffness of beam
$y_1(t), y_2(x, t)$	vertical displacement of rigid block and beam
$H(t)$	vertical displacement of the system bottom
$u_1(t)$	$y_1(t) - H(t)$
$u_2(x, t)$	$y_2(x, t) - y_1(t)$
t_0, \ddot{H}_m	the duration and maximum value of acceleration pulse exerted on the system bottom
σ_0	maximum stress of beam subjected to static uniformly distributed loading ($\rho A \ddot{H}_m$ per unit length)
\ddot{y}_m, σ_m	maximum acceleration of block and maximum stress of beam under shock excitation
k_2, c_2	stiffness and damping coefficient per unit length of material between beam and rigid block
c_1	damping coefficient of material at the bottom of system
$F_8(u)$	force-deflection relation of material at the bottom of system
k_1	initial spring rate of nonlinear material

$$\mu = \rho A l / m \quad k = k_2 l / k_1 \quad c = c_2 l / c \quad \xi_1 = \frac{c_1}{2\sqrt{m_1 k_1}} \quad \gamma_1 = \frac{c_0}{\pi \sqrt{\frac{m_1}{k_1}}} \quad d = \begin{bmatrix} \pi \\ - \\ 1 \end{bmatrix}^2 \sqrt{\frac{EJ}{\rho A}} \sqrt{\frac{k_1}{m_1}} \quad \tau = t / t_0$$

3. INTRODUCTION

Many objects in the real world can be simply treated as a rigid block-simply supported beam system (for example, some works of art and some

* Professor

instruments). Under certain circumstances such as transportation, these objects will be subjected to shock excitation from outside. In order to decrease damage caused by shock, cushioning material with nonlinear properties is often placed at the bottom of the system. Obviously, it is necessary to investigate the nonlinear cushioning properties of this kind of system.

In 1945, R.D. Mindlin [1] studied a rigid block-longitudinal rod system. But actually he studied the rigid block and longitudinal rod respectively, because he assumed that the mass of the rod is much smaller than that of the block, so the interaction between rod and block can be neglected. The latest research on the dynamic responses of rigid block-simply supported beam system is by Xi Dechang [2]-[5]. On the basis of considering the interaction between beam and block, the curves which represent effects of different variables on responses are given, some relevant results are obtained. However, the above work is all limited to linear systems, the nonlinearity of cushioning material is not taken into account.

4. BASIC EQUATIONS

The mechanical model of rigid block-simply supported beam system is shown in Fig. 1, its equations of motion are:

$$\begin{cases} m_1 \ddot{y}_1 + c_1(\dot{y}_1 - \dot{H}) + F_g(y_1 - H) - \int_0^1 k_2(y_2 - y_1) dx \\ - \int_0^1 c_2(\dot{y}_2 - \dot{y}_1) dx + EJ y_2^{(3)}(x=0) - EJ y_2^{(3)}(x=1) = 0 \\ EJ y_2^{(4)} + \rho A \ddot{y}_2 + c_2(\dot{y}_2 - \dot{y}_1) + k_2(y_2 - y_1) = 0 \end{cases} \quad (1a)$$

$$\text{boundary condition: at } x=0,1 \quad y_2=y_1 \quad EJ y_2^{(2)}=0 \quad (1b)$$

$$\text{initial condition: when } t=0 \quad y_1=\dot{y}_1=y_2=\dot{y}_2=0 \quad (1c)$$

In the paper, the force-deflection function of the cushioning material at the bottom of the system is considered as Tangent Elasticity:

$$F_g(u_1) = \frac{2kh}{\pi} \operatorname{tg} \frac{\pi}{2} \frac{u_1}{h} \quad (2)$$

Referring to Fig. 2, k_1 is the initial spring rate and h is the maximum available deflection.

We take the ratios \ddot{y}_{1m}/\ddot{H}_m and σ_m/σ_0 to represent system responses, by noting:

$$w_1 = \sqrt{\frac{k_1}{m_1}} \quad v = u_1 / \left[\frac{\ddot{H}_m}{w_1^2} \right] \quad \delta = h / \left[\frac{\ddot{H}_m}{w_1^2} \right] \quad (3)$$

and expanding $u_2(x, t)$ into the series:

$$u_2(x, t) = \sum_{j=1}^{\infty} \sin \frac{j\pi}{l} x \cdot q_j(t) \quad (4)$$

Where $y_j(x) = \sin \frac{j\pi}{l} x$ is a mode of a simply supported beam, we can get a nonlinear differential-integral equation as below:

$$\left. \begin{aligned} \frac{d^2v}{d\tau^2} + \alpha \frac{dv}{d\tau} + \beta \epsilon_1 \frac{v}{\delta} + \theta \cdot \sum_{j=1,3,\dots} \int_0^\tau \frac{d^2v}{dT^2} \cdot g_j(\tau-T) dT = G(\tau) \\ \text{initial condition: when } \tau = 0, v = \frac{dv}{d\tau} = 0 \end{aligned} \right\} \quad (5a)$$

where $\alpha = 2\pi\epsilon_1\nu_1$

$$\beta = 2\pi\delta\nu_1^2$$

$$\theta = \pi\nu_1$$

$$g_j(\tau - T) = e^{-\eta_0\pi(\tau-T)} \cdot \frac{8}{(j\pi)^2} \cdot \frac{1}{\eta_j^*} \cdot \left\{ 2\epsilon_1 c \eta_j^* \cos \pi \eta_j(\tau-T) + [k + \mu j^4 d^2 - 2\mu \left(\frac{c}{\mu} \epsilon_1\right)^2] \cdot \sin \pi \eta_j(\tau-T) \right\}$$

$$\eta_0 = \frac{c}{\mu} \cdot \epsilon_1 \nu_1$$

$$\eta_j^* = \left[\frac{k}{\mu} + j^4 d^2 - \left(\frac{c}{\mu} \epsilon_1\right)^2 \right]^{1/2}$$

$$\eta_j = \eta_j^* \cdot \nu_1$$

$$G(\tau) = -(\pi\nu_1)^2 \frac{2\ddot{H}(\tau)}{H_m} - (\pi\nu_1)^3 \sum_{j=1,3,\dots} \int_0^\tau \frac{\ddot{H}(T)}{H_m} \cdot g_j(\tau-T) dT \quad (5b)$$

The ratio of acceleration and the ratio of stress can also be obtained:

$$\frac{\ddot{Y}_1(\tau)}{H_m} = \frac{\ddot{H}(\tau)}{H_m} + \frac{d^2v}{d\tau^2} / (\pi\nu_1)^2 \quad (6)$$

$$\frac{\sigma(x, \tau)}{\sigma_0} = \frac{32d^2\nu_1^2}{\pi^2} \sum_{j=1,3,\dots} \frac{j}{\eta_j} \sin \frac{j\pi}{l} x \cdot \int_0^\tau \frac{\ddot{Y}_1(T)}{H_m} \cdot e^{-\pi\eta_0(\tau-T)} \cdot \sin \pi \eta_j(\tau-T) dT \quad (7)$$

5. THE SOLVING OF NONLINEAR DIFFERENTIAL-INTEGRAL EQUATION

With regard to equation (5a), the Splire Function method is used to get numerical solution. That is to assume:

$$\text{When } \tau \in [\tau_i, \tau_{i+1}] \quad v(\tau) = a_i(\tau - \tau_i)^3 + b_i(\tau - \tau_i)^2 + c_i(\tau - \tau_i) + d_i \quad (8)$$

From this, we get:

$$b_{i+1} = 3a_i(\Delta\tau) + b_i$$

$$c_{i+1} = 3a_i(\Delta\tau)^2 + 2b_i(\Delta\tau) + c_i$$

$$d_{i+1} = a_i(\Delta\tau)^3 + b_i(\Delta\tau)^2 + c_i(\Delta\tau) + d_i, \quad \Delta\tau = \tau_{i+1} - \tau_i \quad (9a)$$

$$\text{and } \frac{d^2v}{d\tau^2} \Big|_{\tau=\tau_i} = 2b_i \quad \frac{dv}{d\tau} \Big|_{\tau=\tau_i} = c_i \quad v \Big|_{\tau=\tau_i} = d_i \quad (i=0,1,2,\dots) \quad (9b)$$

Let $\tau_0=0$, then b_0, c_0, d_0 can be easily obtained from equation (5a) and its initial condition, and a_1 is determined by equation (5a) at $\tau=\tau_{i+1}$ based on assumption (8), i.e.

$$\beta \operatorname{tg} \frac{\pi}{2} \cdot \frac{a_1(\Delta \tau)^3 + b_1(\Delta \tau)^2 + c_1(\Delta \tau) + d_1}{\delta} + [6(\Delta \tau) + 3\alpha(\Delta \tau)^2 + \theta \cdot p] a_1 \\ = G(\tau_{i+1}) - (2b_1 + \alpha[2b_1(\Delta \tau) + c_1]) - \theta \cdot q_1 \quad (10a)$$

where p, q_1 are defined as follows:

$$\sum_{j=1,3,\dots} \int_0^{\tau_{i+1}} \frac{d^2 v}{dT^2} \cdot g_j(\tau_{i+1} - T) dT = a_1 p + q_1 \quad (10b)$$

Nonlinear equation (10a) can be solved with the Newton iteration method. After the a_1 are obtained, the acceleration and stress can be calculated from formulae (6) to (9), so following these steps we can get the response of the system for $\tau \geq 0$.

6. RESULTS AND DISCUSSION

In the paper we consider $\ddot{H}(t)$ to be a half sine wave pulse, i.e.

$$\ddot{H}(t) = \ddot{H}_m \sin \pi \frac{t}{t_0} \cdot u(t_0 - t)$$

where $u(t)$ is unit step function. Calculated with the previous formula, the results are given in Fig. 3 to Fig. 6. From these figures we conclude:-

- (1) When other variables remain constant, the change of k , c and d almost have no effect on the acceleration of block; the reason is that the action on the block exerted by the beam through the spring k_2 and damping c_2 is much smaller than the total action on the block exerted by the material at the bottom of system and exerted by the beam through two simply supported ends.
- (2) Within a certain range, the increase of k, c will decrease the stress of the beam substantially. However, σ_m/σ_0 will not decrease very obviously as the value of k becomes large.
- (3) When k is small (< 0.1), σ_m/σ_0 has a peak value at $d = 1.0$ or so. So this situation must be avoided.
- (4) When $1 < \nu_1 < 2$, the acceleration and stress are relatively large. Increasing ξ_1 will decrease them, but the effect is less evident than that when the system resonance occurs under vibration excitation.
- (5) After contrasting the results in this paper with [4], we can find that the maximum acceleration and stress here are larger than that of the linear system. This is because the nonlinear cushioning material with force-deflection relation

$$F_B(u_1) = \frac{2k \cdot h}{\pi} \operatorname{tg} \frac{\pi}{2} \cdot \frac{u_1}{h}$$

is equivalent to a hard spring.

- (6) From Fig. 6 we know the best range of δ is $\delta > 5.0$. The decrease of δ will make the acceleration large. When δ is very large, the system is approximately equivalent to the linear system, so the responses also approach the results of a linear system.

REFERENCES

1. R.D. MINDLIN 1945 Bell System Tech. J.24., Dynamics of Package Cushioning.
2. XI DECHANG, CHEN QINGHUA, ZHENG ZHIYIN, PEN NANLING 1986 5th IAPPI

International Conference on Package, England. 10. Vibration isolation and cushioning of packaged articles connected by an elastic element.

3. XI DECHANG and PEN NANLING 1987 Hang Zhou, China (in Chinese). 1. The isolation of packaged articles connected with an element of simply supported beam.
4. XI DECHANG and PEN NANLING 1987 Hang Zhou, China (in Chinese). 1. The cushioning of packaged articles connected with an element of simply supported beam.
5. XI DECHANG AND CHEN QINGHUA 1987 Hang Zhou, China (in Chinese). 1. The responses of packaged articles connected with an elastic element subjected to random excitation.
6. C.H. HARRIS and C.E. CREDE 1976 Shock and Vibration Handbook. McGraw-Hill, Inc., New York.

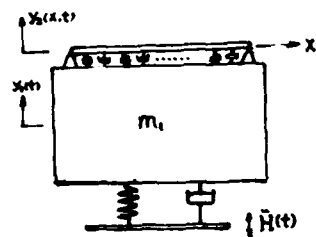


Fig.1

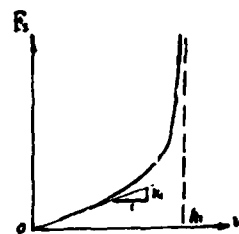
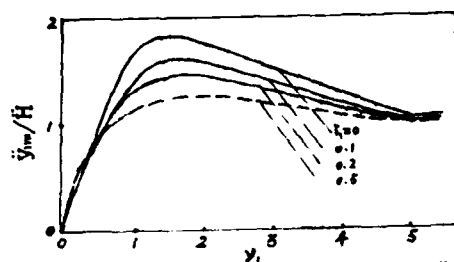
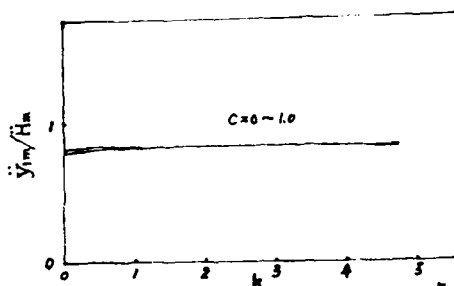
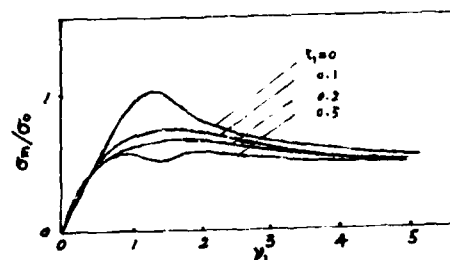


Fig.2



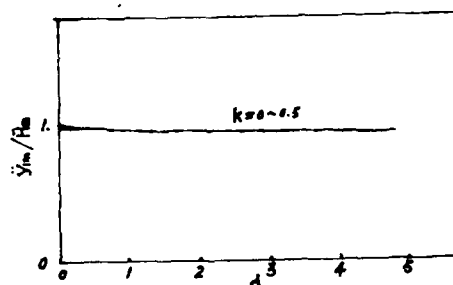
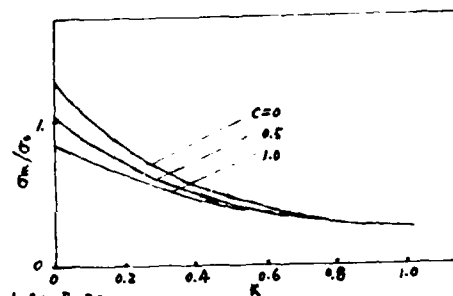
$\mu=0.1 \quad k=0.5 \quad c=0 \quad d=2.0 \quad \delta=5.0$

Fig.3



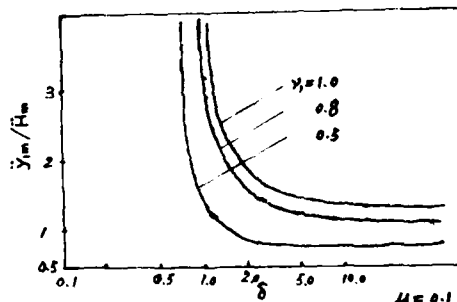
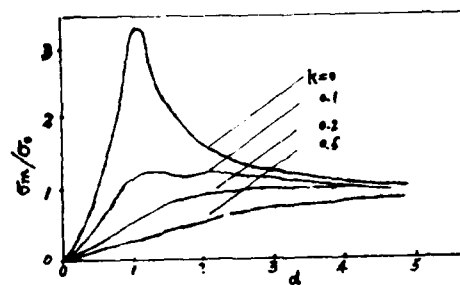
$\mu=0.1 \quad z_1=0.1 \quad y_1=0.5 \quad d=2.0 \quad \delta=5.0$

Fig.4



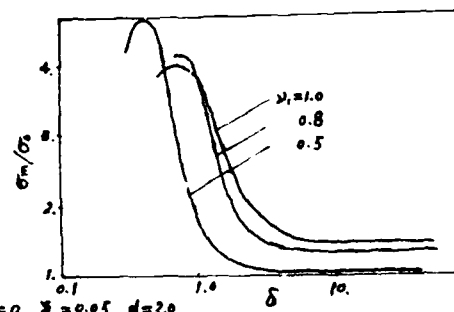
$\mu=0.1 \quad c=z_1=0 \quad y_1=0.5 \quad \delta=5.0$

Fig.5



$\mu=0.1 \quad k=0.1 \quad c=0 \quad z_1=0.05 \quad d=2.0$

Fig.6



DYNAMIC IMPACT OF BEAMS -- A CORRELATION OF EXPERIMENTAL AND THEORETICAL RESULTS

Dr. William P. Schonberg

Department of Mechanical Engineering
University of Alabama - Huntsville
Huntsville, Alabama 35899

1. INTRODUCTION

The transverse impact of beams has long been a problem of theoretical and practical interest in applied mechanics research. Recent theoretical static and dynamic indentation studies by Keer, et.al. (see refs. [1]-[5]) and Schonberg, et. al. [6] have shown that local contact stresses will differ significantly from Hertzian distributions when the region of contact is relatively large. The validity of the theory developed in these studies was demonstrated through comparisons of special case results with the predictions of appropriate elementary beam theories. However, no correlation between experimental results and theoretical predictions was in these investigations. Furthermore, the geometric parameters and material properties considered constituted only a preliminary investigation. As such, the purpose of this paper is two-fold. First, to show, by comparing experimental results with theoretical predictions, that the analytical theory developed by Keer and Lee [3] and Schonberg, et.al. [6] correctly models the low velocity impact response of finite beams. Second, to use that analytical theory in an in-depth investigation of low velocity impact response.

In the first part of the paper, the theoretical solution of the beam impact problem is reviewed. In the second part, data from several experimental impact studies are used to test the validity of the analytical model. Theoretical values of peak central displacement and impact duration are obtained and compared to available experimental values. In the third part of the paper, the theoretical model is used to generate new data for a wide variety of material properties and geometric and impact parameters. Results are obtained for two isotropic materials (steel and aluminum) and for two transversely isotropic materials of different levels of anisotropy (magnesium, which is nearly isotropic; cadmium, which is highly anisotropic). Data concerning newly observed rebound phenomena are presented and discussed.

2. SECTION I -- THEORETICAL SOLUTION METHOD

Consider a beam of finite length $2L$ and thickness h that is struck at its center by a rigid projectile. The beam is supported at its ends by two rotational stiffness springs with equal spring constants K (Figure II.1). The projectile is assumed to impact the beam at a velocity low enough so that penetration or perforation of the beam does not occur. Under this assumption, local deformations are coupled to the global deformations of the beam and are assumed to occur elastically and quasi-statically as in Sun and Huang [7].

The dynamic response of the beam is obtained as the superposition of a static finite layer solution with a dynamic beam theory solution. The static layer solution itself is the superposition of two solutions. The first is an infinite layer solution in which stress and deformation fields are determined by the solution of an appropriate mixed boundary value problem in two-dimensional elastostatics. The second is a static beam theory solution

that accounts for the support conditions at the ends of the beam. Stress and displacement fields are obtained by superimposing associated layer and beam theory expressions:

$$\sigma_{ij}(x, z) = \int_0^c p(x') T_{ij}(x, z; x') dx' + \sigma_{ij}^{SB}(x) \quad (1)$$

$$u_i(x, z) = \int_0^c p(x') U_i(x, z; x') dx' + u_i^{SB}(x) \quad (2)$$

where $p(x)$ is the contact pressure distribution and T_{ij} , U_i are functions of layer geometry and elastic moduli. The superscript $ijSB$ refers to the static beam solution terms. Such a representation gives the layer stresses and strains as functions of an instantaneous contact stress distribution. This result is then placed into the context of a dynamic theory through the superposition of appropriate expressions derived from a standard dynamic beam theory solution. The overall solution thereby gives an accurate description of the local impact stresses as well as the beam bending stresses at points distant from the impact site. Application of boundary conditions at the impact site leads to a Volterra integral equation:

$$\int_0^{c(t)} p(x', t) K(x, x') dx' + \int_0^t \int_0^{c(\tau)} p(x', \tau) M(x, x', \tau) dx' d\tau = Vt - x^2/2R \quad (3)$$

where $K(x, x')$ and $M(x, x', t)$ are functions of geometric, material and impact parameters, V is the initial impact velocity, and R is the radius of curvature of the impactor. The unknown contact pressure distribution and contact length as functions of time are determined at successive time-steps using a technique that combines a standard numerical scheme for Volterra integral equations with an iterative technique developed by Ahmadi, Keer, and Mura [8] for the solution of non-Hertzian contact problems. The reader is referred to the works of Schonberg, et. al. [6] and Keer and Lee [3] for the details of this method as applied to transversely isotropic and isotropic materials, respectively.

3. EXPERIMENTAL VALIDATION

There have been numerous experimental investigations of dynamic impact phenomena. Of those that study central transverse impact of finite beams, the majority usually employed impactors and beams made from similar materials (typically steel, as in ref. [9]). Since the theoretical model assumes a rigid impactor, the experimental studies that were chosen for comparative purposes were those in which a ball or hammer was used to impact a beam of considerably softer material.

Results from twenty experiments were used to check the validity of the analytical model. The experiments are contained in three early photoelastic investigations of low velocity beam impact; the parameters of each experiment are given in Table I.1. It should be noted that the values in Table I.1 are based on information provided in the investigators' reports. In certain instances, the information was incomplete and assumptions had to be made regarding geometry or support conditions. Therefore, analytical predictions need not be exactly equal to experimental results. If the difference between analysis and experiment is on the order of 20 to 25%, then the analytical theory can be considered to adequately model beam impact response.

Additional comments regarding other possible explanations of the differences between analytical results and experimental predictions may be found in the SUMMARY AND CONCLUSIONS.

In the first study, three simply supported castolite beams with different thicknesses were subjected to impacts by a steel hammer [10]. A comparison of experimental impact durations and corresponding analytical predictions are presented in Table I.2 for each beam and for three different impact velocities. The average differences between the experimental results and the theoretical predictions are 10.2%, 26.1%, and 30.5% in Test Sets I, II, and III. The overall average difference for all nine experiments is approximately 22%.

In the second study, two simply supported araldite epoxy-resin beams of different lengths were subjected to central transverse impact [11]. A comparison of experimental maximum central deflections and times at which they occur are presented in Table I.3. The theoretical maximum displacements, Δ_{max} , differ from experimental values by approximately -6% in Test No. 1 and by less than +3% in Test No. 2. The times at which they are predicted to occur, $t_{\Delta,max}$, are virtually identical with the observed times.

In the third study, three simply supported phenolite beams of different lengths were impacted by a steel ball [12]. Comparisons of maximum central displacements and impact durations are presented in Tables I.4 and 5, respectively. In this study, the analytical model was found to underestimate beam displacement by an average of approximately 33% and overestimate impact duration by approximately 22%.

4. ANALYTICAL INVESTIGATION

4.1 Impact Parameters

The elastic and physical properties of the materials employed in this study are given in Tables II.1a and b. For each material, solutions were obtained for simply supported and clamped beams 1 cm thick, 10 and 100 cm long, and for impact velocities of 1 and 10 m/sec. The impactor radius of curvature was varied from .1 cm to 100 cm, and the ratio of beam mass to impactor mass (M) was varied from 0.1 to 10.0. The results are presented in the form of data comparison tables and stress history plots. Tables II.2,3 and Figure II.4 compare the results of impact on steel and aluminum beams; Tables II.4,5 and Figures II.2,3 show results for the magnesium and cadmium beams. Figures II.2,3 show typical impact stress histories. In Tables II.2,3 analytical values of maximum central displacement and impact duration are compared with those obtained from an elementary beam theory analysis [13].

4.2 Results and Observations

4.2.1 Effect of Impactor Curvature

For a given impact velocity and beam configuration, impactor curvature was found to have little effect on the global impact response of the beam. It did, however, have a pronounced effect on local phenomena such as the contact pressure distribution and the size of the contact region. This agrees with the results obtained by Sur and Chen [14] in an impact study using composite laminates. Peak contact stresses were found to rise significantly as R decreased and sometimes even rose above the yield stress. As R increased, peak stresses decreased and overall stress distributions became

severely non-Hertzian. In these cases, peak contact stresses were found to occur near the edges of the contact regions and not at the center of impact.

4.2.2 Effect of Impact Velocity

Contact forces and beam displacements corresponding to different impact velocities were found to be similar except for their respective amplitudes. The differences in the amplitudes were proportional to the relative values of the impact velocities (see Table II.2). This is also in agreement with Sun and Chen [14]. In some cases, high impact velocities produced central deflections that exceeded small deflection theory limits. These cases are indicated by an entry of '***' in the Tables. Revisions in the present theory to accommodate these cases are currently under investigation.

It should be noted that the duration of impact was found to be relatively independent of the impact velocity (Table II.3). This has been observed to be true for very low impact velocities [10,12]. However, for higher impact velocities, this should no longer be the case. The author believes that inclusion of inertial effects in the construction of the static elasticity solution would alter the durations of impact for the higher velocity impacts.

4.2.3 Effect of Mass Ratio

It was observed that massive impactors produced more severe responses than did lighter ones and usually produced force and displacement histories with many peaks. These fluctuations are probably due to the increased participation of the higher modes of vibration of the beam [14]. Heavier beams simply deflected, rebounded, and ejected lighter projectiles. When the beam and impactor were nearly equal in mass, force and displacement histories had only two peaks and occasionally resulted in a multiple impact phenomenon (see Figure II.2 and compare with Figure II.3). In these cases, the beam reached its maximum deflection before the impactor had reversed its trajectory. As the beam deflected upward, a new force maximum was achieved. However, there was no separation in those cases where a projectile was impacting a clamped beam. Clamped beams are not as flexible as simply supported ones and therefore less likely to give rise to double or multiple impact phenomena.

In most of the cases studied, the rebound velocity of the impactor was approximately equal to its initial impact velocity. However, as the ratio of beam mass to impactor mass increased there were significant reductions in the rebound velocity. In these cases, the impactor was released before the beam had returned to its horizontal position. As such, the impactor had not yet recovered all of the energy it had imparted to the beam upon impact. The high inertial resistance of the heavy beam caused a force maximum to be achieved and released before the beam had reversed its trajectory. In Figure II.4 the ratio of the beam displacement at which the impactor was released to the maximum beam displacement ($\Delta_{rel}/\Delta_{max}$) is seen to vary dramatically as the mass ratio increases. It is interesting to note that these curves are independent of impactor radius and velocity and depend only on the material and physical properties of the beam and impactor.

4.2.4 Effect of Material Anisotropy

In previous static indentation studies [1,5], it was shown that the higher bending stiffness and lower transverse stiffness of beams made of highly anisotropic materials produce smaller transverse deflections, smaller contact forces, and larger contact lengths. As can be seen from Tables

II.4,5, this was not necessarily true in the case of dynamic indentation. Examination of elementary beam theory equations [13] reveals that the maximum transverse displacement is indeed inversely proportional to the bending stiffness, but that it is also directly proportional to the mass of the beam. Thus while the higher bending stiffness of cadmium beams should reduce deflections and impact times by approximately 25% as compared to magnesium beams, the high mass density of the cadmium beams will increase deflections nearly 125% resulting in a net increase of almost 70% over magnesium beams. Similar arguments can be used to explain the differences in the durations of impact as well as the peak contact stresses and forces.

The relative sizes of the contact lengths in the cadmium and magnesium beam impacts, however, did agree with those predicted by the static indentation studies holds for the duration of impact. Cadmium beams are less stiff in the transverse direction than magnesium beams (note the relative values of c_{33} in Table II.1b). As such, impacting projectiles penetrated more deeply into cadmium beams than into magnesium beams which resulted in larger contact lengths for the cadmium beams [6].

5. SUMMARY AND CONCLUSIONS

Data from several experimental impact studies were used to test the validity of an analytical model of beam impact response. Theoretical values of central beam displacement and impact duration were obtained and compared to available experimental values. The average differences between predicted and observed values for impact duration and maximum beam displacement are approximately +20% and -27%, respectively. These differences may be attributed to several factors. First, it was assumed that the experimental investigators carefully modelled the beam end conditions. Any deviation from true simply supported ends would affect beam response. Second, all photoelastic materials exhibit a certain amount of time effects (ie. optical or mechanical creep) in response to static and dynamic loadings. The analytical model assumes a perfectly elastic material whose properties do not depend on stress level or strain rate. Third, the analytical model does not include the effects of shear deformation. Inclusion of shear effects would serve to increase the predicted beam displacements. In reviewing the experimental data and the predictions of the analytical model and in light of these observations, it is concluded that the analytical model satisfactorily predicts the low velocity impact response of finite beams.

Using the analytical model, an in-depth study of low velocity projectile impact on isotropic and transversely isotropic beams was performed. For a given impact velocity and beam configuration, impactor curvature was found to have little effect on the global response of the beam, but did have a pronounced effect on local phenomena. The effects of different impact velocities was evident in the relative amplitudes of peak contact forces and impact durations. The differences in the amplitudes were found to be directly proportional to the relative values of the impact velocities. The ratio of the beam mass to impactor mass was found to be an important parameter in determining beam impact response. For some values of this ratio, multiple impact phenomena were observed to occur. Mass ratio effects were also found to be strongly coupled with the effects of material anisotropy in determining relative beam deflections and contact pressure distributions.

6. REFERENCES

1. L.M. KEER and R. BALLARINI 1983 AIAA Journal, 21, 1035 - 1042. Smooth

Indentation of an Initially Stressed Orthotropic Beam.

2. L.M. KEER and G.R. MILLER 1983 Journal of the Engineering Mechanics Division, Transactions of the American Society of Civil Engineers, 109, 706 - 717. Indentation of a Finite Layer.
3. L.M. KEER and J.C. LEE 1985 International Journal of Engineering Science, 23, 987 - 997. Dynamic Impact of an Elastically Supported Beam -- Large Area Contact.
4. L.M. KEER and W.P. SCHONBERG 1986 International Journal of Solids and Structures, 22, 87 - 106. Smooth Indentation of an Isotropic Cantilever Beam.
5. L.M. KEER and W.P. SCHONBERG 1986 International Journal of Solids and Structures, 22, 1033 - 1053. Smooth Indentation of a Transversely Isotropic Cantilever Beam.
6. W.P. SCHONBERG, L.M. KEER and T.K. WOO 1987 International Journal of Solids and Structures, 23, 871 - 896. Low Velocity Impact of Transversely Isotropic Beams and Plates.
7. C.T. SUN and S.N. HUANG 1975 Computers and Structures, 5, 297 - 303. Transverse Impact Problems by Higher Order Beam Finite Elements.
8. N. AHMADI, L.M. KEER and T. MURA 1983 International Journal of Solids and Structures, 19, 357 - 373. Non-Hertzian Contact Stress Analysis for an Elastic Half-Space -- Normal and Sliding Contact.
9. H. SCHWEIGER 1970 Experimental Mechanics, 10, 166 - 169. Central Deflection of a Transversely Struck Beam.
10. A.A. BESTER and M.M. FROCHT 1957 Journal of Applied Mechanics, Transactions of the American Society of Mechanical Engineers, 24, 509 - 514. A Photoelastic Study of Maximum Tensile Stresses in Simply Supported Short Beams Under Central Transverse Impact.
11. A.J. DURELLI and W.F. RILEY 1957 Journal of Applied Mechanics, Transactions of the American Society of Mechanical Engineers, 24, 69 - 76. Experiments for the Determination of Transient Stress and Strain Distributions in Two-Dimensional Problems.
12. Z. TUZI and M. NISIDA 1936 Philosophical Magazine, 21, 448 - 473. Photo-elastic Study of Stresses Due to Impact.
13. W. GOLDSMITH 1960 Impact: The Theory and Physical Behavior of Colliding Solids. London: Edward Arnold.
14. C.T. SUN and J.K. CHEN 1985 Journal of Composite Materials, 19, 490 - 503. On the Impact of Initially Stressed Composite Laminates.

	Study No. 1			Study No. 2		Study No. 3		
	Test Set 1	Test Set 2	Test Set 3	Test No. 1	Test No. 2	Test Set 1	Test Set 2	Test Set 3
Material	Castolite	Castolite	Castolite	Araldite	Araldite	Phenolite	Phenolite	Phenolite
E (N/m ²)	4.826x10 ⁹	4.826x10 ⁹	4.826x10 ⁹	7.58x10 ⁶	8.96x10 ⁶	5.704x10 ⁹	5.704x10 ⁹	5.704x10 ⁹
ν	0.355	0.355	0.355	0.45	0.45	0.40	0.40	0.40
ρ (kg/m ³)	1212	1212	1212	1154	1154	1777	1777	1777
L (cm)	6.35	6.35	6.35	7.62	10.48	16.0	12.0	10.0
h (cm)	2.90	1.93	2.26	2.54	2.54	2.30	2.30	2.30
M	0.0052	0.0035	0.0045	0.50	1.00	0.0246	0.0184	0.0156

Table I.1 -- Experimental Parameters

Velocity (m/sec)	Impact Duration (msec)					
	Test Set 1		Test Set 2		Test Set 3	
	Experimental	Analytical	Experimental	Analytical	Experimental	Analytical
0.244	7.64	8.50	11.11	14.00	8.42	11.00
0.366	7.60	8.50	11.18	14.00	8.49	11.00
0.488	7.44	8.00	10.89	14.00	8.37	11.00

Table I.2 -- Comparison of Experimental Results and Theoretical Predictions for Study No. 1

	Δ_{max} (cm)		$t_{\Delta, max}$ (secs)	
	Experimental	Analytical	Experimental	Analytical
Test No. 1	0.86	0.81	0.13	0.13
Test No. 2	1.12	1.14	0.20	0.21

Table I.3 -- Comparison of Experimental Results and Theoretical Predictions for Study No. 2

Velocity (m/sec)	Maximum Central Displacement (cm)					
	Test Set 1		Test Set 2		Test Set 3	
	Experimental	Analytical	Experimental	Analytical	Experimental	Analytical
0.99	0.20	0.13	0.13	0.09	0.10	0.06
0.83	0.17	0.11	0.11	0.07	0.08	0.05
0.66	0.13	0.09	0.08	0.06	0.06	0.04

Table I.4 -- Comparison of Experimental Results and Theoretical Predictions of Maximum Beam Displacement for Study No. 3

Velocity (m/sec)	Impact Duration (msec)					
	Test Set 1		Test Set 2		Test Set 3	
	Experimental	Analytical	Experimental	Analytical	Experimental	Analytical
0.99	6.31	8.00	4.36	5.40	3.54	4.10
0.83	6.12	8.00	4.40	5.40	3.63	4.10
0.66	6.26	8.00	4.42	5.40	3.59	4.20

Table I.5 -- Comparison of Experimental Results and Theoretical Predictions of Impact Duration for Study No. 3

	STEEL			MAGNESIUM	CADMIUM
	E	ALUMINUM		c_{11}	c_{12}
E	206.8	71.0	c_{11}	58.57	109.2
ν	0.29	0.35	c_{12}	25.01	39.76
ρ	7841.0	2750.0	c_{33}	20.75	37.54
			c_{33}	61.10	46.02
			c_{44}	16.58	15.62
			ρ	1740.0	8650.0

Table II.1a -- Material Properties: Steel and Aluminum (E in GPa; ρ in kg/m³)

Table II.1b -- Material Properties: Magnesium and Cadmium (c_{ij} in GPa; ρ in kg/m³)

	M	STEEL		ALUMINUM	
		Elasticity	Beam Theory	Elasticity	Beam Theory
V=1 m/sec	0.1	5.40	3.96	5.40	4.02
	1.0	1.70	1.49	1.70	1.51
	10.0	0.35	0.94	0.35	0.94
V=10 m/sec	0.1	5.40	3.96	5.40	4.02
	1.0	1.70	1.49	1.70	1.51
	10.0	0.35	0.94	0.35	0.94

	M	STEEL		ALUMINUM	
		Elasticity	Beam Theory	Elasticity	Beam Theory
V=1 m/sec	0.1	0.919	1.194	0.927	1.220
	1.0	0.368	0.304	0.373	0.325
	10.0	0.089	0.050	0.089	0.051
V=10 m/sec	0.1	9.20	12.01	9.28	12.20
	1.0	3.69	3.18	3.73	3.25
	10.0	0.88	0.50	0.89	0.51

Table II.2 -- Maximum Beam Displacement, Simply Supported Beams (mm; L=10.0 cm)

Table II.3 -- Duration of Impact, Simply Supported Beams (msec; L=10.0 cm)

	L/h=10.0			L/h=100.0		
	V	Simply Supported	Clamped	Simply Supported	Clamped	
Peak Force (N)	1 m/sec	151.9	323.6	15.3	32.6	
	10 m/sec	1520.6	3239.1	152.6	326.8	
Peak Stress ($\times 10^7$ N/m ²)	1 m/sec	2.920	4.289	0.591	1.267	
	10 m/sec	8.35	12.735	2.758	4.011	
Max. Displ. (mm)	1 m/sec	0.371	0.178	37.211	17.856	
	10 m/sec	3.718	1.781	***	***	
Impact Duration (msec)	1 m/sec	1.70	0.80	170.00	80.00	
	10 m/sec	1.70	0.80	170.00	80.00	

Table II.4 -- Comparison of Simply Supported and Clamped Results for Magnesium Beams
(R=10.0 cm; h=1.0)

	V	L/h=10.0		L/h=100.0	
		Simply Supported	Clamped	Simply Supported	Clamped
Peak Force (N)	1 m/sec	439.9	935.4	44.2	96.2
	10 m/sec	4400.3	9367.5	442.2	961.5
Peak Stress ($\times 10^7$ N/m ²)	1 m/sec	4.318	6.316	1.342	2.014
	10 m/sec	12.364	17.679	3.908	5.599
Max. Displ. (mm)	1 m/sec	0.625	0.302	62.527	30.417
	10 m/sec	6.253	3.030	***	***
Impact Duration (msec)	1 m/sec	3.00	1.40	300.00	140.00
	10 m/sec	3.00	1.40	300.00	140.00

Table II.5 -- Comparison of Simply Supported and Clamped Results for Cadmium Beams
(R=10.0 cm; h=1.0)

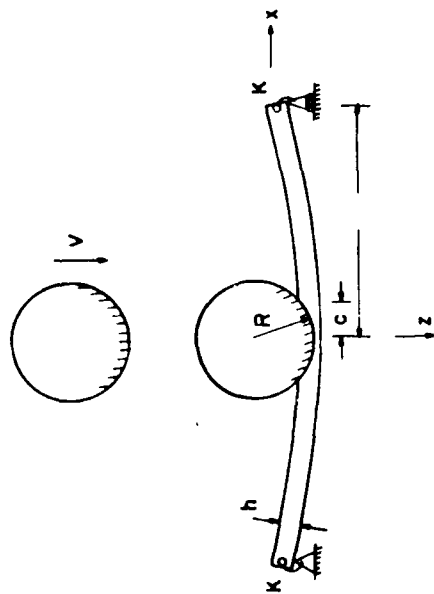


Figure 11.1 -- Problem Configuration - Beam Impact

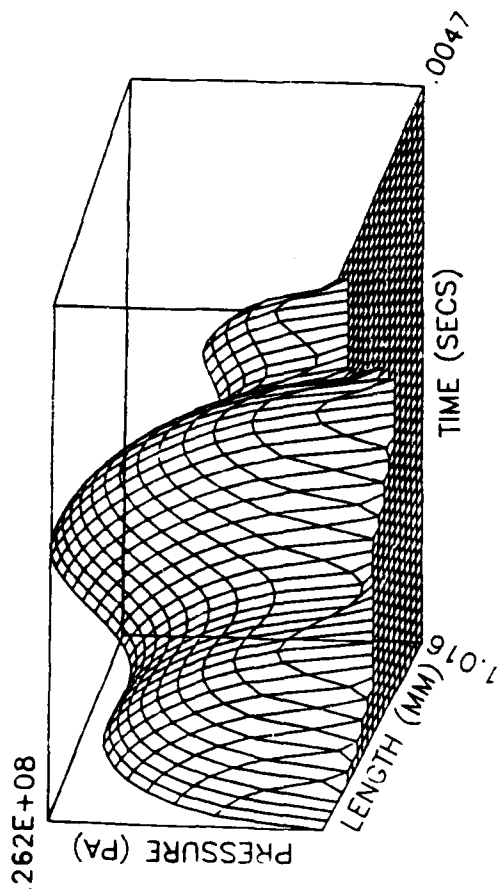


Figure 11.2 -- Contact Pressure Distribution, Simply Supported Cadmium Beam, $V=1$ m/sec, $M=0.5$

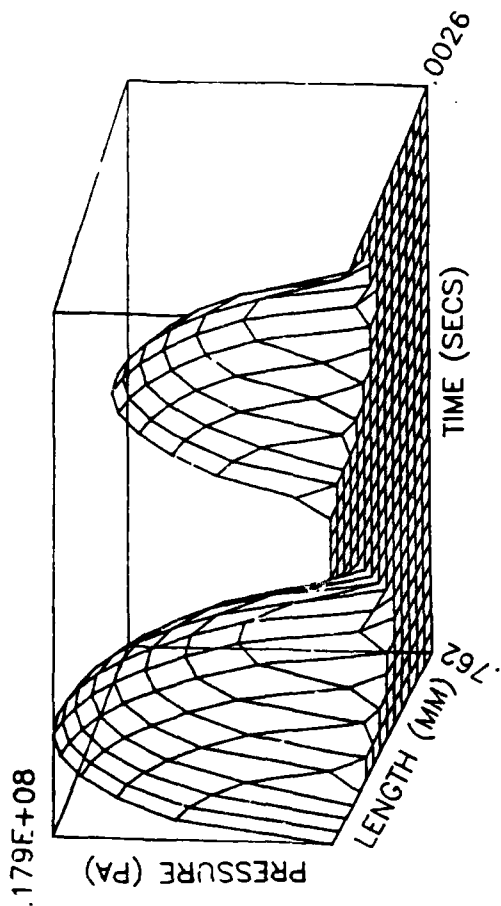


Figure 11.3 -- Contact Pressure Distribution, Simply Supported Cadmium Beam, $V=1$ m/sec, $M=2.5$

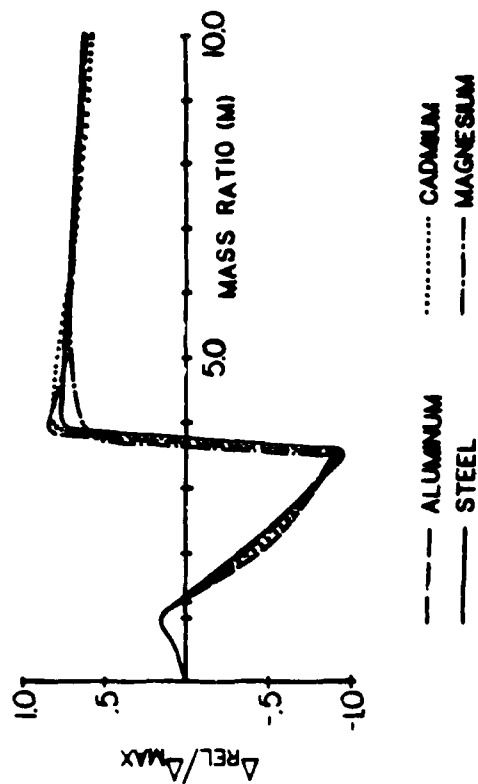


Figure 11.4 -- Beam Displacement at Final Separation

SHOCK TESTING WITH ELECTRODYNAMIC EXCITERS USING OSCILLATORY TRANSIENT EXCITATION

D.H. Trepess and R.G. White

Institute of Sound and Vibration Research
University of Southampton

1. INTRODUCTION

Shipboard equipment in service may undergo shock excitation which could cause damage and result in malfunction. It is necessary, therefore, to representatively shock load equipment prior to it being installed to indicate whether or not the equipment may malfunction in service. In service, shipboard equipment will usually be inertially loaded due to the transient motion of its supports.

If the motion of the supporting structure of the equipment to be shock tested is known, then this could possibly be reproduced by a shock test machine. The motion will be a forced vibration response followed by free vibration, which will generally consist of the summation of vibration modes of the supporting structure, this being composed of a number of decaying sinewaves. This transient motion of the supporting structure could be reproduced in a laboratory shock test, but it would be unique to that piece of equipment, the supporting structure, the position of the equipment and position of adjacent equipment. A variation in any of the above would result in different support motions. However, it is usual that vibrational motion of the supporting structure is unknown.

A general approach to shock testing is therefore needed. Simple test waveforms such as half sine, triangular and rectangular pulses are often specified. These types of transient excitations, however, are not ideal for specification testing or environmental simulation. Simple, single pulses of the above type exhibit regions of zero or very low spectral content. Also, being non-oscillatory in nature, resonant response "build-up" is not achieved in the test item, as would be the case if excited by an oscillatory motion induced by supporting structure resonances, as discussed above. If a single decaying sinusoid is used as a test waveform, the excitation is essentially narrowband, depending on the decay rate, and resonances of the test item may not be stimulated. A transient waveform which is oscillatory in nature and which has attractive spectral characteristics is the rapid frequency sweep [1]. The Fourier transform modulus does not have zeros and the spectrum shape can be readily controlled via the characteristics of the time signal. In simple form, the linear, constant amplitude, rapid frequency sweep has a Fourier transform modulus which is essentially rectangular in shape.

This paper describes how a rapid, linear, acceleration frequency sweep can be amplitude weighted, so when used to excite in phase, the supports of a structure, the structure experiences equal damage potential in a set of its modes of vibration.

A method is described in which, by use of computer control, the frequency response characteristics of the signal generating system (exciter, power amplifier) can be compensated for so that the motion of the exciter table upon which the test item is mounted can be specified.

2. WEIGHTED RAPID FREQUENCY SWEEP TO PRODUCE CONSTANT PEAK MODAL STRESS

The first approach examined was to obtain a shaped or weighted rapid frequency sweep which can be used to excite a structure via its supports so that the maximum stress due to inertial loading is the same in a set of modes of vibration. This was performed for two simple structures, the simply supported beam and the clamped-clamped beam.

The analysis of a simply supported beam excited via acceleration of its supports due to rapid frequency sweep has been performed in reference [2]. A similar analysis for a clamped-clamped beam is given here in Appendix 1.

Both analyses show that only the odd modes of vibration are excited by in phase support motion since the generalised force in the even modes of vibration is zero.

Appendix 1 shows that the maximum stress in a clamped-clamped beam occurring at the supports, for light damping, in all odd modes of vibration from equation A1.22 is given by

$$c\sigma_n = \frac{4/3}{(c\lambda_n l)} \frac{ER_n}{c_l} \ddot{u}_0 \sqrt{\frac{\pi}{a}} \quad (1)$$

where,

the prescript c indicates a clamped-clamped beam,
 σ_n - stress in the n^{th} mode of vibration (n always being odd)
 E - Young's modulus
 $c_l = \sqrt{\frac{E}{\rho}}$ - longitudinal wave speed
 \ddot{u}_0 - excitation acceleration amplitude at each support
 $a = \frac{\omega_2 - \omega_1}{2T}$
 ω_1 - initial angular frequency of frequency sweep
 ω_2 - final angular frequency of frequency sweep
 T - sweep duration
 $R_n = \frac{\cosh \lambda_n l - \cos \lambda_n l}{\sinh \lambda_n l - \sin \lambda_n l}$

$$\lambda_n l = \omega_n^{1/2} l \left(\frac{\rho A}{EI} \right)^{1/4} \quad (2)$$

where,

A - cross-sectional area of the beam
 I - second moment of area of cross-section of the beam
 ρ - density
 l - beam length
 ω_n - the n^{th} angular natural frequency of the beam

Reference [2] shows that for a simply supported beam

$$s\sigma_n = Ed \left[\frac{n^2 \pi^2}{l^2} \right] \frac{1}{\omega_n \pi} \ddot{u}_0 \sqrt{\frac{\pi}{a}} \quad (3)$$

where,

the prescript s indicates simply supported beam
 n - mode number

The following arranges (3) into a similar form to (1):-

For a simply supported beam,

$$\left[\frac{n^2 \pi^2}{l^2} \right] = \omega_n \sqrt{\frac{\rho A}{EI}}$$

For a rectangular beam,

$$I = \frac{bd^3}{12}$$

b - beam width

d - beam thickness

$$\therefore \left[\frac{n^2 \pi^2}{l^2} \right] = \omega_n \left[\frac{12}{c_l^2 d^2} \right]^{1/2} \quad (4)$$

$$n = \omega_n^{1/2} \frac{l}{\pi} \left[\frac{\rho A}{EI} \right]^{1/4}$$

And from (2),

$$\omega_n^{1/2} = \lambda_n \left[\frac{EI}{A\rho} \right]^{1/4}$$

$$\therefore n = \frac{s \lambda_n l}{\pi} \quad (5)$$

After substituting (4) and (5) into (3), the following is obtained:-

$$s \sigma_n = \frac{2 \sqrt{3}}{(s \lambda_n l)} \frac{E}{c_l} \ddot{u}_0 \sqrt{\frac{\pi}{a}} \quad (6)$$

Tabulated values of $\lambda_n l$ for both types of beam are given in Table 1 for all the odd modes up to the 19th mode of vibration.

Now, writing (1) and (6) together to show their similarities,

$$c \sigma_n = \frac{4 \sqrt{3}}{(c \lambda_n l)} \frac{E}{c_l} \ddot{u}_0 \sqrt{\frac{\pi}{a}} R_n \quad (1)$$

(clamped-clamped beam)

$$s \sigma_n = \frac{2 \sqrt{3}}{(s \lambda_n l)} \frac{E}{c_l} \ddot{u}_0 \sqrt{\frac{\pi}{a}} \quad (6)$$

(simply supported beam)

Rearranging (1) and (6) to give

$$\frac{E}{c_l} \ddot{u}_0 \sqrt{\frac{\pi}{a}} \cdot c \sigma_n = \frac{4 \sqrt{3}}{c \lambda_n l} R_n \quad (7)$$

$$\frac{E}{c_l} \ddot{u}_0 \sqrt{\frac{\pi}{a}} \cdot s \sigma_n = \frac{2 \sqrt{3}}{s \lambda_n l} \quad (8)$$

The left hand sides of both (7) and (8) are peak values of stress in each type of beam, multiplied by an identical scale factor. The factor consists of material properties, beam dimensions and sweep excitation parameters.

Now,

$$\lambda_{nl} = \omega_{nl}^2 \cdot \left[\frac{\rho A}{EI} \right]^{1/4} \quad (2)$$

For a rectangular cross-section beam (2) becomes

$$(\lambda_{nl})^2 = \omega_{nl}^2 \cdot \frac{12}{\sqrt{c_l^2 d^2}}$$

$$\therefore (\lambda_{nl})^2 = \frac{\omega_{nl}^2 \cdot 2\sqrt{3}}{c_l d} \quad (9)$$

This demonstrates that the right hand sides of equations (7) (for $n > 3$, i.e. as R_n tends to unity) and (8) are inversely proportional to the square root of the natural frequencies of the respective beams; the constants of proportionality depend on beam dimensions and material properties.

Table 1 gives values of the left hand side of equations (7) and (8), R_n , and for the right hand side of (9) for each odd mode of vibration. The graph in Figure 1 shows how the peak stress in each mode varies with natural frequency.

The axes of the graphs are scaled factors of peak stress and natural frequencies, the scale factors, as mentioned above, depend on material properties, beam dimensions and sweep excitation parameters. This type of presentation has been used for generality.

It should be noted that the symbols X and θ represent peak stress due only to the corresponding beam natural frequency. Therefore, the lines joining the data points do not represent peak stress in the beam at frequencies other than the natural frequencies. These lines serve only to demonstrate how the peak modal stress varies as natural frequency changes.

For the clamped-clamped beam, the peak stress for each odd mode above mode 3 decreases with increasing frequency at a rate of 10 dB per decade. For the simply supported beam, the peak stress decreases again at 10 dB per decade for all of the odd modes of vibration.

In order to achieve equal peak stress in each mode of vibration, the transient support motion needs to be controlled. The required support motion given in the frequency domain is the original acceleration spectrum multiplied by the square root of the angular frequency at which the supports are moving.

The instantaneous frequency of the rapid frequency sweep varies linearly with time. Thus, in the time domain, the signal can be similarly weighted as in the frequency domain to obtain constant peak modal stress. In the time domain a rapid frequency sweep with a constant acceleration amplitude is

$$\ddot{u}(t) = \ddot{u}_0 \sin(at^2 + bt) \quad (10)$$

($2at + b$) being the instantaneous frequency.

Thus, by multiplying (10) by $(2at + b)^{1/2}$ gives a rapid frequency sweep support acceleration waveform which produces equal peak stress in each mode of vibration.

The required signal is thus,

$$(2at + b)^2 \ddot{u}_0 \sin(at^2 + bt)$$

The next stage is to substitute values of the beam properties and sweep parameters into equations (7) and (8) and also to substitute the value of ultimate tensile stress (for the beam material) for the peak stress in the same equations. Then, assuming that the beam deforms linearly up to failure, the value of the acceleration amplitude (\ddot{u}_0) can be calculated in order that the beam should break.

3. CONTROLLED TRANSIENT TESTING

3.1 The Need for Controlled Testing

When using an electrodynamic exciter, a signal of the same form as the required exciter table motion is usually generated electronically and input to a power amplifier; this signal is then applied to the exciter coil. However, the motion of the exciter table does not possess the same spectral characteristics as that of the original electronically generated signal.

In shock testing, the levels of excitation on the equipment under test are important. It is therefore desirable to compensate for the exciter and power amplifier frequency response characteristics. In steady state sinusoidal or slow sweep testing, a feedback system is employed for compensation, but in transient testing, i.e. shock testing, a feedback system is impractical due to response time limitations. A method for compensation in transient testing using the rapid frequency sweep is proposed and demonstrated for a constant amplitude rapid frequency sweep and the proposed weighted frequency sweep described in Section 2.

3.2 Control Technique

An open loop technique is used for frequency response compensation. The method employed is first to measure the frequency response of the generating system through the frequency range of interest. Then, by multiplying the required exciter table motion spectrum by the inverse of frequency response function, the required input spectrum is obtained via inverse Fourier transformation and the time domain signal is obtained. The theory is outlined in Appendix 2.

3.3 Control Implementation

The experimental arrangement for the proposed controlled transient testing technique is shown in Figure 2.

The personal computer is fitted with signal generating (digital to analogue converter) and data acquisition (analogue to digital converter) boards. A signal is created within the computer and generated via the D/A converter at a selected sampling rate. The analogue signal is then applied to the power amplifier and, ultimately, the exciter coil via the low pass smoothing filter. The filter is set to a maximum "cut-off" frequency of half the output sampling rate. The resultant acceleration of the exciter table is recorded by the computer via a charge amplifier, anti-aliasing low pass filter and an analogue to digital converter. At this stage, the computer memory contains output and input signals. The analysis technique described in Section 3.2 can then be implemented so that the required input spectrum can be obtained. Before inverse Fourier transformation, the spectrum is windowed in the frequency range of interest, this is to remove any d.c. offset from the A/D converter and any background noise not within

the frequency range of interest. The inverse Fourier transform is then found, yielding the time domain signal which can be applied to the exciter coil as described above, so the table motion is that required.

3.4 Results

The procedure described was implemented using an electrodynamic exciter with a maximum force output of 200 N.

The compensation was performed for a linear, constant amplitude, rapid frequency sweep and for a linear rapid frequency sweep whose amplitude increased at a rate of 10 dB per decade (as described in Section 2), both over the frequency range 100 Hz to 1000 Hz.

Figures 3 and 4 show the generated and required exciter motion modulus spectrum, the resulting exciter table motion modulus spectrum is shown in Figure 5. The windowed, calculated generator spectrum is shown in Figure 6, the window being shown in Figure 7. The resultant table motion spectrum is shown in Figure 8.

Figure 9 shows the linear rapid frequency sweep increasing at 10 dB per decade; Figure 11 shows the resultant compensated signal, Figure 10 is the required generator signal spectrum.

It can be seen that the spectral characteristics of the compensated exciter table motion (Figures 8 and 11) compare favourably with the required table motion spectrum proving a useful technique, when the relative levels of excitations are important, such as in shock testing.

4.0 CONCLUSIONS

Section 2 demonstrates how a rapid frequency sweep can be shaped so that when used to excite a simple structure via its supports, the peak stress produced in the structure is constant for a set of its modes of vibration.

Section 3 shows how the required excitation level at the exciter table can be obtained via compensation of the frequency response characteristics of the testing system.

By combining the above two techniques, a shock test can be specified which produces equal damage potential to a simple structure in a set of its modes.

ACKNOWLEDGEMENT

This work has been carried out with the support of the Procurement Executive, Ministry of Defence.

REFERENCES

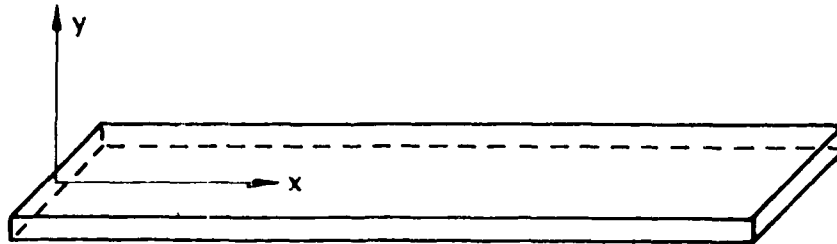
1. R.G. WHITE and R.J. PINNINGTON 1982 Aeronautical Journal. "Practical application of the rapid frequency sweep technique for structural frequency response measurement."
2. R.G. WHITE 1982 Journal of the Society of Environmental Engineers. "Shock testing using a controlled oscillatory waveform."

APPENDIX 1

Calculation of Maximum Stress in a Vibrating Clamped-Clamped Beam

The deflection of a beam vibrating in a mode is given by

$$y_n = q_n(t) \phi_n(x) \quad (A1.1)$$



where,

$\phi_n(x)$ = The n^{th} mode shape

$q_n(t)$ = Generalised displacement, n^{th} mode

From Engineer's bending theory, the stress in a beam due to bending is given by

$$\sigma = \frac{My}{I} \quad (A1.2)$$

where,

M = Bending Moment

y = The perpendicular distance from the neutral axis to the plane of interest

I = Second moment of area of cross-section

For all initially, undeflected beams, the neutral axis is at the same position as the geometric axis. Thus, from equation A1.2, the maximum stress will occur when y is a maximum, i.e. at the surface of the beam.

$$\text{The bending moment is given by } EI \frac{d^2 y}{dx^2} \quad (A1.3)$$

E = Young's Modulus

Combining A2.1, A2.2 and A2.3 to give

$$\sigma_n(x,t) = \frac{Ed}{2} \cdot q_n(t) \frac{d^2 \phi_n(x)}{dx^2} \quad (A1.4)$$

where d is the beam depth.

The response in each mode of vibration is given by the convolution of the generalised force with the corresponding impulse response.

$$\therefore q_n(t) = \int_0^t F_n(\tau) h_n(t - \tau) d\tau \quad (A1.5)$$

F_n = generalised force

$h(t)$ = impulse response

$$h_n(t) = \frac{1}{M_n \omega_{dn}} e^{-\zeta \omega_n t} \sin \omega_{dn} t \quad (A1.6)$$

M_n = generalised mass

ζ = viscous damping ratio

t = time

ω_n = natural frequency

ω_{dn} = damped natural frequency = $\omega_n \sqrt{1 - \zeta^2}$

The generalised mass is given by

$$M_n = \rho A \int_0^l \phi_n^2(x) dx \quad (A1.7)$$

and the generalised force is given by

$$F_n(\tau) = - \rho A \ddot{u} \int_0^l \phi_n(x) dx \quad (A1.8)$$

Now for a clamped-clamped beam,

$$\phi_n(x) = \cosh \lambda_n x - \cos \lambda_n x - R_n (\sinh \lambda_n x - \sin \lambda_n x) \quad (A1.9)$$

where,

$$R_n = \frac{\cosh \lambda_n l - \cos \lambda_n l}{\sinh \lambda_n l - \sin \lambda_n l} \quad (A1.10)$$

and

$$\lambda_n = \left[\frac{\omega_n^2 \rho A}{EI} \right]^{1/4}$$

A = beam cross-sectional area

ρ = density

l = beam length

\ddot{u} = acceleration

Substituting (A1.9) into (A1.7) and evaluating the integral gives the generalised mass for all modes as

$$M_n = \rho A l \quad (A1.11)$$

i.e., the generalised mass = beam mass for all modes,

$$\frac{d^2 \phi_n(x)}{dx^2} = \lambda_n^2 (\cosh \lambda_n x + \cos \lambda_n x - R_n (\sinh \lambda_n x + \sin \lambda_n x)) \quad (A1.12)$$

The maximum value of the second derivative of the mode shape occurs at the end of the beam, i.e. at the supports.

$$\therefore \left[\frac{d^2 \phi_n(x)}{dx^2} \right]_{\max} = 2\lambda_n^2 \quad (A1.13)$$

This value is constant for all modes of vibration.

The generalised force,

$$F_n(t) = - \rho A \ddot{u}(t) \int_0^l \phi_n(x) dx \quad (A1.14)$$

$$\therefore F_n(t) = - \rho A \ddot{u}(t) \left[\frac{4R_n}{\lambda_n} \right] \quad (A1.15)$$

Substituting (A1.6) and (A1.15) into (A1.5) to give,

$$q_n(t) = \int_0^t - \rho A \ddot{u}(\tau) \left[\frac{4R_n}{\lambda_n} \right] \frac{1}{M_n \omega_{dn}} e^{-\zeta \omega_n(t-\tau)} \sin \omega_{dn}(t-\tau) d\tau \quad (A1.16)$$

Assuming that the damping is small and substituting (A1.16) and (A1.13) into (A1.4) gives

$$\begin{aligned} \sigma_n(x, \tau) &= \frac{M_D}{l} \frac{Ed}{M_D \omega_n} \frac{4 R_n \lambda_n}{\lambda_n} \int_0^t \ddot{u}(\tau) \sin[(\omega_n(t-\tau))] d\tau \\ \therefore \sigma_n(x, \tau) &= - \frac{4Ed R_n \lambda_n}{l \omega_n} \int_0^t \ddot{u}(\tau) \sin[\omega_n(t-\tau)] d\tau \end{aligned} \quad (A1.17)$$

For a rapid frequency sweep,

$$\ddot{u}(\tau) = \ddot{u}_0 \sin(a\tau^2 + b\tau)$$

$$a = \frac{\omega_2 - \omega_1}{2T}$$

$$b = \omega_1$$

ω_1 = initial angular frequency

ω_2 = final angular frequency

T = sweep duration

Thus the integral in (A1.17) becomes,

$$\int_0^t \ddot{u}_0 \sin(a\tau^2 + b\tau) \sin \omega_n(t - \tau) d\tau$$

The integral gives,

$$\sqrt{\frac{\pi}{4a}} \ddot{u}_0$$

$$\therefore \sigma_n(x, t) = \frac{-4Ed Rn \lambda n}{i\omega_n} \ddot{u}_0 \sqrt{\frac{\pi}{4a}} \quad (A1.18)$$

Now,

$$\omega_n = \lambda^2 n \left[\frac{EI}{A\rho} \right]^{1/2}$$

for a beam with a rectangular cross-section,

$$\omega_n = \lambda n^2 \left[\frac{E d^2}{\rho 12} \right]^{1/2} = \lambda n^2 \left[\frac{E}{\rho 12} \right]^{1/2} d \quad (A1.19)$$

Substituting into (A2.18),

$$\therefore \sigma_n(x, t) = \frac{-4E Rn}{(\lambda n^2)} \left[\frac{12\rho}{E} \right]^{1/2} \ddot{u}_0 \sqrt{\frac{\pi}{4a}} \quad (A1.20)$$

$$\therefore \sigma_n(x, t) = \frac{-E 4/3 Rn}{(\lambda n^2)} \frac{\ddot{u}_0}{c_l} \sqrt{\frac{\pi}{a}} \quad (A1.21)$$

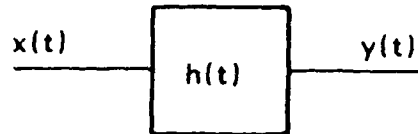
Note The negative sign refers to compression, since it was assumed that the stress varies linearly across the cross-section of the beam then the opposite face will be in tension with the same magnitude of stress.

i.e. (A1.21) becomes,

$$\sigma_n(x, t) = \frac{E 4/3 Rn}{(\lambda n^2)} \frac{\ddot{u}_0}{c_l} \sqrt{\frac{\pi}{a}} \quad (A1.22)$$

APPENDIX 2

Acceleration Generating System Frequency Response Compensation



$x(t)$ - signal generator output

$h(t)$ - acceleration generating system (i.e. power amplifier, shaker) impulse response

$y(t)$ - acceleration signal produced at the table of the exciter

Now,

$$y(\tau) = \int_0^t h(t-\tau) x(\tau) d\tau \quad (A2.1)$$

Fourier transforming,

$$Y(j\omega) = H(j\omega) \cdot X(j\omega)$$

where $Y(j\omega)$, $H(j\omega)$, $X(j\omega)$ are the corresponding Fourier transforms of $y(t)$, $h(t)$ and $x(t)$ respectively.

$H(j\omega)$ is the acceleration generating transfer function.

$$\text{i.e.} \quad H(j\omega) = \frac{Y(j\omega)}{X(j\omega)}$$

If the required output signal is $Z(j\omega)$, then multiplying $Z(j\omega)$ by the inverse transverse function of the acceleration system will give the required exciter spectrum, $W(j\omega)$, to produce $Z(j\omega)$ as the output.

$$\text{i.e.} \quad W(j\omega) = \frac{1}{H(j\omega)} \cdot Z(j\omega) \quad (A2.2)$$

To obtain the required time signal, $W(j\omega)$ is inversed Fourier transformed to give $W(t)$.

Alternatively, $W(t)$ can be calculated in the time domain. This can be achieved by convolving the exciter table motion, time domain signal with the system's impulse response function, as below.

$$W(\tau) = \int_0^t \frac{1}{h(t-\tau)} \cdot Z(\tau) d\tau. \quad (A2.3)$$

TABLE 1

MODE	SIMPLY SUPPORTED			CLAMPED-CLAMPED			
	λ_n	$\omega_n^2 \left(\frac{g}{L} \right)^{1/2}$	$\sigma_n \left(\frac{C_{L-R}}{E_0} \right)^{1/2}$	λ_n	$\omega_n^2 \left(\frac{g}{L} \right)^{1/2}$	R_n	$\sigma_n \left(\frac{C_{L-R}}{E_0} \right)^{1/2}$
1	1	9.8696	1.1026578	4.73004	22.373	0.9825022	1.43909
3	3	80.8264	0.3475326	10.9956	120.903	0.9999465	0.4300475
5	5	246.7401	0.22053134	17.2786	298.5549	0.9999999	0.4009455
7	7	443.6106	0.1575225	15 $\pi/2$	555.168	1.0	0.294042
9	9	799.4379	0.1125175	19 $\pi/2$	890.7317	1.0	0.2321385
11	11	1194.222	0.1002416	23 $\pi/2$	1305.255	1.0	0.1917646
13	13	1647.963	0.08481982	27 $\pi/2$	1798.735	1.0	0.1633567
15	15	2220.841	0.0735106	31 $\pi/2$	2371.178	1.0	0.1422764
17	17	2892.316	0.0646622	35 $\pi/2$	3022.566	1.0	0.124018
19	19	3562.927	0.05803462	39 $\pi/2$	3752.917	1.0	0.11309

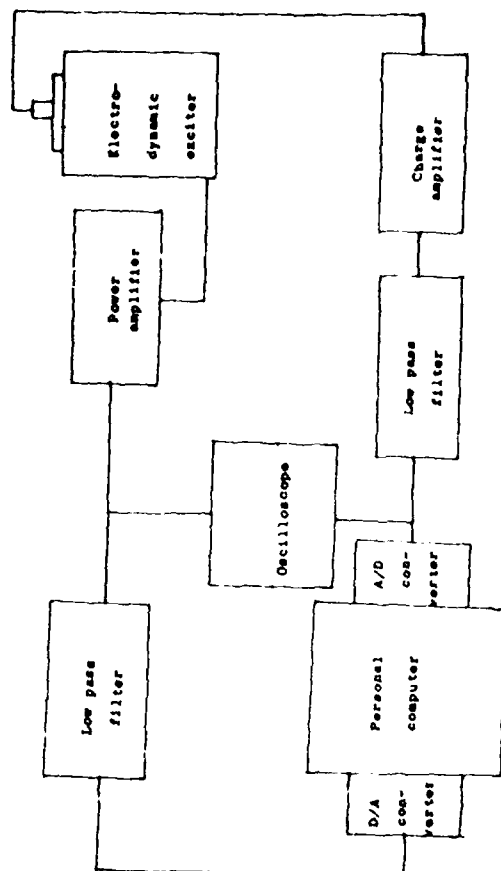


Figure 2: Experimental arrangement for controlled transient testing.

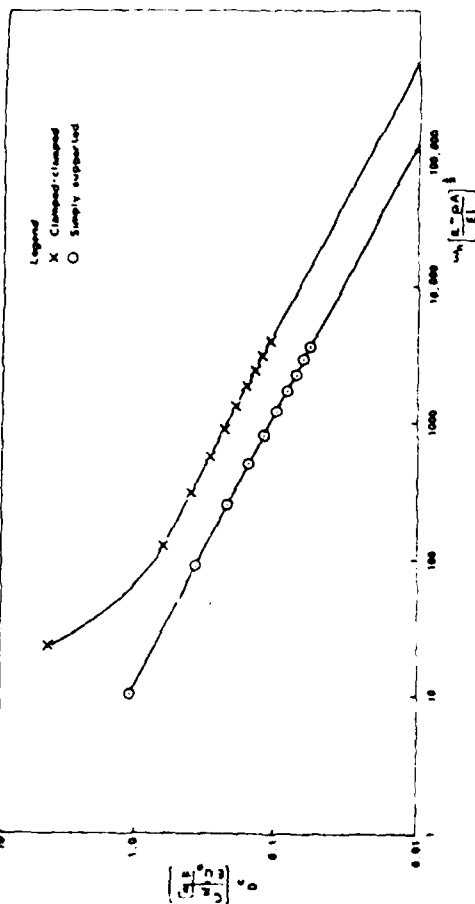


Figure 1: Peak stress in a vibrating beam at each odd natural frequency. Due to in phase acceleration excitation at supports by a linear rapid frequency sweep - constant amplitude.

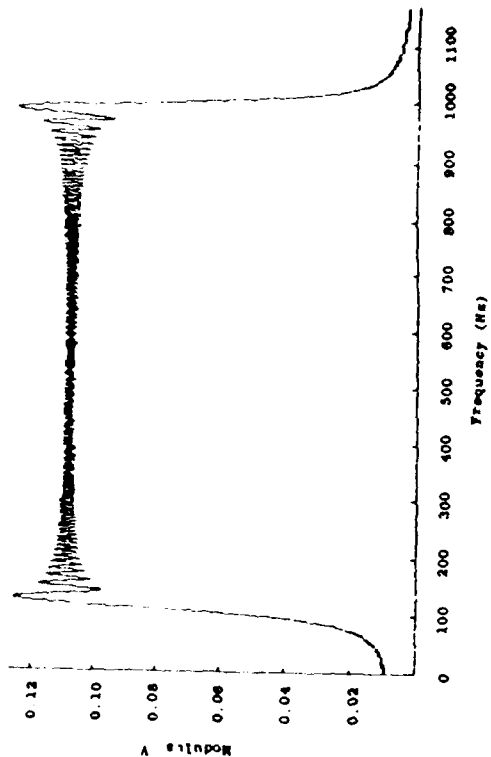


Figure 3: Originally generated modulus spectrum. (Constant amplitude linear rapid frequency sweep.)

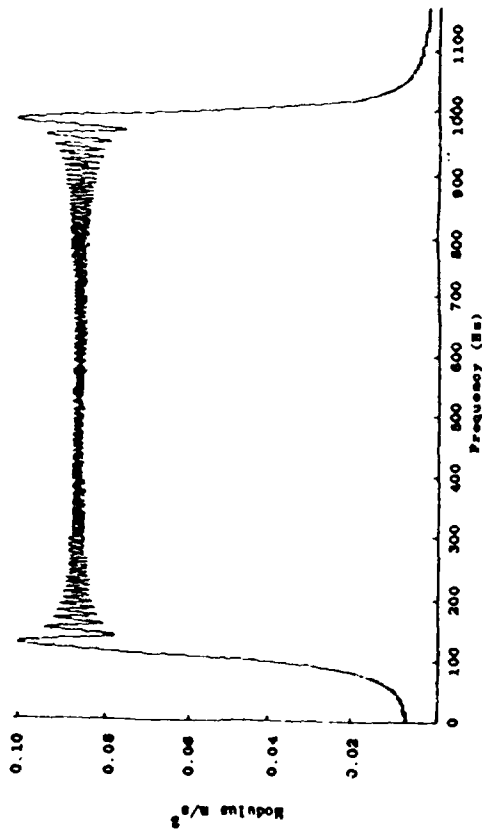


Figure 4: Required exciter table motion modulus spectrum. (Constant amplitude linear rapid frequency sweep.)

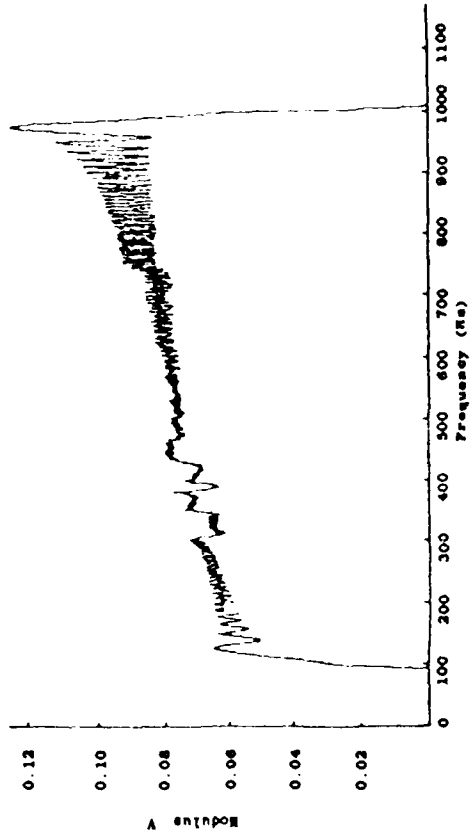


Figure 6: Modulus spectrum of signal to be input to generating system in order to compensate for system frequency response.

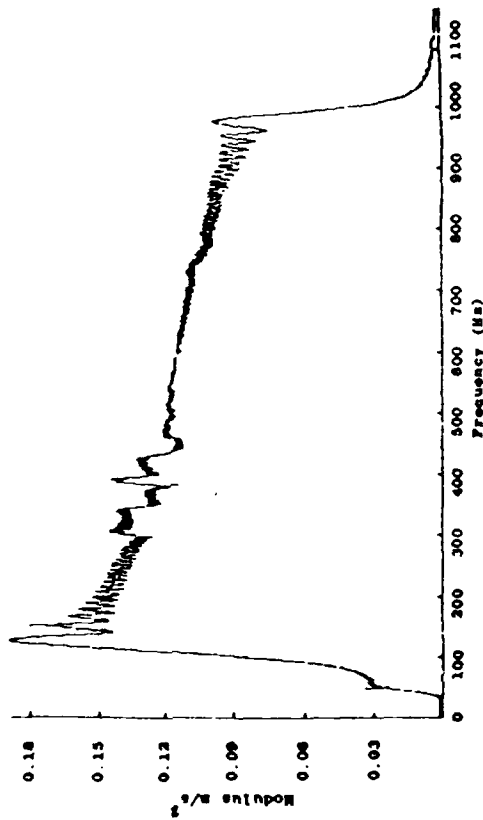


Figure 5: Exciter table motion modulus spectrum.

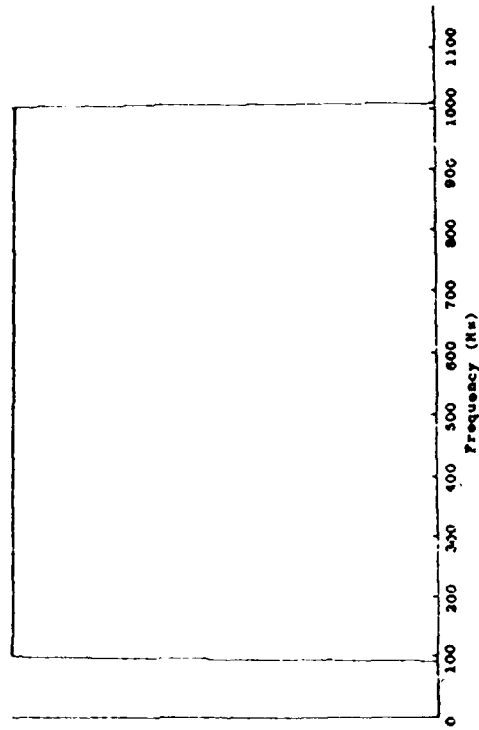


Figure 7: Window modulus spectrum.

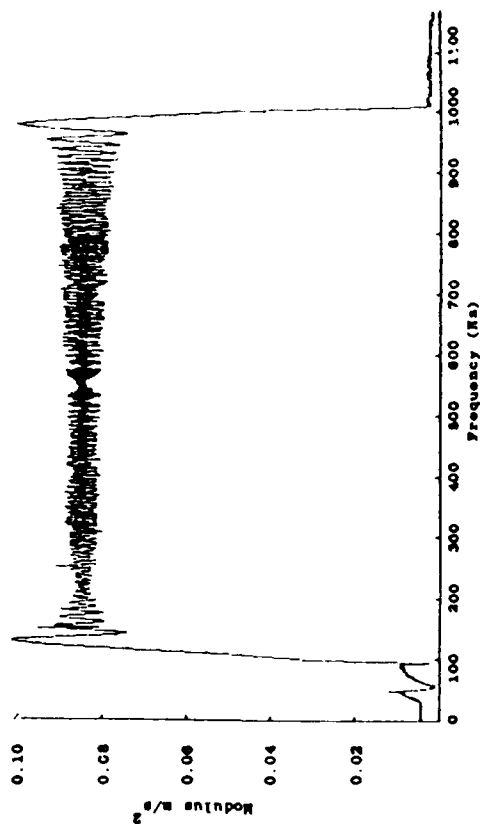


Figure 8: Exciter table motion modulus spectrum obtained after compensation.

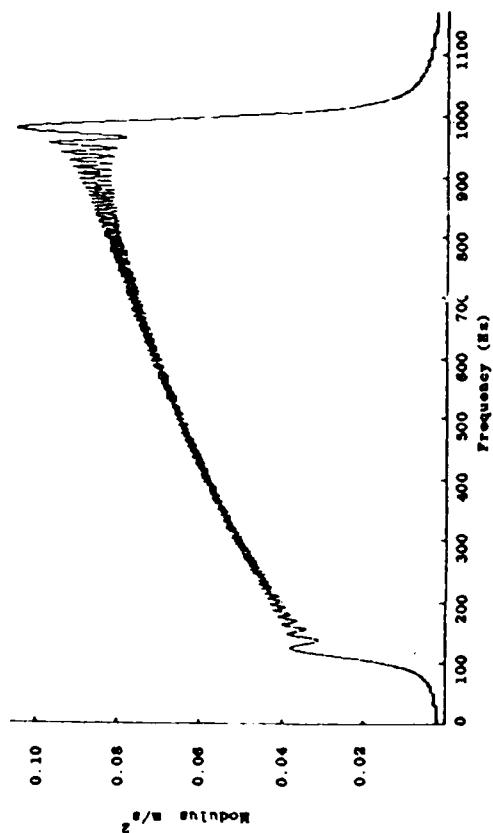


Figure 9: Required exciter table motion modulus spectrum (linear rapid frequency sweep amplitude increasing at 10 dB per decade).

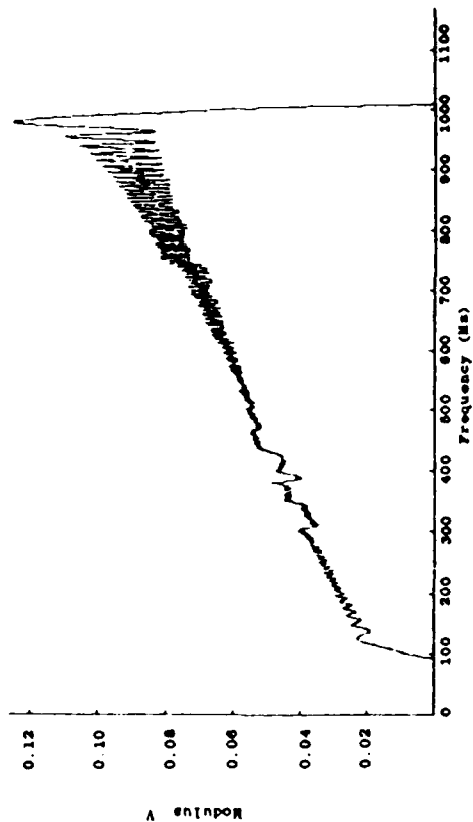


Figure 10: Modulus spectrum of signal to be input to generating system in order to compensate for system frequency response.

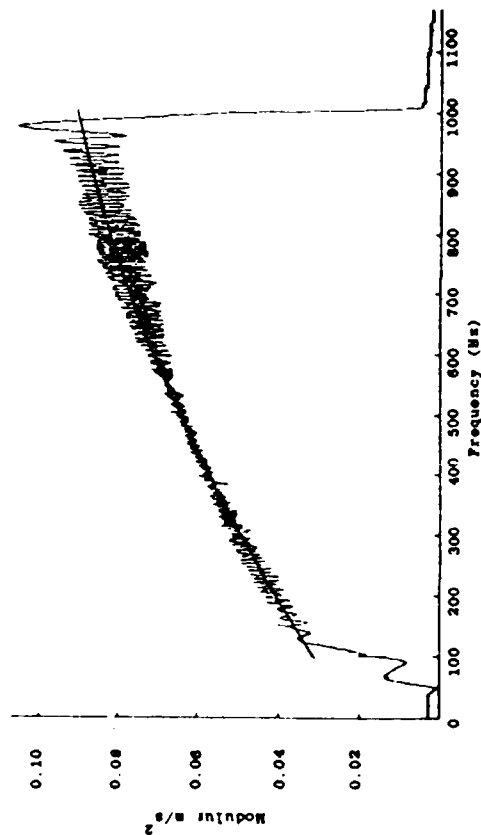


Figure 11: Exciter table motion modulus spectrum obtained after compensation.

A METHOD FOR FINDING AN UPPER BOUND FOR THE RESPONSE OF STRUCTURES TO BLAST WAVES

S.J.C.Dyne, J.K.Hammond and P.Davies

Institute of Sound and Vibration Research

Abstract

The paper presents a technique for prediction of an upper bound for the response of a structure to a shock excitation. The analysis is a development of the work by Davies [6] who used time domain approaches to system response problems and showed how an envelope/Hilbert transform technique could be used to find an upper bound for the response of single input-single output systems. The contribution of this paper is an extension of this to describe the response of structures subject to convecting blast (pressure) waves.

1. INTRODUCTION

Analysis of complicated structures containing large numbers of (possibly coupled) modes can become demanding of computer resources. Model input data are generally either measured experimentally or assumed from theory representing a simplification of the physical model or prototype. Thus experimental results and mathematical model predictions are rarely identical; however, often the full detail of these responses is not required and approximate methods that yield the main features of interest are sought.

This technique involves describing the system impulse response function, the (distributed) input and the response in terms of envelopes. The response envelope can be shown to satisfy an inequality involving the envelopes of the input and of the system and this is used as an upper bound for the system response.

2. ANALYSIS

For a discrete time history $y(n)$ we define the Hilbert transform $\hat{y}(n)$ as the convolution (1)

$$\hat{y}(n) = \sum_{m=-\infty}^{\infty} z(n-m)y(m) \quad (1)$$

where

$$z(m) = \begin{cases} \frac{2}{\pi} \frac{\sin^2(m\pi/2)}{m} & m \neq 0 \\ 0 & m = 0 \end{cases} \quad (2)$$

The implication of the convolution is a filter referred to as a 90° phase shifter from a consideration of the frequency domain, and it should be noted that the transform of a causal sequence is acausal. Furthermore, the infinite limits of the sum prevent exact calculation of the ideal Hilbert transform and methods of finding an approximation to $\hat{y}(n)$ have been

discussed [3]. By analogy with signals in communications systems in a continuous time domain [4] the envelope of a signal is defined as

$$A_y(n) = (y^2(n) + \hat{y}^2(n))^{1/2} \quad (3)$$

An example of a time history and its envelope calculated using this method is given below in figures 1 and 2.

If we now consider a single input-single output discrete system with impulse response $h(n)$ subject to an input $x(n)$, the response $y(n)$ is given as the convolution [5 etc.]

$$y(n) = h(n) * x(n) \quad (4)$$

It can be shown [6] that the envelopes of the response, input and impulse response are related by an inequality giving an upper bound for the response of the system; i.e.

$$A_y(n) \leq A_h(n) * A_x(n) \quad (5)$$

An example is sketched below: Figure 4 shows the right hand side of the inequality superimposed on $A_y(n)$ for a linear second order system with the input shown in figure 3. It can be clearly seen how the envelope of the response is always less than the convolution of the envelopes of the input and impulse response. We show below how this concept may be extended for systems with distributed input.

The general system sketched in figure 5 with impulse response $h(t, r, s)$ may be used to describe a linear system subject to a distributed loading $x(t, s)$, where the independent variables t , r and s represent time, the response function position vector and the input function position vector respectively. The response $y(t, r)$ for example might represent the acceleration of the tip of a mast of a vessel in rough seas, or the stress induced in a component mounting when an aircraft is subject to a pressure wave excitation. The response is again expressed as a convolution of the input and impulse response function: i.e.

$$y(t, r) = \int_S h(t, r, s) * x(t, s) ds \quad (6)$$

where integration is over the domain of influence of $x(t, s)$ and the $*$ denotes the temporal convolution of $h(t, r, s)$ and $x(t, s)$. The Hilbert transform of this relation is taken to give

$$\hat{y}(t, r) = \int_S \hat{h}(t, r, s) * x(t, s) ds \quad (7)$$

combining equations 6 and 7 we have

$$y(t, r) + j\hat{y}(t, r) = \int_S (h(t, r, s) + j\hat{h}(t, r, s)) * x(t, s) ds \quad (8)$$

where j is the root of -1 . Noting that the Hilbert transform of \hat{y} is $-y$ we may take the Hilbert transform again to give

$$\hat{y}(t, r) - jy(t, r) = \int_S (h(t, r, s) + j\hat{h}(t, r, s)) * \hat{x}(t, s) ds \quad (9)$$

multiplying this by j and then adding to equation (8) gives

$$2(y(t, r) + j\dot{y}(t, r)) = \int_S (\dot{h}(t, r, s) + j\ddot{h}(t, r, s)) * (x(t, s) + \dot{x}(t, s)) ds \quad (10)$$

Exploiting the integration inequality [7]

$$\left| \int_a^b f(t) dt \right| \leq \int_a^b |f(t)| dt \quad (11)$$

equation 10 reduces to

$$A_y(t, r) \leq \frac{1}{2} \int_S A_h(t, r, s) * A_x(t, s) ds \quad (12)$$

Thus the response envelope has an upper bound given by the right hand side of inequality (12) which is half the convolution of the impulse response envelope at a point with position vector r due to an input at s , with the envelope of the input at s all integrated over the domain of s .

3. APPLICATION

An example illustrates the use of the inequality. We suppose we should like an upper bound for the response of a beam subject to a convecting pressure wave, (figure 6) and that we know only the envelope of the form of the pressure distribution. The analysis above can be used to compute the envelope of the response to arbitrary input if the envelope of the impulse response is either measured or can be found. In the problem below we compute the response $y(t)$ at a point a distance z from the end of the beam and hence its envelope $A_y(t)$. This is compared with the upper bound for $A_y(t)$ from the distributed convolution

$$\int_0^l A_h(t, z, w) * A_x(t, w) dw \quad (13)$$

A modal method is used for convenience in the computation although it is not a prerequisite for the envelope analysis and other methods including propagating waves or finite elements could be used. An Euler-Bernoulli model is used to describe a beam made from a visco-elastic material with density ρ , Young's modulus E , and damping factor γ . The beam is assumed simply supported with mass m , length l , cross-section S and second moment of area I . The equilibrium equation of motion is [8]

$$\rho S \frac{\partial^2 y}{\partial t^2} + \frac{\partial^2}{\partial z^2} \left[EI \left[\frac{\partial^2 y}{\partial z^2} + \gamma \frac{\partial^3 y}{\partial z^2 \partial t} \right] \right] = x(t, z) \quad (14)$$

where $x(t, z)$ is a convecting field travelling at a constant velocity c of the form

$$x(t, z) = x(t - z/c) \quad (15)$$

The position vectors r and s in inequality (12) become the scalar quantities w and z so the upper bound for the response envelope is given as

$$A_y(t, z) \leq \frac{1}{2} \int_0^l A_h(t, z, u) * A_x(t, u) du \quad (16)$$

The basis of the example is to calculate $y(t, z)$ for a particular location on the beam z_1 . The envelope of this $A_{y_1}(t)$ can be compared with the envelope from the right hand side. We assume equation (14) has a solution

$$y(t, z) = \sum_{r=1}^R q_r(t) \phi_r(z) \quad (17)$$

where R is the mode whose natural frequency is the highest modal frequency below $\frac{1}{2}f_s$ where f_s is the sample rate of the input in discrete form. Substituting (17) into (14) and exploiting the orthogonality property of the modal shapes we derive the ordinary differential equation

$$\ddot{q}_r + \gamma \omega_r^2 \dot{q}_r + \omega_r^2 q_r = \frac{\int x(t, z) \phi_r(z) dz}{\rho S \int \phi_r^2(z) dz} \quad (18)$$

and the mode shape is

$$\phi_r(z) = \sqrt{2} \sin(r\pi z/l) \quad (19)$$

with a normalising factor of $\sqrt{2}$ so that

$$\rho S \int \phi_r^2(z) dz = m \quad (20)$$

the beam mass. For small damping the modal frequency is approximately

$$\omega_r^2 = \frac{EI}{\rho S} \left[\frac{r\pi}{l} \right]^4 \quad (21)$$

We show how the impulse response function can be found: Suppose $x'(t, u)$ is an impulse at $z=z_0$ at $t=0$. i.e.

$$x'(t, z) = \delta(t) \delta(z - z_0) \quad (22)$$

then for small damping

$$q_r(t) = \begin{cases} \frac{\phi_r(z_0)}{m\omega_r} \exp(-\frac{1}{2}\gamma\omega_r^2 t) \sin(\omega_r t) & t > 0 \\ 0 & \text{otherwise} \end{cases} \quad (23)$$

hence the response at z due to a unit impulse at z_0 is

$$h(t, z, z_0) = \sum_{r=1}^R \frac{1}{m\omega_r} \exp(-\frac{1}{2}\gamma\omega_r^2 t) \sin(\omega_r t) \phi_r(z_0) \phi_r(z) \quad (24)$$

from which $A_h(t, z, z_0)$ can be found using the method of equation (3). Equation (24) also enables us to find the response due to the convecting field using equation (6). i.e.

$$y(t, z) = \int_0^l h(t, z, u) * x(t, u) du \quad (25)$$

and since we require the response only at one particular location z_1 we have

$$y_1(t) = \int_0^l h_1(t, u) * x(t, u) du \quad (26)$$

from which $A_{y_1}(t)$ can be found. Finally $A_x(t, u)$ is found directly from $x(t, u)$ and is convolved with $A_h(t, u, z_1)$ and integrated as in equation (12).

4. RESULTS

A Fortran program was used to perform the analysis outlined above by sampling each of the functions in both temporal and spatial variables and using fast Fourier transforms (with zero padding) for the (linear) convolutions and Simpson's method for integration over the spatial variables. Envelopes were calculated using an algorithm based on equations (1), (2) and (3). Physical parameters were given the following values:

beam mass	m	=	2kg
rigidity modulus	EI	=	400Nm ²
beam length	l	=	2m
measurement location	z_1	=	0.7m
damping factor	γ	=	0.001
convecting field velocity	c	=	20ms ⁻¹

The input pressure time history is given in Figure 7. Figure 8 shows the response of the beam from equation (26). The envelope of this response together with the convolution of envelopes from expression 13 is shown in figure 9. We note that the upper bound always exceeds the response envelope confirming the analysis above. Note also that at the peak response the upper bound exceeds the response value by a factor of about two and that the duration of the upper bound is greater than that of the response envelope.

5. CONCLUSIONS

An upper bound can be found for the envelope of the response of a structure subject to distributed loading. Since the value of a function is itself bounded by its envelope an upper bound is found for the peak value of the response of a structure. The only requirements are a knowledge of the envelope of the impulse response of the structure and the envelope of the distributed load. Further computation has shown that the factor by which the upper bound exceeds the response envelope peak is affected by the physical properties of the system - the factor of 2 is typical, but for the system above a faster convection speed reduces the factor to about 1.2.

Impulse response envelopes are required so the computational effort for this analysis is similar to that for traditional techniques such as frequency domain or finite element methods. However, experimental methods can be used to determine the impulse response envelopes at a small number of locations and these may be used by interpolation to find approximations

to the distributed impulse response envelopes and hence the upper bounds.

6. ACKNOWLEDGEMENT

This research has been funded by the MOD (PE) and their support is gratefully acknowledged.

7. REFERENCES

1. A.V. OPPENHEIM and R.W. SCHAFER 1975 *Digital Signal Processing*, Prentice-Hall.
2. L.R. RABINER AND B. GOLD 1975 *Digital Signal Processing*, Prentice-Hall.
3. L.R. RABINER and R.W. SCHAFER 1974 On the behaviour of Minimax FIR digital Hilbert transformers. *Bell Systems Tech. J.* 53(2).
4. J. DUGUNDJI 1958 Envelopes and pre-envelopes of real waveforms. *IRE Trans. on Info. Theory* 4.
5. A. PAPOULIS 1985 *Signal Analysis*, McGraw-Hill.
6. P. DAVIES 1985 *PhD Thesis*, University of Southampton.
7. R.V. CHURCHILL 1960 *Complex Variables and Applications*, McGraw-Hill.
8. G.B. Warburton 1976 *The Dynamical Behaviour of Structures*, Pergamon.

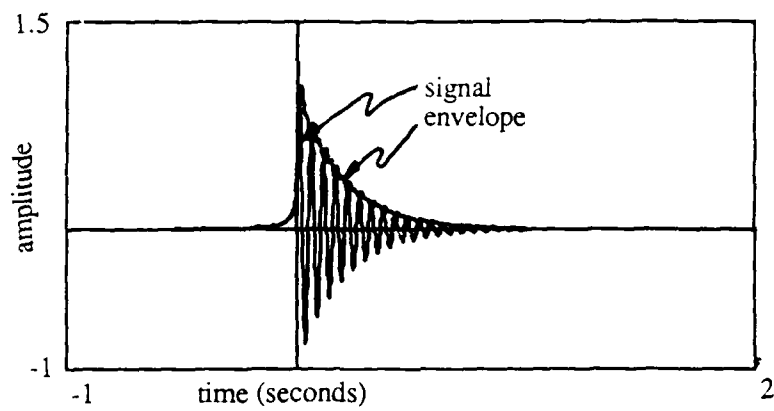


Figure 1: Signal and Envelope

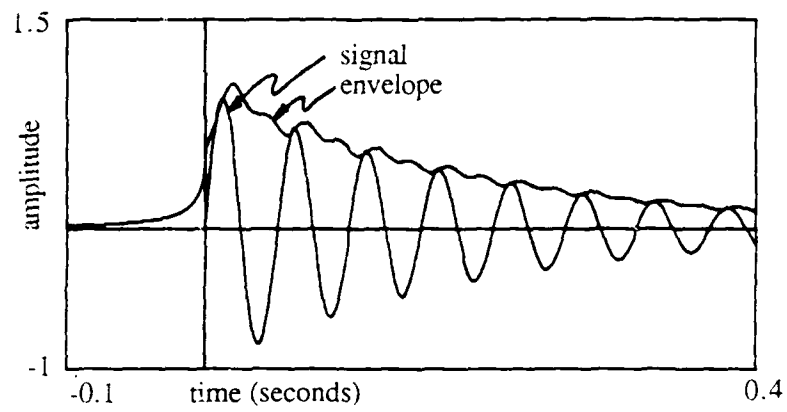


Figure 2: Detail from Figure 1

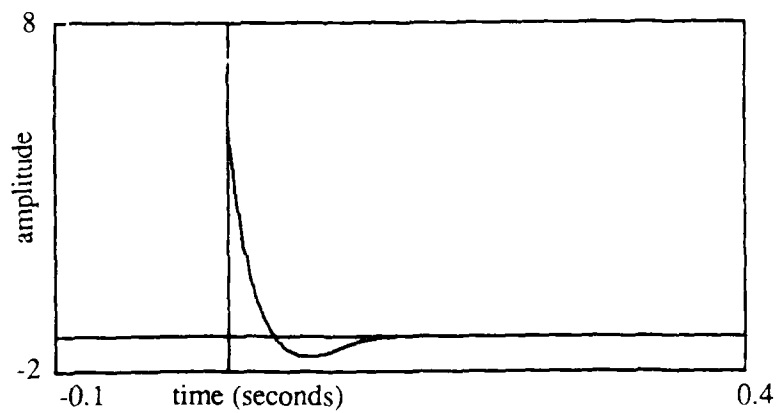


Figure 3: Input to Second Order System

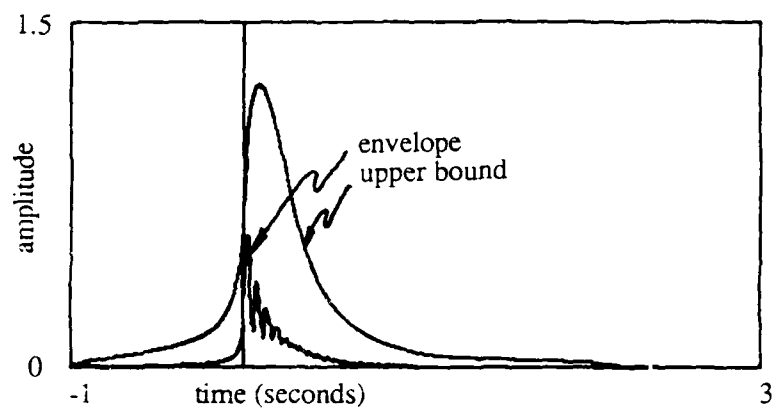


Figure 4: Envelope of the Response of the Second Order System and an Upper Bound for this.

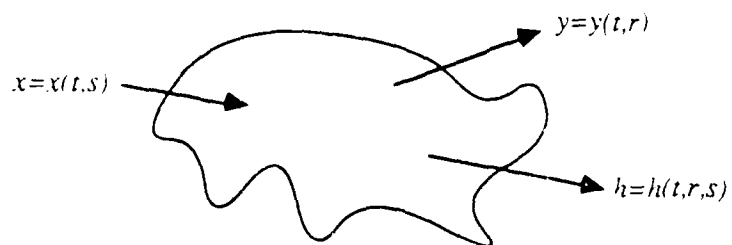


Figure 5: General System with Distributed Properties

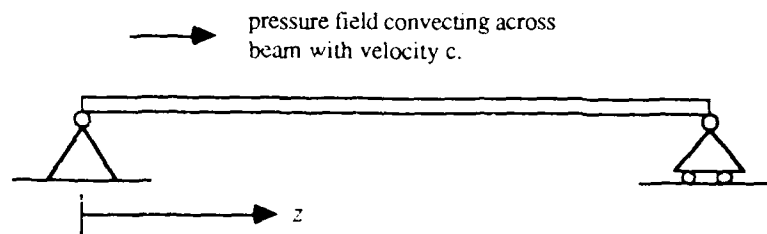


Figure 6: Beam Configuration

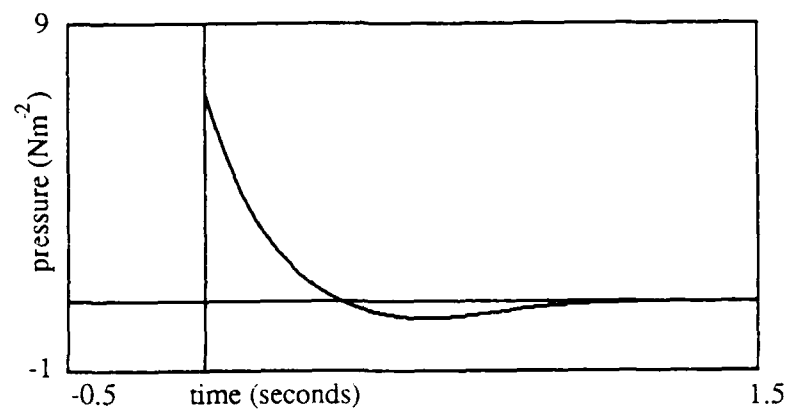


Figure 7: Convecting Pressure Field Time History

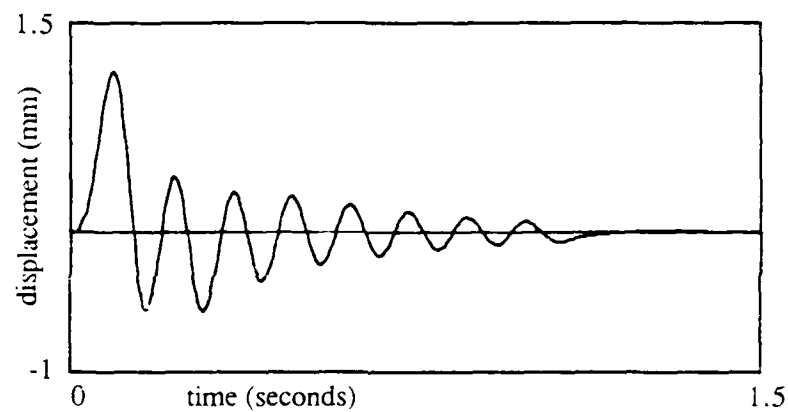


Figure 8: Beam Response, Displacement Time History

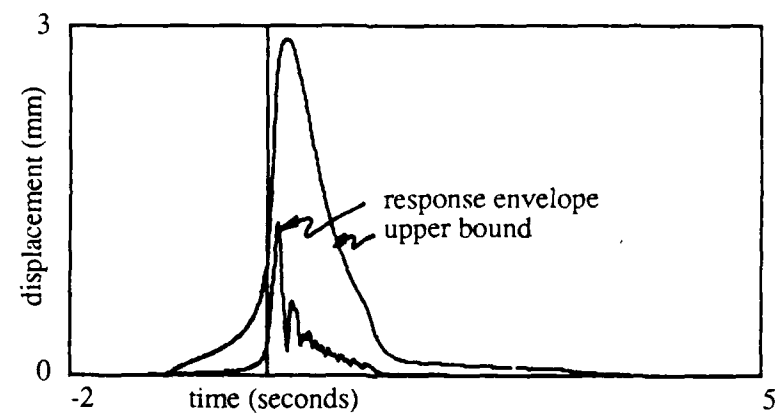


Figure 9: Envelope of Beam Response and Upper Bound for this.

IMPACT COUPLED OSCILLATOR SYSTEMS

D.K.Anderson

C.E.G.B. Berkeley Nuclear Laboratories

1. INTRODUCTION

Much effort is being devoted to the development of analytical models for predicting the dynamic response of complex structures. The well developed methods of linear analysis have proved extremely effective in aiding both the design and assessment of mechanical systems in the engineering environment. There are many situations, however, in which nonlinear effects determine the response of the system. Examples of this kind are afforded by mechanical systems in which a component responds to the applied forcing in such a way that it makes intermittent contact with those adjacent to it. Such contacting motions may lead to wear or other impact damage, particularly if the component settles into a steady state motion in which impacts occur at regular intervals over a prolonged period. In order to assess the likelihood of damage through such a mechanism it is clearly necessary to be able to predict the occurrence of steady state motions and then to determine the relevant parameters e.g. frequency and impact velocity. By their very nature, impacting systems are strongly nonlinear and linearisation techniques have little relevance to such problems.

A number of investigators have considered impacting systems under different types of forcing and it has been found that even in apparently simple systems a great variety of behaviour may be exhibited [1-5]. It has become clear that physical intuition is unreliable and that there is a need for systematic investigation of the types of dynamical behaviour which can occur in this kind of system.

The "dynamical systems" approach has proved particularly effective in the analysis of nonlinear systems of all varieties. In this approach the central idea is that of the phase space in which every point corresponds to a state of the physical system. The problem is then essentially reduced to determining the changes in phase space topology as the control parameters of the system are varied. In this way a global understanding of the system behaviour may be achieved. This is particularly important in systems where there may be more than one steady state motion which can be reached from initial conditions in the range considered possible. In such cases it may be vital to determine the "basins of attraction" of, i.e. those initial conditions which will converge to, each steady state in order to devise practical methods of avoiding those which may be catastrophic for the component under consideration.

Most previously published investigations of such strongly nonlinear systems [1-5] have concentrated on a single degree of freedom approximation for the very good reason that conceptually a two or three dimensional phase space is much easier to visualise than one with higher dimension. Real structures have an infinite number of degrees of freedom; in this paper the effect of energy transference occurring in strongly nonlinear dynamical systems is investigated in a highly idealised conservative system with two degrees of freedom consisting of two simple oscillators which are coupled by impacts occurring when the sum of the displacements is equal to a given value. The simplest real system to which this model corresponds is a beam-like structure whose motion is locally constrained by symmetrically placed

stops, although due to the idealisation the correspondence is by no means exact. The results presented relate to changes in the behaviour of the underlying conservative system as the energy and frequency ratio of the oscillators are varied. The motivation for this investigation was to gain an understanding of the regions in control parameter space which are likely to give rise to periodic steady state solutions of a simple type in systems derived from that considered here by "small" non-conservative perturbations.

To facilitate the analysis the four dimensional phase space is reduced, by taking an appropriate cross section and normalisation of the impact condition to a two dimensional semi-ellipsoidal surface. A nonlinear mapping of an elliptical region onto itself is derived which contains, for impacting motions, all dynamical behaviour exhibited by the full four dimensional "flow" described by the differential equations. The topological properties of this mapping are investigated analytically where possible and otherwise by numerical simulation.

2. SYSTEM AND REDUCTION OF DIMENSION

The simple system considered here is described by the differential equations together with the impact law given below, (1) & (2). For simplicity it is assumed that the masses associated implicitly with the oscillators are equal. This system was obtained from a more general equal mass system by a process of non-dimensionalisation in which all but two control parameters are eliminated leaving the frequency ratio, K , and the system energy, E , remaining.

$$\left. \begin{aligned} \frac{d^2x}{dt^2} + x &= 0 \\ \frac{d^2y}{dt^2} + K^2y &= 0 \end{aligned} \right\} \quad \text{when } |x+y| < 1 \quad (1)$$

where x, y are the displacements in the two degrees of freedom and t is time. Impacts occur when $|x+y|=1$, the impacts are assumed to be instantaneous and perfectly elastic giving the relationship between quantities before and after impact as

$$\begin{aligned} x_+ &= x_- , \quad y_+ = y_- \\ \frac{dx_+}{dt} &= -\frac{dy_-}{dt} , \quad \frac{dy_+}{dt} = -\frac{dx_-}{dt} \end{aligned} \quad (2)$$

where $+$ and $-$ indicate values before and after impact.

As there is no dissipation mechanism in this system there must be conservation of energy:

$$x^2 + K^2y^2 + (dx/dt)^2 + (dy/dt)^2 = 2E = \text{constant}$$

This equation defines a hyper-elliptical surface in the four dimensional phase space which is the subset of Euclidean four-space defined by

$$\{(x, y, dx/dt, dy/dt) \in \mathbb{R}^4 : |x+y| < 1\}$$

Only those motions which lead to impacts are of interest, others being simply those of two uncoupled linear oscillators which are well understood to lie on the surface of a torus. In order to reduce the dimension of the system further therefore, only those points which correspond to an impact i.e. $|x+y|=1$ will be considered. This effectively reduces the space of interest to two semi-ellipsoidal surfaces in Euclidean three-space, Σ^1 and Σ^2 , defined by:

$$\Sigma^1 = \{(x, dx/dt, dy/dt) \in R^3 : x^2 + K^2(1-x)^2 + (dx/dt)^2 + (dy/dt)^2 = 2E, dx/dt + dy/dt > 0\}$$

$$\Sigma^2 = \{(x, dx/dt, dy/dt) \in R^3 : x^2 + K^2(1+x)^2 + (dx/dt)^2 + (dy/dt)^2 = 2E, dx/dt + dy/dt < 0\}$$

corresponding to impact with the $x+y=1$ and $x+y=-1$ impact conditions respectively. This reduction has been effected however by changing the system representation from a continuous "flow" in four-space to a discrete mapping between three dimensional surfaces of section through the flow.

Two further simplifications can now be achieved. The first by noticing that Σ^1 and Σ^2 can in fact be identified since the system possesses symmetry. In practice this means that any point on Σ^2 is normalised, by multiplying all quantities by -1 , into a point of Σ^1 . Thus the mapping is now defined from Σ^1 to itself. The second simplification is effected by projecting the semi-ellipsoidal surface onto its elliptical base so that the mapping becomes one of a plane elliptical region onto itself. This is achieved by changing variables as follows:

$$\text{define : } \phi = (dx/dt - dy/dt)/\sqrt{2}, \psi = (dx/dt + dy/dt)/\sqrt{2}$$

In terms of these variables the definition of Σ^1 becomes:

$$\Sigma^1 = \{(x, \phi, \psi) \in R^3 : x^2 + K^2(1-x)^2 + \phi^2 + \psi^2 = 2E, \psi > 0\}$$

now project down onto the region, Γ , of the plane $\psi=0$ defined by

$$\Gamma = \{(x, \phi) \in R^2 : x^2 + K^2(1-x)^2 + \phi^2 < 2E\}$$

For each value of K there is a limiting energy value below which impacts cannot occur, the elliptical region Γ shrinking to a single point when the system energy is given by:

$$E = K^2/(2(1+K^2))$$

3. THE MAPPING

The explicit mapping equations depend upon whether the next impact after the present one occurs with $x+y=1$ or $x+y=-1$ in the real system; recall that all impacts are normalised so that $x+y=1$. Consider a point (x, ϕ) ; which, by definition, corresponds to a condition immediately before an impact with $x+y=1$. By applying the impact law, (2), to this condition and using the resulting displacements and velocities as initial conditions for the original differential equations, then changing variables back it can be shown that the time to the next impact (i.e. when $|x+y|=1$ next) is given by $t=\tau$ where τ is the first positive root of

$$1 = |-\sqrt{(2E - \{x^2 + K^2(1-x)^2 + \phi^2\})} \cdot (K \sin t + \sin Kt) / (K/2) + \phi(K \sin t - \sin Kt) / (K/2) + x(\cos t - \cos Kt) + \cos Kt| \quad (3)$$

If the expression before taking the absolute value is equal to +1 then the next impact in the system occurs with $x+y=+1$, otherwise it occurs with $x+y=-1$. If the point (x, ϕ) maps onto $(\xi, \Phi) \in \Gamma$ then

$$\xi = \pm (\sqrt{(2E - \{x^2 + K^2(1-x)^2 + \phi^2\})}) \sin \tau / \sqrt{2} - \phi \sin \tau / \sqrt{2} - x \cos \tau$$

and

$$\begin{aligned} \Phi = \pm (\sqrt{(2E - \{x^2 + K^2(1-x)^2 + \phi^2\})}) (\cos \tau - \cos K\tau) / 2 - \phi (\cos \tau + \cos K\tau) / 2 \\ + x (\sin \tau + K \sin K\tau) / \sqrt{2} - K \sin K\tau / \sqrt{2} \end{aligned}$$

where the upper sign is taken if the next impact occurs when $x+y=1$ and the lower sign otherwise.

The question arises as to whether all points of the elliptical region may be mapped onto by, or map into, other points. The answer is yes for all points lying strictly within the ellipse as these correspond to impacts with non-zero velocity. However for points lying on the boundary the situation is more complicated. Let $X(t)=x(t)+y(t)$ and assume that $X(0)=1$, $dX/dt(0)=0$ with $x(0)=x$, $dx/dt(0)=-dy/dt(0)=v$, then from the differential equations:

$$X(t) = x \cos t + v \sin t + (1-x) \cos Kt - v/K \sin Kt, \quad 0 < t < \tau$$

expanding near $t=0$ gives

$$X(t) = 1 - t^2(x + K^2(1-x))/2! + t^3 v(1 - K^2)/3! + t^4(x + K^4(1-x))/4! + \dots$$

from this expression it can be seen that those boundary points with x coordinates satisfying $(x + K^2(1-x)) < 0$ are able to take no part in the mapping as they correspond to trajectories which have penetrated beyond the barrier.

4. FIXED POINTS, STEADY STATE SOLUTIONS AND STABILITY

From the definition of the surface of section it can be seen that periodic points of the mapping correspond to impacting periodic states of the system. A point which, after m applications of the mapping, returns to itself corresponds to an impacting periodic motion of the system. Because the system is conservative the mapping is area preserving (i.e. the Jacobian of the mapping is always equal to one) and no attracting sets can exist. However, under a broader definition than that usually applied in the analysis of dissipative systems a stability type can be assigned to periodic points by looking at the eigenvalues of the Jacobian of the mapping at the fixed point (or of the m -th iterate of the mapping). If the eigenvalues are real then the periodic point is a saddle point with stable and unstable manifolds whose intersections with the surface of section are locally in the direction of the eigenvectors. If the eigenvalues are a complex conjugate pair then the periodic point is neutrally stable. Such points are identifiable in the mapping because they are surrounded by regions of quasi-periodic behaviour. Here the analysis will be mainly confined to the fixed points of the mapping corresponding to single-sided one impact per cycle or symmetrical double-sided two impact per cycle steady states.

The position of the fixed points can be located by noticing that the mapping satisfies the relation

$$2\phi/(2E - \{\xi^2 + K^2(1-\xi)^2 + \phi^2\}) + \xi^2 - K^2(1-\xi)^2$$

$$= -2\phi/(2E - \{x^2 + K^2(1-x)^2 + \phi^2\}) + x^2 - K^2(1-x)^2$$

This relation implies that if $(x, \phi) \in \Gamma$ lies on the contour $S(x, \phi) = C$ of the surface, where

$$S(x, \phi) = 2\phi/(2E - \{x^2 + K^2(1-x)^2 + \phi^2\}) - x^2 + K^2(1-x)^2$$

then (ξ, Φ) will lie on the contour $S(x, -\phi) = C$. By symmetry the two contours only intersect along the line $\phi = 0$ so internal fixed points of the mapping can occur only on this line.

5. THE INTEGRABLE CASE

In general the system described by equations (1) and (2) is not integrable in the sense that there does not exist a second constant of the motion beside the energy. This is evidenced by the appearance of regions of apparently random or stochastic behaviour of the mapping in which no clearly defined invariant curves exist. By contrast, however, when $K=1$ the system is completely integrable, the additional constant being given by the impact velocity or ψ (up to a constant multiplier) in the new variables. In this case the mapping can be written down explicitly:

$$\begin{pmatrix} \xi/\sqrt{2} \\ \phi \end{pmatrix} = \begin{pmatrix} -\cos\tau & -\sin\tau \\ \sin\tau & -\cos\tau \end{pmatrix} \begin{pmatrix} x/\sqrt{2} \\ \phi \end{pmatrix} + \begin{pmatrix} (1+\cos\tau)/\sqrt{2} \\ -\sin\tau/\sqrt{2} \end{pmatrix}$$

where $\tau = 2\tan^{-1}\{1/\sqrt{(4E - 2\{x^2 - (1-x)^2 + \phi^2\})}\}$

which represents precession around the ellipses $2x(x-1) + \phi^2 = \text{constant}$. In this case there is only one fixed point, located at $(x, \phi) = (1/2, 0)$, it is neutrally stable; the whole elliptical region being filled with invariant ellipses on which the behaviour is quasi-periodic. Figure 1 shows a typical mapping diagram illustrating quasi-periodic behaviour, the dashed lines indicate points which are mapped onto each other.

6. FIXED POINT BEHAVIOUR

As the frequency ratio is increased from unity the behaviour of the mapping becomes complicated by the appearance of a region of stochasticity around the upper edge of the elliptical region. This region grows in size with increasing K as the regions of "regular" or quasi-periodic behaviour gradually shrink to become islands in a sea of stochasticity. The existence of stochasticity at all energies (greater than the limiting energy) and for all frequency ratios greater than unity is associated with the breaking of the separatrices which bound the regions of quasi-periodicity surrounding (neutrally stable) periodic points (see [6] for example). In this case a number of periodic points of various orders exist near the upper rim of the elliptical region for small K . Associated with each there is a layer of stochasticity. As K is increased the boundaries between layers are breached resulting in the formation of larger stochastic regions.

Numerical simulation of the mapping has shown that the fixed points behave in a regular way as the energy and frequency ratio are varied. A typical behaviour sequence is illustrated in figure 2 where the energy is

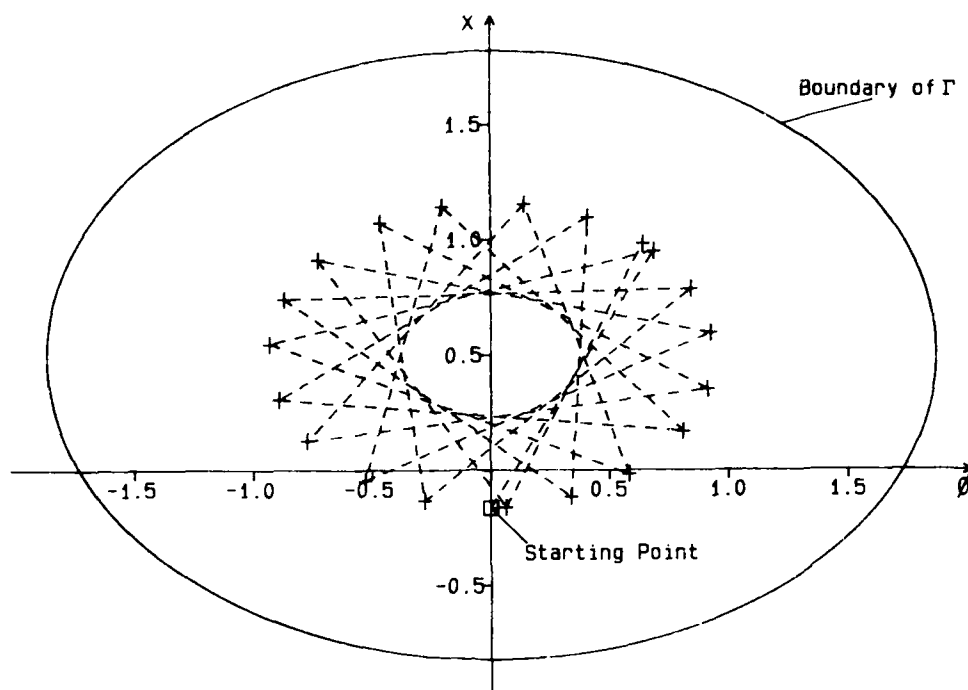


Figure 1: Example of Mapping in the Integrable Case
($E=2.0, K=1.0, 20$ Iterations)

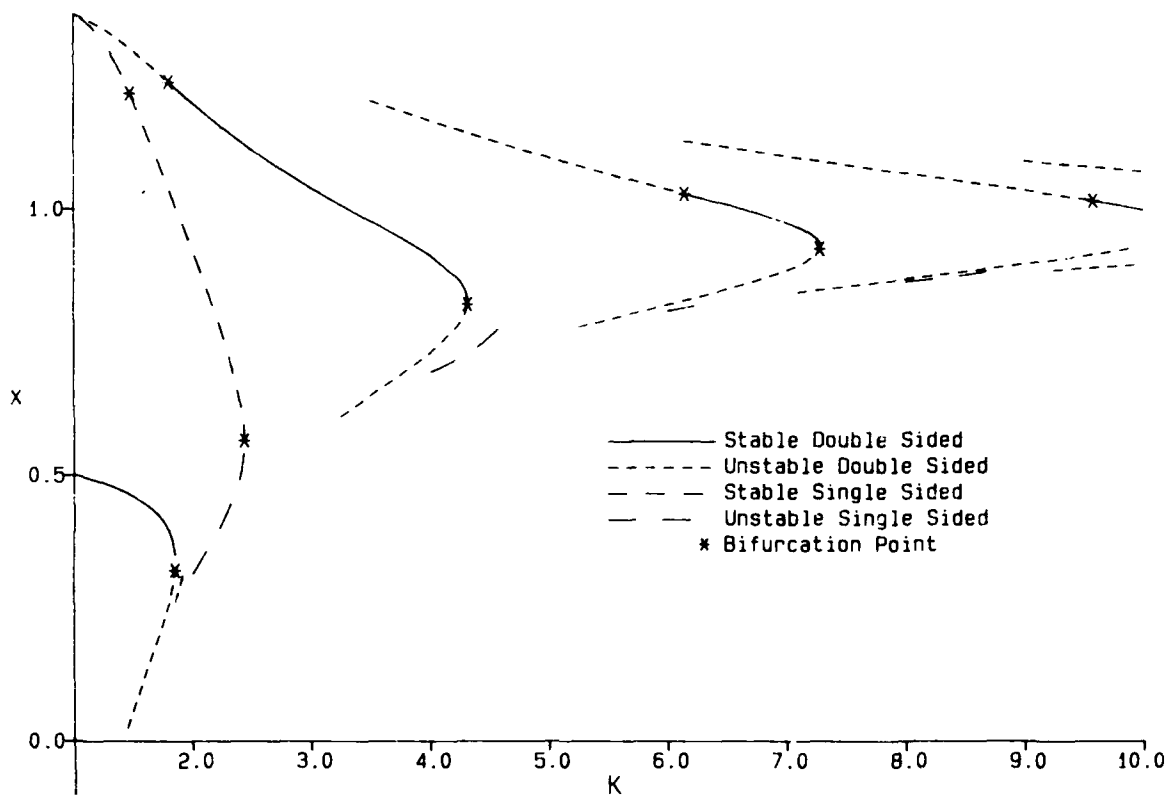


Figure 2: Fixed Point Behaviour for $E=1.0, 1 < K < 10$

fixed and the x coordinates of all fixed points are traced as K is varied. Similar calculations have been carried out for a number of energy values and the assertion that the behaviour shown in figure 2 is qualitatively entirely typical has been confirmed.

For K near unity the mapping is dominated by the fixed point which evolves from that of the integrable case. In this range most of the elliptical region is covered by quasi-periodic behaviour surrounding this neutrally stable point. Invariant curves in the quasi-periodic region are almost elliptical, those close to the fixed point being more so than those close to the boundary. Numerical simulation shows that these curves become more elliptical with increasing system energy. A feature of this regular region is that it appears to remain connected at the bottom of the bounding ellipse of Γ (i.e. the zero velocity point with minimum x value lies on an invariant curve upon which the mapping has quasi-periodic behaviour) until the first unstable point is "born" from the bottom of Γ . After this value of K the quasi-periodic region is completely surrounded by stochasticity. As K is increased further the quasi-periodic-region shrinks. Eventually the bounding invariant curve of the region becomes the intersection with Γ of a homoclinic connexion, composed of branches of the stable and unstable manifolds (see [7]) associated with the unstable fixed point, which have become identified. Finally the neutrally stable and unstable fixed points annihilate in the conservative equivalent of the saddle-node bifurcation, the quasi-periodic region also vanishes. This sequence is illustrated in figure 3(a).

As K is increased from unity unstable fixed points are immediately born from the top edge of Γ . One corresponds to a periodic solution with impacts on a single barrier; a "single sided fixed point", and the other to a periodic solution with successive impacts occurring symmetrically on alternate barriers, a "symmetrical double sided fixed point". Both of these points initially lie within the stochastic region. For each of these fixed points there is a value of K at which bifurcation occurs, resulting in a change of stability type. A necessary and sufficient condition for the occurrence of such a bifurcation is that the eigenvalues of the Jacobian at the fixed point should be equal (either both $+1$ or both -1). In the case of the saddle-node bifurcation discussed above the eigenvalues are positive, this being the only type of bifurcation with this property occurring in this system.

When the eigenvalues are both equal and negative one of several similar bifurcations may occur through which the stability type of the fixed point changes. The eigenvalue sign implies that locally the mapping flips successive iterates from side to side over the fixed point. A change in eigenvalue type from complex to real through the bifurcation results in the disappearance of a pair of periodic points (corresponding to a single two impact per cycle periodic solution). For a range of values of K before bifurcation the unstable fixed point has two homoclinic connexions each of which surrounds a point of the periodic pair and their associated quasi-periodic regions. As the frequency ratio approaches the bifurcation value, the periodic points coalesce and a stable fixed point results. This is an example of a "subcritical flip bifurcation" (figure 3(b)). A change in eigenvalue type from real to complex across the bifurcation results in the production of an unstable asymmetric two impact per cycle periodic pair. The points lie on opposite sides of the, now stable, fixed point; either both lying on a line perpendicular to the $\phi=0$ axis or both on the axis. The periodic pair are connected, at least for a small K range after bifurcation, by two heteroclinic orbits which together form the separatrix between the regular region surrounding the stable fixed point and the stochastic region beyond.

This is an example of the "supercritical flip bifurcation" (figure 3(c)). A particular fixed point may undergo several stability changing bifurcations before it disappears in a saddle node bifurcation.

Fixed points are created at integer values of K at the base of the elliptical region; when K is even a single sided fixed point is created and when K is odd (>1) the new point is double sided symmetrical. They are always created unstable. Fixed points can also be produced "spontaneously" from within a stochastic region as is the case with those points in figure 2 which appear from the upper x range. The production mechanism is the disappearance of an intermediate impact, through a zero velocity impact condition, enabling a solution to become periodic. The opposite event can also occur, viz. the disappearance of a fixed point by the development of an intermediate impact through a zero impact velocity impact condition. This explains the abrupt end of several of the curves representing single sided fixed points when the amplitude becomes sufficient for the occurrence of an impact on the opposite barrier.

Figure 2 indicates that the cycle of fixed point production, stability change and annihilation repeats itself ad infinitum as K is increased. This means that stable fixed points will exist for arbitrarily high values of K , however, numerical simulation indicates that the surrounding quasi-periodic regions become vanishingly small compared with the overall area of Γ . High energy seems to have the opposite effect in that it appears to increase the area of the quasi-periodic region and thus extends the "life" of stable fixed points. Figure 4 indicates those regions in the control parameter plane (for $E, K < 10$) in which stable symmetrical double sided fixed points exist.

7. HIGHER ORDER PERIODIC BEHAVIOUR

Stable periodic behaviour of any order seems possible in this type of system, it is evidenced by the appearance of points which are mapped back onto themselves after $m(>1)$ iterations of the mapping. This point together with all of its iterates forms the "periodic set"; each element of which is surrounded by its own region of quasi-periodic behaviour if the set is stable. Generally the larger the number of points in the periodic set, the smaller the surrounding quasi-periodic region. Consequently, the largest regions of regular behaviour in Γ are associated with low order periodic behaviour, usually either fixed points or periodic sets containing two points. High order periodic sets tend to develop at the edge of the quasi-periodic regions associated with lower order stable periodic sets leading to the well known "islands around islands" phenomenon [6]. These high order islands are relatively short lived and tend to break down rapidly into stochastic regions as the control parameters are changed.

Bifurcations of higher order periodic sets are also possible. The equivalent of the super-critical flip bifurcation in which an unstable two point periodic set becomes stable with the production of an unstable four point set has been observed. High order bifurcation behaviour is difficult to observe numerically as the regular regions associated with the fixed points are hard to find within stochastic areas.

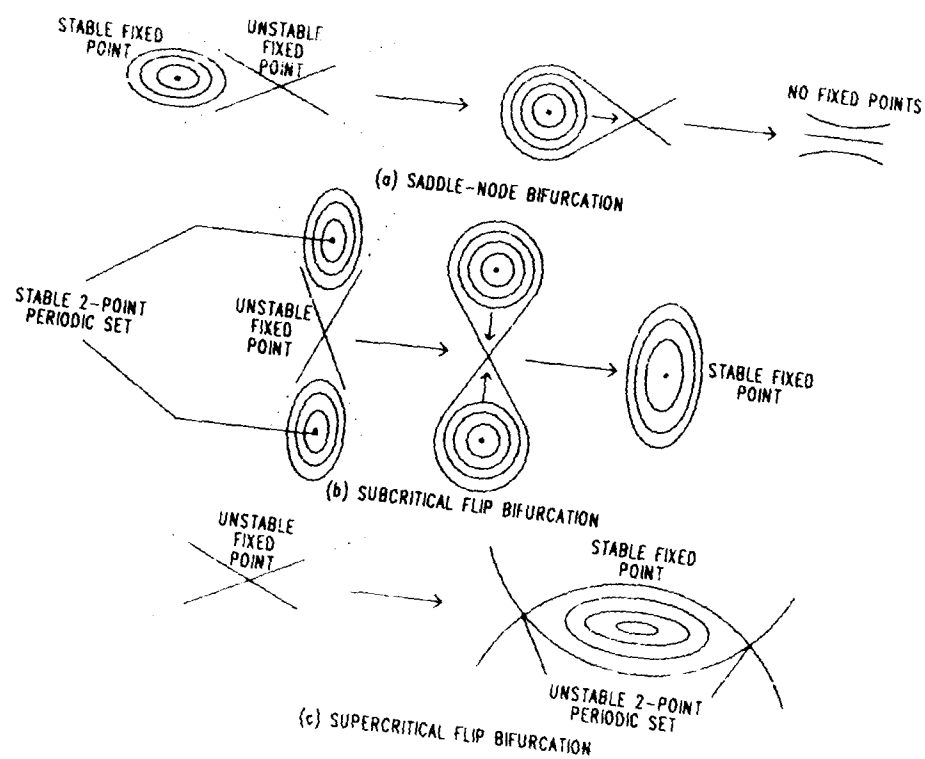


Figure 3: Bifurcations Involving Fixed Points
((b) & (c) may occur in reverse)

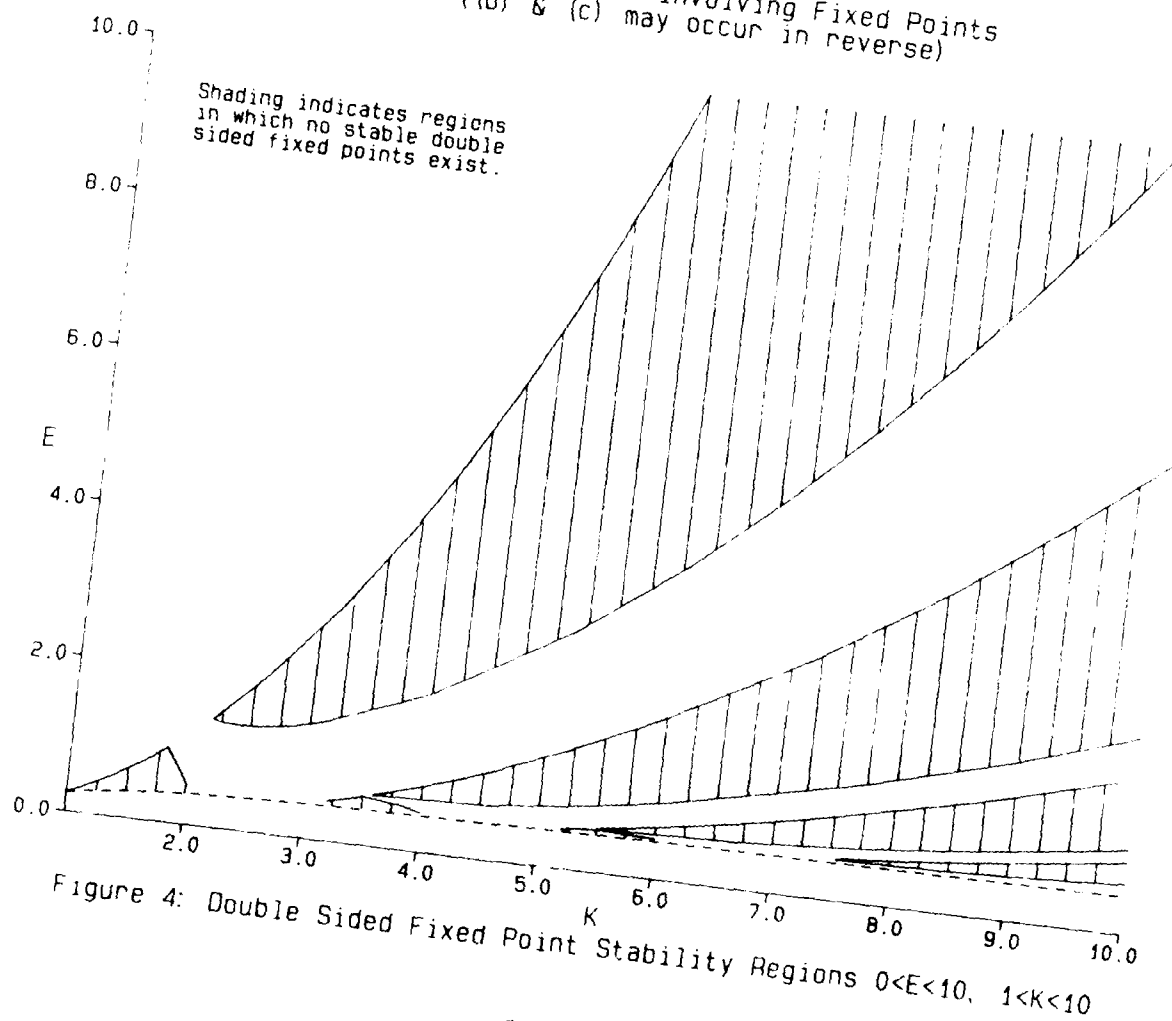


Figure 4: Double Sided Fixed Point Stability Regions $0 < E < 10$, $1 < K < 10$

8. CONCLUSIONS

The analysis of the impact coupled system given above indicates that even in such simple systems a wide variety of phenomena can occur when coupling between degrees of freedom is possible through non-linear mechanisms. The behaviour is neither totally regular (except in the simplest case) nor is it entirely stochastic, indicating that an assumption of ergodicity would not be justified in the analysis of such systems. This may be an important consideration when analysing the response to random excitation particularly if the control parameters are such that large regular regions exist in the phase space of the underlying system. For deterministic systems the "global" analysis shown in figure 4 indicates that steady state solutions of a simple type are most likely to exist when the frequency ratio between the coupled structural modes is close to unity, because it is in this range that the largest regions of regularity occur in the underlying system. For larger frequency ratios the degree of stochasticity is highly energy dependent. Because it is impossible, a priori, to know the bounds on the internal energy within which a particular system will choose to exist, a judgement as to the likelihood of the existence of simple steady states is difficult.

ACKNOWLEDGMENT

This paper is published by permission of the Central Electricity Generating Board.

REFERENCES

1. G.S. WHISTON 1979 Journal of Sound and Vibration 67(1) Impacting Under Harmonic Excitation.
2. F.C. MOON and S.W. SHAW 1983 International Journal of Non-Linear Mechanics Vol.18 No.6 465-477. Chaotic Vibrations of a Beam with Non-linear Boundary Conditions.
3. S.W. SHAW and P.J.HOLMES 1983 Journal of Sound and Vibration 90(1) A Periodically Forced Piecewise Linear Oscillator.
4. S.W. SHAW 1985 Journal of Sound and Vibration 99(2) Forced Vibrations of a Beam with One-Sided Amplitude Constraint: Theory and Experiment.
5. S.W. SHAW 1985 ASME Journal of Applied Mechanics Vol.52 453-458. The Dynamics of a Harmonically Excited System Having Rigid Amplitude Constraints.
6. A.J. LICHTENBERG and M.A. LIEBERMAN 1983 Regular and Stochastic Motion. New York: Springer-Verlag.
7. J.M.T. THOMPSON and H.B. STEWART 1986 Non-Linear Dynamics and Chaos. John Wiley and Son Ltd.

7. FAILURE AND FATIGUE

OVERVIEW OF ACOUSTIC FATIGUE ACTIVITIES AT NASA LANGLEY RESEARCH CENTER

John S. Mixson

Structural Acoustics Branch
NASA Langley Research Center
Hampton, VA 23665-5225

1. ABSTRACT

A number of new aircraft and spacecraft configurations are being considered for future development. These include high-speed turboprop aircraft, advanced vertical takeoff and landing fighter aircraft, and aerospace planes for hypersonic intercontinental cruise or flight to orbit and return. Review of the acoustic environment expected for these vehicles indicates levels high enough that acoustic fatigue must be considered. Unfortunately, the sonic fatigue design technology used for current aircraft may not be adequate for these future vehicles. This has resulted in renewed emphasis on acoustic fatigue research at the NASA Langley Research Center. The overall objective of the Langley program is to develop new methods and information for design of aerospace vehicles that will resist acoustic fatigue without excessive weight penalties.

The program includes definition of the acoustic loads acting on structures due to exhaust jets or boundary layers, and subsequent determination of the resulting stresses within the structure. Material fatigue associated with the high frequency structural stress reversal patterns resulting from acoustic loadings is considered to be an area requiring study, but no activity is currently underway.

2. INTRODUCTION

Sonic fatigue has been recognized as an important consideration for aerospace vehicles since the 1950's. Operational experiences of a variety of aircraft and spacecraft have demonstrated that intense acoustic pressures can actually cause failure of lightweight structures such as skin panels, fuselage rings and stringers, and ribs in wing, flap, and tailplane structures [1]. While these failures may not be catastrophic, the maintenance and repair costs may be considerable. During the 1950's and 1960's considerable research was done to both understand and develop design methods for acoustic fatigue [2, 3].

Figure 1 shows a variety of new vehicle types which are either under development or being considered for development, [4]. All of these vehicles feature increased performance in comparison with currently existing vehicles. Performance increases such as higher speed, greater maneuverability, larger payload, and increased efficiency can be expected to lead to new sonic fatigue problems associated with higher noise loading and lighter weight structures. The effects of extremely high temperatures, new structural materials, and new complex structural configurations must also be taken into account. The existing sonic fatigue technology is not expected to meet the needs of these emerging vehicles, therefore basic research in sonic fatigue has been given renewed emphasis.

This paper will present an overview of the current acoustic fatigue program at the NASA Langley Research Center. Estimation of the acoustic fatigue situation for future vehicles is discussed first to identify needed research areas. Then, current research on acoustic loads prediction and structural response is described, including example results, facilities used, and plans. Acoustic loads research is focused on supersonic heated jets and boundary layers. Structural response research is focused on 1) development of theoretical methods for predicting strain and modal response characteristics; 2) the effects of high temperature on structural response behavior; and 3) fiber-reinforced composite material structures.

SPECIAL NOTE: All dimensional quantities in this paper have been converted from their original English system values into SI system values and rounded to no more than two significant figures. Some numerical inaccuracy and inconsistency may, therefore, appear to be present. For precise values the original sources should be consulted.

3. SONIC FATIGUE ESTIMATION

The vehicles shown in figure 1 are in very early stages of development, therefore no direct information is available on the acoustic loadings, structural response, or fatigue lifetime. An indication of the potential acoustic fatigue problems can be obtained by use of acoustic data from existing similar aircraft, scaling laws, and available design guides [3, 5, 6, 7]

Previous aircraft experience provides a guide to noise levels that may be expected to result in fatigue failures [1]. As shown in figure 2, the shaded bars indicate the noise levels at which acoustic fatigue failures were observed for various types of acoustic loadings. For levels in the range of 140 to 150 dB fatigue damage can occur after many cycles, and for levels of 180 dB or higher damage can occur after only short exposure. The noise pressure scale indicates that sound can exert significant forces, for example 170 dB of normally incident sound would exert about 640 Newtons of force on a 30 cm square panel. The need for lighter weight structures on future aircraft suggests that they may experience fatigue at noise levels similar to those shown in figure 2.

3.1 Aerospace Plane

The aerospace plane concept focuses on two types of mission operation, either sustained hypersonic cruise within the atmosphere, or space launch of payloads into orbit [8]. In either case takeoff is horizontal from a runway and acceleration is rapid. Acoustic loadings should be considered for various phases of flight, including takeoff, ascent, cruise, reentry, and landing.

In the early stages of the takeoff roll the structure in the nearfield of the engine exhaust jet will experience noise levels between 160 and 170 dB. These levels are similar to those measured on the Shuttle and can be estimated from known empirical formulas and exhaust jet parameters. As the speed of the airplane increases, the relative speed between the jet and the freestream decreases so that the intensity of the jet noise sources is decreased. When the local flow speed becomes sonic, the disturbances from the jet cannot propagate upstream to the structure. The speed of Mach 1 is expected to be reached within minutes after takeoff, and then the jet noise loads are expected to become negligible.

Flight envelopes for ascent and cruise operation have been proposed [8], and are shown in figure 3. Use of the data in figure 3 along with standard atmosphere characteristics leads to the result that the aircraft will operate at dynamic pressure values on the order of 48 to 96 kN/m². Maximum fluctuating pressure loads on a structure under a boundary layer have been found to vary in proportion to the dynamic pressure. Empirical scaling laws that relate fluctuating pressure, P_{rms} , to free stream dynamic pressure, Q , are given in the following table [9].

Boundary Layer Type	RMS Pressure, P_{rms}
Attached	$0.006 Q/(1 + 0.14M^2)$
Separated	$0.022Q$
Shock Interaction	$0.14 Q/(1 + 0.5M^2)$

Estimates of acoustic loadings for various vehicle locations, figure 4, indicate levels that are well into the range where acoustic fatigue failures have been observed in the past.

Temperature is expected to be an important parameter when considering structural response and fatigue under aerospace plane flight conditions. Estimated temperatures, figure 5, are high over large areas of the vehicle structure, with large temperature gradients in some regions [10]. These temperatures may affect the acoustic fatigue problem in two ways. First, the structures and materials that are required for reusable high temperature operation are likely to be complex, as shown in figure 6, [11, 12, 13] and to be of the type for which little acoustic fatigue data is available. Second, temperature can influence the acoustic fatigue lifetime in the several ways shown in figure 7. The effects include thermal prestress, thermal buckling (which may result in high stress "oil canning" or "snap-through" behavior), changes of material properties such as Young's modulus, and changes of the fatigue lifetime as expressed in the S-N diagram.

3.2 High Performance Fighters

One feature of increased performance for fighter aircraft is increased maneuverability, as exemplified by the Harrier VSTOL aircraft [14]. Thrust vectoring provides both vertical takeoff and landing capability, and greatly increased maneuverability in forward flight. Most designs feature engine exhaust locations that are forward on the fuselage such that the exhaust jets are directed either onto, or nearly onto, the aircraft structure, figure 8. Estimates indicate that, for some nozzle positions, most of the aircraft is immersed in a noise field with levels above 150 dB, with levels near the nozzle being significantly higher. The exhaust temperatures may exceed 540°C in the region of the nozzle, and therefore the structure needs either high temperature capability or thermal protection devices.

Composite materials are finding increased usage in fighter aircraft [15, 16]. Figure 9 indicates the areas where composites are used on the Harrier II aircraft. It is reported that approximately 30% of the aircraft by weight is made up of composites [16]. Design guides for graphite-epoxy composites are available [17], and appear to be acceptable for current applications. New materials and configurations are still evolving, however, and new V/STOL aircraft of higher performance are under consideration [18, 19], indicating that a continuing program of acoustic fatigue study is desirable.

3.3 Advanced Turboprop Aircraft

New propeller configurations have been under development for some time for large passenger transport aircraft with the objective of saving fuel costs. These propeller blades have a swept-back shape that is intended to increase the aerodynamic performance and to decrease the noise generated for cruise speeds in the range of Mach=0.8. However the noise levels remain in the range where acoustic fatigue must be considered, especially for configurations having the propellers located near the fuselage, figure 10. There are two unique features of this situation. First is the tonal nature of the acoustic field, where the acoustic energy is concentrated at the propeller blade passage frequency (in the range 150 to 250 Hz) and harmonics of that frequency, and where the acoustic field is highly correlated over large areas of the structure. These noise field characteristics cause the response to be especially sensitive to the relative dynamics of the structure and the noise, and must be treated with a different approach than those used for broad band jet or boundary layer noise. The second feature is the unusually long duration of the high noise levels. The propeller noise is highest at the highest tip speed, which occurs during the cruise phase of flight. The exposure time is much longer than usual (for most aircraft the high noise levels occur only for a relatively short time during takeoff and landing), and therefore requires special consideration.

4. ACOUSTIC LOADS RESEARCH

4.1 Boundary Layer Loads

With respect to the vehicle types shown in figure 1, new information on boundary layer loads is most important for the hypersonic (aerospace plane) vehicle. Most available boundary layer loads data are for speeds less than Mach 2.5, with the exception of some data for a maneuverable entry body taken in Mach 4 and Mach 8 wind tunnels [7]. The scatter in the high speed data is large, with overall levels currently estimated within 5 dB and spectrum levels within 10 dB. This uncertainty in levels is inadequate since use of the higher values would probably result in overdesigned structure, and use of lower values may lead to an unsafe design.

New information for the higher speed segments of the flight envelope, figure 3, may not be required because there are indications that fluctuating pressures decrease with Mach number above about Mach 6. When the entry and descent flight profiles are defined, the associated loads can be determined using the same methods as for ascent.

Experimental and theoretical research has been initiated for definition of the fluctuating boundary layer loads for super/hypersonic flight conditions. Experimental studies are focused on development of methods for measurement of fluctuating pressures at Mach numbers up to 6 for temperatures up to 980°C. Langley test facilities being considered include the 8-Foot High-Temperature Structures Tunnel and the 7-Inch Wind Tunnel. A key element is a transducer that can operate at the high temperature and at the high frequencies (several thousand Hertz) required for model studies. Theoretical studies are developing methods to account for the effects of factors such as velocity and temperature gradients on the measurements.

4.2 Jet and Plume Loads

Acoustic loadings due to engine exhaust jets are currently of most interest for the hypersonic vehicle and the high performance fighter configurations, figure 1. Because of the vehicle configurations, with the engine exit located relatively far forward on the fuselage, the exhaust flow impinges on a significant length of fuselage structure. The high performance of the vehicles results in exhaust flows with high velocities and high temperatures. In the vertical landing mode an ASTOVL aircraft, figure 8, may also be subjected to jet loadings due to the "reflection" of the downward-flowing engine exhausts from the landing surface [15]. Available information such as acoustic loadings from free jets [20] and low speed impinging flows [21], can serve as initial guidelines, but are not expected to be sufficient for these future aircraft conditions.

Research is underway on existing configurations, and has been proposed for definition of acoustic loads for configurations and jet conditions approaching the requirements of future vehicles. Test facilities and instrumentation are not available for the actual temperatures that are expected. Figure 11 illustrates a test to define the acoustic pressures and temperatures on a flat plate that is located close to, and parallel to the exhaust axis of a supersonic jet. The nozzle exit is 10 cm wide by 1.3 cm high, and it is designed to operate at exit Mach numbers of 1.35 and 2.0, and at temperatures from ambient to 540°C. Preliminary results indicate that the jet flow is strongly influenced by the presence of the plate and that fluctuating pressure levels are high. The interaction of two supersonic jets is illustrated in figure 12 [22]. The test configuration is a dual nozzle of 0.025 scale with geometry representative of currently operating aircraft. The unsuppressed jets interact to form intense sound waves that propagate upstream, where they could impinge on structure. For this configuration the resonance was suppressed using a slight offset of the operating conditions of one of the nozzles, resulting in a reduction of the peak pressure to about 25% of the unsuppressed value. The facility used for these tests has been used for a variety of studies and has been shown to give results in agreement with full scale results [23]. Modifications of this facility are planned in order to obtain temperatures up to

1400°C and increased flow velocities up to Mach 2 in an outer co-annular nozzle, to more closely represent future vehicles.

For hypersonic vehicles, combustion may be a significant source of acoustic loading on the engine and airframe structure. Theoretical and experimental research has been proposed for definition of the loads and for investigation of active combustion control.

5. STRUCTURAL RESPONSE RESEARCH

5.1 Dynamic Strain Prediction

The great variety of structural materials and configurations called for by future vehicles suggests that an empirical approach may be too costly and time consuming to provide the required acoustic fatigue data in a timely manner. Consequently, an alternate approach employing theoretical methods may be appropriate. A theoretical basis for stress prediction exists [24], and the recent advances in analytical methods (such as finite elements) and computing power are causes for some optimism that renewed efforts could produce satisfactory, improved theoretical methods.

In a recent study [25], several flat panels were subjected to normally incident acoustic waves and their acceleration and strain responses were measured and predicted. Care was taken in setup and calibration of the horn, in mounting the panel, and in maintaining a constant environmental temperature in order to approach ideal test conditions. All four panel edges were supported in rubber-faced clamps. Very good agreement between measured and predicted panel acceleration was achieved. However, the measured strain was consistently less than the predicted strain. Predicted strains were about three times the measured, on average, for an aluminum panel as well as for three composite panels. This result appears to be in general agreement with previous attempts to predict strain for idealized panels [26, eg]. Recent theoretical efforts have treated the boundary conditions in an improved way and have compared Ritz solutions with finite element solutions [27]. Agreement with test results was improved, but not satisfactory.

The configurations currently being studied consist of cantilevered plates that are mechanically excited by base motion, figure 13. A range of plate sizes was studied; the results shown are for a plate having 10 cm x 7.6 cm x 0.08 cm dimensions. The clamping block material and bolt arrangement were varied until agreement was achieved between measured and predicted modal frequencies, and until the plate strains induced by the clamping were felt to be minimized. Shaker excitation was random, band limited to 0-500 Hz, and constant acceleration. The prediction method used the Ritz approach with 16 modes, 16 terms per mode, and was validated by showing agreement with known plate modal frequencies. Measured damping values and base motion are used as inputs, but the results shown used the calculated resonant frequencies. The good agreement shown is typical of the four strain gage locations where comparisons were made. This result may be viewed as a benchmark demonstration of the accurate prediction of dynamic strain response of a plate. Plans include the study of other more realistic boundary conditions, acoustic excitation, and elevated temperatures up to the range of 540°C.

5.2 Non-Linear Strain Response

Intense acoustic loadings can drive flat panels to such large deflections that non-linear, in-plane forces become important. Development of theoretical methods for prediction of panel stress/strain response when large amplitude non-linear effects are important is underway [28].

Some recent results showing non-linear effects for aluminum and composite panels are presented in figure 14 [29]. For this analysis the sound was normally incident, resulting in a constant pressure distribution over the surface of the plate. The frequency spectrum of this pressure was flat, consequently the forcing pressure magnitude on the

plate vibration modes was the same for the three plates, even though the modal frequencies were different due to the different plate stiffnesses. The effective stiffness, D_{eff} , was determined from the modal vibration frequency of the plates. The method of equivalent linearization was used to solve the non-linear equation that resulted from the use of a single mode substitution in the non-linear plate equations. Both linear and non-linear analysis show that the composite panels have more strain than the aluminum panel. For the linear case the magnitudes of the differences can be explained using the mass values, stiffness values, and the approximate formula given at the lower right of the figure. The effect of nonlinearity is shown to depend on the particular composite layup, for example at the highest sound level the strain of the aluminum panel and of the $90/\pm 45/0$ composite panel are both reduced to about 45% of their linear values, but the $0/\pm 45/90$ composite panel is reduced to 37.5% of its linear value.

The analytical methods used for figure 14 have also been used to study the effect of non-linear damping on the large amplitude response of composite panels [30], and to study the effects of transverse shear and plate thickness on panel response to acoustic excitation [31, 32].

5.3 Snap-Through of Buckled Plates

Acoustic excitation can also cause non-linear response behavior in panels that are naturally curved or are curved due to thermal or buckling effects. The non-linear response of panels that are buckled due to in-plane compression has been investigated theoretically [33, 34] and experimentally [35]. Some theoretical results are illustrated in figure 15.

In this analysis, the out-of-plane displacement of a rectangular plate under in-plane compression is represented by a single mode. By including tensile energy due to large displacements, the non-linear force-displacement relation is obtained. When the compressive edge shortening, u , is less than the critical value, u_c , the plate remains flat and the force-displacement curve is monotonically increasing. When $u > u_c$ the curve has a local maximum and a minimum, and therefore the two equilibrium positions A and B. When the vibratory motion about equilibrium position A becomes just sufficiently large, the displacement will "snap-through" to point C and the ensuing motion will take place about equilibrium position B, or snap-through towards A again.

The equivalent linearization technique is used to find the non-linear vibratory response of the buckled plate under random acoustic excitation, and results are shown at the right of the figure. The excitation level parameter α is nondimensionalized such that $\alpha =$ mean square displacement, q_{ms} , for linear response of a flat plate without compression. For a given excitation level, response increases with increasing in-plane compression until the buckled deflection is too large for snap-through on every cycle (persistent snap-through) and the snap-through occurs only intermittently. The figure also shows that as the excitation level increases, the point of maximum response corresponds to increased plate buckling, i.e. larger values of u/u_c . For $\alpha = 2$, the maximum mean square displacement, (and therefore the maximum stress) is about 1.4 times the value with no compression. This increased stress could lead to reduced acoustic fatigue lifetime.

5.4 Response at Elevated Temperature

The effects of elevated temperature are expected to be more important for future vehicles due to the combination of longer duration exposure to both acoustic and thermal loads, larger areas of the structure that are exposed, and the need for lighter weight, reusable structure. As indicated in figure 7, temperature can affect the structural response to acoustic loads through four mechanisms. Preparations are being made for experimental and theoretical study of these mechanisms. The "oil canning", or "snap-through" behavior of a thermally buckled panel might be expected to be similar to the behavior of a

mechanically buckled panel, therefore the results described above in section 5.3 could provide some guidance.

The initial measurements of temperature effects will use the test apparatus sketched in figure 13(a cantilever plate with moving base excitation), and will measure strain response at temperatures up to about 540°C. This configuration will simplify the test hardware to avoid problems such as mechanical attachment of a shaker to a hot test panel, and will allow study of the effects of material property changes without the complicating effects of large prestress or buckling. Exploratory tests with quartz radiant heaters (but no acoustics) show that such temperatures can be obtained and closely controlled using available equipment, but that significant temperature gradients can occur across the plate surface, and through the thickness. Some effects of temperature gradients and material property changes have been calculated [36].

Analysis of panels having combined thermal and acoustic loadings has been initiated using finite element methods and the Von Karman large deflection (non-linear) strain-displacement relations. Material properties were not varied with temperature. Non-linear equations were solved for deflections due to temperature changes that are uniform throughout the panel. Dynamic response to a uniformly-distributed acoustic load was calculated using a Miles single mode solution of linear equations for small amplitude motions about the thermally loaded static equilibrium position. Predicted results for an initially flat, simply supported, panel are shown in figure 16. The thermal static solution (upper right in the figure) shows that center deflection W is zero until the buckling temperature, ΔT_{CR} , is reached. For this panel only 2.8°C temperature change was sufficient to cause buckling. For further temperature increase the deflection follows a strongly non-linear trend. Both deflection shape and stresses from this non-linear static thermal analysis were used as input to the linear dynamic acoustic analysis. The frequency of the first mode, ω , decreases at first due to the increase of inplane stresses as temperature increases, but following buckling at $\Delta T/\Delta T_{CR}=1$, the frequency increases again due to the increasing panel curvature. Panel dynamic deflection, W , and dynamic stress, σ_{rms} , both have a peak value in the neighborhood of the buckling temperature. In particular, the very large stress increase at buckling temperature suggests the increased possibility of acoustic fatigue failure. However, the linear theory is limited to small values of deflection, W , therefore a non-linear dynamic analysis will likely be required for accurate determination of the stresses at temperatures near the buckling temperature. In figure 16, the linear limit has been taken at $W/h=0.5$, resulting in a large non-linear region for the 100 dB noise level.

5.5 Testing at Elevated Temperature

Facilities and test methods for use at high temperature are not well developed, therefore new developments are needed. For example, there is a need to know the resonant frequencies, damping values, and strain response of panels at high temperature (as well as at large amplitudes). An example of a method that is being studied is the Ibrahim Time Domain (ITD) method [37]. This method is intended to measure structural properties while the structure is in steady state response to a random input. The random response time history is sampled to obtain a decay curve, which is then analyzed to obtain the component resonant frequencies and damping values. In a recent study [36] results from the ITD method were compared with results from a standard impulse hammer test of four panels at room temperature. Damping ratio estimates obtained using the ITD method had an average value in the range of 0.01 to 0.03, which is somewhat lower than, but in reasonable agreement with the values of 0.029 to 0.046 obtained from the impulse tests. The natural frequencies identified by the ITD and hammer test methods were in excellent agreement. Since no special test procedures or instrumentation are required, further studies of the ITD method, as well as related methods [38], appear warranted.

The Thermal Acoustic Fatigue Apparatus (TAFA), figure 17, was developed for testing of Space Shuttle thermal protection systems [39, 40, 41]. It uses two electro-

pneumatic sound generators of 30 kW each to produce a progressive wave at levels up to 163 dB rms overall, and can accomodate test panels up to a maximum size of 1.8 m by 1.8 m. Electrical power of 500 kW is available at the test chamber for panel heating. The TAFE is currently being returned to service after an inactive period, and is being fitted with quartz heaters of several types for evaluation. Upgraded acoustic and electrical power capabilities may be required in order to produce the highest sound levels and heat flux values envisioned for future environments.

6. CONCLUDING REMARKS

This paper describes the current status of the acoustic loads and fatigue program at the NASA Langley Research Center. Estimates of the possible acoustic fatigue requirements of future ASTOVL and hypersonic aircraft are discussed, and research topics that are being studied are outlined. It is suggested that near term sonic fatigue technology developments include understanding of the behavior of high temperature and composite structures, improved accuracy in analytical prediction of the strain response of structures, and development of acoustic and thermal test facilities that can produce the environments expected for future aerospace vehicles.

7. ACKNOWLEDGMENTS

The author extends thanks to the following individuals for their contributions of research results and reviews of the paper: J. D. Leatherwood, J. E. Locke, K. H. Lyle, C. Mei, C. F. Ng, C. B. Prasad, J. M. Seiner, and W. E. Zorumski.

8. REFERENCES

1. H. H. HUBBARD and J. C. HOUBOLT 1961 Chapter 48 of the Shock and Vibration Handbook, Edited by C. M. Harris and C. E. Crede, McGraw-Hill. Vibration Induced by Acoustic Waves,
2. W. J. TRAPP and D. M. FORNEY, Jr., Editors 1965 Syracuse University Press. Acoustical fatigue in aerospace structures.
3. F. F. RUDDER, Jr. and H. E. PLUMBLEE, Jr. 1975 AFFDL TR-74-112. Sonic fatigue design guide for military aircraft.
4. ____ 1985 NASA CR 176322. Aeronautical technology 2000: A projection of advanced vehicle concepts. Report of the panel on vehicle applications, National Research Council.
5. E. E. UNGAR, J. F. WILBY and BLISS, D. B., et al 1977 AFFDL TR 76-91, vol. I and II. A guide for estimation of aeroacoustic loads on flight vehicle surfaces.
6. L. C. SUTHERLAND and D. BROWN 1972 AFFDL TR 71-180. Prediction methods for near field noise environments of VTOL aircraft.
7. A. L. LAGANELLI, A. MARTELLUCCI and L. L. SHAW 1983 AIAA Journal, vol. 21, no. 4. Wall pressure fluctuations in attached boundary-layer flow.
8. R. M. WILLIAMS 1986 Aerospace America. National aero-space plane: Technology for America's future.
9. W. E. ZORUMSKI: 1987 NASA TM 100517. Fluctuating pressure loads under high speed boundary layers.

10. R. R. HELDENFELS 1967 NASA SP-148, pp. 471-483. Introductory remarks on structures and materials for hypersonic aircraft. .
11. A. H. TAYLOR, I. O. MACCONOCHIE, L. R. JACKSON and J. A. MARTIN 1983 Astronautics and Aeronautics. Structures and subsystems.
12. A. H. TAYLOR, L. R. JACKSON, J. A. CERRO, and S. J. SCOTTI 1983 AIAA Paper 83-0974. An analytical comparison of two wing structures for Mach 5 cruise airplanes.
13. D. HAYS 1982 NASA CR 3548. An assessment of alternate thermal protection systems for the Space Shuttle orbiter, Vol. I - executive summary. .
14. D. H. S. MORGAN 1986 Aerospace America. Harrier the Viffer.
15. R. DeMEIS 1985 Aerospace America. Designing a V/STOL fighter: McDonnell's AV-8B Harrier II.
16. J. F. SCHIER and R. J. JUERGENS 1983 Astronautics and Aeronautics. They force a fresh look at the design process (Design impact of composites on fighter aircraft, Part I).
17. I. HOLEHOUSE 1980 AFWAL TR 80-3019. Sonic fatigue design techniques for advanced composite aircraft structures.
18. W. J. LEWIS and D. PALFREYMAN 1984 Aerospace America. Supersonic V/STOL ready for technology push
19. K. OWEN 1987 Aerospace America. Beyond Harrier.
20. A. G. R. THOMSON 1972 AGARDograph 162. The estimation of near field sound pressure levels due to jet noise in acoustic fatigue design data.
21. C. M. WILLIS, J. A. SCHOENSTER and J. S. MIXSON 1978 Journal of Aircraft, vol. 15. Acoustics loads on upper-surface-blown powered-lift systems.
22. J. M. SEINER, J. C. MANNING and M. K. PONTON 1986 AIAA Paper 86-1539. Dynamic pressure loads associated with twin supersonic plume resonance.
23. J. M. SEINER, J. C. MANNING and M. K. PONTON 1987 AIAA Paper 87-0244. Model and full scale study of twin supersonic plume resonance.
24. A. POWELL 1965 Acoustical Fatigue in Aerospace Structures, Syracuse University Press, pp. 1-19 An introduction to acoustic fatigue.
25. L. A. ROUSSOS, K. E. HEITMAN and C. E. RUCKER 1986 AIAA Paper 86-1931. Predicted and measured strain response of rectangular panels due to acoustic loading.
26. M. D. OLSEN and G. M. LINDBERG 1970 Aeronautical Report LR-544, National Research Council of Canada. Free vibrations and random response of an integrally-stiffened panel.
27. L. A. ROUSSOS and T. K. BREWER 1987 AIAA Paper 87-0935-CP. Effect of boundary conditions on dynamic strain response of rectangular panels.

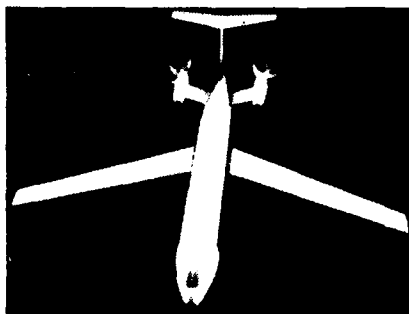
28. C. MEI and K. R. WENTZ 1982 AIAA Journal, vol. 20, pp. 1450-1458. Large amplitude random response of angle-ply laminated composite plates.
29. C. MEI and C. B. PRASAD 1985 Final Report on Task 5, Contract NAS1-17993. Nonlinear random response of composite panels.
30. C. MEI and C. B. PRASAD 1986 AIAA Paper 86-1933. Response of symmetric rectangular composite laminates with nonlinear damping subjected to acoustic loading.
31. C. MEI and C. B. PRASAD 1987 AIAA Paper 87-0933 CP. Effects of large deflection and transverse shear on response of rectangular symmetric composite laminates.
32. C. MEI and C. B. PRASAD 1987 NASA Contractor Report 178313. Influence of large deflection and transverse shear on random response of rectangular symmetric composite laminates to acoustic loads.
33. C. F. NG 1986 Ph.D. Dissertation, Institute of Sound and Vibration Research, Southampton, England. Dynamic behaviour of postbuckled composite plates under acoustic excitation.
34. C. F. NG 1987 AFOSR/ARO Conference on Non-Linear Vibrations, Stability, and Dynamics of Structures and Mechanisms, Blacksburg, Virginia. The analysis of non-linear dynamic behavior of postbuckled plates by simple analytical solution.
35. C. F. NG 1988 Proceedings of the Third International Conference on Recent Advances in Structural Dynamics, Southampton, ENGLAND. The influence of snap-through motion on the random response of curved panels to intense acoustic excitation.
36. J. S. MIXSON and L. A. ROUSSOS 1987 NASA Technical Memorandum 89143. Acoustic fatigue: Overview of activities at NASA Langley.
37. S. R. IBRAHIM and E. C. MIKULCIK 1977 The Shock and Vibration Bulletin, Part 4, Structural Dynamics, Systems Identification, Computer Applications. A method for the direct identification of vibration parameters from the free response.
38. J. N. JUANG and R. S. PAPPAS 1985 Journal of Guidance, Control, and Dynamics, vol. 8, no. 5, pp. 620-627. An Eigensystem realization algorithm for modal parameter identification and model reduction.
39. C. E. RUCKER and R. E. GRANDLE 1973 Fatigue at elevated temperatures. ASTM STP 520. Thermoacoustic fatigue testing facility for space shuttle thermal protection system.
40. C. E. RUCKER and R. E. GRANDLE 1973 AIAA/NASA/ASTM/IES Seventh Space Simulation Conference, Los Angeles, NASA SP 336. Testing of space shuttle thermal protection system panels under simulated reentry thermoacoustic conditions.
41. C. E. RUCKER and J. S. MIXSON 1976 Proceedings of the AIAA/ASME/SAE 17th Structures, Structural Dynamics and Materials Conference. Vibroacoustic testing of space shuttle thermal protection system panels.



Hypersonic Transport



Advanced Fighter



Propeller Transport



Space Transportation

Figure 1.- Future Aerospace Vehicles.

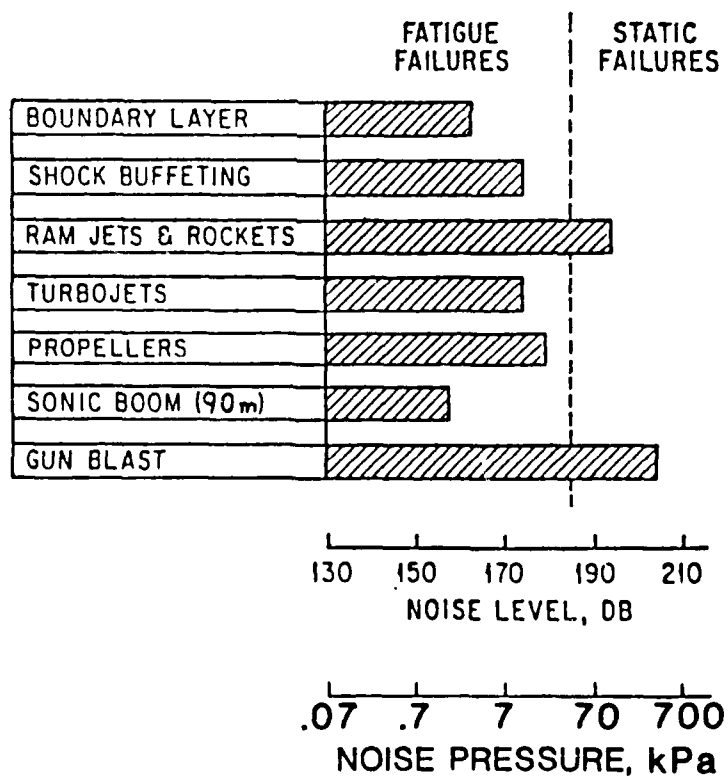


Figure 2.- Noise Levels Effecting Structures [1].

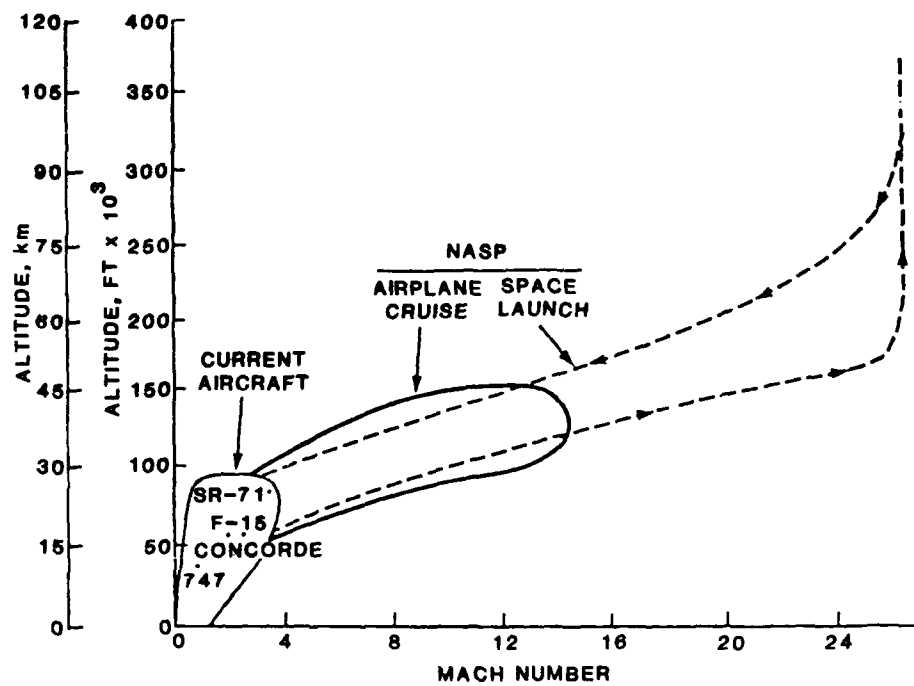


Figure 3.- Proposed Flight Envelope for an Experimental Hypersonic Vehicle [8].

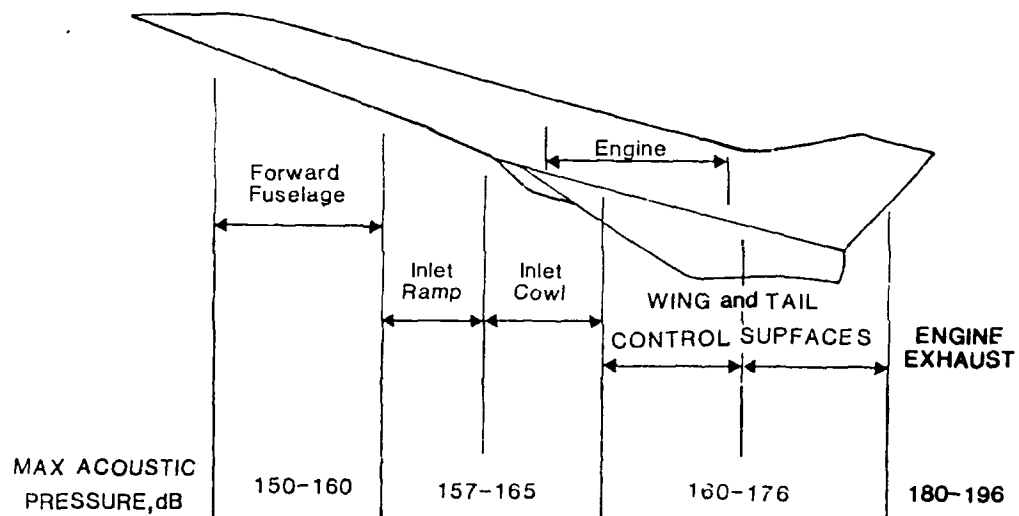


Figure 4.- Generic Design Environments for NASP (National Aerospace Plane).

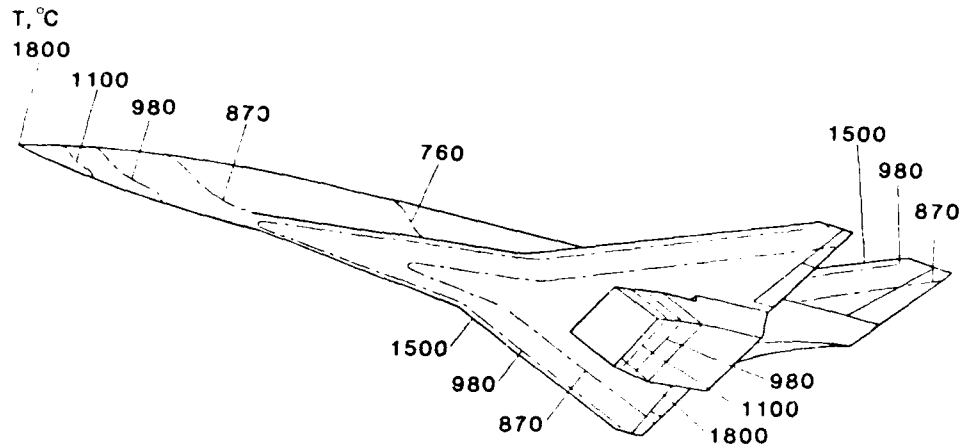
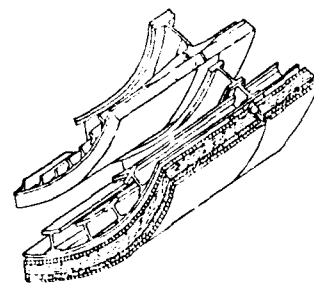
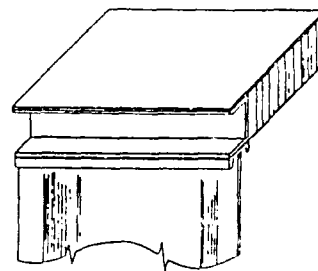


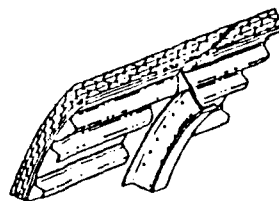
Figure 5.- Equilibrium Surface Temperatures for Cruise at Mach 8 and Dynamic Pressure - 105 kPa [10].



SIDEWALL CONSTRUCTION



HONEYCOMB CORE SANDWICH



TITANIUM MULTIWALL

Figure 6.- Candidate Structural Concepts [11, 12, 13].

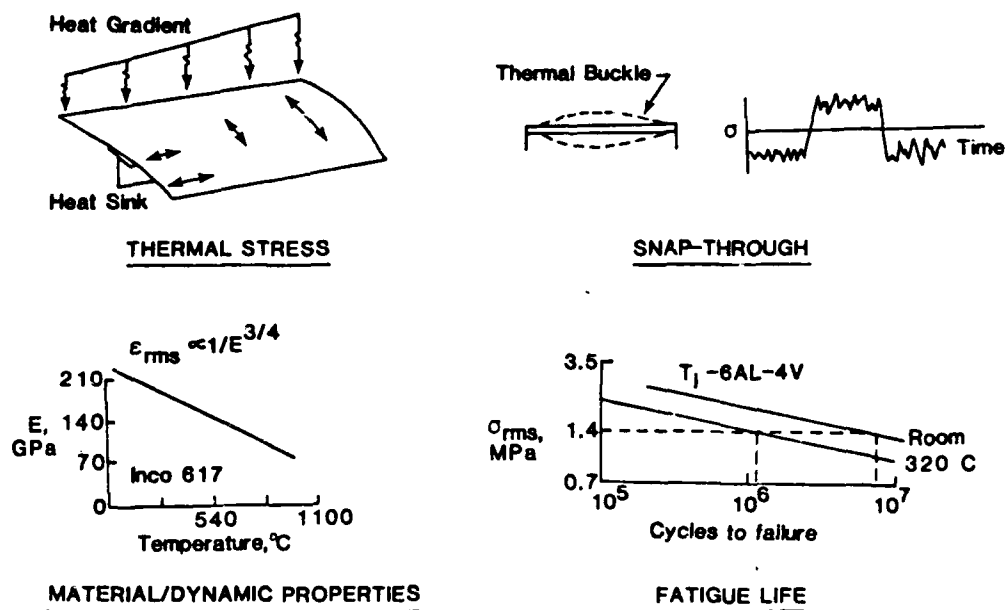


Figure 7.- Thermal Interactions with Acoustic Fatigue.

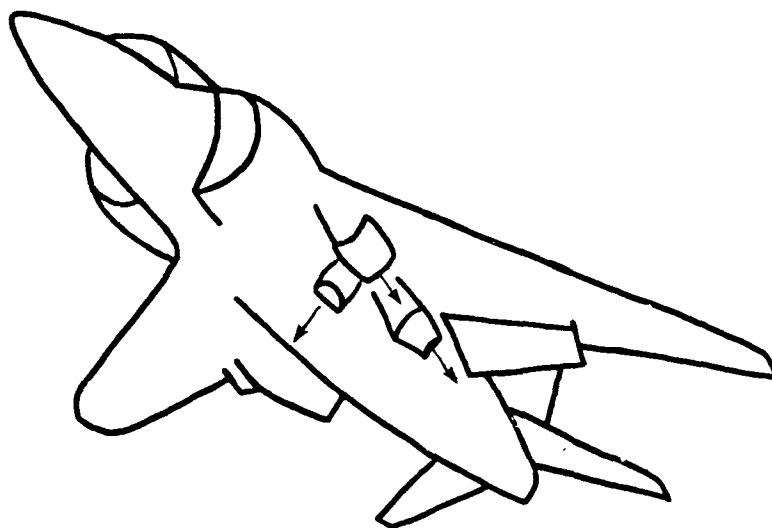
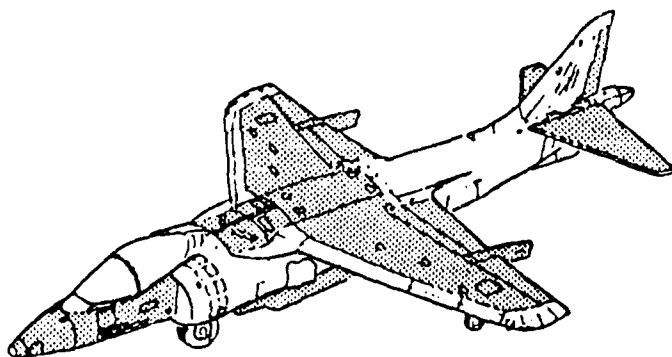


Figure 8.- Engine Exhaust Locations for VSTOL Aircraft.



AV-8B HARRIER II

Figure 9.- Composite Material Usage in Fighter Aircraft [16].

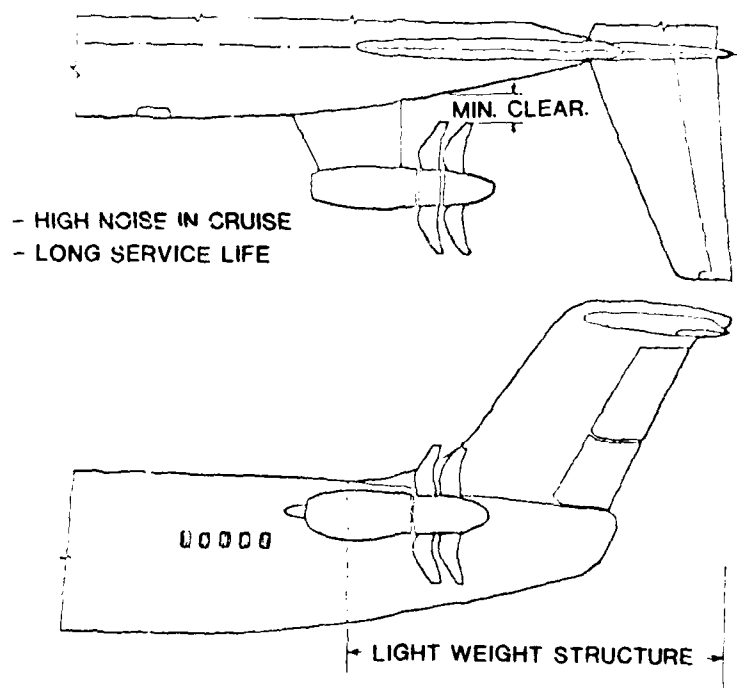


Figure 10.- Sonic Fatigue Considerations for Advanced Turboprop Aircraft.

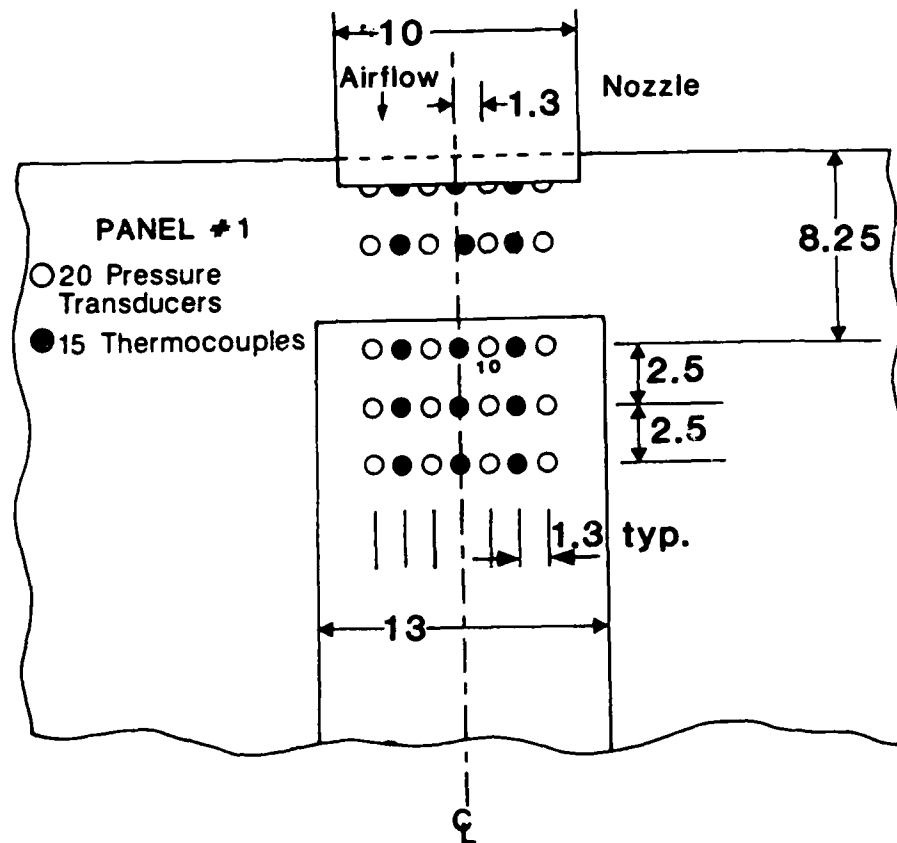


Figure 11.- Apparatus for Measuring Interaction of a Structure with a Supersonic Jet Plume. Dimensions in cm.

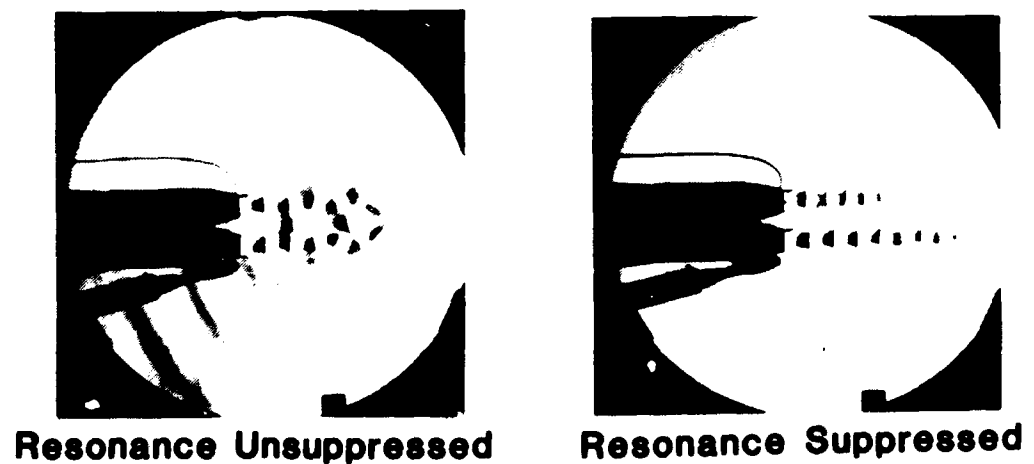


Figure 12.- Load Reduction by Suppression of Resonance of Twin Supersonic Plumes. $M_j = 1.3$ [22]

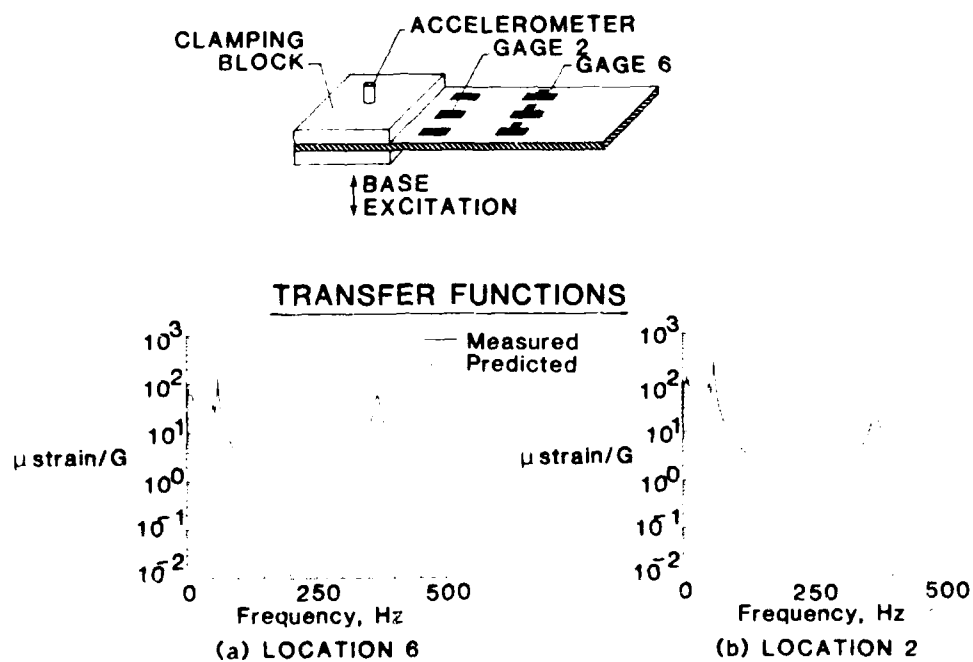


Figure 13.- Prediction of Random Dynamic Strain Response of a Steel Panel at Room Temperature.

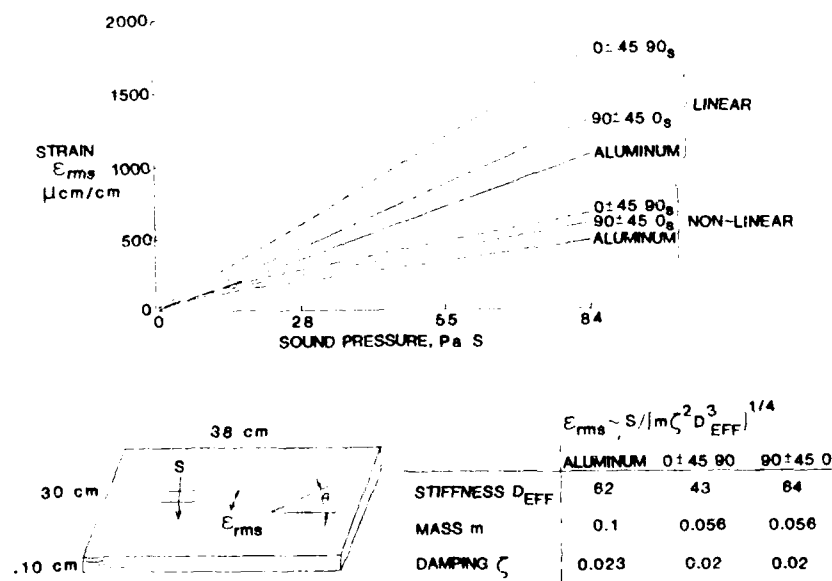


Figure 14.- Effect of Ply Layup Angle on Predicted Acoustic Response of a Graphite-Epoxy Panel [29].

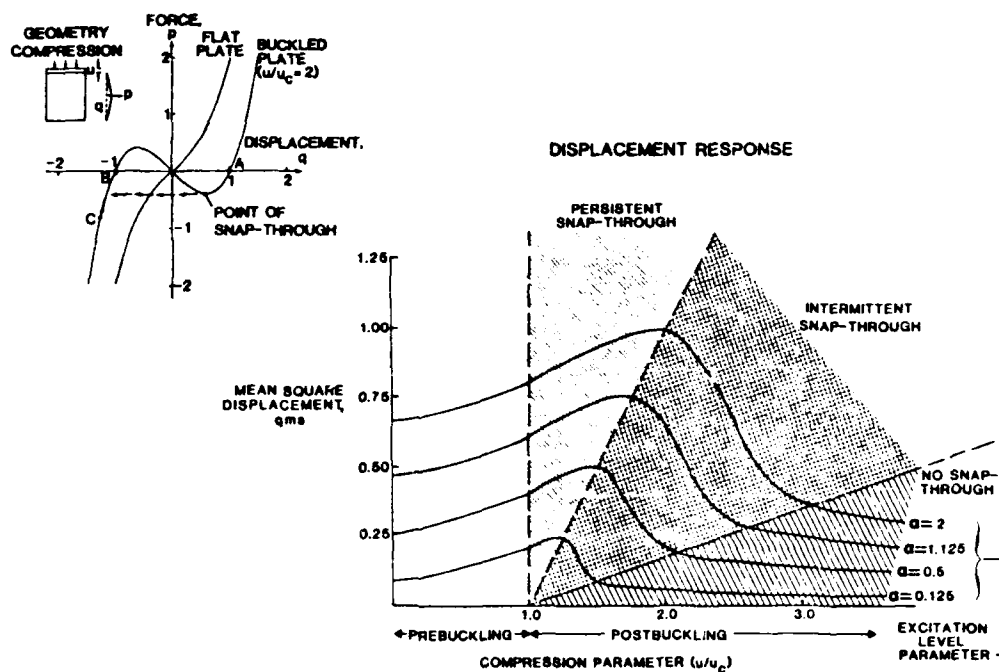


Figure 15.- Theoretical Snap-Through Characteristics of a Buckled Plate under Acoustic Excitation [34].

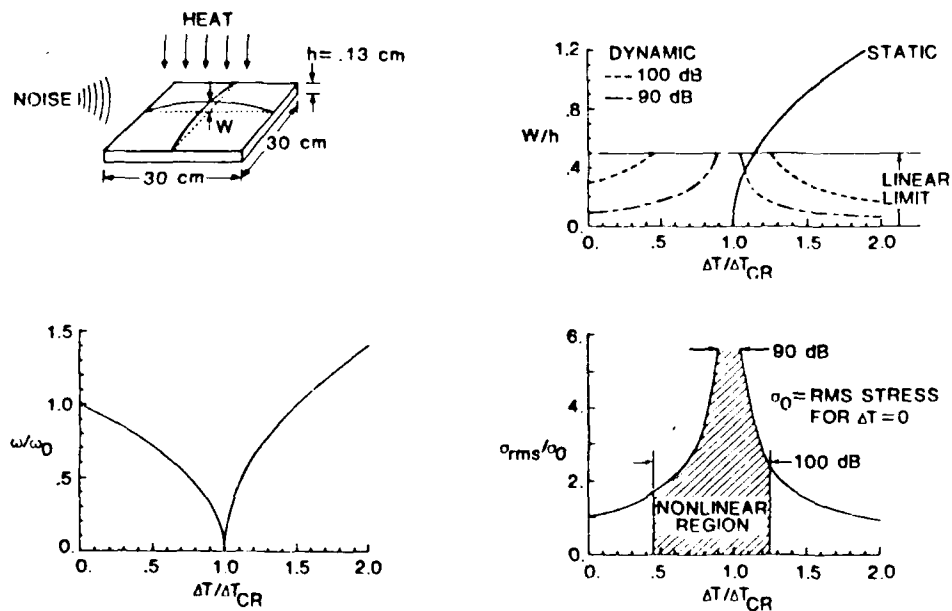


Figure 16.- Effects of Heating on the Acoustic Response of a Flat Panel Calculated using Finite Elements.



Figure 17.- Progressive Wave Thermal-Acoustic Fatigue Test Apparatus at
NASA Langley Research Center.

ACOUSTIC FATIGUE OF STIFFENED STRUCTURES

R. Vaicaitis and S.T. Choi

Department of Civil Engineering and
Engineering Mechanics
Columbia University

1. INTRODUCTION

Acoustic fatigue has become an important factor in structural design and safety of most aircraft and aerospace structures. These problems have been complicated by uncertainty of loads, stress prediction procedures, adverse thermal conditions and lack of proper fatigue damage models. Improved technology base is needed for fatigue live assessment of ASTOVL and STOL aircraft and the proposed new generation orbital and sub-orbital vehicles (NASP) for which experimental and theoretical data base is yet limited [1,2]. The complex acoustic and surface flow pressures acting on various critical components of these flight vehicles need to be prescribed as accurately as possible in order that proper thermal protection systems can be designed. Due to high acoustic loads and severe thermal environment, the structural response is often nonlinear requiring improved mathematical models for dynamic stress and fatigue life prediction [3,4]. Furthermore, with an increasing use of fiber reinforced composite materials, the need for improved solutions increases due to inherent large uncertainties of mechanical and thermal properties of these materials [5-8].

The surface protection systems of aerospace and aircraft structures are usually constructed from discretely stiffened panels or stiffened shells. High cycle fatigue failures have occurred in these structures with the majority of fatigue cracks appearing in the near vicinity of the stiffening element or the stiffener itself [5-9]. This paper presents an analytical study on dynamic response and fatigue damage of discretely stiffened titanium panels to turbulent boundary layer flow and acoustic loads. Preliminary study on the thermal effects due to engine exhaust gases and/or high speed aerodynamic surface flow is given. The objective of the present work is to determine stresses in the stiffened panels and the stiffeners. These results are used in conjunction with sonic fatigue data to estimate fatigue life of these stiffened structures. A generalized transfer matrix procedure is used to calculate dynamic stresses to random pressure inputs [10,11]. The inputs considered in this study include surface pressures corresponding to a truncated Gaussian white noise process, rocket or jet engine exhaust noise and supersonic turbulent boundary layer [12]. Stress response calculations and fatigue life predictions are obtained for several different loading and thermal conditions. Furthermore, expected damage is determined for different stress response peak distributions.

2. THEORY

This section briefly describes the general theory developed for dynamic stress and fatigue life predictions of discretely stiffened flat panels.

2.1 Problem Formulation

Consider a typical stiffened aircraft panel exposed to a turbulent boundary layer flow and/or acoustic pressure on one side and backed by a fluid filled cavity of finite dimensions on the other side as shown in Fig. 1. The dynamic response solution can be developed utilizing the transfer matrix procedure [10,11,13]. Modifications can be incorporated to include thermal, cavity pressure and nonsteady aerodynamic surface flow effects [11]. The basic approach in this development is to determine first the field transfer matrices for the loaded panel and point transfer matrices for the stiffeners. Then, incorporating boundary conditions at the edges of the panel these results can be combined to obtain the response solution for the entire stiffened panel.

The linearized equation of motion for a single panel bay located between any two arbitrary stiffeners is

$$D\nabla^4 w + c\dot{w} + m_p \ddot{w} = p^r(x,y,t) - p^c(x,y,0,t) + p^a(x,y,0,t) + p^T(x,y,t) \quad (1)$$

where $w(x,y,t)$ is the normal displacement to the panel surface, D , c , m_p are plate stiffness, damping and mass per unit area, p^r is the external random pressure (exhaust noise, turbulent boundary layer flow, etc.), p^c is the cavity back up pressure acting on the lower surface of the panel, p^a is the nonsteady aerodynamic pressure due to convected surface flow and p^T is the thermal pressure due to hot exhaust gases or/and aerodynamic heating. The pressure loading terms p^c , p^a and p^T are functions of the transverse displacement w . The solutions for cavity pressure and the nonsteady aerodynamic flow has been developed in ref. 11. If the cavity is sufficiently deep in comparison to panel dimensions, the acoustic back up pressure effects can be neglected [14,15]. However, for shallow cavities significant increase in panel modal frequencies is observed. Such an increase is mostly felt for odd modes. The nonsteady aerodynamic pressure could induce panel flutter when the surface speed reaches supersonic and hypersonic flow regimes [15,16]. The result is nonlinear deflection response and large stress gradients. As shown in refs. 16 and 17, the nonsteady aerodynamic flow effects must be included when panel flutter conditions are reached. At panel flutter, the nonsteady aerodynamic loads completely dominate panel response with random turbulent boundary layer flow pressure contributing only a small amount. In the present study, the cavity pressure and the nonsteady aerodynamic pressure are not included.

The thermal loading acting on the panel can be written as [18]

$$p^T(x,y,t) = -\frac{1}{1-\nu} \nabla^2 M_T + N_x \partial^2 w / \partial x^2 + N_y \partial^2 w / \partial y^2 + 2N_{xy} \partial^2 w / \partial x \partial y \quad (2)$$

where

$$M_T = \alpha E \int_{-h/2}^{h/2} T(x,y,z,t) z dz \quad (3)$$

$$N_x = \frac{Eh}{1-\nu^2} (\nu u / \partial x + \nu \partial v / \partial y) - \frac{N_T}{1-\nu} \quad (4)$$

$$N_Y = \frac{Eh}{1-\nu^2} (\partial v / \partial y + \nu \partial u / \partial x) - \frac{N_T}{1-\nu} \quad (5)$$

$$N_{xy} = \frac{Eh}{2(1+\nu)} (\partial u / \partial x + \partial v / \partial y) \quad (6)$$

$$N_T = \alpha E \int_{-h/2}^{h/2} T(x, y, z, t) dz \quad (7)$$

in which u and v are in-plane displacements corresponding to x and y coordinates, T is temperature distribution in the panel, and α, E, ν, h are thermal expansion coefficient, elastic modulus, Poisson's ratio and panel thickness, respectively. If a panel is restrained along the edges, $u = v = 0$ and $N_x = N_y = -N_T / (1-\nu)$, $N_{xy} = 0$. The in-plane stress resultants N_x and N_y could have a large influence on transverse displacements w and induce thermal buckling of the panel. If the in-plane boundaries are fixed, such a buckling state could be reached even for a relatively small increase in temperature T [18]. However, in the post buckling state further increase in temperature does not result in immediate failure of the panel. Only when thermal stresses reach plastic zone, permanent deformation and failure of the panel occur. For steady state conditions and constant temperature distribution through the thickness of the panel, $M_T = 0$ and $N_T = \alpha E h T$. Furthermore, if the in-plane stress resultants N_x and N_y are not included in the formulation, $p^T = 0$ and there is no effect on transverse displacement w . However, thermal stresses are not equal to zero for these thermal loading conditions.

The random pressure, p^r , acting on the panel arises from sources such as exhaust noise, turbulent boundary layer flow, oscillating shocks, etc. The random pressure data can be expressed in a cross-spectral density form

$$S_p(\xi, \eta, \omega) = S(\omega) R_x(\xi, \omega) R_y(\eta, \omega) \quad (8)$$

where R_x and R_y are spatial correlation coefficients, $S(\omega)$ is the spectral density of pressure fluctuations, and $\xi = x_1 - x_2$, $\eta = y_1 - y_2$ are spatial separations. The empirical expressions for parameters R_x, R_y and $S(\omega)$ are given in ref. 12 for attached and separated turbulence boundary layer flows. Similar expressions are available for random surface pressures generated by jet noise [19].

2.2 Solution Procedure

The response solution procedure in terms of generalized transfer matrix formulation has been developed in ref. 11. The panel shown in Fig. 1 is assumed to be simply supported along the edges normal to the stiffeners. Then, the beam modes along the coordinate x can be written as $Y_n = \sin(n\pi x/a)$. If the panel is taken to be clamped along these edges, a beam mode corresponding to clamped-clamped conditions can be used. Then, deflection response can be written as

$$w(x, y, t) = \sum_{n=1}^{\infty} q_n(y, t) Y_n(x) \quad (9)$$

where q_n are the generalized coordinates. Taking a Fourier transformation of equations (1) and (9), substituting equation (9) into equation (1), utilizing orthogonality and the procedures given in ref. 11, solutions for $\bar{q}_n(y, \omega)$ can be determined. Differentiating these solutions and using the relationship between the various derivatives of $\bar{q}_n(y, \omega)$, the solution can be written in a convenient state vector form $\{Z_n\} = \{\delta_n, \theta_n, M_n, V_n\}$ where $\delta_n, \theta_n, M_n, V_n$ are the components of deflection, slope, moment and shear, respectively. Such a formulation allows for a simple procedure to include any boundary conditions at $y = 0, L$ and to calculate stresses in the panel in terms of known quantities from the state vector. A detailed analysis on response of stiffened panels is given in refs. 10, 11 and 13.

2.3 Thermal Stresses

Thermal stresses in thin plates can be calculated from the equations given in ref. 18. If the edges of the plate are assumed to be restrained in the plane, the stress resultants $N_x = N_y = N_{xy} = 0$. Furthermore, for a uniform temperature distribution $M_T = 0$ and $N_T = \alpha E h T$. Then, the stresses at the plate surface ($z = \pm h/2$) reduce to

$$\sigma_{xx} = 6M_x/h^2 - E\alpha T/(1-\nu) \quad (10)$$

$$\sigma_{yy} = 6M_y/h^2 - E\alpha T/(1-\nu) \quad (11)$$

$$\tau_{xy} = -6M_{xy}/h^2 \quad (12)$$

where M_x, M_y and M_{xy} are the bending and twisting moments. The spectral density $S_{\sigma_{xx}}^s$ of the stress component σ_{xx} at the location s of the panel is

$$S_{\sigma_{xx}}^s(x, \omega) = \left(\frac{6}{h^2}\right)^2 S_{M_x}^s(x, \omega) + \left(\frac{E\alpha T}{1-\nu}\right)^2 \delta(\omega) \quad (13)$$

where $\delta(\omega)$ is the delta function and spectral density of the bending moment $S_{M_x}^s$ can be obtained from

$$S_{M_x}^s(x, \omega) = \sum_{n=1}^{\infty} \left(\nu^2 S_{M_n M_n}^s(\omega) + D^2(1-\nu^2)^2 (n\pi/a)^4 S_{q_n q_n}^s(\omega) - 2D\nu(1-\nu^2)(n\pi/a)^2 S_{q_n M_n}^s(\omega) \right) Y_n^2(x) \quad (14)$$

where the cross-spectral densities $S_{M_n M_n}^s, S_{q_n q_n}^s$ and $S_{q_n M_n}^s$ can be calculated

directly from the response state vector. Similar spectral density expressions can be written for stress components σ_{yy} and τ_{xy} . Then, the root mean square value of stress response is calculated from

$$RMS \left| S_{\sigma_{xx}}^s \right| = \left\{ \left(6/h^2\right)^2 \int_0^{\infty} S_{M_x}^s(x, \omega) d\omega + \left(\frac{E\alpha T}{1-\nu}\right)^2 \right\}^{1/2} \quad (15)$$

In these simplified expressions, stress response due to thermal conditions can be calculated independently from stress calculations due to external random loads. However, if the in-plane stress resultants N_x , N_y and N_{xy} are retained in the governing equation of motion, thermal loads have a direct effect on the characteristic roots and the response solution needs to be developed simultaneously for the total problem. As can be observed from equations (14) and (15), the root mean square value of the stress can be computed directly from known quantities in the state vector.

2.4 Fatigue Life

The key elements in predicting fatigue life of flight structures to random and thermal loads are detailed stress load spectra at a critical point of a structural component and reliable cumulative damage rules for random stress amplitudes. For a multidimensional stress state, the most damaging stress components must be known as well as the choice between the nominal stress and the actual load stress in complex geometries and connections. The load spectra is a function of mission requirements, flight conditions and flight duration. The information on threshold crossings and peak exceedances of stress time histories is needed for the development of stress load spectra. In addition to this information, stress fatigue data in the form of S-N diagrams are needed. Such data are usually obtained from coupon testing either under constant amplitude or random loading. Since stress response of surface protection systems is random, fatigue data from random tests should give the required information for life predictions. However, due to non-Gaussian response characteristics of structures under severe acoustic environment, proper interpretation and utilization of this data are needed when constructing analytical fatigue damage models. Most of the fatigue data for random loading is digested into a form of root mean square (rms) stress versus the number of cycles. For a Gaussian response, the rms stress is a useful quantity to obtain all the required statistics of the response process. The number of cycles in a random process has only a meaningful interpretation for a narrow band process where the response is dominated by a single peak at a prescribed frequency. When the structural response is multi-modal, "the number of cycles" parameter used in plotting the S-N diagrams loses its validity. For non-Gaussian inputs and/or nonlinear stress response, the stress amplitude distribution is non-Gaussian. In this case, not only the rms value but also higher order statistics are needed to characterize the random response process. Using the rms stress value as the sole parameter in predicting fatigue life could lead to erroneous results. Significantly different stress response time histories might have about the same value of rms stress while fatigue life resulting from these stress histories could be vastly different. Thus, alternative procedures are needed to develop damage prediction models. One approach might be to utilize the information of peak distribution of the non-Gaussian stress process and the S-N diagrams corresponding to a constant amplitude stress. To illustrate this procedure, let us consider a general case of a stationary Gaussian stress response process $x(t)$ with a zero mean. The peak distribution can be written as [20]

$$p_x(\xi) = \frac{(1-\alpha^2)^{1/2}}{\sqrt{2\pi} \sigma_x} \exp\left(-\frac{\xi^2}{2\sigma_x^2(1-\alpha^2)}\right) + \frac{\alpha\xi}{2\sigma_x^2} \left[1 + \operatorname{erf}\left(\frac{\xi}{\sigma_x\sqrt{2\alpha^2-2}}\right)\right] \exp\left(-\frac{\xi^2}{2\sigma_x^2}\right) \quad (16)$$

where the parameter α is defined as

$$\alpha = E[N_+(0)]/E[M_T] = \sigma_x^2 / \sigma_{\dot{x}} \sigma_{\ddot{x}} \quad (17)$$

where $E[N_+(0)]$ is the upcrossing rate at the stress at zero threshold level $\xi = 0$ and $E[M_T]$ is the expected number of total peaks. The σ_x^2 , $\sigma_{\dot{x}}^2$ and $\sigma_{\ddot{x}}^2$ are the variances of stress, stress velocity and stress acceleration, respectively.

Two limiting cases of peak distribution can be obtained for $\alpha = 1$ and $\alpha = 0$. A value of $\alpha = 1$ corresponds to a narrow band process and peak distribution reduces to the well-known Rayleigh distribution while for $\alpha = 0$ peak distribution is Gaussian [20,23]. The stress response is usually a narrow band process and peak distribution could be approximated by a Rayleigh distribution.

For a preliminary evaluation of fatigue damage of discretely stiffened panels considered in this study, a damage function $D(\tau)$ is defined for a time interval τ . As τ increases, the damage $D(\tau)$ increases until a value of unity is reached at which failure occurs. If $N(\xi)$ is defined as the number of stress cycles to failure, the total expected damage in the time interval τ can be written as [20,21]

$$E[D(\tau)] = E[M_T(\tau)] \int_{-\infty}^{\infty} (p_x(\xi)/N(\xi)) d\xi \quad (18)$$

where for constant amplitude loading, the expression for $N(\xi)$ can be obtained from the S-N diagram such that $N\xi^\lambda = B$ where λ and B are constants. It should be noted that with this approach the stress ratio $R = -1$. Then, from equations (17) and (18)

$$E[D(\tau)] = \frac{v_0^+ \tau}{B\alpha} \int_{-\infty}^{\infty} \xi^\lambda p_x(\xi) d\xi \quad (19)$$

where $p_x(\xi)$ is given in equation (16) and $v_0^+ = E[N_+(0)]$. For $\alpha = 1$, equation (19) gives

$$E[D(\tau)] = v_0^+ \tau (\sqrt{2} \sigma_x)^\lambda \Gamma(1 + \lambda/2)/B \quad (20)$$

where Γ denotes the Gamma function. For other values of α ($\alpha \neq 0$), equation (19) needs to be evaluated numerically. Furthermore, when the stress response process is non-Gaussian, expected damage can be calculated from equation (18) where now $p_x(\xi)$ is replaced with the appropriate peak distribution and $E[M_T(\tau)]$ is computed from [20]

$$E[M_T(\tau)] = - \int_{-\infty}^{\infty} dx \int_{-\infty}^0 x p_{xxx}(x, 0, x, t) dx \quad (21)$$

in which p_{xxx} is the joint density function of stress, stress velocity and stress acceleration. The variance of damage $D(\tau)$ can also be determined, but the procedure involves lengthy algebraic and numerical computations.

3. NUMERICAL RESULTS

For the calculation of stress response and fatigue damage of the stiffened panel shown in Fig. 1, simplified structures composed of a panel stiffened either with one or two stiffeners has been chosen. The panel and the stringers are made from 6AL-4V titanium material for which the elastic modulus, shear modulus and ultimate strength degradation is given in ref. 22. Response calculations were obtained for the following random inputs: truncated Gaussian white noise pressure, rocket exhaust noise and turbulent boundary layer pressure. The sound pressure levels of these inputs are given in ref. 11. The boundary layer pressure corresponds to separated supersonic flow where boundary layer thickness = 0.203 m, convection velocity = 813 m/sec and altitude = 24,390 m.

The numerical results were obtained for stiffened panels with dimensions $l_1 = l_2 = 0.208$ m, $a = 0.508$ m, $h = 1.52$ mm and $L = 0.416$ m. The thermal expansion coefficient $\alpha = 8.3 \times 10^{-6}$ m/m/°C. The stiffener geometric properties are taken to be the same as given in refs. 11 and 13. Structural damping is introduced by replacing the elastic and the shear moduli by $E(1 + i\eta)$ and $G(1 + i\eta)$ where $\eta = 0.02$.

The stress response spectral density of the stress component σ_{yy} in the panel is given in Fig. 3 for 120 dB Gaussian white noise input and room temperature thermal conditions. Stress response of σ_{xx} is about one half the value of σ_{yy} and the shearing stress τ_{xy} is relatively small [11]. The rms values of the stress response are also included in these figures. Panel stress response corresponding to different types of inputs is shown in Fig. 4. These results correspond to the middle of first panel bay. For the inputs chosen, supersonic turbulent flow induces the largest stresses in the panel. The turbulent flow was assumed to be fully correlated. The effect of flow correlation on panel response is illustrated in Fig. 5.

The total root mean square stress response (dynamic + static) is shown in Fig. 6 for two different temperature distributions in the panel. A uniform temperature distribution produces the largest thermal stresses. The temperature variations with coordinates x and y are illustrated in Fig. 6. As the temperature increases, the rms stress is dominated by the mean stress.

The expected fatigue damage was calculated from equations 19 and 20. Typical fatigue data parameters corresponding to constant amplitude stress tests were chosen for the titanium material under room temperature and elevated temperature conditions. These chosen parameters are $\lambda = 6$, $B = 1.631 \times 10^{21}$ (room temperature), $\lambda = 6$, $B = 1.181 \times 10^{20}$ (elevated temperature). The expected damage corresponding to two root mean square stress values is given in Fig. 7. These results are obtained from equation (20) where the peaks are distributed according to a Rayleigh distribution. The different rms stress values could reflect increase in dynamic response due to increasing input pressure levels. For example, under a uniform noise input of 120 dB, the rms largest stress component in the panel is 30.82 MPa. For larger inputs the stress response is nonlinear and time domain solutions of the nonlinear equations of motion would need to be performed [16] to determine dynamic stress and peak distributions. Thus, the $\sigma_s = 68.95$ MPa used in Fig. 7 is an assumed value merely to illustrate the effect on the expected fatigue damage. The expected damage in Fig. 7 is plotted vs the parameter $v_0 \tau$ (cycles).

Since the dominant response peak is at 140 cps ($v^+ = 140$ cps), about 10% of fatigue life is consumed in 4960 hrs ($\sigma_o = 34.48$ MPa, $T = 27^\circ\text{C}$), 317 hrs ($\sigma_o = 34.48$ MPa, $T = 316^\circ\text{C}$), 53 hrs ($\sigma_s = 68.95$ MPa, $T = 27^\circ\text{C}$) and 4.4 hrs ($\sigma_s = 68.95$ MPa, $T = 316^\circ\text{C}$). Failure ($E[D] = 1$) would occur at 45,635 hrs, 3373 hrs, 596 hrs and 40 hrs, respectively. These preliminary life estimates are based on the condition that mean stress has no effect on fatigue life. Size effects, geometric conditions and mean stress could have significant contributions to fatigue life [5-9].

To illustrate the effect of different peak distributions on fatigue life, the expected damage was calculated utilizing peak distribution given in equation (16). These results are shown in Fig. 8. As can be observed from these results, the effect is not large when different α values are chosen. It should be noted that even if $\alpha \neq 1$, the stress response is linear and Gaussian. For nonlinear and non-Gaussian stress response, peak distributions could be estimated from time domain solutions. Then, equations (18) and (21) are used to calculate fatigue damage.

4. CONCLUSIONS

Transfer matrix procedures were developed to predict stress response of discretely stiffened panels to random pressures. Stress response is dominated by the first few stiffened panel modes. For the conditions chosen in this study, the largest dynamic stresses in the panel are at the location where stiffeners are attached to the skin. Elevated temperatures induce large mean stresses when compared to the dynamic stress levels. Fatigue life is significantly shorter for structures at elevated temperature than for structures under room temperature conditions. To estimate fatigue life under severe acoustic and thermal environment, time domain solutions are needed for nonlinear stress response calculations and peak distributions.

5. REFERENCES

1. R.M. WILLIAMS 1986 Aerospace America. National Aero-Space Plane: Technology for America's future.
2. J.S. MIXSON and L.A. ROUSSOS 1987 NASA TM-89143, Acoustic Fatigue: Overview of Activities at NASA Langley.
3. C. MEI and K.R. WENTZ 1982 AIAA Journal, Vol. 20. Large Amplitude Random Response of Angle-Ply Laminated Composite Plates.
4. C. MEI and C.B. PRASAD 1985 NASA CR-176689. Nonlinear Random Response of Composite Panels.
5. M.J. JACOBSON 1972 AFFDL-TR-71-126. Advanced Composite Joints; Design and Acoustic Fatigue Characteristics.
6. I. HOLEHOUSE 1980 AFWL-TR-80-3019. Sonic Fatigue Design Techniques for Advanced Composite Aircraft Structures.
7. J. SOOVERE 1982 NADC-78169-60. Effect of Acoustic, Thermal and Shear Loading on Flat Integrally Stiffened Graphite/Epoxy Fuselage Panels.

8. J. SOOVERE 1984 The Second International Conference on Recent Advances in Structural Dynamics, University of Southampton, Southampton, England. Dynamic Response and Acoustic Fatigue of Stiffened Composite Structures.
9. F.F. RUDDER, Jr. and H.E. PLUMBLEE, Jr. 1975 AFFDL-TR-74-112. Sonic Fatigue Design Guide for Military Aircraft.
10. R. VAICAITIS and C.S. LYRINTZIS 1987 AIAA-87-0915, Dynamics Specialist Conference, Monterey, CA. Response of Discretely Stiffened Structures.
11. R. VAICAITIS and S.T. CHOI 1987 AIAA-87-2711, AIAA 11th Aeroacoustics Conference, Palo Alto, CA. Response of Stiffened Panels for Applications to Acoustic Fatigue.
12. C.F. COE and W.J. CHYU 1972 NASA TM X-62. Pressure Fluctuation Input and Response of Panels Underlying Attached and Separated Supersonic Turbulent Boundary Layer.
13. Y.K. LIN and B.K. DONALDSON 1969 Journal of Sound and Vibration, Vol. 10, No. 1. A Brief Survey of Transfer Matrix Techniques with Special Reference to Aircraft Panels.
14. E.H. DOWELL and H.M. VOSS 1963 AIAA Journal, Vol. 1. The Effect of Cavity on Panel Vibration.
15. E.H. DOWELL 1974 Aeroelasticity of Plates and Shells, Noordhoff International Publishing, Leyden, The Netherlands.
16. R. VAICAITIS, E.H. DOWELL and C.S. VENTRES 1974 AIAA Journal, Vol. 12, No. 5. Nonlinear Panel Response by a Monte Carlo Approach.
17. E.H. DOWELL 1970 AIAA Journal, Vol. 8, No. 3. Panel Flutter: A Review of Aeroelastic Stability of Plates and Shells.
18. B.A. BOLEY and J.H. WIENER 1966 Theory of Thermal Stresses, John Wiley and Sons, New York.
19. J.A. COCKBURN and A.C. JOLLY 1968 AFFDC-TR-68-2. Structural Acoustic Response, Noise Transmission Losses, and Interior Noise Levels of an Aircraft Fuselage Excited by Random Pressure Fields.
20. Y.K. LIN 1967 Probabilistic Theory of Structural Dynamics, McGraw-Hill, New York.
21. S.H. CRANDALL and W.D. MARK 1963 Random Vibration in Mechanical Systems, Academic Press.
22. E.F. BRUHN 1965 Analysis and Design of Flight Vehicle Structures, Tri-State Offset Co., Ohio.
23. S.O. RICE 1944-1945 Mathematical Analysis of Random Noise, Bell System Tech. J., 23 and 24. Reprinted in N. Wax (ed.), 1963, Selected Papers on Noise and Stochastic Processes, Dover, New York.

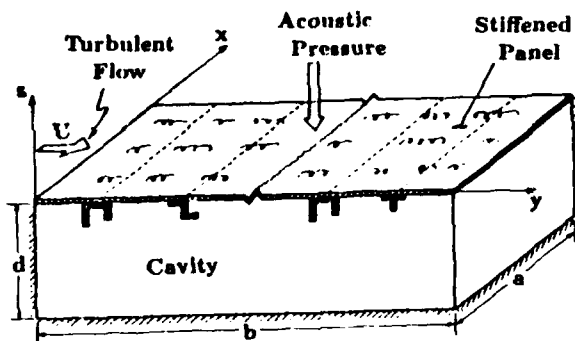


Figure 1. Problem Geometry

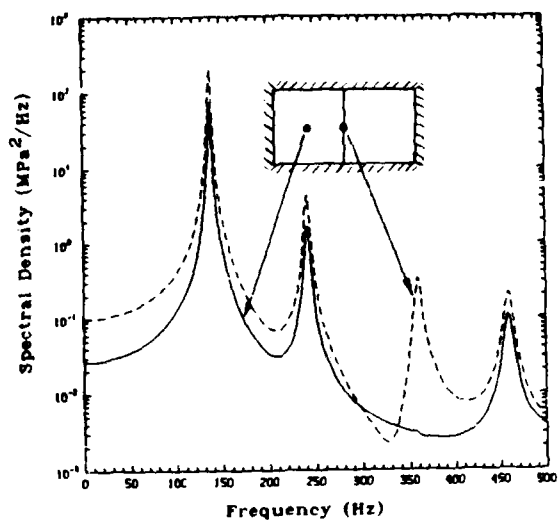


Figure 3. Spectral Density of Stress σ (—rms = 18.31 MPa, ---30.82 MPa)

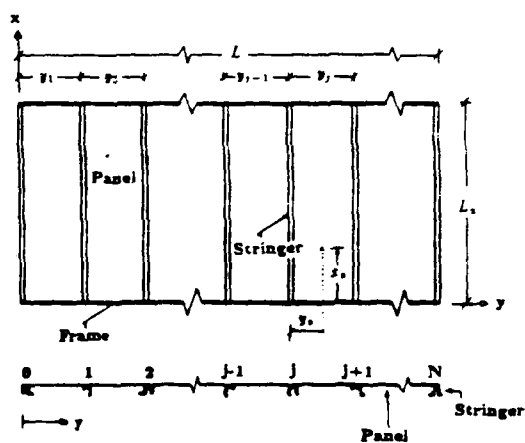


Figure 2. A Discretely Stiffened Panel

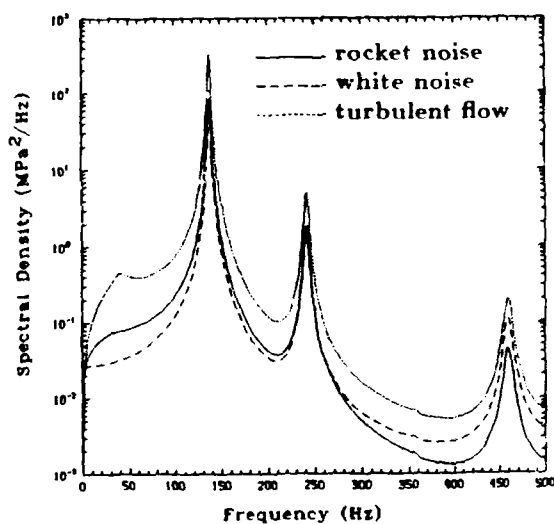


Figure 4. Spectral Density of Stress σ for Different Inputs (—rms = 22.77 MPa, ---18.31 MPa, ... 39.42 MPa)

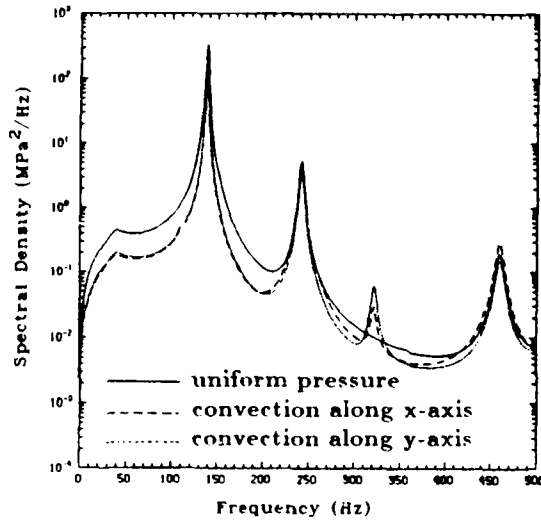


Figure 5. Spectral Density of Stress σ_y for Supersonic Turbulent Flow (—rms = 39.42 MPa, ---22.97 MPa, ...23.48 MPa)

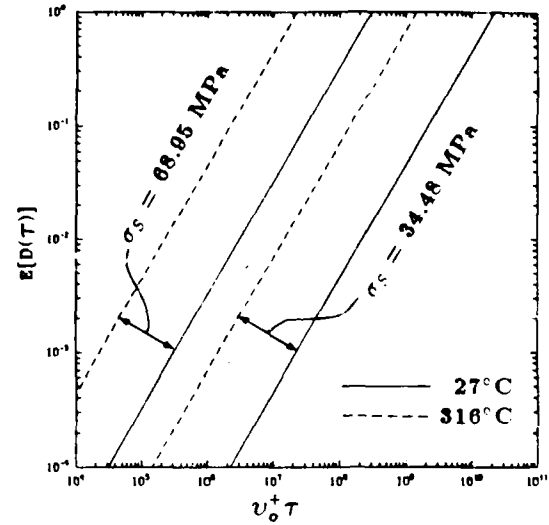


Figure 7. Expected Fatigue of a Stiffened Titanium Panel

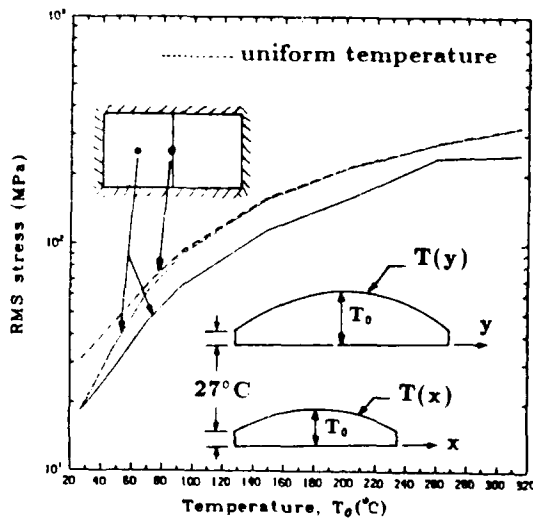


Figure 6. RMS Stress σ_y vs Temperature

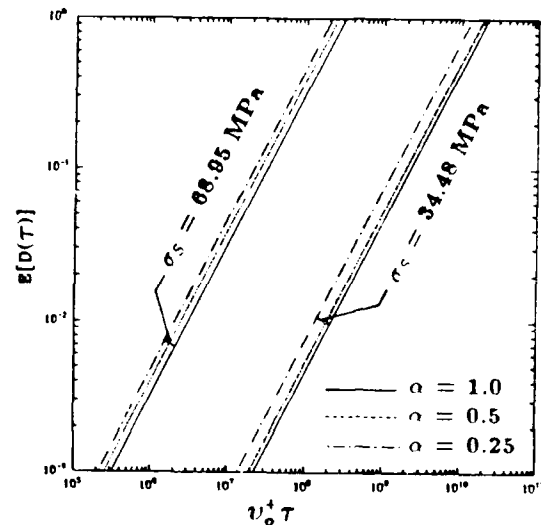


Figure 8. Expected Fatigue Damage for Different Stress Peak Distributions

AN ANALYTICAL INVESTIGATION INTO THE BEHAVIOUR OF COMPOSITES

N.S. Ferguson

Institute of Sound and Vibration Research
University of Southampton

1. INTRODUCTION

A recent study by Gibson [1] reviewed the analytical and experimental investigation into the dynamic properties of advanced composite materials during the period 1983-1986. Development of the modelling and prediction of laminated composite structures is still in progress and this study is in part a review of some of the analytical models available to the engineer and also an investigation into the use of such models in predicting dynamic properties of such materials due to temperature effects, internal damage due to fatigue, etc., and possible extensions in predicting the fatigue life of such composites. Macromechanical modelling of composites is of primary importance to design if one requires overall in-plane and flexural stiffnesses of laminated plates or shells of composite material. The standard approach is to consider the laminate as composed of thin orthotropic layers which may be of different thickness, material and orientations of their principle axes of orthotropy and to apply laminated plate or shell theory (see [2] for further details). Such an approach assumes one has predetermined the characteristics of a typical layer of the composite material possibly by experiment, practice or using a micromechanical model which describes the performance of the layer in terms of its fibre and matrix material. The overall properties are then determined using the plate theory or related analyses such as finite elements. The weaknesses inherent in this approach are twofold. Firstly one must know or be able to predict the behaviour in each individual layer which may require knowledge not just of the interlayer stresses or boundary conditions but also the internal physical behaviour within the layer and secondly the laminated plate theory may not accurately predict the overall behaviour if there is some measure of imperfect bonding between the layers, etc., as the theory assures continuity of displacement and rotations at all the interfaces.

Improvements can thus be obtained by taking account of the constituent fibre and matrix material and also using any known information concerning the composite such as delamination which is present. Advanced three dimensional finite element (F.E.) methods have been developed [3] using a single-cell model of a fibre in the matrix as a basic building block for the models and also it is possible to use standard finite elements to model the layers and releasing some of the interlayer constraints to allow for damage areas to find the direct and shear stresses [4]. Additional methods of analyses are discussed by Chamis [5] and Knight [6]. Simplified micromechanics [2] is a relative simple means of predicting the properties of the individual layers in terms of the fibre and matrix properties and will be applied in this paper in order to observe changes due to changes in the properties, introduction of damage and indicating how the overall behaviour of the composite can be evaluated.

2. THE SIMPLIFIED MICROMECHANICS EQUATIONS (S.M.E.)

The equations are derived using the principles of solid mechanics based on two assumptions, namely that each layer can resist in-plane loads in longitudinal, transverse and shear directions and that the layer, fibre and matrix behave in a linear elastic manner up to fracture. The convention is that the longitudinal direction (1) is along the fibres,

transverse (2) is transverse to the fibres and the in-plane shear is called intralaminar shear. Geometrically the sizes of fibres and interfibre spacing affect the fibre and resin volume ratios, k , or also known as volume fraction. Assuming the relevant parameters are given, some of which can be obtained by considering the geometry, simple equations relating the layer elastic constants and Poisson's ratio can be written in terms of the fibre (subscript f) and matrix (subscript m) properties. These are given in equations (1-6) for a layer with void volume ratio k_v .

$$\text{Longitudinal Modulus} \quad E_L = k_f E_{fL} + k_m E_m \quad (1)$$

(assuming fibre and matrix are subject to same strain)

$$\text{Transverse Modulus} \quad E_T = \frac{E_m}{1 - \sqrt{k_f} (1 - E_m/E_{fT})} \quad (2)$$

$$\text{Shear Modulus} \quad G_{12} = \frac{G_m}{1 - \sqrt{k_f} (1 - G_m/G_{f12})} \quad (3)$$

$$G_{23} = \frac{G_m}{1 - \sqrt{k_f} (1 - G_m/G_{f23})} \quad (4)$$

(3 through thickness of layer)

$$\text{Poisson's Ratio} \quad \nu_{12} = k_f \nu_{f12} + k_m \nu_m = \nu_{13} \quad (5)$$

$$\nu_{23} = \frac{E_T}{2G_{23}} - 1 \quad (6)$$

$$\text{Partial Volumes} \quad k_f + k_m + k_v = 1 \quad (7)$$

The derivation of equations (1-6) is performed by applying the "rule of mixtures" in conjunction with the assumptions made regarding the overall stress and strain behaviour of the composite. For unidirectional composites with orthotropic fibres reasonably good agreement has been obtained using the simplified micromechanics equations (S.M.E.) and the three dimensional finite element analyses [7], the differences possibly due to neighbouring fibre interactions and the Poisson effect through the thickness. Hence for unidirectional properties the S.M.E. can be applied and in this study these equations are applied to each layer of a laminated composite in order to apply laminate theory to obtain the overall bending and in-plane stiffnesses and strengths.

2.1 Thermal Properties using S.M.E.

Caruso [7] investigated the thermal expansion properties of composites using the S.M.E. equations hence these are applicable to

composite structures which are subject to temperature variations. If the composite is not constrained in a manner which would introduce thermal stresses, due to expansion with increased temperature, then the dynamic properties of the composite will still be governed by the Young's Moduli and Poisson's ratio values. White [8] investigated the variation of Moduli with temperature and found insignificant changes at temperatures well below the curing temperature of the carbon fibre composite. The similar material XAS 914C is investigated below at temperatures typical of its proposed working environment.

For a unidirectional composite composed of matrix and fibres with volume fraction ratios 0.6 for the fibre, 0.4 for the matrix with Young's Moduli 220 GPa for the fibres and 3.58 GPa for the matrix material at ambient temperature one can directly apply the S.M.E. equations (1-6) given knowledge on the variation of the individual Young's moduli [8]. These results are given in Table 1.

Table 1 Variation of Young's Moduli (longitudinal) of the composite against temperature.

Note: Individual measurements of resin and fibre moduli have been measured [8], the fibre showing no appreciable variation whilst the resin varies between +45% to -26% of its ambient temperature value. These results have been applied to calculate E for the composite, with E_{FL} the fibre modulus taken as 220 GPa throughout.

Temperature °C	Young's Modulus (matrix) E_m GPa	Young's Modulus (composite) E_c GPa	% Variation E_c from resin temperature (20°C)
-60	5.19	134.076	+0.483
0	3.93	133.572	+0.105
20	3.58	133.432	0
60	3.11	133.244	-0.141
120	2.72	133.088	-0.258

Generally because of the dominance of the fibre properties, $E_f \gg E_m$, and as the fibre is very nearly invariant over the temperature range the overall properties of the composite show very small if not insignificant variation. Clearly this is not the case at high enough temperatures where the matrix material is no longer solid and fibre debonding occurs.

2.2 Effect of Moisture on Composites using S.M.E.

For many applications the composite cannot be assumed to be in a moisture free environment and over a period of time an amount of moisture will be absorbed into the composite. Typically designers consider the case of a composite with 1% absorbed moisture by laminate weight at elevated temperatures, the absorption of moisture at room temperature being small. If one requires a prediction of the moduli of the composite at these temperatures with moisture absorbed using S.M.E. one is required to obtain the volume fractions of fibre to resin to moisture.

An initial approach is to assume that the composite absorbs the moisture with no overall change in volume V and hence the additional mass of the composite is given as $\nu_w \rho_w V$ where ν_w, ρ_w are the volume fraction and density of the moisture. Assuming $\rho_c = \nu_f \rho_f + \nu_m \rho_m$ when dry, assuming no void, then

$$1\% \text{ change in mass } M = \frac{1}{100} \times \rho_c V = \nu_w \rho_w V$$

$$\nu_w = \frac{1}{100} \frac{\rho_c}{\rho_w} \quad (8)$$

If ν_f, ν_m remain in fixed ratio and

$$\nu_f' + \nu_m' + \nu_w = 1 \quad (7)$$

in wet condition, primes denoting volume fractions, then

$$\left[\frac{\nu_f}{\nu_m} \right] = \frac{\nu_f'}{\nu_m'} \quad \text{and} \quad \nu_f' = \frac{1 - \nu_w}{(1 + \nu_m / \nu_f)} = \nu_f (1 - \nu_w) \quad (9)$$

$$\nu_m' = \frac{\nu_m (1 - \nu_w)}{(\nu_f + \nu_m)} = \nu_m (1 - \nu_w) \quad (10)$$

for XAS 914C with 1% moisture, $\nu_f \approx 0.6$, $\nu_m \approx 0.4$ one finds at ambient temperatures the ratio of the longitudinal moduli is

$$\frac{E_{\text{dry}}}{E_{\text{wet}}} = 1.0166$$

using above, in practice

$$\frac{E_{\text{dry}}}{E_{\text{wet}}} = \frac{130 \text{ GPa}}{126 \text{ GPa}} = 1.032$$

In particular, the theoretical prediction for E_c with 1% moisture predicts a decrease in E_c from ambient of $\lambda(\rho_c / \rho_w)\%$ whilst in practice the above results show for a 1% moisture level the theoretical value decreases by 1.63% versus a decrease in 3.2% measured. This leads to a conclusion that for modelling the effect of moisture it is necessary to consider more

than just the effect on the volume ratios of the composite.

3. THE REDUCTION IN THE MECHANICAL PROPERTIES DUE TO FIBRE BREAKAGE AND DEBONDING

The main problem in evaluating the overall properties of a composite due to fibre breakage or debonding is knowing precisely the area and amount of damage. If the area is well defined then to model using F.E. methods one can relax the constraints in the model corresponding to the damaged area, i.e. introduce an area of breakage or debonding by introducing elements with no elastic strength. Alternatively it is proposed that one can use the S.M.E. approach which may not be specific to the position of the damaged area but may still in a statistical sense still give good approximations to the overall strength of the damaged composite.

The theoretical problem of a single fibre in a cylinder of matrix material has been studied by Cox [9]. The effective modulus E_{eff} of such a simple element of the composite can be written in terms of E_f , the Young's Modulus of the fibre, $2a$ the length of the fibre and r_f, r_m the radius of the fibre and matrix cylinder as

$$E_{eff} = E_f \left[1 - \frac{\tanh(\alpha a)}{(\alpha a)} \right] \quad (11)$$

where

$$\alpha^2 = \frac{2\pi G_m}{l \eta (r_m/r_f)} \quad \text{assuming } r_m > r_f \quad (12)$$

and G_m the shear modulus of the matrix. For comparison between the above theoretical result and S.M.E. one can consider the simple problem of a broken fibre embedded in the matrix. For simplicity, the model is idealised and drawn as in Figure 1. It consists of three lengths of fibre in matrix material.

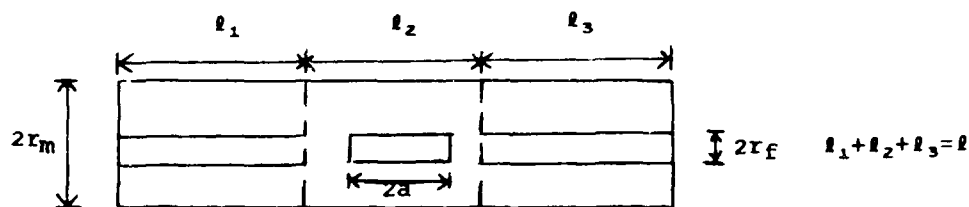


Figure 1. Representation of broken fibre embedded in matrix.

Applying equations (11) and (12) one can find the effective modulus for the middle section and then consider the overall modulus of the single fibre in the matrix over the whole length l . In the longitudinal direction

$$E_{\text{OVERALL}} = E_L \left[\frac{l}{(l-l_2) + \frac{l_2}{1 - \frac{\tanh(\alpha a)}{\alpha a}}} \right] \quad (13)$$

E_L = Young's Modulus for the unbroken fibre in the matrix. If (αa) large, i.e. fibre nearly continuous, then $E_{\text{OVERALL}} \rightarrow E_L$. If (αa) small, i.e.

$$\left[1 - \frac{\tanh(\alpha a)}{(\alpha a)} \right] \rightarrow 0 \quad \text{which implies } E_{\text{OVERALL}} \rightarrow 0,$$

in reality one would expect properties for the middle section to be dominated by the moduli of the matrix material which is much smaller than the fibre moduli.

Consider the S.M.E. approach which only requires E_f, E_m and k_f, k_m for the longitudinal modulus. One must make an assumption concerning the variation of k_f, k_m with the fibre length in the middle section.

If fibre is continuous and there is no void in the composite, then

$$\frac{k_f}{k_m} = \frac{r_f^2}{r_m^2 - r_f^2} \quad \text{and } k_f + k_m = 1 \quad (k_v = 0)$$

hence

$$k_f = \left[\frac{r_f}{r_m} \right]^2 \quad (14)$$

If fibre breakage occurs then effectively k_m remains unaltered but one can consider a reduction in k_f . If the broken fibre is as given in Figure 1, then the fibre volume fraction k_f' is

$$k_f' = \frac{(l-l_2+2a)}{l} k_f = \left[1 - \frac{l_2-2a}{l} \right] k_f$$

$$\text{let } \Delta l = l_2 - 2a$$

hence using S.M.E. one has

$$\begin{aligned} E_2 &= k_f' E_f + k_m E_m \\ &= \left[1 - \frac{\Delta l}{l} \right] E_f + k_m E_m \end{aligned}$$

typically for composites $E_f \gg E_m$ so

$$E_L \approx \left[1 - \frac{\Delta l}{l} \right] E_f \quad (15)$$

$$\text{or } E_L \approx k_f' E_f \quad (16)$$

i.e. a direct linear relationship as a fraction of damaged length of fibre. In many applications where many fibres are broken it may be possible to use expression (16) as a first approximation.

Debonding generally can be described by the length over which the fibre and matrix material are unconnected although in most cases of debonding the fibre and matrix becomes debonded by cracks in the matrix material which may not occur over all the surface of the fibre. A vigorous analysis for the stiffness reduction due to fibre breakage is given by Steif [10]. Assuming a dilute concentration of broken fibres it is possible to consider the model of a single broken fibre using shear lag analysis and then obtain the sectionally averaged longitudinal stress. In the debonded region the shear stress is related to the normal stress by a Coulomb friction law. In order to calculate the stiffness reduction it is possible to approximate the full shear lag analysis by a model which is generally valid except for very short or very long debonds. The approximate result is

$$E_{\text{reduced}} = \frac{E_0}{1 + \rho \left[\frac{2l_d}{L} \right] \frac{E_f}{E_c}} \quad (17)$$

E_0	=	Original modulus of the undamaged composite
$2l_d$	=	Length of debond
E_f	=	Young's modulus of fibre
E_c	=	Young's modulus of the fibre in a cylinder of radius b
	=	E_0 if dilute fibres
L	=	Distance between planes containing fibre breaks
ρ	=	$(a/b)^2$
(a/b)	=	Ratio of radius of broken fibre to radius of unbroken composite surrounding broken fibre
E_{reduced}	=	Reduced Young's Modulus of composite containing fibre breaks

If fibre breaks are very dilute, i.e. $\rho \rightarrow 0$ then

$$E_c \rightarrow E_0$$

$$E_{\text{reduced}} = E_0 \left[1 + \rho \left[\frac{2l_d}{L} \right] \frac{E_f}{E_0} \right]^{-1} \quad (18)$$

If breaks in one plane only then

$$\frac{2l_d}{L} = \frac{\Delta L}{L}$$

as used in expression (15) and approximately,

if $\rho \left[\frac{2l_d}{L} \right] \frac{E_f}{E_c}$ small, one has

$$\begin{aligned} E_{\text{reduced}} &= E_o \left[1 - \rho \frac{\Delta L}{L} \frac{E_f}{E_o} \right] \\ &= E_o - \rho \frac{\Delta L}{L} E_f \end{aligned} \quad (19)$$

$$\text{and } \rho = (a/b)^2 = A_{fB} \left[\frac{L}{2l_d} \right] \quad (20)$$

where A_{fB} = fibre volume fraction for broken fibres

Hence

$$E_{\text{reduced}} = E_o - A_{fB} E_f$$

$$\text{i.e. } E_{\text{reduced}} = E_f (k_f - A_{fB}) + k_m E_m \quad (21)$$

using "Rule of Mixtures" assuming no void, which is the same result using the simple "Rule of Mixtures" result with a reduction in the fibre volume by the volume of the broken fibres.

For accurate prediction of the behaviour of the composite due to debonding one would require the full shear-lag analysis performed by Steif [10] as it takes into account the displacements caused by fibre breaks for short debond lengths. At high debond lengths there is also the additional transfer of the load back to the broken fibre due to friction which must also be included with the shear-lag analysis.

4.0 FATIGUE DAMAGE MECHANICS

Two questions which arise are what is the effect of a damaged area of the composite on the overall properties of the composite and secondly, given a composite in a dynamic environment, how will the area of damage change. The answer to the first question lies in a detailed knowledge of the damage and using the approaches in Section (3) it is possible to describe the overall changes in material properties on a global level although invariably the area of damage is irregular in shape and size and for detailed accurate information one would be required to model the composite using numerical analyses. An alternative approach which has been attempted to give a first order approximation is to consider a plate with a circular area of damage. The damage area can be described as an area of equivalent size as the damage and globally possessing the material properties of the damage which can be specified for the cases of delamination, fibre breakage, debonding, etc. Given that the area is small relative to the size of the plate and is located inside the plate far enough away from the outer edges then one can consider the solution for the static properties of the damaged plate in terms of the solution of a plate containing a circle of different material [12]. This approach is at present being investigated in order to give a first approximation to the solution of a damaged composite plate and statistical confidence limits will be given for the solution.

The question of how damage varies as a function of loading, stress-reversals, temperature, etc., has been attempted by Poursartip et al [11]. The damage D was monitored by a change in modulus of the composite E due to delamination.

The following relationships were used.

$$E = E_0 g(D) \quad (22)$$

D = Damage
 E_0 = Undamaged composite Young's Modulus
 $g(D)$ = Function which related damage with change in modulus, in particular for delamination [13]

$$E = E_0 + (E^\lambda - E_0) A/A_0 \quad (23)$$

E^λ = Modulus of completely delaminated composite
 A/A_0 = Fraction of area of plate delaminated, expression (23) valid under static testing. Poursartip et al [11] assumed a variation of damage D with N , the number of stress cycles at stress amplitude R , cyclic stress range $\Delta\sigma$ as a function f .

$$\frac{dD}{dN} = f(\Delta\sigma, R, D) \quad (24)$$

On substituting (22) into (24) one obtains

$$f = \frac{1}{E_0} \frac{dE}{dN} \bigg/ g'(g^{-1}(E/E_0)) \quad (25)$$

' denotes differentiation of the function. Assuming a simple relationship such as (23) for E and measuring dE/dN one can obtain a function with which one can calculate the fatigue life of the specimen (i.e. when $D=1$), however, that is defined. Expression (23) is valid only for very specific cases where delamination occurs in one layer and the composite is unidirectional hence the need for a general function $g(D)$ for any composite lay-up.

It should also be possible to include the other effects such as temperature, moisture content, etc., by expanding f as a function of more than just three variables but as can be seen from Section (2) and (3) of this study more work is required.

5.0 GENERAL CONCLUSIONS

This study has been conducted in order to obtain first order global estimates of composite behaviour and properties for design engineers interested in environmental effects and fatigue life predictions. To a certain extent this has been achieved using S.M.E. although as can be seen from some of the results thermal effects are minimal whilst moisture content effects are possibly non-linear and further analysis is required for this latter case at elevated temperatures. Increased knowledge of the damage mechanisms is necessary in order to model simply the effects of damaged composites and it is envisaged that this study will be continued in the statistical average model for the damage. Ongoing experimental research on fatigue testing will enable the functions $f(\Delta\sigma, R, D, T, \dots)$ to be determined and likewise comparison will be possible by theoretical predictions of $f(\Delta\sigma, R, D, T, \dots)$ as knowledge of the damage mechanisms becomes quantified.

REFERENCES

1. R.F. GIBSON 1981 Shock Vibration Digest. Dynamic Mechanical Properties of Advanced Composite Materials and Structures: A Review.
2. G.C. SIH and E.P. CHEN (Editors) 1981 Martinus Nijhoff Publishers, The Hague, Netherlands. Mechanics of Fracture 6, Cracks in Composite Materials.
3. J.J. CARUSO 1984 NASA T.M. 83729, NASA Lewis Research Center, Cleveland, Ohio. Application of Finite Element Substructuring to Composite Micromechanics.
4. R.C. DREW 1988 PhD Thesis, ISVR, University of Southampton. An Investigation into Damage Propagation in Carbon-Fibre Reinforced Plastic Composite Materials.
5. C.C. CHAMIS 1984 SAMPE Quarterly, Vol 15(3), 14-23. Simplified Composite Micromechanics Equations for Hygral, Thermal and Mechanical Properties.
6. M. KNIGHT 1982 J of Composite Materials, Vol 16(2), 153-159. Three Dimensional Elastic Moduli of Graphite/Epoxy Composites.
7. J.J. CARUSO and C.C. CHAMIS 1986 J of Composites Technology and Research, Vol 8(3), 77-83. Assessment of Simplified Composite Micromechanics using Three-Dimensional Finite Element Analysis.
8. S.C. GALEA 1988 MPhil Dissertation, University of Southampton, (to be published).
9. H.L. COX 1952 British Journal of Applied Physics, Vol 3, 72-79. The Elasticity and Strength of Paper and Other Fibrous Materials.
10. P.J. STEIF 1984 J of Composite Materials, Vol 17, 153-172. Stiffness Reduction Due to Fiber Breakage.
11. A. POURSATIP, M.F. ASHBY and P.W.R. BEAUMONT 1986 Composites Science and Technology 25 (1986), 193-218. Fatigue Damage Mechanics of a Carbon Fibre Composite Laminate: I-Development of the Model.
12. D.S. DUGDALE and C. RUIZ 1971 McGraw-Hill, London. Elasticity for Engineers.
13. T.K. O'BRIEN 1982 Proc. 1982 Conf. Experimental Mechanics, Hawaii, 236-243. The Effect of Delamination on the Tensile Strength of Unnotched Quasi-isotropic Graphite/Epoxy Laminates.

THE INFLUENCE OF SNAP-THROUGH MOTION ON THE RANDOM RESPONSE OF CURVED PANELS TO INTENSE ACOUSTIC EXCITATION

C. F. Ng

Resident Research Associate
NASA Langley Research Center
Hampton, Virginia, U.S.A.

1. SUMMARY

Assuming a single-mode transverse displacement, a simple formula is derived for the transverse load-displacement relationship of a plate under in-plane compression. The formula is used to derive a simple analytical expression for the non-linear dynamic response of postbuckled plates under sinusoidal or random excitation. The highly non-linear motion of snap-through can be easily interpreted using the single-mode formula. Experimental results are obtained using a buckled aluminum panel using discrete frequency and broadband excitation of mechanical and acoustic forces. Some important effects of the snap-through motion on the dynamic response of the postbuckled plates are described.

2. INTRODUCTION

A typical aircraft panel can be initially curved or subsequently curved due to mechanical or thermal stresses. If a plate is curved, the static and dynamic behavior in the transverse direction can be highly nonlinear. The nonlinearity can take the form of a hardening-spring, a softening-spring or an instability condition with snap-through motion.

The acoustic responses of cylindrical panels are found to be greatly affected by dynamic snap-through motion¹ and better understanding of snap-through motion is needed to predict the dynamic response of curved panels. Theoretical and experimental results of large amplitude vibration of postbuckled plates under sinusoidal excitation were obtained by Yamaki and Chiba², however, snap-through motion was not studied.

The characteristics of snap-through motion in a postbuckled beam under sinusoidal excitation were studied by Tseng and Dugundgi³. A theoretical study of the random response of an initially curved beam including snap-through motion was done by Seide⁴. However, a thorough and straight-forward understanding of the nonlinear behavior (particularly snap-through motion) of general curved plates is difficult to gather from the previous research results. The present study was conducted to fill this gap using a single-mode analysis method and experimental investigation with sinusoidal and random excitation forces on a buckled plate.

3. GENERAL FORMULAE FOR NONLINEAR BEHAVIOR OF PLATES

Assuming an appropriate shape function for the transverse displacement of a plate and using the Rayleigh-Ritz procedure of formulation, the nonlinear equation for equilibrium in the transverse direction is obtained. The detail steps in deriving the following formulae are found in ref. 5.

3.1 Equation for Equilibrium in the Transverse Direction

For a plate under uniaxial compression with uniform edge displacement, the relationship between modal displacement and modal force for the buckling mode is given in ref. 5.

$$q^3 - Rq = p \quad (1)$$

where q , nondimensional displacement parameter, $= Q/Q_p$

Q , modal displacement

Q_p , value of Q at $R=1$

$R = \lambda - 1$

$\lambda = u/u_c$ (the compression parameter)

u = inplane edge shortening displacement

u_c = value of u at which buckling starts

p = nondimensional force parameter, $= P/KQ_p$

P = externally applied modal force

K = linear modal stiffness of the flat plate.

The above formula is applicable to any plate of any boundary condition and aspect ratio if there is no coupling between the various modes. A plot of p versus q for various values of R is shown in Figure 1. From Figure 1 regions of hardening and softening spring behavior are found and there are also regions of negative stiffness, (e.g. between A and B). Notice that for $R = 1$, dynamic motion starting from C will pass through A and B and end up at C.

Static equilibrium positions q_0 are found by putting $p = 0$ in equation (1) and correspond to the points where the curve crosses the q -axis in Figure 1. Note that for $R > 0$, there are three equilibrium values of q ; $q_0 = \sqrt{R}$, $-\sqrt{R}$ and zero. The last value, zero, is an unstable position as the stiffness is negative. We can rewrite equation (1) as

$$q^3 - q_0^2 q = p \quad (2)$$

3.2 Undamped Free Vibration of Postbuckled Plate

From (1) the nondimensional force parameter p for the inertia force is $M\ddot{Q}/KQ_p$ where M is the modal mass. Since $K = \Omega^2 M$ where Ω = resonance circular frequency of the flat plate, and $q = Q/Q_p$, the inertia force parameter is \ddot{q}/Ω^2 .

By adding the inertia force to eq. (2) the free vibration equation is obtained as

$$\frac{1}{\Omega^2} \ddot{q} + (q^3 - q_0^2 q) = 0 \quad (3)$$

With the substitution $\dot{q} = \dot{q} \, dq/dq$, equation 3 can be integrated to obtain \dot{q} . For the initial conditions $\dot{q}(0) = 0$ and $q(0) = q_s$ ($q_s > q_0$) at $t = 0$ the equation can be written

$$\dot{q}^2 = \frac{\Omega^2}{2} (q_s^2 - q^2) (q_s^2 + q^2 - 2q_0^2) \quad (4)$$

Solving the expression for \dot{q} (4) by numerical integration (see ref. 5), time histories for the free vibration of various initial value of q ($q_0 = 1$) were determined and are shown in figure 2. When $q_s < \sqrt{2}$, it can be seen that the period of vibration increases as initial amplitude increases. When $q_s = \sqrt{2} = 1.414$, the period is theoretically infinite as it takes infinite time to approach zero. However, when $q_s = \sqrt{2}$, the period decreases

with increase of amplitude. The displacement also passes through both equilibrium positions, $q = 1$ and $q = -1$, thus indicating snap-through motion. The change of mean position is q_0 (from 1 to 0). Also the r.m.s. value is approximately 1 (the static value) when $q_s = 1.5$. Essentially, the postbuckled plate shows softening spring behavior initially and after snap-through motion accompanied by a change of equilibrium position it shows a hardening spring behavior.

3.3 Random Vibration

The method of equivalent linearization can be used to solve the nonlinear forced vibration equation with damping coefficient of Ω :

$$\frac{1}{\Omega^2} \ddot{q} + 2\frac{\zeta}{\Omega} \dot{q} + (q^3 - q_0^2 q) = p \quad (5)$$

The mean square displacement of a buckled plate, $\langle q^2 \rangle$ due to white noise excitation with spectral density S_{pp} can be obtained for small and large magnitudes (derived in ref. 5).

For small excitations $\alpha < 0.45q_0^4$ ($\alpha = \pi\Omega S_{pp} / 4\zeta$, α is a nondimensional force parameter), there is a no snap-through in the motion and

$$\langle q^2 \rangle = (-q_0^2 + \sqrt{q_0^4 + 3}) / 3, \text{ and } \bar{q} = q_0 \quad (6)$$

For $\alpha > 2q_0^4$ there is persistent snap-through motion in almost every cycle of oscillation and

$$\langle q^2 \rangle = (q_0^2 + \sqrt{q_0^4 + 12\alpha}) / 6, \text{ and } \bar{q} = 0 \quad (7)$$

For $0.45q_0^4 < \alpha < 2q_0^4$ snap-through motion is intermittent, the mean position as well as the mean square values are very unsteady. However, the mean square value can be taken approximately from interpolation between the two end points -- the point of no snap-through and persistent snap-through motion.

From eq. (6) and (7), for $q_0 = 1$, the variation of $\langle q^2 \rangle$ with the excitation parameter α for different values of compression parameter $\lambda(u/u_c)$ is shown in figure 3. The rate of increase of response with excitation is highest when intermittent snap-through motion starts. When persistent snap-through motion is attained, the response increase much more slowly with increases in excitation, showing hardening spring behavior.

From figure 3 and equation (6) and (7), the variation of response with compression parameter for various levels of excitation are plotted as shown in figure 4. For a given excitation level, the response increases with increases in compression as it approaches the buckling point. After initial postbuckling, persistent snap-through occurs and the response continues to increase until a certain point for which only intermittent snap-through motion can be induced. After that point, the response decreases with further increases in compression. The point of maximum displacement corresponds to the point for which the excitation is just sufficient for persistent snap-through motion. Also, the point of maximum response occurs at increasingly greater plate curvatures, or larger values of u/u_c ,

as the excitation level increases. These trends have also been predicted in a qualitative description by Jacobson⁶.

4. EXPERIMENTAL RESULTS WITH ELECTROMAGNETIC SHAKER

4.1 The Test Set-Up

A loading frame with a screw mechanism was used to apply uniform end shortening, u , to a specimen (fig. 5). Dynamic tests on several 0.032 in thick aluminum plates were carried out using point excitation at the center of the plate by an electromagnetic shaker. Displacement response was measured by strain gauges.

4.2 Random Response

Broadband (0-100 Hz) excitation was used to excite random response (Figure 6). The low frequency response (0-20 Hz) dominates the strain response when snap-through motion is initiated at $u/u_c = 4.0$ (Figure 7) and the fundamental modal response is not evident. The dominance of low frequency response for large amplitudes vibration of postbuckled plates was also reported in references 5, 6, and 7.

The variation of mean square strain parameter (square of the ratio of dynamic strain to static strain at $R=1$) with compression parameter is shown in Figure 7. The general trend agrees well with predicted results from the single-mode formula (Figure 4) and the points of maximum responses are near the curve for static values. However, there is a large discrepancy between the experimental results and theoretical prediction for an excitation level of $\alpha = 6$, which indicates that the single-mode representation used in the analysis overpredicts the stiffness of the buckled plate. More modes may be required to represent the deformation pattern and give a lower overall stiffness value.

5. EXPERIMENTAL RESULTS WITH ACOUSTIC EXCITATION OF BUCKLED PLATES

5.1 Test Set-Up

The panel used previously in mechanical excitation was installed in the Langley Thermal Acoustic Fatigue Apparatus (Figure 8) and subjected to a grazing incident progressive wave acoustic field at levels up to 165 dB. Both static and dynamic components of the strain, ϵ , were measured at the midpoint of the bottom edge of the panel.

5.2 Broadband Excitation

Time histories of the total strain were measured for sound levels from 140 dB to 165 dB for two panel configurations, one with the panel flat and unbuckled ($u=0$) and the second with the panel in a curved, buckled configuration ($u = 4 u_c$). The static strain measured in the buckled configuration was 5000 μ -in./in. The vibratory component of the strain is shown at the lower left of figure 9. For the lower sound levels (SPL < 155 dB) the vibratory strain in the buckled panel is less than that in the flat panel. This results from the greater stiffness due to curvature in the buckled panel and from the sound level being too low to cause snap-through. At these levels both curves follow a square-root trend, indicating hardening-spring non-linear response. At levels above 155 dB the sound level is high enough to cause snap-through and the strain increases rapidly with sound level for the buckled panel, following a trend to the square of the sound pressure, indicating softening spring response. The time history at the upper right shows that the panel frequently snaps through from the static equilibrium position with $\epsilon = -5000$ to the other

static equilibrium position with $\epsilon = +3000$, and back again, causing large vibratory strain values. In contrast the flat panel (lower right) vibrates only in the neighborhood of the flat position with $\epsilon = 0$. Figure 10 shows the comparison of the strain response of various SPL for a postbuckled plate of $u = 2.5 u_c$. Again the peak of spectrum of the response is at 0 Hz when snap-through motion starts at 162 dB SPL.

5.3 Frequency Sweep Test

To find out the frequency at which snap-through motion is excited, the postbuckled specimen is subjected to sinusoidal excitation with frequency sweep from 10 to 750 Hz. The sound pressure level is maintained constant for different frequencies by a beat frequency oscillator which automatically adjusts the input to the air modulator. The root mean square value and mean value of the strain response are recorded for the sweep test at SPL of 155 dB (Figure 11). The snap-through motion (indicated by large decrease of mean value) is found at 40, 63, 122, 186 Hz, which are respectively, 1/9, 1/6, 1/3, 1/2 of the linear fundamental frequency 360 Hz and are called superharmonic response. Theoretical results of superharmonic snap-through motion of curved beams is found in ref. 3.

It should be noted that no peak at 122, 186 Hz is found in the response of the panel when snap-through motion is initiated (figure 10). The peak at low frequency of 0-5 Hz may probably due to the frequency of occurrence of the snap-through motion rather than the frequency of the motion itself. Further theoretical and experimental investigation are required to understand this low frequency response due to snap-through.

6. CONCLUSION

From the theoretical and experimental results, the general characteristics of persistent snap-through motion in buckled plates are:

- 1) The mean value of the response is nearly zero instead of the initial static value;
- 2) The r.m.s. response is comparable to the initial static value when the snap-through motion is continuous;
- 3) The snap-through motion is most readily excited by low frequency excitation, usually at a fraction of the fundamental frequency;
- 4) The existence of snap-through causes large and sudden increases in the dynamic response of curved panels and it can be much larger than those obtained in flat panels and can be more significant than other complicating effects like non-linear damping, or multimodal contribution.

These characteristics are all totally different from the stable dynamic motion of linear, hardening-spring or softening-spring types as they all involve instability motion. The use of the single-mode analysis helps to interpret and understand these characteristics easily. However, improvements with use of time integration techniques and inclusion of a few more modes are necessary.

The effect of snap-through motion is not considered in the current sonic fatigue design practice. More experimental work with other types of curved panels like cylindrical and thermally buckled panels are needed to identify the technique to include snap-through motion in the design of aircraft structures.

7. ACKNOWLEDGMENT

The work was done by the author as part of the Research Associateship Program of National Research Council. Technical support from the Structural Acoustics Branch of Langley Research Center is appreciated. Advice from John Mixson, Sherman Clevenson, and assistance of Tracy Miller was very helpful to the research work.

8. REFERENCES

¹M. J. JACOBSON 1983 *Journal of Aircraft*, vol. 20, no.3. Sonic fatigue of advanced composite panels in thermal environments.

²N. Yamaki and M. Chiba 1983 *Thin-Walled Structures*, vol. 1, pp. 3-29. Nonlinear vibrations of a clamped rectangular plate with initial deflection and initial edge displacement.

³W. Y. Tseng and J. Dugudji 1971 *Journal of Applied Mechanics*, pp. 647. Nonlinear vibrations of a buckled beam under harmonic excitation.

⁴P. Seide 1984 *Proceedings of 2nd International Conference in Recent Advances in Structural Dynamics*, Southampton, England. Snap-through of initially buckled beams under uniform random pressure.

⁵C. F. Ng NASA TM 89165 The analysis of non-linear dynamic behavior (including snap-through) of postbuckled plates by simple analytical solution.

⁶M. J. Jacobson 1974 Air Force Flight Dynamics Laboratory. Effect of structural heating on the sonic fatigue of aerospace vehicle structures.

⁷C. F. Ng 1986 Ph.D. Thesis, University of Southampton. Behavior of postbuckled composite plates under acoustic excitation.

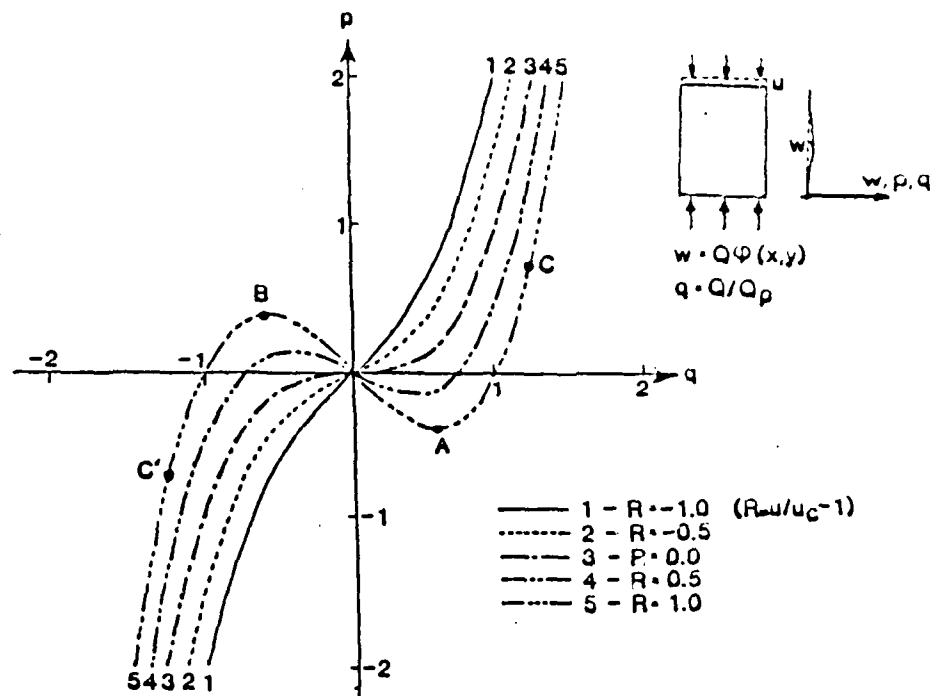


Figure 1. Plots for transverse force equilibrium equation of a plate under in-plane compression.

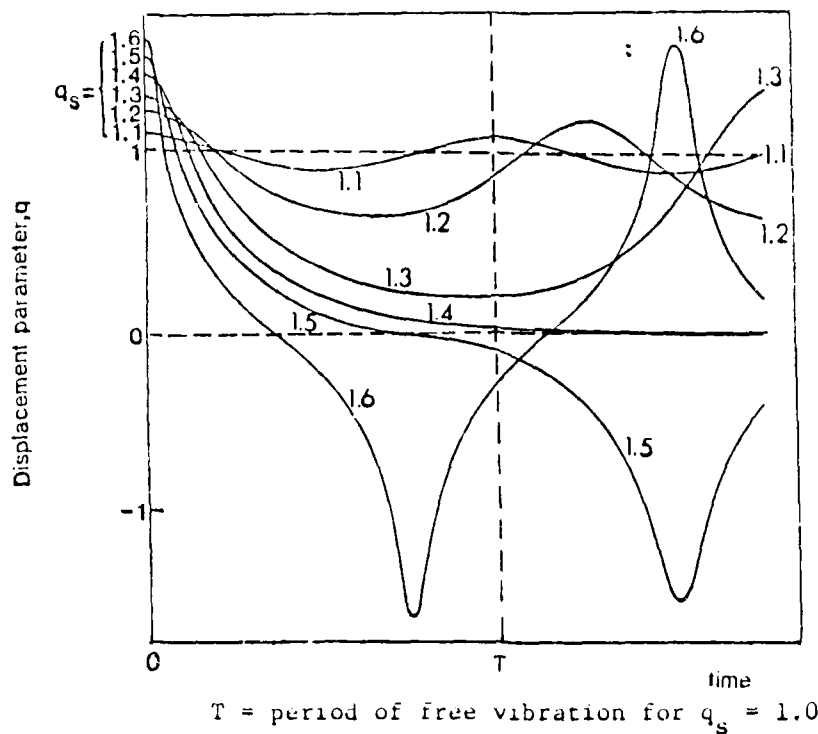


Figure 2. The free vibration of a postbuckled plate for different magnitude of initial displacement, q_s .
 $R = 1$ ($u/u_c = 2$), $q_0 = 1$.

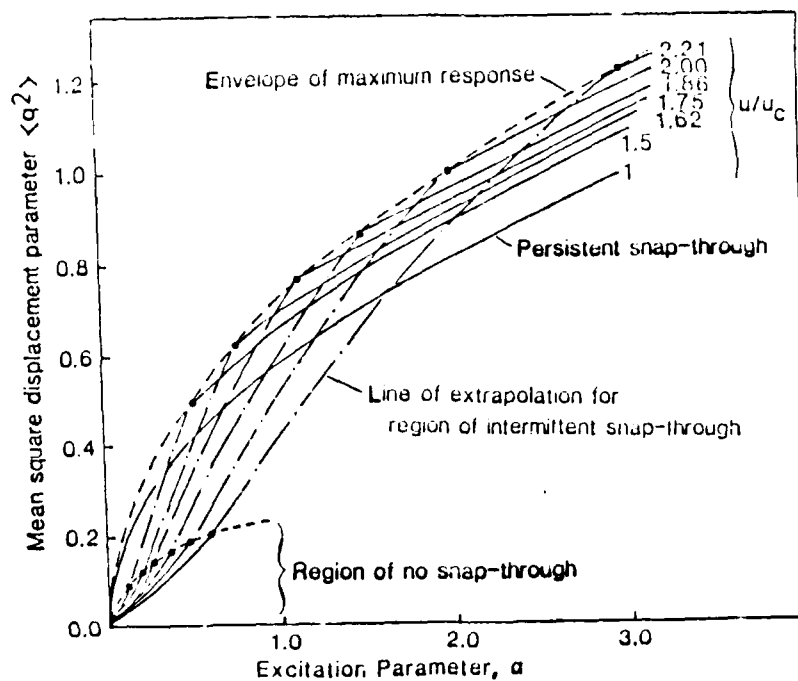


Figure 3. The variation of displacement response with excitation level in a postbuckled plate.

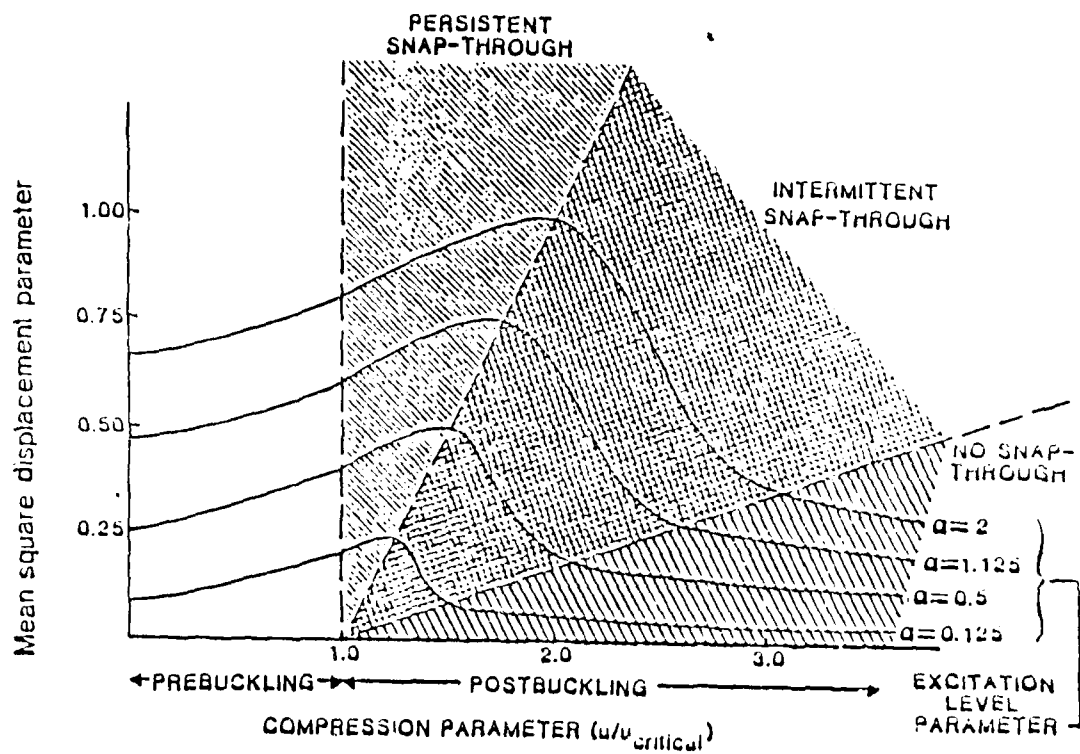
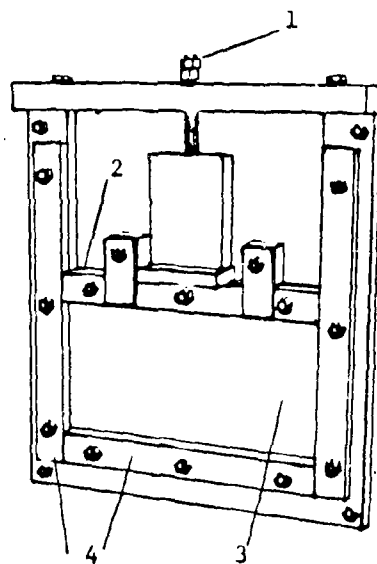


Figure 4. The variation of displacement response of postbuckled plates under white noise excitation.



1. Screw for controlling compression
2. Sliding clamping bar
3. Specimen
4. Clamping bars for sides and bottom edge.

Figure 5. The loading rig

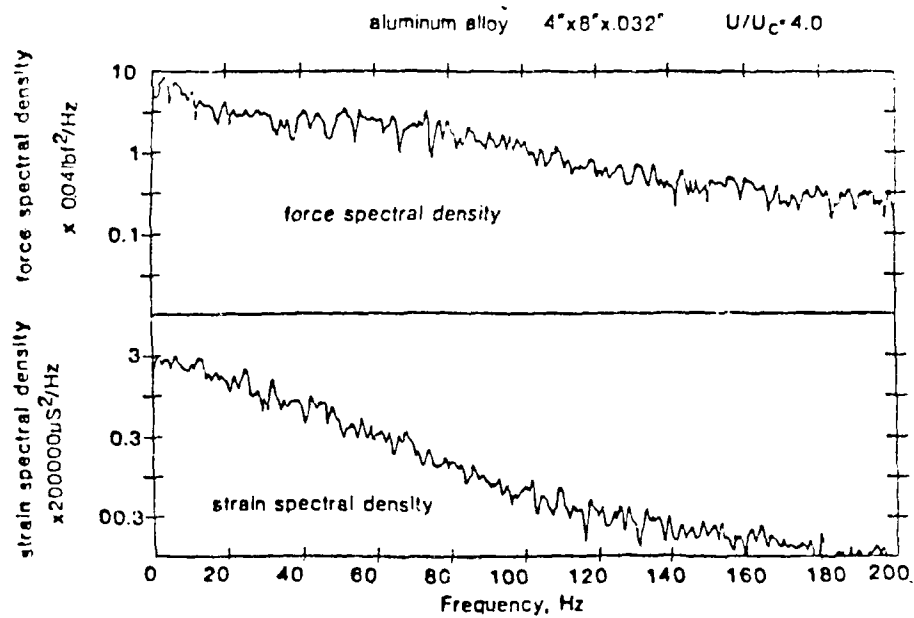


Figure 6. The strain response to random excitation in a postbuckled plate with persistent snap-through.

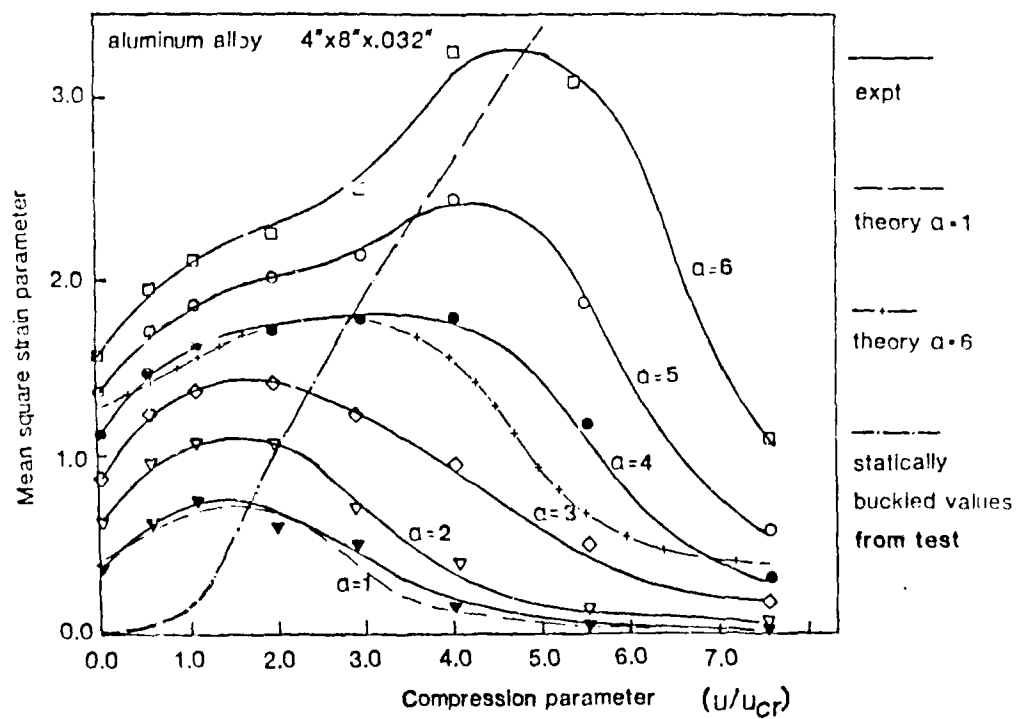


Figure 7. Variation of random strain response with increasing compression in an isotropic plate.

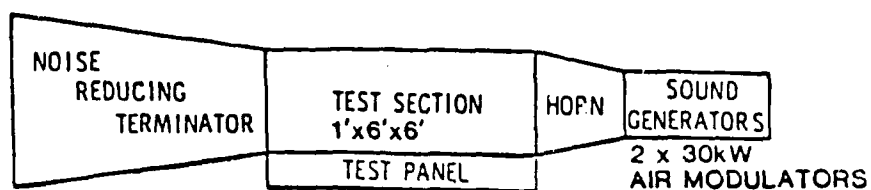


Figure 8. The schematic diagram of the acoustic facility.

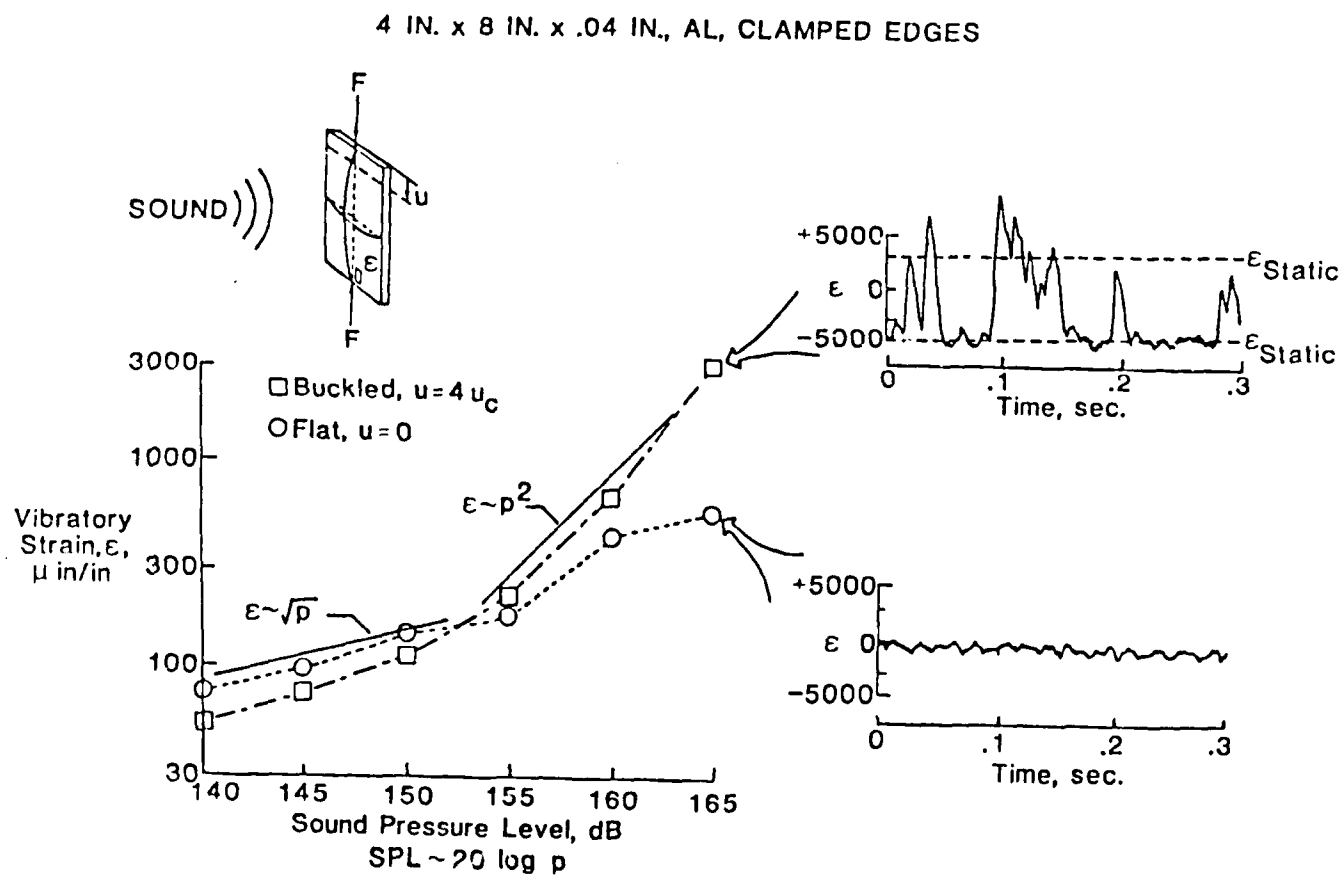


Figure 9. The acoustic responses of flat and buckled plates

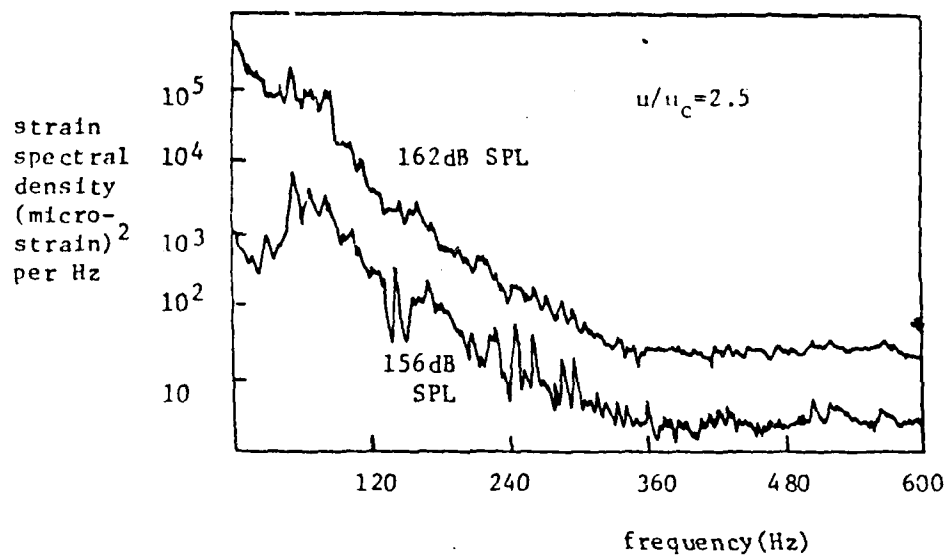


Figure 10. The acoustic responses of a postbuckled plate under different excitation level.

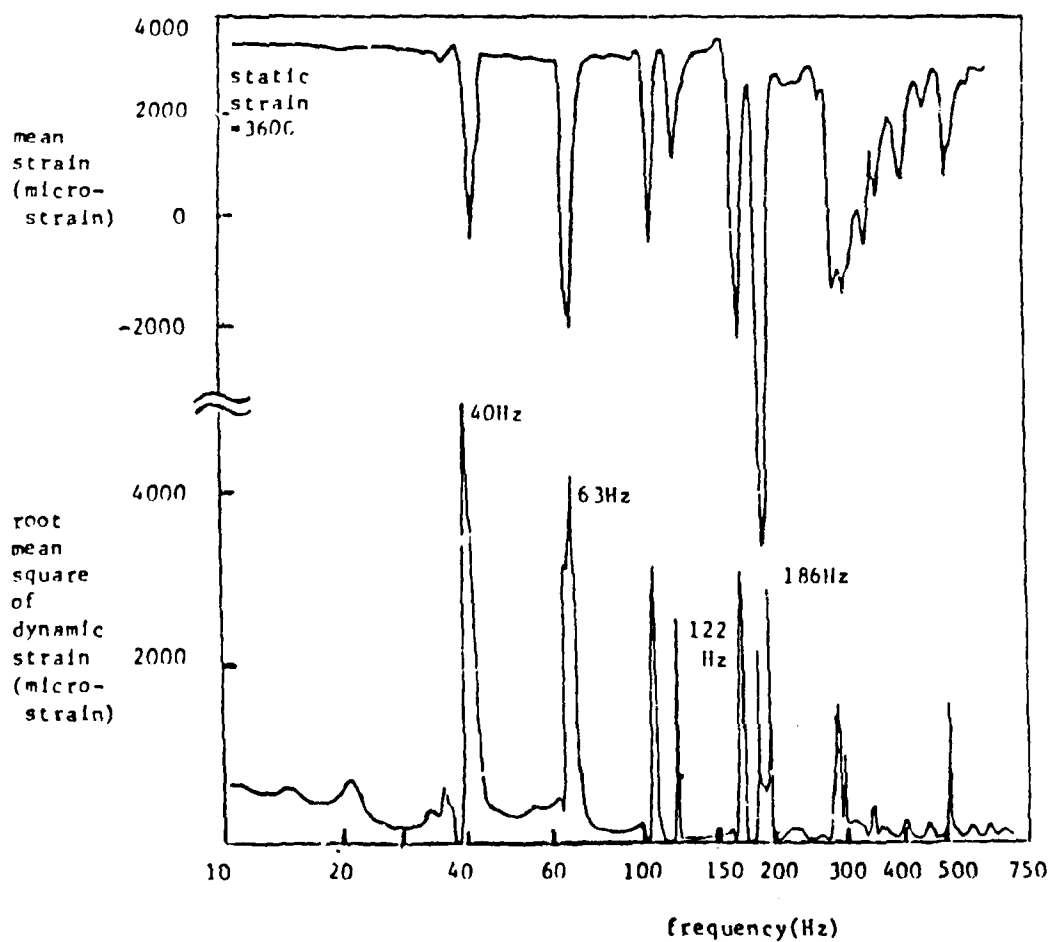


Figure 11. The sinusoidal sweep test of a postbuckled plate at 155 dB SPL.

EFFECT OF TEMPERATURE ON ACOUSTICALLY INDUCED STRESSES IN SOME CFRP PLATES

S.C. Galea and R.G. White

Institute of Sound and Vibration Research
University of Southampton

1. INTRODUCTION

Carbon fibre reinforced plastics now make significant contributions in the overall structure of modern aircraft. Their introduction was realised due to their better specific stiffness and strengths compared with conventional aerospace materials such as Al alloys. In recent years, these materials have been used extensively in advanced V/STOL aircraft such as the MCAIR AV-8B/GR MK 5 [1]. In such cases certain areas of the aircraft structure may be subjected to intense combined acoustic and thermal loadings. Loading type and magnitude will depend on aircraft configuration (particularly the proximity of the fuselage to the engine) and the particular manoeuvre. Of major importance is the ground effect during VTOL operations where engine exhaust reflections cause substantial increases in the thermal/acoustic environment. Also, aerodynamic heating and boundary layer turbulence during high speed flight may cause degrading thermal/acoustic environments in conventional advanced aircraft. Limited acoustic fatigue data have indicated that the acoustic fatigue life of stiffened CFRP panels is reduced when subjected to elevated temperatures [2,3,4]. Coupon fatigue tests, at elevated temperatures, of wet, impact damaged specimens suggest a 50% reduction in the acoustic fatigue life [5].

An estimate of acoustic fatigue life of CFRP panels can be attempted by using a simple single mode response technique [6,7] to predict induced strains in conjunction with experimentally determined acoustic fatigue data [8,9]. In order to use this technique it is necessary to assess the validity of the fundamental mode approximation in estimating the induced strain levels due to random acoustic excitation. This approach depends on the linearity of the system and on the use of the normal mode technique. Results have indicated that this approach is valid for conventional materials, e.g. Al alloy, and for 'thick' CFRP plates at room temperature [7,10]. The thickness criterion here is that plates of 6 layers or less tend to have non-linear behaviour even at relatively low sound pressure levels (> 140 dB) [11]. However, for conventional and 'thick' CFRP plates, when plate deflections are large compared to plate thickness (i.e. at extremely high overall sound pressure levels ~ 160 dB) non-linear response does occur.

The objective of this investigation was to determine the response of CFRP plates under broadband acoustic excitation at elevated temperatures and to then compare these experimental results with those predicted by the single, fundamental mode formula. In order to use such a prediction method the modal response of the CFRP plate must be known. An investigation was also carried out to evaluate the variations in modal response (viz. resonant frequencies and modal damping) of a clamped plate with temperature.

2. EXPERIMENTAL TECHNIQUE AND ANALYSIS

The two panels tested were constructed from Ciba Geigy 'Fiberox' XAS/914c carbon fibre/epoxy resin system. These plates, designated here as Plates A2 and B, were of 14 plies and 16 plies with $[+45,0,0,90,0,-45,0]_{\text{sym}}$

and $[+/-45,0,90,+/-45,0,90]_{\text{sym}}$ lay-up, respectively. The fibre volume fraction was typically 0.60 and plate thicknesses were 1.75 mm and 2.0 mm, respectively. Both plates were layed up by hand, then moulded and cured in a heated press. Overall size of the panels was 500 mm by 350 mm, but when placed in the clamping frame the exposed area was 450 mm by 300 mm, the long dimension being parallel to the 0 degree plies.

The variation of the frequency response and damping of the fully clamped CFRP plates with temperature was investigated using point excitation with a coil and magnet arrangement. Figure 1a shows a schematic diagram of the experimental set-up. The plate was excited by the coil and magnet using random noise generated by the analyser. To excite the first four modes of both plates a frequency bandwidth of 0 - 500 Hz was used. Since the force is proportional to coil current, the force signal was taken as the voltage across a 1 ohm resistor connected in series with the coil. Strain gauge pairs, located in positions shown in Figure 1b, were used to monitor the bending strain response of the plate. The force and the bending strain response signals were then acquired on a multi-channel Wavetek 804 A signal analyser. The analysis involved calculating the spectral densities (psd) of the strains and the force signals ($S_{ff}(f)$ and $S_{pp}(f)$) and then evaluating the modulus of the frequency response function, $|H(f)|^2$, i.e. $S_{ff}(f)/S_{pp}(f)$. Up to 50 averages were used to calculate the psd. The modal viscous damping ratio, ζ_n for mode n , was measured by using the logarithmic decrement method. This involved sinusoidally exciting the plate and then fine tuning the excitation frequency until maximum response occurred (i.e. resonance frequency, f_n). The modal viscous damping ratio could then be attained by applying the logarithmic decrement method on the decay signal of the bending strain response.

An array of four 1kW tungsten halogen elements heated the CFRP plate, as illustrated in Figure 1. Two Variacs, each placed in series with two elements, were used to vary the thermal output of the heating array, to produce a plate front surface temperature of 80°C to 120°C. Temperature profiles of the plates were measured, with a hand held thermocouple surface probe, to determine spatial variations of temperature. When the heated face was 120°C, Plate A2 showed a variation in temperature through the thickness of the plate of 10°C, and to the outer edges of the non heated face of 30°C. During testing the plates were instrumented with two K type thermocouples on the heated face and one on the back non heated face. One of the thermocouples on the front face was used as a sensor for a temperature controller connected to relays in series with the heating elements (see Figure 1). This was to ensure that the plate surface temperature would never exceed 140°C. The procedure for an elevated temperature test was to leave the plate unclamped during heating, then once the desired temperature had been reached and had stabilised (i.e. after 45 minutes) the plate was clamped. This procedure was followed to eliminate the build-up of thermal stresses, during heating, due to the differential thermal expansion rates of the steel clamping frame and the CFRP plate. Frame heating, which could cause frame warp, was kept to a minimum by constructing an aluminium foil enclosure around the perimeter of the plate, between the plate and the heating panel. This eliminated radiative heating of the steel frame, and upon heating the plate to 120°C the frame temperature did not exceed 35°C.

An investigation of the acoustic/thermal response of CFRP plates to broad band excitation was carried out by installing the above plates in the acoustic progressive wave tunnel (PWT) of the ISVR and using the 4 kW heating panel mentioned above. Figure 1b shows the experimental set-up. The Wyle Laboratories WASS 3000 siren is capable of generating overall sound pressure levels (OSPL) up to 163 dB of broad band noise in the test

section of the tunnel. A CFRP plate, clamped in a vertical steel frame, as used for the frequency response investigation, was installed so that it formed one of the vertical walls of the test section of the PWT. Note that individual strains were recorded in order to evaluate in-plane strains as well as bending strains (only bending strain results will be presented here). No temperature compensating strain gauges were used in this case. Here the effects of temperature on the strain gauges were eliminated by balancing the bridges after flow conditions and the plate temperature had stabilised, i.e. immediately before activating the siren and acquiring data.

The plates were excited by broad band excitation in the frequency range 20 - 600 Hz and OSPLs 135 to 160 dB in steps of 5 dB. Sound pressure measurements were taken by a B & K type 4330 microphone mounted at the centre of the test section, i.e. in front of the mid-point of the plate. The positions of the strain gauge pairs are shown in Figure 1b. Strain and pressure signals were filtered via low pass filters and stored digitally on the ISVR 15 channel workstation and then transferred to a VAX 11/780 via a digital tape. Data record lengths of 10s were stored enabling over 30 segment averages in the psd calculations. Data manipulation of the strain and pressure signals gave the following parameters:

(a) The strain psd, $S_{\epsilon\epsilon}(f)$, gives an indication of the modal influence on the spectral response of the plate due to random excitation. Of particular interest is the variation of resonant behaviour with increasing excitation levels and temperature.

(b) The running integral across the strain spectral density with frequency gives an indication of the contribution of each mode to the mean square strain response. This parameter is normalised by dividing by the overall mean square strain.

(c) Probability density function (pdf) of the strain signal which should be Gaussian for a linear response. If the response becomes non-linear then the pdf of the strain may tend to one side of the mean or the peak may appear sharp. An indication of system non-linearity can be obtained by calculating the third and fourth moments of the pdf. The former is the skewness which describes the degree of asymmetry, for a Gaussian system the pdf is symmetric, hence the skewness is 0. The latter moment is the kurtosis which gives the degree of sharpness of the peak, for Gaussian systems this parameter is 3.

3. PREDICTION OF CFRP PLATE RESPONSE

3.1 Natural Frequency Estimation

Estimates of CFRP plate natural frequencies were calculated by using the Rayleigh-Ritz method and by the ANSYS finite element (FE) program. The first method was applied via a program supplied by ESDU data sheet [12]. Both methods allow the user to input material properties and thickness of each lamina followed by the laminate lay-up, or the in-plane/flexural stiffness matrix of the laminate can be input directly into the program. The former program only accepts specially orthotropic laminated plates, i.e. balanced laminates with thickness, elastic properties and orientations symmetric about the laminate centre plane. The only restriction in the ANSYS FE program was found to be in the degree of anisotropy allowed, i.e. the ratio of direct elastic modulus to transverse elastic modulus must be less than about 13. The material properties used here were those apparent material properties measured from dynamic tests carried out on beam specimens made from the same material and lay-up as the plates.

In the ANSYS FE model an 8-node layered shell element was used. Sufficient accuracy was attained by modelling the plate using a 10 x 6 array of elements (i.e. 273 nodes). This element also has a stress stiffening capacity, and allows the material properties to be entered as functions of temperature. Coefficients of thermal expansion of each ply can also be included, thus the influence of interply residual thermal stresses can be determined.

3.2 Prediction of Acoustically Induced RMS Strains in a CFRP Plate

The stiffened panel of a fuselage skin can be assumed to be an array of fixed edge plates which vibrate independently of each other. Assuming that the fundamental mode dominates the response, then the mean square stress can be given by [6],

$$\overline{\sigma^2(t)} = \frac{\pi}{4\zeta_1} f_1 S_{pp}(f_1) \sigma_0^2 \quad (1)$$

where f_1 = the fundamental resonance frequency of the clamped plate (Hz),
 ζ_1 = the fundamental modal viscous damping ratio,
 $S_{pp}(f_1)$ = acoustic spectral density at f_1 (Pa²/Hz),
 σ_0 = surface stress at the point of interest due to a uniform pressure of unit magnitude.

Other assumptions here are that the resonant modes of the plate are well separated, damping is small, the pressure is in phase over the plate and the acoustic pressure spectrum is flat over the frequency range considered. Stress variations through the laminate will vary from ply to ply depending on the elastic modulus, so this parameter may be misleading if only the surface stresses are monitored. Most fatigue and design work on CFRP structures is accomplished by using surface strain values rather than surface stresses. Predictions of RMS strains are achieved by ϵ_0 , instead of σ_0 , which is the surface strain at the point of interest due to a uniform pressure of unit magnitude.

All of the above parameters, except for damping, can be either calculated or measured. The viscous damping is either approximated as 0.025 for a CFRP plate within an array or can also be measured. The ESDU data sheet [7] was used to calculate RMS surface strains. The data input to this program consisted of measured apparent elastic properties, which enabled calculation of ϵ_0 , and experimentally determined values of f_1 , ζ_1 and $S_{pp}(f_1)$.

4. RESULTS

4.1 Natural Frequencies

The natural frequencies calculated using the Rayleigh-Ritz and the FE method are compared with the measured values in Table 1. As usual, the prediction methods overestimate fundamental natural frequencies, also lack of rigidity of the clamping frame would cause the measured values to be low. Otherwise agreement is quite good for f_1 but there is considerable error in the higher order modes. The ANSYS results also include predictions of mode shapes of Plate A2 which agree with those observed. Plate B had to be slightly preheated before clamping to eliminate the initial warp of the plate. Table 2 gives the variation of natural frequency and viscous damping ratio with temperature. The fundamental natural frequency of both plates reduced by 16% as the temperature increased to 120°C. This was surprising since predictions of fundamental

natural frequencies due to reductions in material properties, caused by elevated temperatures, showed a reduction of only 2%. Hence, it would appear that other parameters influence the above phenomenon. One possible explanation is the reduction of internal residual thermal stresses as the temperature approaches the glass transition temperature of the matrix. Table 2 also shows a general trend for damping to decrease with increasing temperature. Elevated temperature tests carried out on the 914 resin showed the damping to be a minimum between 60° - 80°C, which could be an explanation for the low value of ζ_1 at 80°C.

4.2 Acoustic Progressive Wave Tunnel Results

A 2.5 kPa static pressure in the test section of the tunnel, due to the excessively high flow rates required to operate the siren, caused the plates to deflect in the 1,1 mode (up to one plate thickness for Plate A2). This deformation induced stress stiffening in the plates causing the natural frequencies to increase. An analysis using ANSYS, including static pressure, gave a prediction for f_1 of 174 Hz, for Plate A2, which agreed very well with that observed viz. 170 Hz. In general, plate natural frequencies remained constant or slightly decreased with increasing OSPL. This is in contrast with the thin CFRP plates, i.e. 4 plies only, tested by White [11] who found f_1 to increase dramatically with increasing OSPL. But thin plates tend to behave in a non-linear manner at moderate OSPL. The effect of temperature was to decrease f_1 further. For example, f_1 for Plate A2, at an OSPL of 160 dB, decreased by 14% from its room temperature value as the plate was heated to 120°C.

Typical variations of bending strain spectral densities with increasing OSPL are shown in Figure 2. This illustrates the reduction in modal response as the acoustic excitation level increases. Figure 3 shows the typical variation of the percentage contribution of the first mode to the overall RMS bending strain (w), at SG 2 for Plates A2 and B, with increasing OSPL. As illustrated, w drops as OSPL increases, the variation being the greatest for Plate A2 (the thinner of the two plates). The variation with temperature appears to be greatest for Plate A2 at SG 2 (see Figure 3). For this plate w increased when the plate was heated to 80°C but then decreased to the value at room temperature upon heating further to 120°C.

No significant trends were observed in the skewness and kurtosis values, other than the skewness values (i.e. the degree of asymmetry of the pdf), for Plate A2, showed a slight increase due to heating at high OSPL. It appears that elevated temperatures do not cause the bending strain response of these particular CFRP plates to become non-linear at a lower OSPL, as was expected.

In general, RMS bending strains do not vary greatly with temperature, however a slight increase can be observed at 80°C, compared to values at room temperature and 120°C, for Plate A2 at SG 1 and SG 2. Assuming that f_1 and $S_{pp}(f_1)$ are constant, then this could be due to the observed decrease in damping of the plate at this temperature, since RMS strain response $\propto 1/\sqrt{\zeta_1}$. Using measured values of f_1 , ζ_1 , apparent elastic properties and $S_{pp}(f_1)$, and the ESDU data sheet [7], which uses eqn. (1), the estimated values of RMS surface strains were determined. Figures 4 and 5 show these values compared with measured results for Plate A2 at SG 1 and Plate B at SG 3, respectively. Note that the values of damping used here were those measured when the plate was positioned in the PWT. As can be seen in Table 2, these values are much higher than those obtained in the frequency response tests when the plate was away from the chamber. The increase in damping is due to the pumping action of the plate on the

confined mass of air in the chamber. The estimated RMS surface strain results agree well with the measured values. Estimated RMS surface strains become less accurate at high OSPL, as is expected, due to the plate response becoming non-linear and hence the basic assumption of modal response becomes invalid.

5. CONCLUSIONS

The natural frequencies of the CFRP plates decreased slightly with increasing temperature. This was not entirely due to reductions in material properties with increasing temperature but was probably caused by other effects such as reductions in residual thermal stresses.

Elevated temperatures did not significantly change the bending strain response of the CFRP plates tested under broadband acoustic excitation. Non-linear effects were observed to occur with increasing OSPL for both plates. The thicker plate, Plate B, still exhibited a large fundamental mode contribution to the overall RMS bending strain even at high OSPL (up to 160 dB). For these plates and for the particular carbon fibre/epoxy resin system used here, the single mode response method accurately predicted the RMS bending strains at room temperature and at elevated temperatures (up to 120°C) under broadband random acoustic excitation up to OSPL of 160 dB.

ACKNOWLEDGEMENT

The authors would like to thank the RAE Farnborough for their sponsorship of this work via an unclassified research agreement. Considerable thanks are also due to Mr. R.P. Mousley of the RAE for his guidance and encouragement throughout the programme of work.

REFERENCES

1. B.L. RILEY 1986 22nd John Player Lecture, Inst. of Mech. Eng. Proc. V. 20, N. 50. AV-8B/GR MK 5 airframe composite applications.
2. J. SOOVERE 1985 Journal of Aircraft, V. 22, N. 4, April. The effect of acoustic/thermal environments on advanced composite fuselage panels.
3. M.J. JACOBSON 1983 Journal of Aircraft, V. 20, N. 3, March. Sonic fatigue of advanced composite panels in thermal environments.
4. J. SOOVERE 1982 NADC-78169-60, Feb. Effect of acoustic, thermal and shear loading on flat integrally stiffened Graphite/Epoxy fuselage panels.
5. J. SOOVERE 1982 Journal of Aircraft, V. 19, N. 4, April. Sonic fatigue testing of an advanced composite aileron.
6. B.L. CLARKSON 1968 The Aero. Journal of the Royal Aero. Society, V. 72, N. 695, November. Stress in skin panels subjected to random acoustic loading.
7. ESDU 1983 Item No. 84008, Engineering Science Data Unit, London, November. Estimation of RMS strains in laminated skin panels subject to random acoustic loading.

8. I. HOLEHOUSE 1984 PhD Thesis, ISVR, University of Southampton. Sonic fatigue design techniques for advanced composite airplane structures.
9. ESDU 1984 Item No. 84027, Engineering Science and Data Unit, London, November. Endurance of fibre reinforced composite, laminated structural elements subjected to simulated random acoustic loading.
10. R.G. WHITE and R.F. MOUSLEY 1987 Proc. of the 4th International Conf. on Composite Structures, Paisley, 27-29 July. Vol. 1, pp 519-535. Dynamic response of CFRP plates under the action of random acoustic loading.
11. R.G. WHITE 1978 Composites, V. 9, pp 251-258. A comparison of some statistical properties of the responses of aluminium alloy and CFRP plates to acoustic excitation.
12. ESDU 1983 Engineering Sciences Data Unit. Item No. 83036. Natural frequencies of rectangular, specially orthotropic laminated plates.



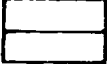
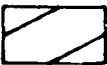


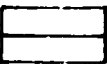

MODE	ESDU	ANSYS	MEASURED	ANSYS MODE SHAPES
1,1	103	100	96	
2,1	183	177	180	
1,2	238	230	242	
2,2	304	294	294	
1,1	144	135	134	
2,1	222	217	243	
1,2	352	332	322	
2,2	355	334	370	

Plate A2

Plate B

(all values in Hz)

Table 1. Comparison of estimated and measured natural frequencies of fully clamped CFRP plates (measured apparent elastic properties used).

	20°C	80°C	120°C	20°C	80°C	120°C
f_1 (Hz)	96	85	80	134	116	112
ζ_1	0.0085	0.0035	0.007	0.0125	0.011	0.009
ζ_1^*	0.020			0.030		
	PLATE A2			PLATE B		

Table 2. Variation of CFRP plate natural frequencies and viscous damping with temperature.

(* value of damping with plate in position in acoustic progressive wave tunnel.)

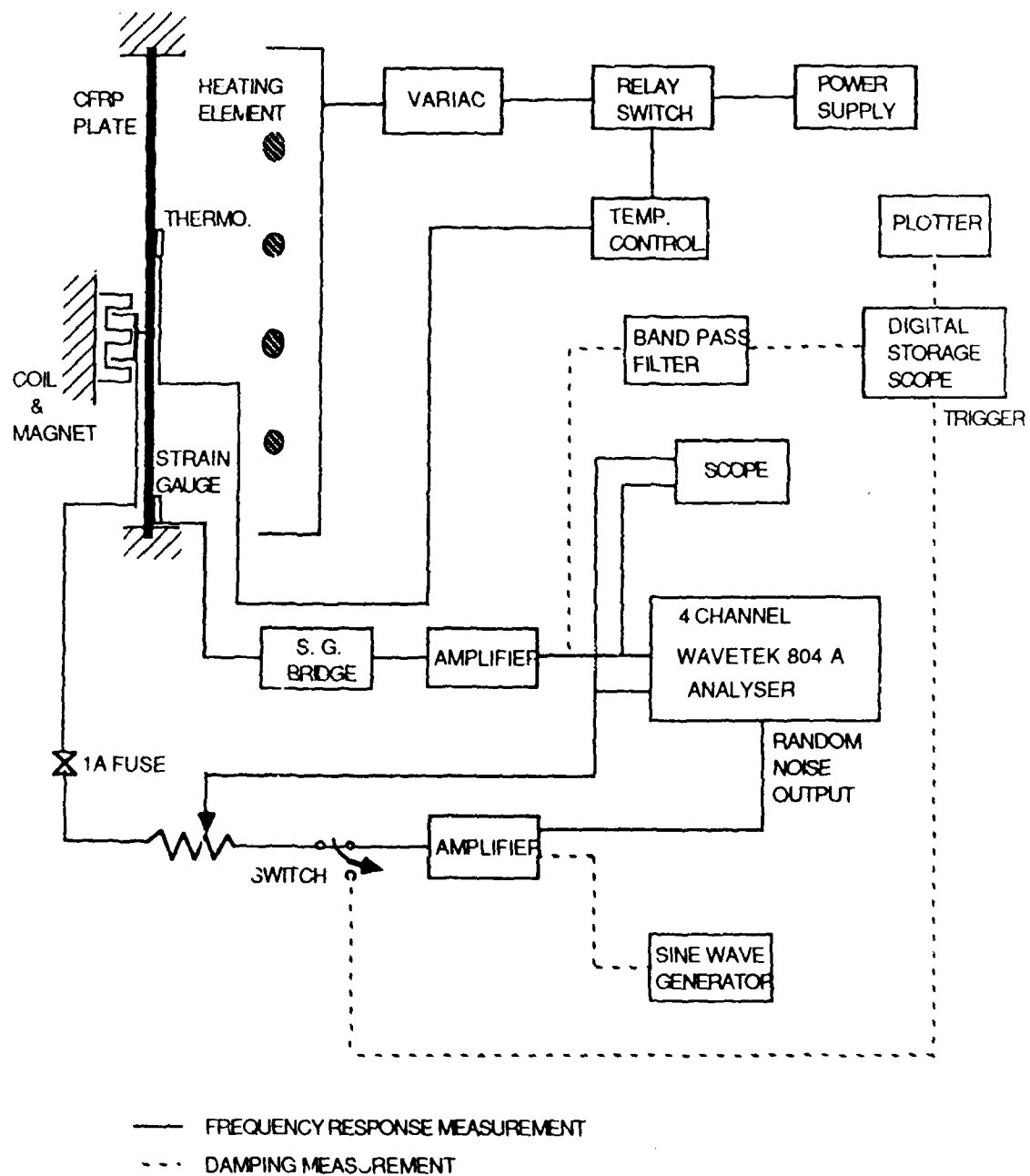


Figure 1a) : Schematic diagram of the experimental setup for measuring some natural frequencies of a clamped CFRP plate.

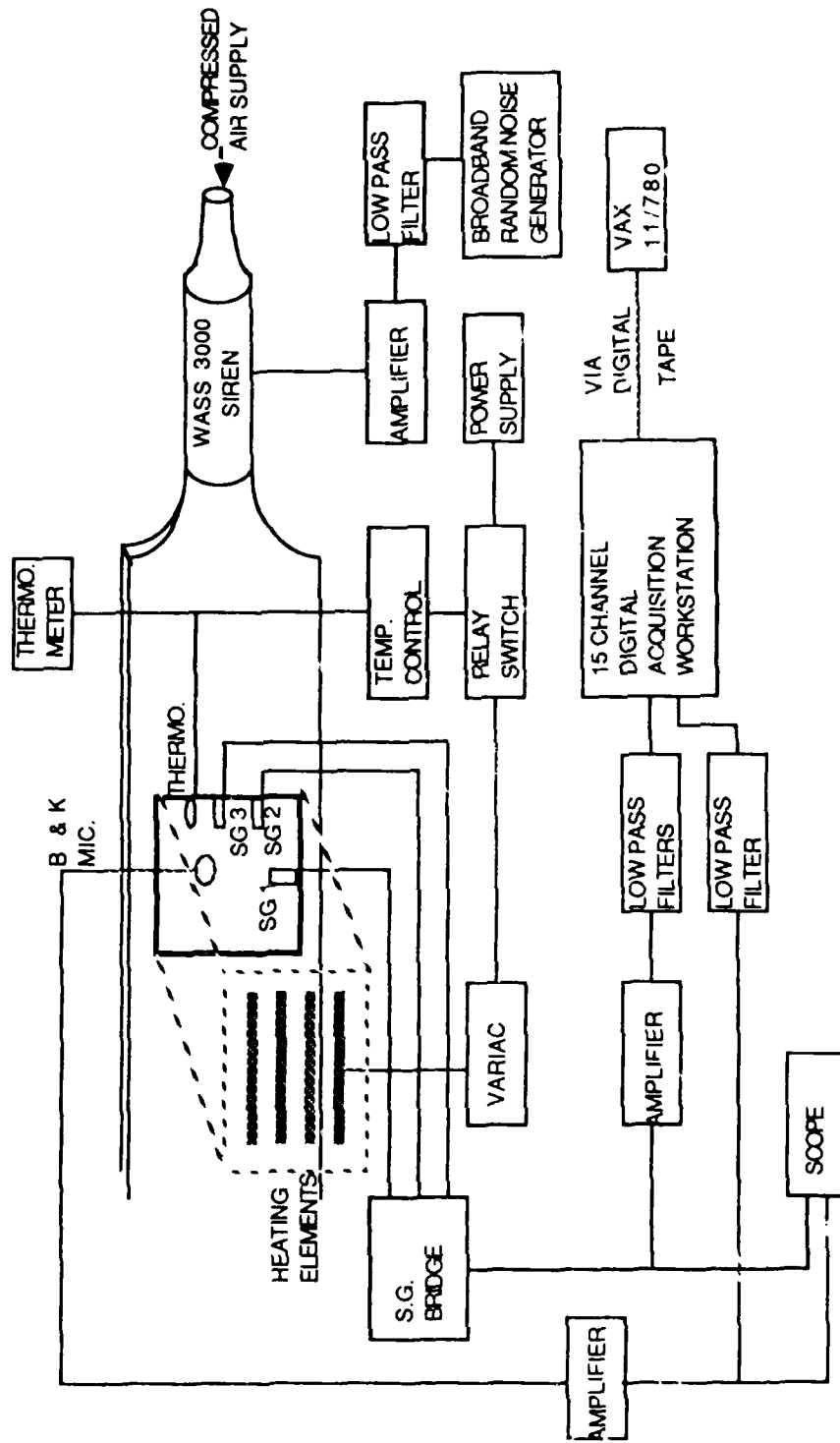


Figure 1b) : Schematic diagram of the experimental setup to acoustically excite a CFRP plate and for data analysis.

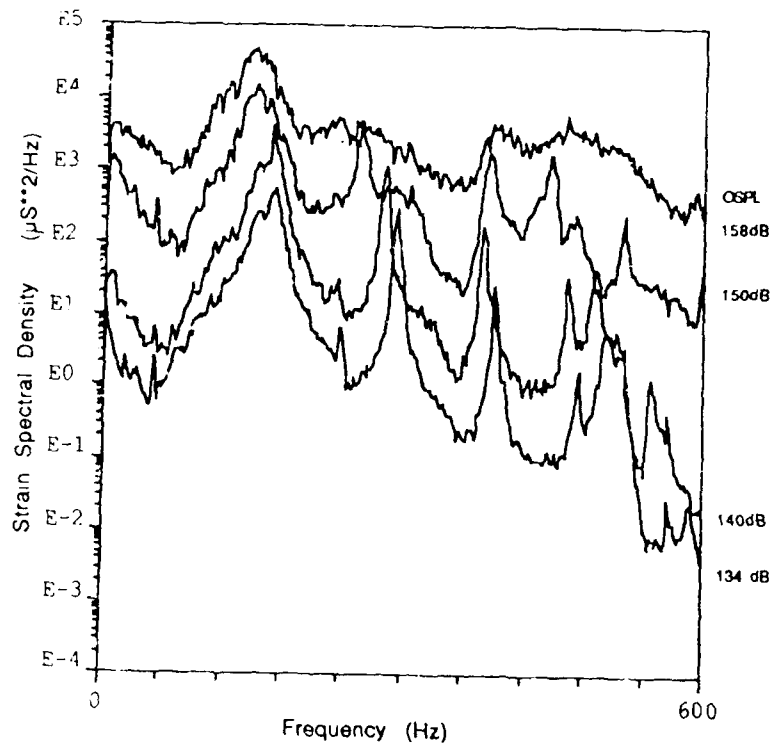


Figure 2 : Typical variations of bending strain spectral density with increasing OSPL
(Plate A2 ; SG 3 ; 120°C)

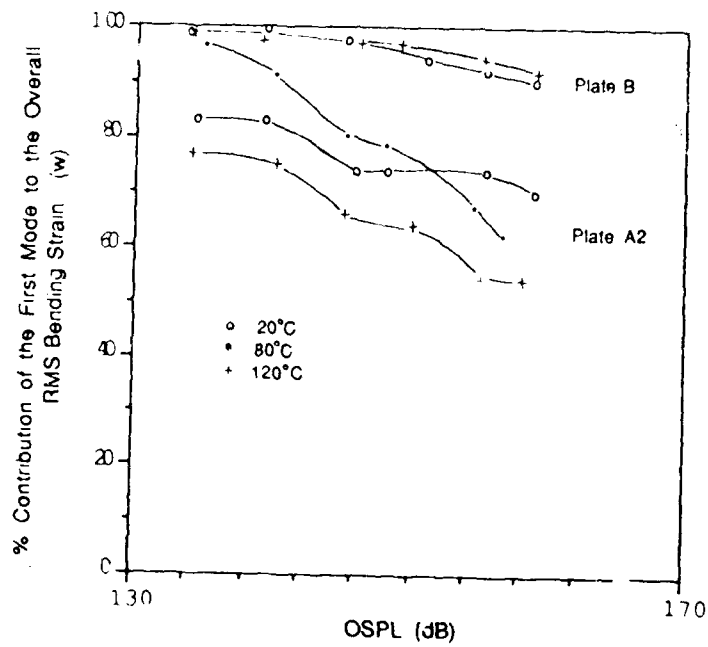


Figure 3 : Variation of % contribution of the fundamental mode to the overall RMS bending strain with OSPL and temperature for SG 2.

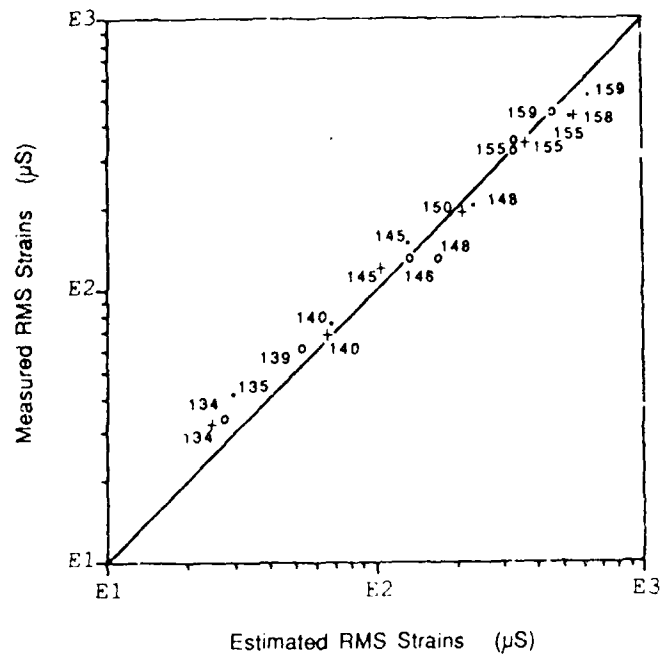


Figure 4 : Comparision of measured and estimated RMS bending strains in a CFRP plate under broadband acoustic excitation .
(Plate A2 ; SG 1 ; o 20°C, * 80°C, + 120°C)

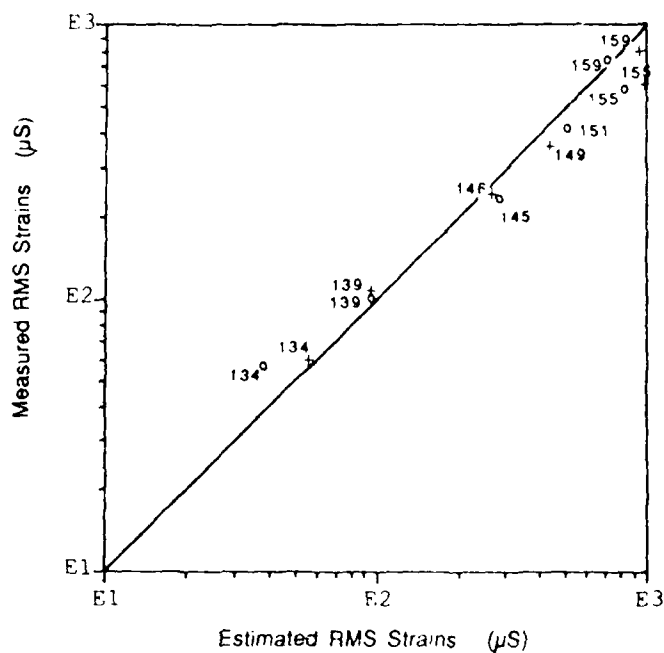


Figure 5 : Comparision of measured and estimated RMS bending strains in a CFRP plate under broadband acoustic excitation.
(Plate B ; SG 3 ; o 20°C, + 120°C)

TWO METHODS FOR THE DETECTION OF FAILURE IN MECHANICAL SYSTEMS

by

* Patricia Davies and **J.K.Hammond

* Ray W. Herrick Laboratories, School of Mechanical Engineering, Purdue University.

** Institute of Sound and Vibration Research, University of Southampton.

ABSTRACT

When a component in a complicated system fails the system may continue to function. However, this failure may lead finally to a total system failure and so early detection of a component failure could be very important. This paper describes two approaches to the detection of failure in a system. The first approach takes the response of a system and models it as white noise passed through a linear filter. The parameters of this filter and the input to the system are estimated and monitored for deviations from *normal* behaviour. The second approach is to examine the envelope and instantaneous frequency of the response of the system and monitor it for changes during a transient excitation of the system.

1. INTRODUCTION

The area of condition monitoring and machinery health is, and has been, the object of much research [1,2,3,8,9,13,14]. This is because it is important to be able to detect changes in a system's behaviour in order to assess whether a system is about to stop working or start operating in a dangerous mode. Early detection of problems with machines can save the time taken to, and expense of, repairing a machine and, in addition, can add to the safety of the machine operation. The types of changes to a system discussed in this paper are where a component in a system fails. This system will be modelled as a linear system whose impulse response is the sum of damped sinewaves and the failure will be modelled as one of these damped sinewaves changing its frequency and decay.

Two methods for the detection of the failure of a component in a system are described in the next section of this paper. The first method is one that can be used while the machine is operating; it relies on the ability to model the machine's response as white noise passed through a linear filter and involves monitoring the estimates of this filter's coefficients and its input. The second approach is to monitor the envelope and instantaneous frequency of the response of the system to a transient excitation. This approach can be used in two ways: firstly if the failure occurs during the transient test then sudden changes in the envelope and instantaneous frequency could be used to detect it, and secondly if the failure has already occurred the envelope of the response of the damaged system could be compared with the envelope of the response of the undamaged system stored from previous tests. The second approach is only useful if it is possible to repeat the excitation signal.

2. THEORY

In this section an outline of the theory used in the two methods is given, together with a description of how this theory may be used to detect the changes to the system under test.

2.1 *Monitoring white noise excited systems*

The response of the system is modelled as white noise passed through a linear, autoregressive moving average filter. Let $e(n)$ denote the input and $r(n)$ denote the response then the model can be expressed as:

$$r(n) = -c_1 r(n-1) - c_2 r(n-2) - \dots - c_{NC} r(n-NC) + e(n) + d_1 e(n-1) + d_2 e(n-2) + \dots + d_{ND} e(n-ND) \quad (1)$$

This model expresses the response of the system as the weighted sum of past response values and present and past values of the excitation signal. The model is often expressed in its z-transform form, $R(z) = H(z)E(z)$, where $R(z)$ and $E(z)$ denote the z-transforms of $r(n)$ and $e(n)$ respectively and,

$$H(z) = \frac{1 + d_1 z^{-1} + d_2 z^{-2} + \dots + d_{ND} z^{-ND}}{1 + c_1 z^{-1} + c_2 z^{-2} + \dots + c_{NC} z^{-NC}} \quad (2)$$

$H(z)$ is the z-transform of the sampled impulse response of the system, denoted by $h(n)$. $r(n)$ is known but $e(n)$, the input noise series, the c_i and the d_j , the coefficients of the filter are not. Using an approximate likelihood method described in references [15] and [16], the coefficients and the input noise series, $e(n)$, can be estimated. The method relies on the statistical properties of $e(n)$, that is, $e(n)$ should be a Gaussian distributed white noise series.

A system whose impulse response is the sum of damped sinusoids can be modelled using an autoregressive moving average model [3,6]. Systems of this type are sometimes called multimodal systems and the roots of the denominator polynomial in equation (2) are related to the frequency and damping of each of the modes. An example of such a system may be a viscously damped structure although usually a system of this type would have an infinite number of modes. It can be shown that each mode adds two autoregressive coefficients (the c_i) and two moving average coefficients (the d_j) to the model, thus the resulting model would have an infinite number of terms. However if interest is in the response of the structure over a limited frequency range the system can be approximately modelled by using an autoregressive moving average model of finite order. This is discussed more fully in [3].

The failure is modelled as one of the modes of the system changing its characteristics. This change in natural frequency and/or damping is reflected in a change in the coefficients of the model, so by continuously estimating and monitoring the parameters of the filter model of the system the time of failure should be detected. Another utilization of the digital modelling approach is to generate a filter model of the system and use it to predict the input. When the model no longer accurately reflects the system behaviour the estimated input characteristics will change. Hence by monitoring the response characteristics the failure can be detected.

In reference [4] this digital model approach was used on a real system. Here the application of the method was slightly different to that described above. It was assumed that the system behaviour was very complicated and the component failure that had occurred would not change

the system behaviour very much but would manifest itself as an added impulsive excitation to the system. The digital filter approach was used to predict the input to the system. It was shown that the impulsive behaviour, not always apparent in the response of a system is more clearly visible in the estimated excitation signal. These results were achieved with digital filter models that modelled only the overall characteristics of the system as computational limitations restricted the complexity of model that could be constructed.

In order to illustrate the effectiveness of this technique figure 1 shows the response of a linear system whose excitation is white noise with some impulses buried in it and figure 2 shows the estimated excitation signal generated by using the digital filter technique described above.

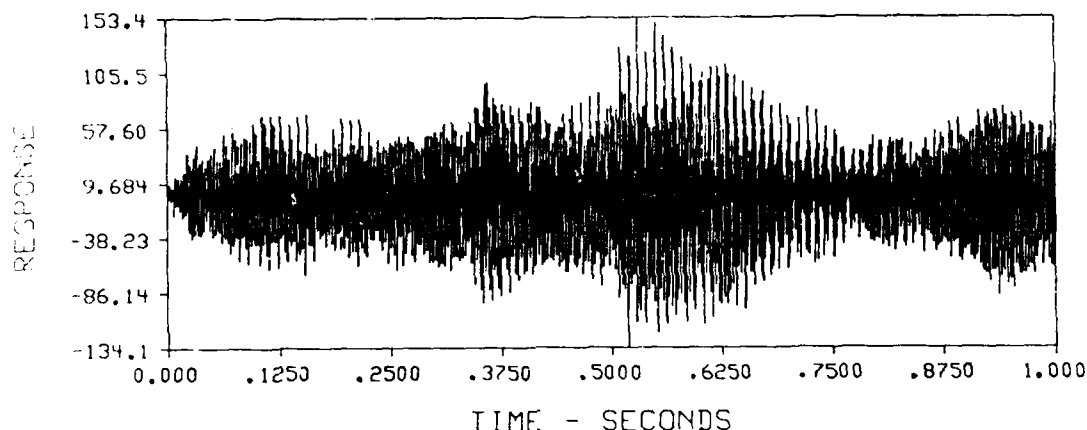


Figure 1: Response of multimodal system to white noise plus impulses excitation.

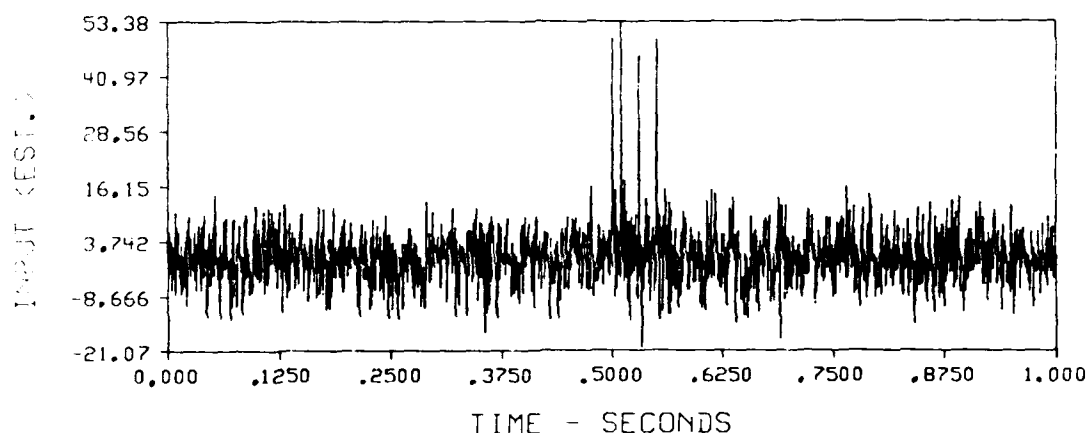


Figure 2: Estimated input to multimodal system.

2.2 Monitoring the envelope and instantaneous frequency of the response

The second method for the detection of a change to a system is that of monitoring the envelope and instantaneous frequency of the response of the system. Before illustrating how the envelope and instantaneous frequency of the response of a system may be used to detect the

change to the system a brief outline of their definition and how to calculate them will be given.

A signal $y(t)$ can be thought of as the real part of a complex analytic signal $\sigma_y(t)$. In turn this complex analytic signal can be thought of as a complex analytic function evaluated along a line in a complex plane. The real and imaginary parts of a complex analytic function are related, this relationship is expressed by the Cauchy Riemann equations [7,12]. The imaginary part of the complex signal denoted by $\hat{y}(t)$ is known as the Hilbert transform of $y(t)$. There are many different Hilbert transforms, each one derived from considering regions in a complex plane over which a complex function is analytic. In reference [10] some of the Hilbert transform relationships used most commonly in signal processing applications are described.

The Hilbert transform relationship that is used here is given below in equation (3).

$$\hat{y}(t) = \frac{1}{\pi} \int_{-\infty}^{\infty} \frac{y(\tau)}{(t - \tau)} d\tau \quad (3)$$

This is a convolution of $y(t)$ with $1/\pi t$. $1/\pi t$ is sometimes referred to as a Hilbert transformer. The effect of this transformation on a cosine signal is to change it into a sinusoid of the same frequency and amplitude. The Fourier transform of the Hilbert transformer is j for negative frequencies and $-j$ for positive frequencies, where j is the square root of -1 . The Hilbert transformer has the effect of phase shifting frequency components in a signal by plus or minus ninety degrees.

Instead of using continuous infinite length signals, signals are usually of finite length and sampled. A digital Hilbert transformer is designed so that it will take the sampled signal and produce a sampled version of the Hilbert transform of the continuous signal. The design of such a Hilbert transformer is discussed in detail in references [10] and [11]. Very broadly the design process is to construct a finite impulse response digital filter such that it matches as closely as possible the desired frequency response of a Hilbert transformer over a limited frequency range. As the number of coefficients included in the digital filter increases the frequency range over which the filter acts as an effective Hilbert transformer gets larger. The digital filter Hilbert transformer used in subsequent examples in this paper effectively transforms frequency components between 0.02 and 0.48 times the sampling frequency. The transformation of frequency components outside this frequency range are subject to errors.

Having the tools to generate the Hilbert transform of a signal it is now possible to generate the envelope and instantaneous frequency of the signal. The expression for the analytic signal can be written as:

$$\sigma_y(t) = y(t) + j \hat{y}(t) = A_y(t) e^{j\Phi_y(t)} \quad (4)$$

where

$$A_y(t) = \left\{ y^2(t) + \hat{y}^2(t) \right\}^{1/2} \quad \text{and} \quad \Phi(t) = \tan^{-1} \left\{ \frac{\hat{y}(t)}{y(t)} \right\}. \quad (4a)$$

$A_y(t)$ is the envelope of the signal and $\Phi_y(t)$ is the phase. Differentiating $\Phi_y(t)$ will give the instantaneous frequency of the signal.

As an illustration figure 3(a) shows the response of a system with three natural frequencies, between 500 and 515 Hertz and damping ratios between .001 and .004. The system was excited by an impulsive force, a highly damped sinewave of frequency 1250 Hertz. The change was made to the second mode of the system, the damping ratio was changed to 100 times its previous value. The change occurred at .1 seconds. Figure 3(b) shows the envelope of the response signal

and 3(c) shows the instantaneous frequency. The change to the system produces sharp changes in the envelope and instantaneous frequency of the signal. The instantaneous frequency also undergoes rapid changes as the envelope gets close to zero, these are partly due to the problems of calculating the phase and its derivative when both the signal and its Hilbert transform are close to zero.

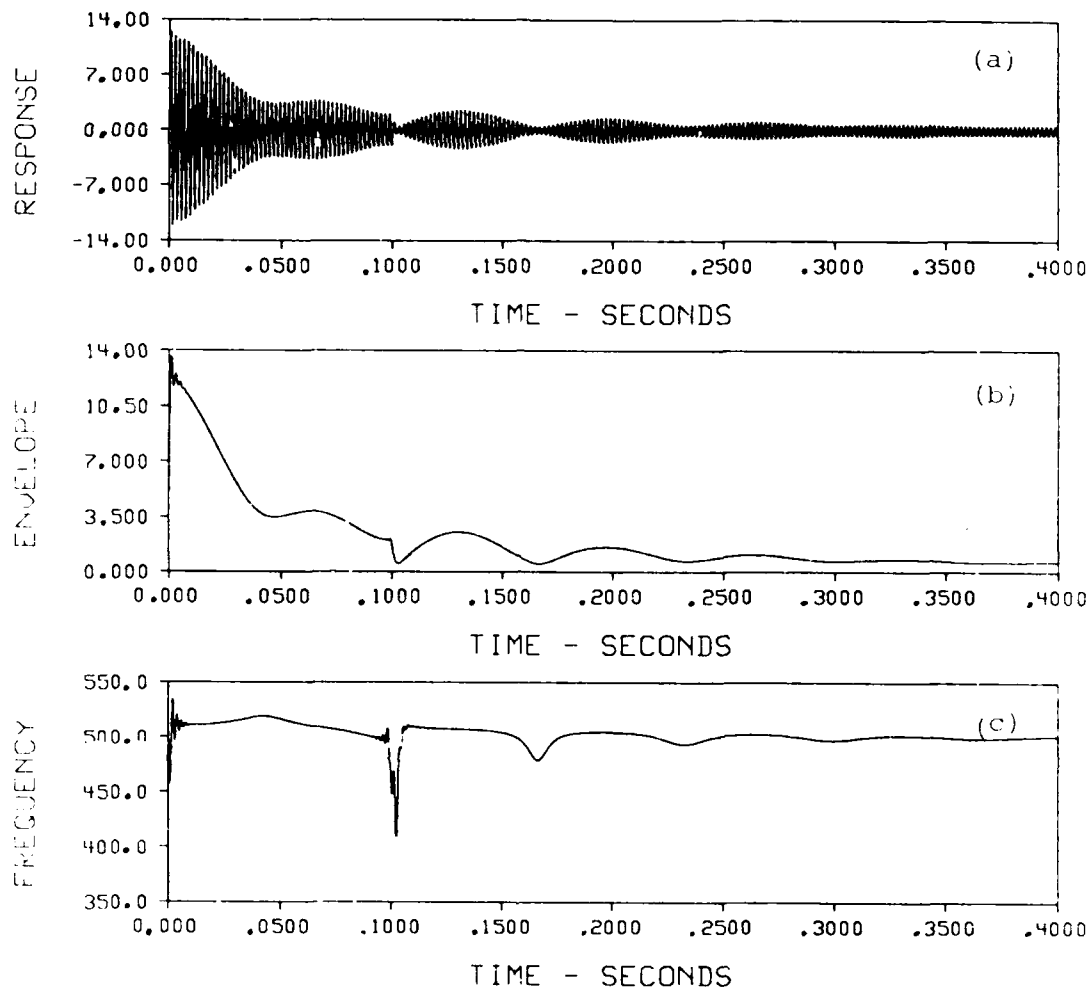


Figure 3: (a) response of system, (b) envelope of response and (c) instantaneous frequency. System changed at .1 seconds.

In general a system may well have a more complicated transfer function than the three mode transfer function considered here. This envelope and instantaneous frequency method can still be used, although the response signal would have to be split into bandlimited signals using digital filters before the envelope and instantaneous frequency of each band is calculated. This is because the instantaneous frequency of a narrowband signal can be written as $\omega_c + \psi(t)$, where ω_c is the center frequency of the band and $\psi(t)$ reflects the variation in the instantaneous frequency of this bandlimited signal about the center frequency. For narrowband signals this variation would, in general, be small and thus any change to the system would be reflected as a sharp change to this instantaneous frequency signal. Figure 4 shows the instantaneous frequency of the response of a system with ten natural frequencies from 30 to 500 Hertz. The excitation

was the same as for the system whose response is shown in figure 3 and the change to the system affecting one mode took place at .1 seconds. The large fluctuations in the instantaneous frequency due to the broadband characteristics of the signal means that the instantaneous frequency is no longer an effective means of detecting the change to the system.

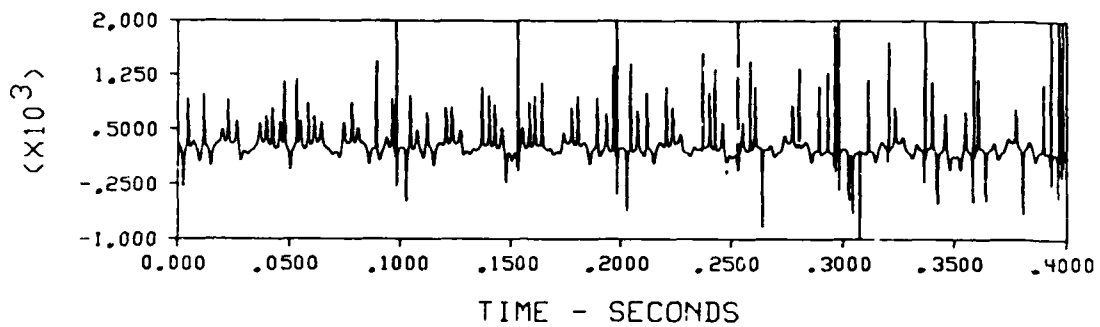


Figure 4: The instantaneous frequency of a broadband signal.

3. EXAMPLES

3.1 White noise excited systems

In figure 5 is shown the response of a system to white noise excitation. At .5 seconds one of the three modes of the system changes its natural frequency and damping. Figure 6 shows the estimated autoregressive moving average parameters as a function of time. At .5 seconds the change in the system is reflected in the change to the parameter values. In this example the change to the system was very dramatic. The natural frequency of the mode trebled and the damping ratio became ten times its previous value. For less dramatic changes to the system the change in the autoregressive moving average parameters is less noticeable.

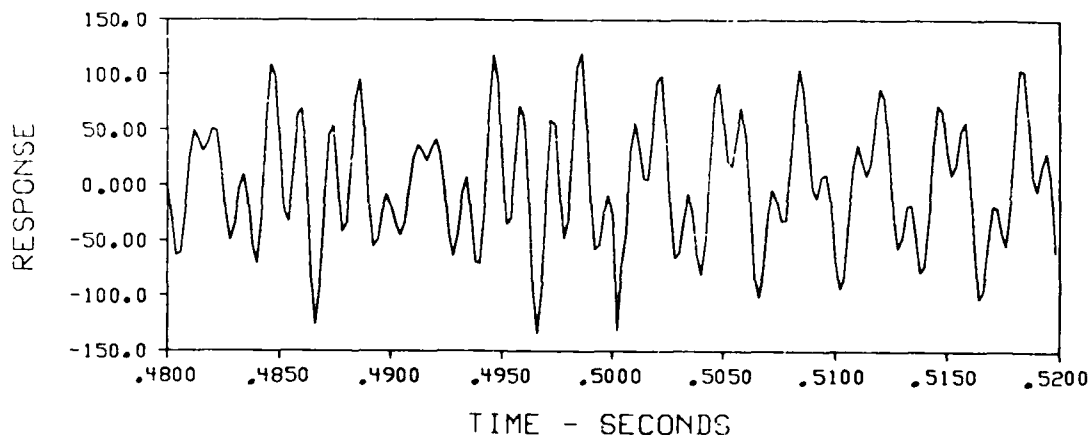


Figure 5: Response of a modal system to white noise excitation. System change occurs at .5 seconds.

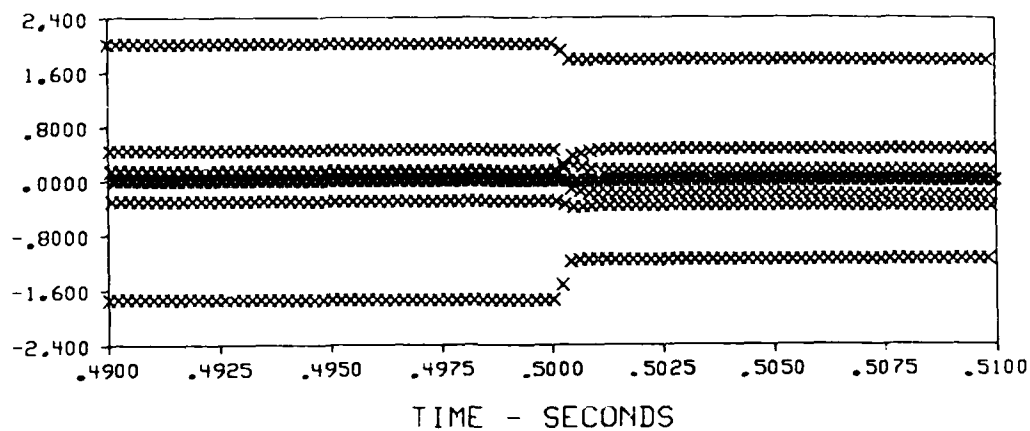


Figure 6: Estimated autoregressive moving average parameters.

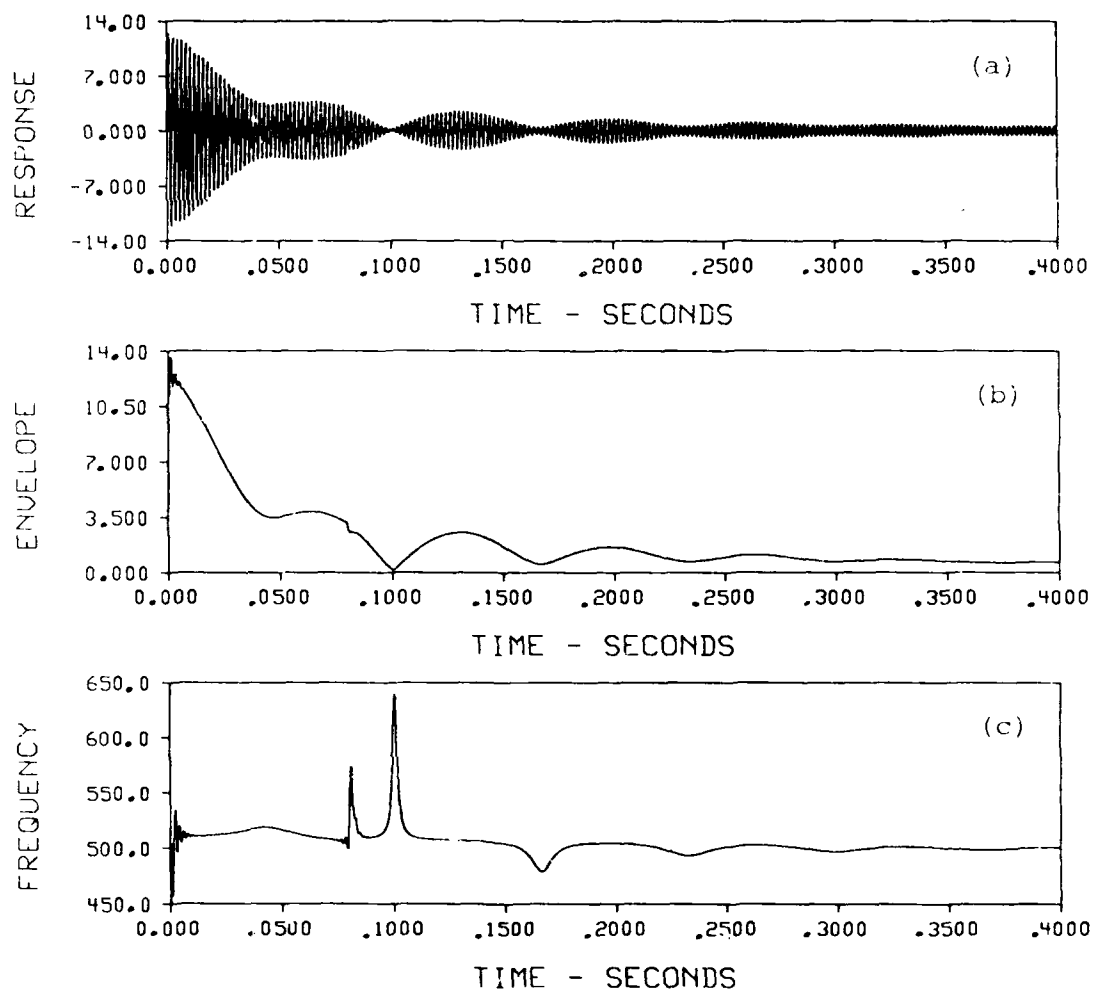


Figure 7: The response, the envelope of the response and the instantaneous frequency. The change to the system occurred at .08 seconds.

3.2 Transient Response tests

The system whose response is shown in figure 3 was used again, this time the system change occurred at 0.08 seconds. Figure 7 shows the response, its envelope and the instantaneous frequency. Here the change in the envelope when the system changes is small. The change in the instantaneous frequency is large. However, when the envelope is close to zero there is also a large change in the estimated instantaneous frequency. One of the problems of monitoring the instantaneous frequency for changes to the system would be to differentiate between these two reasons for the large fluctuation of the instantaneous frequency.

Another method that can be used to detect changes to a signal is the cepstrum [10]. The theoretical background will not be discussed here. The power cepstrum of a signal is the inverse Fourier transform of the log of the squared modulus of the Fourier transform of the signal. The log operation is performed to change multiplicative components in the spectrum into additive components. The discontinuity in the original signal produces ripples in the spectrum. The frequencies of the ripples are related to the time at which the discontinuity occurred in the original signal. The final inverse Fourier transform produces features at the time of the original discontinuity and also at multiples of this time. In this context we show how the cepstrum may be used to enhance the discontinuity feature in the envelope time history. Figure 8 shows the cepstrum of the envelope. The 'time' axis shown is often called the queffrequency axis (frequency of oscillations in the spectrum).

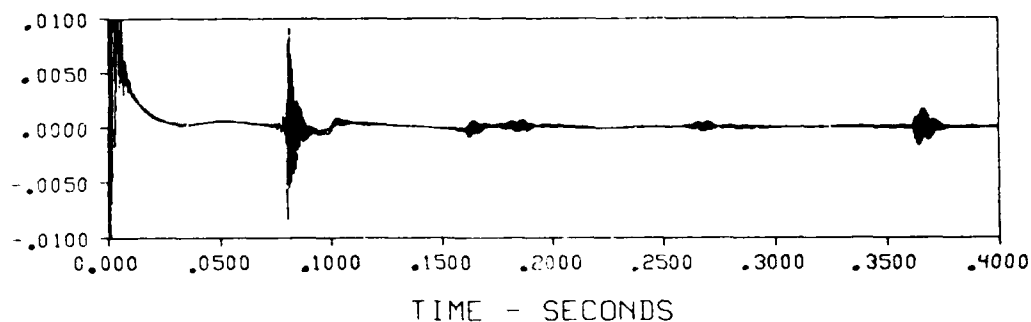


Figure 8: The cepstrum of the envelope of the response signal. The change occurred at .08 seconds.

4. SUMMARY

This paper has highlighted two methods that could be used to detect changes to a system by monitoring the response of that system. The systems modelled were modal systems whose impulse response could be modelled as the sum of damped sinusoids, and the change in the system was the alteration of the frequency and damping ratio of one of the modes of the system.

For systems whose response could be modelled as white noise passed through a linear filter it was shown that the change to the system could be detected from monitoring estimates of the coefficients of the linear filter. An advantage of this approach is that the estimation and monitoring of the parameters can be implemented online, although further work is required to make the estimation algorithms robust. One of the problems with this method is that the model

of the system needs to be very accurate in order to detect subtle changes to the system. The parameters of models that only model the global features of a complicated system's behaviour will not vary very much when a subtle change to the system occurs. Another application of this digital filter approach reported in reference [4] was to use it to generate an estimate of the excitation to the system and to monitor this estimated excitation for abnormalities. The detection of changes to a system that manifest themselves as an extra impulsive excitation is enhanced using this method over that achieved by monitoring the response only. This was found to be true even when the filter model was crude and only modelled the global features of the system's behaviour.

It was shown that changes to a system undergoing transient excitation could be detected by monitoring the envelope and instantaneous frequency of the response of that system. When the change occurred the envelope and instantaneous frequency underwent sharp changes. Monitoring of the instantaneous frequency only can lead to problems because the calculated instantaneous frequency undergoes large changes when the signal envelope is close to zero as well as at the time when the system undergoes a change. The envelope and instantaneous frequency are generated using finite impulse response digital filters and so there is scope to implement their calculation in hardware. Signals monitored using this technique need to be narrowband, because broadband signals have envelopes and instantaneous frequencies that have large fluctuations. These fluctuations cannot be distinguished from those occurring because of the system change.

It has been demonstrated that both methods could be useful for the detection of changes in a system. The methods need to be applied to real systems with component failures in order to evaluate their usefulness in a practical situation.

REFERENCES

1. D.H.BELL 1985 *Vibration Analysis to Improve Reliability and Reduce Failure - a collection of papers presented at the Design Automation Conference, Cincinnati, Ohio. Sponsored by the Reliability, Stress Analysis and Failure Prevention Committee, Design Engineering Division of the American Society of Mechanical Engineers.* An enveloping technique of early stage detection and diagnosis of faults in rolling element bearings.
2. P.BRADSHAW and R.B.RANDALL 1983 *MSA-Mechanical Signature Analysis, a collection of papers presented at the 9th biennial conference on Mechanical Vibration and Noise, Dearborn, Michigan. Sponsored by the Design Engineering Division, American Society of Mechanical Engineers.* Early detection and diagnosis of machine faults on the Trans Alaska pipeline.
3. P.DAVIES 1985 *Ph.D Thesis, Institute of Sound and Vibration Research, University of Southampton.* The application of time domain methods to the analysis of vibration (and acoustic) data.
4. P.DAVIES 1987 *Proceedings of the fifth International modal analysis conference, London.* Estimation and analysis of the input to a system for the detection of abnormalities in the excitation signal.
5. P.DAVIES and J.K.HAMMOND 1986 *Journal of Sound and Vibration* **111**(1),93-113. The use of signal envelopes to describe the bandlimited response of a class of systems and to define an alternative shock spectrum.

6. P.DAVIES and J.K.HAMMOND 1984 *Transactions of the American Society of Mechanical Engineers, Journal of Vibration, Acoustics, Stress and Reliability in Design* **106**,40-48. A comparison of Fourier and parametric methods for structural system identification.
7. F.B.HILDEBRAND 1949 *Advanced Calculus for Engineering*. Prentice-Hall Inc.
8. M.S.LAN and Y.NAERHEIM 1985 *Sensors and Controls for Manufacturing - a collection of papers presented at the Winter Annual Meeting of the American Society of Mechanical Engineers, Miami Beach, Florida..* In-process detection of tool breakage in milling.
9. R.H.LYON 1987 *Machinery Noise and Diagnostics*. Butterworth Publishers MA.
10. A.V.OPPENHEIM and R.W.SCHAFER 1975 *Digital Signal Processing*. Prentice-Hall.
11. L.R.RABINER and B.GOLD 1975 *Theory and application of digital signal processing*. Prentice-Hall Inc., Englewood Cliffs, New Jersey.
12. E.SKUDRZYK 1971 *The Foundations of Acoustics*. Springer Verlag, New York.
13. R.M.STEWART 1982 *Chapter 23 in Noise and Vibration (ed. R.G.White and J.G.Walker): Applications of signal processing techniques to machinery health monitoring*. Ellis Horwood Ltd.
14. D.A.WALLACE and M.S.DARLOW 1985 *Paper presented at the American Society of Mechanical Engineers' Conference on Mechanical Vibration and Noise at Cincinnati, Ohio, September 1985*. Signal processing of transient phenomena using Fourier transform techniques.
15. P.YOUNG 1984 *Recursive Estimation and Time-Series Analysis*. Springer Verlag.
16. P.YOUNG 1976 *International Journal of Control* **V23 No 5**, 593-612. Some observations on instrumental variable methods of time series analysis.

8. NONLINEAR TECHNIQUES

MODAL INTERACTIONS IN THE NONLINEAR RESPONSE OF STRUCTURAL ELEMENTS-THEORY AND EXPERIMENT

A. H. Nayfeh

Department of Engineering Science and Mechanics
Virginia Polytechnic Institute and State University
Blacksburg, Virginia 24061

and

L. D. Zavodney

Department of Engineering Mechanics
The Ohio State University
Columbus, Ohio 43210

The influence of modal interactions (i.e., internal or autoparametric resonances) on the nonlinear response of structural elements to a harmonic excitation was investigated both theoretically and experimentally. The method of multiple scales was used to determine the equations describing the modulation of the amplitudes and phases of the interacting modes for the case of a two-to-one internal resonance. Primary excitations of either of the interacting modes was considered. Steady-state periodic and aperiodic responses were determined. Conditions for the existence of amplitude- and phase-modulated responses were obtained. Solutions are presented showing period-multiplying bifurcations leading to chaos. To verify the theoretical predictions, we performed an experiment using a two-degree-of-freedom model consisting of two light-weight beams and two concentrated masses. The experimental results are in qualitative agreement with the theoretical results. A video tape of some of the observed nonlinear phenomena will be shown.

1. INTRODUCTION

Recently, the nonlinear response of internally coupled oscillators to a harmonic excitation has received considerable attention (Nayfeh and Mook [1]; Nayfeh [2]). They model the nonlinear response of ships, elastic pendulums, robots, shells, arches, bowed structures, and beams and plates under static and dynamic loadings. If u_1 and u_2 are the generalized coordinates of the two linear normal modes, then the governing equations have the form

$$\begin{aligned} \ddot{u}_1 + \omega_1^2 u_1 + 2\mu_1 \dot{u}_1 + \delta_1 u_1^2 + \delta_2 u_1 u_2 + \delta_3 u_2^2 + \delta_4 \dot{u}_1^2 + \delta_5 \dot{u}_1 \dot{u}_2 \\ + \delta_6 \dot{u}_2^2 + \delta_7 u_1 \ddot{u}_1 + \delta_8 u_2 \ddot{u}_1 + \delta_9 u_1 \ddot{u}_2 + \delta_{10} u_2 \ddot{u}_2 \\ + (h_{11} u_1 + h_{12} u_2) \cos \omega t = F \cos \omega t, \end{aligned} \quad (1)$$

$$\begin{aligned} \ddot{u}_2 + \omega_2^2 u_2 + 2\mu_2 \dot{u}_2 + \alpha_1 u_1^2 + \alpha_2 u_1 u_2 + \alpha_3 u_2^2 + \alpha_4 \dot{u}_1^2 + \alpha_5 \dot{u}_1 \dot{u}_2 \\ + \alpha_6 \dot{u}_2^2 + \alpha_7 u_1 \ddot{u}_1 + \alpha_8 u_2 \ddot{u}_1 + \alpha_9 u_1 \ddot{u}_2 + \alpha_{10} u_2 \ddot{u}_2 \\ + (h_{21} u_1 + h_{22} u_2) \cos \omega t = G \cos \omega t, \end{aligned} \quad (2)$$

where only linear and quadratic terms have been retained. Here, ω_1 and ω_2 are the linear undamped natural frequencies of the system, ω is the excitation frequency, the μ_n are the viscous damping coefficients of the two modes, and F , G , α_n , δ_n , and h_{mn} are constants.

In this paper, we consider the case $\omega_2 \approx 2\omega_1$ and $\omega = \omega_1$ or ω_2 . Special cases of the present problem were studied using various techniques by Sethna [3], Nayfeh, Mook and Marshall [4], Yamamoto and Yasuda [5], Sethna and Bajaj [6],

Mayfeh and Mook [1], Hatwal, Mallik and Ghosh [7], Haddow, Barr and Mook [8], Miles [9], and Mayfeh [10]. Four first-order ordinary differential equations that describe the modulation of the amplitudes and the phases of the interacting two modes were derived by Sethna [3] and Miles [9] using the method of averaging, and Nayfeh, Mook and Marshall [4], Haddow, Barr and Mook [8], and Nayfeh [10] using the method of multiple scales. These equations were used to determine the fixed points and their stability. The stable fixed points correspond to periodic responses. For some range of system and excitation parameters, Hopf bifurcations exist. The fixed points of the averaged equations lose their stability when the real part of a complex conjugate pair of eigenvalues changes sign from negative to positive. In these ranges, steady-state periodic responses do not exist. Instead, the response consists of amplitude- and phase-modulated motion, and for small damping, the amplitude and phases may experience period-multiplying bifurcations and chaos. Sethna [3] used an analog computer to integrate the averaged equations in this interval and found periodic amplitudes and phases. Nayfeh, Mook and Marshall [4] integrated a special form of equations (1) and (2) in this range and obtained amplitude- and phase-modulated responses. Later, Yamamoto and Yasuda [5] observed amplitude- and phase-modulated responses in their analog-computer simulations of a special form of equations (1) and (2). Hatwal, Mallik and Ghosh [7] reported numerical results for a special form of equations (1) and (2) showing periodically modulated motions and chaos. Miles [9] reported numerical calculations of the averaged equations showing chaotic and periodically modulated solutions. Nayfeh and Zavodney [11] experimentally observed amplitude- and phase-modulated responses in a simple mechanical system. Nayfeh, Balachandran, Colbert and Nayfeh [12] observed amplitude- and phase-modulated responses in the same mechanical system when the second mode is excited by a primary resonance.

2. ANALYSIS

We use the method of multiple scales (Nayfeh [13], [14]) to determine a second-order uniform expansion of the solution of equations (1) and (2) when $\omega_1 \approx 2\omega_2$. To this end, we introduce a small dimensionless parameter ϵ as a bookkeeping device and seek a uniform expansion in the form

$$u_1 = \epsilon u_{11}(T_0, T_1) + \epsilon^2 u_{12}(T_0, T_1) + \dots, \quad (3)$$

$$u_2 = \epsilon u_{21}(T_0, T_1) + \epsilon^2 u_{22}(T_0, T_1) + \dots, \quad (4)$$

where $T_0 = t$, a fast scale characterizing motions with the frequencies ω_1 , ω_2 , and Ω , and $T_1 = \epsilon t$, a slow scale characterizing the modulations of the amplitudes and phases with damping and the resonances. Moreover, we order the damping coefficients and the excitation amplitudes F and G so that their influence balances the nonlinearity. Consequently, we replace u_i by ϵu_i and F and G by ϵF and ϵG , respectively. Substituting equations (3) and (4) into equations (1) and (2) and equating coefficients of like powers of ϵ on both sides, we obtain:

Order ϵ

$$D_0^2 u_{11} + \omega_1^2 u_{11} = 0, \quad (5)$$

$$D_0^2 u_{21} + \omega_2^2 u_{21} = 0; \quad (6)$$

Order ϵ^2

$$\begin{aligned} D_0^2 u_{12} + \omega_1^2 u_{12} = & -2D_0 D_1 u_{11} - 2\mu_1 D_0 u_{11} - \delta_1 u_{11}^2 - \delta_2 u_{11} u_{21} \\ & - \delta_3 u_{21}^2 - \delta_4 (D_0 u_{11})^2 - \delta_5 D_0 u_{11} D_0 u_{21} - \delta_6 (D_0 u_{21})^2 - \delta_7 u_{11} D_0^2 u_{11} \\ & - \delta_8 u_{21} D_0^2 u_{11} - \delta_9 u_{11} D_0^2 u_{21} - \delta_{10} u_{21} D_0^2 u_{21} - (h_{11} u_{11} + h_{12} u_{21}) \cos \omega T_0 \\ & + F \cos \omega T_0, \end{aligned} \quad (7)$$

$$\begin{aligned} D_0^2 u_{22} + \omega_2^2 u_{22} = & -2D_0 D_1 u_{21} - 2\mu_2 D_0 u_{21} - \alpha_1 u_{11}^2 - \alpha_2 u_{11} u_{21} \\ & - \alpha_3 u_{21}^2 - \alpha_4 (D_0 u_{11})^2 - \alpha_5 D_0 u_{11} D_0 u_{21} - \alpha_6 (D_0 u_{21})^2 - \alpha_7 u_{11} D_0^2 u_{11} \\ & - \alpha_8 u_{21} D_0^2 u_{11} - \alpha_9 u_{11} D_0^2 u_{21} - \alpha_{10} u_{21} D_0^2 u_{21} - (h_{21} u_{11} \\ & + h_{22} u_{21}) \cos \omega T_0 + G \cos \omega T_0, \end{aligned} \quad (8)$$

where $D_n = \partial/\partial T_n$.

The general solution of equations (5) and (6) can be expressed as

$$u_{n1} = A_n(T_1) \exp(i\omega_n T_0) + cc \quad (9)$$

where cc stands for the complex conjugate of the preceding terms and the A_n are arbitrary functions of T_1 to this order of approximation; they are determined by imposing the solvability conditions (elimination of secular and small-divisor terms) at the next level of approximation. To proceed further, we need to specify the resonances under consideration.

2.1 The Primary Resonance of First Mode

To express quantitatively the nearness of the resonances, we introduce the detuning parameters σ_1 and σ_2 defined according to

$$\omega_2 = 2\omega_1 + \epsilon\sigma_1 \quad \text{and} \quad \Omega = \omega_1 + \epsilon\sigma_2. \quad (10)$$

Substituting equation (9) into equations (7) and (8) and using equations (10), we obtain

$$\begin{aligned} D_0^2 u_{12} + \omega_1^2 u_{12} = & -2i\omega_1 (A_1' + \mu_1 A_1) e^{i\omega_1 T_0} \\ & - 4\omega_1 A_1 A_2 A_1 e^{i(\omega_1 T_0 + \sigma_1 T_1)} + \frac{1}{2} F e^{i(\omega_1 T_0 + \sigma_2 T_1)} + cc + NST, \end{aligned} \quad (11)$$

$$\begin{aligned} D_0^2 u_{22} + \omega_2^2 u_{22} = & -2i\omega_2 (A_2' + \mu_2 A_2) e^{i\omega_2 T_0} \\ & - 4\omega_2 A_2 A_1^2 e^{i(\omega_2 T_0 - \sigma_1 T_1)} + cc + NST, \end{aligned} \quad (12)$$

where the prime indicates the derivative with respect to T_1 , NST stands for terms that do not produce secular terms, and

$$4\omega_1\Lambda_1 = \delta_2 + \delta_5\omega_1\omega_2 - \delta_8\omega_1^2 - \delta_9\omega_2^2, \quad (13)$$

$$4\omega_2\Lambda_2 = \alpha_1 - \alpha_4\omega_1^2 - \alpha_7\omega_1^2. \quad (14)$$

For a uniform expansion, the A_n must be chosen so that the terms in equations (11) and (12) that produce secular terms must vanish, thereby yielding the solvability conditions

$$2i\omega_1(A_1' + \mu_1 A_1) + 4\omega_1\Lambda_1 A_2 A_1 e^{-i\sigma_1 T_1} - \frac{1}{2} F e^{i\sigma_2 T_1} = 0, \quad (15)$$

$$2i(A_2' + \mu_2 A_2) + 4\Lambda_2 A_1^2 e^{-i\sigma_1 T_1} = 0. \quad (16)$$

To analyze the solutions of equations (15) and (16), we express the A_n in the polar form

$$A_1 = \frac{1}{2} a_1 (\Lambda_1 \Lambda_2)^{-1/2} e^{i\beta_1} \quad \text{and} \quad A_2 = \frac{1}{2} a_2 (\Lambda_1)^{-1} e^{i\beta_2}. \quad (17)$$

Substituting equations (17) into equations (15) and (16) and separating real and imaginary parts yields

$$a_1' = -\mu_1 a_1 - a_1 a_2 \sin \gamma_1 + f \sin \gamma_2, \quad (18)$$

$$a_2' = -\mu_2 a_2 + a_1^2 \sin \gamma_1, \quad (19)$$

$$a_1 \beta_1' = a_1 a_2 \cos \gamma_1 - f \cos \gamma_2, \quad (20)$$

$$a_2 \beta_2' = a_1^2 \cos \gamma_1, \quad (21)$$

where

$$\gamma_1 = \sigma_1 T_1 + \beta_2 - 2\beta_1, \quad \gamma_2 = \sigma_2 T_1 - \beta_1, \quad (22)$$

$$f = F \sqrt{\Lambda_1 \Lambda_2} / 2\omega_1. \quad (23)$$

It turns out that for the physical systems mentioned above $\Lambda_1 \Lambda_2 > 0$. Therefore, to the first approximation, the solution of equations (1) and (2) is

$$u_1 \approx \frac{a_1(t)}{\sqrt{\Lambda_1 \Lambda_2}} \cos[\omega_1 t + \beta_1(t)], \quad u_2 \approx \frac{a_2(t)}{\Lambda_1} \cos[\omega_2 t + \beta_2(t)], \quad (24)$$

where the amplitudes a_n and phases β_n are governed by equations (18)-(22).

Equations (18)-(22) are generic and describe the behavior of the responses of all two-degree-of-freedom systems with quadratic nonlinearities whose frequencies are in the ratio of two-to-one when the lower mode is excited by a primary excitation.

Periodic solutions of equations (1) and (2) correspond to the fixed points of equations (18)-(22), which in turn correspond to $a_1' = a_2' = 0$ and $\gamma_1' = \gamma_2' = 0$. It follows from equations (22) that

$$\beta_1' = \sigma_2 = \nu_1 \quad \text{and} \quad \beta_2' = 2\sigma_2 - \sigma_1 = \nu_2. \quad (25)$$

Then, the fixed points of equations (18)-(22) are given by

$$a_1^6 + 2(\mu_1\mu_2 - \nu_1\nu_2)a_1^4 + (\mu_1^2 + \nu_1^2)(\mu_2^2 + \nu_2^2)a_1^2 - f^2(\mu_2^2 + \nu_2^2) = 0 \quad (26)$$

and

$$a_2 = a_1^2(\mu_2^2 + \nu_2^2)^{-\frac{1}{2}}. \quad (27)$$

The stability of a particular fixed point with respect to a perturbation proportional to $\exp(\lambda T_1)$ is determined by the zeros of

$$\begin{aligned} &\lambda^4 + 2(\mu_1 + \mu_2)\lambda^3 + (\mu_1^2 + \mu_2^2 + 4\mu_1\mu_2 + \nu_1^2 + \nu_2^2 - a_2^2 + 4a_1^2)\lambda^2 \\ &+ [2\mu_1\mu_2^2 + 2\mu_1^2\mu_2 + 2\mu_1\nu_2^2 + 2\mu_2\nu_1^2 - 2\mu_2a_2^2 + 4(\mu_1 + \mu_2)a_1^2]\lambda \\ &+ \mu_1^2\mu_2^2 + \mu_1^2\nu_2^2 + \mu_2^2\nu_1^2 + \nu_1^2\nu_2^2 - \mu_2^2a_2^2 - \nu_2^2a_2^2 + 4\mu_1\mu_2a_1^2 \\ &- 4\nu_1\nu_2a_1^2 + 4a_1^4 = 0. \end{aligned} \quad (28)$$

According to the Routh-Hurwitz criterion, at least one root of equation (28) has a positive real part, and hence a fixed point given by equations (26) and (27) is unstable if all of the following conditions are not satisfied:

$$r_1r_2 - r_3 > 0, \quad r_3(r_1r_2 - r_3) - r_1^2r_4 > 0, \quad r_4 > 0, \quad (29)$$

where r_1, r_2, r_3 , and r_4 are, respectively, the coefficients of $\lambda^3, \lambda^2, \lambda^1$, and λ^0 in equation (28). The violation of the second condition in (29) would imply the existence of a pair of complex conjugate λ with a positive real part, and hence replacing the inequality by an equality yields the parameters for the Hopf bifurcation.

Representative variations of a_1 and a_2 with σ_2 for given values of σ_1, μ_1 , and μ_2 are shown in Fig. 1. The local stability of a fixed point is determined from conditions (29). The unstable parts are shown by the broken lines in Fig. 1. As one varies the control parameter σ_2 and hence Ω , the fixed points lose their stability in one of two ways: either an eigenvalue crosses the imaginary axis into the right-half plane along the real axis or a pair of complex-conjugate eigenvalues cross the imaginary axis into the right-half plane. The first type of instability corresponds to the jump phenomenon, whereas the second type corresponds to the extensively studied problem of the Hopf bifurcation (Marsden and McCracken, [15]). Based on the Hopf bifurcation theorem (Hale [16]), the modulation equations (18)-(22) are expected to exhibit limit-cycle oscillations near the Hopf-bifurcation values Ω_1 and Ω_2 . Sethna and Bajaj [6] carried out a bifurcation analysis for the latter case and determined the amplitudes of the limit cycles. Hence, the amplitudes a_n and phases β_n of u_1 and u_2 are expected to modulate with time, and consequently u_1 and u_2 are expected to be aperiodic. Sethna [3] integrated the averaged equations using an analog computer in the interval $\Omega_1 \leq \Omega \leq \Omega_2$ and found that the a_n and β_n are periodic. A digital solution (Nayfeh, Mook, Marshall, [4]) of a special case of equations (1) and (2) for a value of Ω in the interval $\Omega_1 \leq \Omega \leq \Omega_2$ is shown in Fig. 2; it represents an amplitude- and phase-modulated motion. Similar results were obtained by Yamamoto and Yasuda [5] and Nayfeh and Raouf [17] using analog and digital simulations, respectively. Numerical solutions of equations (18)-(22) show that the limit-cycle solutions may undergo period-doubling bifurcations, leading to chaos (Miles, [9]).

2.2 Primary Resonance of Second Mode

In this case, we introduce the detuning parameters σ_1 and σ_2 defined according to

$$\omega_2 = 2\omega_1 + \epsilon\sigma_1 \quad \text{and} \quad \Omega = \omega_2 + \epsilon\sigma_2. \quad (30)$$

Using equations (30) in eliminating the terms that produce secular terms from u_{12} and u_{22} , we obtain in place of equations (15) and (16), the following modulation equations:

$$2i(A_1' + \mu_1 A_1) + 4\Lambda_1 A_2 A_1 e^{-i\sigma_1 T_1} = 0, \quad (31)$$

$$2i\omega_2(A_2' + \mu_2 A_2) + 4\omega_2 \Lambda_2 A_1^2 e^{-i\sigma_1 T_1} - \frac{1}{2} G e^{i\sigma_2 T_1} = 0, \quad (32)$$

where the Λ_n are defined in equations (13) and (14).

Substituting the polar form given by equations (17) into equations (31) and (32) and separating real and imaginary parts, we obtain the equations describing the modulation of the amplitudes and phases with time. These equations are used to determine the steady-state solutions (fixed points) and their stability.

In this case, there are two possible steady-state solutions. First,

$$a_1 = 0 \quad \text{and} \quad a_2 = \frac{g}{\sqrt{\sigma_2^2 + \mu_2^2}}, \quad g = G/2\omega_2, \quad (33)$$

and the response is given by

$$u_1 = 0 \quad \text{and} \quad u_2 = a_2 \cos(\Omega t - \gamma_2) + \dots, \quad (34)$$

where γ_2 is a constant; this is essentially the linear solution. The first mode is unexcited and the amplitude of the second mode increases linearly with the amplitude g of the excitation. Second,

$$a_1 = (\Lambda_1 \Lambda_2)^{-\frac{1}{2}} [x_1 \pm (f_2^2 \Lambda_1^2 - x_2^2)^{\frac{1}{2}}]^{\frac{1}{2}}, \quad (35)$$

$$a_2 = a_2^* = |\Lambda_1|^{-1} [\mu_1^2 + \frac{1}{4} (\sigma_1 + \sigma_2)^2]^{\frac{1}{2}}, \quad (36)$$

where

$$x_1 = \frac{1}{2} \sigma_2 (\sigma_1 + \sigma_2) - \mu_1 \mu_2, \quad (37)$$

$$x_2 = \sigma_2 \mu_1 + \frac{1}{2} \mu_2 (\sigma_1 + \sigma_2), \quad (38)$$

The response in this case is given by

$$u_1 = a_1 \cos(\frac{1}{2} \Omega t - \frac{1}{2} \gamma_1 - \frac{1}{2} \gamma_2) + \dots, \quad (39)$$

$$u_2 = a_2^* \cos(\Omega t - \gamma_2) + \dots. \quad (40)$$

We note a very interesting feature of the second solution, namely, the amplitude a_2 of the directly excited second mode is independent of the amplitude g of the excitation, whereas the amplitude a_1 of the first mode that is not directly excited is a function of the excitation amplitude.

Carrying out a stability analysis of the fixed points, as in the preceding section, we find that the eigenvalues determining the stability of the linear solution are

$$\lambda = -\mu_1 \pm \sqrt{\Lambda_1^2 a_2^2 - v_1^2}, \quad -\mu_2 \pm i v_2, \quad (41)$$

where

$$v_1 = \frac{1}{2} (\sigma_1 + \sigma_2) \quad \text{and} \quad v_2 = \sigma_2. \quad (42)$$

It follows from equations (41) that the linear solution is stable if and only if $a_2 \leq \mu_1 + v_1$ or $a_2 \leq a_2$. On the other hand, the eigenvalues determining the stability of the nonlinear solution are given by

$$\begin{aligned} \lambda^4 + 2(\mu_1 + \mu_2)\lambda^3 + [\mu_2^2 + 4\mu_1\mu_2 + v_2^2 + 4\Lambda_1\Lambda_2a_1^2]\lambda^2 \\ + [2\mu_1\mu_2^2 + 2\mu_1v_2^2 + 4\Lambda_1\Lambda_2(\mu_1 + \mu_2)a_1^2]\lambda \\ + 4\Lambda_1\Lambda_2a_1^2[\Lambda_1\Lambda_2a_1^2 + \mu_1\mu_2 - v_1v_2] = 0. \end{aligned} \quad (43)$$

Using the Routh-Hurwitz conditions (29), we find that the necessary and sufficient conditions that none of the roots of equations (43) have positive real parts are

$$\Lambda_1\Lambda_2a_1^2 + \mu_1\mu_2 - v_1v_2 > 0, \quad (44)$$

$$\begin{aligned} 4\mu_1\mu_2(\mu_2^2 + v_2^2)(4\mu_1^2 + 4\mu_1\mu_2 + \mu_2^2 + v_2^2) + 8(\mu_1 + \mu_2)^2\Lambda_1\Lambda_2a_1^2 \\ \cdot (\mu_2^2 + 2\mu_1\mu_2 + 2v_1v_2 + v_2^2) > 0. \end{aligned} \quad (45)$$

Condition (44), in conjunction with equations (35) and (36), implies that the solution corresponding to the positive sign is stable whereas the solution corresponding to the negative sign is unstable. The violation of condition (45) would imply the existence of a pair of complex-conjugate roots of equation (43) with a positive real part. When $v_1v_2 > 0$, condition (45) is satisfied for all values of μ_1, μ_2 , and g . On the other hand, when $v_1v_2 < 0$, condition (45) may be violated, depending the values of the v_n, μ_n , and g .

Figure 3 shows the variation of a_1 and a_2 with g for $\Lambda_1 = 0.5, \Lambda_2 = 0.25, \sigma_1 = 0.0, \sigma_2 = 0.0, \mu_1 = 0.005$, and $\mu_2 = 0.005$. In this case, $v_1 = 0.0, v_2 = 0.0$, and $x_1 = -0.000025$. Since $x_1 < 0$, equation (35) has one real root when $g \geq \zeta_2$, where $\zeta_2 \approx 0.00005$. Since conditions (44) and (45) are satisfied, this root is stable. Consequently, when $g \leq \zeta_2$, the response is given by equation (34); the first mode is not excited because $a_1 = 0$ and the amplitude of the second mode is proportional to g . When $g > \zeta_2$, the response is given by equations (39) and (40) where $a_2 = a_2^* = 0.01 = \text{constant}$ for all values of g greater than ζ_2 and a_1 is given by equation (35). Hence, if an experiment is performed by setting $\Omega \approx \omega_2$ and the detunings and damping coefficients are such that $x_1 < 0$ and $v_1v_2 > 0$, one expects the second mode to dominate. This is initially so. But as g increases beyond a critical value ζ_2 , a_2 remains constant and equal to a_2^* (i.e., second mode saturates) and the extra energy is spilled over into the first mode. The saturation value a_2^* can be very small if $\sigma_1 + \sigma_2$ and μ_1 are small. The saturation phenomenon was first discovered by Nayfeh, Mook and Marshall [4] in connection with the pitching and rolling of ships. They found that a ship whose pitch frequency is approximately twice the roll frequency exhibits undesirable roll characteristics, as observed by Froude in 1863. To

verify the perturbation result, Nayfeh, Mook, and Marshall [4] integrated a special form of equations (1) and (2) for a long time and determined the amplitudes of u_1 and u_2 . The results of the numerical simulation are in excellent agreement with those predicted by the perturbation solution, as shown in Figure 3.

As a second example, we let $\Lambda_1 = 1.0$, $\Lambda_2 = 0.5$, $\mu_1 = \mu_2 = 0.02$, $\sigma_1 = -0.03$, and $\sigma_2 = 0.12$, then $v_1 = 0.045$, $v_2 = -0.03$, and $x_1 = -0.00095$. Hence, equation (35) has one real root for all values of $g \geq \zeta_2$, where $\zeta_2 = 0.00178$, condition (44) is satisfied for all $g > \zeta_2$, but condition (45) is violated for all values of $g \geq \zeta_3$, where $\zeta_3 = 0.003$. Consequently, the response consists of a pure second mode when $g \leq \zeta_2$, a combined periodic first and second modes given by equations (39) and (40) with a_2 being equal to $a_2 = 0.04924$ when $\zeta_2 < g < \zeta_3$, and an amplitude- and phase-modulated combined first and second modes when $g \geq \zeta_3$.

Figure 4 shows the variation of a_1 and a_2 with g when $\Lambda_1 = 0.5$, $\Lambda_2 = 0.25$, $\sigma_1 = 0.0$, $\sigma_2 = 0.025$, and $\mu_1 = \mu_2 = 0.005$. In this case, $v_1 = 0.0125$, $v_2 = 0.025$ and $x_1 = 0.0002875$. Hence, equation (35) has only one real root, which satisfies conditions (44) and (45) when $g > \zeta_2$, where $\zeta_2 = 0.00068$. It has two real roots when $\zeta_1 \leq g \leq \zeta_2$, where $\zeta_1 = 0.0038$. The larger root satisfies conditions (44) and (45), and hence it is stable, whereas the smaller root satisfies condition (45) but violates condition (44), and hence it is unstable.

Figure 5 shows frequency-response curves for the case $\Lambda_1 = 1.0$, $\Lambda_2 = 0.5$, $\mu_1 = \mu_2 = 0.02$, $\sigma_2 = 0.12$, and $g = 0.1$. Again the unstable portions are represented by broken lines. In addition to the jump phenomenon, Figure 5 shows the interval $-0.047 \leq \sigma_1 \leq -0.0127$, in which a pair of complex-conjugate roots of equation (43) with a positive real part, implying the existence of a Hopf bifurcation. In this interval, the response is amplitude- and phase-modulated combined first and second modes. Nayfeh and Raouf [17] presented digital results showing amplitude- and phase-modulated responses of a special form of equations (1) and (2) and period-multiplying bifurcations of the solutions of the averaged equations.

3. EXPERIMENT

3.1 Primary Resonance of First Mode

To observe these amplitude- and phase-modulated motions, we conducted an experiment using a mechanical system consisting of two light-weight beams and two concentrated masses as shown in Fig. 6 and described in Appendix A. A similar model was used by Haddow, Barr and Mook [8] to observe saturation when $\Omega \approx \omega_2$ and the response when $\Omega \approx \omega_1$. The model was excited by a 250 lb electrodynamic shaker driven by a 2500 watt power amplifier. The shaker was driven by a sinusoidal waveform generated by a waveform synthesizer that has a 0.0001 Hz resolution. The response of the system to a harmonic excitation at the base is governed by a special form of equations (1) and (2). The lengths L_1 and d were adjusted so that the linear natural frequencies of the system were approximately in the ratio of two-to-one (i.e., $f_2 \approx 2f_1$). The linear resonant frequencies were determined to be $f_1 = 8.03$ Hz and $f_2 = 16.25$ Hz by performing a routine modal analysis using random excitations. Since the damping in the structure is very small, these resonant frequencies are very close to the linear natural frequencies. The associated mode shapes obtained theoretically are shown in Fig. 6. Relative displacements of the two masses were measured by strain gages mounted near the bases of the beams. The excitation frequency f was slowly varied (in steps of 0.0001 Hz) up and down between 7.6 Hz and 8.6 Hz while keeping all other parameters constant, including the table acceleration. The acceleration level of the table was kept constant by a digital computer that was used as a closed-loop feedback controller.

The response was analyzed using an FFT analyzer and the steady-state amplitudes a_1^* and a_2^* of the two modes comprising the total displacement w_1 of M_1 for the periodic cases were determined. They are plotted in Fig. 7 as a function of f . The a_i^* are measures that are proportional to the amplitudes a_i of the modes. This happens because in general, the governing partial differential equation is typically separated into spatial and temporal functions, such as

$$v(s,t) = \sum_j r \psi_j(s) G_j(t)$$

where r is a scaling factor, the $\psi_j(s)$ are the spatial functions, typically the linear eigenfunctions, and the $G_j(t)$ are the temporal modulations, which appear in equations (1) and (2). The displacement of mass m_1 can be related to the surface strain at the base of beam 1 as measured by the strain gage provided the mode shape (eigenfunction) is known. Hence, we are measuring a discrete value of $\psi(s)$ to indicate the value of $\psi(L_1)$ which is a function of the mode shape; the magnitudes a_i^* will be proportional to the values of $\psi(s)$ at the gage location and will be scaled by r and modulated by $G(t)$. The excitation frequencies marking the transition from periodic to aperiodic responses are marked in Fig. 7 as the Hopf-bifurcation points. The experimental results in this figure are qualitatively in agreement with the theoretically determined frequency-response curves in Fig. 1.

Representative time traces of the displacement w_1 of mass M_1 are shown in Fig. 8 before and after the Hopf bifurcation; this displacement is a linear combination of the generalized coordinates u_1 and u_2 of the two modes. The displacements of the individual modes were obtained by filtering the signal and are shown in Fig. 9. These experimentally determined time traces are qualitatively in agreement with those obtained numerically and are shown in Fig. 2. The constant-amplitude response that occurs before the bifurcation corresponds to a stable fixed point (point attractor) in the projection of the trajectory on the $a_2 - a_1$ plane. These amplitudes were simultaneously monitored on an oscilloscope as the system experienced a bifurcation. The constant amplitude periodic motion gave rise to an aperiodic motion whose nature changed as the unstable region was penetrated. As the frequency approached the other "Hopf-bifurcation point", the aperiodic motion gave way to a constant amplitude periodic motion. Fig. 10 shows a projection of the long-time trajectory on the $u_2 - u_1$ plane. Before the bifurcation, the periodic response is stationary and appears as a "figure eight" since the nonlinearity adjusts the frequencies of the two modes so that the response period of one mode is exactly twice that of the other mode. Inside the unstable region the "figure eight" response is observed to evolve because the two modes are constantly exchanging energy.

3.2 Primary Resonance of Second Mode

In this case, the lengths of the beams were adjusted so that the the first two natural frequencies were found to be approximately 7.62 Hz and 15.23 Hz.

To demonstrate the instability of the structure when $g > \zeta_2$, we excited the structure near the second natural frequency 15.23 Hz at a low amplitude. The response consisted of only the second mode, as predicted by linear theory. When the structure was excited at a larger amplitude the second mode responded with the amplitude predicted by the linear theory as expected. However, after about 500 cycles, the first mode appeared and began to grow, while simultaneously the second mode diminished. This was readily observed in the FFT of the response, and seen as a distorted waveform on the oscilloscope. Thus the linear solution was seen to be unstable and both the first and second modes appeared in the response as predicted by the nonlinear theory and in contrast with the predictions of the linear theory. An interesting point regarding this phenomenon is that the level of excitation was so small that vibration at approximately 15.23 Hz was not even discernable when one's hand was placed on the shaker

table. Thus it was observed that the nonlinearities present were affecting the response dramatically even at extremely low levels of excitation.

To demonstrate the saturation phenomenon, the amplitude of excitation was increased slightly while keeping the excitation frequency fixed at 15.23 Hz. The response, after the transients decayed, showed that the amplitude of the second mode (15.23 Hz) did not increase -- rather the energy went into the first mode. This was seen on the FFT as an increased peak at the frequency (7.62 Hz) of the first mode. The waveform, originally consisting of the second mode 15.23 Hz waveform, became distorted as it gradually became dominated by the first mode. Further increases in the amplitude of the excitation continued to increase only the amplitude of the first mode in the steady-state condition. Initially the amplitude of the second mode increased, as observed in the instantaneous FFT of the response; however, as the amplitude of the second mode increased, it pulled up the amplitude of the first mode. This interaction eventually decayed to the steady-state response in which the amplitude of the second mode returned to its saturated level, while the amplitude of the first mode was noticeably higher. The results are documented in a video tape.

Recently, the same model was used by Nayfeh, Balachandran, Colbert, and Nayfeh [12] to observe amplitude- and phase-modulated motions. They developed the hardware and software necessary to demodulate the amplitude- and phase-modulated response. An example is shown in Fig. 11.

4. SUMMARY

We have presented in this paper observations of amplitude- and phase-modulated responses of a two-degree-of-freedom mechanical system with quadratic nonlinearities to a harmonic excitation. The linear natural frequencies of the system were tuned so that they were approximately in the ratio of two-to-one and the excitation frequency was slowly varied up and down around the lower natural frequency. We observed the transition from periodic to aperiodic motions, indicating the occurrence of a Hopf bifurcation. Moreover we excited the system near the second natural frequency and verified the saturation phenomenon and the instability of the linear solution. Furthermore, amplitude- and phase-modulated responses of the same mechanical system were recently observed by Nayfeh, Balachandran, Colbert, and Nayfeh.

ACKNOWLEDGEMENT

This work was supported by the Air Force Office of Scientific Research under Grant No. AFOSR-86-0090, and the National Science Foundation under Grant No. MSM-8521748.

Appendix A: Description of the Model

The model was fabricated from mild steel according to the following dimensions: $L_1 = 158.8$ mm, $L_2 = 152.4$ mm, and $d = 89.2$ mm. The cross-sectional dimensions of beam 1 are 1.651 mm x 12.83 mm and beam 2 are 0.507 mm x 12.70 mm. The mass density per unit length are $\rho_1 = 0.164$ g/mm and $\rho_2 = 0.057$ g/mm. The cross-sectional dimensions of mass 1 are 19.0 mm x 19.0 mm and mass 2 are 15.9 mm x 12.7 mm. The depths are such that their total mass, including the mounting screws, is $m_1 = 31.1$ g and $m_2 = 40.0$ g. Using these dimensions, the frequency of the third mode (characterized by the out-of-plane motion of beam 2 caused by the torsion of beam 1) is far removed from the frequency of the second mode; hence a two-mode formulation is adequate to describe the response of the model. We have conducted experiments with similar models whose dimensions are more than twice those of this model; all that is required is the two-to-one internal resonance and higher resonances far removed.

Appendix B: Description of Test Procedure

The test model was excited by a 250 lb electrodynamic shaker driven by a 2500 watt power amplifier. Sinusoidal waveforms used to drive the shaker were generated by a waveform synthesizer that had a 0.0001 Hz resolution. Frequency sweeps were made in small steps of 0.0001 Hz to minimize the transient response. The acceleration level of the table was held constant (as the frequency was swept) by a digital computer used as a closed-loop feedback controller.

The amplitude of each mode was monitored on an FFT analyzer. The natural frequencies and mode shapes were obtained by performing a routine modal analysis using a random excitation.

Since any one transducer location will detect one mode more directly than another mode, the amplitudes of the responses shown in Figure 4, 5, 6, and 7 are to be understood as being proportional to the amplitude of the mode, not a direct measurement of the mode. For this reason, no scale is put on these plots. During the large amplitude response shown in Figure 4, the peak-to-peak amplitude of m_1 was on the order of 5 mm, or approximately 3% of L_1 .

REFERENCES

1. A. H. NAYFEH and D. T. MOOK 1979 Nonlinear Oscillations. New York: Wiley-Interscience.
2. A. H. NAYFEH 1988a Application of the Method of Multiple Scales to Nonlinearly Coupled Oscillators. Chapter for the Lasers, Molecules, and Methods, a Volume in the Advances in Chemical Physics Series.
3. P. R. SETHNA 1965 Journal of Applied Mechanics 32, 576-582. Vibrations of dynamical systems with quadratic nonlinearities.
4. A. H. NAYFEH, D. T. MOOK, and L. R. MARSHALL 1973 Journal of Hydrodynamics 7, 145-152. Nonlinear coupling of pitch and roll modes in ship motions.
5. T. YAMAMOTO and K. YASUDA 1977 Bulletin of the Japanese Society of Mechanical Engineering 20, 168-175. On the internal resonance in a nonlinear two-degree-of-freedom system forced vibrations near the lower resonance point when the natural frequencies are in the ratio 1:2).
6. P. R. SETHNA and A. K. BAJAJ 1978 Journal of Applied Mechanics 43, 895-902. Bifurcations in dynamical systems with internal resonance.
7. H. HATWAL, A. K. MALLIK and A. GHOSH 1983 Journal of Applied Mechanics 50, 663-668. Forced nonlinear oscillations of an autoparametric system - part 2: chaotic responses.
8. A. G. HADDOW, A. D. S. BARR, and D. T. Mook 1984 Journal of Sound and Vibration 97, 451-473. Theoretical and experimental study of modal interaction in a two-degree-of-freedom structure.
9. J. W. MILES 1984 Physica D 13, 247-260. Resonantly forced motion of two quadratically coupled oscillators.
10. A. H. NAYFEH 1988b accepted for publication Journal of Ship Research. On the undesirable roll characteristics of ships in regular seas.
11. A. H. NAYFEH and L. D. ZAVODNEY 1988 accepted for publication, Journal of Applied Mechanics. Experimental observation of amplitude- and phase-modulated responses of two internally coupled oscillators to a harmonic excitation.
12. A. H. NAYFEH, B. BALANCHANDRAN, M. A. COLBERT, and M. A. NAYFEH, under preparation. Theoretical and experimental investigation of complicated responses of a two-degree-of-freedom structure.
13. A. H. NAYFEH 1973 Perturbation Methods. New York: Wiley-Interscience.
14. A. H. NAYFEH 1981 Introduction to Perturbation Techniques. New York: Wiley-Interscience.
15. J. E. MARSDEN and M. McCracken 1976 Hopf Bifurcation and its Applications. New York: Springer-Verlag.
16. J. K. HALE 1963 Oscillations in Nonlinear Systems. New York: McGraw Hill.
17. A. H. NAYFEH and R. A. RAOUF 1986 AIAA Paper No. 86-0964, a Collection of Technical Papers, pp. 555-563; also accepted for publication in the International Journal of Solids and Structures. Nonlinear oscillation of circular cylindrical shells.

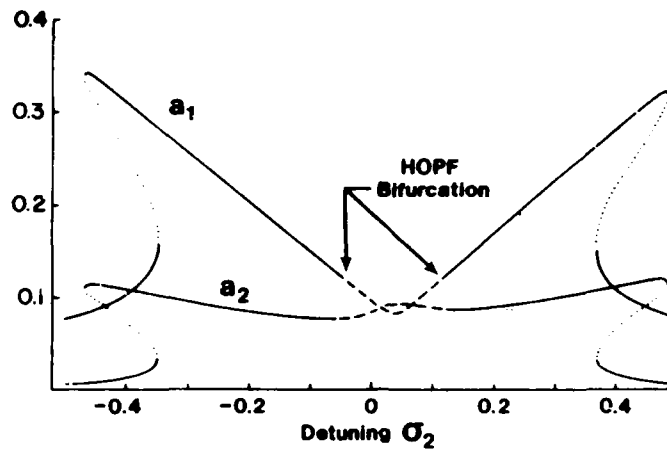


Figure 1. Theoretically determined frequency-response curves when the excitation frequency is nearly equal to the lower frequency. $\sigma_1 = 0.08$, $\mu_1 = \mu_2 = 0.075$, $f = 0.075$: solid curves, stable;, unstable with at least one eigenvalue being positive; ----, unstable with the real part of a complex-conjugate pair of eigenvalues being positive.

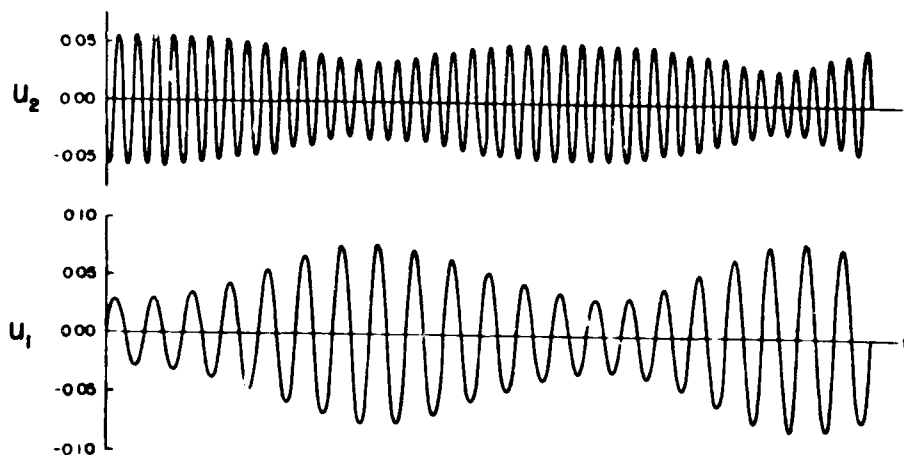


Figure 2. The long-time behavior of a numerically calculated amplitude- and phase-modulated motion of a special case of equations (1) and (2): all δ_i and α_i are zero except $\delta_2 = -1$, $\alpha_1 = 1$, $\omega_1 = 0.5$, $\omega_2 = 1.0$, $\alpha = 0.5$, $\mu_1 = \mu_2 = 0.85$, $F = 0.001$, $G = C$, and $h_{mn} = 0$.

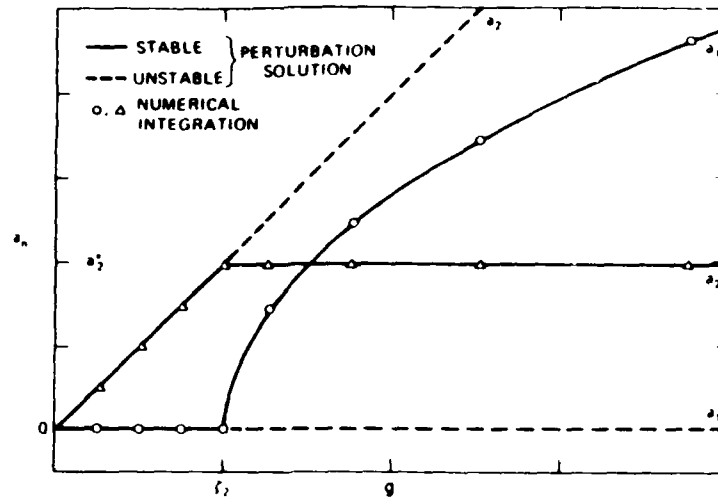


Figure 3. Amplitudes of the response as a function of the amplitude of the excitation when the second mode is excited by a primary resonance: all δ_1 and α_1 are zero except $\delta_2 = -1$, $\alpha_1 = 1$, $\omega_1 = 0.5$, $\omega_2 = 1.0$, $\sigma_2 = 0$, $\mu_1 = \mu_2 = 0.005$, $h_{mn} = 0$, and $F = 0$.

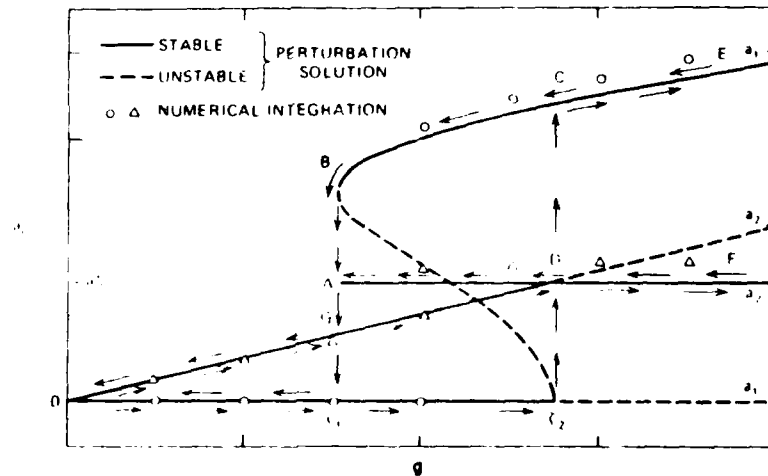


Figure 4. Amplitudes of the response as a function of the amplitude of the excitation when the second mode is excited by a primary resonance: all δ_1 and α_1 are zero except $\delta_2 = -1$, $\alpha_1 = 1$, $\omega_1 = 0.5$, $\omega_2 = 1.0$, $\sigma_2 = 0.025$, $\mu_1 = \mu_2 = 0.005$, $h_{mn} = 1$, and $F = 0$.

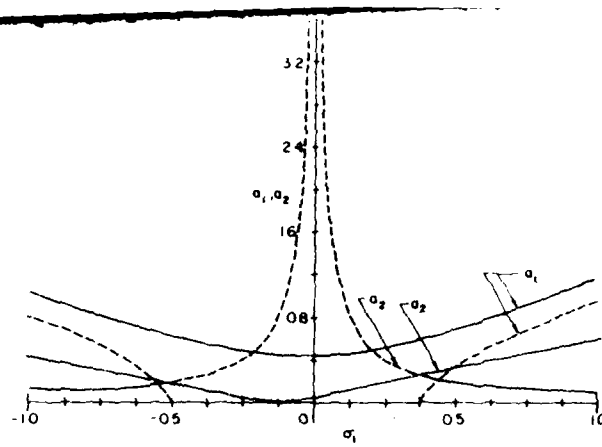


Figure 5. Frequency-response curves for the case $\Lambda_1 = 1.0$, $\Lambda_2 = 0.5$, $\mu_1 = \mu_2 = 0.02$, $\sigma_2 = 0.12$, $g = 0.1$.

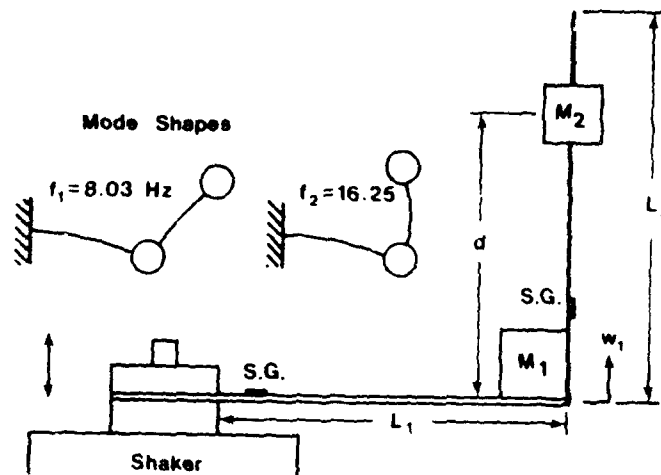


Figure 6. Two-degree-of-freedom model tuned for a 2:1 internal resonance and accompanying linear mode shapes. Beam 1: 1.651 mm x 12.83 mm x 158.7 mm, $\rho_1 = 0.164$ g/mm, $m_1 = 31.1$ g; Beam 2: 0.507 mm x 12.70 mm x 1552.4 mm, $\rho_2 = 0.057$ g/mm, $m_2 = 40.0$ g; $d = 89.2$ mm.

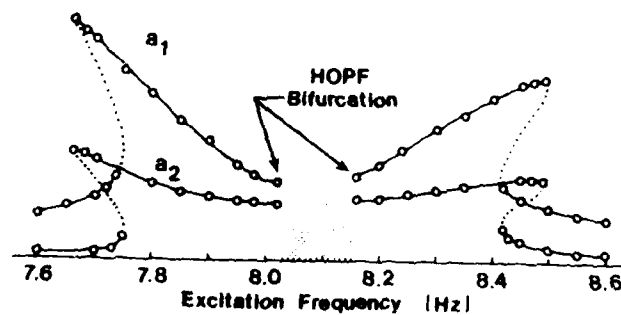


Figure 7. Experimentally determined frequency-response curves when the excitation frequency f is near the first natural frequency $f_1 = 8.03$ Hz; the shaded region corresponds to aperiodic long-time motions. These amplitudes are proportional to the actual amplitudes of the modes of the structure.

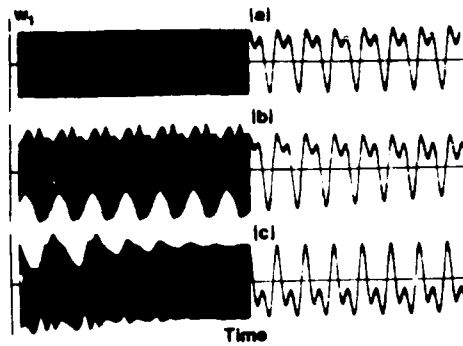


Figure 8. Time traces of the displacement of mass M_1 before and after the bifurcation from periodic to aperiodic responses. The left portion shows the envelope of modulation by compressing time, and the right portion shows a sample with an expanded time scale; (a) $f = 8.02$ Hz, (b) $f = 8.03$ Hz, (c) transition from $f = 8.15$ Hz to $f = 8.16$ Hz.

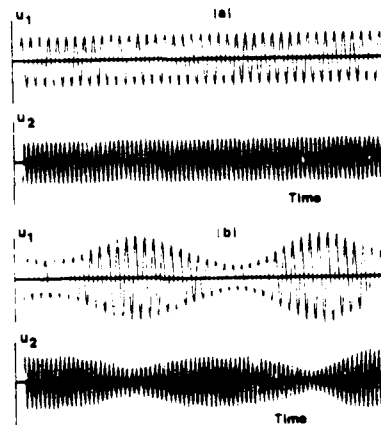


Figure 9. Modal components of the displacement of mass M_1 as a function of time (a) before the bifurcation ($f = 8.02$ Hz) and (b) after the bifurcation ($f = 8.03$ Hz). These traces were filtered from the data of Figure 5. The higher harmonics that appear most noticeably in u_2 are a consequence of the sampling frequency of the digital scope and were not present in the analogue waveform.

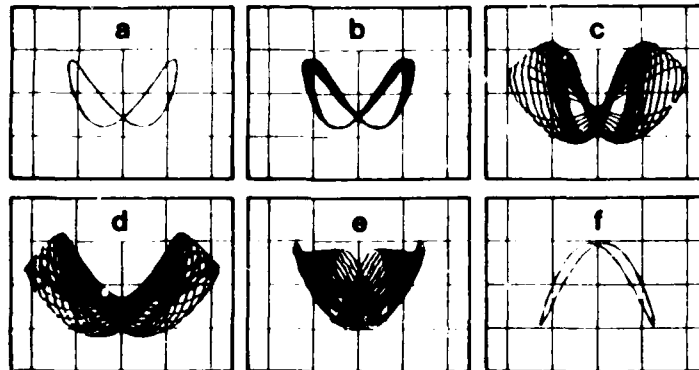


Figure 10. Variation of the displacement u_2 of the second mode with the displacement u_1 of the first mode: (a) periodic motion before the bifurcation, $f = 8.02$ Hz; (b) aperiodic motion just after the bifurcation, $f = 8.025$ Hz; (c-e) aperiodic motion in the unstable region, $8.03 < f < 8.15$; and (f) return to a periodic motion $f = 8.16$ Hz. Only portions of a "complete cycle" are shown for the aperiodic responses because the overlapping of a complete cycle obscures the projection of the amplitude- and phase-modulated motion.

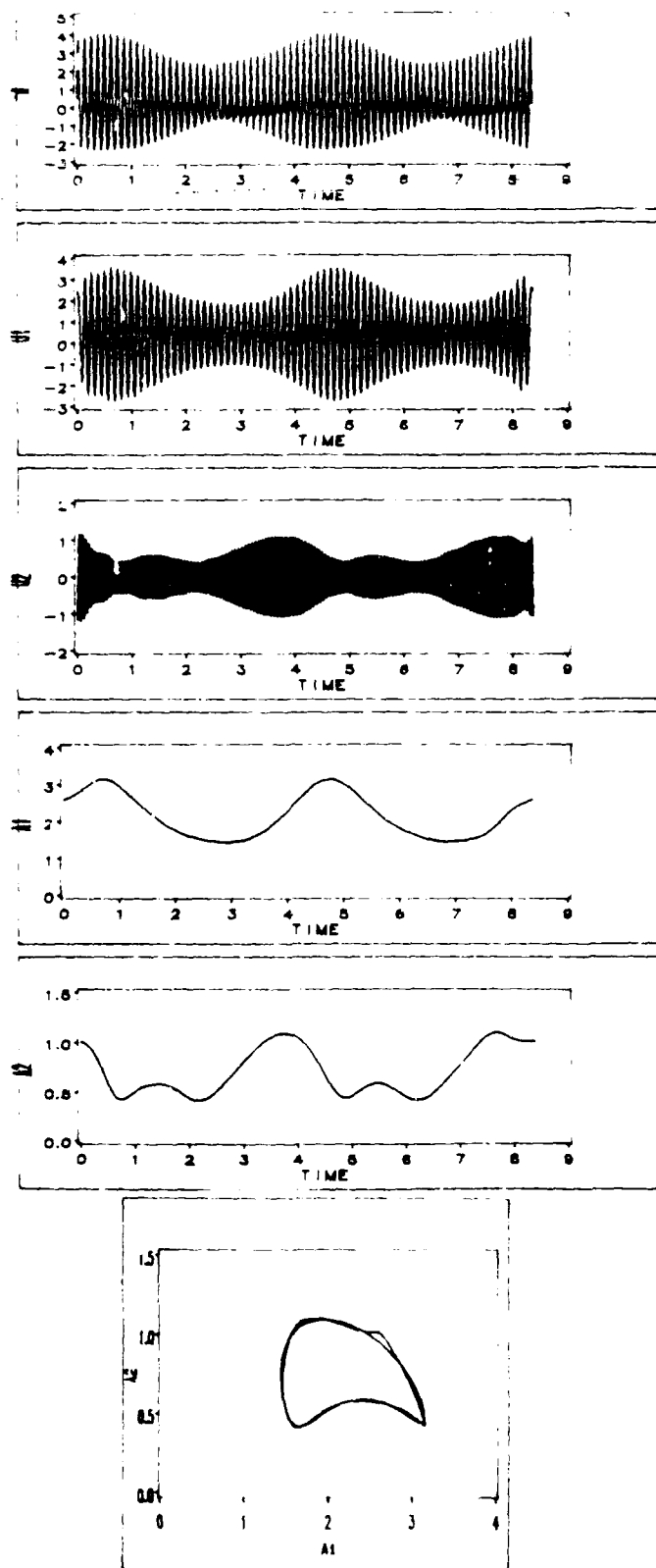


Figure 11. (a) Long-time history of the displacement of mass M_1 .
 (b) Long-time history of the modal components of the displacement of mass M_1 .
 (c) Long-time history of the modal amplitudes.
 (d) Variation of the long-time amplitude of the second mode with that of the first mode.

DISSIPATIVE STEP BY STEP INTEGRATION METHODS IN NONLINEAR STRUCTURAL DYNAMICS

C. Hoff

University California Berkeley

ABSTRACT

In general, nonlinear dynamic problems modeled by finite elements can only be solved numerically with step by step integration methods. In the case of low frequency response an unconditionally stable method with numerical dissipation is required. The time step can then be chosen as large as possible. Higher frequencies caused by spatial discretization and numerical noise have to be damped out while lower frequencies must not be influenced. In this paper a new unconditionally stable implicit single step method with controllable numerical dissipation is presented. The new method has some advantages over known dissipative methods. The performance of the new method for nonlinear systems is shown and the usefulness of the numerical dissipation is demonstrated. Some comments are made to solution strategies with equilibrium check and energy control.

1. INTRODUCTION

In the last twenty years a lot of effort has been done to solve the structural dynamic equation of motion for nonlinear systems numerically. It is worthwhile to mention all important developments but instead of this we refer to a good overview given in [1]. A recent state-of-the-art report can be found in [2]. Various very sophisticated multistep methods of higher order exist for the numerical solution of ordinary differential equations, see e.g. [3]. For the particular problem of the partial differential equation discretized in space by finite elements or finite differences the spatial error becomes dominant if higher order methods in time are used. Therefore most of the current computer programs work with time step schemes up to second or third order. The present paper deals with stiff problems coming from a discretized structure with a large number of degrees of freedom, a broad eigenfrequency spectrum and nonlinear inner forces.

For responses of the system which lie in the lower spectrum of eigenfrequencies relatively large time steps are allowed to approximate the solution accurately. An unconditionally stable algorithm with arbitrary large step size is required. Unconditionally stable algorithms are restricted to the theorem of Dahlquist [4] who stated that the highest accuracy of an unconditionally stable linear multistep method can not exceed the order of two and that an unconditionally stable method can never be explicit. The accuracy can only be increased with nonlinear multistep methods. The idea of Padé approximation applied to the first order form of the dynamic equation leads to third and fourth order accuracy with unconditional stability, see e.g. [5], [6], [7], [8]. The gain in accuracy must be paid with double sized matrices and a larger bandwidth compared to lower order methods. This paper is restricted to one step second order unconditionally stable methods with single matrix size.

If the time step is chosen as large as possible the higher frequencies are approximated badly. Higher frequencies in the system are caused by the finite element spatial discretization and numerical noise. It is desired to damp them out with a controllable numerical dissipation which does not influence the lower frequency range. The dissipation must be controlled by a parameter which is independent of the step size. Various dissipative methods were designed in the past, see e.g. [9], [10], [11], among others. The new θ_1 -method presented in this paper has some advantages over the old methods. The derivation of the algorithm can be found in [12]. A comparison with other dissipative algorithms is made in [13] and will not be repeated here. The purpose of this paper is the application to nonlinear systems.

The nonlinearity strongly effects the accuracy and the stability of the step-by-step integration methods. For linear systems it is relatively simple to prove stability. The mathematical theory is well

established, see e.g. [14]. For generally nonlinear systems we can only give necessary conditions of stability. A good overview of stability conditions for nonlinearities is given in [15]. There is no guarantee of failure in some special cases. One problematic example for the widely used trapezoidal rule of Newmark [16] is given in [17]. Although the trapezoidal rule was proven to be stable in the energy norm [18] for nonlinear systems, the algorithm fails for particular time step sizes. This example is an additional reason to introduce numerical dissipation. Careful checks of the equilibrium and energy balance are also necessary to improve the reliability of a nonlinear algorithm.

First the new θ_1 -method including Newmark's trapezoidal rule is presented in the form of a predictor-corrector scheme convenient for nonlinear systems. Practical convergence criteria are discussed to insure the stability of the calculation. Two examples of nonlinear systems are presented to show the behavior of the step-by-step integration methods.

2. ALGORITHM FOR NONLINEAR PROBLEMS

We assume a structure which is discretized by finite elements, finite differences or boundary elements, see e.g. [19]. The coupled matrix equation of motion with viscous damping and given initial conditions has to be solved:

$$M \ddot{u}(t) + C \dot{u}(t) + f(u(t)) = p(t) \quad (1)$$

$$u(t=0) = u_0$$

$$\dot{u}(t=0) = \dot{u}_0$$

M , C , K denote the mass, damping and stiffness matrix respectively. The displacement and its time derivatives are $u(t)$, $\dot{u}(t)$, $\ddot{u}(t)$, the dot denotes derivation with respect to time.

The step-by-step integration methods solve the problem numerically from one time step to the next. The internal nodal forces $f(u(t))$ are nonlinear in the displacements $u(t)$. The simplest and often the only possible way to solve (1) is to linearize $f(u(t))$ in each time step. The following incrementation is introduced:

$$u(\tau) = u_n + \Delta u(\tau) \quad t_n \leq \tau \leq t_{n+1}$$

$$f(u(\tau)) = f_n + K_n \Delta u(\tau) \quad (2)$$

$$K_n = \left. \frac{\partial f}{\partial u} \right|_{u=u_n} \quad \text{tangent stiffness matrix}$$

$$f_n = f(u_n) \quad \text{nodal forces at time } t_n$$

Step-by-step integration methods assume special approximations of the displacement, velocity and acceleration over the time interval. The Newmark- β method e.g. assumes a linear acceleration, a quadratic velocity and a cubic displacement over the time interval. For a special choice of the free parameters the algorithm is up to second order accurate without numerical dissipation. As already mentioned the numerical dissipation may be desirable in some cases. The recently developed θ_1 -method [12], [13] possesses controllable numerical dissipation. The same order of approximation functions as in the Newmark- β method is used but with different time constant coefficients. The following scheme describes the new method:

$$\bar{a}_{n+1} = (1-2\Theta_1^2) a_n - 4\Theta_1^3 \frac{1}{\Delta t} v_n \quad (3)$$

$$\bar{v}_{n+1} = (4\Theta_1^4 - 6\Theta_1^3 + 1) v_n + (2\Theta_1^3 - 3\Theta_1^2 + \Theta_1) \Delta t a_n$$

$$K_n = K(d_n)$$

$$f_n = f(d_n)$$

$$\Delta p^* = (1-\Theta_0) p_n + \Theta_0 p_{n+1} - f_n - M \bar{a}_{n+1} - C \bar{v}_{n+1} \quad (4)$$

$$K^* = 4\Theta_1^2 \frac{1}{\Delta t^2} M + (3-2\Theta_1) 2\Theta_1^2 \frac{1}{\Delta t} C + K_n$$

$$K^* \Delta d^* = \Delta p^*$$

$$a_{n+1} = \bar{a}_{n+1} + 4\Theta_1^2 \frac{1}{\Delta t^2} \Delta d^*$$

$$v_{n+1} = \bar{v}_{n+1} + (1-\Theta_1) \Delta t a_n + (3-2\Theta_1) 2\Theta_1^2 \frac{1}{\Delta t} \Delta d^* \quad (5)$$

$$d_{n+1} = d_n + (1-\Theta_1) \Delta t v_n + \Delta d^*$$

$$0.95 \leq \Theta_1 \leq 1 \quad (6)$$

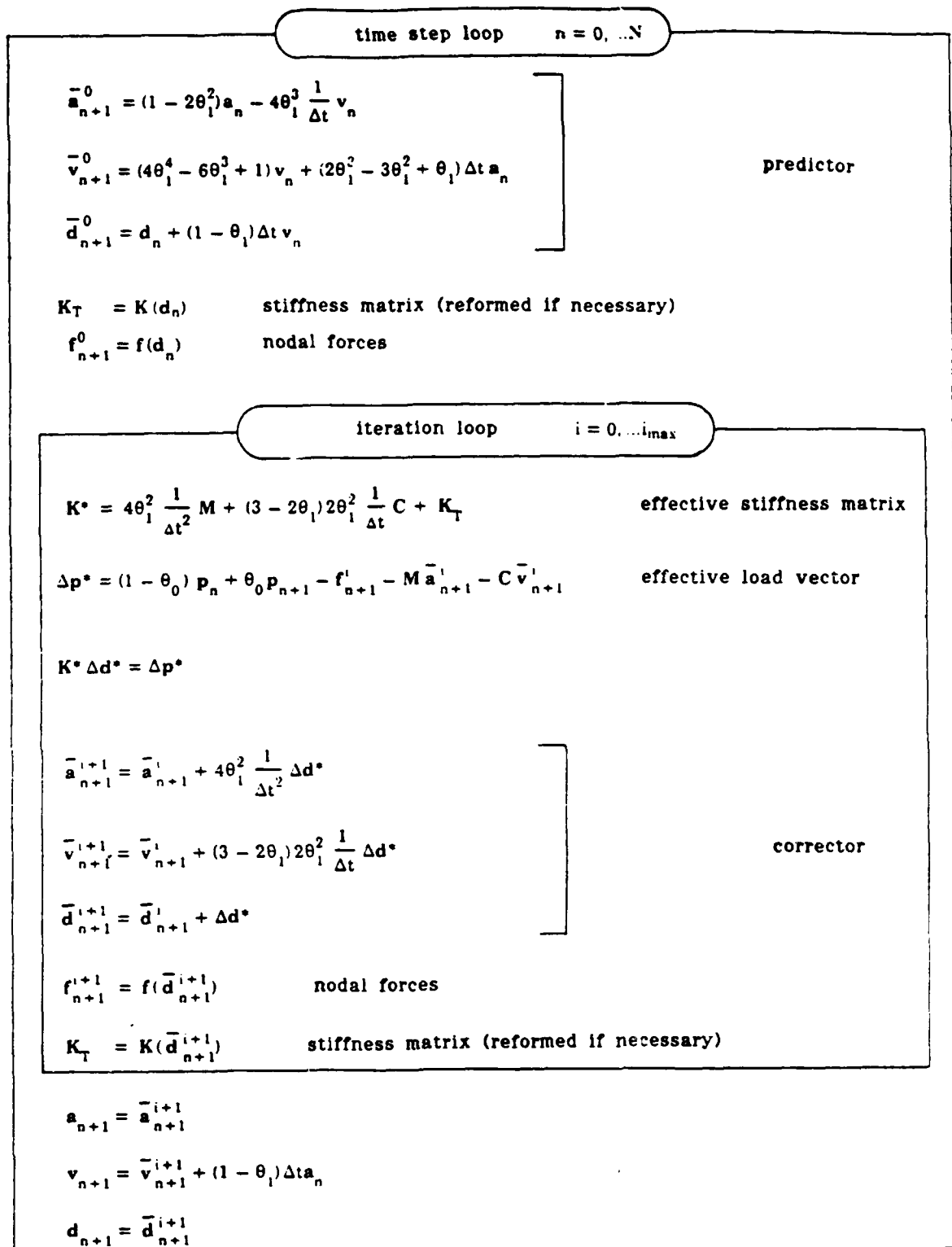
The time constant parameter θ_1 controls the numerical dissipation in the high frequency range. With $\theta_1 < 1$ the dissipation increases, for $\theta_1 = 1$ the algorithm is free of dissipation and becomes identical to Newmark's trapezoidal rule, see e.g. [1]. The special properties of the algorithm are worked out in [12] and [13]. The algorithm is second order accurate for θ_1 in the range of (6). The influence of the lower frequency range is not significant for the accuracy. Compared to the Newmark- β method two additional vector operations in each time step are necessary. This is the price for introducing numerical dissipation. Compared to other dissipative algorithms the advantages of the new method are a better behavior in the first time steps (overshooting), higher accuracy for damped and undamped systems (second order), no spurious root in the lower frequency range and a better performance for nonlinear systems, for details see [13]. The θ_1 -method can be implemented as shown in table 1. A Newton- Raphson strategy is used to solve the nonlinear equation iteratively.

3. ITERATION STRATEGIES AND CONVERGENCE CHECKS

As already mentioned the convergence of the step-by-step integration methods and even more the convergence of the Newton- Raphson iteration can not be guaranteed in general. A reliable algorithm must control the out-of-balance forces or residuals $r_{n+1} = \Delta p^*$ which must be iteratively go to zero. If a simple equilibrium balance without iteration in each time step is performed the solution may diverge in the case of large time steps. An equilibrium iteration within the time step leads to a solution path which is closer to the exact solution. The out-of-balance forces r_{n+1} must be lesser than a sharp boundary ϵ which is close to the machine accuracy.

$$r_{n+1} = p_{n+1} - f_{n+1} - M a_{n+1} \quad \text{residual forces} \quad (7)$$

$$\|r_{n+1}\|_2 \leq \epsilon_r \|f_{n+1}\|_2 \quad (8)$$



Tab. 1 : Iterative predictor multicorrector scheme of the Θ_1 -method in nonlinear problems

The equilibrium check does not guarantee an overall convergence. Multiple roots and saddle points of the nonlinear equation will not be recognized. In time history calculations an accumulation of energy may occur as a consequence of the linearization process even if (8) is fulfilled in every time step. To control this in a practical calculation we have only an energy quantity available from the discrete system during the time history which is not exact. But we can give estimates by introducing the following energy quantities :

$$A_{n+1} = A_n + \Delta A \quad \text{external energy} \quad (9)$$

$$\Delta A = \mathbf{d}_n^T (\mathbf{p}_{n+1} - \mathbf{p}_n) + \Delta \mathbf{d}^T \mathbf{p}_{n+1}$$

$$E_{n+1} = T_{n+1} + W_{n+1} \quad \text{internal energy} \quad (10)$$

$$T_{n+1} = T_n + \Delta T \quad \text{kinetic energy} \quad (11)$$

$$\Delta T = \frac{1}{2} \mathbf{v}_{n+1}^T \mathbf{M} \mathbf{v}_{n+1} - \frac{1}{2} \mathbf{v}_n^T \mathbf{M} \mathbf{v}_n$$

$$W_{n+1} = W_n + \Delta W \quad \text{strain energy} \quad (12)$$

$$\Delta W = \frac{1}{2} \Delta \mathbf{d}^T (\mathbf{f}_{n+1} + \mathbf{f}_n) + \frac{1}{2} \Delta \mathbf{d}^T (\mathbf{r}_{n+1} + \mathbf{r}_n) + \Delta S$$

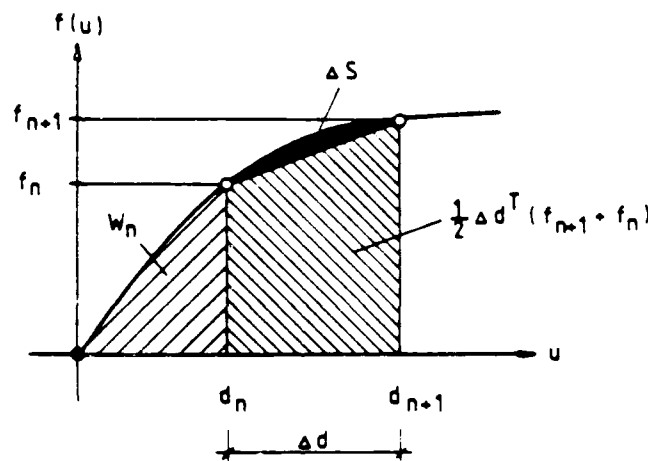


Fig. 1 : Strain energy for the internal nonlinear forces

For the external energy A_{n+1} (9) linear loads \mathbf{p}_n are assumed. In the case of plasticity, friction or damping additional energy terms must be taken into account. They are neglected here for simplicity. The kinetic energy (11) can be calculated exactly if the velocities are exact. The strain energy (12) can only be approximated in the nonlinear case. The out-of-balance forces \mathbf{r}_{n+1} and \mathbf{r}_n can be reduced to zero with equilibrium iterations. If we assume $W(f)$ linear within the time step the term ΔS will be zero. But in general we can not neglect the nonlinear part ΔS , see figure 1. If the tangent stiffness \mathbf{K}_n at time t_n is available we can calculate a lower and upper bound or a rough estimate of ΔS :

$$0 < |\Delta S| < \left| \frac{1}{2} \Delta d^T (f_n + K_n \Delta d - f_{n+1}) \right| \quad (13)$$

$$\Delta S = \frac{1}{6} \Delta d^T (f_n + K_n \Delta d - f_{n+1}) \quad (14)$$

The energy can now be controlled by the following criteria:

$$E_{n+1} \leq (1 + \epsilon_E) E_n + \Delta A \quad (15)$$

If the term ΔS in (12) is neglected it can be shown by inserting (7) - (12) into (15) that the criteria leads to

$$\frac{1}{2} \Delta d^T (r_{n+1} + r_n) \leq \epsilon_E E_n \quad (16)$$

The Newmark trapezoidal rule for example conserves the energy in the sense of (16) neglecting ΔS if (8) is fulfilled, see also [18]. Although (16) is fulfilled the term ΔS accumulates in some special cases causing a drift of the numerical solution, see [17] for details. The trial to repair the scheme with a Lagrangian constraint equation [17] remains on a discrete energy quantity which is not exact because ΔS is still neglected. It may be better to use the estimate (14) for an improved energy control.

In comparison to the trapezoidal rule dissipative methods are able to compensate the accumulation of ΔS in the higher frequency range so that a refined energy control with (14) is rather necessary. It will be shown in the next chapter that the introduction of numerical damping is a reliable alternative to avoid energy accumulation from stiffness jumps in the higher frequency range.

4. EXAMPLES

To demonstrate the effects of the numerical solution with step-by-step integration methods two single degree-of-freedom systems are used. In multidegree-of-freedom systems the effects may be smoothed over the structure and not be recognized.

4.1. Hardening Spring

A geometric nonlinear spring is tested, see figure 2. This example has been used by several authors, see e.g. [5], because it is convenient to show the accuracy of the step-by-step integration algorithm in the nonlinear case. The undamped free vibration of the spring with an initial displacement is described by the equations:

$$m \ddot{u}(t) + f(u(t)) = 0 \quad (17)$$

$$u(t=0) = u_0$$

$$\dot{u}(t=0) = 0$$

$$f(u) = 2 \left\{ S \frac{u}{(l^2 + u^2)^{1/2}} + EF \left[\frac{u}{l} - \frac{u}{(l^2 + u^2)^{1/2}} \right] \right\} \quad (18)$$

$$K(u) = \frac{\partial f}{\partial u} = 2 \left\{ S \frac{l^2}{(l^2 + u^2)^{1.5}} + EF \left[\frac{1}{l} - \frac{l^2}{(l^2 + u^2)^{1.5}} \right] \right\} \quad (19)$$

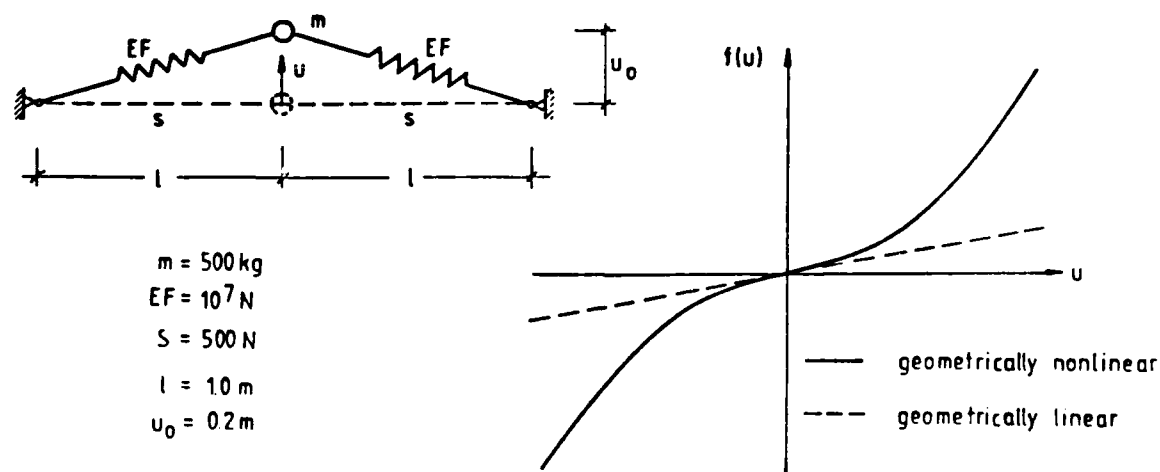


Fig. 2 : Geometrically nonlinear spring

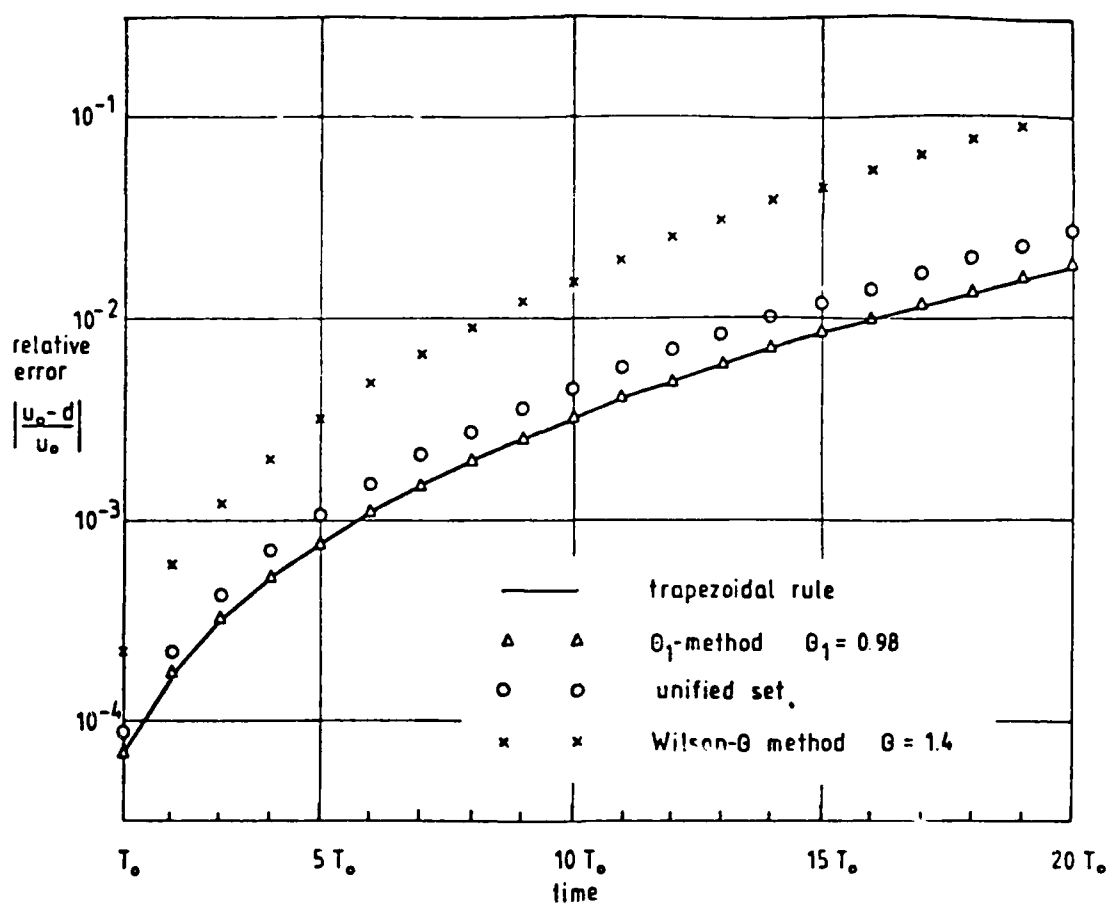


Fig. 3 : Relative period error in the maximum displacement during 20 periods with constant time step size $\Delta t/T_0 = 1/200$

The equation (17) is solved numerically by the following methods :

- Newmark's trapezoidal rule
- θ_1 - method with $\theta_1 = 0.98$
- unified set from [20] with parameters from table II in [20] to get spectral identity to the α -method of Hilber with $\alpha = -0.05$
- Wilson θ method with $\theta = 1.4$

The force (18) is linearized in each time step with the tangent stiffness (19). No iteration is performed within the time step to show the accuracy of the time step algorithm alone. In every period the mass must return to the initial position. This requirement is used to define the error in the displacement amplitude. A calculation with very short time steps converges to the quasi exact period $T_0 = 0.264\ 791\ 269$ s. This period is divided into N time steps Δt . The accumulation of the error from one to twenty periods with a constant time step ($N = 200$ time steps per period) is shown in figure 3. The θ_1 - method shows a good accuracy which is very close to the most accurate trapezoidal rule. Other dissipative methods must pay for the introduction of numerical damping with a loss of accuracy.

4.2. Bilinear Softening Spring

The stability of the methods is now tested for a suddenly softening spring, see figure 4. This example has already been used in [17] to investigate the behavior of Newmark's trapezoidal rule. It is a very theoretical system but stiffness jumps can often occur and it is of general interest to know what happens with the algorithms at nondifferentiable points of the internal forces $f(u(t))$. The main interest for this example is the stability of the algorithms and not the accuracy. The free vibration with an initial velocity is solved numerically :

$$\ddot{u}(t) + f(u(t)) = 0 \quad (20)$$

$$u(t=0) = u_0 = 0$$

$$\dot{u}(t=0) = \dot{u}_0 = 25$$

$$f(u) = \begin{cases} 100 u & |u| \leq 2 \\ 200 & |u| > 2 \end{cases} \quad (21)$$

The problems of this example arise from the accumulation of the error ΔS in the strain energy. By refining the time steps, the quasi- exact period $T_0 = 0.670\ 918$ with the amplitude $u_{\max} = 2.56643$ is determined. The effects of the out- of- balance forces r_n and r_{n+1} are eliminated completely with three iterations per time step.

Newmark's trapezoidal rule and the θ_1 - method with $\theta_1 = 0.98$ are compared. The figure 6 shows the energy over time for the step size $\Delta t = 0.3 T_0 = 0.2$. The trapezoidal rule overestimates the energy strongly. This behavior is known from [17]. The overestimation occurs only in the range of $0.2 T_0 \leq \Delta t \leq 0.4 T_0$. The θ_1 - method dissipates the effect of ΔS in the desired manner over the whole frequency range. Time step sizes $\Delta t > 0.05 T_0$ occur in multi- degree- of freedom systems in the higher frequency range, when unconditionally stable implicit methods are used. It is desired to damp these frequencies out if they are not excited. The θ_1 - method is able to maintain its dissipative property in the higher frequency range even for nonlinear problems.

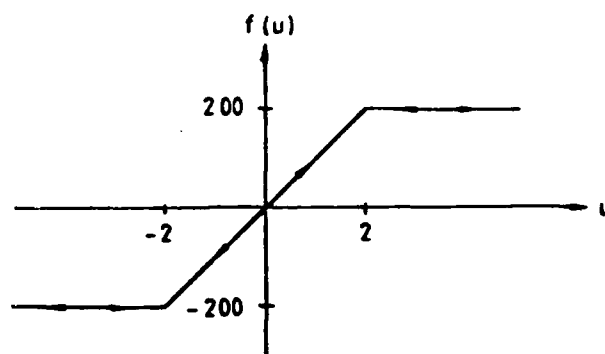


Fig. 4 : Force in a bilinear spring

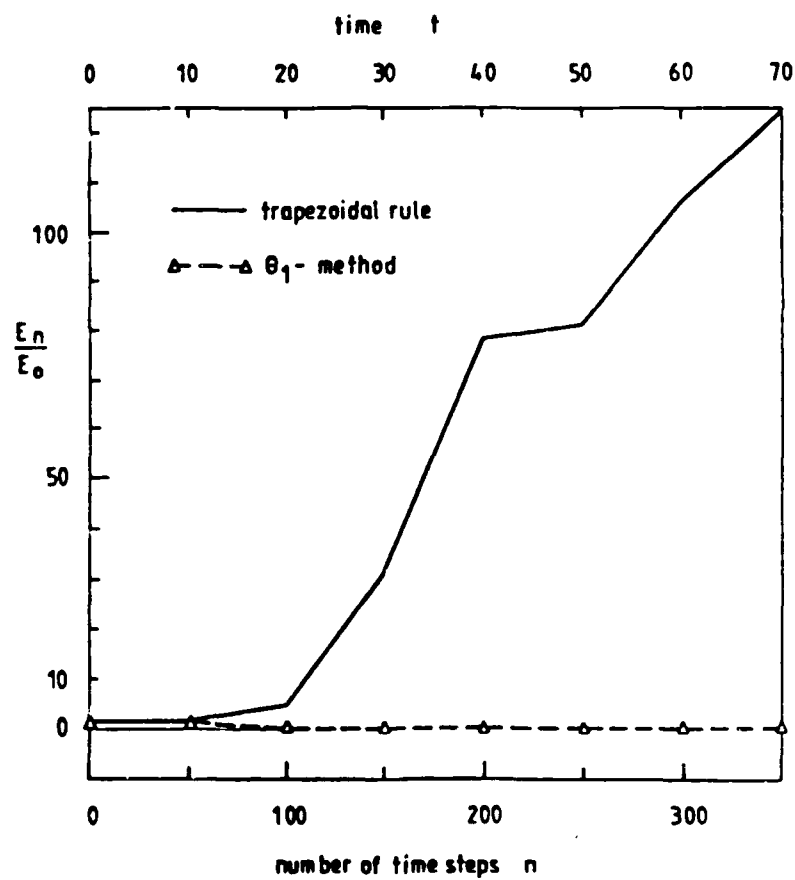


Fig. 5 : Energy during 350 time steps with $\Delta t = 0.3T_c = 0.2$

5. CONCLUSIONS

It was shown that the θ_1 - method is a reliable algorithm to treat nonlinear dynamic problems. The accuracy in the lower frequency range is close to Newmark's trapezoidal rule which is known as the most accurate second order method. The θ_1 - method possesses the desired dissipation in the higher frequency range which even works for extreme stiffness jumps. The computational effort is not increased significantly compared to Newmark's trapezoidal rule. In the case of lower frequency response the θ_1 - method is a powerful tool to solve nonlinear dynamic problems.

Further investigations are necessary to show the behavior of the method in large scale systems compared to other known methods. More theoretical insight is required for the energy criteria to control the algorithm. The energy can only be calculated in a discretized form and has to be used carefully because it is not the real energy of the system. In this particular point further research has to be done to obtain reliable control criteria for the algorithms.

REFERENCES

- [1] Belytschko, T.; Hughes, T.J.R.; *Computational Methods for Transient Analysis*, Vol.1 in *Computational Methods in Mechanics*, North Holland Elsevier Publishers, Amsterdam (1983)
- [2] W.L. Wood, *Some Transient and Coupled Problems - A State-of-the-Art-Review*, Chapter 8 in *Numerical Methods in Transient and Coupled Problems*, Ed. R.W. Lewis, E. Hinton, P. Bettess and B.A. Schrefler, John Wiley & Sons Ltd. (1987)
- [3] E.Hairer, S.D.Norsett, G.Wanner, *Numerical Solution of Ordinary Differential Equations*, Springer Series in Computational Mathematics, Springer Verlag Berlin, New York (1987)
- [4] G. Dahlquist,
A Special Stability Problem for Linear Multistep Methods, BIT 3, pp 27 - 43 (1963)
- [5] M. Gellert, *A Direct Integration Method for the Analysis of a Certain Class of Nonlinear Dynamic Problems*, Ing. Archiv 48, pp 403- 415 (1979)
- [6] L. Brusa, L. Nigro, *A One Step Method for Direct Integration of Structural Dynamic Equations*, Int.J.Num.Meth.Eng. 15, pp 685- 699 (1980)
- [7] D.M. Trujillo,
The Direct Numerical Integration of Linear Matrix Differential Equations Using Pade Approximations, Int.J.Num.Meth.Eng.9, pp 259- 270 (1975)
- [8] R.M.Thomas, I. Gladwell, *The Methods of Gellert and of Brusa and Nigro are Pade Approximant Methods*, Int.J.Num.Meth.Eng. 20, pp 1307- 1322 (1984)
- [9] H.M. Hilber, T.J.R. Hughes, R.L. Taylor, *Improved Numerical Dissipation for Time Integration Algorithms in Structural Dynamics*, Earthquake Eng.& Struct.Dyn. 5, pp 283- 292 (1977)
- [10] D.D. Adams, W.L. Wood, *Comparison of Hilber- Hughes- Taylor and Bossak- α methods for the Numerical Integration of Vibration Equations*, Int.J.Num.Meth.Eng. 17, pp 765- 771 (1983)
- [11] G. Bazzi, E. Anderhegger, *The p- Family of Algorithms for Time- Step Integration with Improved Numerical Dissipation*, Earthquake Eng.& Struct. Dyn. 10, pp 537- 550 (1982)
- [12] C. Hoff, P.J. Pahl, *Development of an Implicit Method with Numerical Dissipation from a Generalized Single Step Algorithm for Structural Dynamics*, accepted for publication in Comp.Meth.Appl.Mech.Eng. (1987)

- [13] C. Hoff, P.J. Pahl, *Practical Performance of the θ_1 -Method and Comparison with Other Dissipative Algorithms in Structural Dynamics*, accepted for publication in *Comp. Meth. Appl. Mech. Eng.* (1987)
- [14] J.D. Lambert, *Computational Methods in Ordinary Differential Equations*, John Wiley & Sons (1977)
- [15] K. Dekker, J.G. Vekker, *Stability of Runge- Kutta Methods for Stiff Nonlinear Differential Equations*, CWI Monographs, North Holland Elsevier Publishers (1984)
- [16] N.M. Newmark, *A Method of Computation for Structural Dynamics*, Proc. ASCE 85, EM3, pp 67- 94 (1959)
- [17] T.J.R. Hughes, *Stability, Convergence and Growth and Decay of Energy of the Average Acceleration Method in Nonlinear Structural Dynamics*, *Comp. & Struct.* 6., pp 313- 324 (1976)
- [18] T. Belytschko, D.F. Schoeberle, *On the Unconditional Stability of an Implicit Algorithm for Nonlinear Structural Dynamics*, *ASME J. Appl. Mech.* 17, 865- 869 (1975)
- [19] O.C. Zienkiewicz, W.L. Wood, N.W. Hine, R.L. Taylor, *A Unified Set of Single Step Algorithms, Part 1: General Formulation and Applications*, *Int. J. Num. Meth. Eng.* 20, pp 1529- 1552 (1984)

ON SOME ASPECTS OF OPERATIONAL ERROR DISTRIBUTION AND
PROPAGATION IN DIRECT INTEGRATION FOR NONLINEAR DYNAMICS

F. Brancaleoni and C. Valente

Department of Structural and Geotechnical Engineering
University of Rome "La Sapienza"

1. INTRODUCTION

Performance evaluation criteria of integration algorithms for the direct time solution of linear or nonlinear discrete structural dynamics problems are stability, accuracy and high mode components filtering properties, overshoot characteristics, implementation effort, error propagation behaviour. The latter item, to which this paper is devoted, is growing in importance with the present diffusion of large scale dynamic analyses comprising geometric and material nonlinearities.

Attention is herein given to operational error, which, with the definition first given by Felippa and Park [1,2], is the error introduced by inexactness in the solution of the algebraic equations that must be solved at each time station. For linear problems such inexactness is strictly related to the solution precision in finite arithmetics of a set of linear equations and it can hence be dealt with by adequate procedures and by increasing the number of significant digits in the computation. In nonlinear analyses on the contrary the operational error is related to the precision of the step solution of the nonlinear problem and it hence depends on the scheme adopted, typically linearized or iterative, with convergence controlled by different possible criteria, based on tolerances specified by the analyst. Such tolerances are, to limit the computational error, usually considerably larger than the machine precision: consequently, the errors attainable for linear systems are far smaller or negligible when compared to those characteristic of non linear ones.

It is known that when adopting direct integration algorithms operational errors undergo propagation and amplification while progressing with the solution, according to laws associated to the operator class and to the implementation path adopted [1,2,3]. Though, the research work carried out on error propagation in structural dynamics applications has always been based on the assumption of uniform distribution between two extremal values. While this has provided useful guidelines for the understanding of the phenomenon, neither of the two latter hypotheses can be considered acceptable in non linear applications. Nothing does in fact suggest specifically a uniform distribution; as to the extremal limiting values it must be noted that in standard procedures tolerances are typically specified in terms of generalized forces, while the equation solution is carried out in generalized displacements or in their derivatives. With a nonlinear force-displacement relationship the tolerance limits on forces do not correspond to fixed limits for displacements, making the second assumption untrue.

A first section of the present paper is hence devoted to providing information on the possible error distributions in non linear problems. Their main features are conveniently exemplified and discussed on the basis of numerical experiments on simple oscillators: some points concerned with further aspects arising in multi d.o.f. cases are also mentioned. The data obtained, while far from being exhaustive, are sufficient to allow the

proposal of simplified theoretical error distributions associated with the different situations determined. Such distributions are in a second section treated within the framing of an algorithm for the analysis of error propagation, a preliminary version of which was proposed by one of the authors in [4]. It is assessed that also the distribution of the step error affects the propagation characteristics significantly. Amplification characteristics for representative integration operators are determined and discussed on wide ranges of reduced frequencies (frequency/time step ratios). Results are presented both in form of evolution histories and of error spectra.

2. OPERATIONAL ERROR DISTRIBUTION

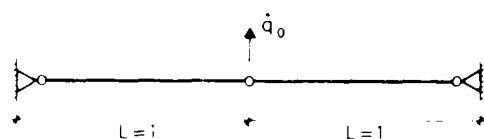
2.1 Discussion on simple systems

Once tackled in a systematic manner, the problem of possible operational error distributions reveals rather complex, so that some of its main features can be best illustrated preliminarily on simple single d.o.f. cases. The test case considered is concerned with the analysis of free oscillations with geometric nonlinearities and namely those of a three pins elastic strut with vertical initial velocity conditions, see fig. 1a. The corresponding type of nonlinearity is continuous and is illustrated in the force-displacement graph of fig. 1b, where also the displacement level reached in the test oscillations considered is shown. A small amount of tensile prestressing provides non-zero initial geometric tangent stiffness; the ratio between maximum and minimum tangent stiffness with the range covered during the oscillations is reported on the same graph. The solution scheme adopted uses locally the implementation path described in section 3. and the average acceleration method as integration operator, with a total lagrangian formulation. The local solution at each time step is achieved via Newton-Raphson iteration. The solutions referred to as "exact", as compared to "approximate" for error determination, were also determined numerically; care was given to avoiding influence of machine precision and of algorithmic frequency and phase distortion. The convergence criterion adopted is based on the reduction of an unbalanced nodal forces norm below a specified value, which simplifies in this case to the unbalanced vertical force in the centre node. One further aspect must be stressed: in the following shall be presented results obtained with different tolerances, sometimes labeled as "large" or "small". Aiming at investigating ranges of interest for the analysts, all the cases examined produce results expected to make sense in typical applications, even if they span from "rough" to "very precise" in everyday structural analysis terminology. As a whole, the procedures and cases considered are intended to be representative of standard cases in engineering computations for nonlinear dynamics problems.

The first example presented refers to a tolerance in force that can be considered "large": the associated static displacement error for the linearized initial configuration is of 5% of the maximum displacement during vibrations, while decreasing rapidly for increasing displacement. Fig. 2 shows the operational error time evolution in a branch centered around a maximum of the free oscillations response. The error decreases regularly in the first part, to increase also regularly subsequently and to show in the second part sudden decreases followed by again regularly increasing branches. The cause of such configuration, which was found to be typical, is simple: each regular part of the error evolution is associated to a constant number of iterations in the local step solution. When the response evolves towards its maximum (A zone) the structural nonlinearity

decreases and to such number of iterations corresponds a decreasing error. Once the maximum has been attained and the displacement decreases, the non-linearity grows and so does the error (B zone), until the number of iterations becomes insufficient to allow respecting the specified tolerance (point C). One more iteration is then added and the error collapses, to resume its growth (D zone) until the number of iterations becomes insufficient again and the phenomenon repeats. The behaviour about the response peak is better depicted in the enlargement in fig. 3. It can also be seen that the error has the same sign throughout the part of response considered. The corresponding distribution histogram is shown in fig. 4. The fewer sparse larger displacement errors are associated to the response branch about the initial configuration (minimum stiffness).

When decreasing the tolerance such picture changes progressively; an "intermediate" precision case (static displacement error associated to the force tolerance 0.5% of the maximum displacement) shows the error distribution of fig. 5. Several new characteristic features are better pointed out by a "small" tolerance case (static displacement error associated to the force tolerance 0.005% of the maximum displacement). Fig. 6 shows a brief part of the corresponding response for a branch with increasing non-linearity. The pattern commented before is replaced by a far less regular one; the increase of error at constant number of iterations does still take place, but the growth is not monotonic and its decrease at number of iterations variation produces often also a change of the error sign. Such marked irregularity implies a significant change of the distribution: the errors show a potentially very dangerous trend towards concentration at a number of restricted fields of either sign, see fig. 7.



Truss element properties:
 Young's modulus 1
 Cross sectional area 1
 Unstrained length $L_0 = 0.99L$

Fig. 1a - One d.o.f. geometrically nonlinear test oscillator

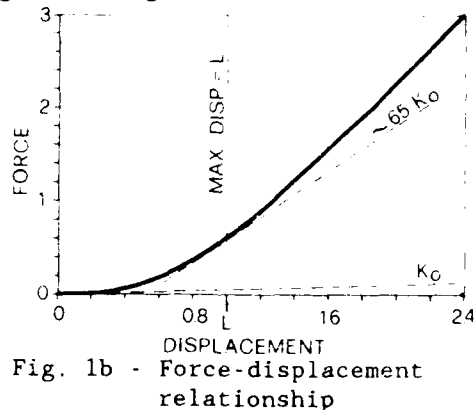


Fig. 1b - Force-displacement relationship

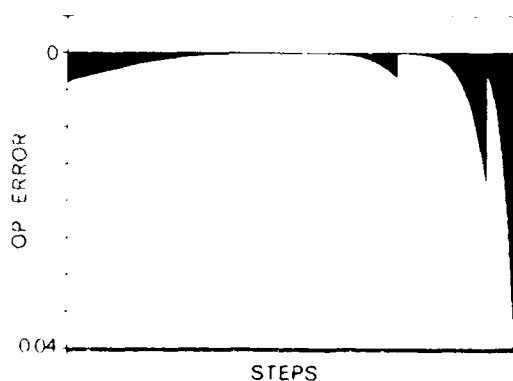


Fig. 2 - Operational error evolution, "large" tolerance

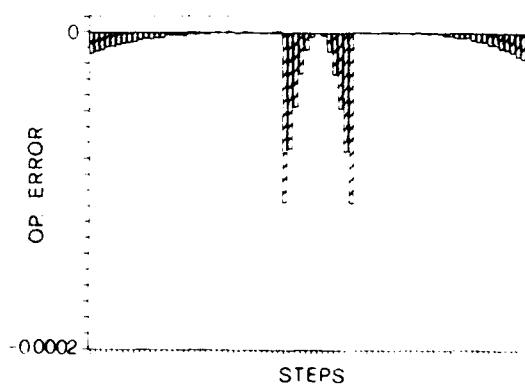


Fig. 3 - Detail of fig. 2, as therein indicated

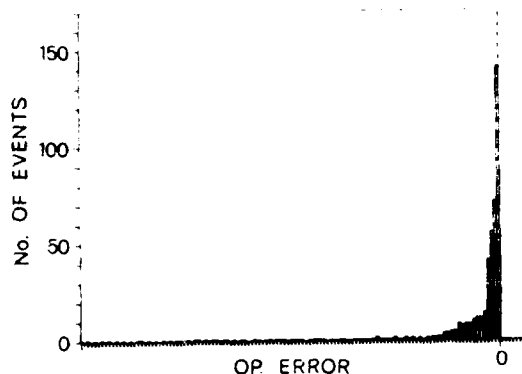


Fig. 4 - Operational error distribution, "large" tolerance

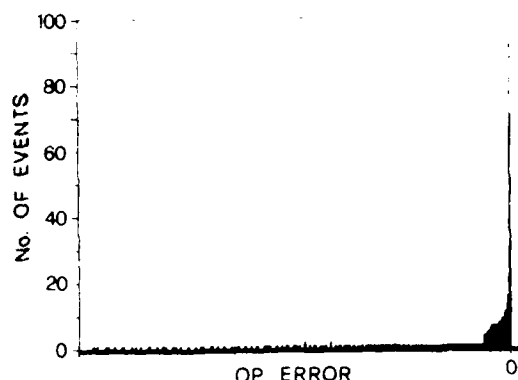


Fig. 5 - Op. error distribution, "intermediate" tolerance

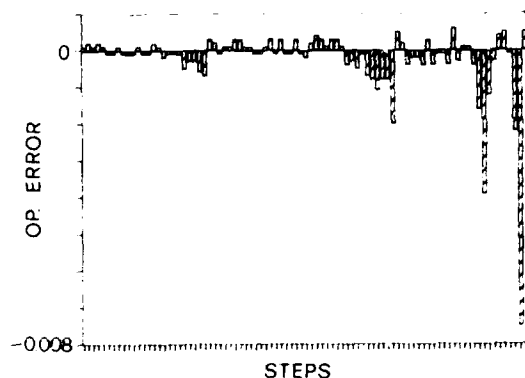


Fig. 6 - Operational error evolution, "small" tolerance

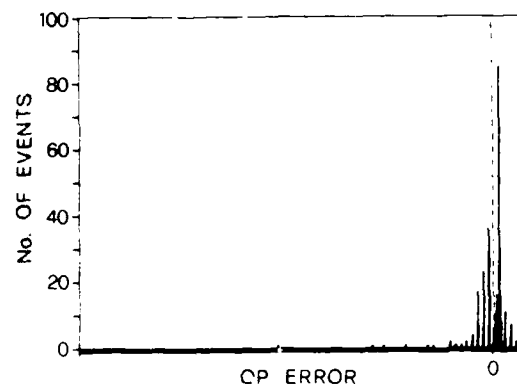


Fig. 7 - Operational error distribution, "small" tolerance

2.2 Remarks

The results shown, despite their limitations, allow to state that operational errors occurring in nonlinear dynamics solution procedures are characterized by evident peculiarities, each connected to different situations. In particular the effects of varying nonlinearity and tolerance levels have been demonstrated. Within one d.o.f. structures the same conclusions have been found to stand also for other standard solution strategies, such as constant stiffness iteration procedures. In multi d.o.f. cases the picture becomes far more complex, as several further variables play a significant rôle. Among them can be quoted convergence criteria and types of loading, plus the different error distributions for different degrees of freedom caused by the possible uneven location of nonlinearities on the structure. The study of multi d.o.f. cases cannot be restricted within the limits of this paper; it has been considered of more interest in the present stage of the work to propose a number of simplified theoretical error distributions derived from those observed experimentally and to study their propagation behaviour in actual time integration procedures.

Five artificial error distributions have been considered. The first two, labeled A and B, do not descend from experimental evidence and are to be assumed as reference ones. Case A is characterized by uniform error between two extremal values, as proposed in [4,5], fig. 8a. Case B has a

Gauss distribution with zero mean and given standard deviation, fig. 8b. Three distributions are associated to the results shown, see fig.s 8 c,d,e, and namely to a number of selected characteristic zones: it has been in fact deemed, for an easier interpretation of the phenomenon, not to attempt a simultaneous simulation of the whole set of experimental distributions. Case C and D, associated with the situations of fig.s 6 to 9 assumed to take place symmetrically or non symmetrically, are produced by a couple or a single Gauss distribution with means $-\epsilon + \epsilon$ and $+\epsilon$ respectively, plus a given standard deviation. Case E, associated with situations such as that shown in fig. 4, is produced by an half gaussian distribution, again with given standard deviation. Note that the graphs of fig. 8 show error distributions as artificially generated and adopted in the numerical propagation analysis procedure described in section 3. The fewer large sparse errors connected with low stiffness high non linearity branches of the response have not been considered in this stage.

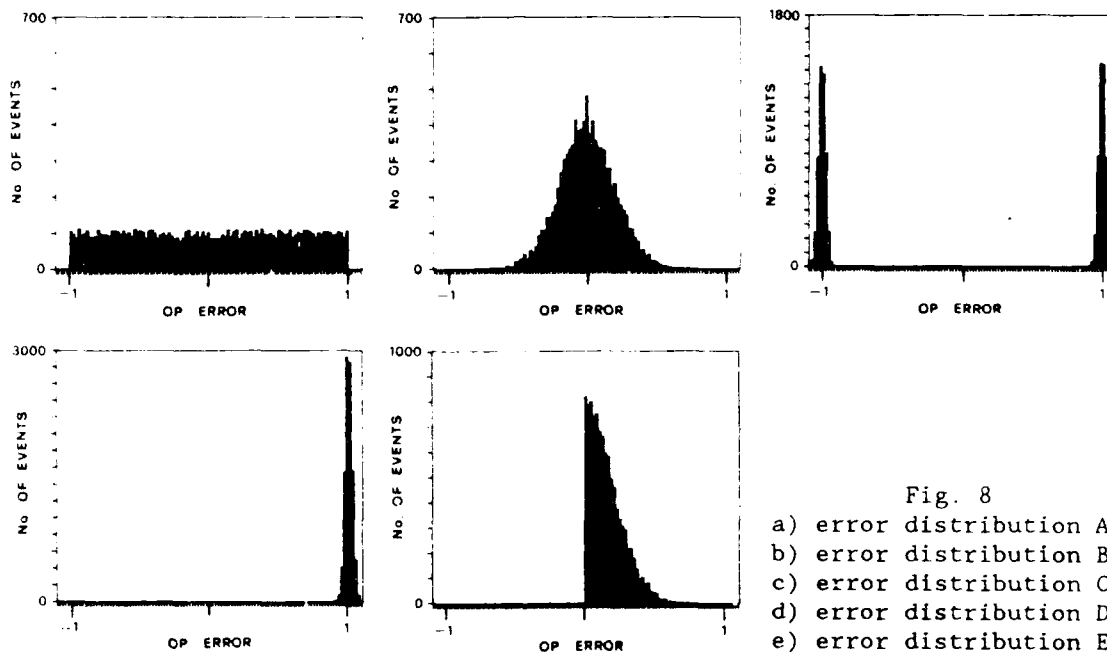


Fig. 8

- a) error distribution A
- b) error distribution B
- c) error distribution C
- d) error distribution D
- e) error distribution E

3. OPERATIONAL ERROR PROPAGATION

3.1 Implementation paths

A linear multistep method (LMM) specialized to second order ordinary differential equations (ODE) can be written in the general form:

$$\left. \begin{aligned} \sum_{i=0}^m \alpha_i q_{n-i} &= \Delta t \sum_{i=0}^m \beta_i q_{n-i} \\ \sum_{i=0}^m \gamma_i q_{n-i} &= \eta \Delta t^2 \sum_{i=0}^m \delta_i q_{n-i} \end{aligned} \right\} \begin{aligned} m \geq 1, n \geq m \\ \alpha_0 \neq 0, \gamma_0 \neq 0 \end{aligned} \quad (1)$$

where for direct consistency it must be $\beta_1 = \delta_1$ and the normalization $\alpha_0 = \gamma_0 = 1$ is assumed and η is the associated necessary scalar. Following [8], the known terms of (1) at past time stations can be collected in separate vectors as:

$$[a_n^d, b_n^d, c_n^d] = [d_{n-1}, \dots, d_{n-m}] \begin{bmatrix} \alpha_1 & \beta_1 & \gamma_1 \\ \vdots & \vdots & \vdots \\ \alpha_m & \beta_m & \gamma_m \end{bmatrix}, \quad (2)$$

where d stands for any displacement variable or its time derivative. The algorithm can so be rewritten separating known terms at stations $n-1$, i.e. the so called historical terms h , plus unknown ones at station n :

$$\begin{Bmatrix} q_n \\ \dot{q}_n \end{Bmatrix} = \begin{Bmatrix} \Delta t_\beta \dot{q}_n \\ \Delta t_\delta \ddot{q}_n \end{Bmatrix} + \begin{Bmatrix} h_n^q \\ \bar{h}_n^q \end{Bmatrix}, \quad (3)$$

with $\Delta t_\beta = \Delta t \beta_0$ and $\Delta t_\delta = \eta \Delta t \beta_0$, while the historical terms are:

$$\begin{aligned} h_n^q &= \Delta t b_n^q - a_n^q \\ \beta_0 \bar{h}_n^q &= \Delta t_\delta b_n^q - b_n^q + (a_n^q - c_n^q)/\Delta t \end{aligned} \quad (4)$$

Substituting (3) into the standard second order linear equations of motion written at opportune time stations and solving in displacements one obtains:

$$A_n q_n = l_n \quad (5)$$

where the step matrix A_n and the generalized load vector l_n are:

$$\begin{aligned} A_n &= M + \Delta t_\delta D + \Delta t_\beta \Delta t_\delta K \\ l_n &= M(\Delta t_\delta \Delta t b_n^q - c_n^q) + \Delta t_\delta D h_n^q + \Delta t_\beta \Delta t_\delta f_n \end{aligned} \quad (6)$$

Different implementation paths are possible for the above formulation, see [1,2], in connection to different orders of the operations to carry out at each time station. The one selected here, see table 9, to exemplify the error propagation behaviour is spontaneous for second order ODE and among the most commonly used in finite element codes. Note that for second order ODE all the implementation paths proposed to date are affected by significant error amplification and the one shown is no exception.

Table 9 - Implementation path for second order algorithms

- i) Compute historical terms h_n^q , \bar{h}_n^q from available quantities at past time stations
- ii) Compute generalized loading term l_n
- iii) Compute step matrix A_n
- iv) Solve in displacements at current station $q_n = A_n^{-1} l_n$
- v) Compute velocities and accelerations at current station \dot{q}_n , \ddot{q}_n from displacements q_n through the algorithmic difference formulae (1).
- vi) Advance to next time station

3.2 Error propagation analysis

The largest operational error introduced in any implementation of time integration procedures is associated to the part in which the solution of the linear or nonlinear set of equations is carried out, such as step iv) of table 9. The proposed technique for the analysis of the operational error propagation is based on numerical experiments in which while performing a time integration procedure the said equations set is solved with high digital precision and an artificial error vector Ξ of given distribution is added to such solution at each time station; step iv) of table 9 would e.g. become:

$$q_n = A_n^{-1} \dot{q}_n + \Xi$$

In the following the propagation shall be studied for a single d.o.f. linear oscillator, so reducing the artificial error to a scalar ξ , to which the distributions A to E discussed in 2.2 are given. The behaviour is known to be strongly affected by the $\Delta t/T_0$ ratio: the analysis of different stepsizes for a one d.o.f. case is representative of the amplification behaviour for the modal response of stiff ODE systems.

The LMM formula considered is the average acceleration method (AAM): this aspect warrants some further discussion. References [1-4] have clearly shown that the propagation characteristics of a LMM method are affected far more significantly by the implementation path than by its algorithmic properties, but for $\Delta t/T_0 > 1$ (large stepsizes), where the algorithmic damping becomes important and, if present, cancels the response for the corresponding frequencies. The AAM operator has no algorithmic damping: it can hence be considered representative of the behaviour of any standard LMM for $\Delta t/T_0 < 1$ (small stepsizes) and only of LMM possessing no amplitude decay for $\Delta t/T_0 > 1$. The large stepsizes range for LMM with amplitude decay is, being canceled, of no special interest.

Evolution histories for the A distribution and five $\Delta t/T_0$ values (0.001, 0.1, 1, 10, 1000) are reported in fig. 10. The extremal values given to the artificial error are of ± 1 , so that the response can be interpreted directly as an amplification factor of the maximum operational error. The known trend [3,4] towards high values in the very large and very small stepsize ranges, with lower values for the intermediate ones, is evident. The detail histories reported for a number of cases show that the spurious oscillations take place with a period related to the inverse of the $\Delta t/T_0$ ratio for small steps, while converging asymptotically towards $2\Delta t$ for the large ones. This latter aspect is due to the known property of LMM with no algorithmic damping, which concentrate all the energy associated to periods smaller than the integration step on a oscillation having continuous sign inversion and hence $2\Delta t$ period. The response obtained is always the sum of two harmonic components, the first on the oscillator frequency, plus a spurious one with the said characteristics.

The same pattern is encountered for the distributions C, D, E, fig.s 11 to 13, for which only three stepsizes are exemplified, but with considerable variations of the amplification factor values and of its dependence on the integration step. In all the cases considered a stabilization of the amplification factor has been attained after an adequate number of steps (not always reached in the graphs), also confirming known theoretical results based on asymptotic estimate techniques[2,6,7]. Note that the error distribution B has not been reported, due to its lesser interest.

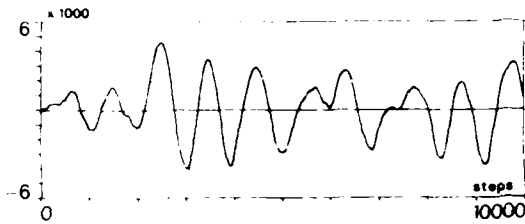


Fig. 10 - Error distribution A

- a) $\Delta t/T_0 = 0.001$ (10^4 steps)
- b) $\Delta t/T_0 = 0.1$ (10^4 steps+detail on 10^3)
- c) $\Delta t/T_0 = 1$ (10^3 steps+detail on 10^2)
- d) $\Delta t/T_0 = 10$ (10^3 steps+detail on 50)
- e) $\Delta t/T_0 = 1000$ (10^3 steps+detail on 50)

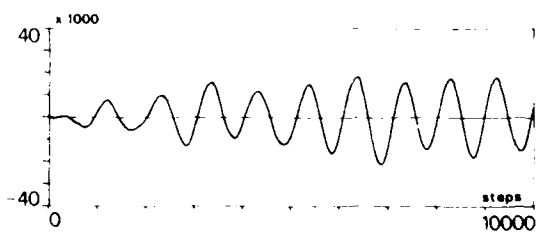
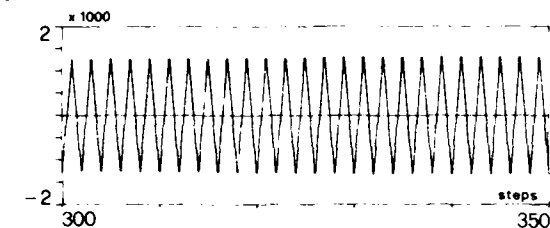
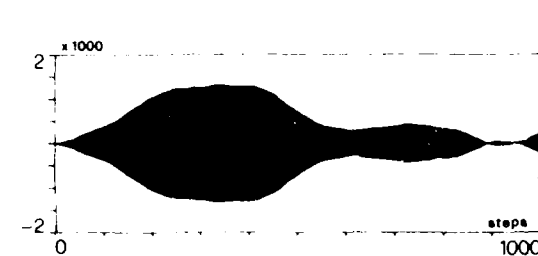
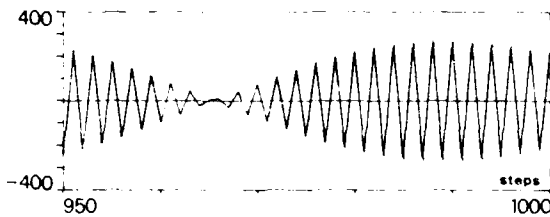
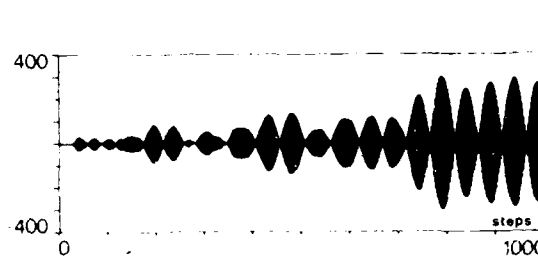
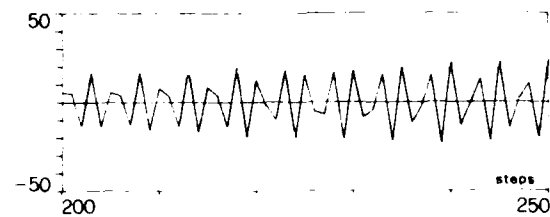
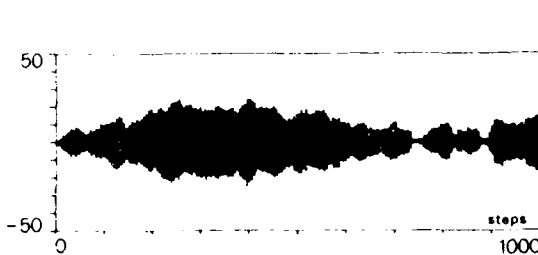
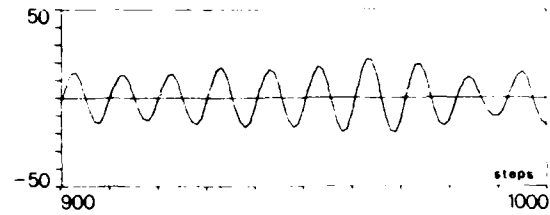
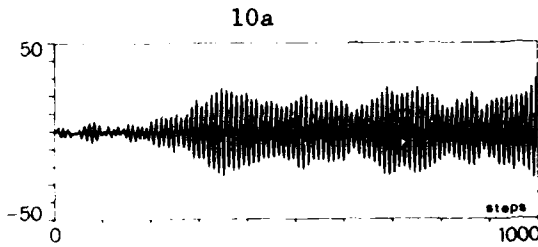


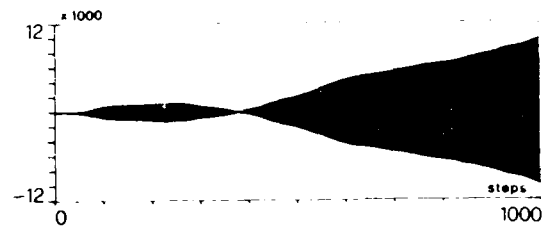
Fig. 11 - Error distribution C

- a) $\Delta t/T_0 = 0.001$ (10^4 steps)
- b) $\Delta t/T_0 = 1$ (10^3 steps)
- c) $\Delta t/T_0 = 1000$ (10^3 steps)

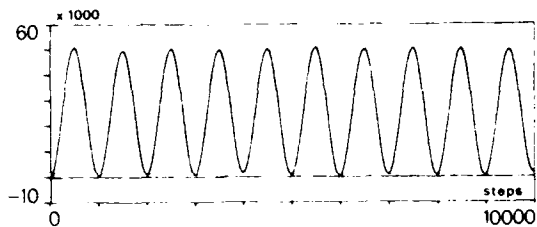
11a



11b



11c



12a

Fig. 12 - Error distribution D

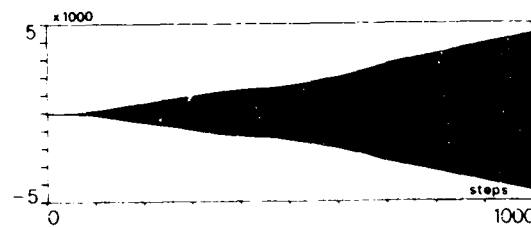
a) $\Delta t/T_0 = 0.001$ (10^4 steps)

b) $\Delta t/T_0 = 1$ (10^3 steps)

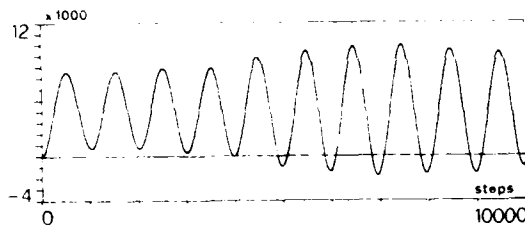
c) $\Delta t/T_0 = 1000$ (10^3 steps)



12b



12c



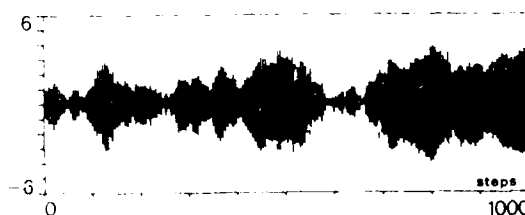
13a

Fig. 13 - Error distribution E

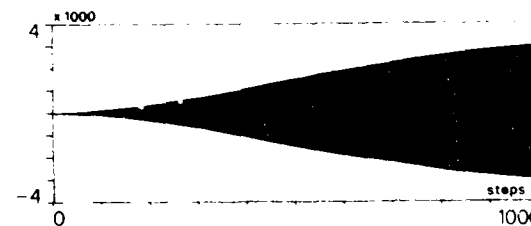
a) $\Delta t/T_0 = 0.001$ (10^4 steps)

b) $\Delta t/T_0 = 1$ (10^3 steps)

c) $\Delta t/T_0 = 1000$ (10^3 steps)



13b



13c

4. FINAL REMARKS AND CONCLUSION

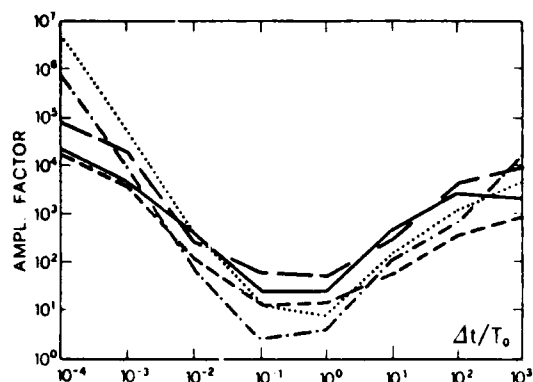
The results of sect.3 are summarized in the spectrum of fig. 14, which shows the maximum error amplification factor versus the $\Delta t/T_0$ ratio for a linear single d.o.f. oscillator and the five distributions studied. The influence of this latter aspect is evident: the amplification factor can in fact change of orders of magnitude with respect to the reference case A (uniform error). Especially severe are the non symmetrical distribu-

tions, with very high amplification for small steps, plus a peculiar low propagation in the intermediate range.

In nonlinear dynamics, with solution accuracy dominated by user specified tolerances, the operational error propagation experimented is such to seriously endanger the results. The field treated appears hence of extreme interest in computational mechanics: among other topics, the analysis of operational error distribution, with attention to multi d.o.f. systems, and the consideration of alternative implementations warrant further study. For the latter aspect note that to date acceptable propagation behaviour has been obtained [1-4] only via previous reduction to first order of the second order ODE systems arising in structural dynamics.

Fig. 14 - Error amplification spectra for different distributions

Distribution A —————
 Distribution B - - - - -
 Distribution C ————
 Distribution D
 Distribution E - . - . -



5. REFERENCES

1. K.C. PARK, C.A. FELIPPA 1978 ASME Journal of Applied Mechanics, 603-611, Vol. 45. *Computational Aspects of Time Integration Procedures in Structural Dynamics - Part 2: Error Propagation.*
2. C.A. FELIPPA, K.C. PARK 1978 ASME Journal of Applied Mechanics, 595-602, Vol. 45. *Computational Aspects of Time Integration Procedures in Structural Dynamics - Part 1: Implementation.*
3. F. BRANCALEONI, V. CIAMPI 1981 Proc. IX In.. Congress IKM, Weimar. *A General Approach to the Analysis and the Use of Linear Multistep Methods in Structural Dynamics.*
4. F. BRANCALEONI, V. CIAMPI 1982 Proc. VI Conference AIMETA, Genua. *Characteristics and Behaviour of a New Family of Linear Operators for the Evolution Analysis of Discrete Problems (in Italian).*
5. F. BRANCALEONI, V. CIAMPI 1981 Proc. In.. Conf. SMIRT VI, Paris. *Improved Error Propagation Behaviour of Linear Multistep Methods for Transient Structural Analysis.*
6. P. HENRICI 1963 *Error Propagation for Difference Methods.* New York: John Wiley and Sons.
7. P. HENRICI 1962 *Discrete Variable Methods in Ordinary Differential Equations.* New York: John Wiley and Sons.
8. P.S. JENSEN 1974 In.. J. Comp. Struct., Vol. 4, 615-626. *Transient Analysis of Structures by Stiffly Stable Methods.*

R. F. Smith and H. C. B. Hyder

Thermal Hydraulics Division, Maxwell Laboratory, Lincoln, New Zealand

1. INTRODUCTION

In shell and tube heat exchangers used in process plants or in the power generation industry, several vibration mechanisms may exist resulting from fluid flow, thermal expansion, and seismic activity. These vibrations cause tube wear and failure. In general, the tube supports have a significant influence on the magnitude and ease of assembly. Thus it is not surprising that tube vibrations will cause tube damage due to impacting and fretting. The presence of loose supports promotes strong non-linearity in the response of the tube as found from experimental investigations on typical heat exchanger tubes [1]. The prediction of wear damage is especially important in nuclear steam generators and the most important wear mechanism has been found to be one involving impact with sliding. In this area of non-linear vibrations, much work has been reported on single-degree of freedom impacting systems under harmonic forcing [2, 3] and multi-degree of freedom impacting systems under random excitation [4].

The work presented in this paper describes an initial study of the behaviour of loosely supported heat exchanger tubes. A mathematical model describing the motion of a beam impacting against a support is presented, based upon the assumption that the motion of the beam is linear between impacts but highly non-linear at the time of impact. The objectives are firstly to establish the importance of parameters which may influence the tube response such as tube clearance, alignment and secondly, to examine the parameters which may govern the wear rate (ie impact rate, impact velocity, time between successive impacts). This model is formulated in a format for use as a computer simulation algorithm. The results obtained using the algorithm are presented for a pinned-pinned beam undergoing free vibration with an intermediate loose support.

2. THEORETICAL MODEL OF IMPACTING BEAM

In this section, a mathematical model is presented which describes the motion of the beam and its impact dynamics. This model is formulated in a format that is suited for the purposes of computer simulation. The results for a particular case are based on the model which will be presented in subsequent sections.

First, it should be noted that the beam motion is highly non-linear with the beam velocity being discontinuous at the point of impact. This implies that conventional numerical integration techniques such as the Runge-Kutta method are inapplicable. In this study, a special technique has been developed which incorporates a simplifying feature of this particular non-linear motion; this feature being that between successive impacts, the motion of the beam is linear. Thus for each time interval between impacts, the beam motion may be represented by a modal summation of the form

$$\xi(x,t) = \sum_{j=1}^N q_j(t) \phi_j(x) \quad (1)$$

where $q_j(t)$ is the principal displacement of the j th mode, $\phi_j(x)$ is the j th mode shape and $\xi_j(x,t)$ is the actual displacement of the beam at any time t . For modelling purposes, a finite number of modes N is used although in principle, an infinite number of modes are required. The mode shapes $\phi_j(x)$ which prescribes the beam motion between impacts correspond to modes where the intermediate supports (at which impacts may occur) are absent.

Since a linear model is appropriate for equation (1), each principal co-ordinate q_j satisfies the oscillator equation

$$\ddot{q}_j + \omega_j^2 q_j = 0 \quad (2)$$

yielding solutions of the form

$$q_j(t) = A_j \cos(\omega_j t) + B_j \sin(\omega_j t) \quad (3)$$

where A_j and B_j are defined by the initial conditions at the start of each time interval. No damping terms have been included in the formulation of equation (2) for the purposes of this study although this could quite easily be included. In addition, it is assumed that there are no losses of energy and that the intermediate supports are rigid. The latter assumption implies that at each impact, the beam receives an impulse which causes it to rebound instantly from the support (ie zero contact time).

For the simulation exercise to work, it is necessary to piece together the various time intervals between impacts, ie to model each impact and relate the beam displacement and velocity just before the impact to the new displacement and velocity at the beginning of the next time interval just after impact.

The simulation algorithm is described as follows. Beginning with the linear equation of motion of the beam, using equation (1), the response is simulated exactly by taking small time steps. Eventually, a time is reached where it is found that the beam has penetrated the support. Using the method of bisections, the exact time of impact is obtained hence enabling the displacement and velocity of each principal mode to be calculated at the instant just prior to the impact. It is then necessary to calculate the new tube displacement and velocity at the instant just after the impact. For simplicity, let the time at which the impact occurs be denoted by $t=0$. In addition, let the displacement and velocity just before and after the impact to be denoted by $\xi(x,0_-)$, $\xi(x,0_+)$ and $\dot{\xi}(x,0_-)$, $\dot{\xi}(x,0_+)$ respectively. A similar notation applies for the principal co-ordinates. As the impact has no time duration, the displacement before and after the impact will be identical (ie $\xi(x,0_-) = \xi(x,0_+)$ and $q_j(x,0_-) = q_j(x,0_+)$). Hence, only the velocity remains to be calculated. Let the impulse that the tube received from the support be denoted by P . Since the impulse can be idealised as a force applied for an infinitesimally small duration, the impulse applied to each principal mode may be calculated by the usual method for determining principal forces from actual applied forces. Thus, the impulse applied to each mode is given by $P\phi_j(x)$ where $\phi_j(x)$ is the value of the mode shape at the location x where the beam touches the support. The new velocity of each mode $\dot{q}_j(0_+)$ can be calculated from the impulse equation

$$\dot{q}_j(0_+) = \dot{q}_j(0_-) + P\phi_j(x_0)/m_j \quad (4)$$

where m_j is the principal mass of the j th mode. P can be calculated based on the assumption of conservation of energy. The impulse does not add energy to the system but merely redistributes the total energy between the various modes. Because no energy is lost as a result of the impact, the total energy before and after an impact remains constant. In addition, because the displacement is unchanged at the impact, the strain energy in the beam remains unchanged. Hence, for equating the total energy before and after the impact, only the kinetic energy needs to be considered. Thus the total beam kinetic energy before and after impact is given by

$$\sum_j^N \frac{1}{2} m_j [\dot{q}_j(0_-)]^2 = \sum_j^N \frac{1}{2} m_j [q_j(0_-) + P\phi_j(x_0)/m_j]^2 \quad (5)$$

using equation (4). This can be simplified to

$$\sum_j^N \frac{1}{2} m_j (2\dot{q}_j(0_-) P\phi_j(x_0)/m_j + P^2 \phi_j^2(x_0)/m_j) = 0 \quad (6)$$

Since P is independent of the summation, equation (6) may be rewritten as

$$P \sum_j^N \dot{q}_j(0_-) \phi_j(x_0) + P^2 \sum_j^N \frac{1}{2} \phi_j^2(x_0)/m_j = 0 \quad (7)$$

The solutions to the above equation are

either $P = 0$ (no impact) or

$$P = - \frac{\sum_j^N \dot{q}_j(0_-) \phi_j(x_0)}{\sum_j^N \frac{1}{2} \phi_j^2(x_0)/m_j}$$

P can thus be calculated from known values of $\dot{q}_j(0_-)$ using the above equation. Hence from equation (4), $\dot{q}(0_+)$ is obtained.

3. COMPUTER SIMULATION

Simulation of the displacement response of the tube was carried out on a PDP 11/60 computer. For each case study, time histories were generated for the displacement response of the tube at the support location and at a nominal midspan location L_2 (see figure 1) over a duration of two minutes. In addition, impact velocities and the time duration between successive impacts were recorded. Ten degrees of freedom were considered in each case and the energy associated with each degree of freedom was computed. A sample rate of 15,000 samples per second was used to achieve accurate resolution of the times between impacts. The results presented here refer to the free vibration of a mild steel beam with pinned end supports as shown in figure 1. The beam is 1m in length with the intermediate support located at 0.49 m from one end. The gap between the stops at the intermediate support is 1.8 mm (ie the maximum beam displacement at the support will be ± 0.9 mm when centred between the stops).

Computer simulations were carried out to examine the effects of tube misalignment with the support by resetting the lateral position of the stops in relation to the beam position at zero deflection. The amount of misalignment Q is expressed as a percentage and is defined as

$$Q = (1 - \frac{C_1}{C}) \times 100\% \quad (9)$$

where C = maximum beam deflection at the support when centred between the stops

C_1 = distance between the upper stop and the beam at static equilibrium

C_2 = distance between the lower stop and the beam at static equilibrium

and $C_1 + C_2 = 2C$

Results were obtained for misalignments Q of 0%, 50%, 100%, 150% and 200%.

Further tests were carried out to investigate the effect of increasing energy level in the system for each case of misalignment used. This was achieved by prescribing different initial conditions namely, displacement, velocity and mode of vibration. For this investigation, ten energy levels were used, ie 0.05 Nm, 0.1 Nm, 0.5 Nm, 1 Nm, 5 Nm, 10 Nm, 15 Nm, 20 Nm, 25 Nm and 30 Nm.

Additional simulations were carried out to examine firstly, the effect of changing the mode of vibration into which the energy is first introduced into the system and secondly, the effect of the intermediate support location with a constant level of energy in the system.

4. EFFECT OF INITIAL CONDITIONS

Three different energy levels were used to carry out this investigation. The intermediate support was located at midspan (ie $L_1 = 0.5$ m) and time histories were generated for the beam response at the support location L_1 and at the nominal midspan location $L_2 = 0.75$ m. Comparisons of the response were made between (i) constant energy of 0.8 Nm introduced separately into mode 1 and mode 3, (ii) constant energy of 6.3 Nm introduced separately into mode 3 and mode 5 and (iii) constant energy of 25 Nm introduced separately into mode 5 and 7.

Figures 2a and 2b typically show the displacement spectral densities at the support location L_1 and nominal midspan location L_2 respectively for case (i). It is clearly evident that the responses were shown to be almost identical and therefore independent of mode number $n = 1$ and 3. Results obtained for cases (ii) and (iii) were also found to be consistent with the above trends. Hence, it can be concluded that the redistribution of energy among the various modes of vibration as a result of impacting at the support is independent of the initial conditions. However, it is only true for the case being considered here (ie. energy is conserved in the system).

5. EFFECT OF SUPPORT LOCATION

Simulations were carried out to examine the effect of varying the position of the support on the beam response with constant energy in the system. Three support positions were tested, namely $L_1 = 0.45$ m, 0.475 m and 0.5 m for five different energy levels of 0.1 Nm, 0.8 Nm, 3.25 Nm, 6.3 Nm and 25 Nm. Results obtained in all cases tested exhibited very similar trends as typified by figure 3a showing the displacement spectral densi-

ties at the three different support location with an energy level of 0.1 Nm. It is evident that by moving the support away from the midspan position (ie. $L_1 = 0.5\text{m}$), the level of impacting will decrease for constant energy input hence the non-linearity in the response will comparatively be of a lesser degree. This would imply that less energy redistribution will occur hence most of the energy is retained in the lower order resonances. This is indicated by the level and the peaky nature of the higher order resonances at $L_1 = 0.45\text{ m}$ and 0.475 m . With the support at midspan, two effects can be observed from the response. Firstly, some of the resonances are not excited by virtue of the support being at a nodal position. Secondly, the non-linearity of the response is comparatively greater as indicated by a small shift in the lowest resonance frequency and a greater broadening effect of the higher order resonances possibly due to increased energy redistribution. These trends are even more pronounced for the highest energy level tested as shown in figure 3b.

6. EFFECT OF TUBE MISALIGNMENT AND ENERGY LEVEL

Five different settings of tube misalignment were used in this study (ie. $Q = 0, 50, 100, 150$ and 200%) and for each setting, ten different levels of energy were tested, namely 0.05, 0.1, 0.5, 1, 5, 10, 15, 20, 25 and 30 Nm. In all the cases tested, the position of the intermediate support was located at $L_1 = 0.495\text{ m}$ such that it would not coincide with a nodal position. Similarly, the simulated response at the nominal midspan position was monitored at $L_2 = 0.71$ and not at 0.75 m . analysis of the results were carried out in the following manner:-

- (i) Displacement spectral densities (DSD) of the response were computed to investigate the effects of non-linearity (ie frequency shifting, broadening of resonance peaks etc).
- (ii) Statistical moments were computed to determine the nature of the responses (ie. standard deviation, skewness, kurtosis). For example, for a Gaussian process, the skewness and kurtosis values are 0 and 3 respectively. Alternatively, normalised probability density functions (PDF) of the responses were obtained to highlight the nature of the responses. Normalisation of the data was carried out by subtracting the mean value from each data point and dividing by its standard deviation. In this manner it is possible to make comparisons between different cases of misalignment and energy level.
- (iii) Examination of the statistics of the impacts at the support were carried out by monitoring the impact rate (no of impacts/sec) and the probability density function of the time between successive impacts.
- (iv) The energy redistribution resulting from the impacts was examined by monitoring the percentage contribution of the energy in each of the principal co-ordinates q_j to the total energy of the system.

6.1 Effect of Misalignment

With no misalignment of the beam, the displacement spectral densities (DSDs) of the response at the nominal midspan position ($L_2 = 0.71\text{m}$) for increasing levels of energy are shown in figure 4a and the corresponding PDFs are shown in figure 4b. At the lowest energy level of 0.05 Nm, the DSD indicated that the response was predominantly due to the lowest resonance at 60Hz and characterised by its PDF as being periodic in

nature. This resonance frequency corresponded closely to the fundamental resonance of a pinned-pinned beam with the intermediate support absent. Similarly, the higher order responses corresponded to those of the pinned-pinned boundary condition.

With more energy in the system, it was found that there was increasing non-linearity once significant impacting occurred. This was highlighted from the DSDs by large frequency shifts in the lowest resonance, significant broadening of the peaks and eventually being overwhelmed by off-resonant contributions, and the emergence of new resonances (eg. at 315 Hz and 1020 Hz for the highest energy level tested). At the highest energy level tested, the resonance frequencies corresponded closely to those for a pinned-pinned-pinned beam indicating that the intermediate support was effectively acting as a pinned support. The corresponding PDFs showed that the responses were becoming very Gaussian in nature with skewness and kurtosis values close to 0 and 3 respectively.

With increasing misalignment, the trends were found to be very similar once significant impacting had occurred (ie. for energy levels greater than 0.5 Nm), as typified by figure 5a for the case with misalignment 0 : 200%. The frequencies of the observed resonance peaks for large energy levels were correlated to those of a pinned-pinned-pinned beam. The PDFs showed that the responses had Gaussian characteristics even at the lowest energy level tested as shown in figure 5b.

Figure 6 illustrates the variation of the impact rate with energy in the system for different levels of tube misalignment. For energy levels below 0.5 Nm, it can be seen that the impact rate was significantly dependant upon increasing misalignment. At higher energy levels, very little variation of the impact rate was observed with misalignment; showing a proportionality constant of approximately 0.5 between the impact rate and the energy level. The variations observed at the low energy levels could possibly be due to discrimination between the number of positive and negative impacts for different misalignments. At the lowest energy level of 0.05 Nm, the impact rate was shown to have increased with increasing misalignment. Closer inspection of the impact rate by separating the total number of impacts into positive and negative impacts revealed that with misalignments greater than 50%, the impacts were all positive. At the next energy level, the impacts were found to be composed of a large proportion of positive impacts and some negative impacts. It can be seen that the impact rate had significantly dropped for misalignments of 150% and 200%. This was probably due to the fact that for negative impacts to occur, the beam would effectively require a longer duration to move from one stop to the other and vice-versa, hence reducing the overall impact rate.

The PDFs of the times between successive impacts indicated high positive skewness and the majority of impacts have time durations ranging from 0.1 msec to 1 msec for high impact rates (ie. energy levels greater than 15 Nm). The distributions corresponding to energy levels between 5 Nm and 10 Nm were also positively skewed but covered time durations ranging from 0.1 msec to 2.5 msec. This form of analysis may be useful when considering estimation of wear damage because from knowledge of the distribution, it is possible to assess whether chattering of the beam was predominant (short time durations).

Figure 7 illustrates a typical three-dimensional display of the energy distribution among the principal co-ordinates q_j for increasing

levels of energy in the system. The energy in each principal co-ordinate is defined as a percentage of the total energy in the system. The plot is shown for the case of zero misalignment. It can be seen that even at the lowest energy level, some distribution of the energy (introduced originally into the 1st mode) has occurred, as indicated by contributions found at the higher principal co-ordinates. With increasing energy level, more distribution of energy was clearly evident as a result of an increase in the impact rate, and was generally found to have been spread evenly over the higher principal co-ordinates with the exception being q_2 . However, no clear trends were observed with increasing misalignments.

7. DISCUSSION

The results obtained from the simulations clearly indicated that the beam motion was random with a Gaussian distribution even for cases with moderate levels of energy in the system. Perhaps such an effect may be surprising despite the absence of any random number generation and the simulation being purely deterministic. It is therefore interesting to examine whether or not periodic motion is possible, based on the assumptions that there are no external forces or damping and no energy loss. The simplest example of periodic motion could be that of a beam impacting against one rigid stop where the time duration between successive impacts was constant. If periodic motion was possible, the velocity of each principal co-ordinate \dot{q}_j at the start of each period would have to be the same (ie $\dot{q}_j(0_+) = \dot{q}_j(0_+ + T)$ where T is the period). This would imply that the energy in mode j was the same at each time interval. Such circumstances are impossible since the effect of each impact is to change the energy in each mode (as shown in equation (7)). Hence, periodic motion of the above type proposed is clearly impossible.

A possible type of periodicity would be in circumstances where there was a periodic sequence of impacts such that the energy in each mode at the start of each period was identical. However, the results from this study have not indicated the presence of such forms of periodicity. The indication from this study was that for the non-linear system being modelled, chaotic motion was most likely to occur.

The findings from this study have indicated that even in free vibration, the response of such a simple beam model showed quite complicated behaviour. It does point to the fact that further theoretical studies are required to achieve a better understanding of the parameters governing energy redistribution in the system and to include more features such as damping, external forcing and more supports (rigid or flexible) into the current model.

8. CONCLUSIONS

A simple theoretical model for the free vibration of a loosely supported beam has been proposed and was formulated for computer simulation purposes. The simulations have shown that the beam responses were very random in nature even for low levels of impacting and in the majority of cases, exhibited Gaussian characteristics. It has also been shown that the beam response characteristics with a constant level of energy in the system were independent of the mode of vibration into which the energy was first introduced. The non-linearity of the beam response was characterised by significant shifts in resonance frequency and broadening of peaks with increasing energy in the system. At high levels of impacting,

the resonance frequencies of the beam response corresponded to natural modes of vibration for the pinned- pinned beam with the intermediate support acting as a pinned support. Misalignment of the beam with the support did not influence the response characteristics significantly for cases where the energy level was greater than 0.5 Nm; this being reflected by the impact rate being relatively unaffected by increasing misalignment at constant energy level.

ACKNOWLEDGEMENTS

The work described in this paper was undertaken as part of the Underlying Research programme of the UKAEA.

REFERENCES

1. H.G.D. GOYDER 1987 Proc.Int.Conf. on Flow Induced Vibrations, Bowness on Windermere, England, paper K4, 467 - 476. The structural dynamics of the tube vibration problem.
2. S.W. SHAW and P. HOLMES 1983 Journal of Sound and Vibration 90, 129 - 155. A periodically forced piecewise linear oscillator.
3. G.S. WHISTON 1983 Journal of Sound and Vibration 86, 557 - 562. An analytical model of two dimensional impact/sliding response to harmonic excitation.
4. H.C.DAVIES 1980 Journal of Sound and Vibration 68, 479 - 487. Random vibration of a beam impacting stops.

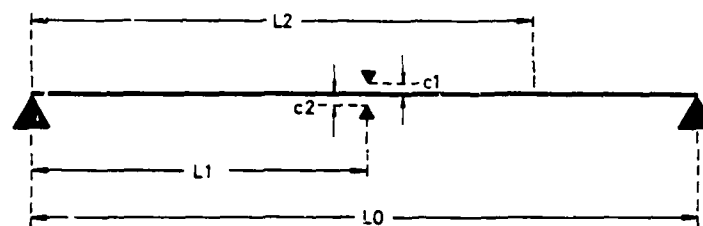


FIG. 1 BEAM MODEL USED FOR COMPUTER SIMULATION

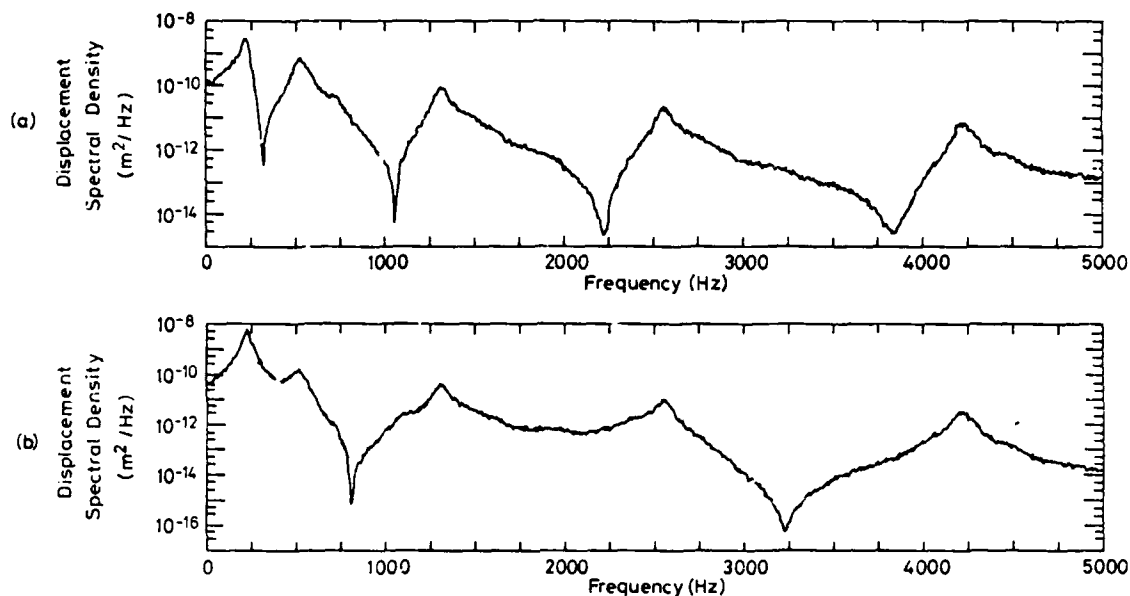


FIG. 2 COMPARISON OF RESPONSE SPECTRAL DENSITIES WITH CONSTANT ENERGY LEVEL (0.8Nm) USING DIFFERENT INITIAL CONDITIONS AT (a) SUPPORT $L_1=0.5m$ AND (b) NOMINAL MIDSPAN $L_2=0.75m$

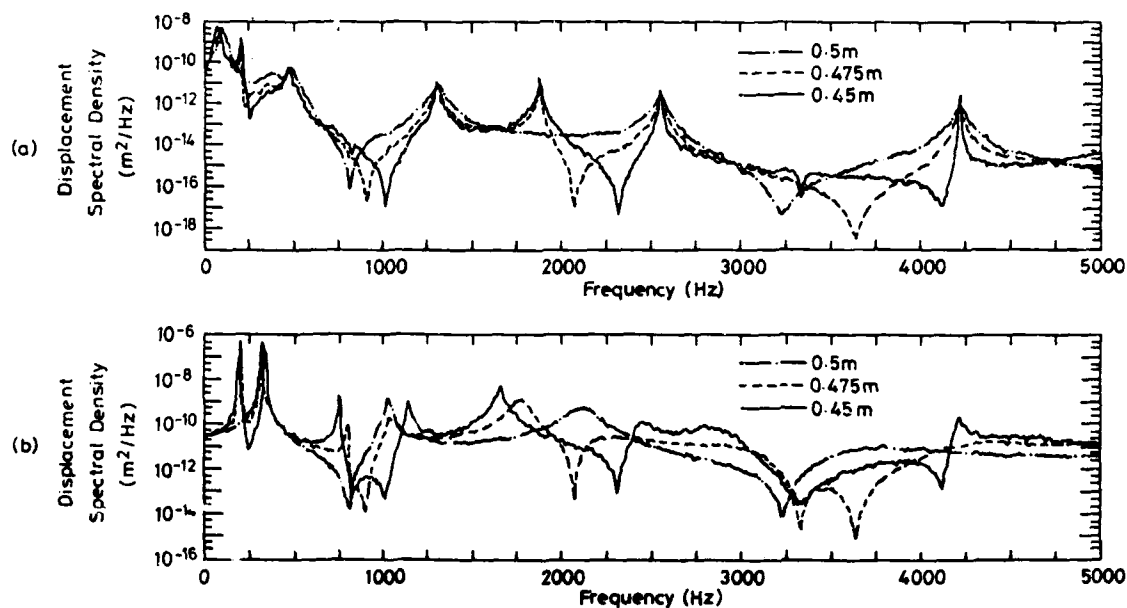


FIG. 3 RESPONSE SPECTRAL DENSITIES OBTAINED AT $L_2=0.75m$ WITH SUPPORT LOCATED AT $L_1=0.45m$, $0.475m$ AND $0.5m$ FOR ENERGY LEVELS (a) 0.1Nm (b) 25Nm

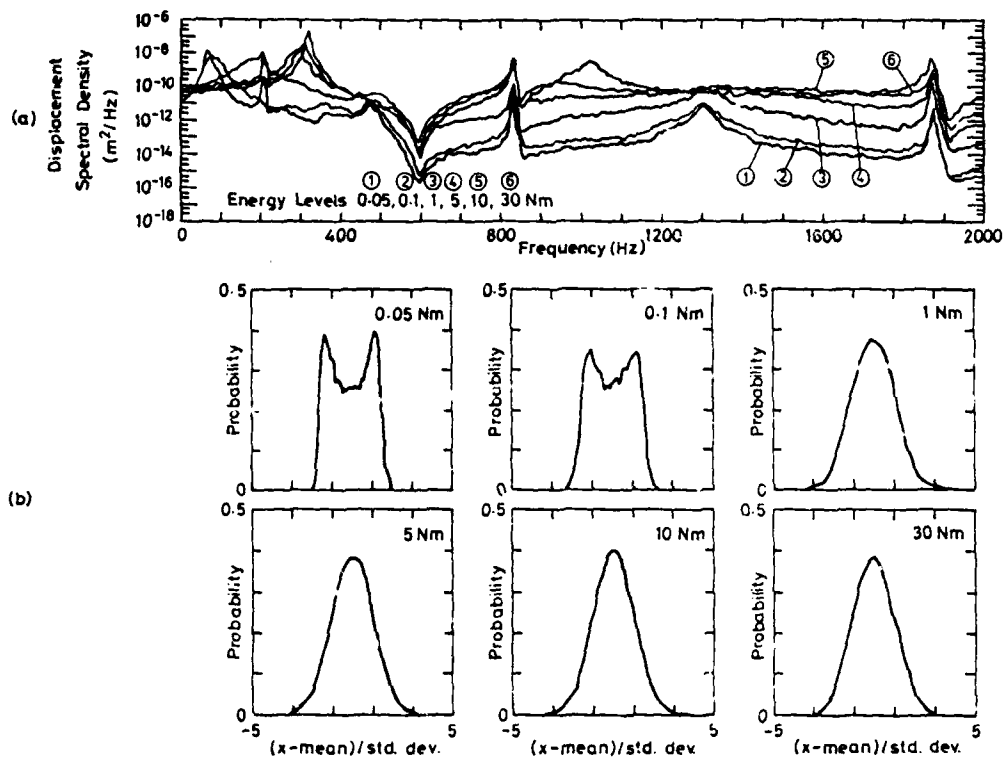


FIG. 4 (a) SPECTRAL DENSITIES AND (b) PROB. DENSITIES OF THE BEAM RESPONSE OBTAINED AT $L_2=0.71m$ FOR DIFFERENT ENERGY LEVELS (MISALIGNMENT $Q=0\%$)

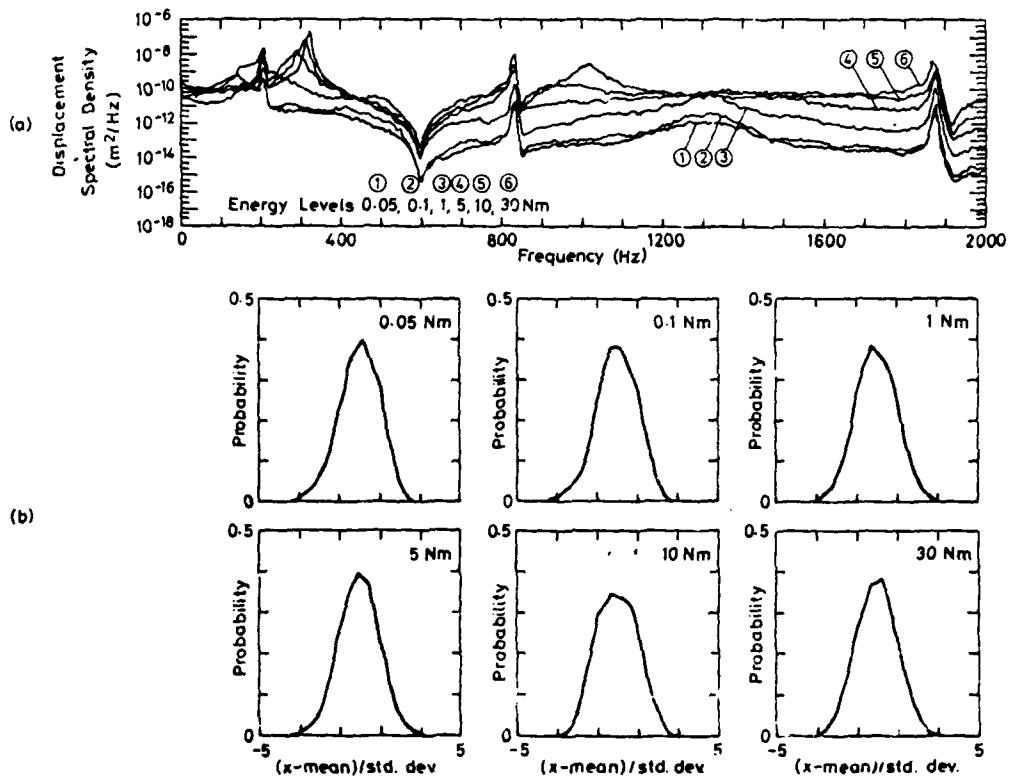


FIG. 5 (a) SPECTRAL DENSITIES AND (b) PROB. DENSITIES OF THE BEAM RESPONSE OBTAINED AT $L_2=0.75m$ FOR DIFFERENT ENERGY LEVELS (MISALIGNMENT $Q=200\%$)

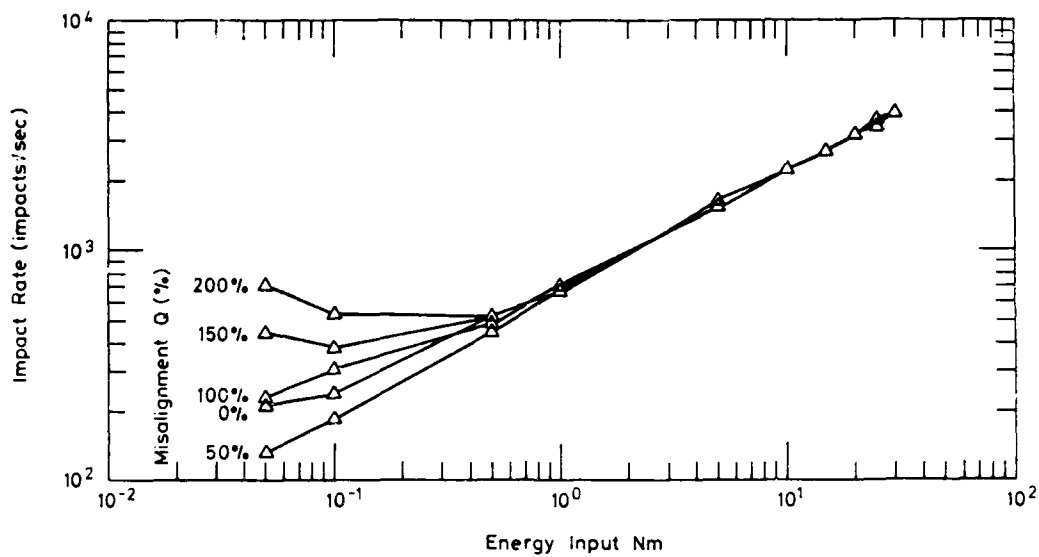


FIG. 6 EFFECT OF IMPACT RATE WITH ENERGY LEVEL FOR DIFFERENT TUBE MISALIGNMENTS

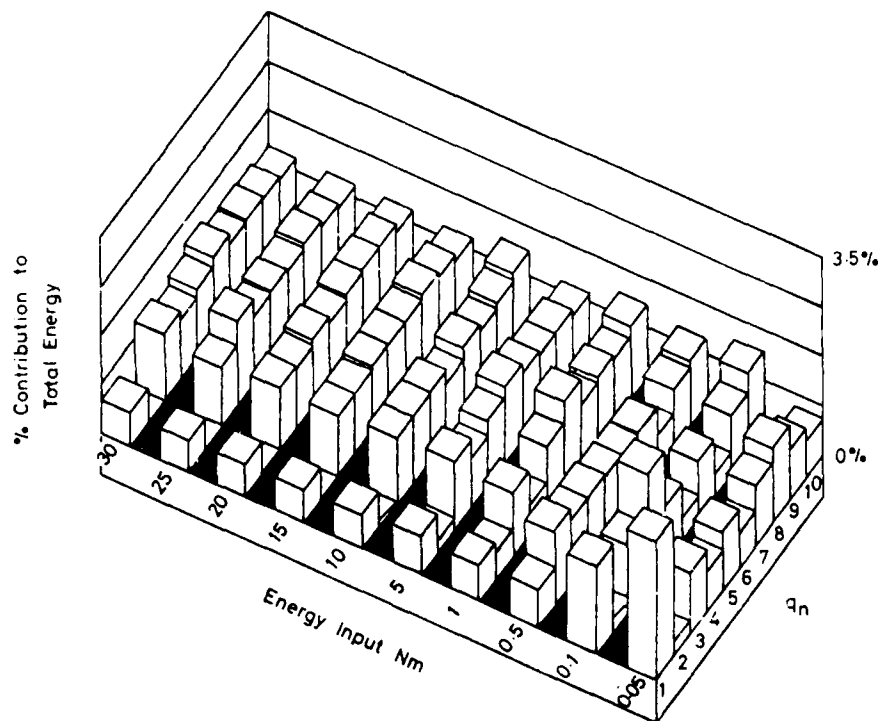


FIG. 7 3-D PLOT OF ENERGY DISTRIBUTION AMONG PRINCIPAL COORDINATES FOR DIFFERENT ENERGY LEVELS (MISALIGNMENT $Q=0\%$)

NON-LINEAR VIBRATIONS OF FLUID LOADED CYLINDRICAL SHELLS

Paulo B. Gonçalves

Department of Civil Engineering - PUC - Rio - 22453 - Brasil

Ronaldo C. Batista

COPPE/UFRJ, C.P. 68506, Rio, 21945, Brasil

1. INTRODUCTION

The vibration of circular cylindrical shells, either in air or in heavy fluid, is of practical importance in many branches of engineering. Although numerous papers have been written on the non-linear vibrations of cylindrical shells in air, on the basis of various shell theories [1-6], no such non-linear analysis appears to have been consistently done for fluid loaded cylindrical shells.

The purpose of the present paper is to present a model for the non-linear dynamic interaction between a fluid and a thin elastic shell, and to investigate the effects of shell and fluid parameters on the non-linear structural vibration response in terms of frequencies.

For the shell itself, the dynamic version of Sanders non-linear equations for the case of small strains and moderately small rotations are employed, neglecting only the rotation about the normal in the expressions for the middle surface strains [7]. By including in-plane inertia effects and avoiding the approximations of the shallow shell theory, generally used in non-linear analysis of shells [8], the results are applicable for a wide range of wave lengths and also for cases of excitation at the higher frequencies of the shell. It is assumed that the shell is filled with - or immersed in - an ideal fluid which performs a potential motion during vibration of the cylindrical shell.

The coupling via hydrodynamic pressure and the normal velocity continuity is taken into account whilst sliding between the fluid and the shell is allowed.

Turning to possible fluid non-linearities, these will generally come into play when the vibration amplitudes are significant. Reference [9] considered the non-linear terms in the dynamic fluid pressure and in the boundary condition at the surface of the cylinder. That study demonstrated that these effects are of secondary order for completely filled or submerged shells, provided that the movement of the shell surface is moderately small. Thus, the non-linear terms in the fluid equations will be neglected in the present investigation.

2. THEORY

The physical problem considered is the determination of the non-linear response of an isotropic, elastic, thin-walled, cylindrical shell filled with - or immersed in - an ideal fluid initially at rest. The geometry, displacement components and co-ordinate system are defined in fig. 1.

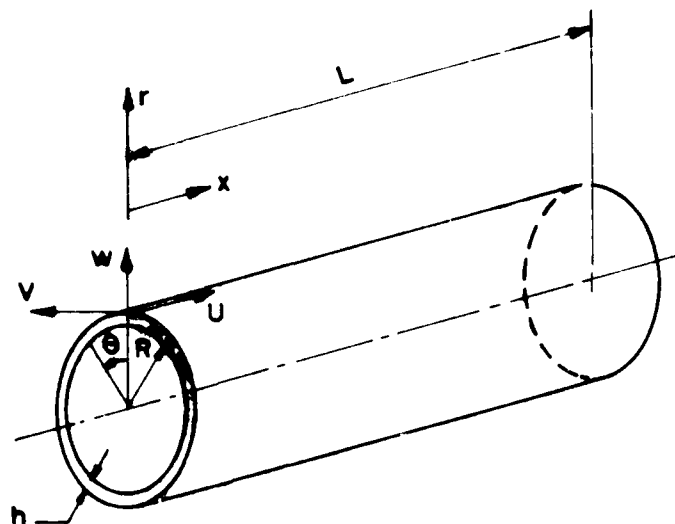


Fig. 1 - Co-ordinate system, displacements and geometry

The shell equations of motion may be expressed in dimensionless form as

$$\{u_{,\xi} + \delta w_{,\xi}^2 + v[(v_{,\theta} + w) + \delta(w_{,\theta} - v)^2]\}_{,\xi} + a[u_{,\theta} + v_{,\xi} + 2\delta w_{,\xi}(w_{,\theta} - v)]_{,\theta} + \Delta a[w_{,\xi\theta} + (u_{,\theta} - 3v_{,\xi})/4]_{,\theta} - \gamma^2 u = 0$$

$$\{v_{,\theta} + w + \delta(w_{,\theta} - v)^2 + v[u_{,\xi} + \delta w_{,\xi}^2]\}_{,\theta} + a[u_{,\theta} + v_{,\xi} + 2\delta w_{,\xi}(w_{,\theta} - v)]_{,\xi} + 2\delta w_{,\xi} \cdot \{a[u_{,\theta} + v_{,\xi} + 2\delta w_{,\xi}(w_{,\theta} - v)]\}_{,\xi} + 2\delta(w_{,\theta} - v) \cdot \{(v_{,\theta} + w) + \delta(w_{,\theta} - v)^2 + v[u_{,\xi} + \delta w_{,\xi}^2]\}_{,\xi} - 3\Delta a[w_{,\xi\theta} + (u_{,\theta} - v_{,\xi})/4]_{,\xi} - \Delta[(w_{,\theta\theta} - v_{,\theta}) + v w_{,\xi\xi}]_{,\theta} - \gamma^2 v = 0$$

$$v u_{,\xi} + v_{,\theta} + w + \delta[(w_{,\theta} - v)^2 + v w_{,\xi}^2] - \{2\delta w_{,\xi}[u_{,\xi} + \delta w_{,\xi}^2 + v(v_{,\theta} + w) + \delta v(w_{,\theta} - v)^2]\}_{,\xi} - \{2\delta(w_{,\theta} - v) \cdot [(v_{,\theta} + w) + \delta(w_{,\theta} - v)^2 + v u_{,\xi} + \delta v w_{,\xi}^2]\}_{,\theta} - \{2\delta a(w_{,\theta} - v)[u_{,\theta} + v_{,\xi} + 2\delta w_{,\xi}(w_{,\theta} - v)]\}_{,\xi} - \{2\delta a w_{,\xi}[u_{,\theta} + v_{,\xi} + 2\delta w_{,\xi}(w_{,\theta} - v)]\}_{,\theta} + \Delta[w_{,\xi\xi} + v(w_{,\theta\theta} - v_{,\theta})]_{,\xi\xi} + \Delta[(w_{,\theta\theta} - v_{,\theta}) + v w_{,\xi\xi}]_{,\theta\theta} + 4a\Delta[w_{,\xi\theta} + (u_{,\theta} - 3v_{,\xi})/4]_{,\xi\theta} + \gamma^2 w - \lambda = 0 \quad (1)$$

In the foregoing the following parameters were introduced

$$\begin{aligned} \delta &= h/2R & \xi &= X/R & (\cdot) &= \partial/\partial t & u &= U/h & v &= V/h & w &= W/h \\ \Delta &= h^2/12R^2 & \gamma &= [\rho_s R^2 (1 - \nu^2)/E]^{1/2} & a &= (1 - \nu)/2 \\ \lambda &= p R^2 (1 - \nu^2)/E h^2 \end{aligned} \quad (2)$$

in which E is the modulus of elasticity, ν is Poisson's ratio, ρ_s is the shell density, p is the radial pressure and t is time.

For a fluid loaded shell the radial pressure can be written as

$$p = p_d + p_f \quad (3)$$

where p_d is the applied dynamic pressure and p_f is the dynamic fluid pressure due to the shell surface motion.

In this investigation, the shell boundary conditions are assumed to be the "classical simply supported" boundary conditions, thus:

$$u,_{\xi} = v = w = w,_{\xi\xi} = 0 \text{ at } \xi = 0, \ell \quad (4)$$

where $\ell = L/R$.

For a complete cylindrical shell, such as the one considered here, all components of displacements must satisfy the circumferential periodicity condition. This condition assures that all the physical quantities will be continuous and single-valued along the circumferential co-ordinate.

The fluid is assumed to be non-viscous and incompressible so that it can be described by a potential function $\phi(r, \theta, x, t)$. The equations describing the fluid motion in dimensionless quantities are [11]

$$\bar{\phi},_{\xi\xi} + (\bar{\phi},_{\eta}/\eta) + (\bar{\phi},_{\theta\theta}/\eta^2) + \bar{\phi},_{\eta\eta} = 0 \quad (5)$$

$$\bar{p}_f = -\gamma \bar{\phi} \quad (6)$$

where

$$\eta = r/R \quad \bar{\phi} = \gamma \phi/R^2 \quad \bar{p}_f = \gamma^2 p_f/R^2 \rho_F \quad (7)$$

in which ρ_F is the density of the fluid medium.

The kinetic condition of impenetrability gives

$$\bar{\phi},_{\eta} = 2 \gamma \delta \dot{w} \text{ at } \eta = 1 \quad (8)$$

3. MODAL SOLUTION

From previous investigations [1-6] on modal solutions for non-linear vibrations of cylindrical shells in vacuum it is observed that, in order to obtain a consistent solution, the sum of modal functions for the displacements must satisfy all boundary conditions and continuity requirements. Moreover it must contain the most significant modes to the first approximation of non-linearity, in special, the axisymmetric modes which, as pointed out by Evesen [8], play an important role in the outcome of the results.

Here the following approximated solution for w

$$w = w_0 \cos^2 \omega t [\cos 2 q \xi - (\cos 4 q \xi)/4 - (3/4)] + \\ + w_1 \cos \omega t \sin q \xi \cos n \theta \quad (9)$$

was achieved through a perturbation procedure [9] and includes both axisymmetric and asymmetric modes which attend the boundary conditions (4). In (9) ω is the radian frequency, n is the number of circumferential waves and

$$q = m \pi R/L \quad (10)$$

in which m is the number of axial half waves.

By retaining in u and v all the modes that couple with w_0 and w_1 through quadratic and cubic products of displacements and their spatial derivatives in (1) and taking into account the boundary conditions (4), one obtains for u and v [9]

$$\begin{aligned} u = & u_0 \cos^2 \omega t [\sin 2q\xi - (\sin 4q\xi)/2] + u_1 \cos \omega t \cos q\xi \cos n\theta + \\ & + u_2 \cos^2 \omega t \cos 2n\theta [\sin 2q\xi - (\sin 4q\xi)/2] + \\ & + u_3 \cos^3 \omega t \cos n\theta \cos 3q\xi + u_4 \cos^5 \omega t \cos n\theta \cos 5q\xi + \\ & + u_5 \cos^6 \omega t [\sin 6q\xi - (3 \sin 8q\xi)/4] \end{aligned} \quad (11)$$

$$\begin{aligned} v = & v_1 \cos \omega t \sin q\xi \sin n\theta + v_2 \cos^2 \omega t \sin 2n\theta (\cos 2q\xi - 1) + \\ & + v_3 \cos^3 \omega t \sin n\theta \sin 3q\xi + v_4 \cos^5 \omega t \sin n\theta \sin 5q\xi \end{aligned}$$

It is useful to note that these functions and consequently all force and moment resultants satisfy the circumferential periodicity condition.

For the internal fluid case, the boundary condition (8) suggests seeking the solution for the velocity potential in the form.

$$\begin{aligned} \bar{\phi} = & A_1 I_n(qr) \omega \sin \omega t \sin q\xi \cos n\theta + A_2 I_0(2qr) \omega \sin 2\omega t \cos 2q\xi + \\ & + A_3 I_0(4qr) \omega \sin 2\omega t \cos 4q\xi + A_4 [r^2 - 2(\xi^2 - \ell\xi)] \omega \sin 2\omega t \end{aligned} \quad (12)$$

where I_n is the n^{th} modified Bessel function of the first kind [11].

Substituting the expressions for w and $\bar{\phi}$ into equation (8), one can write the amplitudes A_i of $\bar{\phi}$ in terms of w_1 and w_0 as follows

$$\begin{aligned} A_1 = & -2 \gamma \delta w_1 \{q [I_{n-1}(q) - (n/q) I_n(q)]\}^{-1} \\ A_2 = & -\gamma \delta w_0/q I_1(2q); A_3 = \gamma \delta w_0/8 q I_1(4q); A_4 = 3 \gamma \delta w_0/4 \end{aligned} \quad (13)$$

For a shell immersed in a fluid, a similar solution, in terms of the modified Bessel function of the second kind, K_n , can be easily obtained [9]. By employing the principle of superposition, one can also obtain the solution for a fluid-filled shell immersed in a fluid.

Finally, expressions (9), (11) and (12) are substituted into equations (1) and (6) and a Galerkin procedure is employed to obtain a system of twelve coupled non-linear algebraic equations for the modal amplitudes u_i , v_i and w_i . These equations are unfortunately too long to be presented here; the interested reader will find them in reference [9]. The complexity of the algebraic equations precludes the possibility of closed-form solution. Nevertheless Newton-Raphson method can be effectively used to solve these

equations in relatively few iterations. Through this procedure one obtains the relation between the frequency and the vibration amplitudes which allows one to study the influence of fluid and shell parameters on the degree and type of non-linearity involved in the frequency response. The plot of a response - frequency relationship is usually referred to as the "backbone" curve.

4. RESULTS

In the analysis of the results the following frequency ratios are introduced

$$\Lambda_V = \Omega_V / \Omega_{0V} \quad \Lambda_F = \Omega_F / \Omega_{0F} \quad (14)$$

where $\Omega_V (= \gamma \omega_V)$ and $\Omega_F (= \gamma \omega_F)$ are the lowest frequency parameters (associated with predominantly radial motion) for, respectively, a shell in vacuum and a shell in a fluid medium, and Ω_{0V} and Ω_{0F} are the corresponding linear free vibration frequencies [12].

The results indicated in figures 2 to 4 show how variations in the geometrical parameters (L/R , h/R) and wave numbers (m, n) affect the degree and type of non-linearity. Figure 2 shows the variations of Ω/Ω_0 (Λ_V or Λ_F) with the maximum radial amplitude w_{max} for given values of n and figure 3 shows the influence of the axial wave length parameter ($L/m R$) on the results. These results demonstrate that the non-linearity increases as the number of circumferential and axial waves increases.

The curves in figure 4 were obtained for a fixed L/h ratio and different values of the radius R . For each geometry the wave numbers (m, n) are those associated with the minimum natural frequency in the spectrum. As shown in figure 4, the non-linearity associated with the minimum natural frequency increases as the ratios h/R and L/R decreases, i.e., strong non-linearities occur for the case of thin and/or short cylinders.

The effect of the fluid region on the shell behaviour can be separated in two different parts: the inertia effects associated with the classical radial mode ($w_1 \cos n \theta \sin q \xi \cos \omega t$) and the inertia effects associated with the secondary radial modes (axisymmetric modes). As shown in figure 2 for $n=6$ (dash and point curve), if only the inertia effects associated with the classical radial mode are retained, the non-linearity for a fluid-filled shell is weaker than that predicted for a shell in vacuum. This "added mass" effect is also responsible for the significant reduction in the linear free vibration frequencies of a fluid-filled shell [12]. On the other hand, if the fluid effects associated with the shell secondary modes are also taken into account, the non-linearity for a fluid-filled shell, as shown in figure 2, is much stronger than that predicted for a shell in vacuum. This strong softening effect is due to the increase of the inertia effects associated with second-harmonic terms in the non-linear equations of motion [9,14]. From the results, one can also observe that the degree of non-linearity increases as the ratio ρ_F/ρ_S increases.

For the case of forced vibrations, the applied loading was chosen such that only one mode is directly excited

$$p_d = \bar{P} \cos n \theta \sin q \xi \cos \omega t \quad (15)$$

Figure 5 illustrates the response curves for forced vibrations of a

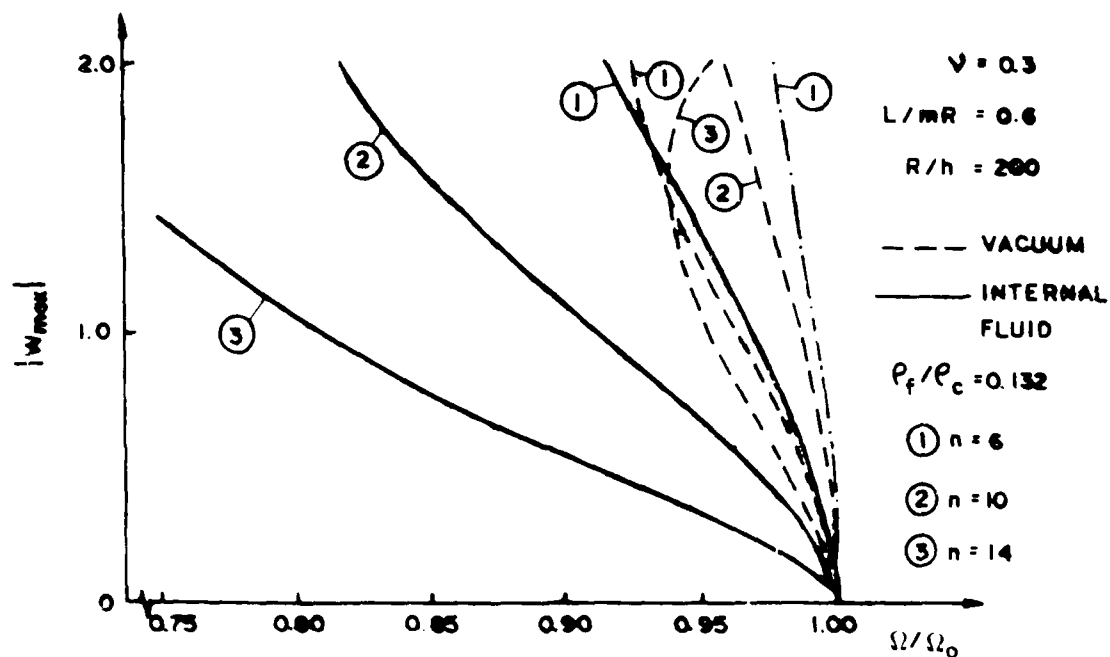


Figure 2 - Influence of the circumferential wave number, n , on the non-linear vibrations of the shell.

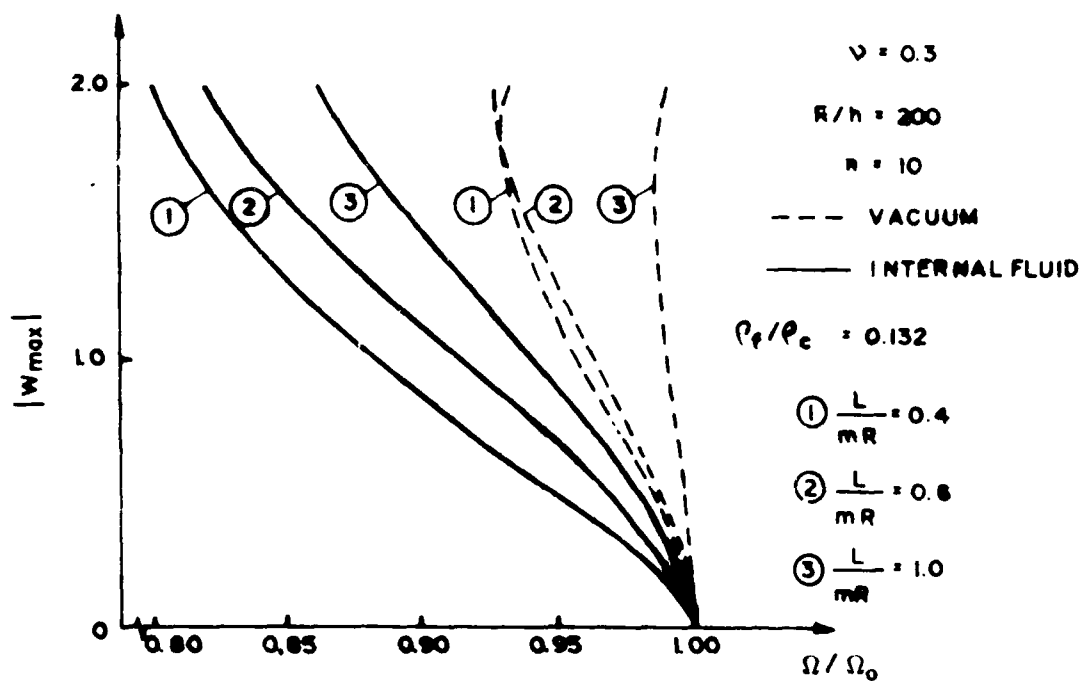


Figure 3 - Influence of large amplitudes on the vibration frequency for various values of the axial wave length L/mR .

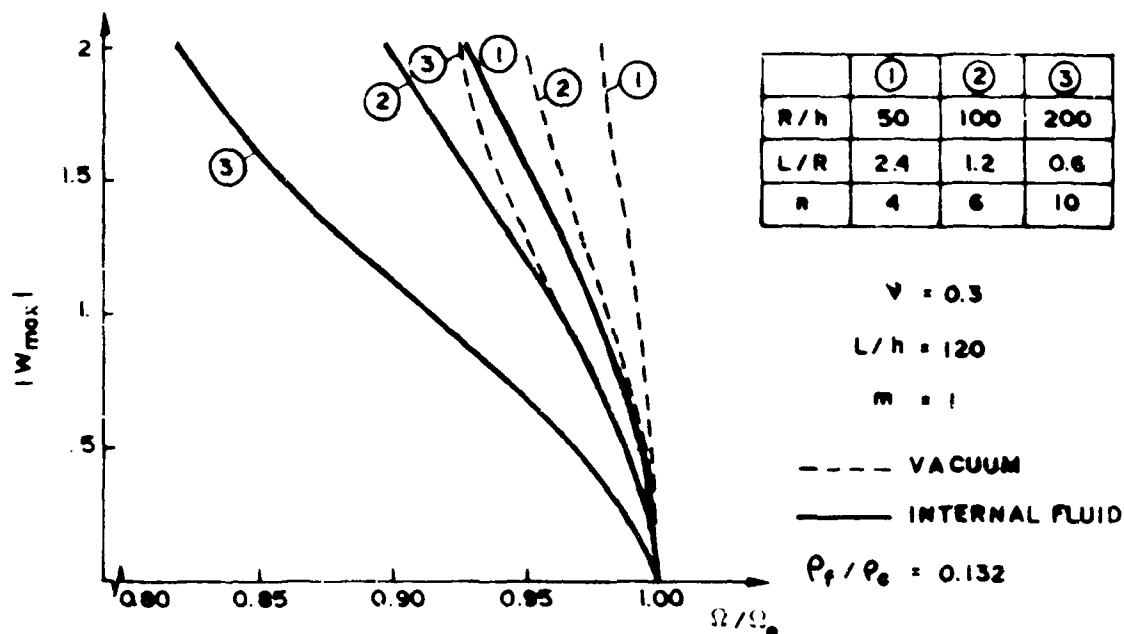


Figure 4 - Influence of the shell geometrical parameters (L/R , h/R) on the non-linear behaviour of a shell at the fundamental frequency.

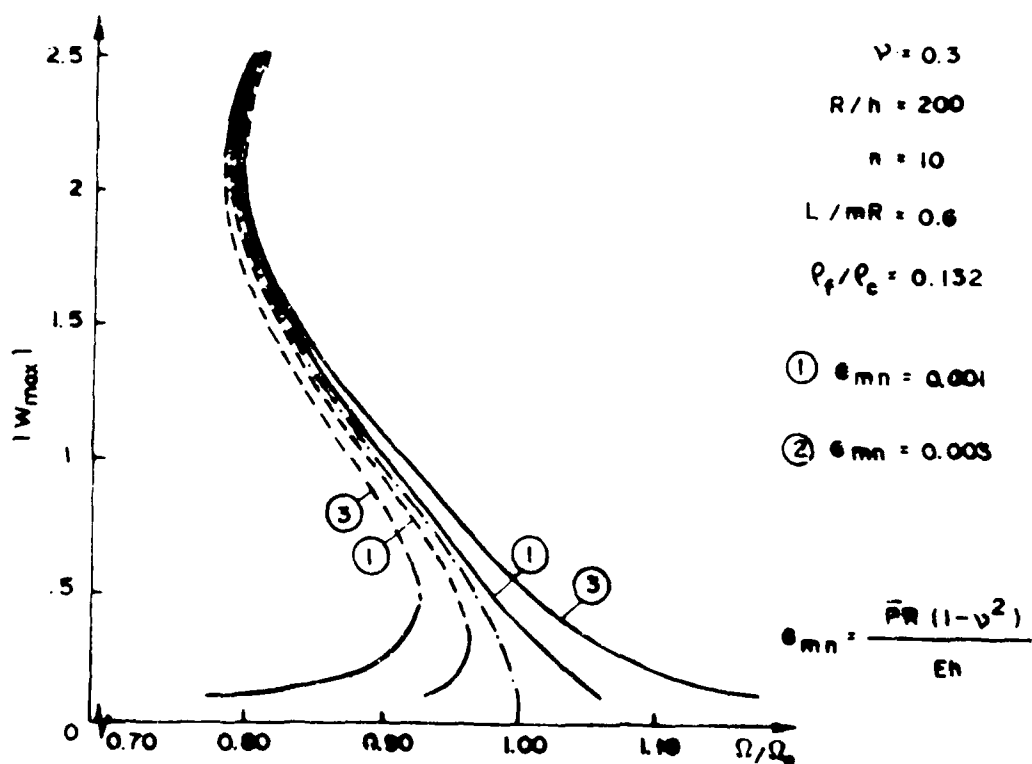


Figure 5 - Single mode response of a fluid filled shell. Forced and free vibrations.

fluid-filled shell. The unstable solution, i.e., the physically impossible solution is denoted by a dashed line. The existence of more than one stable solution for a given frequency of excitation explains the possible appearance of discontinuous jumps in amplitude. Which amplitude does exist depends upon the past history of the system. If the excitation frequency is varied, a jump will occur whenever a point of infinite slope in figure 5 is reached [13,14]. The loci of the vertical tangencies in figure 5 together with the backbone curve maps on the boundaries of a instability region, which, as shown by Stoker [13], corresponds to the first instability region of the Mathieu equation.

One must bear in mind that in a real system dissipation is always present. The presence of dissipative forces will diminish the instability region and give rise to a rounded peak on the skewed resonance curve, whose location depends upon the relative amount of damping [13,15].

Although it is not discussed here, the same softening behaviour is expected for a cylindrical shell immersed in a fluid and also for the case when both the internal and external surfaces of the shell are fluidically loaded.

5. CONCLUSIONS

The effect of a fluid medium on the degree and type of non-linearity of a thin-walled cylindrical shell was investigated.

It has been shown, for a broad range of wave numbers (m,n) and geometric ratios ($L/R, h/R$), that, for excitation at the fundamental frequency, the non-linearity is initially of a softening type. This initial frequency behaviour is due to the non-linear coupling, that reduces the membrane stiffness of the shell and gives rise to inertia effects associated with second-harmonic terms.

Regarding the effect of the fluid, it has been observed that a fluid-filled shell exhibits a stronger non-linearity than a shell in vacuum. For both cases the non-linearity increases whenever the numbers of axial and circumferential waves increase and the ratios h/R and L/R decrease.

By employing a consistent shell theory, and by obtaining a solution that satisfies the imposed boundary and continuity conditions and retains the most important secondary modes, the present analysis overcomes many of the shortcomings encountered in previous studies for shells in vacuum. Hence, the present formulation for the shell problem is capable of furnishing consistent solution for a wide range of geometric parameters and wave numbers.

REFERENCES

1. H.N. CHU 1961 J. Aerospace Sci. 28, 602-609. Influence of large amplitudes on the flexural vibrations of a thin circular cylindrical shell.
2. D.A. EVESEN 1963 AIAA Journal 1, 2857-2858. Some observations on the nonlinear vibrations of orthotropic cylindrical shells.
3. E.H. DOWELL and C.S. VENTRES 1968 Int. J. Solids Structures 4,

- 973-991. Modal equations for the nonlinear flexural vibrations of a cylindrical shell.
4. S. ATLURI 1972 Int. J. Solids Structures 8, 549-569. A perturbation analysis of non-linear free flexural vibrations of a circular cylindrical shell.
 5. J.H. GINSBERG 1973 J. Appl. Mech.-ASME 40, 471-477. Large amplitude forced vibrations of simply supported thin cylindrical shells.
 6. H. RADWAN and J. GENIM 1976 J. Appl. Mech.-ASME 43, 370-372. Non-linear vibrations of thin cylinders.
 7. J.L. SANDERS Jr. 1963 Q. Appl. Math. 21, 21-36. Nonlinear theories for thin shells.
 8. D.A. EVESEN 1974 Thin Shell Structures Ed. Fung and Sechler. Nonlinear vibrations of circular cylindrical shells. New Jersey: Prentice Hall.
 9. P.B. GONÇALVES 1987 Ph.D. Thesis, COPPE-Federal University of Rio de Janeiro. Non-linear dynamic interaction between a fluid and thin shells.
 10. H. LAMB 1945 Hydrodynamics. New York: Dover Publications.
 11. N.W. McLACHLAN 1934 Bessel Functions for Engineers. Oxford: Oxford Press
 12. P.B. GONÇALVES and R.C. BATISTA 1987 Journal of Sound and Vibration 113, 59-70. Frequency response of cylindrical shells partially submerged or filled with liquid.
 13. J.J. STOKER 1950 Nonlinear Vibrations. New York: Interscience Publishers, Inc.
 14. V.V. BOLOTIN 1965 Dynamic Stability of Elastic Systems. San Francisco: Holden-day.
 15. H.A. NAYFEH and T.D. MOOK 1979 Nonlinear Oscillations. New York: Wiley.

9. RANDOM VIBRATION OF NONLINEAR SYSTEMS

RECENT ADVANCES IN NONLINEAR RANDOM VIBRATION

Y. K. Lin

Center for Applied Stochastics Research

Florida Atlantic University

1. INTRODUCTION

The subject random vibration deals with uncertainty in the behavior of dynamical systems. The cause for uncertainty may be unpredictability of exact time-histories of excitations, imperfection or lack of accurate information in the modeling of physical problem, or combination of these. Mathematically speaking, modeling a dynamic system amounts to setting up the governing equations of motion, and specifying the initial and boundary conditions. Thus, various types of uncertainty are represented as random variables and random processes in the modeling which can only be characterized in terms of probabilistic or statistical properties.

The present paper will focus on nonlinear governing equations, and will be restricted only to uncertain excitations. In a discretized form, such equations may read

$$\frac{d}{dt} X_j = f_j(X, t) + g_{jk}(X, t) F_k(t);$$
$$j = 1, 2, \dots, N; \quad k = 1, 2, \dots, M \quad (1)$$

in which t is the time variable, X_j are components of the system response vector X , $F_k(t)$ are random processes representing the random excitations, and a repeated subscript in a product indicates a summation. Functions f_j and g_{jk} are generally nonlinear; however, their functional forms are deterministic. For practical purposes, this representation by a set of first order ordinary differential equations is sufficiently general. A higher order equation can be replaced by several first order ones, a distributed system governed by a partial differential equation can be discretized using, for example, a Galerkin procedure, and an integral-differential equation can be converted to a set of ordinary differential equations.

Two types of random excitation are possible. A particular $F_k(t)$ is a multiplicative (or parametric) excitation if its accompanying factor $g_{jk}(X, t)$ depends explicitly on the response X ; it is an additive (or external) excitation if its accompanying factor does not depend on X . In other words, a multiplicative excitation appears as the coefficient of an unknown in the governing equations whereas an additive excitation appears as an inhomogeneous term. The roles played by the two types of random excitations are fundamentally different.

2. EXACT SOLUTIONS

Exact solutions for randomly excited nonlinear systems are difficult to obtain. The possibility for exact solutions exists if the random excitations can be idealized as Gaussian white noises. In such a case the

response of a system to random excitations, represented as a vector in a state space, is a Markov vector. The probability density of a Markov vector, conditional on the knowledge of the initial state, is governed by a parabolic partial differential equation, called the Fokker-Planck equation, which can be derived from the equations of motion. Still, exact solutions for the Fokker-Planck equation is known only for very special first order nonlinear systems, which are of little interest to structural engineers. For higher order systems, solutions have been obtained for the reduced Fokker-Planck equations; namely, Fokker-Planck equations without the time derivative term. The unknown in a reduced Fokker-Planck equation is the unconditional probability density of the system response when it reaches the state of statistical stationarity. This can occur if the f_j and g_{jk} functions in equation (1) do not depend explicitly on t , and if energy can be dissipated from the system to balance the input energy from the excitations.

The Fokker-Planck equation has the general form of

$$\frac{\partial}{\partial t} q + \frac{\partial}{\partial x_j} G_j = 0 \quad (2)$$

where q is an abbreviated symbol for the unknown conditional probability density $q_X(x, t | x_0, t_0)$, and G_j is the probability flow in the j th direction given by

$$G_j = A_j(x)q - \frac{1}{2} \frac{\partial}{\partial x_k} [B_{jk}(x)q] \quad (3)$$

In (2) and (3), a lower case symbol represents the possible value of a random quantity. For example, x is a possible value of X , x_j a possible value of X_j , etc. This convention will be followed throughout the paper. In equation (3) A_j and B_{jk} are called the first and second derivate moments (also known as the drift and diffusion coefficients), respectively, which can be obtained from the equations of motion as follows using the well-known rules of Wong and Zakai [1]:

$$A_j(x) = f_j(x) + \pi K_{\ell s} g_{rs} \frac{\partial}{\partial x_r} g_{jl}(x) \quad (4)$$

$$B_{jk}(x) = 2\pi K_{\ell s} g_{jl} g_{ks} \quad (5)$$

In (4) and (5) each $K_{\ell s}$ is a constant, representing the joint spectral density of $F_\ell(t)$ and $F_s(t)$, which are now restricted to be Gaussian white noises so that an exact probabilistic solution can be obtained. $K_{\ell s}$ is related to the cross-correlation function of $F_\ell(t)$ and $F_s(t)$ as

$$E[F_\ell(t_1)F_s(t_2)] = 2\pi K_{\ell s} \delta(t_1 - t_2) \quad (6)$$

An exact solution, if obtainable, must satisfy the initial condition

$$q_X(x, t_0 | x_0, t_0) = \prod_{j=1}^N \delta(x_j - x_{j,0}) \quad (7)$$

and appropriate boundary conditions. If the total probability measure must be preserved, then the boundary conditions must be natural, namely,

$$G_j = 0 \text{ at the boundaries} \quad (8)$$

As indicated earlier, we shall be interested in the stationary state solutions, governed by the reduced Fokker-Planck equation

$$\frac{\partial}{\partial x_j} G_j = 0 \quad (9)$$

$$G_j = A_j(x)p_s(x) - \frac{1}{2} \frac{\partial}{\partial x_k} [B_{jk}(x)p_s(x)] \quad (10)$$

where $p_s(x)$ is the stationary probability density of X independent of t . Equation (9) is solved with the boundary conditions (8).

2.1 The Case of Stationary Potential

The special case of stationary potential considered by Stratonovich [2] is one in which the probability flow vanishes everywhere not only at the boundaries, namely

$$A_j(x)p_s(x) - \frac{1}{2} \frac{\partial}{\partial x_k} [B_{jk}(x)p_s(x)] = 0 \quad (11)$$

Without loss of generality, write the solution for (11) as

$$p_s(x) = C \exp(-\phi) \quad (12)$$

This solution form guarantees that the probability density, if it exists, is non-negative for a positive normalization constant C . Substituting (12) into (11), one obtains

$$B_{jk} \frac{\partial \phi}{\partial x_k} = \frac{\partial}{\partial x_k} B_{jk} - 2A_j \quad (13)$$

These are N equations for ϕ . If a consistent ϕ function can be obtained from (13), then the stochastic system belongs to the class of stationary potential.

For a first order system, for which the state space is one-dimensional, namely $N = 1$, the probability flow must vanish everywhere if it vanishes at the boundaries. Then (13) reduces to

$$B \frac{d\phi}{dx} = \frac{d}{dx} B - 2A \quad (14)$$

Solving for ϕ

$$\phi = \ln B - 2 \int AB^{-1} dx \quad (15)$$

Unfortunately, as to be explained later, oscillatory dynamic systems do not belong to the class of stationary potential. Since structural systems are usually oscillatory a more general procedure is needed and will be discussed in the next section.

2.2 The Case of Generalized Stationary Potential

Circulatory probability flows are generally present in a multi-dimensional state space. To provide for additional flexibility in obtaining a solution to equation (9), we split the drift and diffusion coefficients as follows [3,4]

$$A_j = A_j^{(1)} + A_j^{(2)} \quad (16)$$

$$B_{jk} = B_{jk}^{(j)} + B_{kj}^{(k)} \quad (17)$$

Equation (17) retains the symmetry condition for diffusion coefficients; i.e. $B_{jk} = B_{kj}$. Substituting (16) and (17) into (9), one obtains

$$\frac{\partial}{\partial x_j} \left[A_j^{(1)} p_s - \frac{\partial}{\partial x_k} B_{jk}^{(j)} p_s \right] + \frac{\partial}{\partial x_j} [A_j^{(2)} p_s] = 0 \quad (18)$$

Let $A_j^{(1)}$ be associated with the vanishing probability flow, and $A_j^{(2)}$ associated with the circulatory probability flow. Then for p_s expressed in the form of (12), it can be shown that

$$\frac{\partial}{\partial x_j} A_j^{(2)} = A_j^{(2)} \frac{\partial \phi}{\partial x_j} \quad (19)$$

$$A_j^{(1)} = \frac{\partial}{\partial x_k} B_{jk}^{(j)} - B_{jk}^{(j)} \frac{\partial \phi}{\partial x_k} \quad (20)$$

The superscript (j) in (20) does not imply a summation. There are a total of $n + 1$ equations for ϕ in the set of (19) and (20). The problem is solvable if a consistent ϕ function can be obtained from these equations. Such a solvable problem is said to belong to the case of generalized stationary potential [3,4]. It is of interest to note that if the system is in a state known as detailed balance [e.g. 5,6], then the two parts of each drift coefficient $A_j^{(1)}$ and $A_j^{(2)}$ correspond to the so-called irreversible and reversible parts, respectively. However, (19) and (20) are more general, and are applicable to systems not in detailed balance.

2.3 Applications

The above solution technique will now be applied to single-degree-of-freedom second order systems of the type

$$\ddot{Z} + \psi(Z, \dot{Z}) = \theta_k(Z, \dot{Z}) W_k(t) \quad (21)$$

where $W_k(t)$ are Gaussian white noises with delta type correlations; i.e.

$$E[W_k(t) W_l(t+\tau)] = 2\pi K_{kl} \delta(\tau) \quad (22)$$

Equation (21) is equivalent to two first order equations in the form of (1)

$$\begin{aligned} \frac{d}{dt} X_1 &= X_2 \\ \frac{d}{dt} X_2 &= -\psi(X_1, X_2) + \theta_k(X_1, X_2) W_k(t) \end{aligned} \quad (23)$$

It follows from (4) and (5) that

$$\begin{aligned} A_1 &= x_2, \\ A_2 &= -\psi(x_1, x_2) + \pi K_{kl} \theta_l(x_1, x_2) \frac{\partial}{\partial x_2} \theta_k(x_1, x_2) \\ B_{11} &= B_{12} = B_{21} = 0, \quad B_{22} = 2\pi K_{kl} \theta_k(x_1, x_2) \theta_l(x_1, x_2) \end{aligned}$$

Split the drift and diffusion coefficients into

$$A_1^{(1)} = 0, \quad A_1^{(2)} = x_2$$

$$A_2^{(1)} = -\psi(x_1, x_2) + \pi k_{k\ell} \theta_\ell \frac{\partial}{\partial x_2} \theta_k + \lambda_x / \lambda_y$$

$$A_2^{(2)} = -\lambda_x / \lambda_y, \quad B_{22}^{(2)} = \frac{1}{2} B_{22}, \quad B_{12}^{(1)} = -B_{21}^{(2)}$$

where λ is an arbitrary function of $x = x_1$ and $y = \frac{1}{2}x_2^2$, and is twice

differentiable with respect to its arguments. The physical meaning of λ will be discussed later. Then application of (19) and (20) results in

$$x_2 \frac{\partial \phi}{\partial x_1} + (\lambda_x / \lambda_y) \frac{\partial \phi}{\partial x_2} - \frac{\partial}{\partial x_2} (\lambda_x / \lambda_y) = 0 \quad (24)$$

$$B_{12}^{(1)} \frac{\partial \phi}{\partial x_2} = \frac{\partial}{\partial x_2} B_{12}^{(1)} \quad (25)$$

$$B_{21}^{(2)} \frac{\partial \phi}{\partial x_1} + \pi K_{k\ell} \theta_k \theta_\ell \frac{\partial \phi}{\partial x_2} = \frac{\partial}{\partial x_1} B_{21}^{(2)} + \psi(x_1, x_2) + \pi K_{k\ell} \theta_k \frac{\partial}{\partial x_2} \theta_\ell - \lambda_x / \lambda_y \quad (26)$$

The general solution of (24) is

$$\phi(x_1, x_2) = -\ln \lambda_y + \phi_0(\lambda) \quad (27)$$

where $\phi_0(\lambda)$ is an arbitrary function of λ . In order that (25) and (26) can also be satisfied, the ψ and θ_k functions must be related as

$$\begin{aligned} \psi(x_1, x_2) = & \pi x_2 K_{k\ell} \theta_k \theta_\ell [\lambda_y \phi_0'(\lambda) - \lambda_{yy} / \lambda_y] \\ & - \pi K_{k\ell} \theta_\ell \frac{\partial}{\partial x_2} \theta_k + \lambda_x / \lambda_y + D(x_1) e^{\phi_0(\lambda)} / \lambda_y \end{aligned} \quad (28)$$

where $D(x_1)$ is an arbitrary function of x_1 alone. Equation (28) provides a restriction between the constitutive law of the system, as represented by ψ and θ_k on one hand, and the spectral densities $K_{k\ell}$ on the other, so that the exact solution for the stationary probability density is obtainable using the present procedure.

The well-known case [7,8] of linear damping, nonlinear spring, and an additive Gaussian white noise excitation

$$\ddot{Z} + \beta \dot{Z} + g(Z) = W(t), \quad \beta > 0 \quad (29)$$

corresponds to a single $\theta = 1$ and

$$\psi(x_1, x_2) = \beta x_2 + g(x_1) \quad (30)$$

Then letting $D(x_1) = 0$ and

$$\lambda = y + \int_0^x g(u) du = \frac{1}{2}x_2^2 + \int_0^{x_1} g(u) du \quad (31)$$

equation (28) reduces to

$$\phi_0'(\lambda) = \frac{\beta}{\pi K} \quad (32)$$

where K is the spectrum of the white noise. Furthermore, $\phi(\lambda) = \phi_0(\lambda)$ in this case. Thus

$$\begin{aligned} p_S(x_1, x_2) &= C \exp\left(-\frac{\beta}{\pi K} \lambda\right) \\ &= C \exp\left\{-\frac{\beta}{\pi K} \left[\frac{1}{2} x_1^2 + \int_0^{x_1} g(u) du\right]\right\} \end{aligned} \quad (33)$$

which is a valid probability density if λ is positive for large $|x_1|$.

Without specifying the form for the λ function, but still letting $D(x_1) = 0$ and restricting to a single additive excitation, one obtains from (28)

$$\phi_0'(\lambda) = \frac{\psi(x_1, x_2) - \lambda_x/\lambda_y + \pi K x_2 (\lambda_{yy}/\lambda_y)}{\pi K x_2 \lambda_y} \quad (34)$$

Note that the right hand side of (34) must be a function of λ alone. If this is satisfied, then (34) can be used to obtain the required $\phi_0(\lambda)$.

The solution obtained by Caughey and Ma [9] corresponds to

$$\psi(x_1, x_2) = \lambda_x/\lambda_y + \pi K x_2 [\lambda_y h(\lambda) - \lambda_{yy}/\lambda_y] \quad (35)$$

where $h(\)$ is an arbitrary function subject to a rather general restriction to be specified later. Substitution of (35) into (34) results in

$$\phi_0'(\lambda) = h(\lambda) \quad (36)$$

and a stationary probability density

$$p_S(x_1, x_2) = C \lambda_y \exp \left[- \int_0^\lambda h(v) dv \right] \quad (37)$$

The λ and h functions must be such that the right hand side of (37) is normalizable. This extremely simple result is obtained under a rather artificial assumption that the constitutive law of the system itself, namely $\psi(x_1, x_2)$ is dependent on the spectrum K of the excitation.

The physical meaning of the λ function can be revealed by considering the deterministic case of undamped free motion governed by

$$\ddot{x} + \lambda_x/\lambda_y = 0 \quad (38)$$

Since $\dot{x} = (1/2)(d\dot{x}^2/dx) = dy/dx$, the above equation can be replaced by

$$d\lambda = \lambda_x dx + \lambda_y dy = 0 \quad (39)$$

Therefore, $\lambda(x, y)$ is not truly arbitrary; it represents the total energy in the conservative system (38). It should be noted, however, that this physical interpretation must be modified if multiplicative random excita-

tion appears in the coefficient of the first derivative term in a second order differential equation.

Equations (19) and (20) have been applied to obtain new solutions for systems under both additive and multiplicative excitations [4,10]. The following two examples will illustrate some of the possibilities.

The first example is described by

$$\ddot{Z} + \left[\alpha + \frac{\beta}{2} (\dot{Z} + \omega_0^2 Z)^2 + W_2(t) \right] \dot{Z} + \omega_0^2 [1 + W_1(t)] Z = W_3(t) \quad (40)$$

where $W_1(t)$, $W_2(t)$ and $W_3(t)$ are independent Gaussian white noises with spectra K_{11} , K_{22} and K_{33} , respectively. Under the restriction $\omega_0^2 K_{11} = K_{22}$ the stationary probability density for $Z=X_1$ and $\dot{Z}=X_2$ is given by [14]

$$p_S(x_1, x_2) = C \left(\lambda + \frac{K_{33}}{2K_{22}} \right)^{-\gamma} \exp \left(- \frac{\beta}{2\pi K_{22}} \lambda \right) \quad (41)$$

where $\gamma = \frac{1}{2} \left(\frac{\alpha}{\pi K_{22}} + 1 - \frac{\beta}{\pi K_{22}^2} K_{33} \right)$ and $\lambda = \frac{1}{2} x_2^2 + \frac{1}{2} \omega_0^2 x_1^2$

Equation (41) is a generalization of a result obtained previously by Dimantberg [10] for the special case $K_{33} = 0$, namely, when the additive random excitation is absent, in which case, the value for γ is restricted to $\gamma < 1$; otherwise, the right hand side of (41) is not normalizable. This can occur, of course, only if $\alpha < 0$ and $K_{22} > |\alpha|/\pi$. It means that the trivial solution $Z=\dot{Z}=0$ is unstable in probability when $K_{22} > |\alpha|/\pi$.

The second example is an interesting nonlinear oscillator capable of exhibiting limit cycle and bifurcation behaviors, governed by [11].

$$\ddot{Z} + Z^2 \left[\beta + \frac{4\alpha}{Z^2 + \dot{Z}^2} \right] \dot{Z} + [1 + W(t)] Z = 0 \quad (42)$$

where $\beta > 0$, and $W(t)$ is a Gaussian white noise multiplicative excitation with a spectral density K . Without the random excitation, the equation has a non-trivial solution, corresponding to a stable limit-cycle if $\alpha < 0$. If $\alpha > 0$, then the only stable configuration is the trivial $Z = 0$.

The stationary probability density for $Z=X_1$ and $\dot{Z}=X_2$ is found to be

$$p_S(x_1, x_2) = C(x_1^2 + x_2^2)^{2\alpha/\pi K} \exp \left[- \frac{\beta}{2\pi K} (x_1^2 + x_2^2) \right] \quad (43)$$

Equation (43) implies that if $\alpha > 0$ then a nontrivial stationary probability density exists only if $K > 2\alpha/\pi$. Thus, $2\alpha/\pi$ represents a critical spectral level for the multiplicative excitation at which bifurcation occurs, and below which the trivial solution is stable in probability. When a stationary probability density of the system response exists ($K > 2\alpha/\pi$), its shape depends on whether $\alpha \geq 0$ or $\alpha < 0$. It can be shown that if $\alpha \geq 0$, then the probability density p_S has a peak at $x_1^2 = x_2^2 = 0$. On the other hand, if $\alpha < 0$, then p_S has a maximum at $x_1^2 + x_2^2 = 4|\alpha|/\beta$ and it tends to zero as $x_1^2 + x_2^2$ approaches to either zero or infinity. This

implies that the probability density has a shape shown in Fig. 1, and the most probable values for the response lie on the circle

$x_1^2 + x_2^2 = 4 |\alpha| / \beta$, which is the stochastic analogue of the limit cycle.

To the knowledge of the writer, the class of generalized stationary potential, satisfying (19) and (20), includes all the stochastic systems whose exact probability solution in the stationary state are known to date. When both multiplicative and additive random excitations are present, restriction on the system parameters and excitation spectral levels are generally required to obtain such solutions.

3. EQUIVALENT STOCHASTIC SYSTEMS

It is possible that responses of two dynamical systems under different sets of random excitations can share an identical probability distribution. Such systems are said to be stochastically equivalent. Given a stochastic system with a known probability density, a procedure has been devised to identify or construct its equivalent systems [12].

Return to (19) and (20) since these equations define the class of generalized stationary potential for which exact solutions are presently possible. In order to satisfy (19), let

$$A_i^{(2)} = \frac{\partial}{\partial x_j} \delta_{ij}^{(1)} - \delta_{ij}^{(1)} \frac{\partial \phi}{\partial x_j} \quad (44)$$

where δ_{ij} is anti-symmetric; namely, $\delta_{ij}^{(1)} = -\delta_{ji}^{(1)}$. Adding (20) and (44),

$$A_i = \frac{\partial}{\partial x_j} (B_{ij}^{(1)} + \delta_{ij}^{(1)}) - (B_{ij}^{(1)} + \delta_{ij}^{(1)}) \frac{\partial \phi}{\partial x_j} \quad (45)$$

Now since B_{ij} is symmetric, it is always possible to write

$$B_{ij}^{(1)} = \frac{1}{2} B_{ij} + \delta_{ij}^{(2)} \quad (46)$$

where $\delta_{ij}^{(2)}$ are also anti-symmetric. Then equation (45) becomes

$$A_i = \frac{\partial}{\partial x_j} \left(\frac{1}{2} B_{ij} + \delta_{ij} \right) - \left(\frac{1}{2} B_{ij} + \delta_{ij} \right) \frac{\partial \phi}{\partial x_j} \quad (47)$$

where $\delta_{ij} = \delta_{ij}^{(1)} + \delta_{ij}^{(2)}$ is again anti-symmetric. The set of n equations in (47), which replaces the set of $n+1$ equations in (19) and (20), is simpler since the process of splitting A_i and B_{ij} are now replaced by a single process of selecting δ_{ij} . With the knowledge of the solution of one stochastic system, namely, the knowledge of ϕ , we can construct a large number of equivalent stochastic systems by selecting physically meaningful combinations of B_{ij} and δ_{ij} matrices.

Equation (47) is a relation in terms of the drift and diffusion coefficients. In terms of original system equations of the form of (1) this relation may be expressed as

$$f_j = \pi K_{ls} g_{rs} \frac{\partial}{\partial x_r} g_{jl} - \pi K_{ls} g_{jl} g_{rs} \frac{\partial \phi}{\partial x_r}$$

$$+ \frac{\partial}{\partial X_r} \delta_{jr} - \delta_{jr} \frac{\partial \phi}{\partial X_r} \quad (48)$$

The f and g functions here do not depend explicitly on t since (47) or (48) are derived on the assumption of a stationary solution. If the g functions are kept to be the same as those of a given stochastic system whose stationary probability density is known, then by varying the δ_{jr} matrix, we obtain equivalent stochastic systems having the same reduced Fokker-Planck equation. This restrictive case has been investigated previously by San Miguel and Chaturvedi [13]. From the present analysis, it is clear that sharing an identical reduced Fokker-Planck equation is not a necessary condition for equivalent stochastic systems. Different reduced Fokker-Planck equations are obtained by varying both the g functions and the δ_{jr} matrix. As examples, we cite the following stochastically equivalent systems [12]:

$$\begin{aligned} \ddot{Z} + \beta Z^2 \dot{Z} + g(Z) &= ZW(t) \\ \ddot{Z} - \pi K \dot{Z} + \beta \dot{Z}^3 + g(Z) &= \dot{Z}W(t) \\ \ddot{Z} + \beta \dot{Z}[1 + (K_{22}/K)Z^2] + g(Z) &= W(t) + ZW_2(t) \\ \ddot{Z} + (\beta - \pi K_{33})\dot{Z} + \beta \dot{Z}[(K_{22}/K)Z^2 + (K_{33}/K)\dot{Z}^2] \\ &+ g(Z) = W(t) + ZW_2(t) + \dot{Z}W_3(t) \end{aligned}$$

where $W(t)$, $W_2(t)$ and $W_3(t)$ are assumed independent, having spectral densities K , K_{22} and K_{33} , respectively. These systems share the same stationary probability density as that of system (29), namely equation (32), although their Fokker-Planck equations are different.

It is of interest to note that there exists a narrower class of equivalent stochastic systems whose responses share not only the stationary probability distribution, but also the transient nonstationary probability distribution under identical initial conditions. This narrower class is said to be stochastically equivalent in the strict (or strong) sense, whereas the wider class discussed above is referred to as being stochastically equivalent in the wide (or weak) sense [12].

4. APPROXIMATE SOLUTIONS

When both multiplicative and additive random excitations are present, restrictions usually must be imposed on the relationship between the noise spectra and some system parameters in order to obtain an exact stationary-state solution for the response of a nonlinear system at the present time. In practical engineering applications, the excitation spectral levels cannot be so restricted; therefore, approximate procedures are often needed to obtain the solutions.

4.1 Cumulant-Neglect Closure

One versatile scheme to obtain approximate solutions is the cumulant-neglect closure [14,15] which can be applied easily if random excitations

are Gaussian white noises or filtered Gaussian white noises. Return to (1) and convert these equations to the Itô type stochastic differential equations as follows [e.g. 16]

$$dX_j(t) = m_j(X,t)dt + \sigma_{j\ell}(X,t)dB_\ell(t) \quad (49)$$

where $B_\ell(t)$ are independent unit Wiener processes, and

$$m_j(X,t) = A_j(X,t) \quad (50)$$

$$\sigma_{j\ell}(X,t) \sigma_{k\ell}(X,t) = B_{jk}(X,t) \quad (51)$$

The right hand sides of (50) and (51) are the same drift and diffusion coefficients in (4) and (5), but with x replaced by X . However, these coefficients can now depend on t , and the results in this section are not restricted to the stationary response. One can then obtain equations for the statistical moments for $X(t)$ by using Itô's differential rule [17]

$$\frac{d}{dt} E[F(X,t)] = E\left[\frac{\partial F}{\partial t} + (m_j \frac{\partial F}{\partial X_j} + \frac{1}{2} \sigma_{j\ell} \sigma_{k\ell} \frac{\partial^2 F}{\partial X_j \partial X_k})\right] \quad (52)$$

and by letting F be X_i , $X_i X_r$, $X_i X_r X_s$, etc. For nonlinear systems, the equations for statistical moments form an infinite hierarchy, and they can only be solved approximately using a suitable closure scheme.

The statistical moments are related to cumulants as follows [2,18]:

$$\begin{aligned} E[X_j] &= \kappa_1[X_j] \\ E[X_j X_k] &= \kappa_2[X_j, X_k] + \kappa_1[X_j] \kappa_1[X_k] \\ E[X_j X_k X_\ell] &= \kappa_3[X_j, X_k, X_\ell] + 3 \{ \kappa_1[X_j] \kappa_2[X_k, X_\ell] \}_s \\ &\quad + \kappa_1[X_j] \kappa_1[X_k] \kappa_1[X_\ell] \\ E[X_j X_k X_\ell X_m] &= \kappa_4[X_j, X_k, X_\ell, X_m] + 3 \{ \kappa_2[X_j, X_k] \kappa_2[X_\ell, X_m] \}_s \\ &\quad + 4 \{ \kappa_1[X_j] \kappa_3[X_k, X_\ell, X_m] \}_s + 6 \{ \kappa_1[X_j] \kappa_1[X_k] \kappa_2[X_\ell, X_m] \}_s \\ &\quad + \kappa_1[X_j] \kappa_1[X_k] \kappa_1[X_\ell] \kappa_1[X_m] \\ &\dots\dots\dots \end{aligned} \quad (53)$$

where $\kappa_j[]$ denotes a j th cumulant, and $\{ \}_s$ indicates a symmetrizing operation with respect to its arguments; namely, taking the arithmetic mean of different permuted terms similar to the one within the braces. In a cumulant-neglect closure, all the cumulants higher than a given order N are set to zero. The statistical moments of an order higher than N can then be expressed in terms of lower order moments using (53). Very accurate results have been obtained using this scheme [14] as long as the spectral levels of multiplicative random excitations are not too high so that the system is far from stochastic bifurcation or instability [19,20].

It is of interest to note that for a random process defined on $(-\infty, \infty)$, neglecting κ_n for $n > 2$ is equivalent to the so-called Gaussian closure; namely, approximating this random process by a Gaussian process.

Gaussian closure, however, is the simplest and of the lowest order among non-trivial cumulant-neglect closures. Furthermore, if the excitations are white noises or filtered white noises, then Gaussian closure leads to the same results as statistical equivalent linearization. A review of recent contributions to the equivalent linearization schemes has been given by Spanos [21]. Another closure scheme, using a truncated Gram-Charlier or Edgeworth series [22,23] has a similar accuracy as that of cumulant closure; however, it is more difficult to apply to multi-degree-of-freedom systems when a multidimensional Gram-Charlier series is required.

4.2 Generalized Equivalent Linearization

The development of generalized equivalent linearization scheme by Brückner and Lin [24] was motivated by two reasons: (1) a cumulant-neglect closure of an order $N > 2$ does not guarantee a non-negative probability density everywhere, (2) the traditional equivalent linearization, which leads to the same result as that of Gaussian closure, replaces the original nonlinear system with a linear system devoid of parametric excitation; therefore, it is unsuitable to treat the case when random parametric excitations are also present.

In a generalized equivalent linearization scheme, the original Itô system, (49) is replaced by a linear Itô system as follows:

$$dX_j(t) = (a_{jk}X_k + b_j)dt + (c_{jrs}X_r + d_{js})dB_s(t) \quad (54)$$

The equations for the first and second order statistical moments are closed; they may be determined from

$$\frac{d}{dt} E[X_j] = a_{jk} E[X_k] + b_j \quad (55)$$

$$\begin{aligned} \frac{d}{dt} E[X_j X_r] = & a_{rs} E[X_j X_s] + a_{jk} E[X_r X_k] \\ & + c_{jkl} c_{rpl} E[X_k X_p] + b_r E[X_j] + b_j E[X_r] \\ & + c_{jkl} d_{rl} E[X_k] + c_{rpl} d_{jl} E[X_p] + d_{jl} d_{rl} \end{aligned} \quad (56)$$

The constants a_{jk} , b_j , c_{jrs} and d_{js} are determined by minimizing the mean-square errors

$$\epsilon_j = E\{[m_j(X) - a_{jk}X_k - b_j]^2\} \quad (57)$$

$$\begin{aligned} \epsilon_{jr} = E\{[X_j m_r(X) + X_r m_j(X) + \sigma_{jl}(X) \sigma_{rl}(X) - a_{rs} X_j X_s \\ - a_{jk} X_r X_k - c_{jkl} c_{rpl} X_k X_p - b_r X_j - b_j X_r \\ - c_{jkl} d_{rl} X_k - c_{rpl} d_{jl} X_p - d_{jl} d_{rl}]^2\} \end{aligned} \quad (58)$$

To carry out the minimization process, the evaluation of certain moments higher than the second order is still required. However, when the optimal constants so obtained are substituted into Eq.(54), the linearized system does possess a non-negative probability density.

4.3 Stochastic Averaging

Method of stochastic averaging was developed by Stratonovich [2] based primarily on physical arguments. It was later justified and interpreted rigorously by Khasminskii [25], Papanicolaou and Kohler [26]. The first application to structural systems was due to Ariaratnam in the analysis of column stability under random axial load [27]. Lin and co-workers have used the procedure to investigate the effects of atmospheric turbulence on the motions of helicopter blades [e.g. 28,29,30,31], and of long-span bridges [32,33]. Namachchivaya and Ariaratnam [34] and Namachchivaya [35,36] applied the method to Hopf bifurcation in the presence of stochastic excitations. A review of the general subject and many other contributions was given by Roberts and Spanos [37].

According to Stratonovich [2] the response of a dynamic system to random excitation may be approximated by a Markov vector, if the correlation times of all the excitations are short compared with the relaxation time of the system. Then the coefficients in the corresponding Itô type differential equations (49) can be obtained from the original physical equations (1) as follows:

$$m_j = f_j(X, t) + \int_{-\infty}^0 \frac{\partial}{\partial X_l} g_{jk}(X, t) g_{ls}(X, t + \tau) E[F_k(t) F_s(t + \tau)] d\tau \quad (59)$$

$$\sigma_{jl} \sigma_{kl} = \int_{-\infty}^{\infty} g_{jr}(X, t) g_{ks}(X, t + \tau) E[F_r(t) F_s(t + \tau)] d\tau \quad (60)$$

It is of interest to note that the right hand sides of (59) and (60) reduce to the same forms as those of (4) and (5), respectively, if the random excitations are delta-correlated.

If the right hand sides of the physical equations (1) are small in some sense, implying that the state variables are slowly varying, then the results obtained in (59) and (60) can be further simplified by time-averaging over t . This additional time averaging not only makes the drift and diffusion coefficients independent of time, but very frequently it also renders a group of state variables to become uncoupled from the others, thus permitting a reduction of the dimensions of the state space being considered. The latter advantage is very significant from an analytical point of view and is the main reason for the popularity of the stochastic averaging procedure. If the system is linear or slightly nonlinear, the unknowns in the original physical equations can be transformed to polar-coordinate variables corresponding to slowly varying amplitudes and phases, making the time-averaging applicable. Alternatively, the unknowns can be transformed to complex random processes in conjugate pairs. The absolute magnitude of a complex random process is equivalent to an amplitude process, and the ratio between the imaginary and real parts is the arctangent of a phase process. This alternative scheme was used by Ariaratnam and Tam [38] to linear systems with many degrees of freedom. Brückner and Lin [39] have shown that it can also be applied advantageously to nonlinear cases, and when used in conjunction with the cumulant-neglect procedure, the number of equations to be solved simultaneously is reduced greatly.

Since time-averaging is often the key to make a problem solvable, it is of interest to comment on two cases for which time-averaging are still applicable without requiring that the right hand sides of all the first order physical equations be small. The first case is a weakly damped single-degree-of-freedom oscillator with a strongly nonlinear stiffness, governed by

$$\ddot{X} = -g(X) + \epsilon f(X, \dot{X}) + \epsilon^{1/2} h_1(X, \dot{X}) F_1(t) \quad (61)$$

where ϵ is a small positive number and for simplicity the $F_i(t)$ are assumed to be white noises. Introduce an energy process [2]

$$V = \frac{1}{2} \dot{X}^2 + G(X) = \frac{1}{2} \dot{X}^2 + \int_0^X g(u) du \quad (62)$$

Equation (61) can be replaced by the following two first order equations

$$\dot{X} = \pm \sqrt{2(V-G)} \quad (63)$$

$$\begin{aligned} \dot{V} = & \pm \sqrt{2(V-G)} \{ \epsilon f(X, \pm \sqrt{2(V-G)}) \\ & + \epsilon^{1/2} h_1(X, \pm \sqrt{2(V-G)}) F_1(t) \} \end{aligned} \quad (64)$$

These two equations can be converted to the following Itô type equations

$$dX = \pm \sqrt{2(V-G)} dt \quad (65)$$

$$dV = \epsilon m dt + \epsilon^{1/2} \sigma dB(t) \quad (66)$$

where according to (4), (5), (50) and (51)

$$m = \pm \sqrt{2(V-G)} \{ f + (\pi K_{ij}) h_j \frac{\partial}{\partial V} [\pm \sqrt{2(V-G)} h_i] \} \quad (67)$$

$$\sigma = \sqrt{4\pi K_{ij}(V-G) h_i h_j} \quad (68)$$

The unknown V in (70) is slowly varying, but the unknown X in (65) is not. Invoking a theorem due to Khasminskii [40] Zhu [41] performed a time-averaging on the right-hand-side of (70) as follows:

$$\bar{m} = \frac{1}{T} \int_R \{ f + \pi K_{ij} h_j \frac{\partial}{\partial V} [\pm \sqrt{2(V-G)} h_i] \} dX \quad (69)$$

$$\bar{\sigma}^2 = \pm \frac{1}{T} \int_R 2\pi K_{ij} \sqrt{2(V-G)} h_i h_j dX \quad (70)$$

where integration on t has been replaced by integration on X using (65), R is the integration domain defined as $V \geq G$, and

$$T = \pm \int_R [2(V-G)]^{-1/2} dX \quad (71)$$

Since the integrands are expressed in terms of $\pm \sqrt{2(V-G)}$, the value of each

integral is obtained by adding the results from separate integrations for the plus and the minus signs. Substituting \bar{m} and $\bar{\sigma}$ for m and σ , respectively, in (66), we obtain an Itô equation for V which is devoid of X . Similar analyses have also been carried out by Spanos [42] and Roberts [43] for systems under only additive random excitations.

Another exceptional case, considered by Namachchivaya and Lin [44], is described by the following equations of motion

$$\begin{aligned}\ddot{Z}_1 + 2\alpha_1 \dot{Z}_1 + \Omega_1^2 Z_1 &= f_1(Z, \dot{Z}, \mu) + A_{1j}(\mu) Z_j W(t) \\ \ddot{Z}_2 + 2\alpha_2 \dot{Z}_2 + \Omega_2^2 Z_2 &= f_2(Z, \dot{Z}, \mu) + A_{2j}(\mu) Z_j W(t)\end{aligned}\quad (72)$$

where μ is a parameter, $\Omega_i^2 = \omega_i^2(\mu) + \alpha_i^2(\mu)$, α_i and ω_i are damping parameters and natural frequencies, respectively, and f_i are only weakly nonlinear. As μ increases, the first mode becomes close to instability while the second mode remains highly damped. We then transform Z_1 and \dot{Z}_1 to the amplitude and phase counterparts, and at the same time make the substitution

$$\begin{aligned}Z_2 &= [\cos\omega_2 t + \omega_2^{-1} \alpha_2 \sin\omega_2 t] Y_1 + (\omega_2^{-1} \sin\omega_2 t) Y_2] e^{-\alpha_2 t} \\ \dot{Z}_2 &= [-(\omega_2^{-1} \Omega_2^2 \sin\omega_2 t) Y_1 + (\cos\omega_2 t - \omega_2^{-1} \alpha_2 \sin\omega_2 t) Y_2] e^{-\alpha_2 t}\end{aligned}\quad (73)$$

The new equations satisfy the condition for time averaging, and the resulting Itô equation for the amplitude of the first mode is devoid of other variables. This method was developed on the basis of a theorem due to Papanicolaou and Kohler [45]. It can be applied to cases involving a very large number of degrees of freedom. However, if more than one mode can become critical, then transformation to conjugate pairs of complex processes is simpler [46].

4.4. Energy Dissipation Balancing [47]

Consider a single-degree-of-freedom system, governed by equations of the type of (23). An exact stationary probability solution can be found if the ψ and θ functions are related according to (28). Restricting to $D(x_1) = 0$ and to λ of the form of (31), relation (28) is simplified to

$$\psi(x_1, x_2) = \pi x_2 K_{k\ell} \theta_k \theta_\ell \phi'(\lambda) - \pi K_{k\ell} \theta_k \frac{\partial}{\partial x_2} \theta_\ell + g(x_1) \quad (74)$$

This equation specifies a class of solvable problems.

Given a problem with a ψ function not in the form of (74), it is possible to write

$$\psi(x_1, x_2) = u(x_1, x_2) + g(x_1) + \pi K_{k\ell} \theta_\ell \frac{\partial}{\partial x_2} \theta_k \quad (75)$$

Then, using (12) as an approximate solution, the error involved is

$$\epsilon = u(x_1, x_2) - \pi x_2 K_{k\ell} \theta_k \theta_\ell \phi' + 2\pi K_{k\ell} \theta_\ell \frac{\partial}{\partial x_2} \theta_k \quad (76)$$

A reasonable criterion for the choice of $\phi'(\lambda)$ is to equate the average

energy dissipations between the given system and the substituting system [47] for which the exact solution is obtainable; namely letting

$$\int x_2 \epsilon p_s(x_1, x_2) dx_1 dx_2 = 0 \quad (77)$$

where p_s is chosen to be the stationary probability density of the substituting system.

As an example, consider a van der Pol type oscillator

$$\ddot{Z} + \alpha \dot{Z} + \beta Z^2 \dot{Z} + \gamma \dot{Z}^3 + Z + ZW_1(t) + \dot{Z}W_2(t) + W_3(t) \quad (78)$$

By equating $Z = X_1$ and $\dot{Z} = X_2$ and comparing with (23), we can identify that $\theta_1 = x_1$, $\theta_2 = x_2$, $\theta_3 = 1$ and $\psi(x_1, x_2) = \alpha x_2 + \beta x_1^2 x_2 + \gamma x_2^3 + x_1$

$$\pi K_{kl} \theta_l \frac{\partial}{\partial x_k} \theta_k = \pi (K_{21} x_1 + K_{22} x_2 + K_{23}) \quad (79)$$

From (75),

$$\psi(x_1, x_2) = u(x_1, x_2) + g(x_1) + \pi (K_{21} x_1 + K_{22} x_2 + K_{23}) \quad (80)$$

Therefore,

$$\begin{aligned} g(x_1) &= x_1(1 - \pi K_{21}) - \pi K_{23} \\ u(x_1, x_2) &= (\alpha - \pi K_{22})x_2 + \beta x_1^2 x_2 + \gamma x_2^3 \end{aligned} \quad (81)$$

It follows from (31) that

$$\lambda = \frac{1}{2} x_2^2 + \frac{1}{2} (1 - \pi K_{21})(x_1 - x_{1,0})^2 \quad (82)$$

where $x_{1,0} = \pi K_{23} / (1 - \pi K_{21})$. In order for λ to be always positive, it requires that $1 - \pi K_{21} > 0$ which is a necessary condition in probability.

The integration in (77) can be simplified by a transformation $x_1 = [2\lambda / (1 - \pi K_{21})]^{1/2} \cos \theta + x_{1,0}$, and $x_2 = (2\lambda)^{1/2} \sin \theta$, resulting in

$$\phi'(\lambda) = \frac{2(\alpha + \pi K_{22}) + (\beta + 3\gamma)\lambda}{2\pi(1 - \pi K_{21})(K_{11}x_{1,0} + 2K_{31}x_{1,0} + K_{33}) + \pi[K_{11} + 3K_{22}(1 - \pi K_{21})]\lambda} \quad (83)$$

The approximate stationary probability density is

$$p_s(x_1, x_2) = C \exp \left[- \int \phi'(\lambda) d\lambda \right] \quad (84)$$

The reader is referred to [47] for details.

It is of interest to note that if only the additive random excitations are present then the approximate probability density obtained on the basis of energy dissipation balancing coincides with that obtained from a least mean-square error criterion proposed by Caughey [48]; however, the two results are different if multiplicative random excitations are present. In the latter case, the energy dissipation criterion leads to correct bifurcation and/or instability conditions in some known examples while the least mean-square error criterion or stochastic averaging [47,49] do not.

5. CONCLUDING REMARKS

The length limitation of this paper does not permit a thorough review of all important advances which took place in recent years toward solving nonlinear random vibration problems. It is therefore appropriate to suggest additional materials for interested readers. The earlier review by Caughey [50] remains most authoritative for works prior to 1971. A large portion of a survey, entitled, "Methods of Stochastic Dynamics" is devoted to nonlinear stochastic systems. For the very useful analytical tools of equivalent linearization and stochastic averaging, [21] and [37] are again suggested.

Because of the familiarity of the materials at hand, it is perhaps unavoidable that much account is given to works carried out by the writer and his associates. Many very important contributions are not mentioned, and they are by no means less significant.

6. ACKNOWLEDGEMENTS

This paper is prepared under grant AFOSR-88-0005 from the Air Force Office of Scientific Research, Air Force Systems Command, USAF, monitored by Dr. Anthony Amos. The US Government is authorized to reproduce and distribute reprints for Governmental purposes notwithstanding any copyright notation thereon. Thanks are due to Mr. G. Q. Cai with whom the writer has had numerous helpful discussions.

7. REFERENCES

1. E. WONG and M. ZAKAI 1965 Internal Journal of Engineering Sciences 4, 213-229. On the relation between ordinary and stochastic equations.
2. R. L. STRATONOVICH 1963 Topics in the Theory of Random Noise. Vol. 1. New York: Gordon and Breach.
3. Y.K. LIN, Y. YONG and G.Q. CAI 1987 Stochastic Structural Mechanics. Lecture Notes in Engineering 31, 268-280. New York: Springer-Verlag. Exact solution for nonlinear systems under parametric and external white-noise excitations.
4. G.Q. CAI and Y.K. LIN 1988 Internal Journal of Nonlinear Mechanics. On exact stationary solutions of equivalent nonlinear stochastic systems. To appear.
5. R. GRAHAM and H. HAKEN 1971 Zeitschrift fur Physik, 203, 289-302. Generalized thermo-dynamic potential for Markov systems in detailed balance and far from thermal equilibrium.
6. Y. YONG and Y.K. LIN 1987 Journal of Applied Mechanics, 54, 414-418. Exact stationary-response solution for second order nonlinear systems under parametric and external white-noise excitations.
7. A. ANDRONOV, L. PONTRYAGIN and A. WITT 1940 Zh. Eksperim, i Teor. Fiz. 3, 165-180. On the statistical investigation of dynamical systems, in Russian.

8. A. KRAMERS 1940 Physica, 7, 284-304. Brownian motion in a field of force and diffusion model of chemical reactions.
9. T. K. CAUGHEY and F. MA 1983 International Journal of Nonlinear Mechanics, 17, 137-142. The exact steady-state solution of a class of nonlinear stochastic systems.
10. M. F. DIMENTBERG 1982 International Journal of Non-Linear Mechanics, 17, 231-236. An exact solution to a certain nonlinear random vibration problem.
11. Y.K. LIN and G.Q. CAI 1988 Journal of Applied Mechanics. Exact stationary-response solution for second order nonlinear systems under parametric and external white-noise excitations, Part II. To appear.
12. Y.K. LIN and G.Q. CAI 1988 Journal of Applied Mechanics. Equivalent stochastic systems. To appear.
13. M. SAN MIGUEL and S. CHATURVEDI 1980 Zeitschrift fur Physik B 40, 167-174. Limit cycles and detailed balance in Fokker-Planck equations.
14. W.F. WU and Y.K. LIN 1984 International Journal of Nonlinear Mechanics, 19, 349-362. Cumulant-neglect closure for nonlinear oscillators under random parametric and external excitations.
15. R.A. IBRAHIM, A. SOUNDARARAJAN and H. HEO 1985 Journal of Applied Mechanics, 52, 965-970. Stochastic response of nonlinear dynamics systems based on non-Gaussian closure.
16. Y. K. LIN 1986 Probabilistic Engineering Mechanics 1, 23-27. Some observations on stochastic averaging method.
17. K. ITÔ 1951 Nagoya Mathematical Journal, Japan 3, 55-65. On a formula concerning stochastic differentials.
18. Y.K. LIN 1967 Probabilistic Structural Dynamics. New York: McGraw-Hill (Reprinted with revision 1976: Krieger Publishing Co., Malabar, FL.)
19. S.T. ARIARATNAM 1980 In New Approaches to Nonlinear Problems in Dynamics, Ed. P.J. Holmes, SIAM Publications, Philadelphia, PA, 470-473. Bifurcation in nonlinear stochastic systems.
20. J.Q. SUN and C.S. HSU 1987 Journal of Applied Mechanics, 54, 649-655. Cumulant-Neglect Closure for Nonlinear Systems under Random Excitations.
21. P.D. SPANOS 1981 Applied Mechanics Reviews, 34, 1-8. Stochastic Linearization in Structural Dynamics.
22. S.A. ASSAF and L.D. ZIRKIE 1976 International Journal of Control, 23, 477-492. Approximate analysis of non-linear stochastic systems.

23. S.H. CRANDALL 1980 International Journal of Nonlinear Mechanics, 15, 303-313. Non-Gaussian closure for random vibration of non-linear oscillator.
24. A. BRUCKNER and Y.K. LIN 1987 International Journal of Nonlinear Mechanics, 22, 227-235. Generalization of the equivalent linearization method for nonlinear random vibration problems.
25. R.Z. ZHASMINSKI 1966 Theory of Probability and Applications. II(3), 390-405. A limit theorem for the solution of differential equations with random right hand sides.
26. G.C. PAPANICOLAOU and W. KOHLER 1974 Communication on Pure and Applied Mathematics, 27, 641-668. Asymptotic theory of mixing stochastic ordinary differential equations.
27. S.T. ARIARATNAM 1965 Proceedings, International Conference on the Dynamic Stability of Structures, 255-265. Oxford: Pergamon Press. Dynamic stability of a column under random loading.
28. Y.K. LIN, Y. FUJIMORI and S.T. ARIARATNAM 1979 AIAA Journal, 17, 545-552. Rotor blade stability in turbulent flow, Part I.
29. Y. FUJIMORI, Y.K. LIN and S.T. ARIARATNAM 1979 AIAA Journal, 17, 673-678. Rotorblade stability in turbulent flow, Part II.
30. J.E. PRUSSING and Y.K. LIN 1982 Journal of American Helicopter Society 27, 51-57. Rotor blade flap-lag stability in turbulent flow.
31. J.E. PRUSSING and Y.K. LIN 1983 Journal of American Helicopter Society 28, 42-46. A closed form analysis of rotor blade flap-lag stability in hover and low-speed forward flight in turbulent flow.
32. Y.K. LIN 1979 Journal of Engineering Mechanics, ASCE 105 EM6, 921-932. Motion of suspension bridges in turbulent winds.
33. C.G. BUCHER and Y.K. LIN 1988 Journal of Engineering Mechanics ASCE. Stochastic stability of bridges considering coupled modes. To appear.
34. N. SRI NAMACHCHIVAYA and S.T. ARIARATNAM 1987 International Journal of Nonlinear Mechanics 22, 363-372. Stochastically perturbed Hopf bifurcation.
35. N. SRI NAMACHCHIVAYA 1988 Journal of Applied Mechanics. Hopf bifurcation in the presence of both parametric and external stochastic excitations. To appear.
36. N. SRI NAMACHCHIVAYA 1988 Journal of Applied Mathematics and Computation. Stochastic bifurcations. To appear.
37. J.B. ROBERTS and P.D. SPANOS 1986 International Journal of Nonlinear Mechanics 21, 111-134. Stochastic averaging an approximate method of solving random vibration problems.

38. S.T. ARIARATNAM and D.S.F. TAM 1979 Z. Angew. Math. Mech. 59, 79-84. Random vibration and stability of a linear parametrically excited oscillators.
39. A. BRÜCKNER AND Y.K. LIN 1987 International Journal of Nonlinear Mechanics 22, 237-250. Applications of complex stochastic averaging to nonlinear random vibration problems.
40. R.Z. KHASHINSKII 1968 Kibernetika 4, 260-279. On the averaging principal for stochastic differential Itô equations (in Russian).
41. W.Q. ZHU 1982 Proceedings, IUTAM Symposium on Random Vibration and Reliability, Frankfurt/Oder, ed. K. Hennig, 347-357. Berlin: Akademie. Stochastic averaging of energy envelope of nearly Lyapunov systems.
42. P.D. SPANOS 1982 Proceedings, IUTAM Symposium on Random Vibration and Reliability, Frankfurt/Oder, ed. K. Hennig, 327-337. Berlin: Akademie. Approximate analysis of random problems through stochastic averaging.
43. J.B. ROBERTS 1982 Proceedings, IUTAM Symposium on Random Vibration and Reliability, Frankfurt/Oder, ed. K. Hennig, 285-294. Berlin: Akademie. Energy methods for nonlinear systems with non-white excitation.
44. N. SRI NAMACHCHIVAYA and Y.K. LIN 1987 Stochastic Structural Mechanics. Lecture Notes in Engineering 31, 281-310. New York: Springer-Verlag. Application of stochastic averaging for systems with high damping.
45. G.C. PAPANICOLAOU and W. KOHLER 1976. Communications in Mathematical Physics, 46, 217-232. Asymptotic analysis of deterministic and stochastic equations with rapidly varying components.
46. C.G. BUCHER and Y.K. LIN 1988 Effect of spanwise correlation of turbulence field on the motion stability of long-span bridges. To appear.
47. G.Q. CAI and Y.K. LIN 1988 Internal Journal of Nonlinear Mechanics. A new approximate solution technique for randomly excited nonlinear oscillators. To appear.
48. T.K. CAUGHEY 1986 Journal of Probabilistic Mechanics 1, 2-4. On the response of nonlinear oscillators to stochastic excitation.
49. Y. K. LIN and G.Q. CAI 1988 Developments in Theoretical and Applied Mechanics 14. Energy dissipation balancing -- an approximate solution technique for nonlinearly damped system under random excitations. To appear.
50. T.K. CAUGHEY 1971 Advances in Applied Mechanics, II, 209-253. Nonlinear theory of random vibration.

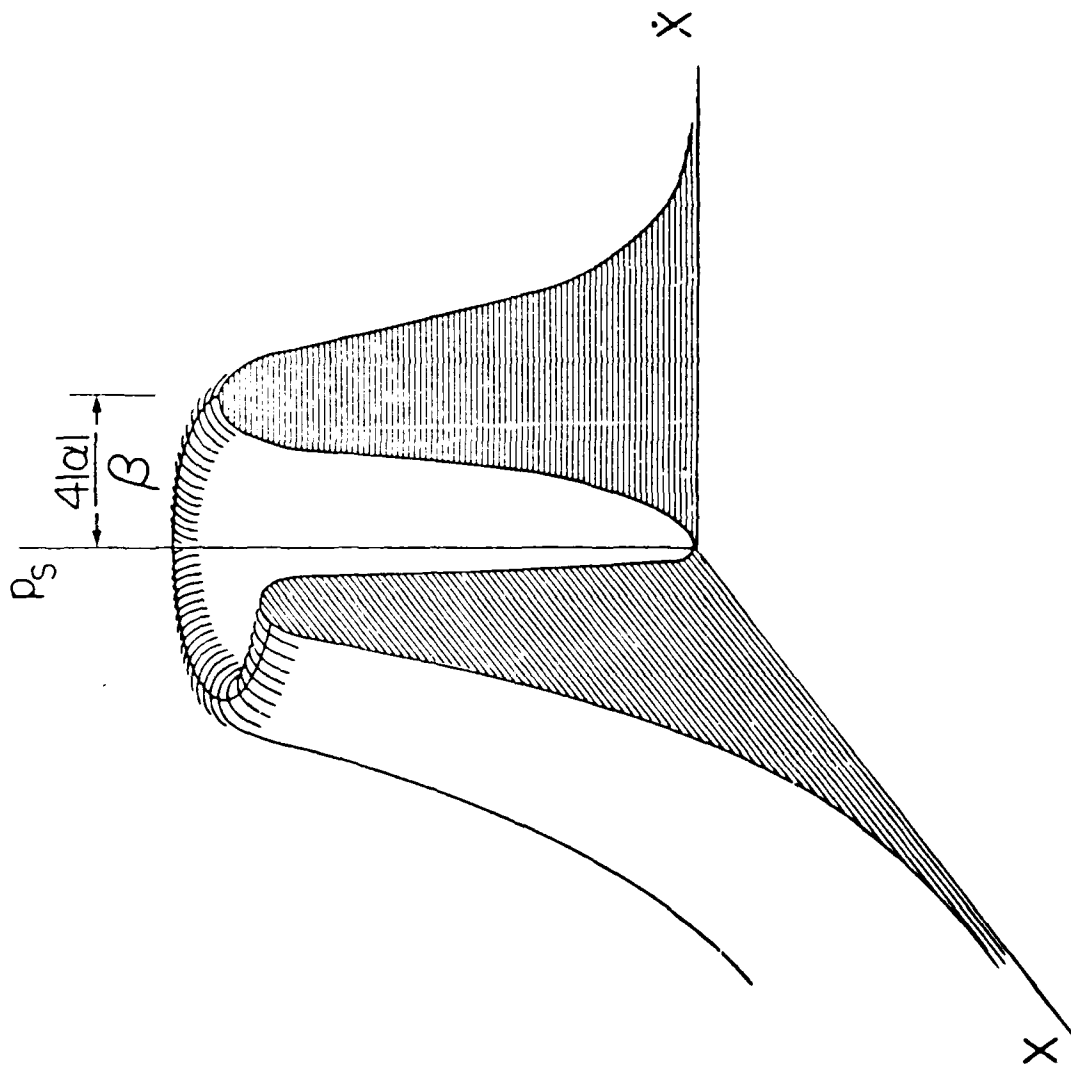


Fig. 1 A stationary probability density (with the right-front quarter removed), depicting the stochastic analogue of limiting-cycle behavior of a non-linear system under parametric excitation.

CONSIDERATION OF NON-GAUSSIAN RESPONSE PROPERTIES BY USE OF STOCHASTIC EQUIVALENT LINEARIZATION

H.J. Pradlwarter, G.I. Schuëller and X.-W. Chen

Institute of Engineering Mechanics
University of Innsbruck, Austria

1. INTRODUCTION

Although it is well known that the response of nonlinear structures subjected to Gaussian random excitation is non-Gaussian, it is, nevertheless, usually assumed to be Gaussian distributed, in particular when the technique of Equivalent Linearization (EQL) is applied to calculate the response in terms of its second moments. Due to this unrealistic assumption a biased estimate of the response statistics is obtained. The bias increases with increasing nonlinearity. In this context it is claimed e.g. in [1] that linear systems exist which lead - at least for white noise excitation - exactly to the first statistical moments of the response of the respective *true* nonlinear systems. The adjective "*true*" is used here, and in the following, to indicate the actual nonlinear system and the statistics of the actual nonlinear response which can presently only be found by simulation of a sufficiently large sample size (e.g. 10 000).

For the purpose of discussing the implications of this statement, consider a n -th order non-linear system which follows the differential equation,

$$\frac{dy}{dt} = g(y) + w(t) \quad (1)$$

where y is the generalized response vector of the true nonlinear system, $w(t)$ is a vector of independent white noise components and g a n -dimensional non-linear function. In other words, there exists a linear system, with the true coefficient matrix $[A]$ and linear response x , following the linear differential equation

$$\frac{dx}{dt} = [A(t)] \cdot x(t) + w(t) \quad (2)$$

such that

$$E\{x\} = E\{y\} \text{ and } E\{x \cdot x^T\} = E\{y \cdot y^T\} \quad (3)$$

where x^T indicates the transposed vector of x .

The true coefficient matrix $[A]$ can be determined by [1]

$$[A] = [E\{g(y) \cdot y^T\}] \cdot [E\{y \cdot y^T\}]^{-1} \quad (4)$$

Of course, the two matrices on the right hand side of eq. (4) are not known when the equivalent linearization technique is applied. Indeed, there would be no need to linearize, since all that is obtained by EQL is generally a biased estimate of the matrix $E\{y \cdot y^T\}$. However, the above results enable one to investigate the conditions which are required to obtain the true coefficient matrix $[A]$ and, consequently, the unbiased estimates for the second moments of the nonlinear response, i.e. $E\{y \cdot y^T\}$.

For applications of the EQL technique an additional condition is quite important. If the true joint distributions are used to determine the expectations, i.e.

$$[E\{g(y) \cdot y^T\}] = \int_{-\infty}^{+\infty} \dots \int_{-\infty}^{+\infty} [g(y) \cdot y^T] f_y(y) dy \quad (5)$$

the true coefficient matrix can be derived. For practical applications this statement is only useful for those cases for which it is possible to construct the joint distribution $f_y(y)$ only from known expectations $E\{y\} = E\{x\}$ and $E\{y \cdot y^T\} = E\{x \cdot x^T\}$. In other words, if the shape of the joint distribution is known as function of $E\{y\}$ and $E\{y \cdot y^T\}$, the true coefficient matrix can be obtained.

In practice, however, it is very difficult to formulate the shape of non-Gaussian joint distributions, although it is often possible to approximate the true shape of probability distributions of components of the response vector y , i.e. marginal distributions of $f_{y_i}(y_i)$.

In this paper, it is assumed that only the true shape of the marginal distributions can be approximated by physical considerations. The procedure is demonstrated by the use of the smoothly varying hysteretic model as proposed in [2] and later generalized and adapted for the use of EQL in [3] to represent a wide class of hysteretic behavior.

For simplicity a SDOF-hysteretic system under nonstationary white noise excitation is considered. The second moments $E\{x \cdot x^T\}$ of the linearized model in eq. (2) can either be obtained by applying a Lyapunov matrix equation or by modal analysis, where the determination of complex eigenvalues and eigenvectors is required. Since modal analysis is more general and suitable for MDOF systems consisting of a large number of degrees of freedom subjected to nonstationary non-white excitation, e.g. evolutionary spectra, complex modal analysis will be utilized in the further developments.

2. METHOD OF ANALYSIS

2.1 The Technique of EOL and Complex Modal Analysis

Using the approach as suggested in [3] the equation of motion for a SDOF system may be written

$$m\ddot{y} + c\dot{y} + \alpha ky + (1 - \alpha)kz = b(t) \quad (6)$$

where $b(t)$ represents a random excitation, m the mass, c the viscous damping coefficient, α the post-to-preyielding factor, k the stiffness, y the displacement response where a dot indicates derivation with respect to time. The auxiliary variable z may be described by the following nonlinear differential equation [3]

$$\dot{z}_N = a\dot{y} + \beta|\dot{y}| |z|^{n-1}z - \gamma\dot{y}|z|^n \quad (7)$$

The parameters a , β , γ and n are parameters controlling the shape of the hysteretic loops.

In the concept of EQL, the nonlinear eq. (7) is replaced by a linear differential equation, i.e. by

$$\dot{z}_L = c_1 y + c_2 \dot{y} + c_3 z \quad (8)$$

where the linearization coefficients are determined such that

$$E \{ (\dot{z}_N - \dot{z}_L)^2 \} \rightarrow \text{Minimum} \quad (9)$$

i.e. the mean square of the difference between the nonlinear (N) and the linear (L) models is minimized. It can be shown that the condition in eq. (9) is satisfied if (see eq. (4))

$$(c_1, c_2, c_3) = E \{ \dot{z}_N \cdot y^T \} \cdot [E \{ y \cdot y^T \}]^{-1} \quad (10)$$

where the vector y is introduced to represent the nonlinear response

$$y^T = (y_1, y_2, y_3) = (y, \dot{y}, z) \quad (11)$$

At this stage it should be pointed out, that the linearization coefficient c_1 in eq. (8) is zero only for Gaussian distributed response quantities, but is generally nonzero for non-Gaussian response.

the linearized characteristic equations

$$\begin{bmatrix} \dot{y}_L \\ \dot{z}_L \end{bmatrix} = \begin{bmatrix} 0 & 1 \\ -\alpha k/m & -c/m \end{bmatrix} \begin{bmatrix} y_L \\ z_L \end{bmatrix} + \begin{bmatrix} 0 \\ b(t) \end{bmatrix} \quad (12)$$

are not valid for general cases, as they are derived in [4] under the assumption of Gaussian response, from which $c_1 = 0$ follows.

Using the state vector approach, the linear equation of motion, i.e. eq. (6) along with the linearized auxiliary variable z in eq. (8) can be written in the form

$$\frac{d\mathbf{x}}{dt} = [\mathbf{A}(t)] \mathbf{x} + \mathbf{b}(t) \quad (13)$$

where

$$\mathbf{x} = \begin{bmatrix} y_L \\ \dot{y}_L \\ z_L \end{bmatrix}; \quad [\mathbf{A}(t)] = \begin{bmatrix} 0 & 1 & 0 \\ -\alpha k/m & -c/m & -(1-\alpha)k/m \\ c_1(t) & c_2(t) & c_3(t) \end{bmatrix};$$

$$\mathbf{b}(t) = \begin{bmatrix} 0 \\ b(t) \\ 0 \end{bmatrix} \quad (14)$$

In order to distinguish clearly between the linearized Gaussian response \mathbf{x} and the nonlinear non-Gaussian response \mathbf{y} , two different notations are introduced

The second moments $E[\mathbf{x} \cdot \mathbf{x}^T]$ of the response of the time variant system (eq. (13)) can be obtained in a rather straight forward procedure. It is applicable to nonstationary excitation, including evolutionary spectra (see e.g. [5], [6]). More details of the procedure are found in [7] which deals exclusively with the evaluation of the first two moments of the stochastic response of a time variant linear system. There it is shown that the continuously time variant linear system can be approximated by a system considered to be time invariant within consecutive short time intervals. Moreover, an algorithm is introduced to evaluate efficiently the characteristic equations utilizing the solution of the respective previous time step and to evaluate the response due to an arbitrary evolutionary spectrum.

$$\begin{aligned} E[\mathbf{x} \cdot \mathbf{x}^T] &= \int_{-\infty}^{\infty} \int_{-\infty}^{\infty} \mathbf{x}(t) \mathbf{x}^T(t+\tau) \exp(-j\omega\tau) d\omega d\tau \\ &= \int_{-\infty}^{\infty} \mathbf{x}(t) \mathbf{x}^T(t+\tau) \exp(-j\omega\tau) d\omega d\tau \end{aligned}$$

obtained when assuming Gaussian response. For this purpose two SDOF-systems with identical structural parameters of mass $m = 6.708 \cdot 10^6$ kg, stiffness $k = 9.26 \cdot 10^8$ N/m, damping $c = 0$ and white noise intensity $I(t) = 2\pi S_0(t) = 0.4$ t [m²/sec³] is investigated for two different post-to preyielding factors α

$$(a) \alpha = \alpha_a = 0 \text{ and } (b) \alpha = \alpha_b = 0.05$$

The parameters controlling the shape of hysteretic loops in eq. (7) are selected as follows:

$$a = 1; \beta = \gamma = 4.44 \text{ m}^{-1}; n = 1$$

In Fig. 1, the true standard deviation σ_{y1} of the displacement response is compared with the standard deviation σ_{x1} obtained by EQL. From this Figure, it is seen that the displacement response is considerably underestimated by the method of EQL, although the velocity response is predicted quite well (see Fig. 6).

The simulated results are based on 10 000 samples. Fig. 1 also shows the results when using the true linearization coefficients as calculated according to eq. (10) utilizing the 10 000 response quantities Y_i and the nonlinear eq. (7). In terms of second moments the agreement between the optimal linear response and the true response is excellent which verifies the relation defined by eq. (3).

In Fig. 2 the true linearization coefficients are then compared with the linearization coefficients obtained when assuming Gaussian response quantities. This figure reveals considerable differences, indicating a strong influence of the assumed distribution of the response quantities.

2.2 Consideration of Non-Gaussian Response Properties

An efficient way to estimate realistic marginal distributions of the nonlinear response quantities is the introduction of nonlinear transformations such as

$$y_i = h_i(x_i) \quad (15)$$

which are established on the basis of physical considerations. For this purpose any conceivable nonlinear transformation function can be utilized, however under the condition that it meets the requirement stated above by eq. (3), i.e.:

$$E\{x\} = E\{y\} \text{ and } E\{x \cdot x^T\} = E\{y \cdot y^T\} \quad (3)$$

This can be accomplished in two steps. First, the transformation $h_i(x)$ is selected such that the following conditions

$$E\{h_i(x_i)\} = E\{x_i\} \text{ and } E\{h_i^2(x_i)\} = E\{x_i^2\} \quad (16)$$

are satisfied. Secondly, modified Gaussian correlation coefficients ρ_{ij} are evaluated from the following integral equation

$$\rho_{ij} = \frac{E\{x_i x_j\}}{\sqrt{E\{x_i^2\} E\{x_j^2\}}} = \int_{-\infty}^{+\infty} \int_{-\infty}^{+\infty} h_i(x_i) h_j(x_j) f_{X_i, X_j}(x_i, x_j; \rho'_{ij}) dx_i dx_j \quad (17)$$

satisfying for $i \neq j$ the requirement $E\{y_i y_j\} = E\{x_i x_j\}$. Experience shows that it is usually sufficient to evaluate ρ'_{ij} in one step by

$$\rho'_{ij} = \frac{\rho_{ij}}{\left(\int_{-\infty}^{+\infty} \int_{-\infty}^{+\infty} h_i(x_i) h_j(x_j) f_{X_i, X_j}(x_i, x_j; \rho_{ij}) dx_i dx_j \right)} \quad (18)$$

where $f_{X_i, X_j}(x_i, x_j; \rho_{ij})$ represents a jointly Gaussian distribution with correlation coefficients ρ_{ij} .

Following these nonlinear transformations, which lead to a more realistic characterization of the marginal distribution, the expectations defined by eq. (5) can be approximated by

$$E\{g(y) y^T\} \approx \int_{-\infty}^{+\infty} \int_{-\infty}^{+\infty} [g(y(x)) y^T(x)] f_X(x; R') dx \quad (19)$$

where $f_X(x; R')$ denotes a jointly Gaussian distribution with a correlation matrix R' containing the correlation coefficients defined by eq. (18) and eq. (17) respectively:

$$[R'] = \begin{bmatrix} 1 & . & . & . \\ . & 1 & \rho'_{12} & . \\ . & \rho'_{12} & 1 & . \\ . & . & . & 1 \end{bmatrix} \quad (20)$$

These expectations as evaluated from eq. (19) are used in eq. (4) to improve the linearization coefficients and, consequently, the estimates for the second moments of the nonlinear response.

So far the analysis is generally applicable. In the following, these considerations are applied to a particular case where only the restoring force is non-Gaussian. All components of the state vector $y = (y_1, y_2, y_3)^T$ of a SDOF-system are generally non-Gaussian distributed. It is well known that the displacements y_1 and the velocities y_2 show a tendency towards a two-sided exponential type distribution. However, the deviation of the true distributions $f(y_1)$ and $f(y_2)$ from a Gaussian distribution is always far less than for the third component y_3 , i.e. the auxiliary variable $z=y_3$. Therefore, in a first step, it is reasonable to take only the non-Gaussian response properties of the auxiliary variable $z=y_3$ into account.

Since the auxiliary variable z in eq. (7) is confined to the range

$$-b \leq z \leq b \quad \text{where } b = \left(\frac{a}{\beta + \gamma} \right)^{1/n} \quad (21)$$

the probability density function (PDF) of z is actually bounded and its probability mass is concentrated in the upper and lower bounds for those cases where the response exceeds the yielding displacements. To account for this fact, the transformation

$$z = y_3 = h_3(x_3) = \text{sign}(x_3) \cdot b \cdot \left[1 - e^{-\frac{\kappa}{b} x_3} \right] \quad (22)$$

is suggested, where κ is selected such that eq. (16) is satisfied. The corresponding non-Gaussian distribution

$$f_{y_3}(z_3) = \frac{b}{\kappa (b - |z|) \sqrt{2\pi\sigma_3^2}} \exp \left[-\frac{1}{2} \left(\frac{b}{\kappa\sigma_3} \ln \left(1 - \frac{|z|}{b} \right) \right)^2 \right] \quad (23)$$

agrees fairly well with distributions obtained from simulation. This is demonstrated in Fig. 3 where PDF's according to eq. (23) are compared with PDF's from simulations for various ratios $\lambda = \sigma_3/b$.

In a next step, taking $E\{y \cdot y^T\}$ from simulation, the linearization coefficients (c_1, c_2, c_3) are calculated by using eq. (19) and eq. (10). In Fig. 4, these coefficients are compared with the true linearization coefficients. It is seen that the agreement is quite good, especially when compared with coefficients resulting from an assumed Gaussian response. However, the simple fact that the true coefficients are approximated much better by the non-Gaussian coefficients than by the Gaussian, is a necessary but not sufficient condition for obtaining an improved estimate of the second moment of the response. For example, when disregarding eq. (17) or eq. (18) by assuming $\rho_{ij} = \rho'_{ij}$, the non-Gaussian linearization coefficients still agree fairly well with the true values, while the

response statistics obtained might become worse.

Now, when evaluating the nonstationary response by using an EQL algorithm within an iterative procedure, the linearization coefficients have to be calculated repeatedly, i.e. several hundred times. In case the response is Gaussian distributed, where eq. (15) simplifies to an identity relation, eq. (19) can often be evaluated explicitly without any time consuming numerical integration. Such an explicit formulation for the nonlinear eq. (7) was first shown in [3]. In the present case where a nonlinear transformation (eq. (15)) is introduced, eq. (18) and eq. (19) have to be evaluated numerically with a considerable increased numerical effort in terms of CPU-time. It should be mentioned at this point that if the computational procedure is not modified as suggested in the Appendix, the computational effort might be of the same order as required by simulation. It should be noted that by use of the suggested procedure, however, the CPU-time for computing eq. (18) and (19) are negligible when compared to the numerical effort required for evaluation the second moment of the response.

3. NUMERICAL RESULTS

The algorithm based on the previous section is applied for the two examples as defined in section 2. In the first example (see Appendix), convergence is obtained after $M = 3$ steps. The non-Gaussian response quantities are calculated only for a limited number of time steps, i.e. for $t = 2, 10, 20$ and 30 seconds. For all other time instants, interpolation is used (see Appendix). The results obtained by EQL and assuming a non-Gaussian distributed restoring forces are presented in Fig. 4. The improvements achieved by the suggested procedure are significant, especially in the first case, where the non-Gaussian properties of the displacement- as well as velocity response have been neglected and the assumed distributions of the restoring forces do not fit the actual PDFs, i.e. they resemble their characteristics only (see Fig. 3).

Fig. 5 shows the nonstationary standard deviation $\sigma_x(t)$ of the displacement response for both examples. The result obtained for Gaussian and non-Gaussian response properties as well as Monte-Carlo simulation (10,000 samples) are plotted. For standard deviations of $\sigma_x < 0.3$ m the agreement with the simulated results is excellent. For the case of $\sigma_x > 0.3$ m also considerable improvements are achieved. It should be noticed, that the response for $\sigma_x = 0.2$ m is already strongly nonlinear, where the displacements consist mainly of elastic deformations δ (drift) with $\sigma_\delta/\sigma_x = 0.90$. Contradicting the conclusions stated in [8], the excellent agreement between prediction and simulation demonstrates clearly that EQL is indeed capable to predict accurately the displacement response of a strongly yielding system. In Fig. 6 the standard deviations σ_y obtained for the velocity response are compared. For both cases, the agreement with simulated results is for Gaussian and non-Gaussian response quantities, quite satisfactory.

Finally, in Fig. 7 the standard deviations σ_z of the auxiliary variable z , representing the nonlinear restoring force, are compared. The agreement between the standard deviation obtained by EQL adapting non-Gaussian properties and simulated results is excellent. The results coincide almost completely for the entire time range.

4. CONCLUSIONS

It has been shown that non-Gaussian properties of the nonlinear stochastic response can be taken into account within the framework of EQL to improve considerably the prediction of second moments of the response.

A concept adapting non-Gaussian response properties has been introduced. The concept is applicable for any type of nonlinearity and readily extended for MDOF-systems. Non-Gaussian marginal distributions of components of the response are introduced by means of nonlinear transformations $y(x) = h(x)$ between the nonlinear response y and the linearized response x . These transformations allow the incorporation of physical properties of the nonlinear response.

The applicability of the suggested method has been demonstrated by calculating the second moments of a hysteretic SDOF-system by considering merely the non-Gaussian properties of the restoring force. The considerable improvements achieved are quite encouraging to pursue the suggested approach.

5. ACKNOWLEDGEMENT

This research was supported by the Austrian Science Foundation (WF) under Project No. S 30-02 which is gratefully acknowledged by the authors.

6. REFERENCES

- 1 F. KOZIN 1987 Lecture Notes in Engineering 31, 259 - 267, Stochastic Structural Mechanics, Y.K. Lin and G. I. Schuëller (Eds.), Springer Verlag, Berlin. Parameter Estimation and Statistical Linearization.
- 2 R. BOUC 1967 Proceedings of the 4th Conference on Nonlinear Oscillation, Prague, Czechoslovakia. Forced Vibration of Mechanical Systems with Hysteresis.

3. Y.K. WEN 1976 *Journal of Engineering Mechanics Division, ASCE* 102, 249 - 264. Method for Random Vibration of Hysteretic Systems.
4. T.S. ATALIK and S. UTKU 1976 *Journal of Earthquake Engineering and Structural Dynamics* 4, 411 - 420. Stochastic Linearization of Multidegree of Freedom Nonlinear Systems.
5. T.-P. CHANG, T. MOCHIO and E. SAMARAS 1986 *Probabilistic Engineering Mechanics* Vol 1 No 3, 157 - 166. Seismic Response Analysis of Nonlinear Structures.
6. H.J. PRADLWARTER and G.I. SCHUELLER 1987 *Proceedings of IUTAM-Symposium on Nonlinear Stochastic Dynamic Engineering Systems*, F. Ziegler and G.I. Schuëller (Eds.), 3 - 21, Springer Verlag, Berlin-Heidelberg-New York-Tokyo. Accuracy and Limitations of the Method of Equivalent Linearization for Hysteretic Multi-Storey Structures.
7. H.J. PRADLWARTER and X.W. CHEN 1988 *Report-88*, Institute of Engineering Mechanics, University of Innsbruck, Austria. Evaluation of the Covariance Matrix of the Response of MDOF-Systems Loaded by an Evolutionary Spectrum.
8. W.D. IWAN, M.A. MOSER and L.G. PAPARIZOS 1987 *Proceedings of IUTAM-Symposium on Nonlinear Stochastic Dynamic Engineering Systems*, F. Ziegler and G.I. Schuëller (Eds.), 444 - 455, Springer Verlag, Berlin-Heidelberg-New York-Tokyo. The Stochastic Response of Strongly Nonlinear Systems with Coulomb Damping Elements.

APPENDIX

Computational Scheme for NGEQL Algorithm

INITIAL CALCULATION

(a) Calculate for a Gaussian distributed response

(a1) The second moments $E \{ \mathbf{x}^{(0)}(t) \mathbf{x}^{T(0)}(t) \} = [\mathbf{R}(t)]^{(0)}$

(a2) The "Gaussian" linearization coefficients $\mathbf{c}^{(0)}(t)$, e.g. $\mathbf{c}^{T(0)}(t) = (0, c_2^{(0)}(t), c_3^{(0)}(t))$

ITERATION $i = 1, 2, 3, \dots, M$

(b) Calculate for a few well distributed instances t_{kj} the non-Gaussian linearization coefficients

$\mathbf{c}^{(i)}(t_{kj})$ on the basis of second moments $[\mathbf{R}(t)]^{(i-1)}$

(c) Establish a relation $\mathbf{c}^{(i)}(t) = \mathbf{c}^{(i)}(\mathbf{c}^{(0)}(t))$ to interpolate for an arbitrary time t the non-Gaussian linearization coefficients $\mathbf{c}^{(i)}(t)$

(d) Calculate with $\mathbf{c}^{(i)}(t)$ new second moments

$$[\bar{\mathbf{R}}(t)]^{(i)} = E \{ \mathbf{x}^{(i)}(t) \mathbf{x}^{T(i)}(t) \}$$

(e) Calculate the matrix of second moments

$$[\mathbf{R}(t)]^{(i)} = \nu \cdot [\bar{\mathbf{R}}(t)]^{(i)} + (1-\nu) [\mathbf{R}(t)]^{(i-1)}; 0 < \nu < 2$$

(f) Check convergence

If $\| [\mathbf{R}(t)]^{(i)} - [\mathbf{R}(t)]^{(i-1)} \| > \varepsilon \| [\mathbf{R}(t)]^{(i)} \|$, then start new iteration with (b), else stop iteration.

For the example (section 2.1) it is assumed that the non-Gaussian linearization coefficients are interpolated between the time steps $[t_a, t_b]$, where $\mathbf{c}^{(i)}(t_a)$ and $\mathbf{c}^{(i)}(t_b)$ have been calculated in (b).

Then for $t_a < t < t_b$, $\mathbf{c}^{(i)}(t)$ can be determined by

$$\mathbf{c}^{(i)}(t) = \begin{bmatrix} \alpha_{21} & \alpha_{31} \\ \alpha_{22} & \alpha_{32} \\ \alpha_{23} & \alpha_{33} \end{bmatrix} \cdot \begin{bmatrix} c_2^{(0)}(t) \\ c_3^{(0)}(t) \end{bmatrix}$$

where the coefficients of the matrix $[\alpha_{ij}]$ are evaluated from

$$\begin{bmatrix} \alpha_{21} & \alpha_{31} \\ \alpha_{22} & \alpha_{32} \\ \alpha_{23} & \alpha_{33} \end{bmatrix} = [c^{(0)}(t_a), c^{(0)}(t_b)] \cdot \begin{bmatrix} c_2^{(0)}(t_a) & c_2^{(0)}(t_b) \\ c_3^{(0)}(t_a) & c_3^{(0)}(t_b) \end{bmatrix}^{-1}$$

FIGURE CAPTIONS

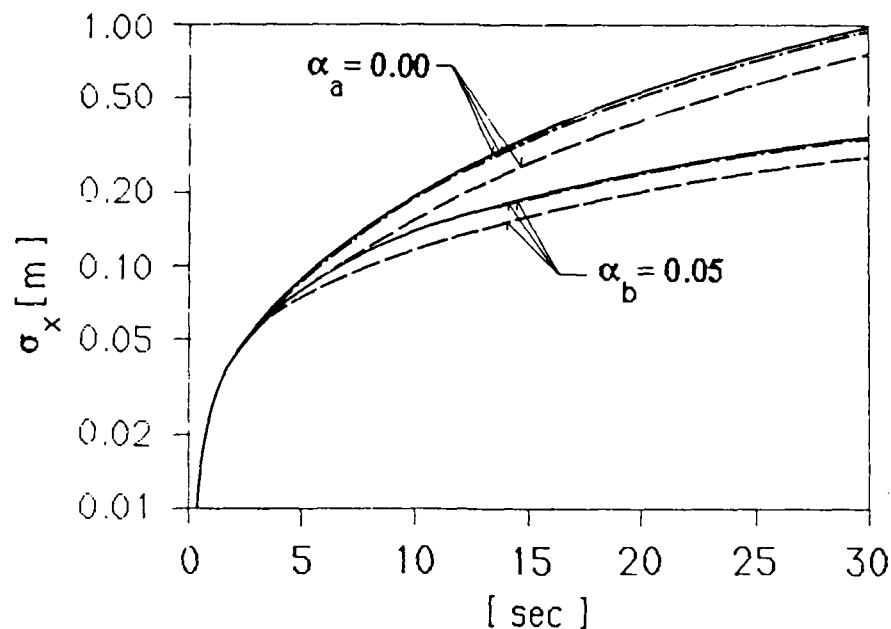


Fig. 1: Standard deviation of displacements obtained by use of — simulation, — — — EQL and - · - · - true linear system.

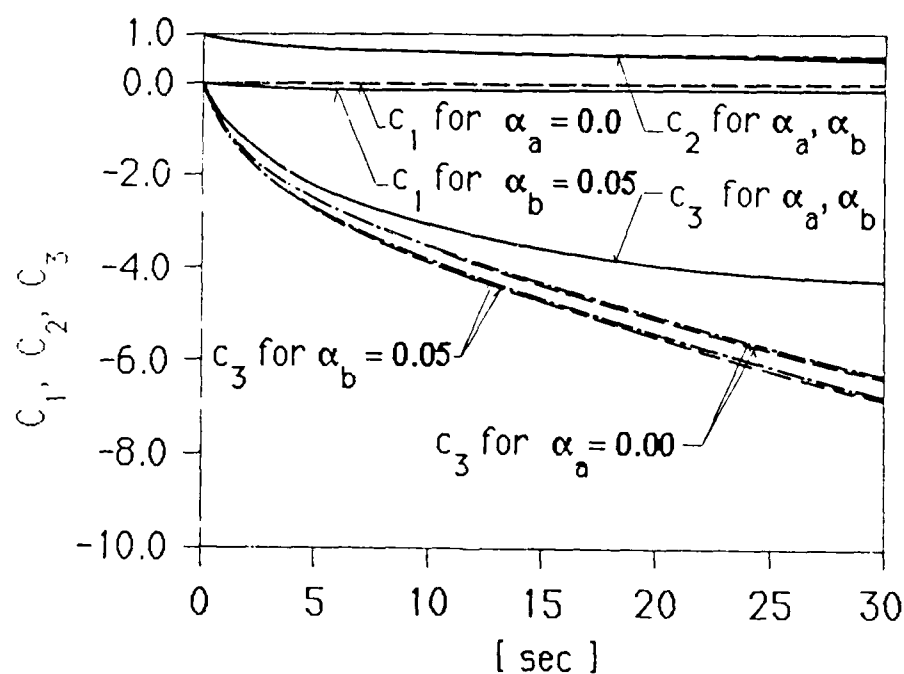


Fig. 2: Linearization coefficients for several cases: — true coefficients (non-Gaussian), — — — EQL and - · - · - Gaussian.

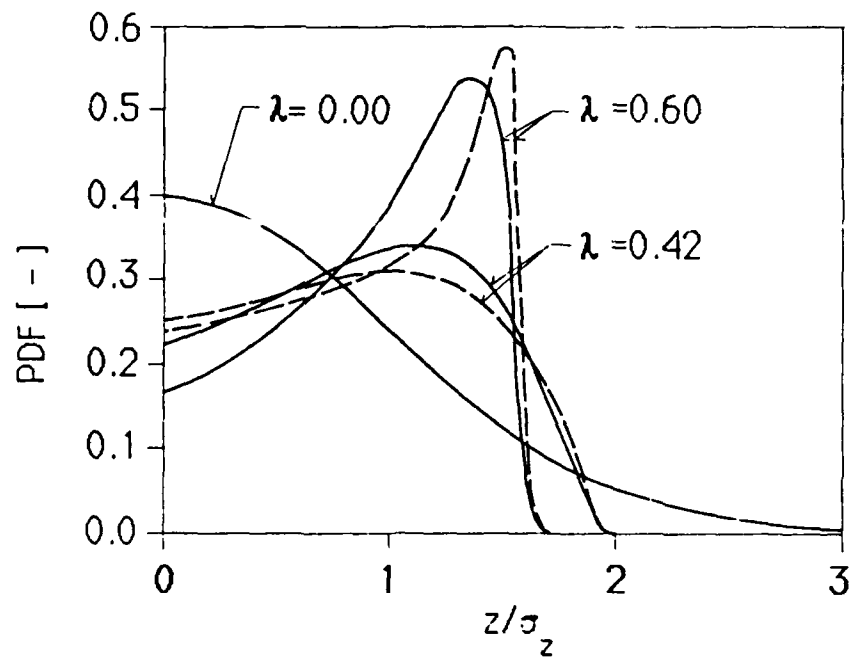


Fig. 3: PDF of auxiliary variable z : --- simulation (smoothed), — assumed PDF according to eq. (3)

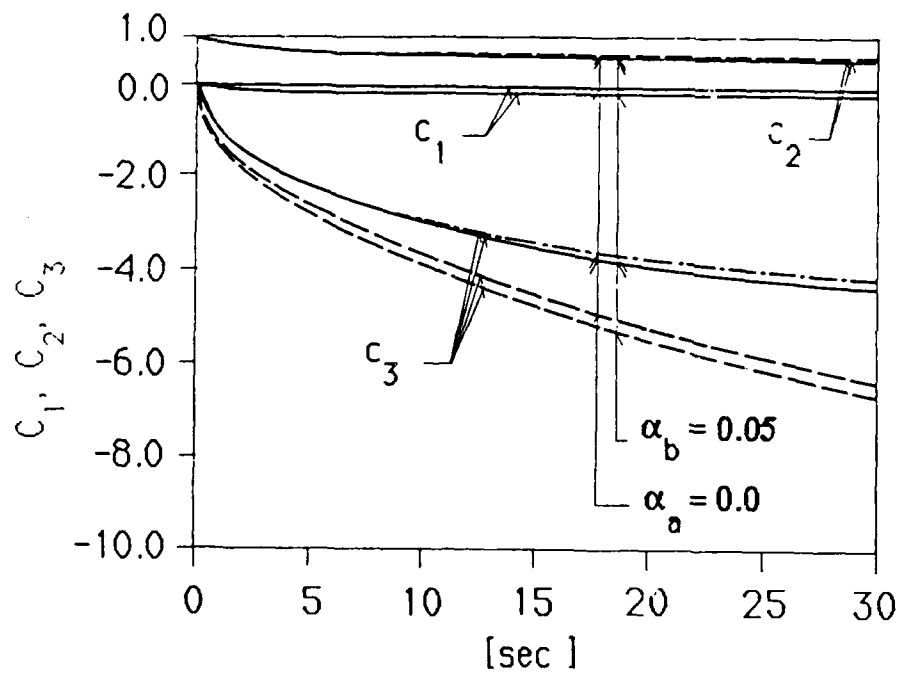


Fig. 4: Linearization coefficients for several cases: — true coefficients, --- Gaussian response, -.- non Gaussian response.

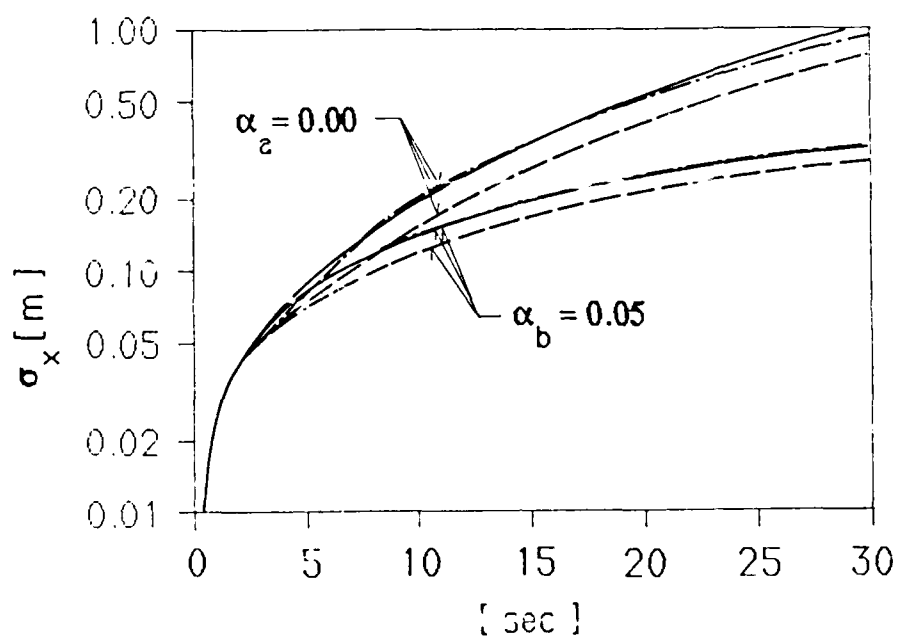


Fig. 5: Standard deviation of displacement obtained by use of ——— simulation, — — — EQL with Gaussian response, - · - · - non-Gaussian EQL (NGEQL).

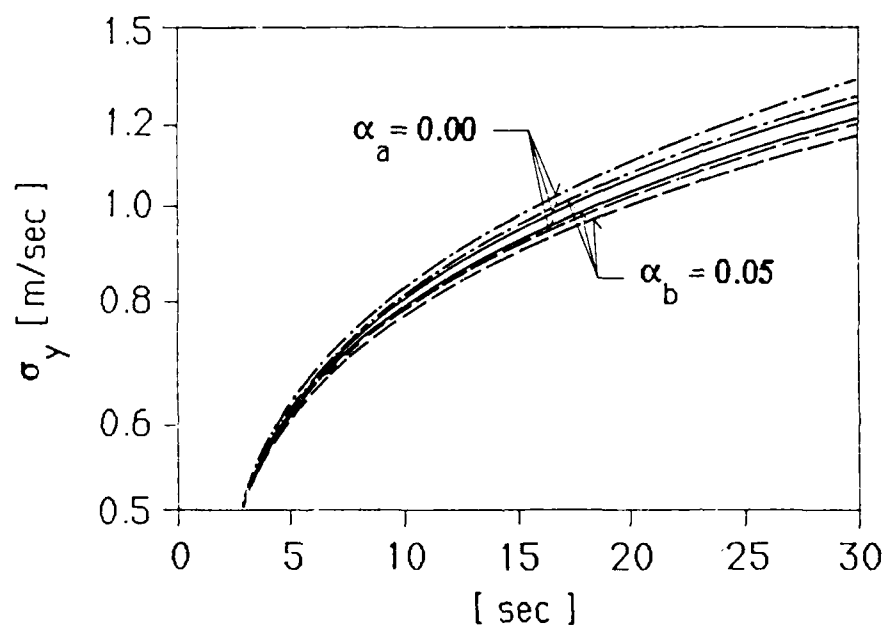


Fig. 6: Standard deviation of response velocities obtained by use of ——— simulation, — — — EQL with Gaussian response, - · - · - non-Gaussian EQL (NGEQL).

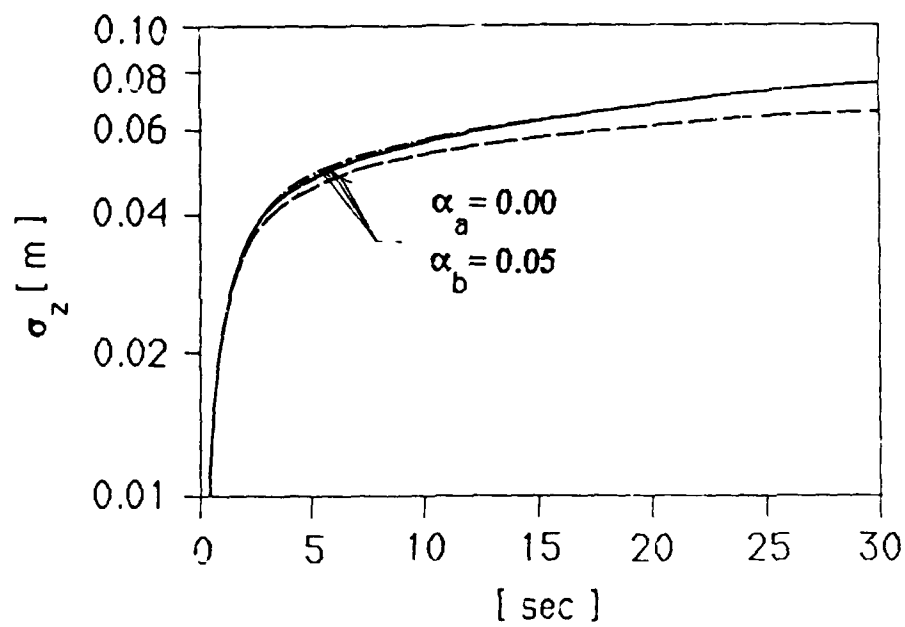


Fig. 7: Standard deviation of auxiliary variable z obtained by use of ——— simulation,
 ---EQL with Gaussian response, - . - . - non-Gaussian EQL (NGEQL).

RANDOM VIBRATION OF HYSTERETIC SYSTEMS

G. Tsiatas¹ and H. Sadid²

Civil and Environmental Engineering
Washington State University
Pullman, WA 99164-2910
U.S.A.

I. INTRODUCTION

Hysteretic systems are widely used to model the yielding behavior of materials and structures. Hysteresis is also exhibited in structures where sliding occurs between different parts. Because of the importance of hysteretic modeling, especially in earthquake engineering, considerable work has been done in this area [1,2,3].

Characteristic of hysteretic behavior is that the restoring force depends on the past time history of the displacement. Since the problem is a nonlinear one, ordinary methods of random vibration such as the frequency domain approach cannot be used. Several techniques, including equivalent linearization and Gaussian closure, have been utilized for the analysis of hysteretic structures. These methods give approximate results since the response can deviate significantly from a Gaussian distribution.

The purpose of this work is twofold. First, an analytical procedure based on Ito stochastic differential equations and Ito calculus is utilized for the study of a particular type of hysteretic behavior and second, two closing schemes for the infinite hierarchy of the moment equations are compared.

2. THEORY

2.1 State-Space Formulation

Many different models of hysteretic behavior have been proposed. Here, a nonlinear hysteretic oscillator with the following equation is considered [4],

$$\ddot{x} + 2h\dot{x} + \phi(x, \dot{x}) = f(t) \quad (1)$$

where, x is dimensionless relative displacement, h is the critical viscous damping and $\phi(x, \dot{x})$ is the restoring force given by:

$$\phi(x, \dot{x}) = rx + (1-r)\text{sgn}\dot{x} \quad (2)$$

The restoring force depends on the displacement and the sign of the velocity. The variable r is the rigidity ratio, i.e., the ratio of stiffness between elastic and plastic regions. Figure 1 illustrates the restoring force for different values of r . The case $r=1$ corresponds to an elastic system whereas $r=0$ denotes elastoplastic behavior. In general,

¹ Assistant Professor
² Graduate Student

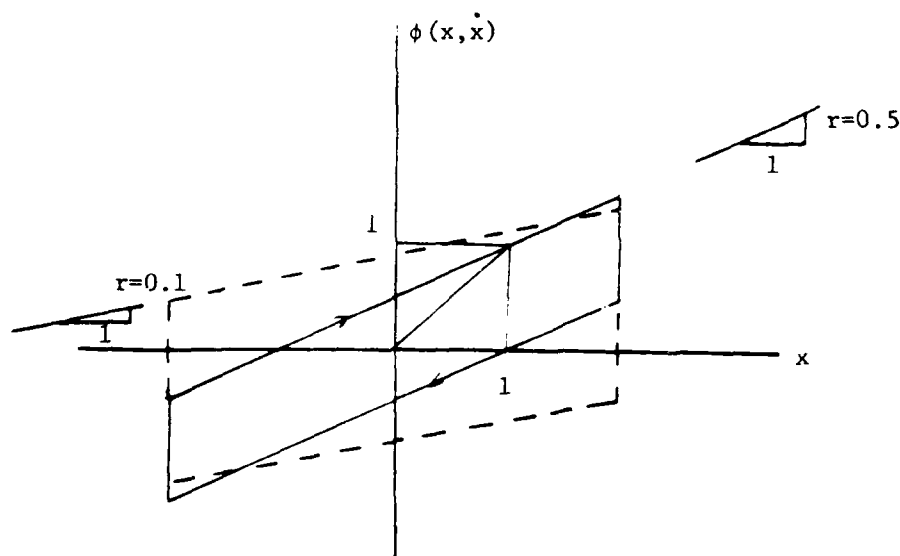


Fig. 1 Hysteretic Restoring Force

smaller values of r indicate stronger nonlinearity. The loading term, $f(t)$, is considered to be a stationary white noise process with uniform power spectral density function equal to $S_0/(2\pi)$.

By introducing the state variables

$$x_1 = x$$

$$x_2 = \dot{x},$$

equation (1) transforms into a first order differential equation of the form

$$\begin{bmatrix} \dot{x}_1 \\ \dot{x}_2 \end{bmatrix} = \begin{bmatrix} x_2 \\ -2hx_2 - rx_2 - rx_1 - (1-r)\text{sgn}x_2 \end{bmatrix} + \begin{bmatrix} 0 \\ 1 \end{bmatrix} f(t) \quad (3)$$

It should be mentioned that extension of the method to evolutionary, non-white excitation can be easily made. Non-stationarity can be achieved by multiplying the excitation by a modulating deterministic function whereas non-whiteness is achieved by passing white noise through filters. In that case additional state variables should be included.

The solution of equation (3) is a Markov process whose behavior is best studied using an Ito stochastic differential equation of the form [5],

$$dx(t) = \underline{f}(t, \underline{x})dt + \underline{G}(t)dw(t)$$

where $w(t)$ is a Wiener process. The transition probability density of $\underline{x}(t)$ obeys the associated Fokker-Plauck equation. This is a parabolic differential equation whose solution cannot be found easily for a general case. For engineering purposes though, it is usually sufficient to determine the statistical moments of the response.

2.2 Moment Equations

Let $g(t, \underline{x})$ be a function of the state variables and time t . Using Ito's lemma and basic properties of Ito calculus the following differential equation governing the expectation of $g(t, \underline{x})$ can be derived:

$$\begin{aligned} \frac{d}{dt} E[g(t, \underline{x})] &= E\left[\frac{\partial g(t, \underline{x})}{\partial t}\right] + \sum_{i=1}^n E\left[\frac{\partial g(t, \underline{x})}{\partial x_i} f_i(t, \underline{x})\right] + \\ &\frac{1}{2} \sum_{i,j=1}^n E\left[\frac{\partial^2 g(t, \underline{x})}{\partial x_i \partial x_j} (G Q G^T)_{ij}\right] \end{aligned} \quad (4)$$

where Q is the strength matrix of the Wiener process $W(t)$. It should be noted that the same equation can be derived by multiplying the Fokker-Planck equation by $g(t, \underline{x})$ and taking ensemble averages.

By choosing suitable expressions for $g(t, \underline{x})$, a set of differential equations governing the statistical moments of \underline{x} can be obtained. For systems starting from rest with zero mean, odd order moments are zero. Therefore, only equations for the even moments are derived.

By substituting $g(t, \underline{x}) = x_1^2$, $x_1 x_2$, and x_2^2 successively in (4) a system of equations for the second order moments can be derived. If $m_{ij} = E[x_1^i x_2^j]$, then

$$\begin{aligned} \dot{m}_{20} &= 2m_{11} \\ \dot{m}_{11} &= m_{02} - 2hm_{11} - rm_{20} - (1-r)E[x_1 \operatorname{sgn} x_2] \\ \dot{m}_{02} &= -4hm_{02} - 2rm_{11} - 2(1-r)E[x_2 \operatorname{sgn} x_2] + S_0 \end{aligned} \quad (5)$$

Similarly, letting $g(t, \underline{x}) = x_1^4$, $x_1^3 x_2$, $x_1^2 x_2^2$, $x_1 x_2^3$ and x_2^4 the following equations for the fourth order moments are obtained.

$$\begin{aligned} \dot{m}_{40} &= 4m_{31} \\ \dot{m}_{31} &= 3m_{22} - 2hm_{31} - rm_{40} - (1-r)E[x_1^3 \operatorname{sgn} x_2] \\ \dot{m}_{22} &= 2m_{13} - 4hm_{22} - 2rm_{31} - 2(1-r)E[x_1^2 x_2 \operatorname{sgn} x_2] + S_0 m_{20} \\ \dot{m}_{13} &= m_{04} - 6hm_{13} - 3rm_{22} - 3(1-r)E[x_1 x_2^2 \operatorname{sgn} x_2] + 3S_0 m_{11} \\ \dot{m}_{04} &= -8hm_{04} - 4rm_{13} - 4(1-r)E[x_2^3 \operatorname{sgn} x_2] + 6S_0 m_{02} \end{aligned} \quad (6)$$

For linear systems under white noise excitation the moment equations form a closed system. However, for nonlinear systems, the moment equations form an infinite hierarchy of equations, that is, equations for moments of specific order include moments of higher order. In such a case the system cannot be solved without some approximation. In equations (5) and (6), the ensemble averages involving the signum function may involve moments of higher order.

Different schemes have been used to truncate the infinite hierarchy. A popular approach is to make the assumption that the state vector is Gaussian distributed. Then, higher order moments are expressed in terms of first and second order moments and the infinite hierarchy is closed. However, for strong nonlinearities, this scheme may not give satisfactory results because the deviation from the Gaussian assumption can be considerable. A different method involves the use of a non-Gaussian approximation of the density function which can be used to express higher order moments in terms of lower ones. Both schemes are used in the present investigation.

Following the Gaussian closure scheme, the joint probability density function of the displacement and velocity is considered normal, given by:

$$p(x_1, x_2) = \frac{1}{2\pi\sigma_1\sigma_2\sqrt{1-\rho^2}} \exp \left\{ \frac{-1}{2(1-\rho^2)} \left[\frac{(x_1-\mu_1)^2}{\sigma_1^2} - \frac{2\rho(x_1-\mu_1)(x_2-\mu_2)}{\sigma_1\sigma_2} + \frac{(x_2-\mu_2)^2}{\sigma_2^2} \right] \right\} \quad (7)$$

In equation (7), μ_1 and μ_2 are the means of the state variables which for this case are zero. Also, $\sigma_1 = \sqrt{m_{20}}$, $\sigma_2 = \sqrt{m_{02}}$ and $\rho = \frac{m_{11}}{\sigma_1\sigma_2}$. Using equation (7), the ensemble averages involving the signum function in equations (5) and (6) can be approximated by lower order moments. Then, the system is truncated and it can be solved for any required statistical moments.

The non-Gaussian approach assumes a non-Gaussian joint density function for the state variables. Such a density can be given by the following Edgeworth expansion [6]:

$$p^*(x_1, x_2) = p(x_1, x_2) - \frac{1}{3!} \sum_{k,l,m} \kappa_{k,l,m} \frac{\partial^3 p(x_1, x_2)}{\partial x_k \partial x_l \partial x_m} + \frac{1}{4!} \sum_{k,l,m,r} \kappa_{k,l,m,r} \frac{\partial^4 p(x_1, x_2)}{\partial x_k \partial x_l \partial x_m \partial x_r} + \dots \quad (8)$$

where $p(x_1, x_2)$ is the Gaussian joint probability density function given by equation (7), and the κ 's are the cumulants. Since the odd order moments are zero, the third order cumulant ($\kappa_{k,l,m}$) is zero. By assuming that

cumulants above certain order are zero, equation (8) can be used to express higher order moments in terms of lower ones and therefore truncate the infinite hierarchy. In the present work cumulants above fourth order are considered zero. Then, equation (8) can be used to express ensembles involving the signum function in terms of lower order moments.

3. NUMERICAL RESULTS

Numerical calculations were carried out to determine the response of the hysteretic oscillator and compare the two different closing schemes. A Runge-Kutta method of order four was used for the solution of the system of moment equations. The response quantities of interest are the mean-square displacement and velocity.

Figures 2 and 3 show the time variation of these statistical moments. The damping ratio assumed is 1%, the rigidity ratio is 0.5 and the dimensionless spectral magnitude is 1.0. It is seen that the Gaussian assumption underestimates the mean-square responses at the stationary level by about 11%. Figures 4 and 5 show the stationary mean-square displacement and velocity for different values of the rigidity ratio r .

4. CONCLUSIONS

A simple hysteretic oscillator under stationary white noise excitation was considered. The mean-square displacement and velocity were computed using a Gaussian and a non-Gaussian closing scheme. The mean-square velocity is an increasing function of the rigidity ratio r whereas the mean-square displacement has a minimum at about $r=0.35$. The Gaussian assumption underestimates the response especially for lower rigidity ratios (stronger nonlinearities).

5. ACKNOWLEDGEMENT

Support from National Science Foundation under Grant CEE-8504972 is gratefully appreciated.

REFERENCES

1. T.K. CAUGHEY 1960 Journal of Applied Mechanics, ASME, Vol. 27, 649-652. Random Excitation of a System with Bilinear Hysteresis.
2. Y.K. WEN 1976 Journal of the Engineering Mechanics Division, ASCE, Vol. 102, No. EM2, 249-263. Method for Random Vibration of Hysteretic Systems.
3. J.B. ROBERTS 1978 Journal of Applied Mechanics, ASME, Vol. 45, 923-928. The Response of an Oscillator with Bilinear Hysteresis to Stationary Random Excitation.
4. T. KOBORI, R. MINAI and K. ASANO 1974 Theoretical and Applied Mechanics, University of Tokyo, Vol. 24, 239-248. Random Response of the Nonlinear System with Hysteretic Characteristics.
5. I. ARNOLD 1974 Stochastic Differential Equations: Theory and Application, John Wiley.
6. R.A. IBRAHIM 1985 Parametric Random Vibration, Research Studies Press, Ltd.

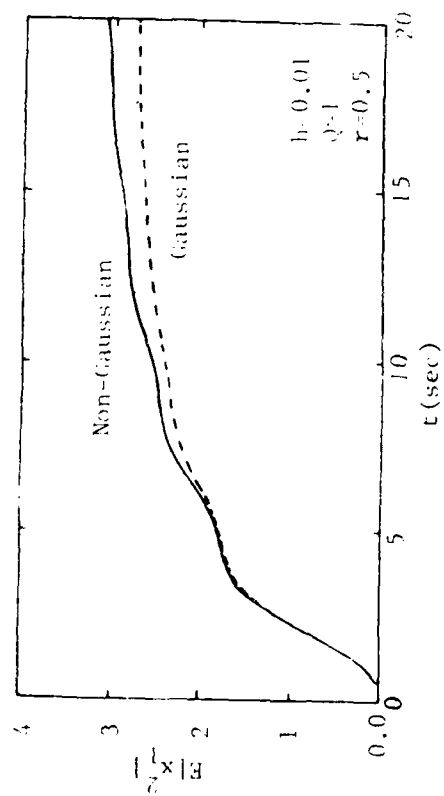


Fig. 2 Mean Square Displacement

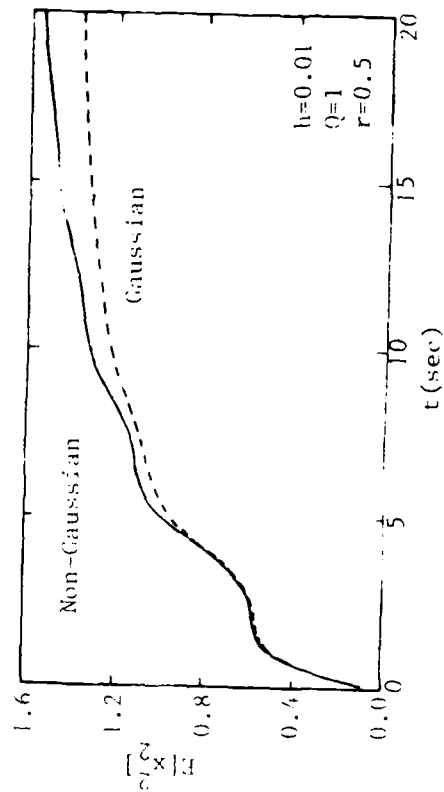


Fig. 3 Mean Square Velocity

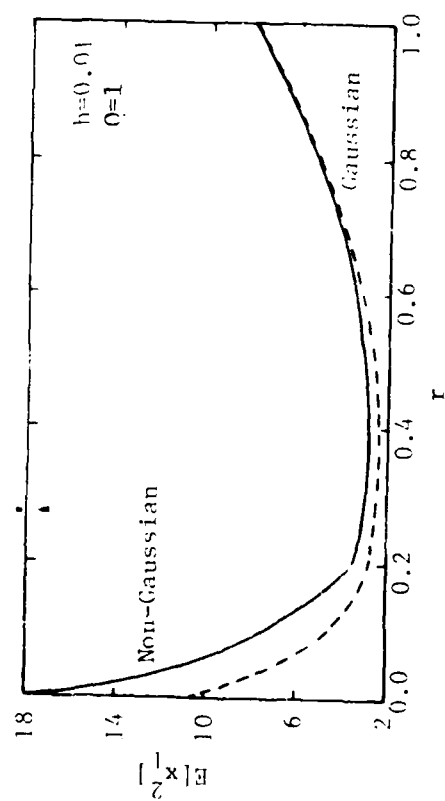


Fig. 4 Stationary Mean Square Displacement

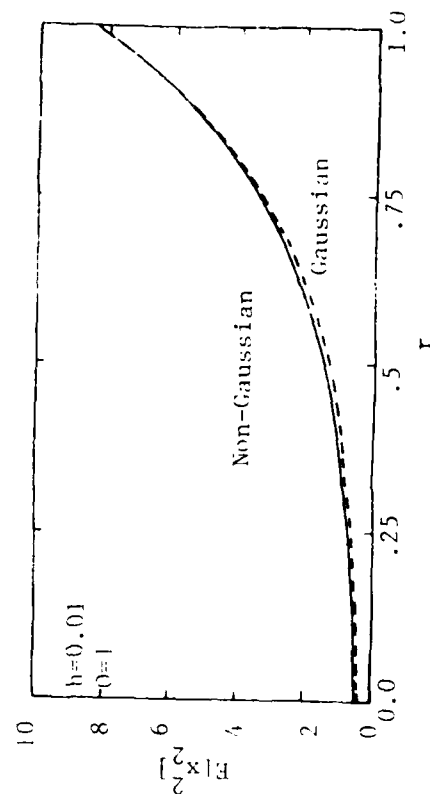


Fig. 5 Stationary Mean Square Velocity

A METHOD FOR THE DYNAMIC ANALYSIS OF RANDOMLY EXCITED STRUCTURES
WITH FRICTIONAL CONSTRAINTS

M.J.H. Fox

CEGB Berkeley Nuclear Laboratories, Berkeley, Glos.

1. INTRODUCTION

Frictional constraints are an almost universal feature of engineering structures occurring, for example, wherever components are riveted or bolted together, or are constructed of contacting laminations or strands. Through their contribution to system damping they may control the overall dynamics of the structure, as well as affecting local stiffness properties. At the same time, because they are non-linear in nature, they pose problems for dynamic analysis of the structure. If the constraints are assumed to obey a simple form such as Coulomb's Law, they may be included in a theoretical model whose response to a deterministic input force may be found by a numerical integration procedure. For complex structures, with many frictional constraints, this may be an extremely costly and time-consuming process.

When the input force is random rather than deterministic, analysis is still more difficult. A pseudo-random simulated input force with the correct statistical properties may be generated, and an explicit response to this calculated. However the duration of response required to obtain an adequate statistical representation of the output from a non-linear system is likely to make this method prohibitively expensive. An alternative approach relies on an attempt to characterize the structure by linear natural modes, frequencies and damping factors and to apply the well-developed theory of the response of linear structures to random excitation. This may be successful if response calculations are restricted to the range of excitation for which the linear model was developed, but cannot be used for extrapolation, as friction loaded constraints may change from a 'sticking' to a 'sliding' condition or vice versa, drastically altering system damping.

In this paper, a procedure is proposed for carrying out assessments of structures with frictional constraints under random excitation, and experimental verification of it is presented. The procedure is applied for the case where a simple Coulomb friction law is assumed, but could be extended to more complex representations of friction.

2. FORMULATION OF THE METHOD

The process is iterative with two stages per iteration. On each iteration the constraints are divided into two sets, those assumed to be in a 'sticking' condition, and those in a 'sliding' condition. This division is supported by earlier calculations on a deterministically excited structure by Fox [1] where transition from a complete frictional constraint to near continuous sliding was found to take place over a narrow range of applied external force.

The first stage on each iteration involves an evaluation of system response in the presence of non-linear frictional forces at the constraints assumed to be sliding. The sticking constraints are assumed to give zero translation or rotation at the corresponding points on the structure. The evaluation is carried out using the method of equivalent linearisation as

described by Lin [2] and Iwan & Yang [3]. The technique, although only approximate, is most successful in predicting mean parameters of the response, especially the energy dissipation rate. This is closely related to material wear rate, often the effect of most concern in a frictionally constrained system. The method is based on finding an approximate, linear set of equations which are in some sense the 'best' representation of the non-linear system under the assumed conditions of excitation. Because this excitation is assumed to take the form of broad band stationary random forcing with a Gaussian probability distribution, the response of the linear set of equations to the forcing will also be Gaussian (see, for example, Davenport & Root [4]). The criterion used to find the 'best' linear approximation is then that its parameters should be such as to minimise the expected value (under the resulting linear response) of the square of the difference between each of the original, non-linear equations and its linearised counterpart. Because the friction force is assumed here to obey a simple, velocity dependent, Coulomb law the effect is to introduce additional linear damping terms into the equations of motion which would govern the system in the absence of any constraints at the friction points.

In the second stage of the process the rms reaction forces at the constraints assumed to be sticking are evaluated. If any of these are found to exceed the available frictional force the corresponding constraints are moved from the 'sticking' set to the 'sliding' set, and a new model is used as a basis for the equivalent linearisation step. It may be that using the new model one of the other sticking degrees of freedom will be found to have already exceeded the limiting friction. This represents a 'cascade' situation, where the freeing of one constraint causes one or more further degrees of freedom to become free simultaneously. In this case, the new model is immediately abandoned and the next model in the sequence, with one more sliding degree of freedom, is considered.

The iteration is continued until a self-consistent solution is reached. As the process is based on transferring constraints from the 'sticking' to the 'sliding' set, and not vice versa, it must be started from a state with the maximum possible number of sticking constraints.

It is often most efficient to carry out evaluations for a range of forcing levels from zero up to the maximum envisaged. The process is then started, for very low level excitation, by assuming that all constraint points are sticking. An exception to this arises where contact between two surfaces is over a very small area. In this case, the friction forces, although adequate to prevent translational motion of the structure, may have inadequate moment to prevent rotation about an axis perpendicular to the plane of contact. In structures such as long beams with several frictional constraint points it may, therefore, be appropriate to treat such rotations as sliding degrees of freedom from the outset. The corresponding frictional moments may either be neglected, if sufficiently small, or their equivalent linearised damping may be included with linear system damping from the start.

The linear model constructed for each forcing level may be used to extrapolate to higher forcing levels up to the point at which it first predicts an rms reaction force at a sticking constraint higher than the available constraining friction force. At this point the model is changed as described above. In this way, although iteration is required to establish the response at higher forcing levels, each model constructed in the process

(except those immediately abandoned in 'cascade' situations) is itself relevant to a particular range of forcing levels.

3. EQUIVALENT LINEARISATION

At each stage of the process described in section 2, it is required to find the response of a system with known constraint points to the given, random, external excitation force and the sliding friction forces at the sliding degrees of freedom. This is most easily done in terms of the natural modes of the given system (in the absence of friction forces at the sliding degrees of freedom). The equation for the generalised displacement, q_i , of the i th mode is then:

$$\ddot{q}_i + \eta_i \omega_i \dot{q}_i + \omega_i^2 q_i + \sum_j \Psi_i(x_j) F_j \operatorname{sgn}(\dot{y}(x_j))/m_i = \sum_k f_k(t) \Psi_i(\hat{x}_k)/m_i \quad (1)$$

where ω_i , η_i and m_i are the natural frequency, loss factor and modal mass of the i th mode, $\Psi_i(x_j)$, $\Psi_i(\hat{x}_k)$ are the values of the i th mode shape at the slip points x_j and the external force application points \hat{x}_k , F_j , $\dot{y}(x_j)$ are the limiting friction force and the velocity at the sliding degree of freedom at x_j and $f_k(t)$ is the external applied force at point \hat{x}_k .

An approximate equation for the i th mode:

$$\ddot{q}_i + T_i \dot{q}_i + \omega_i^2 q_i = \sum_k f_k(t) \Psi_i(\hat{x}_k)/m_i \quad (2)$$

is now set up, in which the effects of the friction forces at the sliding degrees of freedom have been included in a modified linear damping term. A further assumption is being made here, in that explicit modal cross-coupling terms, which would produce additional correlation between the equivalent linearised modes are not included in (2). However, implicit coupling is present, in the sense that T_i will be found to depend on response in the other modes.

The error introduced in the i th equation by the linearisation is:

$$e_i = T_i \dot{q}_i - \eta_i \omega_i \dot{q}_i - \sum_j \Psi_i(x_j) F_j \operatorname{sgn}(\dot{y}(x_j))/m_i$$

The condition applied to find T_i is then that the expected value of the square of this error term should be minimised, so that:

$$\frac{\partial}{\partial T_i} (E(e_i^2)) = 2E \left[T_i \dot{q}_i^2 - \eta_i \omega_i \dot{q}_i^2 - \dot{q}_i \sum_j \Psi_i(x_j) F_j \operatorname{sgn}(\dot{y}(x_j))/m_i \right] = 0 \quad (3)$$

Evaluation of the expected value requires a knowledge of the response of the system, which itself requires a value for T_i to be found. However, as the system now being considered is linear it is known that the response will be Gaussian, and so (3) may be used to yield an equation for T_i . It will, however, be an implicit equation, requiring an iterative solution.

Given a starting value for T_i , the $E(\dot{q}_i^2)$ terms in (3) may be straightforwardly evaluated as the mean square response of the system governed by equations (2) (see for example reference [4])

$$E(\dot{q}_1^2) = \int_0^\infty \frac{\sum_k \Psi_1(\hat{x}_k)^2 S_{kk}(\omega) \omega^2 d\omega}{m_1^2 ((\omega^2 - \omega_1^2)^2 + \omega^2 \omega_1^2 T_1^2)} \quad (4)$$

where $S_{kk}(\omega)$ is the power spectral density function of the force $f_k(t)$, and it is assumed that the different $f_k(t)$ are uncorrelated. To evaluate the last term in (3) it is necessary to consider the joint probability density function of the velocity $\dot{y}(x_j)$ at the point x_j and the modal generalised velocity \dot{q}_1 . Since the response is Gaussian:

$$p(\dot{y}_j, \dot{q}_1) = \frac{1}{2\pi \det(S)} \exp \left(-\frac{1}{2} (\dot{y}_j, \dot{q}_1) S^{-1} \begin{pmatrix} \dot{y}_j \\ \dot{q}_1 \end{pmatrix} \right)$$

where $\dot{y}_j = \dot{y}(x_j)$ and

$$S = \begin{bmatrix} E(\dot{y}_j^2) & E(\dot{y}_j \dot{q}_1) \\ E(\dot{y}_j \dot{q}_1) & E(\dot{q}_1^2) \end{bmatrix}, \text{ the correlation matrix. So:}$$

$$S^{-1} = \begin{bmatrix} E(\dot{q}_1^2) & -E(\dot{y}_j \dot{q}_1) \\ -E(\dot{y}_j \dot{q}_1) & E(\dot{y}_j^2) \end{bmatrix} / \det(S)$$

Then, in (3)

$$E(\dot{q}_1 \operatorname{sgn}(\dot{y}_j)) = \frac{2}{2\pi\sqrt{D}} \int_0^\infty d\dot{y}_j \int_{-\infty}^\infty d\dot{q}_1 \dot{q}_1 \exp((-E(\dot{q}_1^2)\dot{y}_j^2 - E(\dot{y}_j^2)\dot{q}_1^2 + 2E(\dot{q}_1 \dot{y}_j)\dot{y}_j \dot{q}_1)/2D)$$

where $D = \det(S)$.

$$= \frac{1}{\pi\sqrt{D}} \int_0^\infty d\dot{y}_j \int_{-\infty}^\infty d\dot{q}_1 \left(\dot{q}_1 - \frac{E(\dot{q}_1 \dot{y}_j)}{E(\dot{y}_j^2)} \dot{y}_j + \frac{E(\dot{q}_1 \dot{y}_j)}{E(\dot{y}_j^2)} \dot{y}_j \right) \exp(\dots)$$

$$= \frac{1}{\pi\sqrt{D}} \int_0^\infty d\dot{y}_j \frac{E(\dot{q}_1 \dot{y}_j)}{E(\dot{y}_j^2)} \dot{y}_j \sqrt{\frac{2\pi D}{E(\dot{y}_j^2)}} \exp \left((-E(\dot{q}_1^2) + \frac{E(\dot{q}_1 \dot{y}_j)^2}{E(\dot{y}_j^2)}) \dot{y}_j^2 / 2D \right)$$

$$\begin{aligned}
&= \sqrt{\frac{2}{\pi}} \frac{E(\dot{q}_i \dot{y}_j)}{[E(\dot{y}_j^2)]^{3/2}} \frac{D}{E(\dot{q}_i^2) - E(\dot{q}_i \dot{y}_j)^2 / E(\dot{y}_j^2)} \\
&= \sqrt{\frac{2}{\pi}} \frac{E(\dot{q}_i \dot{y}_j)}{E(\dot{y}_j^2)^{1/2}} \quad (5)
\end{aligned}$$

Since $D = \text{Det } (S) = E(\dot{q}_i^2)E(\dot{y}_j^2) - E(\dot{q}_i \dot{y}_j)^2$.

Now $\dot{y}_j = \sum_l \Psi_l(x_j) \dot{q}_l$, and so

$$\left. \begin{aligned}
E(\dot{q}_i \dot{y}_j) &= \sum_l \Psi_l(x_j) E(\dot{q}_i \dot{q}_l), \text{ and} \\
E(\dot{y}_j^2) &= \sum_k \sum_l \Psi_k(x_j) \Psi_l(x_j) E(\dot{q}_k \dot{q}_l)
\end{aligned} \right\} \quad (6)$$

in terms of the modes and modal generalised velocities, while by analogy with (4)

$$E(\dot{q}_i \dot{q}_j) = \text{Re} \int_0^\infty \frac{\sum_k \Psi_i(\hat{x}_k) \Psi_j(\hat{x}_k) S_{kk}(\omega) \omega^2 d\omega}{m_i m_j [(\omega^2 - \omega_i^2)(\omega^2 - \omega_j^2) + \omega^2 \omega_i \omega_j T_i T_j - i\omega [\omega_i T_i (\omega^2 - \omega_j^2) - \omega_j T_j (\omega^2 - \omega_i^2)]]}$$

From an initial estimate:

$$T_{i0} = \eta_i \omega_i$$

then, assuming the applied forcing spectrum $S_{kk}(\omega)$ and the modal

characteristics are known, it is possible to set up an initial modal correlation matrix $E(\dot{q}_i \dot{q}_j)$. Then (3), (5) and (6) give an improved estimate

$$T_i^{-1} = \eta_i \omega_i + \sqrt{\frac{2}{\pi}} \left(\frac{F_j \Psi_i(x_j) \sum_l \Psi_l(x_j) E(\dot{q}_i \dot{q}_l)}{\sqrt{\sum_k \sum_l \Psi_k(x_j) \Psi_l(x_j) E(\dot{q}_k \dot{q}_l)}} \right) / m_i E(\dot{q}_i^2)$$

and the process may be repeated until convergence is achieved.

It should be noted that the inter-modal correlations implied by (7) arise only from the external applied forcing; as mentioned earlier, the friction forces are assumed not to contribute to such correlations.

4. EXPERIMENTAL DESIGN

An experimental rig was set up to test the applicability of the proposed procedure in a particular case. The experiment involved the measurement of input power, frictional energy dissipation rates, and the spatial variation of rms acceleration in two configurations of a system with

non-linear (sliding) frictional constraints. It was also necessary to determine experimentally the characteristics of corresponding linear configurations with constraint points either sticking or left completely free, as the natural modes of these systems are required in the procedure as described in section 3.

The rig consisted of a 3.05m long steel tube of 12.7mm diameter and 1.6mm wall thickness restrained at two points by being clamped between silicone rubber pads (figure 1). These were arranged to provide comparatively little restraint to rotation perpendicular to the axis of the tube, while being stiff to translational motions. At each of two further points on the tube stainless steel faced slides could be pressed against the tube with an adjustable preload, or they could be left free. At a further point on the tube an electrodynamic shaker was attached to the tube, in a direction in the plane of the slides, when these were attached. The applied force could be measured by a force transducer in the shaker link, while similar transducers in the slide mountings measured the sliding force being exerted on the slides. The response of the system was measured using an accelerometer which could be moved along the tube as required. It was sufficiently light to have negligible effect on the system dynamics.

The system was excited by supplying a broadband random signal in the 0-250 Hz frequency range to the shaker, the overall level of the signal being variable. For all runs a response survey was carried out by moving the accelerometer to a number of positions along the tube at a constant force input, and the corresponding rms acceleration values in the 0-200 Hz frequency range were recorded. Input power was found from the real part of the input force-velocity cross spectrum, obtained by frequency domain integration of the force-acceleration cross spectrum with the accelerometer at the shaker attachment point. For runs with sliding points energy dissipation at these points was measured by the same technique. In all runs the input force spectrum was measured and recorded for use as input to the theoretical model.

Four runs were carried out. As the forcing level was increased from very low values at which the slides acted as translational constraints on the tube, friction was overcome first at the top slide. The resulting state of the system with sliding occurring at this slide only was taken as the condition for the first run. It proved to be quite a difficult situation to reproduce, careful adjustment of applied force and slide preloads being required to avoid sliding at the lower slide.

The next run was a reference run with the top slide removed to give complete freedom to the tube there. The modal analysis program MIDAS [5] was used to define the natural frequencies and mode shapes of the linear system used as a basis for the equivalent linearisation step.

As the forcing level was further increased, sliding was initiated at the lower slide also. Run three relates to this situation, although the preloads, and hence limiting friction forces, are different from those in the first run. The fourth run is the reference case for run 3, in which the tube is constrained only at the permanent top and bottom constraint points, being free to move at the levels of the two slides.

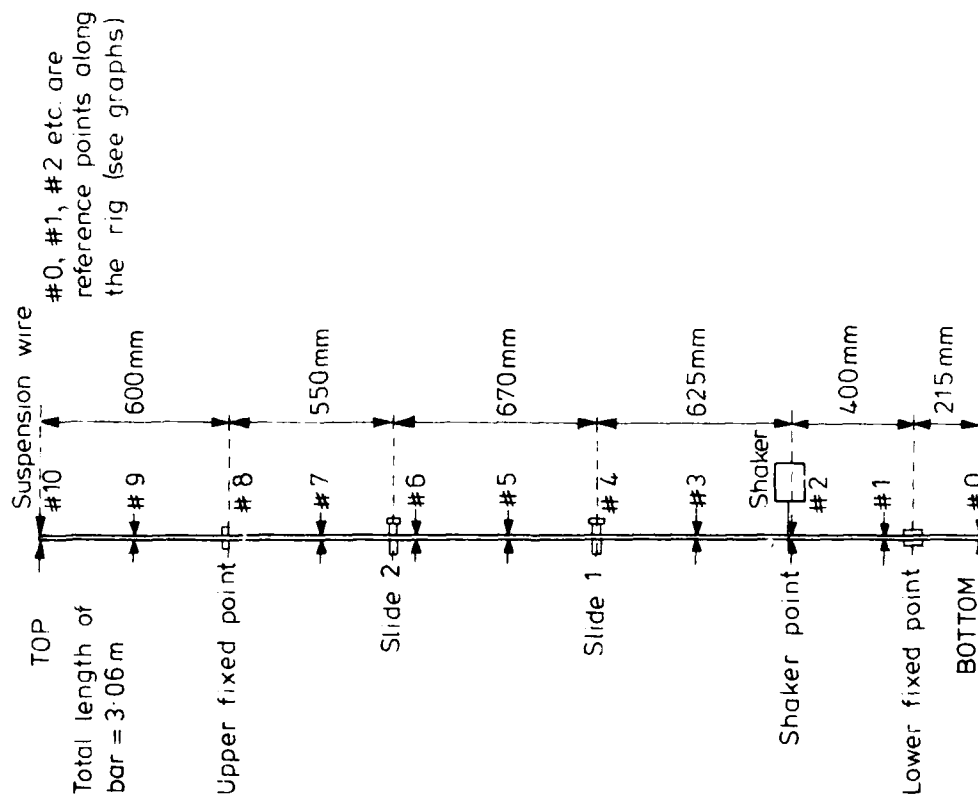


Figure 1 Experimental Rig Design

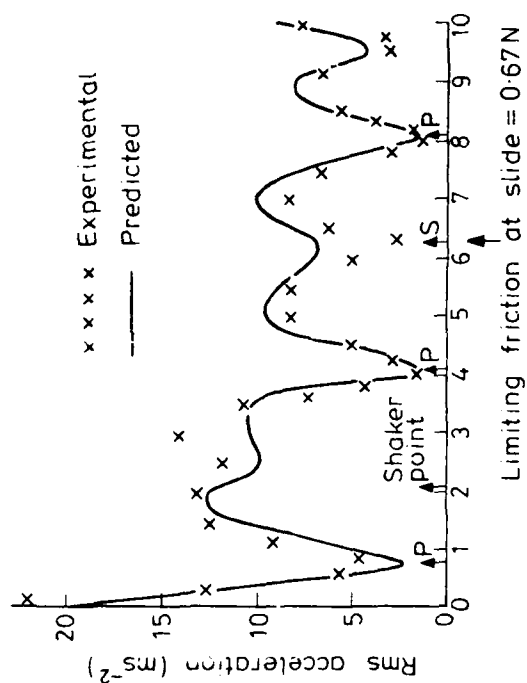


Figure 2 Experimental and Predicted Response, Run 1

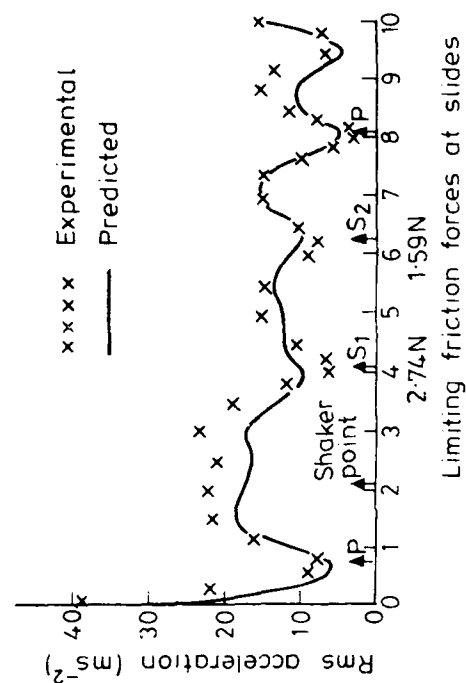


Figure 3 Experimental and Predicted Response, Run 3

The underlying linear mode shapes and frequencies of the system in the two states considered were obtained from the two reference runs. In run 4, where the tube was free at the level of both slides, however, it proved to be difficult to obtain good data for the higher modes. In this case, therefore, six modes were obtained by modal analysis, and supplemented by a further four obtained from finite element analysis, using the finite element code BERDYNE [6]. It would in general be possible to use finite element analysis to define the linear reference systems throughout. This was not done in this case as it was found to be difficult to represent the receptances of the two permanent restraints in a finite element model.

As a check on the combination of mode shape and frequencies chosen the response for the reference runs was calculated theoretically using them in conjunction with the measured input force spectrum. The predicted response was then compared with the measured acceleration profile along the tube. The agreement was found to be very close in both cases.

Using the modes defined in run 2, the theory of section 3 was applied to find the response in the presence of the friction force at the top slide. The appropriate value of limiting friction was evaluated as the component of measured sliding force at this slide coherent with tube velocity at this level. This helped to eliminate uncorrelated additions to the sliding force signal caused by surface irregularities. The results for rms acceleration are shown as a continuous line in figure 2. The crosses in this figure show the measured acceleration values for this run. The comparison is very good, except near the slide position. Here the measured acceleration profile shows a pronounced dip, while the theory indicates only slightly reduced values. The measured and predicted power inputs for both this run and the reference run are shown in table 1, with the corresponding values for power dissipation at the slide. A large increase in power input, from 9.3 to 26mW, is measured when the slide is added, and this is well represented by the theory. The predicted energy dissipation rate at the slide, 14mW, is about 50% higher than the 9.5mW measured. The difference between the power input and the rate of energy dissipation at the slide represents the energy lost to other damping mechanisms. This is somewhat higher than in the reference case due to a higher force input caused by a change in the system impedance at the shaker.

		Run 1	Run 2	Run 3	Run 4
Power Input	Measured	26mW	9.3mW	83mW	33mW
	Predicted	25mW	9.7mW	105mW	37mW
Dissipation at Top Slide	Measured	9.5mW	-	30mW	-
	Predicted	14mW	-	39mW	-
Dissipation at Bottom Slide	Measured	-	-	31mW	-
	Predicted	-	-	56mW	-

Table 1. Measured and Predicted Power Inputs/Dissipation Rates

The corresponding predicted and measured acceleration profiles for run 3 are shown in figure 3, with power input and dissipation being shown in table 1. Again, agreement is generally good, although response at the slider locations is overpredicted, leading to an overprediction of power dissipation at the sliders and an underprediction of response in the vicinity of the shaker.

It is not unexpected that the method should overpredict response at frictional constraints which are only just above the 'sticking' phase. The increasing significance of the friction forces at a given constraint point as the external excitation level is reduced will tend to produce correlations between the responses of the different modes in such a manner as to bring the structure to rest at the constraint point. These cross-correlations are not allowed for in the theory. The energy dissipation rate for a given overall response level is thus overestimated, and the response level away from the constraint correspondingly underestimated. From a practical point of view, it is necessary to be aware that there is a transition region between the areas of applicability of two models: one with a pure 'stick' condition at the constraint and the other a pure 'slip' condition. In this region, it is necessary to consider the predictions of both models in assessing response.

6. CONCLUSIONS

A procedure has been suggested for analysing the response of a linear elastic structure with one or more frictional constraints to stationary random Gaussian excitation. The method may be used either iteratively, or as a means of establishing response for a range or increasing excitation levels, starting from zero. On each iteration or for each band of force levels a division is made of the frictional constraints between 'sticking' and 'sliding' conditions. The assessment at each stage involves the determination of equivalent linear terms to be added to a model of the structure in the absence of frictional constraints to allow for their effect. For the simple Coulomb friction law considered these take the form of additional damping terms.

An experimental verification of the procedure has been carried out on a simple beam structure in the laboratory. It has been found to be successful in predicting overall levels of response and energy dissipation. Response and local energy dissipation are well represented in the neighbourhood of constraints with well established sliding, but are somewhat overpredicted near constraints just beyond the sticking condition.

The procedure may therefore be regarded as the basis for a conservative assessment procedure for systems with a failure mode related to total energy dissipation at frictional contact sites. It is necessary to recognise an area of uncertainty in the region of transition from 'stick' to 'slide' at each constraint point, and to take the more pessimistic of the two corresponding models into account. More sophisticated friction models could be incorporated as a refinement to the procedure.

ACKNOWLEDGEMENT

This paper is published by permission of the Central Electricity Generating Board.

REFERENCES

1. M.J.H. FOX 1984 2nd International Conference on Recent Advances in Structural Dynamics, Southampton, April 1984. The Effect of Small Clearances and Friction Loaded Constraint Points on Bending Wave Energy Transmission in a Long Beam.
2. W.D. IWAN and I.M. YANG 1972 J. Applied Mechanics, June 1972, 545-550. Application of Statistical Linearization Techniques to Non-linear Multi-degree-of-Freedom Systems.
3. Y.K. LIN 1967 Probabilistic Theory of Structural Dynamics pp 283-288. New York: McGraw-Hill.
4. W.B. DAVENPORT and W.L. ROOT 1958 Random Signals and Noise Chapter 9. New York: McGraw-Hill.
5. R.F. DURRANS 1980 CEEB Report RD/B/N4917 MIDAS - Phase II, A Program for the Modal Analysis of Structures.
6. M.J.H. FOX 1984 BERSAFE User Guides Volume 5. A User's Guide to BERYNE, Phase II, Level 3. CEEB Berkeley Nuclear Laboratories.

A FINITE ELEMENT LARGE DEFLECTION MULTIPLE-MODE RANDOM RESPONSE ANALYSIS OF BEAMS SUBJECTED TO ACOUSTIC LOADING

C. K. Chiang and Chuh Mei

Department of Mechanical Engineering and Mechanics
Old Dominion University, Norfolk, Virginia

1. INTRODUCTION

The finite element method has been proved to be an effective and versatile approach for analysis of structures of complex geometry and support conditions. Application of the finite element methods to linear random response analysis of complex structures have been reported, for example, in references [1-3]. A comprehensive literature search revealed that there were only three articles that investigated large deflection random response of structures using the finite element methods. Hwang and Pi [4] were apparently the first to study nonlinear acoustic response of plate using the finite element method. A first-order and a second-order nonlinear element stiffness matrices were developed to account for the large deflection effect. The nonlinear finite element problem was handled as a linearized eigenvalue solution with iterations. Numerical results were obtained for a simply supported rectangular plate subjected to raindrop type and uniform intensity random acoustic loadings. The acceleration spectra at the plate center at three acoustic load levels were obtained. The maximum frequency shift of the fundamental mode was approximately 4.5%. They cautioned that when the input acoustic pressure level is too high for a given plate configuration, the iterative eigenfrequencies become complex numbers; this indicates that the proposed finite element procedure is no longer applicable.

Busby and Weingarten [5] used the finite element method only to obtain the nonlinear differential equations of motion in terms of the normal mode coordinates. The equivalent linearization method was then applied for solution of these equations. Mean square deflections at the midspan were obtained for simply supported and clamped beams. No comparison with other approximate solutions were given in both papers [4,5]. Mei and Chiang [6] recently have extended the finite element method to large deflection random response of beams and rectangular plates. The formulation was restricted to a single-mode approach. The finite element single-mode results were compared with the solutions using the Fokker-Planck-Kolmogorov (FPK) equation method [7] and the equivalent linearization (EL) method [8,9]. Good agreement has been reported [6] among the three methods.

In this study, a finite element multiple modes procedure is developed for the large deflection random response analysis of beams subjected to acoustic pressure. The excitation is assumed to be stationary, ergodic and Gaussian with zero mean; its magnitude and phase are uniform over the beam surfaces. Both simply supported and clamped beams are studied. The finite element results of root-mean-square (RMS) nondimensional maximum deflection, RMS maximum micro-strain and equivalent linear frequency for beams at various sound pressure levels are obtained and compared with solutions using the EL method [8,9].

2. MATHEMATICAL FORMULATION

2.1 Linear Analysis

Once the mass and linear stiffness matrices for a beam element are available, the undamped linear system equations of motion are obtained by assembling the element matrices and applying the kinematic boundary conditions, and it can be written as

$$[M_b]\{\ddot{\eta}_b\} + [K_b]\{\eta_b\} = \{P(t)\} \quad (1)$$

where $[M_b]$ and $[K_b]$ denote the system mass and linear stiffness matrices related to bending, respectively, $\{\eta_b\}$ denotes the vector of system bending nodal displacements, and $\{P(t)\}$ denotes the vector of nodal forces.

In order to transfer the equations of motion to the normal coordinates, the eigenproblem of the undamped linear free vibration is to be solved

$$\omega_j^2 [M_b]\{\phi\}_j = [K_b]\{\phi\}_j \quad j = 1, 2, \dots, m \quad (2)$$

where ω_j is the linear frequency of vibration of the j -th mode, and $\{\phi\}_j$ is the corresponding j -th mode shape normalized to unity of the largest component, where the sign of each mode shape based on the area under each mode shape is adjusted to be positive. Apply a coordinate transformation, from the nodal displacements to the normal coordinates, by

$$\begin{matrix} \{\eta_b\} \\ m \times 1 \end{matrix} = \begin{matrix} [\phi] \\ m \times n \times n \end{matrix} \begin{matrix} \{q\} \\ n \times 1 \end{matrix} \quad n \leq m \quad (3)$$

where each column of the modal matrix $[\phi]$ is a normal mode $\{\phi\}_j$, and $\{q\}$ represents a vector of normal coordinates. Substituting equation (3) into equation (1) and premultiplying by the transpose of $[\phi]$, equation (1) becomes

$$[M]\{\ddot{q}\} + [K]\{q\} = \{p(t)\} \quad (4)$$

where the modal mass M_j , stiffness K_j and force $p_j(t)$ are given by the expressions

$$M_j = \{\phi\}_j^T [M_b] \{\phi\}_j / \int \{\phi\}_j dx \quad (5)$$

$$K_j = \{\phi\}_j^T [K_b] \{\phi\}_j / \int \{\phi\}_j dx \quad (6)$$

$$p_j = \{\phi\}_j^T \{P\} / \int \{\phi\}_j dx \quad (7)$$

where $\int_0^L \{\phi\}_j dx$ is the area under mode shape and is positive, and L is the total length of the beam.

With the modal damping ratio $\zeta (= c/c_{cr})$ obtained either from experiment or from existing data, the j -th row of modal equation (4) can be expressed as

$$\ddot{q}_j + 2\zeta\omega_j \dot{q}_j + \omega_j^2 q_j = p_j/M_j \quad j=1,2,\dots,n \quad (8)$$

The mean square response of j-th linear modal amplitude from equation (8) is

$$E(q_j^2)_0 = \int_0^\infty S_p(\omega) |H_j(\omega)|^2 d\omega \quad (9)$$

where the subscript 0 denotes for linear solution, $S_p(\omega)$ is the spectral density function of the pressure excitation p_j , and the frequency response function is given by

$$H_j(\omega) = \frac{1}{M_j(\omega_j^2 - \omega^2 + 2i\zeta\omega_j\omega)} \quad (10)$$

For lightly damped ($\zeta < 0.05$) structures, the frequency response curve is highly peaked at ω_j and equation (9) yields

$$E(q_j^2)_0 = \frac{\pi S_p(\omega_j)}{4 M_j^2 \zeta \omega_j^3} \quad j=1,2,\dots,n \quad (11)$$

In practice, the spectral density function is usually given in terms of the frequency f in Hz. Substitute $S_p(\omega) = S_p(f)/2\pi$ where $S_p(f)$ has the units $(N/m)^2/Hz$ for beam, the mean-square modal amplitude becomes

$$E(q_j^2)_0 = \frac{S_p(f_j)}{8 M_j^2 \zeta \omega_j^3} \quad (12)$$

The natural frequencies ω_j were found to be well separated and for the case of light damping; the i-th linear mean-square displacement, taking into account the autocorrelation terms only, is

$$E(n_i^2) \approx \sum_{j=1}^n \phi_{ij}^2 E(q_j^2)_0 \quad i=1,2,\dots,m \quad (13)$$

with $E(q_i q_j) = 0$ for $i \neq j$.

2.2 Large Deflection Formulation

Once the mean-square values of linear displacements are determined from equation (13), the deflection of the structure under harmonically excited steady-state case based on linear theory is given by

$$\{n_b\}_{iter=0} = \sqrt{2} \begin{Bmatrix} \text{RMS } n_1 \\ \text{RMS } n_2 \\ \vdots \\ \text{RMS } n_m \end{Bmatrix} \quad (14)$$

Corresponding to this deflection shape, there exists an axial force

$$N_x = EA (u_{,x} + \frac{1}{2} w_{,x}^2) \quad (15a)$$

where E is the Young's modulus and A is the cross-section area. Since linear modes $\{\phi\}_j$, $j=1, 2 \dots n$, equation (3), are used in the analysis; the term $u_{,x}$ has no contribution to the axial force N_x . Equation (15a) becomes

$$N_x = EA (\frac{1}{2} w_{,x}^2) \quad (15b)$$

The potential energy of the membrane force undergoing large transverse deflection is

$$V = \int N_x (u_{,x} + \frac{1}{2} w_{,x}^2) dx \quad (16)$$

Substituting equation (15b) in equation (16) and by introducing a linearizing function g which is defined as

$$g = \frac{1}{2} w_{,x} \quad (17)$$

it yields the potential energy functional

$$V = \frac{EA}{2} \int (2gu_{,x}w_{,x} + 2g^2 w_{,x}^2) dx \quad (18)$$

The finite element used in the present formulation is the common beam element with six degrees-of-freedom. The displacement functions are

$$\begin{aligned} w &= a_1 + a_2x + a_3x^2 + a_4x^3 \\ u &= a_5 + a_6x \end{aligned} \quad (19)$$

The six generalized coordinates

$$\{a\}^T = [a_1, a_2, \dots, a_6] \quad (20)$$

can be determined from the element nodal displacements

$$\{\delta\}^T = [\{\delta_b\}^T, \{\delta_m\}^T] \quad (21)$$

with element bending displacements $\{\delta_b\}^T = [w_1, w_{x1}, w_2, w_{x2}]$, and element axial or membrane displacements $\{\delta_m\}^T = [u_1, u_2]$. The relation between the generalized coordinates and the nodal displacements can be evaluated from equation (19) and can be written as

$$\{a\} = [T]\{\delta\} \quad (22)$$

The terms in the potential energy can be expressed in terms of the element nodal displacements as

$$u_x = [0 \ 0 \ 0 \ 0 \ 0 \ 1] \{a\} = [C][T]\{\delta\} \quad (23)$$

$$w_x = [0 \ 1 \ 2x \ 3x^2 \ 0 \ 0] \{a\} = [D][T]\{\delta\} \quad (24)$$

thus, equation (18) can be expressed as

$$V = \frac{1}{2} \{\delta\}^T [\bar{k}]\{\delta\} \quad (25)$$

$$\text{with } [\bar{k}] = EA [T]^T \int_0^l (g[C]^T[D] + g[D]^T[C] + 2g^2[D]^T[D]) dx [T] \quad (26)$$

$$= [\bar{k}_{mb}] + [\bar{k}_{bm}] + [\bar{k}_b]$$

where l is the beam element length. Evaluation of the element geometrical stiffness matrix $[\bar{k}]$ is based on numerical integration using a five-point Gaussian integration which can exactly integrate for polynomial of order of nine.

2.3 Solution Procedure

For a given sound spectrum level $S_p(f)$, the beam deflection of equation (14) can be determined. The geometrical stiffness matrices are then obtained for all the elements using equation (26). Assembling the finite elements and applying the kinematic boundary conditions, the equations of motion are of the form

$$\begin{bmatrix} M_b & 0 \\ 0 & M_m \end{bmatrix} \begin{Bmatrix} \ddot{\eta}_b \\ \ddot{\eta}_m \end{Bmatrix} + \left(\begin{bmatrix} K_h & 0 \\ 0 & K_m \end{bmatrix} + \begin{bmatrix} \bar{K}_b & \bar{K}_{bm} \\ \bar{K}_{mb} & 0 \end{bmatrix} \right) \begin{Bmatrix} \eta_b \\ \eta_m \end{Bmatrix} = \begin{Bmatrix} P(t) \\ 0 \end{Bmatrix} \quad (27)$$

where $[\bar{K}]$ denotes the system geometrical stiffness matrix. The modal equations (8) become

$$\ddot{q}_j + 2\zeta\omega_j \dot{q}_j + \Omega_j^2 q_j = p_j/M_j \quad j=1,2,\dots,n \quad (28)$$

where the equivalent linear frequency Ω_j for j -th mode is determined from

$$\Omega_j^2 [M]\{\phi_e\}_j = ([K] + [R])\{\phi_e\}_j \quad (29)$$

in which $\{\phi_e\}_j$ is the equivalent linear normal mode. The mean-square modal amplitude for lightly damped structures, from equation (28), is

$$E(q_j^2)_1 = \int_0^\infty S_p(\omega) |H_j(\omega)|^2 d\omega$$

$$= \frac{S_p(F_j)}{8 M_j^2 \zeta \omega_j \Omega_j^2} \quad (30)$$

where the subscript 1 denotes for the first iterative solution, $F_j = \Omega_j/2\pi$ is the equivalent linear frequency in Hz, and the frequency response function is

$$H_j(\omega) = \frac{1}{M_j (\Omega_j^2 - \omega^2 + 2i\zeta\omega\omega_j)} \quad (31)$$

The i-th mean-square displacement is

$$E(n_i^2) = \sum_{j=1}^n \phi_{ij}^2 E(q_j^2)_1 \quad (32)$$

and the iterative process can now be repeated with

$$\{n_b\}_{iter}^T = \sqrt{2} \text{ RMS } [n_1, n_2, \dots, n_m] \quad (33)$$

as the updated deflection shape for the next iteration. Convergence is considered achieved when the difference of the RMS amplitudes satisfies the relation

$$\left| \frac{(\text{RMS } q_j)_{iter} - (\text{RMS } q_j)_{iter-1}}{(\text{RMS } q_j)_{iter}} \right| < 10^{-3} \quad (34)$$

for all $j=1,2,\dots,n$.

2.4 Strains

Once the convergence of modal amplitude is satisfied, the bending strain components at the two nodes ($x=0, x=l$) of the k-th beam element can be determined from

$$(\epsilon_x)_b = -zw_{,xx}$$

$$= \sum_{i=1}^n -z [0 \ 0 \ 2 \ 6x \ 0 \ 0] [T][\beta]_k \{\phi\}_i q_i$$

$$= \sum_{i=1}^n -z [B][T][\beta]_k \{\phi\}_i q_i \quad (35)$$

where $[\beta]_k$ is the connectivity matrix between the k -th element nodal displacements and the system nodal displacements as $\{\delta\}_k = [\beta]_k \{n\}$. The maximum bending strains within each element are evaluated with z at the top or bottom surfaces ($z = \pm \frac{h}{2}$), and equation (35) can be written as

$$(\epsilon_x)_b = \sum_{i=1}^n (C_1)_i q_i \quad (36)$$

The membrane strain component of the k -th element can be obtained from

$$\begin{aligned} (\epsilon_x)_m &= u_{,x} + \frac{1}{2} w_{,x}^2 \\ &= \sum_i [C][T][\beta]_k \{\phi\}_i q_i + \frac{1}{2} \sum_i \sum_j q_i \{\phi\}_i^T [\beta]_k^T [T]^T [D]^T [D][T][\beta]_k \{\phi\}_j q_j \\ &= \sum_{i=1}^n (C_2)_i q_i + \sum_{i=1}^n \sum_{j=1}^n (C_3)_i (C_3)_j q_i q_j \end{aligned} \quad (37)$$

Since for Gaussian random processes with zero-mean, the modal amplitudes follow the relations

$$E(q_i q_j q_k) = 0 \quad (38)$$

$$\begin{aligned} E(q_i q_j q_k q_\ell) &= E(q_i q_j) E(q_k q_\ell) \\ &+ E(q_i q_k) E(q_j q_\ell) + E(q_i q_\ell) E(q_j q_k) \end{aligned} \quad (39)$$

The mean-square strain is then related to the converged mean-square modal amplitudes, with $E(q_i q_j) = 0$ for $i \neq j$, as

$$\begin{aligned} E(\epsilon_x^2) &= \sum_i \sum_j [(C_1)_i + (C_2)_i][(C_1)_j + (C_2)_j] E(q_i q_j) \\ &+ \sum_i \sum_j \sum_k \sum_\ell [(C_3)_i (C_3)_j (C_3)_k (C_3)_\ell] E(q_i q_j q_k q_\ell) \end{aligned} \quad (40)$$

3. RESULTS AND DISCUSSION

The primary purpose of this study is to extend the finite element method using multiple modes for analyzing large deflection random response of structures subjected to acoustic loads. Numerical results for beams are obtained and compared with other approximate solutions to assess the accuracy of the present finite element formulation. Boundary conditions considered are simply supported and clamped, and inplane edges are immovable at the ends ($u=0$ at $x=0$ and L).

In all the presented analyses, only one-half of the beam which is divided equally into fifteen elements is used. The beam reported in references [6, 8 and 9] are used here for analysis. The beam is made of 2024-T3 aluminum. The dimensions and material properties are:

width	$b = 2 \text{ in. (5.08 cm)}$
thickness	$h = 0.064 \text{ in. (0.1626 cm)}$
length	$L = 12 \text{ in. (30.48 cm)}$
Young's modulus	$E = 10.5 \times 10^6 \text{ psi (70.395 GPa)}$
mass density	$\rho = 0.2588 \times 10^{-3} \text{ lb - sec}^2/\text{in.}^4$ $(2765.7606 \text{ kg/m}^3)$
damping ratio	$\zeta = 0.01$

Table 1 shows the RMS (maximum beam deflection/radius of gyration) at various sound spectrum levels (SSL) between 90 and 130 dB (re. 2×10^{-5} Pa) for a simply supported beam and a clamped beam using single mode and multiple modes in the analyses. To demonstrate the accuracy of the finite element (FE) results, approximate RMS maximum deflections obtained by using the EL method [8,9] and the FPK equation [7] approach (exact solution to the forced Duffing equation) are also given. It can be seen that even a single-mode finite element solution is adequate to provide reasonable accurate deflections.

Figure 1 shows the three equivalent linear frequencies $F(\text{Hz})$ versus SSL using FE and EL methods. Dash lines represent linear frequencies. It clearly demonstrates that the present FE formulation using equation (29) gives excellent equivalent linear frequency predictions as compared to the EL solutions for all three modes. The finite element results from solving $[M_b]\{\ddot{\eta}_b\} + ([K_b] + [\bar{K}_b])\{\eta_b\} = \{P(t)\}$ are denoted by FE*; it gives good agreement for fundamental mode which contributes the most in evaluating RMS displacement.

Figure 2 shows the RMS maximum strain versus SSL using FE and EL methods for simply supported and clamped beams. The FE* gives good agreement as compared to the EL solution, since both methods are formulated in terms of the transverse displacement only and neglected the axial displacement and axial inertia.

4. CONCLUSIONS

A finite element method has been presented to analyze large deflection multiple mode random response of beams subjected to acoustic loadings. Geometrical stiffness matrix was developed for a beam element to account for the membrane force due to large deflections. The membrane force in each element is evaluated at the Gaussian points. Solution procedure based on an iterative scheme was described. Numerical examples were given for simply supported and clamped beams at various sound spectrum levels. The beam formulation included the incorporate of inplane displacement and inplane inertia. Finite element random response predictions compared very well with the approximate solution using EL method.

ACKNOWLEDGEMENT

The work is supported by Flight Dynamics Laboratory, Air Force Wright Aeronautical Laboratories under Grant F33615-86-C-3230 and by NASA-Langley Research Center under Grant NAS1-17993-22.

Table 1 Comparison of RMS maximum deflections for simply supported beam and clamped beam using different methods

	FPK method	EL method [8, 9]		FE method		
	single mode [7]	single mode	three modes	single mode	three modes	five modes
Simply Supported						
90	0.3198	0.3194	0.3194	0.3212	0.3175	0.3174
100	0.8615	0.8456	0.8456	0.8648	0.8522	0.8520
110	1.8867	1.7938	1.7937	1.8645	1.8231	1.8227
120	3.6248	3.3843	3.3834	3.5569	3.4663	3.4637
130	6.6134	6.1325	6.1289	6.5217	6.4275	6.4174
Clamped						
90	0.1005	0.1005	0.1006	0.1006	0.0980	0.0978
100	0.3155	0.3154	0.3156	0.3159	0.3078	0.3076
110	0.9392	0.9354	0.9357	0.9449	0.9231	0.9223
120	2.3549	2.2850	2.2845	2.3591	2.3113	2.3099
130	4.8720	4.5952	4.5883	4.8742	4.7361	4.7335

Three modes - mode 1, 3 and 5.

Five modes - mode 1, 3, 5, 7 and 9.

REFERENCES

1. L. D. Jacobs and D. R. Lagerquist 1968 Wright-Patterson Air Force Base, Ohio, AFFDL-TR-68-44. Finite Element Analysis of Complex Panel to Random Loads.
2. S. S. Dey 1979 Computer Methods in Applied Mechanics and Engineering 20, 173-194. Finite Element Method for Random Response of Structures Due to Stochastic Excitation.
3. M. D. Olson 1972 Computers and Structures 2, 163-180. A Consistent Finite Element Method for Random Response Problems.
4. C. Hwang and W. S. Pi 1972 AIAA Journal 10, 276-282. Nonlinear Acoustic Response Analysis of Plates Using the Finite Element Method.
5. H. P. Busby and V. I. Weingarten 1973 ASCE Journal Engineering Mechanics, 55-68. Response of Nonlinear Beam to Random Excitation.
6. C. Mei and C. K. Chiang 1987 AIAA 11th Aeroacoustic Conference, Paper 87-2713. A Finite Element Large Deflection Random Response Analysis of Beams and Plates Subjected to Acoustic Loading.
7. V. V. Bolotin 1984 Random Vibrations of Elastic Systems, 290-292, 314-316. Martinus Nijhoff Publishers.
8. C. B. Prasad and C. Mei 1987 AIAA 11th Aeroacoustic Conference, Paper 87-2712. Multiple Mode Large Deflection Random Response of Beams with Nonlinear Damping Subjected to Acoustic Excitation.
9. C. B. Prasad 1987 Ph.D. Dissertation, Old Dominion University. The Effect of Nonlinear Damping on the Large Deflection Response of Structures Subjected to Random Excitation.

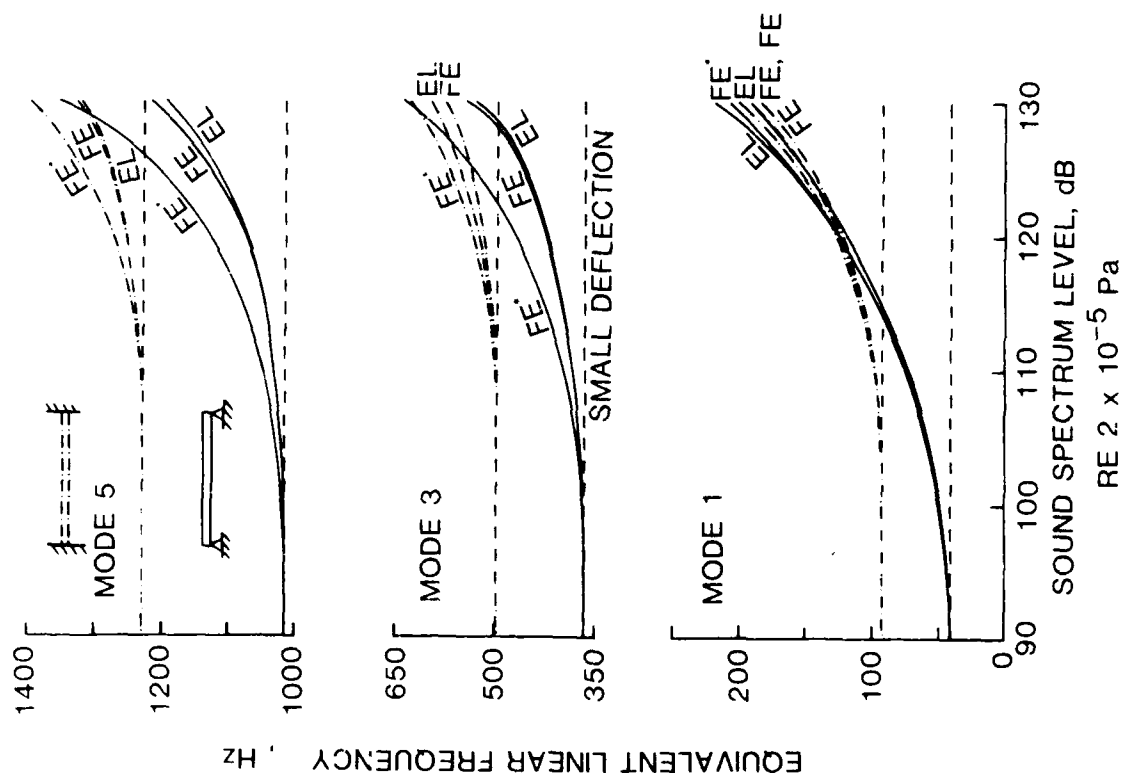


Figure 1 Equivalent linear frequencies for beams ($r_s = 0.01$).

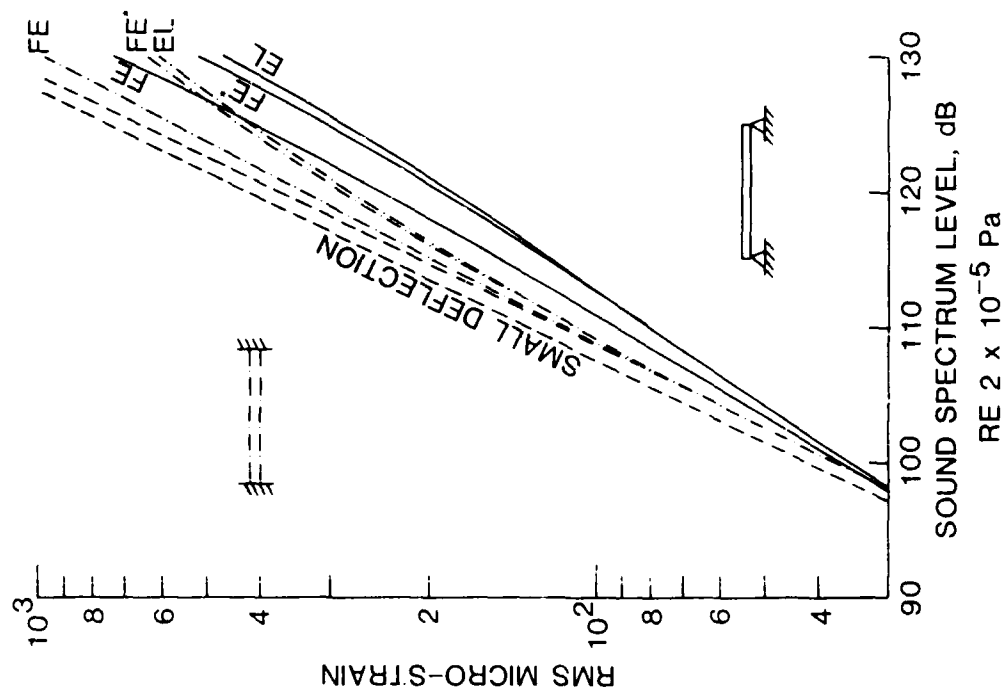


Figure 2. RMS maximum strain for beams using three modes ($r_s = 0.01$).

NON LINEAR STOCHASTIC DYNAMICS OF FRAMES

F. Casciati and L. Faravelli

Dept. of Structural Mechanics
University of Pavia - Italy

SUMMARY - Nonlinear stochastic dynamics of frames can be conducted by stochastic equivalent linearization in two different ways. Either a global hysteretic constitutive law is associated with each storey or it is introduced for each region where inelastic deformation may concentrate.

When second order geometric effects cannot be neglected, both the approaches can be extended. However, the first, and simpler, procedure presents some inconveniences which are emphasized in this paper.

1. INTRODUCTION

General state-of-art reports in stochastic dynamics [1][2] emphasize the versatility of stochastic equivalent linearization in approaching non-linear problems. Their use is especially suitable for estimating the dynamic response of systems, structures as well as continua [3], under stochastic excitation. In particular, for complex hysteretic multi-degree-of-freedom systems there are not alternative tools of analysis which are presently operative.

A basic improvement, in view of practical applications, was proposed in Refs. [4][5][6] and [7] where the algorithms, originally introduced for plane structures, are extended to three-dimensional frames. It is well known, in fact, that for spatial systems plane analysis is incompatible with the hysteretic nature of the material constitutive law.

The actual response of frames, however, is significantly influenced also by geometrical effects, i.e. by the interaction between vertical loads and horizontal displacements at the top of columns. These effects are generally of non-linear nature, since the axial force in the columns depends on the top displacement which, in turn, depends on the axial force... Nevertheless, in several cases of practical interest the static axial force in the columns remains nearly constant during the dynamic excitation, avoiding the non-linearity of the problem.

The so called "geometrical second order effects" can be approximately taken into account by the geometric stiffness matrices of the vertical elements [8]. In this paper attention is focused on the consequences that the introduction of such a matrix leads in the stochastic-linearization coefficients and in the response characteristics.

2. GOVERNING RELATIONS

From the computational point of view each storey of the frame under investigation is conveniently modelled by a single

oscillator with one degree-of-freedom in the plane and three in the space. If the hysteretic constitutive laws of these oscillators are known on experimental basis, then the dynamic analysis of the frame reduces to solve a system of first order differential equations [4]:

$$\dot{\underline{d}} + \underline{Q} \underline{d} = \underline{F} \quad (01)$$

In Eq. (01) \underline{Q} is a structural matrix which groups the coefficients of the equations of motion and the coefficients of the linearized equations which express the storey constitutive laws. The vector \underline{d} contains displacements, velocities and general response quantities. The vector \underline{F} denotes the external action assumed to be stochastic and stationary. The reader is referred to the appendix for the mechanical meaning of the expressions leading to Eq.(01).

The linearization coefficients \underline{C} and \underline{H} (a pair for each constitutive law) introduced in Eq.(A5) are unknown "a priori". Therefore, also the matrix \underline{Q} , which contains these coefficients, is unknown. Nevertheless, for Gaussian excitation, the dependence of \underline{C} and \underline{H} on the covariance matrix $\underline{\Sigma}$ of \underline{d} is assigned. It follows that, guessing initial values for \underline{C} and \underline{H} , the analyst can find the root-mean-square description of the response by iteratively solving the well known Liapounov equation:

$$\underline{Q} \underline{\Sigma} + \underline{\Sigma} \underline{Q}^T = \underline{f} \quad (02)$$

with

$$\underline{f} = \langle \underline{F} \underline{F}^T \rangle \quad (03)$$

An alternative approach [9] [6] [7], leading to a solving system which again is formally given by Eq. (01), assigns the hysteretic constitutive law in each of the regions where inelastic deformation concentrate. The main disadvantage is that the number of these regions may be very large. For instance, in a single-storey plane frame the first approach leads to a system (01) of dimension 3. The present procedure requires at least 6 constitutive equations (one for each of the two ends of the three elements) to be added to the two first order differential equations which describe the floor motion.

On the other hand, the advantage of this alternative approach is that the constitutive law must not be identified, as the storey relationship needs: it can be determined directly from the geometrical and mechanical properties of the single section. A more detailed design is therefore possible by such an analysis.

Moreover, this second approach can also take advantage from the solution algorithms discussed in Ref. [10]: a sort of modal analysis for non-classically damped systems. The possibility of neglecting the higher modes in the analysis of the equivalent linear system, in fact, may reduces the computational effort which the solution of Eq. (02) requires.

3. GEOMETRICAL NON-LINEARITIES

The possibility of extending the simpler procedure can be investigated by studying the oscillator of Figure 1a). A mass is supported by a rigid column of length ℓ with at the bottom a hysteretic spring of elastic stiffness k_θ : let θ the rotation in the spring and M the associated moment. Since the displacement at the top is $u=\theta\ell$ and the corresponding force is $W=M/\ell$, the elastic stiffness of the system comes out to be:

$$k = k_\theta / \ell^2 \quad (04)$$

Representing the hysteretic constitutive law of the spring by the classical endochronic model of Ref. [11], the first order equation of motion can be written

$$m \ddot{\theta} \ell + c \dot{\theta} \ell + \alpha k_\theta \theta / \ell + (1-\alpha)k_\theta z / \ell = -m a_g \quad (05)$$

where c is the damping term, α is the hardening ratio and z is the auxiliary variable by which the hysteretic component is expressed. The hardening ratio must be at least 3 or 4% in order to obtain satisfactory displacements estimates in classical equivalent linearization. The external excitation is here provided by the horizontal support-acceleration a_g .

The resulting linearized constitutive law is:

$$\dot{z} = C \dot{\theta} + H z \quad (06)$$

Introduction of the second order geometric effects leads to add to Eq. (05) the term $[-mg\theta \ell / \ell]$

$$m\ddot{\theta} \ell + c\dot{\theta} \ell + (\alpha k_\theta / \ell - mg)\theta + (1-\alpha)k_\theta z / \ell = -m a_g \quad (07)$$

The static elastic equilibrium is stable for

$$mg\ell < k_\theta \quad (08)$$

i.e.

$$\ell < k\ell^2/mg \quad (09)$$

From Eq. (09) one finds

$$\ell > \ell_c = g/\omega^2 \quad (10)$$

where, as usual, $\omega^2 = k/m$. However, since $\alpha < 1$, the coefficient of θ in Eq. (07) can become negative before instability occurs and, hence, can assume values close to zero. This situation has been shown to give rise to indeterminate displacements in Ref. [11] and this prevent one from extending the simpler procedure to the analysis of problems with significant second-order geometrical effects. The example of the next section will quantify this lack of accuracy.

By contrast, the approach which takes into account the constitutive laws of all the regions where inelastic deformation may occur is still working even when geometrical non-linearities are not negligibles. For this purpose, the

geometrical stiffness matrix must be added to the elastic stiffness matrix of each structural element [8][12].

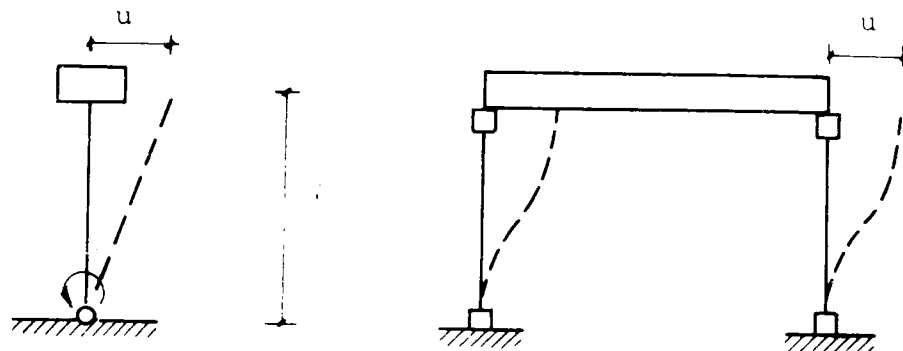


Figure 1 - a) The single-degree-of-freedom system for which the equation of motion is written in order to underline the inconsistency of the results achieved by stochastic equivalent linearization when second order geometrical effects are considered. b) Plane frame idealization with potential plastic hinges: no inconsistency arises in this case.

4. A NUMERICAL EXAMPLE

Consider a unit-mass oscillator with circular frequency $\omega = (1.5) \cdot (2\pi)$ rad/sec, damping $c = 2 \beta \omega$ with $\beta = .10$, yielding displacement $u_y = (.3) \cdot (2.54)$ cm and hardening ratio $\alpha = .25$ [11]. The associated critical length (Eq. (10)) is $l_c = (4.34) \cdot (2.54)$ cm.

Let the stochastic excitation a_g be a white-noise whose intensity is such that the resulting peak acceleration of a time history of duration 4sec is $.2g$. ($G_0 = 5.11 \cdot (2.54)^2 \text{ cm}^2/\text{s}^3$)

In Ref. [13] the following results were obtained for the variances of u and du/dt : $(.083) \cdot (2.54)^2 \text{ cm}^2$ and $(4.56) \cdot (2.54)^2 \text{ cm}^2/\text{s}^2$. Moreover the linearization coefficients were $C = .77$ and $H = -2.75$.

These results were checked by Eq. (05) obtaining the values summarized in Table I. The variability of the linearization coefficient H is due to the convergence criterion of the solving iterative procedure. The term $\text{Cov}[\dot{u}z]$ gives a measure of the energy dissipated in the hysteretic spring.

Table II provides the results of the same set of analyses but obtained making use of Eq. (07) instead of Eq. (05). This means that the second order geometrical effects are taken into account by the simple idealization of Figure 1a). The analysis of Table II shows the progressive decrease of C and $|H|$ as l decreases. Also, as l decreases, the variance of z ($\text{Var}[z]$) and

the measure of the dissipated energy $\text{Cov}[\dot{\theta}z]$ increase. The variance of the rotation rate $\text{Var}[\dot{\theta}]$ is characterized by a general decrease with respect to the corresponding values calculated without second order geometrical effects. Moreover, if one plots the values of $\text{Var}[\dot{\theta}]$ in Table II versus l , a peak is found at $l = 7 \cdot (2.54)$ cm. Note that the actual critical length l_{ca} is the lower values of l for which it is not possible to obtain convergence. It was found to be $l = 6 \cdot (2.54)$, i.e. higher than the critical length l_c in Eq. (09). Its evaluation requires the introduction of a stability criterion. From Table II the change of sign of the derivative $d(\text{Var}[\dot{\theta}])/dl$ seems to be a possible candidate for this stability criterion.

Table I - Properties of the response of the oscillator considered in the numerical example. The geometrical nonlinearities are neglected. Lengths in inches.

Length of the column	$\text{Var}[\theta]$	$\text{Var}[z]$	$\text{Var}[\dot{\theta}]$	$\text{Cov}[\dot{\theta}z]$	C	H
20	.00021	.000079	.0114	.00028	.77	-2.75
17.39	.00027	.000103	.0151	.00036	.77	-2.75
10	.00083	.00032	.0461	.0011	.77	-2.66
7	.00169	.00064	.093	.0023	.77	-2.73
6.5	.00197	.00074	.108	.0026	.77	-2.73
6	.00206	.00078	.113	.0028	.77	-2.73

Table II - Properties of the response of the oscillator considered in the numerical example. The geometrical nonlinearities are included. Lengths in inches.

Length of the column	$\text{Var}[\theta]$	$\text{Var}[z]$	$\text{Var}[\dot{\theta}]$	$\text{Cov}[\dot{\theta}z]$	C	H
20	.00081	.000088	.0101	.00031	.75	-2.68
17.49	?	.000119	.0132	.00042	-	-
10	.0023	.00041	.0340	.0014	.72	-2.53
7	.00164	.0010	.048	.0035	.66	-2.30
6.5	.0015	.0013	.044	.0044	.63	-2.17
6	.0013	.0014	.039	.0046	.61	-2.08

Inaccuracy problems arise when attention is focused on the rotation θ (i.e. the displacement $u=\theta\ell$). It is worth noting, in fact, that when the coefficient of θ in Eq. (07) becomes zero ($\ell = (17.39) \cdot (2.54)$ cm), no solution can be found. Moreover, in the neighbourhood of this length the rotation is overestimated according with the effect pointed out in Ref. [11]. For instance, the variance of θ for $\ell = 10 \cdot (2.54)$ cm is almost twice the one for $\ell = 7 \cdot (2.54)$ cm! This situation makes unreliable the model of Fig 1a), since θ is just the variable which governs the second order geometrical effects.

Table III - Properties of the response of the frame in Figure 1b). The geometrical effects are neglected. Lengths in inches.

Hardening ratio	Mass	Var[u]	Var[\dot{u}]	C _{min}	H _{min}
5%	.168	.11	7.13	.506	-51.3
10%	.168	.10	7.53	.501	-92.5
12.5%	.168	.10	7.76	.500	-109.7
15%	.168	.10	8.00	.498	-109.7
20%	.168	.11	9.32	.495	-199.3

Table IV - Properties of the response of the frame in Figure 1b). The geometrical effects are included. Lengths in inches.

Hardening ratio	Mass	Var[u]	Var[\dot{u}]	C _{min}	H _{min}
10%	.168	.111	7.43	.503	-91.9
10%	.210	.171	7.64	.503	-103.1

The previous analyses have been partially repeated over the frame of Fig. 1b). Its height is $H=300$ cm and its length $L=550$ cm. The mass is concentrated at the girder level: its original value is $.168 \text{ t} \cdot \text{s}^2/\text{cm}$. The stiffnesses of the elements are selected in such a way that the same equations of motion are written in the elastic field. The constitutive law is introduced at the six end-sections of the three beam-elements. The yielding moment in the plastic hinges of the columns is selected as $ku_y^2/4$. The hardening ratio ϵ of these bending moment-rotation relationships should be selected to provide the global hardening of 25% considered above. For this purpose the following values of ϵ were introduced: 5%, 10%, 12.5%, 15% and 20%. Table III summarizes the results achieved.

The comparison of the results of Table III with the ones of Table I shows that both displacements and velocities are underestimated by the model of Fig. 1a). Moreover, $\text{Var}[u]$ and $\text{Var}[\dot{u}]$ are unsensitive to changes in the value of the hardening ratio ξ . This justifies the selection of $\xi = 10\%$ as the basis of the further analyses developed in view of a short comparison with the results of Table II.

Geometrical second-order effects are investigated by adding the corresponding geometric stiffness matrix to the elastic stiffness matrices of the columns. This has been made for two values of the supported mass: .168 and .210 t s²/cm, respectively. The results are given in Table IV.

In this case no problem arises when the stochastic equivalent linearization algorithm is used. The hysteretic constitutive law, in fact, does not involve directly the horizontal displacement u and, hence, the solving procedure is no longer sensitive to the amount of the second-order geometrical effects as it occurs for the analyses of Table II.

5. CONCLUSIONS

Although stochastic equivalent linearization is more and more adopted in practical engineering applications, there are some circumstances that prevent one from implementing its simpler form in automatic analysis procedures. This paper has emphasized the inaccuracy of the results one obtains in particular situations when second order geometrical effects are included.

However, this lack of accuracy can be completely avoided by using frame idealizations more sophisticated [9], whose greater computational effort can be strongly reduced by adopting frequency domain solution algorithms [10].

ACKNOWLEDGEMENT

The financial support of the Ministry of Public Education (MPI) is here acknowledged.

REFERENCES

1. P. SPANOS 1981 Applied Mechanics Reviews, 34, 1, 1-8. Stochastic Linearization in Structural Dynamics.
2. Y.K. LIN, F. KOZIN, Y.K. WEN, F. CASCIATI, S.I. SCHUELLER, A. DER KIUREGHIAN, O. DITLEVSEN and F.H. VANMARCKE 1986 Structural Safety, 3, 167-194. Methods of Stochastic Structural Dynamics.
3. F. CASCIATI and L. FARAVELLI 1988 Research Studies Press, Letchworth. Fragility Analysis of Complex Structural Systems.
4. Y.K. WEN, Y.J. PARK and A.H-S. ANG 1986 in F. Casciati and L. Faravelli (eds.) Methods of Stochastic Structural Mechanics, SEAG, Pavia. Random Vibration of Hysteretic Systems under Bi-directional Ground Motions. (see also Earth. Eng. & Struct. Dyn., 14, 543-557)
5. Y.J. PARK and A.M. REINHORN 1986 Proc 3rd US Nat. Conf. on Earth. Eng., Charleston, 991-1002. Earthquake Response of Multistory Buildings under Stochastic Biaxial Ground Motions.
6. F. CASCIATI and L. FARAVELLI 1987 Proc. 9th SMIRT Confer., Lausanne, vol. M, 453-458. Stochastic Equivalent Linearization in 3-D Hysteretic Frames.
7. F. CASCIATI and L. FARAVELLI 1988 accepted for publication in the Journal of Engineering Mechanics, Proc. ASCE. Stochastic Equivalent Linearization for 3D Frames.
8. R.W. CLOUGH and J. PENZIEN 1975 McGraw Hill. Dynamics of Structures
9. F. CASCIATI and L. FARAVELLI 1985 Nuclear Engineering and Design, 90, 341-356. Methods of Nonlinear Stochastic Dynamics for the Assessment of Structural Fragility.
10. M.P. SINGH, G. MALDONADO, R. HELLER and L. FARAVELLI 1987 Proc. IUTAM Symposium on Nonlinear Stochastic Dynamic Engineering Systems. Modal Analysis of Nonlinear Hysteretic Structures for Seismic Motions.
11. F. CASCIATI and L. FARAVELLI 1986 in F. Casciati and L. Faravelli (eds.) Methods of Stochastic Structural Mechanics, SEAG, Pavia. Non Linear Stochastic Dynamics by Equivalent Linearization.

12. F. CASCIATI and L. FARAVELLI 1988 accepted for publication in Res Mechanica. Hysteretic 3-D Frames under Stochastic Excitation
13. F. CASCIATI 1987 Proc. ICASP 5, Vancouver, 2, 1165-1172. Non-Linear Stochastic Dynamics of Large Structural Systems by Equivalent Linearization

APPENDIX - Deriving Eq.(01)

The equations of motion of the frame are

$$\ddot{\underline{u}} + \underline{m}^{-1} \underline{c} \dot{\underline{u}} + \underline{m}^{-1} \underline{D} \underline{V} - \underline{m}^{-1} \underline{W}(t) = 0 \quad (A1)$$

with \underline{m} denoting the mass matrix, \underline{c} the damping matrix and $\underline{W}(t)$ the external dynamic excitation. \underline{u} is the vector of the inter-storey displacements, \underline{V} is the vector of the restoring forces of the single storeys and \underline{D} is an appropriate matrix. Each V_j is proportional to the inter-storey drift u_j in the linear case. More generally one writes

$$V_j = V_j(u_j, \dot{u}_j) \quad (A2)$$

where $V_j(\cdot, \cdot)$ denotes a given non-linear function. It is convenient to write

$$V_j = A_j z_j + E_j u_j \quad (A3)$$

and

$$\dot{z}_j = a_3 \dot{u}_j - a_4 z_j |\dot{u}_j| |z_j|^{a_5-1} - a_5 \dot{u}_j |z_j|^{a_6} \quad (A4)$$

where z is an auxiliary variable and the quantities a_1, \dots, a_6 are the parameters of the hysteretic model.

Eqs. (A1), (A3) and (A4) form the non-linear solving system of equations. Since the non-linearity is only in Eq. (A4), it is sufficient to write it in the form:

$$\dot{z}_j = C_j \dot{u}_j + H_j z_j \quad (A5)$$

for obtaining, with Eqs. (A1) and (A3), a linear system of equations. After elimination of \underline{V} , it leads to Eq. (01).

In Eq. (A5) C_j and H_j are the linearization coefficients that, for Gaussian excitation $\underline{W}(t)$, can be written as known functions of the variances of z_j and v_j and the coefficient of correlation of these variables [9][12][13].

The constitutive law, generally, is not given for the storey but, rather, at the single point or section of the frame. In this case Eq. (A4) (and hence Eq. (A5)) is written locally and relates the local inelastic deformation with its static counterpart. The storey restoring force V_j in Eq. (A1) has therefore a more complicate expression in terms of these new kinematic and static variables. Nevertheless, simple matrix algebra leads again to write Eq. (01). The reader is referred to Refs. [9] and [12] for the details.

10. PARAMETRIC EXCITATION

RECENT ADVANCES IN VIBRATION ANALYSIS OF SYSTEMS WITH RANDOM PARAMETRIC EXCITATIONS

C.W.S. To*

Department of Mechanical engineering
The University of Western Ontario
London, Ontario, Canada, N6A 5B9

ABSTRACT

In this article systems subjected to random parametric excitations are considered. Attention is paid on publications appeared in the literature between 1981 and 1987. Those published prior to 1981 are not considered here as they had already been reviewed elsewhere. Both quantitative and qualitative aspects of the analysis are included. The quantitative analysis techniques reviewed are the Fokker-Planck equation approaches, methods of stochastic averaging, truncated hierarchy techniques, and various other methods.

1. INTRODUCTION

For safety and economic reasons modern mechanical and structural systems have to be designed to withstand various intensive excitations. The diversity and uncertainty of these excitations make it a necessity to treat them as random processes. Among them are random parametric excitations.

There are many categories of the differential equations governing the dynamic behaviour of random parametrically excited systems. Let us consider a general equation of the form:

$$\ddot{\underline{X}}(t) + f(\underline{X}(t), \dot{\underline{X}}(t), t) = \underline{Y}(t) \quad (1)$$

with the initial condition $\underline{X}(0) = \underline{X}_0$ and $\dot{\underline{X}}(0) = \dot{\underline{X}}_0$, where $\underline{X}(t)$ is an n -dimensional displacement vector (the solution process) and f is a time-dependent vector of order n . If $\underline{Y}(t)$ is also a random process then the equation models a system that is subject to both random parametric excitation and non-parametric excitation, $\underline{Y}(t)$. The latter form of excitation is usually referred to as an external excitation.

The solution of equation (1) is usually very difficult. In general only approximate solutions are obtainable in most cases for the response process [1].

In this review article systems subjected to parametric excitations are considered. Our attention is on systems investigated between 1981 and 1987. Systems studied prior to 1981 are not included here as they had already been reviewed by Ibrahim [2], Arnold and Kliemann [3], Ibrahim [4], and Kozin [5].

Essentially, there are two directions of work reported in the literature. The main thrust of one direction is concerned with the prediction of response of the systems. Techniques used are regarded as

*Associate Professor and NSERC Research Fellow

quantitative. These are the Fokker-Planck equation (FPE) approaches, methods of stochastic averaging, truncated hierarchy techniques, and various other methods. The other direction of development is concerned with the stability analysis of the systems. Techniques used in this direction are referred to as qualitative. These include movement and Lyapunov stabilities. Where an explicit representation of the solution process is possible the stochastic stability definitions reviewed include: stability in the mean, asymptotical stability in the mean, mean square stability, and asymptotically mean square stability.

2. FOKKER-PLANCK EQUATION (FPE) APPROACHES

This method is applicable to systems which can be represented by a set of Ito differential equations of the form:

$$d\tilde{X}(t) = f(\tilde{X}(t), t)dt + G(\tilde{X}(t), t)d\tilde{B}(t) \quad (2)$$

$$(\tilde{X}(t_0) = \tilde{X}_0, t \geq t_0)$$

where $d\tilde{B}(t) = \tilde{W}(t)dt$ is an m -dimensional vector stochastic process whose components are Gaussian white noise while \tilde{B} is the corresponding Brownian motion process. $G(\tilde{X}(t), t)$, known as diffusion matrix, is an $n \times m$ matrix function and \tilde{X}_0 is independent of $\tilde{W}(t)$. $f(\tilde{X}(t), t)$, known as drift vector, is a vector function of the solution process $\tilde{X}(t)$ and time and can either be linear or nonlinear. Of course, \tilde{X} in (2) is different from that in (1). Here, \tilde{X} is the state vector while \tilde{X} that in (1) is the displacement vector. The Fokker-Planck equation (FPE) corresponding to equation (2) is however given by:

$$\frac{\partial p(\tilde{X}, t | \tilde{X}_0, t_0)}{\partial t} = - \sum_{j=1}^n \frac{\partial}{\partial X_j} [f_j(\tilde{X}, t)p] + \sum_{i,j=1}^n \frac{\partial^2}{\partial X_i \partial X_j} [(GDG^T)_{ij}p] \quad (3)$$

where D is the white noise intensity matrix. Another form of FPE based on the statistical properties of continuous Markov processes is the following parabolic partial differential equation:

$$\frac{\partial p(\tilde{X}, t | \tilde{X}_0, t_0)}{\partial t} = - \sum_{j=1}^n \frac{\partial}{\partial X_j} [\alpha_j(\tilde{X}, t)p] + \frac{1}{2} \sum_{i,j=1}^n \frac{\partial^2}{\partial X_i \partial X_j} [\alpha_{ij}(\tilde{X}, t)p] \quad (4)$$

where $\alpha_j(\tilde{X}, t)$ and $\alpha_{ij}(\tilde{X}, t)$ are the derivative moments which can be derived by limit operations applied directly to the equations of motion. Unfortunately, equations (3) and (4) give different results for the problem of random parametric excitation although they agree for externally excited linear systems. This paradox in the different forms of the Fokker-Planck equation has been examined by Gray and Caughey [6] and Mortensen [7]. References [6] and [7] agree that when $G(\tilde{X}(t), t)$ in equation (2) above is not a function of $\tilde{X}(t)$ the solutions to (3) and (4) are identical.

It is important to point out that in Section 5.2.1 of [4] a different and incorrect explanation was given. It gave the difference between the white noise $w(t)$ and the physical wide band excitation $\xi(t)$ as the origin of the problem. In other words, what was suggested was that if $\xi(t) = w(t)$ the Wong and Zakai [9] correction term was not

necessary. This is not true as it is in contradiction to the finding in [6]. To see why let us consider the following equation of motion for a single-degree-of-freedom (SDOF) system subjected to both parametric and non-parametric white noise excitations:

$$\ddot{x}(t) + 2\xi\omega_n [1 + w(t)]\dot{x}(t) + [a_1 + a_2w(t)]x(t) = w(t) \quad (5)$$

where, for simplicity, a_1 and a_2 are constant parameters and the rest of the symbols have their usual meaning. The corresponding Ito's equation is

$$\frac{dx(t)}{dt} = \begin{Bmatrix} \dot{x}_2 \\ -a_1x_1(t) - 2\xi\omega_n x_2(t) \end{Bmatrix} + \begin{Bmatrix} 0 & 0 \\ 0 & 1 - a_2x_1(t) - 2\xi\omega_n x_2(t) \end{Bmatrix} \begin{Bmatrix} 0 \\ w(t) \end{Bmatrix} \quad (6)$$

where $x(t) = \begin{Bmatrix} x_1(t) \\ x_2(t) \end{Bmatrix}$, and $x_2(t) = \frac{dx_1(t)}{dt}$.

Comparing equations (2) and (6) one finds that $G(x(t), t)$ is, in need, a function of $x(t)$. Therefore, the Wong-Zakai correction is required in order to enable the solution of equation (5) using the Ito's approach in agreement with that applying the Stratonovich calculus [7].

Closed form solutions of the Fokker-Planck equation are rarely obtainable. However, in many cases, it is possible to derive some moment equations, which may be algebraic or differential depending on whether the solution being sought is stationary or non-stationary, respectively. These moment equations are derived by multiplying the Fokker-Planck equation by suitable functions and integrating the resulting equation over the entire probability space. For the transition probability density given in equation (3), it can be shown that the moment equations are of the form [1]

$$\frac{d}{dt} E\{h(\tilde{X}, t)\} = \sum_{j=1}^n E\{f_j \frac{\partial h}{\partial X_j}\} + \sum_{i,j=1}^n E\{(GDG^T)_{ij} \frac{\partial^2 h}{\partial X_i \partial X_j}\} + E\{\frac{\partial h}{\partial t}\} \quad (7)$$

where $h(\tilde{X}, t)$ is an arbitrary function and $E\{\cdot\}$ designates ensemble average. From equation (7), the moment equation for any order can be obtained by choosing the appropriate function $h(\tilde{X}, t)$.

For linear systems with white noise coefficients the moment equations are uncoupled and so they are easy to handle. In cases where there is non-linearity, the moment equations become coupled with moments of higher orders. The system of moment equations thus form a set of the so-called infinite hierarchy equations [1] and some closure techniques have to be applied to truncate the infinite hierarchy. A number of these closure schemes have been proposed in the literature and shall be reviewed in a subsequent section.

Dimentberg [9] obtained an exact analytical solution of the FPE for a particular second order system

$$\ddot{X} + 2\alpha\dot{X} [1 + \eta(t)] + \beta_1\dot{X}(X^2 + \dot{X}^2/\Omega^2) + \Omega^2X[1 + \xi(t)] = r(t) \quad (8)$$

where $\xi(t)$, $\eta(t)$, $r(t)$ are statistically independent stationary Gaussian processes of the white noise type with respective intensities D_ξ , D_η and D_r . The stationary joint probability density function (pdf) was found to be governed by the equation:

$$y \frac{\partial p}{\partial x} = \Omega^2 x \frac{\partial p}{\partial y} + \frac{\partial}{\partial y} [(2\alpha - 2\alpha^2 D_\eta)y] + \frac{1}{2} \frac{\partial^2}{\partial y^2} [(4\alpha^2 y^2 D_\eta + \Omega^4 x^2 D_\xi + D_r)p]$$

and for the special case when

$$\Omega^2 D_\xi = 4\alpha^2 D_\eta$$

It was pointed out that in a stochastic system that is stable with probability one, there can be no oscillation in the absence of external excitations.

Exact solutions of the Fokker-Planck-Kolmogorov (FPK) equation for the stationary joint probability density (jpd) of the state variables for certain multi-dimensional dynamic systems [10] have also been provided.

Other multi-degree-of-freedom (MDOF) systems with parametric and non-parametric random excitations were considered by Lin and Shih [11], To [12], and To and Orisamolu [13]. In [12, 13] equation (7) was used and the corresponding second moment equations were solved with the fifth-order Runge-Kutta algorithm. In [13] a bimodal approach was adopted for response moments of discretized plates with geometrical non-linearity of small deformation. Non-stationary random excitations and responses were included. The structures were modelled with more than 200 DOF.

3. METHODS OF STOCHASTIC AVERAGING

The original stochastic averaging method was introduced by Stratonovich [14]. It may be viewed as an extension of the deterministic averaging procedure of Bogoliubov and Mitropol'sky to the field of random differential equations. This method is applicable to systems of lightly damped and subject to broad-band random excitations.

It entails the introduction of amplitude and phase angle transformations of the form:

$$X(t) = a(t) \cos(\omega_0 t + \Phi) \quad (9)$$

where the amplitude envelope process, $a(t)$, and the phase process, Φ , are slowly varying with respect to time t .

Dimentberg [15] applied the moment equations and stochastic averaging technique to linear systems with random parametric excitation.

Dimentberg et al. [16] employed the averaging method to investigate the stochastic oscillations of a non-linear second order system that is simultaneously excited by periodic and broadband random parametric excitations:

$$\ddot{x} + (2\delta + bx^2 + \beta\dot{x}^2)\dot{x} + \Omega^2 [1 + r \sin \nu t + \xi(t)]x = 0 \quad (10)$$

where $\xi(t)$ is a stationary centred broadband random process of known

spectral density. Equation (10) models the oscillations of a helicopter rotor blade with due allowance for horizontal turbulence components. This is a more general model than the one given by Lin et al. [17, 18].

Prussing [19] used the Wong and Zakai correction with the stochastic averaging method to illustrate that an unstable deterministic system can indeed be stabilized by parametric white noise contrary to earlier claims by some authors. This fact was first reported and verified with simulation by Mitchell and Kozin [20].

Schmidt [21] analyzed systems with quadratic and cubic restoring forces, and cubic damping forces, excited by white noise parametric loading. The analysis included a second order averaging accounting for the influence of non-linear stiffness contributions. Roberts [22] employed the stochastic averaging method to evaluate the uncoupled roll motion of a ship in random sea waves. The analysis included non-white restoring moment and the effect of non-linear damping. The parametric excitation in the governing equation of motion was the pitch angle which was assumed to be a stationary process. Ibrahim [23] studied the simultaneous occurrence of self-excited and random parametric vibrations in water lubricated bearings of submarines.

Ibrahim and Soundararajan [24] also used the Stratonovitch stochastic averaging procedure (while incorporating the Wong and Zakai correction term) to investigate the non-linear liquid free surface oscillations of a partially filled container subject to random parametric excitations. It was stated that a comparison with the experimental results of Daizeil revealed that the results from the averaging procedure gave better correlation than those from the Fokker-Planck equation.

Stochastic averaging of the response energy envelope was considered by Zhu [25, 26] to provide a mathematical basis in the Stratonovich sense that the Markov property is conserved when the odd monotonically increasing continuous function representing the system elastic restoring force is non-linear and the excitation is white.

The response of a string to random parametric excitation was studied by Chen and Huang [27]. They showed that the introduction of non-linear damping brought the originally unstable string into a bounded stable limit cycle. The standard stochastic averaging method was used by Dimentberg [28] to deal with a linear oscillator with external and parametric excitations.

Up to this point the methods reviewed in this section are concerned with SDOF systems. Very limited number of publications addresses MDOF non-linear systems subjected to parametric excitations. Noteworthy is the work of Schmidt and Schulz [29] in which the stochastic averaging method was applied to evaluate the jpd of a non-linear two-degree-of-freedom (2 DOF) system. Results were considered incomplete as the constant of integration was difficult to determine. Recently, Lin [30] presented a physical interpretation of the stochastic averaging method. It was pointed out that Stratonovich's procedure was not suitable to problems with periodic variation of some coefficients in the governing equations as they would be eliminated by time-averaging. Examples are rotor blades of a helicopter [17, 18] or a wind turbine [31]. It is also not suitable for problems with the excitation treated as a uniformly modulated process [30]. Roberts and Spanos [32] reviewed results

obtained by applying the method of stochastic averaging to random vibration problems. In a recent work Bruchner and Lin [33] had extended the stochastic averaging procedure of Ariaratnam and Tam [34], which was originally employed to analyze linear systems under random parametric excitations, to non-linear systems under both stationary random parametric and non-parametric excitations. The accuracy of the procedure was tested in two examples for which exact solutions are known. The main advantage of the method for MDOF systems is that fewer equations need to be solved when the infinite hierarchy is truncated.

4. TRUNCATED HIERARCHY TECHNIQUES

Consider equation (1). If it describes linear systems under parametric and non-parametric white noise excitations the associated moment equations are a set of finite and uncoupled deterministic differential equations whose solutions are readily obtained by procedure of calculus. If the excitations are uniformly modulated white noise processes the associated moment equations can be integrated by some numerical scheme to provide the solutions. However, when the systems are non-linear the moment equations are coupled and form an infinite hierarchy set. Exact solutions then are infeasible and the application of approximate techniques become inevitable. A common approximation is the truncation of this higher order moment(s) by means of several ad-hoc procedures. To obtain a finite set of equations for which solutions can be obtained, it is required that any truncation scheme should at least preserve the moment properties for it to be valid.

The infinite hierarchy equations of a set of first order non-linear Ito's equations may be written as

$$\frac{dM_i}{dt} = F_i(M_1, M_2, \dots, M_i, M_{i+1}, \dots) \quad (11)$$

where $i = 1, 2, \dots$ and $M_i(t=0) = 0$. M_i are the exact solutions of the infinite set. All closure schemes reduce the system described by equation (11) to a finite set of the form:

$$\frac{dm_i}{dt} = G_i(m_1, m_2, \dots, m_N) \quad (12)$$

where $i=1, 2, \dots, N$ and $m_i(t=0) = b_i$. Here m_i are the approximate solutions after truncation. A "good" truncation scheme is one that minimizes the error $(M_i - m_i)$ while preserving the moment properties. Bellman et al. [35, 36] establishes two lemmas that guarantee the preservation of moment properties.

4.1 Gaussian Closure Schemes

These are procedures in which the response (or a certain function of the response) is approximated by a Gaussian distribution so that all cumulants of order greater than two vanish identically. This leads to moments of order greater than two being expressed in terms of the first and second moments. These methods are alternatively referred to as the methods of 'cumulant discard'. Clearly, these methods are inadequate when the system response is very much different from being Gaussian.

which is likely to be the case when parametric random excitations are presented and the system non-linearity is not small.

Iyengar and Dash [37] have shown that where the excitation is non-Gaussian, the technique leads to the best estimate in a minimum mean square error sense. Wu and Lin [38] have also shown that the accuracy of the computed second moments can be improved by retaining the cumulants up to the fourth order. Ibrahim and associates have also used the scheme to solve various problems [24, 39-41]. In [40] a two DOF linear structure with parametric excitation was considered. The term associated with the parametric excitation was disregarded when the normal mode transformation was used by assuming that the discrete mass at the free end was locked. No physical justification or heuristic reason was given. It should be pointed out that the techniques in [39-41] are only applicable to systems with small non-linearities.

4.2 Non-Gaussian Schemes

Ibrahim and associates [39-42] have also applied a non-Gaussian closure scheme to deal with various problems. In the non-Gaussian closure scheme, with the fifth order moment terms retained in the solution for a two DOF system, 69 equations were solved numerically using the fifth and sixth order Runge-Kutta algorithms available in the International Mathematical and Statistical Library (IMSL). Clearly, for systems with many DOF the procedure is computationally infeasible. Moreover, in his work [43] Crandall pointed out that a pitfall that might be encountered in applying the method of non-Gaussian closure with Gram-Charlier density was that the resulting non-linear algebraic equations might have no real solution.

5. OTHER METHODS

Szopa [44] employed a method based on the application of a stochastic Volterra integral equation of the second kind to study the probabilistic characteristics of the response of a multi-degree-of-freedom system. Numerical calculations concerning the variance of the response of a two-degree-of-freedom system were presented.

Huang [45] used the spectral method to investigate the dynamic behaviour of structures with periodic random parameters. By expanding the spatial periodic random functions in Fourier series to obtain expressions for correlation functions, he solved for the natural frequencies and normal modes and was able to estimate their mean values and variances from the random Fourier coefficients. It is obvious that the accuracy of this method is limited, among other things, by the point of truncation of the Fourier series.

Fuh et al. [46] determined numerically the response statistics of coupled torsion-flapping rotor blade to atmospheric turbulence. Parametric and external excitations were considered.

Recently, weakly non-linear systems excited by independent, stationary and Gaussian parametric and non-parametric disturbances were studied by Menh [47], using the successively approximation technique. Young and Chang [48] used the method of equivalent external excitation to predict the stationary variances of the states of non-linear oscillators

disturbed by both stochastic parametric and external excitations. Some exact solutions and Monte Carlo simulations were compared with the predicted results. The method, though does not require the probability densities of the stationary states to be jointly Gaussian, does hinge on the validity of using the equivalent external excitation to maintain the same propagation of moments up to the second order. Brückner and Lin [49] presented a generalized equivalent linearization method that can handle non-linear SDOF and MDOF systems subjected to both parametric and external random white noise excitations. While it is a powerful method for statistical moments it cannot be employed to study stochastic stability or bifurcation problems. It was illustrated that for a non-linear SDOF oscillator excited by parametric and external, independent Gaussian white noises 27 non-linear differential equations had to be integrated numerically. Therefore, for systems with a large number of DOF it would be infeasible computationally.

In another interesting development Hernandez-Machado and San Miguel [50] had presented an approximate correlation function of a non-linear non-stationary non-Markovian process. The non-Markovian processes studied were defined by the Langevin-type stochastic differential equations. The method can be applied to non-linear MDOF systems subjected to both non-Markovian parametric and external loadings. This method has been employed by Kapitaniak [51] to determine the solution and stability conditions of Hill's equation with natural frequency and damping coefficients modelled as Ornstein-Uhlenbeck noise.

6. STOCHASTIC STABILITY METHODS

There are various established stability concepts for the analysis of deterministic responses. There are even more stochastic stability concepts for the analysis of systems involved with stochastic responses as there are four different modes of convergence of probability theory. These are convergence in distribution, convergence in probability, convergence in mean square and almost sure convergence [1]. Thus, there are at least four times as many concepts of stochastic stability as for the deterministic problem. However, not all of the possible definitions of stochastic stability are of interest because, in a particular application, they may be too weak to be of any practical significance [52].

The bulk of the studies carried out in the past are concerned with moment stabilities. This involves with the generation or estimation of response moments so that information concerning the requirements for stability can be obtained. Methods for response moment generation or estimation have already been dealt with in the foregoing sections and therefore are not repeated here.

Another area of studies involves the concept of Lyapunov stability. This is based on the Lyapunov direct method. The latter can be regarded as an extension and generalization of the energy method of mechanics. It seeks to determine the system stability conditions without actually carrying out the solution of the differential equations. To achieve this, a scalar function satisfying certain properties is devised for the system. Such a scalar function is defined in the entire phase space and its total time derivative is evaluated along a trajectory of the system. With the information of this function, known as the Lyapunov function,

the stability of the equilibrium (or null) solution is investigated. The different forms of definitions of stochastic Lyapunov stability are obtained from their deterministic counterparts by simply changing the modes of convergence appropriately. Because of the many definitions of stochastic stability, the existence of a vast literature, and the space available in this paper we can only touch on a limited number of significant results and techniques. Interested readers are referred to reviews in [2-5, 53]. [53] is a shorter version of [5].

Danilin and Yahdykin [54] studied the conditions of exponential stability and stability in probability of the equilibrium solution of stochastic difference equations with Markov parametric excitations. Chow and Chiou [55] combined the analysis of Lyubarski and Robotnikov [56], and Kozin [57] to derive conditions for the mean square and almost sure asymptotic stability in terms of the size and the correlation length of a bounded random parametric excitation. Geman [58] presented a technique based on the law of large numbers to obtain the almost sure stability condition of a set of non-linear differential equations coupled through random coefficients. Approximate conditions for almost sure stability of the equilibrium state of linear systems were studied by Ahmadi and Glockner [59]. Auslender and Mil'shtein [60] introduced the "Lyapunov index" to examine the stochastic stability of linear systems of the Ito and Stratonovich types. Sufficient stability conditions for asymptotic stability, almost sure asymptotic stability, and uniform stochastic stability for cylindrical shells in terms of the intensities of the radial and axial loads and the damping coefficient were investigated by Kurnik and Tylikowski [61], and Tylikowski [62]. The necessary and sufficient conditions for almost sure asymptotic stability of the planar response of a non-linear string under a narrow-band Gauss-Markov process were determined by Richard and Anand [63] using a combination of perturbation method, variational calculus and a technique based on the generalization of Van de Pol's method.

Sufficient stability criteria for column subjected to white noise, Gaussian and general stationary random loadings were established by Ahmadi and Glockner [64]. The stability conditions for certain class of non-stationary random excitation were also discussed. However, it should be noted that if the system is subjected to non-stationary random excitations and has positive damping the stability question does not arise.

The dynamic stability of elastic frames subjected to an earthquake Gaussian white noise was considered by Abdel-Rahman and Ahmadi [65]. In this work different necessary and sufficient conditions for the mean-square stability of equilibrium were developed. Computed results for SDOF and MDOF structures were compared with those obtained by digital simulation technique and the existing almost sure stability criteria. It was concluded that the simulation results suggested that the mean-square stability was more reliable when compared with the almost sure stability. Lin and associates [19, 66-68] investigated various concepts of Stochastic stability in rotor dynamics. Phillis [69] studied the entropy stability of continuous dynamic systems. Potapov [70] considered the stability of structural elements subjected to stationary loads. Semenov and Smirnov [71] investigated the stability of linear stochastic systems with periodically non-stationary parametric excitation. Narayanan [72] examined the stochastic stability of fluid conveying tubes. Watt and Barr [73] investigated the stability boundary for pseudo-random

parametric excitation of a linear oscillator.

Recently, as pointed out in the last section, stability conditions of Hill's equation excited by Ornstein-Uhlenbeck noise were obtained by Kapitaniak [51]. An earlier and similar problem was investigated by Kliemann and Rümelin [74]. Here similar means that the parametric excitation is the Ornstein-Uhlenbeck Gaussian process. As noted in [5], further clarification of the result in [74] would be desirable.

In a recent article Wiens and Sinha [75] applied the Lyapunov direct method to discrete systems. They presented a method for constructing the Lyapunov function that is specially suitable for the study of the almost sure asymptotic stability of the systems.

Finally the excellent work on the exact stability region of systems with jump process coefficients by Loparo and Blankenship [76] should be included here.

7. CONCLUDING REMARKS

Over a period of 7 years some 60 papers have appeared in the open literature. This reflects a great interest in systems disturbed by random parametric excitations. However, more remains to be studied for MDOF non-linear systems excited by parametric non-stationary processes.

About 95% of the publications are based on Markovian properties of the excitation processes. From the practical standpoint non-Markovian excitation processes such as the Ornstein-Uhlenbeck process are likely to receive more attention in the future. The lack of reliable experimental and digital computer simulation data will certainly motivate researchers to provide them in the near future. Moreover, computer symbolic manipulation software packages, such as Macsyma are likely to play a role in promoting the area of vibration of linear and weakly nonlinearly systems excited by random parametric disturbances.

Finally, it should be remarked that bifurcation problems of nonlinear systems to random parametric excitations have recently been investigated [77-78].

ACKNOWLEDGEMENT

Support from the Natural Sciences and Engineering Research Council (NSERC) of Canada under Grant No. A5704 and comments as well as suggestions from the two referees are gratefully acknowledged.

REFERENCES

1. Soong, T.T., Random Differential Equations in Science and Engineering, Academic Press Inc. (1973).
2. Ibrahim R.A. "Parametric Vibration Part VI: Stochastic Problems (2)", Shock and Vibration Digest, 13, pp. 23-25 (1981).
3. Arnold, L. and Klieman, W., "Qualitative Theory of Stochastic Systems", Probab. Analysis and Related Topics (Edited by Bharucha-Reid, A.H.), Academic Press, 3 (1981).
4. Ibrahim, R.A., Parametric Random Vibration, Research Studies Press Ltd., England (1985).
5. Kozin, F., "Some Results on Stability of Stochastic Dynamical Systems", Random Vibration - Status and Recent Developments (Edited by Elishakoff, I. and Lyon, R.H.), pp. 163-191 (1986).
6. Gray, A.H., Jr. and Caughey, T.K., "A Controversy in Problems Involving Random Parametric Excitation", J. Math. and Phys., 44, p. 288-296 (1965).
7. Mortensen, R.E., "Mathematical Problems of Modelling Stochastic Non-linear Dynamic System", NASA CR-1168 (1968).
8. Wong, E. and Zakai, M., "On the Relation Between Ordinary and Stochastic Equations", International Journal of Engineering Science, 3 (2), pp. 213-229 (1965).
9. Dimentberg, M.F., "An Exact Solution to a Certain Non-Linear Random Vibration Problem", International Journal of Non-Linear Mechanics, 17 (4), pp. 231-236 (1982).
10. Dimentberg, M.F., "Exact Solutions of the Fokker-Planck-Kolmogorov Equation for Certain Multidimensional Dynamic Systems", Journal of Applied Mathematics and Mechanics, 47 (4), pp. 458-460 (1983).
11. Lin, Y.K. and Shih, T.Y., "Vertical Seismic Load Effect on Building Response", ASCE Journal of Eng. Mech., 108 (EM2), pp. 331-343 (1982).
12. To, C.W.S., "Random Modal Interaction of A Two Degree-of-Freedom Structure", Proc. ASME PVP Conference, Chicago, Illinois, PVP-113 (1986).
13. To, C.W.S. and Orisamolu, I.R., "Response of Discretized Plates to Transversal and In-plane Non-stationary Random Excitations", J. Sound and Vibration, 114 (3), 481-494 (1987).
14. Stratonovich, R.L., Topics in the Theory of Random Noise, Vol. 1 and 2, Gordon and Breach, New York (1963).
15. Dimentberg, M.F., "Method of Moments in Problems of Dynamics of systems with Randomly Varying Parameters", J. Appl. Math. and Mech., 46, pp. 161-166 (1983).

16. Dimentberg, M.F., Isikov, N.E. and Model, R., "Vibration of a System with Cubic Non-linear Damping and Simultaneous Periodic and Random Parametric Excitation", *Mechanics of Solids*, 16 (6), pp. 19-21 (1981).
17. Lin, Y.K., Fujimori, Y. and Ariaratnam, S.T., "Rotor Blade Stability on Turbulent Flows - Part I", *American Institute of Aeronautics and Astronautics Journal*, 17 (6), pp. 545-552 (1979).
18. Fujimori, Y., Lin, Y.K. and Ariaratnam, S.T., "Rotor Blade Stability in Turbulent Flows - Part II", *American Institute of Aeronautics and Astronautics Journal*, 17 (7), pp. 673-678 (1979).
19. Prussing, J.E., "Stabilization of an Unstable Linear System by Parametric White Noise", *Journal of Applied Mechanics, Transactions of ASME*, 48, pp. 198-199 (1981).
20. Mitchell, R. and Kozin, F., "Sample Stability of Second-Order Linear Differential Equations with Wide Band Noise Coefficients", *SIAM Journal of Applied Mathematics*, 27 (4), pp. 571-605 (1974).
21. Schmidt, G., "Vibrations Caused by Simultaneous Random Forced and Parametric Excitations", *Z. Angew. Math. Mekh.* 60 (9), pp. 409-419 (1981, in German).
22. Roberts, J.B., "Effect of Parametric Excitation on Ship Rolling in Random Waves", *J. Ship Research*, 26 (4), pp. 246-253 (1982).
23. Ibrahim, R.A., "Self-excited Vibration of a Non-linear System with Random Parameters", *Shock and Vibration Bulletin*, 53 (1), pp. 135-144 (1982).
24. Ibrahim, R.A. and Sondararajan, A., "Non-linear Parametric Liquid Sloshing Under Wide Band Random Excitation", *Journal of Sound and Vibration*, 91 (1), pp. 119-134 (1983).
25. Zhu, W.Q., "Stochastic Averaging of the Energy Envelope of Nearly Liapunov Systems", *Proc. of the IUTAM Symposium on Random Vibrations and Reliability, Frankfurt/Oder, G.D.R., 1982* (Edited by Hennig, K.), pp. 347-357. Akademie, Berlin (1983).
26. Zhu, W.Q., "On the Method of Stochastic Averaging of Energy Envelope", *Proc. of the International Workshop on Stochastic Structural Mechanics, Innsbruck, November, 1982. Report 1-83*, pp. 17-26, University of Innsbruck (1983).
27. Chen, W.L. and Huang, T.C., "The Stability and Response of a Randomly Excited Hanging String in A Fluid", in *Random Vibrations* (Edited by Huang, T.C. and Spanos, P.D.), *ASME WAM, AMD-Vol. 65*, pp. 25-34 (1984).
28. Dimentberg, M.F., "Correlation and Spectral Characteristics of the Square of the Oscillation Amplitude of A system with External and Parametric Random Excitation", *Mech. Solids*, 19 (2), pp. 70-72 (1984).

29. Schmidt, G. and Schulz, R., "Non-linear Random Vibrations of Systems with Several Degrees of Freedom", Proc. of the IUTAM Symposium on Random Vibrations and Reliability, Frankfurt/Oder, G.D.R., 1982 (Edited by Hennig, K.), pp. 307-316. Akademie, Berlin (1983).
30. Lin, Y.K., "Some Observations on the Stochastic Averaging Method", Probabilistic Engineering Mechanics, 1 (1), pp. 23-27 (1986).
31. Hong, R.C.Y., "Response of a Wind Turbine Blade To Seismic and Turbulent Wind Excitations", Ph.D. Thesis, Dept. of Aeronautical and Astronautical Engineering, University of Illinois at Urbana-Champaign (1984).
32. Roberts, J.R. and Spanos, P.D., "Stochastic Averaging: An Approximate Method of Solving Random Vibration Problems", Int. J. Non-linear Mechanics, 21 (2), pp. 111-134 (1986).
33. Brüchner, A. and Lin, Y.K., "Application of Complex Stochastic Averaging To Non-linear Random Vibration Problems", Int. J. Non-linear Mechanics, 22 (3), pp. 237-250 (1987).
34. Ariaratnam, S.T. and Tam, D.S.F., "Moment Stability of Coupled Linear System Under Combined Harmonic and Stochastic Excitation", in Stochastic Problems in Dynamics, (Edited by Clarkson, B.L.), Pitman, London, pp. 90-105 (1977).
35. Bellman, R. and Richardson, J.M., "Closure and Preservation of Moment Properties", Journal of Mathematical Analysis and Applications, 23, pp. 639-644 (1968).
36. Wilcox, R.M. and Bellman, R., "Truncation and Preservation of Moment Properties for Fokker-Planck Equation", Journal of Mathematical Analysis and Applications, 37, pp. 532-542 (1970).
37. Dash, P.K. and Iyengar, R.N., "Analysis of Randomly Time Varying Systems by Gaussian Closure Technique", Journal of Sound and Vibration, 83 (2), pp. 241-251 (1982).
38. Wu, W.F. and Lin, Y.K., "Cumulant-Neglect Closure for Non-Linear Oscillators Under Random Parametric and External Excitations", International Journal of Non-Linear Mechanics, 19 (4), pp. 349-362 (1984).
39. Ibrahim, R.A. and Heo, H., "Autoparametric Vibration of Coupled Beams Under Random Support Motion", ASME Paper No. 85-DET-184 (1985).
40. Ibrahim, R.A. and Heo, H., "Structural Modal Analysis Under Random External and Parametric Excitations", Proc. 3rd Intl. Modal Analysis Conference, Orlando, Florida, 1, pp. 260-266 (1985).
41. Ibrahim, R.A., "Numerical Solution of Non-linear Problems in Structural Dynamics", Proc. Intl. Conference on Computational Mechanics, Tokyo, Japan, 2, pp. XI. 155-160 (1986).

42. Ibrahim, R.A. and Soundararajan, A., "An Improved Approach for Random Parametric Response of Dynamic Systems with Non-linear Inertia", Intl. J. Non-linear Mechanics, 20, (4), pp. 309-323 (1985).
43. Crandall, S.H., "Non-Gaussian Closure for Random Vibration of Non-linear Oscillators", International Journal of Non-linear Mechanics, 15, pp. 303-313 (1980).
44. Szopa, J., "Response of a Multidegree-of-freedom System of Variable Coefficients to Random Excitation", Zeitschrift für Angewandte Mathematik und Mechanik, 62 (7), pp. 321-328 (1982).
45. Huang, W.H., "Vibration of Some Structures with Periodic Random Parameters", American Institute of Aeronautics and Astronautics Journal, 20 (7), pp. 1001-1008 (1982).
46. Fuh, J.S., Hong, C.Y.R., Lin, Y.K. and Prussing, J.E., "Coupled Flap-torsional Response of a Rotor Blade in Forward Flight due to Atmospheric Turbulent Excitations", J. Amer. Helicopter Soc., 28 (7), pp. 3-12 (1983).
47. Menh, N.C., "Response of Weakly Non-linear Dynamical Systems Subjected to Random Parametric and External Excitations", Journal of Sound and Vibration, 113 (1), pp. 1-8 (1987).
48. Young, G.E. and Chang, R.J., "Prediction of the Response of Non-linear Oscillators Under Stochastic Parametric and External Excitations", Intl. J. Non-linear Mechanics, 22 (2), pp. 151-160 (1987).
49. Brüchner, A. and Lin, Y.K., "Generalization of the Equivalent Linearization Method for Non-linear Random Vibration Problems", Intl. J. Non-linear Mechanics, 22 (3), pp. 227-235 (1987).
50. Hernandez-Machado, A. and San Miguel, M., "Dynamical properties of non-Markovian Stochastic Differential Equations" J. Math. Phys., 25 (4), pp. 1066-1075 (1984).
51. Kapitaniak, T., "Non-Markovian Parametrical Vibration", Intl. J. Engineering Science, 24 (8), pp. 1335-1337 (1986).
52. Kozin, F., "A Survey of Stability of Stochastic Systems", Automatica, 5, pp. 95-112 (1969).
53. Kozin, F., "Stability of Stochastic Dynamical System", J. Probabilistic Engineering Mechanics, 1 (1), (1986).
54. Danilin, A.B. and Yadykin, I.B., "Exponential Stability of Stochastic Finite-Difference Systems", Automation and Remote Control, 42 (4), pp. 440-445 (1981).
55. Chow, P.L. and Chiou, K.L., "Asymptotic Stability of Randomly Perturbed Linear Periodic Systems", SIAM J. Appl. Math., 40 (2), pp. 315-326 (1981).

56. Lyubarski, G.Y. and Robotnikov, Y.L., "On Differential Equations with Random Coefficients", Theory Probability and Applications, 8, pp. 290-298 (1963).
57. Kozin, F., "On Relations Between Moment Properties and Almost Sure Liapunov Stability for Linear Stochastic Systems", J. Math. Anal. Appl., 10 (2), pp. 342-352 (1965).
58. German, S., "Almost Sure Stable Oscillations in a Large System of Randomly Coupled Equations", SIAM J. Appl. Math., 42 (4), pp. 695-703 (1982).
59. Ahmadi, G. and Glockner, P.G., "Approximate Stability Criteria For Some Second Order Linear Differential Equations with Stationary Gaussian Random Coefficients", ASME J. Appl. Mech., 49, pp. 648-648 (1982).
60. Auslender, E.I. and Mil'shtein, G.N., "Asymptotic Expansions of the Liapunov Index for Linear Stochastic Systems With Small Noise", Appl. Math. Mech., 46 (3), pp. 277-286 (1982).
61. Kurnik, W. and Tylikowski, A., "Stochastic Stability and Non-stability of a Cylindrical Shell", Ing.-Arch., 53, pp. 363-369 (1983).
62. Tylikowski, A., "Dynamic Stability of a Non-linear Cylindrical Shell", ASME J. Appl. Mech., 51, pp. 852-856 (1984).
63. Richard, K. and Anand, G.V., "Non-linear Resonance in Strings Under Narrow Band Random Excitation, Part I: Planar Response and Stability", Journal of Sound and Vibration, 86 (1), pp. 85-98 (1983).
64. Ahmadi, G. and Glockner, P.G., "Dynamic Stability of a Kelvin-Viscoelastic Column", Journal of Engineering Mechanics, Proceedings of ASCE, 109 (4), pp. 990-999 (1983).
65. Abdel-Rahman, S. and Ahmadi, G., "Stability of Frames Subjected to Random Earthquake Loadings", 22nd Annual Technical Meeting, Society of Engineering Science, Paper No. ESP22/85070 (1985).
66. Lin, Y.K. and Prussing, J.E., "Concepts of Stochastic Stability in Rotor Dynamics", J. Amer. Helicopter Soc., 27 (2), pp. 73-74 (1982).
67. Prussing, J.E. and Lin, Y.K., "Rotor Blade Flap-Lag Stability in Turbulent Flows", J. Amer. Helicopter Soc., 27 (2), pp. 51-57 (1982).
68. Prussing, J.E. and Lin, Y.K., "A Closed-Form Analysis of Rotor Blade Flap-Lag Stability in Hover and Low Speed Forward Flight in Turbulent Flow", J. Amer. Helicopter Soc., 28 (7), pp. 42-46 (1983).
69. Phillis, J.A., "Entropy Stability of Continuous Dynamic Systems", Intl. J. Control, 35, pp. 323-340 (1982).

70. Potapov, V.D., "Stability of Structure Elements Subjected to Stationary Loads", J. Appl. Mech. and Tech. Phys., 22, pp. 574-578 (1982).
71. Semenov, V.A. and Smirnov, A.I., "On the Stability of Linear Stochastic Systems With Periodically Non-stationary parametric Excitation", Mech. Solids, 18 (1), pp. 14-20 (1983).
72. Narayana, S., "Stochastic Stability of Fluid Conveying Tubes", Proc. IUTAM Symp. on Random Vibrations and Reliability (Edited by Hennig, K.), pp. 273-283. Akademie, Berlin (1983).
73. Watt, D. and Barr, A.D.S., "Stability Boundary For Pseudo-Random Parametric Excitation of a Linear Oscillator", ASME J. Vibration Acoust. Stress and Reliab. in Design, 105, pp. 326-331 (1983).
74. Kliemann, W. and Rümelin, W., "On the Growth of Linear Systems Parametrically Disturbed by a Diffusion Process", Report No. 27, Department of Mathematics, University of Bremen (1981).
75. Wiens, G.J. and Sinha, S.C., "On the Application of Lyapunov's Direct Method to Discrete Dynamic Systems with Stochastic Parameters", J. Sound and Vibration, 94 (1), pp. 19-31 (1984).
76. Loparo, K.A. and Blankenship, G.L., "Almost Sure Instability of a Class of Linear Stochastic Systems with Jump Process Coefficients", Proc. of the Workshop in Liapunov Exponents, Springer-Verlag Lecture Notes in Math., No. 1186 (1986).
77. Sri Namachchivaya, N. and Ariaratnam, S.T., "Stochastically Perturbed Hopf Bifurcation", Int. J. Nonlinear Mechanics, 22(5), pp. 363-372 (1987).
78. To, C.W.S., Lin, R., Huang, K.L., and Lu, Q.S., "Stochastically Perturbed Bifurcations in Two Nonlinearly Coupled Systems", to appear.

PARAMETRIC INSTABILITIES AND CHAOTIC AMPLITUDE MODULATIONS IN A SYSTEM WITH TWO DEGREES-OF-FREEDOM

D. A. Streit

Department of Mechanical Engineering, The Pennsylvania State University,
University Park, PA 16802

A. K. Bajaj and C. M. Krousgrill

School of Mechanical Engineering, Purdue University,
West Lafayette, IN 47907

1. INTRODUCTION

Multi-degree-of-freedom, weakly nonlinear systems with parametric excitation have been studied quite extensively in the literature [1-9]. It is well known that interesting and complex dynamical responses arise in case of primary, secondary and combination resonances. Traditionally, asymptotic methods such as the method of multiple time scales and the method of averaging have been used to reduce the system equations to an autonomous system in amplitude and phase variables. The averaged equations depend on the external parameters such as the amplitude and the frequency of parametric excitation, as well as on the nature of the relationship between the linear frequencies of the system. These equations, being highly nonlinear, have mostly been studied for their constant solutions. It has been found that the steady state response can be multivalued, representing stable and unstable periodic response.

In some 2-DOF systems with specific internal and parametric resonances, it has been observed that there may be a range of excitation frequency over which all the nonzero solutions are unstable. Some studies [3,4] have attempted to understand the dynamics of the averaged equations over this frequency interval. They clearly show by numerical integration that the averaged equations can possess complex dynamical behavior including period-doubling bifurcations and chaotic motions. The period-doubling bifurcations arise in limit cycle solutions resulting from the Hopf bifurcation of the steady state response. The solutions of the original system are then expected to be amplitude-modulated motion.

In this work we study the effect of parametric combination resonance on 2-DOF systems governed by

$$\ddot{\underline{z}} + \underline{\Omega}^2 \underline{z} + \epsilon \left[c(\dot{z}_1 + \dot{z}_2) + (k + \sigma \cos \eta t)(z_1 + z_2) + \alpha(z_1 + z_2)^2 \right] \begin{Bmatrix} 1 \\ \eta^2 \end{Bmatrix} = 0, \quad (1)$$

where $\underline{\Omega}^2 = \text{diag}(\omega_1^2, \omega_2^2)$, and $\underline{z} = [z_1, z_2]^T$.

The parameter c represents a linear damping coefficient, k represents a stiffness detuning parameter, σ and Ω are the amplitude and frequency, respectively, of the parametric excitation, α is the strength of the quadratic nonlinearity, ω_1 and ω_2 are the natural frequencies of the unforced, undamped system and η is a constant coupling parameter. The small motion parameter, ϵ , is used in developing an asymptotic expansion around the zero solution of (1) such that as $\epsilon \rightarrow 0$, the expansion will represent the linear differential equations of a stationary conservative system. These equations describe the modal response of flexible mechanical systems such as oscillating machinery mounted on an isolation pad and originated from a study of flexible robotic manipulators [10].

Combination resonances of the type $\Omega = \omega_1 + \omega_2$ and $\omega_1 = 2\omega_2$ are considered in this study. The method of multiple time scales is used to obtain an autonomous fourth order system representing the amplitude and the phase dynamics on a slow time scale. In addition to steady-state constant solutions, periodic as well as more complex and chaotic motions are shown to exist. The original equations (1) are then numerically studied to investigate the correspondence between the solutions of the original system and those of the amplitude equations.

2. ANALYSIS

The method of multiple time scales is used to obtain approximate solutions to (1). The solutions can be written in terms of a uniform expansion in ϵ

$$z_j = z_j^{(0)} + \epsilon z_j^{(1)} + \epsilon^2 z_j^{(2)} + \dots \quad (2)$$

Additionally, for the first order approximation sought, two time scales $T_0 = t$ ("fast time") and $T_1 = \epsilon t$ ("slow time") are used. The time derivatives can be written with respect to the two scales as

$$\frac{d}{dt} = D_0 + \epsilon D_1 + \dots, \quad \frac{d^2}{dt^2} = D_0^2 + \epsilon 2D_0 D_1 + \dots \quad (3)$$

where $D_i = \partial/\partial T_i$. Substituting (2) and (3) into (1), retaining through $O(\epsilon)$ terms and equating like power terms gives the following two sets of equations:

$$\epsilon^0 \text{ terms: } D_0^2 \underline{z}^{(0)} + \underline{\Omega}^2 \underline{z}^{(0)} = 0, \quad (4)$$

$$\begin{aligned} \epsilon^1 \text{ terms: } D_0^2 \underline{z}^{(1)} + \underline{\Omega}^2 \underline{z}^{(1)} &= -2 D_0 D_1 \underline{z}^{(0)} - [\epsilon D_0 (z_1^{(0)} + z_2^{(0)}) \\ &+ (k + \sigma \cos \Omega t)(z_1^{(0)} + z_2^{(0)}) + \alpha (z_1^{(0)} + z_2^{(0)})^2] \left[\frac{1}{\eta^2} \right]. \end{aligned} \quad (5)$$

The general solution of equations (4) can be written as:

$$z_j^{(0)} = A_j(T_1) e^{i\omega_j T_0} + cc \quad (6)$$

where "cc" represents the complex conjugate of the previous expressions. Substituting (6) into (5) results in the equation

$$\begin{aligned} D_0^2 \underline{z}^{(1)} + \underline{\Omega}^2 \underline{z}^{(1)} &= -2 \left[\begin{array}{c} A_1' i \omega_1 e^{i\omega_1 T_0} \\ A_2' i \omega_2 e^{i\omega_2 T_0} \end{array} \right] \left[\begin{array}{c} cc \\ cc \end{array} \right] - \left[\epsilon (A_1 i \omega_1 e^{i\omega_1 T_0} + A_2 i \omega_2 e^{i\omega_2 T_0} + cc) \right. \\ &+ (k + \sigma \cos \Omega T_0) (A_1 e^{i\omega_1 T_0} + cc + A_2 e^{i\omega_2 T_0} \\ &\left. + cc) + \alpha (A_1 e^{i\omega_1 T_0} + cc + A_2 e^{i\omega_2 T_0} + cc)^2 \right] \left[\frac{1}{\eta^2} \right], \end{aligned} \quad (7)$$

where $(\)' = D_1(\)$.

The solvability equations for A_1 and A_2 of (6) are found by the removal of secular terms (terms leading to resonance) in (7). As discussed in [10], eight relations between ω_1 , ω_2 , and Ω can lead to such resonances in this problem. Of these eight, the combination resonance of $\omega_1 = 2$, $\omega_2 = 1$ and $\Omega = \omega_1 - \omega_2$ is the one investigated here. For this case, the removal of secular terms on the right side of (7) produces the complex differential equations:

$$4iA_1' + 2icA_1 + kA_1 + 0.5\sigma A_2 + \alpha A_2^2 = 0, \quad (8)$$

$$2iA_2' + (icA_2 + kA_2 - 0.5\sigma A_1 + 2\alpha A_1 \bar{A}_2)\eta^2 = 0, \quad (9)$$

where \bar{A}_2 is the complex conjugate of A_2 .

Equations (8) and (9), referred to as the amplitude equations, represent solvability conditions for A_1 and A_2 in (6). These equations can be transformed to a more convenient form by defining:

$$A_1(T_1) = 0.5 a_1(T_1) e^{i\beta_1(T_1)}, \quad A_2(T_1) = 0.5 a_2(T_1) e^{i\beta_2(T_1)}. \quad (10)$$

Substituting (10) into (8) and (9) and separating the real and the imaginary parts results in four, first order differential equations in terms of the amplitude and the phase variables:

$$2a_1(\gamma_2' - 2\gamma_1') + 0.5ka_1 + 0.25\sigma a_2 \cos \gamma_1 + 0.25\alpha a_2^2 \cos \gamma_2 = 0, \quad (11)$$

$$2a_1' + ca_1 - 0.25\sigma a_2 \sin \gamma_1 - 0.25\alpha a_2^2 \sin \gamma_2 = 0, \quad (12)$$

$$a_2(\gamma_2' - \gamma_1') + (0.5ka_2 + 0.25\sigma a_1 \cos \gamma_1 + 0.5\alpha a_1 a_2 \cos \gamma_2)\eta^2 = 0, \quad (13)$$

$$a_2' + (0.5ca_2 + 0.25\sigma a_1 \sin \gamma_1 + 0.5\alpha a_1 a_2 \sin \gamma_2)\eta^2 = 0, \quad (14)$$

where $\gamma_1 = \beta_1 - \beta_2$ and $\gamma_2 = \beta_1 - 2\beta_2$.

It should be noted that constant solutions to (11) - (14) represent periodic, first order approximations for $z_1(t)$ and $z_2(t)$. Since these equations are homogeneous, the zero solution ($a_1 = a_2 = 0$) always exists. The stability of these zero solutions will be discussed in the next section.

Non-zero constant solutions to (11) - (14) can be shown to be:

$$a_2 = \pm \frac{2}{1-\alpha} [k^2(l^2 - 1)^2 + c^2(l^2 + 2)^2]^{-1/2}, \quad a_1 = \frac{a_2}{l}, \quad (15)$$

with

$$\sin \gamma_1 = \frac{2c}{1-\sigma} (l^2 + 4)^{-1/2}, \quad \cos \gamma_1 = \frac{2k}{1-\sigma} (l^2 - 2)^{-1/2}, \quad (16)$$

$$\sin \gamma_2 = \frac{2c(l^2 + 2)}{1-\alpha a_2}, \quad \cos \gamma_2 = \frac{2k(1-l^2)}{1-\alpha a_2},$$

where

$$1^2 = [d \pm \sqrt{(d^2 - 4e)}] \quad (17)$$

and

$$d = \frac{8c^2 - 4k^2 - (0.5\sigma)^2}{2(k^2 + c^2)}, \quad e = \frac{4(k^2 + 4c^2)}{(k^2 + c^2)}.$$

The existence of these amplitude solutions requires that the radicand in (17) be non-negative, i.e., $d^2 - 4e \geq 0$. The maximum value (c_{\max}) of damping constant c for which solutions exist is therefore found by enforcing the condition $d^2 - 4e = 0$ and solving for c . This maximum value of c for $k = 0$ can be readily found to be

$$c_{\max} = \left[\sigma / \sqrt{32 \omega_1 \omega_2} \right] = \sigma / 8. \quad (18)$$

The amplitudes of response a_1 and a_2 at this maximum value of c reduce to a_1^* and a_2^* which are given by the simple expressions:

$$[a_1^*] = 3\sigma/8\alpha, \quad [a_2^*] = 3\sigma/4\alpha. \quad (19)$$

It is easy to see that the qualitative nature of the constant amplitude solutions (15)-(16) is unaffected by a change in the value of coupling parameter η . Changes in coupling parameter effect only a simple scaling of those solutions. The stability of those solutions, however, depends significantly on the value of coupling parameter η .

3. STABILITY ANALYSIS

The stability of a constant solution \underline{w}_0 to a set of N first order, autonomous nonlinear differential equations

$$\underline{w}'(T_1) = \underline{f}(\underline{w}(T_1)) \quad (20)$$

is determined from the linearized equations

$$\dot{\underline{w}}(T_1) = \underline{J} \underline{\hat{w}}(T_1) \quad (21)$$

where

$$\underline{\hat{w}}(T_1) = \underline{w}(T_1) - \underline{w}_0, \quad \underline{J} = \left[\frac{\partial f_i}{\partial w_j} \right]_{\underline{w} = \underline{w}_0}. \quad (22)$$

For this work, (20) will correspond to either the complex amplitude equations (8) and (9) or the amplitude-phase equations (11)-(14).

Let λ_j ($j = 1, 2, \dots, N$) represent the eigenvalues of the Jacobian matrix \underline{J} . If $\text{Real}(\lambda_j) < 0$ for all j , then the constant solution \underline{w}_0 is stable, and if $\text{Real}(\lambda_j) > 0$ for any j , the constant solution \underline{w}_0 is unstable. If any $\text{Real}(\lambda_k) = 0$ with the remaining $\text{Real}(\lambda_j) < 0$ ($j \neq k$), then the stability of \underline{w}_0 must be determined by nonlinear means.

Considering the zero solution $\underline{w}_0 = (0, 0)^T$ of (8) and (9), the Jacobian matrix can be written as:

$$\underline{J} = \begin{bmatrix} 0.25(ik - 2c) & i 0.125 \sigma \\ i 0.25 \sigma \eta^2 & 0.5(ik - c) \eta^2 \end{bmatrix}. \quad (23)$$

The eigenvalues of \underline{J} are:

$$\lambda_{1,2} = \frac{1}{4} \left[ik(\eta^2 + \frac{1}{2}) - c(\eta^2 + 1) \right] + \frac{1}{4} \left[c^2(\eta^2 + 1)^2 - k^2(\eta^2 + \frac{1}{2})^2 - \frac{\sigma^2}{2} \eta^2 \right]^{1/2} \quad (24)$$

$$ick(2\eta^2 + 1)(\eta^2 + 1)^{1/2}.$$

It can be shown from (24) that at least one root, say λ_1 , has a nonpositive real part. If the remaining root λ_2 has a positive real part, then the zero solution is unstable. In fact, it can be shown that for the coupled oscillators ($\eta \neq 0$) and for nonzero damping ($c \neq 0$), the zero solution of (8) and (9) is always asymptotically stable.

The stability of the non-zero constant solutions given by (15) - (16) is best understood through the 4×4 Jacobian matrix obtained from the amplitude equations (11) - (14). This Jacobian matrix and its corresponding eigenvalues will not be presented here, but will be evaluated numerically for the special cases discussed in the next section.

4. DISCUSSION OF RESULTS

For this investigation, the amplitude of parametric excitation is set to $\sigma = U^2/8$ and the coefficient of quadratic nonlinear term is set to $\alpha = U^2/4$ where $U^2 = 0.454865$. The damping c is varied from 0 to $c_{\max} = 0.015625 U^2$. In addition, the detuning k is varied from $-0.2 U^2$ to $0.2 U^2$. Many different values of coupling parameter η have been studied. However results for only one case of $\eta = -1.097638$ are presented here.

The amplitude curves as a function of detuning k for three different damping c are shown in Figures 1-3. Solid lines indicate stable constant solutions whereas dashed lines indicate unstable constant solutions. The zero solution (a_1, a_2) = (0, 0) is always asymptotically stable except for the points $k = \pm 0.0625 U^2$ for $c = 0$. These two points correspond to where unstable solution branches a_1 and a_2 touch the k -axis (Figure 1). As c is increased, the nonzero solution branches lift off the zero axis. As $c \rightarrow c_{\max}$, stable and unstable branches collapse around the nonzero solution a_1' and a_2' at $k = 0$.

Figures 1-3 show that there is an interval in detuning k where the upper solution branch is unstable. This occurs at $\pm k_H$ and is due to a Hopf bifurcation where the eigenvalues of J , the Jacobian matrix, cross the imaginary axis with nonzero imaginary part. As c increases, the response curves shrink but the unstable portion persists until the solutions themselves cease to exist.

It was seen in the last section that the response amplitudes are independent of the coupling parameter η whereas their stability certainly depends on it. By changing η , the portion of the response curve that is unstable due to Hopf bifurcation can be completely or partly stabilized. More details can be found in [11].

It is very interesting to investigate the dynamic response of the amplitude equations where the constant solutions are unstable by Hopf bifurcation. Figure 2 shows the response curves for $c = 0.012 U^2$ with Hopf bifurcation points at $\pm k_H$. Note from equations (11) - (14) that the amplitude solution and the corresponding stability is symmetric about the $k = 0$ axis and therefore, only the region from $k = -k_H$ to $k = 0$ need be considered. When $k = -k_H$ stable constant solutions are observed. For $-k_H < k < 0$, all nonzero constant solutions are unstable. As discussed in the last section the zero solution is stable. For this range of k , the system response has been investigated numerically. Equations (11) - (14) have been integrated using the IMSL 5th and 6th Order Runge-Kutta routine. Results of these integrations are shown in Figures 4 and 5 where

$$V_1 = a_1 \cos(\gamma_1 - \frac{\gamma_1}{2}) \text{ and } V_2 = a_1 \sin(\gamma_2 - \frac{\gamma_1}{2}).$$

Figure 4 clearly shows the period-doubling sequence starting from a limit cycle close to $k_H = -0.049116 U^2$. The response for $k = -0.04303 U^2$ is chaotic. Further increase in k results in an abrupt appearance of regular but period 3 motion which again undergoes period-doubling into chaos.

The results of the amplitude equations discussed here show that these equations may have periodic as well as chaotic motions. Because of the averaging or asymptotic analysis performed, we expect that at least for small enough ϵ , there is a one-to-one correspondence between these solutions of the averaged equations and the solutions of the original coupled system (1). Thus, the constant and periodic solutions of the amplitude equations correspond respectively to periodic and amplitude modulated solutions of (1). To verify these results, we set $\epsilon = 0.1$ and then numerically integrate equation (1) using initial conditions obtained from

$$z_1(t) = a_1 \cos(2\gamma_1 - \gamma_1 + \omega_1 t), z_2(t) = a_2 \cos(\gamma_1 - \gamma_2 + \omega_2 t)$$

where a_1, a_2, γ_1 and γ_2 are determined by (15) - (16). The periodic solutions and the bifurcations can be characterized by time response as well as by the Poincare section which shows the section of the steady state motion. For a periodic solution of period $2\pi/\Omega$, the section has only one point. For motion on a 2-torus, the section should consist of a set of points forming a closed curve. A dense set of points indicates almost periodic motion with two noncommensurate frequencies. A finite number of points indicates a phase-locked, closed or periodic motion on the 2-torus. As a system parameter is varied the motion on the torus may get unstable and lead to some other motion. Figure 6 shows the Poincare sections projected onto the $(z_1 - z_2)$ plane. Transient motions leading to a fixed point are shown for $k = -0.047 U^2$. Thus, the 2 DOF system has a periodic motion whereas the asymptotic analysis predict almost periodic or modulated response. The section of the steady state motion for $k = -0.016 U^2$ is a closed curve indicating that the motion is on a 2-torus. Further increase in k leads to the 2-torus losing stability and the section for $k = -0.0415 U^2$ represents a torus-doubled solution. This phenomenon is called torus-doubling bifurcation [12]. The process of torus-doubling can ultimately lead to the destruction of smooth torus surface and the onset of chaotic behavior. It is interesting to note that the detuning intervals for the original system are slightly shifted compared to those predicted by the asymptotic analysis. Also the Poincare sections are quite similar to the continuous solutions of the amplitude equations. This is to be expected at least for small enough ϵ since the vectorfield of the averaged or amplitude equations then approximates the Poincare map of the original system in standard form [13].

5. CONCLUDING REMARKS

In this work, a two-degree-of-freedom system is analyzed for its response when driven parametrically near a combination resonance. The method of multiple time scales is used to show that stable limit cycle periodic response coexists with stable zero equilibrium. Thus, the motion is highly dependent on initial conditions.

For a particular coupling parameter value, the constant solutions of the amplitude equations become unstable by a Hopf bifurcation resulting in limit cycle solutions. As the detuning is varied, these limit cycle oscillations destabilize by period-doubling, leading eventually to chaotic motions in the amplitude equations. This implies that the original system has periodic solutions which become unstable and bifurcate into amplitude

modulated motion. The amplitude modulations themselves undergo period-doubling leading to chaotic amplitude modulations.

The original coupled oscillators are then numerically integrated for $\epsilon \leq 0.1$. The asymptotic analysis results are found to be qualitatively consistent except for a small shift in the detuning interval over which the corresponding motions exist and are stable.

REFERENCES

1. A. H. NAYFEH and D. T. MOOK 1979 *Nonlinear Oscillations*. New York: Wiley-Interscience.
2. R. A. IBRAHIM and A.D.S. BARR 1978 *Shock and Vibration Digest* **10**, 9-24. Parametric vibration Part II: mechanics of nonlinear problems.
3. A. H. NAYFEH and L. D. ZAVODNEY 1986 *Journal of Sound and Vibration* **107**, 329-350. The response of two-degree-of-freedom systems with quadratic nonlinearities to a combination parametric resonance.
4. J. BECKER and J. MILES 1986 *Journal of Applied Mathematics and Physics (ZAMP)* **37**, 641-650. Parametric excitation of an internally resonant double pendulum, II.
5. A. H. NAYFEH and A.E.S. JEBRIL 1987 *Journal of Sound and Vibration* **115**, 83-101. The response of two-degree-of-freedom systems with quadratic and cubic nonlinearities to multifrequency parametric excitation.
6. E. G. TEZAK, A. H. NAYFEH and D. T. MOOK 1982 *Journal of Sound and Vibration* **85**, 459-472. Parametrically excited nonlinear multidegree-of-freedom systems with repeated natural frequencies.
7. A. H. NAYFEH 1983 *Journal of Sound and Vibration* **88**, 547-557. The response of two-degree-of-freedom systems with quadratic non-linearities to a parametric excitation.
8. K. B. ASMIS and W. K. TSO 1972 *Journal of Applied Mechanics* **39**, 832-834. Combination and internal resonance in a non-linear two-degrees-of-freedom system.
9. W. K. TSO and K. G. ASMIS 1974 *International Journal of Non-Linear Mechanics* **9**, 269-277. Multiple parametric resonance in a non-linear two-degree-of-freedom system.
10. D. A. STREIT 1986 Doctoral Dissertation; Purdue University. Dynamics and stability of robotic manipulators with parametric excitation.
11. D. A. STREIT, A. K. BAJAJ and C. M. KROUSGRILL 1987 *Journal of Sound and Vibration* (to appear). Combination parametric resonance leading to periodic and chaotic quadratic nonlinearities.
12. K. KANEKO 1984 *Progress of Theoretical Physics* **72**, 202-215. Oscillation and doubling of torus.
13. J. GUCKENHEIMER and P. HOLMES 1983 *Nonlinear Oscillations, Dynamical Systems, and Bifurcations of Vectorfields*. New York: Springer-Verlag.

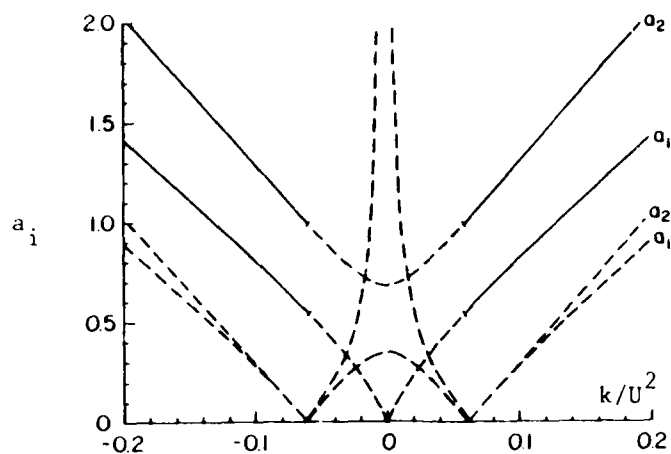


Figure 1. Amplitude response curves for $C = 0.0001 U^2$.

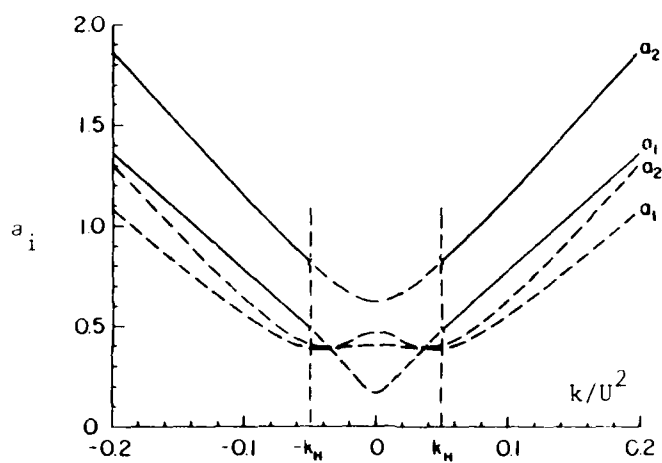


Figure 2. Amplitude response curves for $C = 0.012 U^2$.

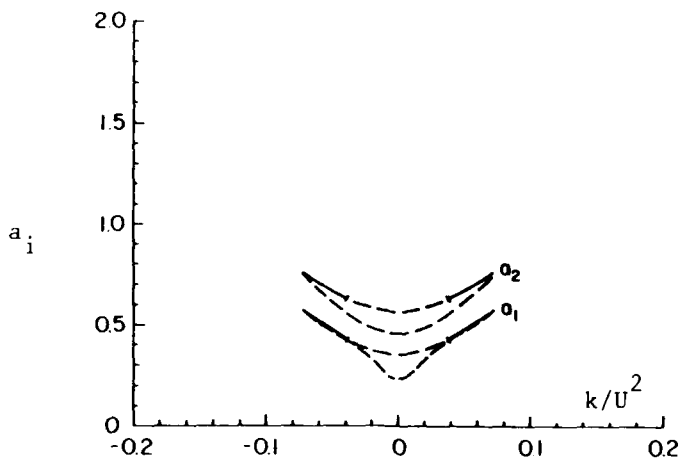


Figure 3. Amplitude response curves for $C = 0.0148 U^2$.

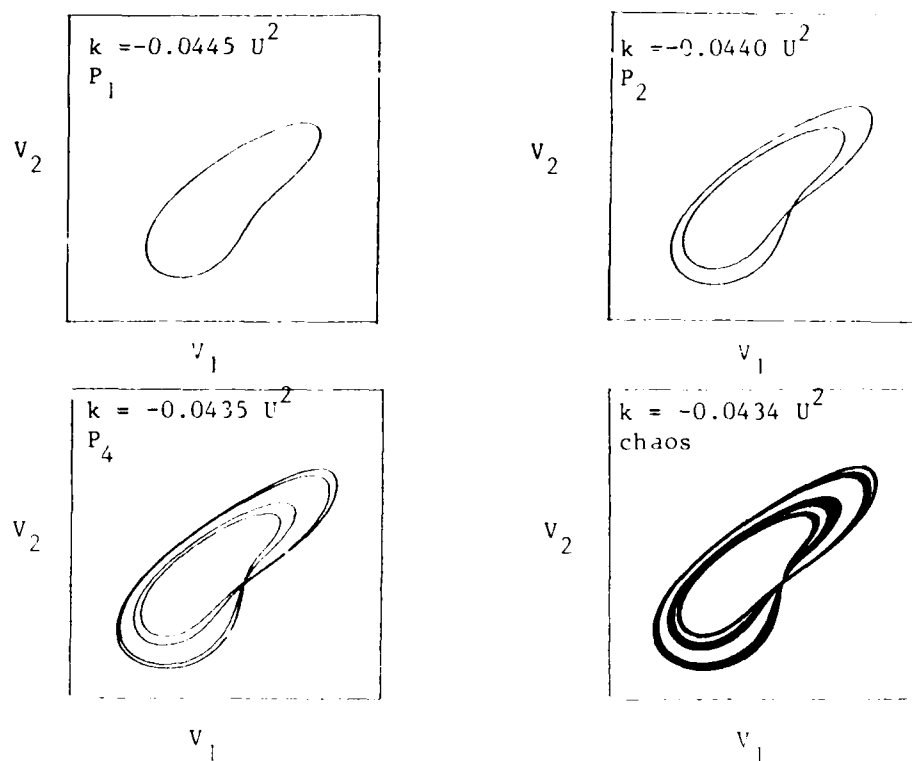


Figure 4. First period-doubling sequence for $C = 0.012 U^2$

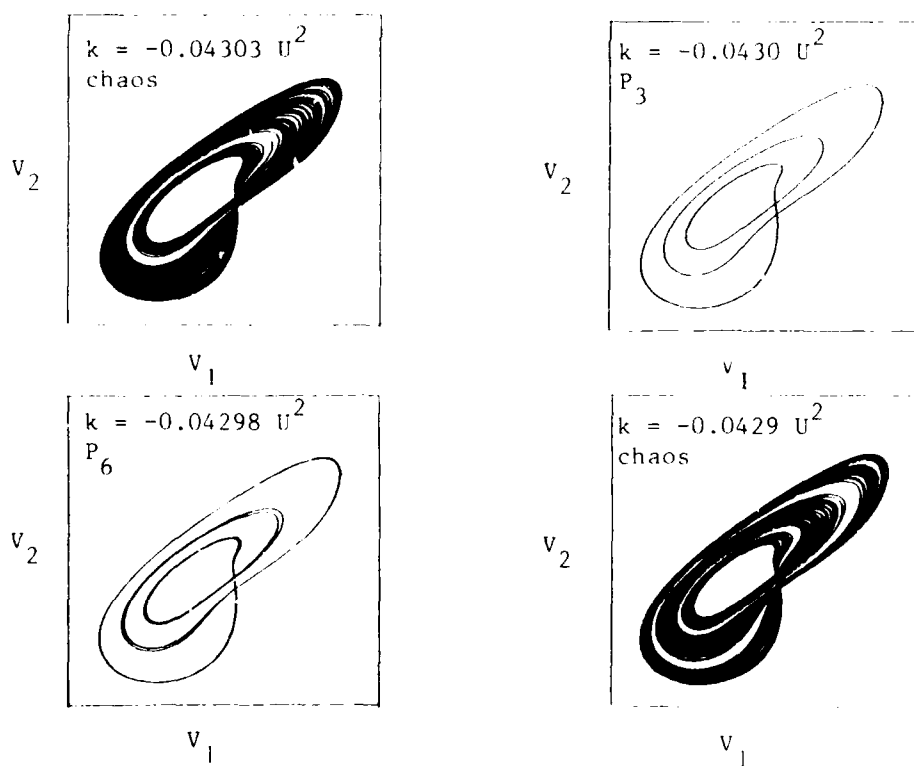


Figure 5. Second period-doubling sequence for $C = 0.012 U^2$.

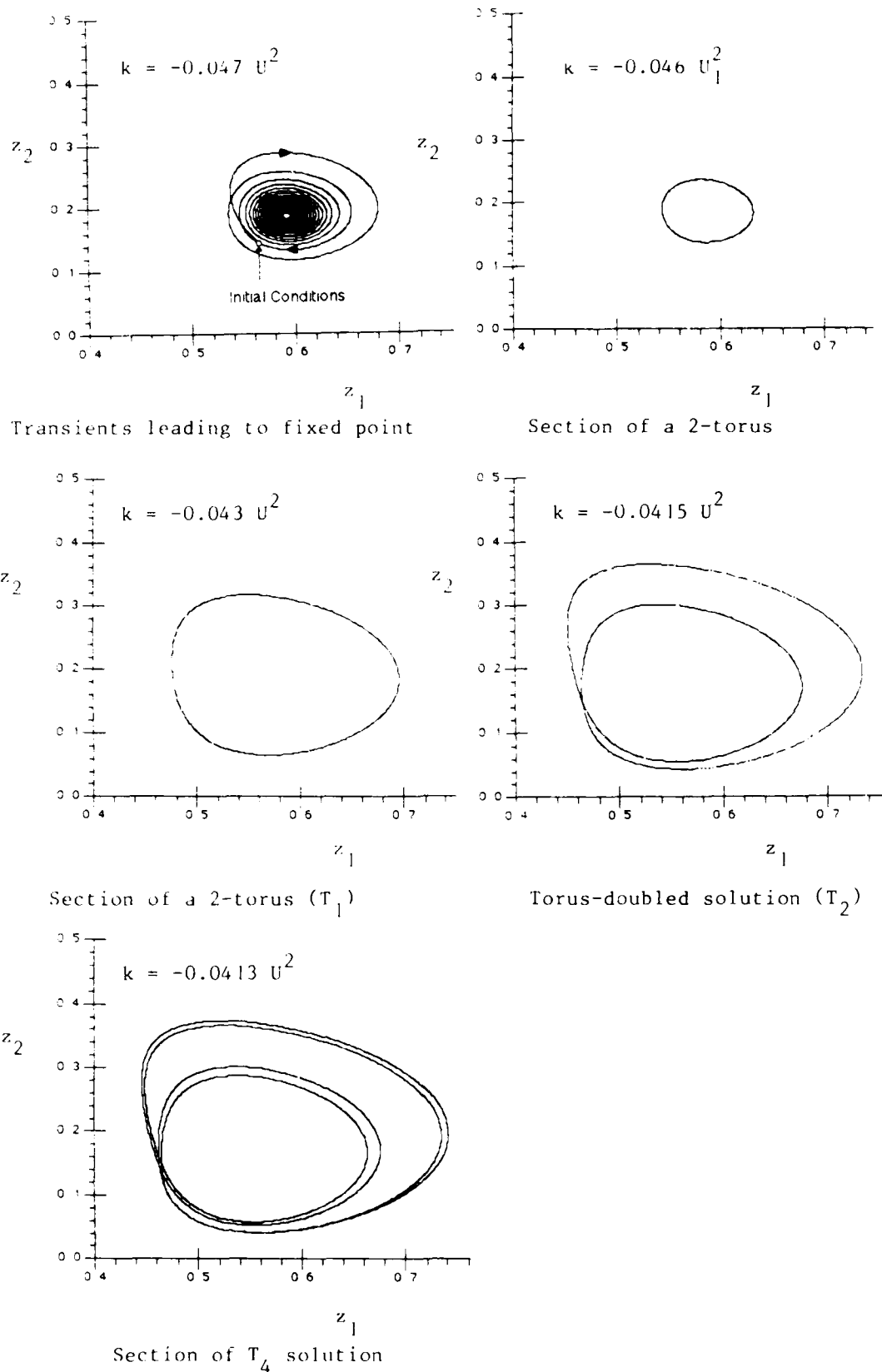


Figure 6. Poincaré sections for the motion of the coupled oscillators.

COMBINATION RESONANCES OF PARAMETRICALLY-EXCITED RECTANGULAR PLATES

G.L. Ostiguy and H. Nguyen

Ecole Polytechnique
Montreal, Canada

1. INTRODUCTION

It has been known that when a rectangular plate sustains an in-plane load of the form $N(t) = N_0 + N_1 \cos \lambda t$, where $\cos \lambda t$ is a harmonic function of time, the plate may become laterally unstable over certain regions of the (N_0, N_1, λ) parameter space. This phenomenon is referred to as dynamic or parametric instability.

When the natural frequencies of the system are distinct, and in the absence of internal resonances and combination resonances, the periodic in-plane load can excite only one normal mode at a time. Then, at the principal parametric resonance, the exciting frequency λ lies near twice the natural frequency or in other words, the frequency of the lateral (parametric) vibration is half the load frequency λ . In contrast with this simple resonance, parametric combination resonances may also occur. This kind of resonance is characterized by the fact that the system in question resonates simultaneously in more than one normal mode and all resonant modes are directly excited by the parametric excitation.

Parametric instability of elastic structures has been investigated by a number of authors; a comprehensive analysis of this kind of problem, together with numerous references, can be found in [1-3]. Parametric resonance of rectangular plates under periodic in-plane forces has been studied previously and its instability behavior has been considerably clarified [4]. However, a survey [5] of the literature reveals that work on the dynamic stability of thin elastic plates under periodic in-plane loads has been often limited to the investigation of principal parametric resonances. Studies of parametric combination resonances have not been too numerous and confined mainly to square plates [6-8] or almost square plates [9]. Furthermore, in [6] and [9] no result associated with combination resonance was shown, and in [7] and [8] a linear theory was used to investigate the mechanical model. It is well known that the linear theory can only predict the frequencies at which lateral vibrations would occur, and determining the amplitude of vibration requires a nonlinear formulation.

The present work deals primarily with the problem of the occurrence of parametric combination resonances and covers an existing gap in our understanding of the combination resonance phenomena of structures. The rectangular plate under investigation is acted upon by periodic in-plane forces uniformly distributed along two opposite clamped edges; the other two edges are simply supported and stress-free. The analysis is based on the dynamic analog of the von Karman's large-deflection theory and the governing equations are satisfied using the orthogonality properties of the assumed functions. The temporal response of the damped system is determined by the generalized asymptotic method, and only combination resonances are considered and investigated in this work. General rectangular plates are used, the aspect ratio of the plate being regarded as an additional parameter of the system. The effects of various system parameters on a combination resonance are also evaluated.

2. FORMULATION OF THE PROBLEM

2.1 Statement of the Problem

The specific conceptual model under investigation is a rectangular plate subjected to the action of periodic in-plane forces uniformly distributed along two opposite edges. The geometry of the plate and the load configuration are shown in Fig. 1. The plate is referred to the right-handed cartesian system of coordinates, the x-y plane being in the middle surface of the plate and the origin at its lower left corner.

The plate is initially flat, of uniform thickness, elastic, homogeneous and isotropic. It is also assumed that the plate thickness h and the resulting displacements are small compared with the wavelength of lateral vibrations. This restriction allows us to use a thin plate theory. As a consequence, we can assume that the loading frequencies over which lateral (out-of-plane or parametric) vibrations occur are considerably below the natural frequencies of longitudinal (in-plane) vibrations, and in-plane inertia forces can be neglected.

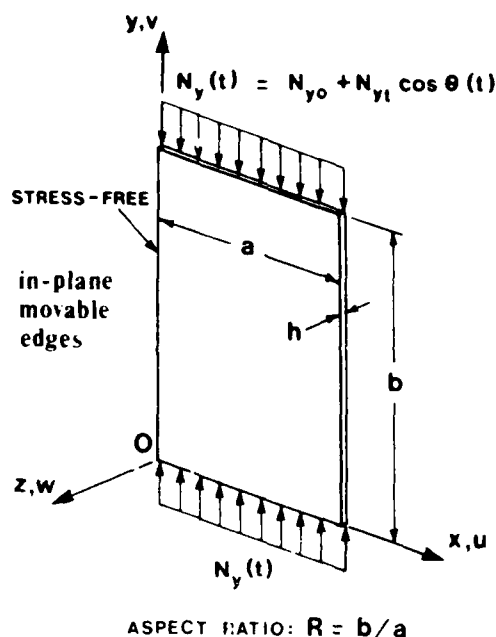


FIG. 1 Plate and load configuration

2.2 Basic Equations

The plate theory used in this analysis may be described as the dynamic analog of the von Karman's large-deflection theory and is derived in terms of the stress function f and the lateral displacement w . The differential equations governing the nonlinear flexural vibrations of the plate can be written in the non-dimensional form

$$R^4 F_{,\zeta\zeta\zeta\zeta} + 2R^2 F_{,\zeta\zeta\eta\eta} + F_{,\eta\eta\eta\eta} = R^2 [W^2_{,\zeta\eta} - W_{,\zeta\zeta} W_{,\eta\eta}] \quad (1)$$

$$R^4 W_{,\zeta\zeta\zeta\zeta} + 2R^2 W_{,\zeta\zeta\eta\eta} + W_{,\eta\eta\eta\eta} = c [R^2 (F_{,\eta\eta} W_{,\zeta\zeta} - 2F_{,\zeta\eta} W_{,\zeta\eta} + F_{,\zeta\zeta} W_{,\eta\eta}) - R^4 W_{,\tau\tau}] \quad (2)$$

in which a comma denotes partial differentiation with respect to the corresponding coordinates and where

$$\begin{aligned} \zeta &= x/a, & \eta &= y/b, & W &= w/h, & R &= b/a, \\ F &= f/Eh^2, & \tau &= t[Eh^2/\rho a^4]^{1/2}, & c &= 12(1-\nu^2). \end{aligned} \quad (3)$$

The non-dimensional in-plane loading, $N_{\eta}(\tau) = N_{\eta 0} + N_{\eta 1} \cos \Lambda \tau$, combined with the stretching of the middle surface owing to large deflections of the plate, gives rise to the dimensionless membrane forces which are then related to the non-dimensional stress function F by

$$(N_{\zeta}, N_{\eta}, N_{\zeta\eta}) = (F_{,\eta\eta}/R^2, F_{,\zeta\zeta}, -F_{,\zeta\eta}/R) \quad (4)$$

$$\text{where } (N_{\zeta}, N_{\eta}, N_{\zeta\eta}) = [a^2/Eh^3](N_x, N_y, N_{xy}) \quad (5)$$

in which N_x , N_y and N_{xy} are membrane forces. The in-plane loading, acting on the boundary, is taken into account in the boundary conditions.

2.3 Boundary Conditions

The boundary conditions are related to both the lateral displacement W and the stress function F . The stress conditions assumed in this analysis are as follows: stress-free (unloaded) edges and uniformly stressed (loaded) edges. Thus, these stress conditions may be expressed in the dimensionless form as

$$\begin{aligned} F_{,\eta\eta} = F_{,\zeta\eta} &= 0 & \text{at } \zeta &= 0, 1 \\ F_{,\zeta\zeta} = -N_{\eta}(\tau), \quad F_{,\zeta\eta} &= 0 & \text{at } \eta &= 0, 1. \end{aligned} \quad (6)$$

In this work, the two unloaded edges of the plate are assumed to be simply supported and the other two loaded edges clamped. The supporting conditions in this case are written as

$$\begin{aligned} W = R^2 W_{,\zeta\zeta} + \nu W_{,\eta\eta} &= 0 & \text{at } \zeta &= 0, 1 \\ W = W_{,\eta} &= 0 & \text{at } \eta &= 0, 1. \end{aligned} \quad (7)$$

The problem consists in determining functions F and W which satisfy the governing equations, together with the boundary conditions.

3. METHOD OF SOLUTION

A solution of equations (1) and (2) is sought in the form of double series

$$F(\zeta, \eta, \tau) = -\frac{1}{2}\zeta^2 N_{\eta}(\tau) + \sum_{mn} F_{mn}(\tau) X_m(\zeta) Y_n(\eta) \quad (8)$$

$$W(\zeta, \eta, \tau) = \sum_{pq} W_{pq}(\tau) \Phi_p(\zeta) \Psi_q(\eta) \quad (9)$$

where X_m , Y_n , Φ_p and Ψ_q are beam eigenfunctions given by

$$X_m(\zeta) = \cosh \alpha_m \zeta - \cos \alpha_m \zeta - \left(\frac{\cosh \alpha_m - \cos \alpha_m}{\sinh \alpha_m - \sin \alpha_m} \right) (\sinh \alpha_m \zeta - \sin \alpha_m \zeta) \quad (10)$$

$$Y_n(\eta) = \cosh \alpha_n \eta - \cos \alpha_n \eta - \left(\frac{\cosh \alpha_n - \cos \alpha_n}{\sinh \alpha_n - \sin \alpha_n} \right) (\sinh \alpha_n \eta - \sin \alpha_n \eta);$$

$$\Phi_p(\zeta) = \sin p\pi\zeta \quad (11)$$

$$\Psi_q(\eta) = \left(\frac{\sinh \alpha_q - \sin \alpha_q}{\cosh \alpha_q - \cos \alpha_q} \right) (\cosh \alpha_q \eta - \cos \alpha_q \eta) + \sinh \alpha_q \eta - \sin \alpha_q \eta.$$

These beam functions satisfy the relevant boundary conditions. In equations (8) and (9), F_{mn} and W_{pq} are undetermined functions of the non-dimensional time τ .

Applying the approach of generalized double Fourier series [10], using the orthogonality properties of the assumed functions, solving for the coefficients F_{mn} in terms of W_{pq} , omitting all indices associated with the spatial mode in the x direction ($p=1$) lead to a system of nonlinear ordinary differential equations for the time functions as follows:

$$\ddot{W}_v + \sum_q K_q W_q + N_{\eta} \sum_s P_s W_s + \sum_{i,j,k} \frac{M_{ij}^{(1)}}{l_{qs}} W_i W_j W_k = 0 \quad (12)$$

By finding the eigenvalues and eigenvectors of the linear part of equation (12), the latter can be written in terms of normal coordinates such that the linear part of the resulting equation is uncoupled and introducing linear viscous damping in the final results, we obtain

$$\ddot{W}_m + 2C_m \dot{W}_m + \Omega_m^2 W_m - 2\cos\theta \sum_n \mu_m^{(n)} \Omega_n^2 W_n + \sum_{i,j,k} M_m^{(1)} k W_i W_j W_k = 0 \quad (13)$$

where

$$\Omega_m^2 = [\omega_m^2 (1 - N_{\eta 0} / N_m)]^{1/2}, \quad \mu_m^m = N_{\eta} / 2(N_m - N_{\eta 0}) \quad (14)$$

in which N_m represents the static critical load according to linear theory. In equation (13), Ω_m is the free vibration circular frequency of the rectangular plate loaded by a constant component of the in-plane force, μ_m^n is the load parameter, C_m is the coefficient of viscous damping and $\theta(\tau)$ is the total phase angle of harmonic excitation.

Taking the first three terms in the expansion for the lateral displacement, the continuous system is reduced to a three-degree-of-freedom system and we have the following set of temporal equations of motion:

$$\begin{aligned} \ddot{W}_1 + \Omega_1^2 W_1 = & -2C_1 \dot{W}_1 + 2\cos\theta (\mu_1 \Omega_1^2 W_1 + \mu_1^2 \Omega_2^2 W_2 + \mu_1^3 \Omega_3^2 W_3) \\ & + (\Gamma_{11} W_1^3 + \Gamma_{12} W_1^2 W_2 + \Gamma_{13} W_1^2 W_3 + \Gamma_{14} W_1 W_2^2 + \Gamma_{15} W_1 W_3^2 \\ & + \Gamma_{16} W_2^3 + \Gamma_{17} W_2^2 W_3 + \Gamma_{18} W_2 W_3^2 + \Gamma_{19} W_3^3 + \Gamma_{110} W_1 W_2 W_3) \\ \ddot{W}_2 + \Omega_2^2 W_2 = & -2C_2 \dot{W}_2 + 2\cos\theta (\dots \mu_2 \dots) + (\dots \Gamma_2 \dots) \\ \ddot{W}_3 + \Omega_3^2 W_3 = & -2C_3 \dot{W}_3 + 2\cos\theta (\dots \mu_3 \dots) + (\dots \Gamma_3 \dots) \end{aligned} \quad (15)$$

The above set of equations constitute the final form assumed by the equations of motion. They represent a system of second-order nonlinear differential equations with periodic coefficients, which may be considered as extensions of the standard Mathieu-Hill equation.

4. SOLUTION OF THE TEMPORAL EQUATIONS OF MOTION

The method of asymptotic expansion in powers of a small parameter ϵ , developed by Mitropolskii [11] and generalized by Agrawal and Evan-Iwanowski [12], is used to solve the previous set of equations of motion. Assuming that the present system is weakly nonlinear and that the instantaneous frequency of excitation and the load parameter vary slowly with time, the temporal equation of motion (13) can be written in the following asymptotic form:

$$\ddot{W}_m + \Omega_m^2 W_m = \epsilon [-2C_m \dot{W}_m + 2\cos\theta \sum_n \mu_m^{(n)} \Omega_n^2 W_n - \sum_{i,j,k} M_m^{(1)} k W_i W_j W_k] \quad (16)$$

Confining ourselves to the first order of approximation in ϵ , we seek a solution of equation (16) in the following form:

$$w_m = a_m(T) \cos \psi_m(T) \quad (17)$$

where $T = \epsilon\tau$ represents the "slow" time, and where a_m and ψ_m are functions of time defined by the system of differential equations

$$\begin{aligned} \frac{da_m}{dT} &= \dot{a}_m = \epsilon A_m^{\text{II}}(T, \theta, a, \psi) \\ \frac{d\psi_m}{dT} &= \dot{\psi}_m = \Omega_m(T) + \epsilon B_m^{\text{II}}(T, \theta, a, \psi) \end{aligned} \quad (18)$$

and $d\theta(\tau)/d\tau = \Lambda(T)$ is the instantaneous frequency of the external in-plane excitation. Functions $A_m^{\text{II}}(T, \theta, a, \psi)$ and $B_m^{\text{II}}(T, \theta, a, \psi)$ are selected in such a way that equation (17) will, after replacing a_m and ψ_m by the functions defined in equations (18), represent a solution of equation (16).

Following the general scheme of constructing asymptotic solutions and considering an additive combination resonance involving only two spatial forms of vibration, which is the case of the present analysis, then after some tedious transformations and manipulations, we can arrive finally at a system of equations describing the nonstationary response of the discretized system.

5. STATIONARY RESPONSE

The region of parametric combination instability and the stationary response associated with the combination additive resonance $\Lambda = \Omega_1 + \Omega_3$ may be calculated as a special case of the nonstationary motions in the resonant regime described previously.

Stationary values for the specified parametric combination resonance are given by

$$a_1 = \frac{2}{\left[\frac{3\Gamma_{11}}{2\Omega_1} + \frac{\Gamma_{14}}{\Omega_1} + \frac{\Gamma_{32}}{\Omega_3} + \frac{3\Gamma_{36}}{2\Omega_3} \left[\frac{C_1\mu^3\Omega_1^2(\Lambda+\Omega_1-\Omega_3)}{C_3\mu^3\Omega_3^2(\Lambda-\Omega_1+\Omega_3)} \right] \right]^{1/2}} \times$$

$$\left[\Lambda - \Omega_1 - \Omega_3 + \left[\frac{C_1}{C_3} \right]^{1/2} + \left[\frac{C_3}{C_1} \right]^{1/2} \right] \left[\frac{\mu^3\Omega_1^2\Omega_3^2}{(\Lambda+\Omega_1-\Omega_3)(\Lambda-\Omega_1+\Omega_3)} - C_1C_3 \right]^{1/2} \quad (19)$$

$$a_3 = a_1 \left[\frac{C_1\mu^3\Omega_1^2(\Lambda+\Omega_1-\Omega_3)}{C_3\mu^3\Omega_3^2(\Lambda-\Omega_1+\Omega_3)} \right]^{1/2} \quad (20)$$

In equation (19), of which the amplitude of vibration associated with the first mode is evaluated, only positive real values for the amplitude are admitted and the \pm sign indicates the possibility of two solutions: the larger of the two solutions is stable while the lower solution is unstable and physically unrealizable. The steady-state amplitude associated with the third spatial form of vibration is then calculated in using equation (20).

Near the resonance, that is $\Lambda \approx \Omega_1 + \Omega_3$, the frequency relationships in the radical of equation (20) can be modified as follows: $\Lambda + \Omega_1 + \Omega_3 \approx 2\Omega_1$ and $\Lambda - \Omega_1 + \Omega_3 \approx 2\Omega_3$. Since the damping coefficients and the loaded natural frequencies appearing in the aforementioned equation are strictly positive, it follows that one of the conditions for the occurrence of this kind of combination resonance is

$$\text{sign } \mu_1^3 = \text{sign } \mu_3^3 \quad (21)$$

We now consider the complete equation (19) for the amplitude of the response. Here again, however, it is necessary that the last inner radical be nonimaginary in order that the physical amplitude of the response be real. This places a condition on the relationship between the product of loading parameters and the product of damping coefficients. The required condition is

$$\mu_1^3 \mu_3^3 = \mu^2 \frac{C_1 C_3 (\Lambda + \Omega_1 + \Omega_3) (\Lambda - \Omega_1 + \Omega_3)}{\Omega_1^2 \Omega_3^2} \quad (22)$$

This condition simply means that the product of loading parameters must be strong enough to overcome the effect of the damping forces acting on the plate. Otherwise, a physically realizable solution does not exist.

The base width of the stationary response is the only region in which vibrations may normally initiate. By setting $a_1 = 0$ in equation (19) and introducing the decrement of viscous damping $\Delta = 2 - C_m \Omega_m$, we obtain

$$\begin{aligned} \Lambda^4 - 2(\Omega_1 + \Omega_3)\Lambda^3 + 4\Omega_1\Omega_3 + (\Delta^2 - (\Omega_1 + \Omega_3)^2)\Lambda^2 + 2(\Omega_1 + \Omega_3)(\Omega_1 - \Omega_3)^2\Lambda \\ + (\Omega_1 - \Omega_3)^2(\Omega_1 + \Omega_3)^2 + 1 + (\Delta^2 - \Omega_1^2 - \Omega_3^2 - \Omega_1\Omega_3(\Omega_1 + \Omega_3^2))\mu_1^3\mu_3^3 = 0 \end{aligned} \quad (23)$$

The foregoing equation makes it possible to locate in the (μ, Λ) parameter space the boundaries of the region of instability associated with the specified combination resonance of the summed type.

6. NUMERICAL RESULTS AND DISCUSSION

In order to get more insight into various aspects of the problem and to highlight the influence of various system parameters on the stability characteristics and the response of rectangular plates associated with combination resonances, numerical evaluation of the solution was performed for a wide variety of cases and the results shown in Figs. 2 through 8 are typical of those obtained. The specified values of the plate parameters and material constants used for the numerical calculations are given in Table 1.

Based on the conditions (21) and (22) for the occurrence of combination resonances in the general case, the numerical evaluation of the specimens considered reveals that, for the first three modes of vibration, only a combination resonance of the summed type involving the first and the third spatial form of vibration is possible. Hence, only the resonance relationship $\Lambda = \Omega_1 + \Omega_3$ is used throughout the present analysis.

TABLE 1. Specifications of plate parameters

Specimen	Dimensions (mm) a x b x h	Aspect Ratio R
P.1	293 x 508 x 1	1.734
P.2	254 x 508 x 1	2
P.3	200 x 508 x 1	2.54

Modulus of Elasticity: $E = 2.385 \text{ GPa}$
Poisson's Ratio: $\nu = 0.45$
Density: $\rho = 1200 \text{ kg/m}^3$

Figure 2 shows the region of instability associated with the specified combination resonance, and at the same time the effect of varying linear damping on this instability zone. As can be seen, an increase in Δ has the beneficial effect of increasing the amount of withdrawal of the instability region from the frequency ordinate $\Lambda_1 (\Omega_1 + \Omega_3)$. A moderate amount of damping can also preclude the possibility of combination resonance, even for large excitation amplitudes.

The results shown in Fig. 3 indicate that the aspect ratio R can play a certain role in determining the combined stability characteristics of rectangular plates with this particular case of boundary conditions. Reference to this figure shows that an increase of the aspect ratio does decrease the length of the combination instability zone, where the computed data corresponding to the upper limits of the boundaries of this combined region are associated with a given value of the dynamic component of the in-plane load. This implies that, considering only the occurrence of the aforementioned combination resonance, an increase in R has a somewhat stabilizing effect on the system.

In contrast with the previous system parameters, an increase of the static (N_{y0}) or dynamic (N_{yt}) component of the in-plane load is usually destabilizing for the system under study. As is known, an increase in N_{y0} lowers the natural frequencies of the system and, consequently, shifts the instability region associated with a combination resonance to lower load frequencies as shown in Fig. 4. This means that a variation of the static component of the in-plane load may render a stable plate unstable. Simultaneously, an increase in the static or dynamic component of the in-plane load lengthens, or widens, the combination instability zone. This implies that the occurrence of this combination resonance augments with an increase of the periodic load amplitudes.

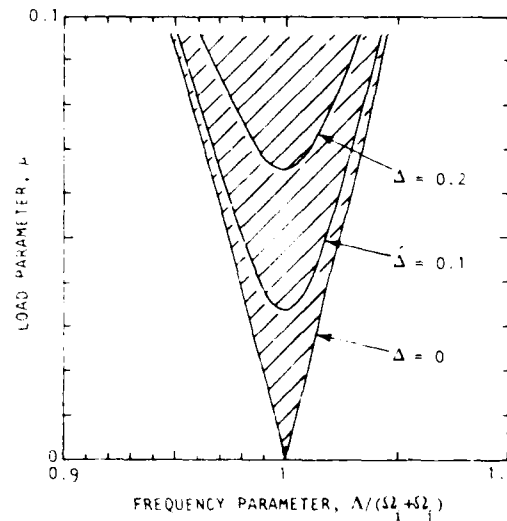


FIG. 2 Region of instability associated with any combination additive resonance involving two modes of vibration

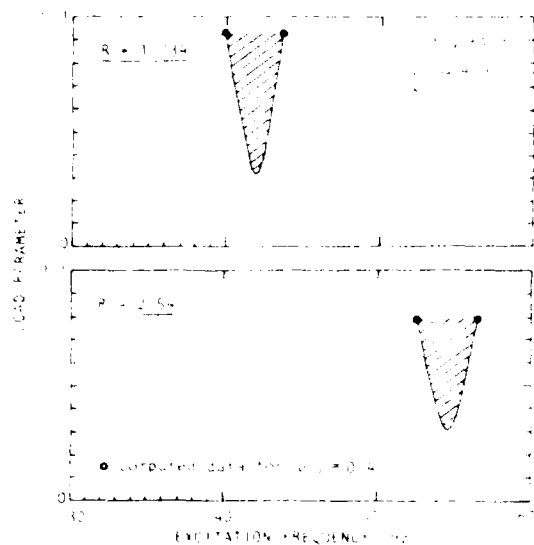


FIG. 3 Effect of varying the aspect ratio on the combination instability zone

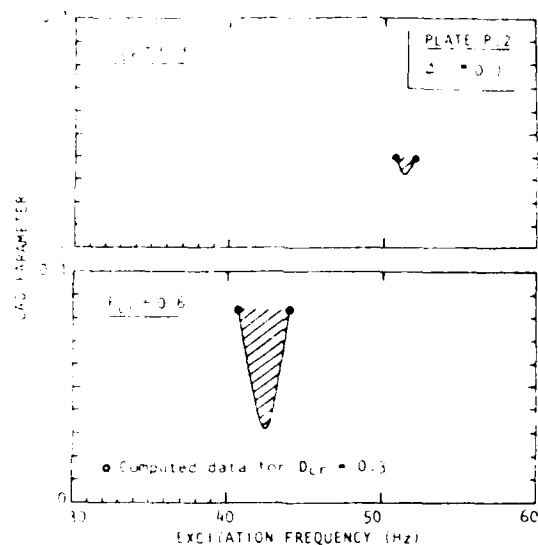


FIG. 4 Effect of varying static in-plane load N_{y0} on the combination instability zone

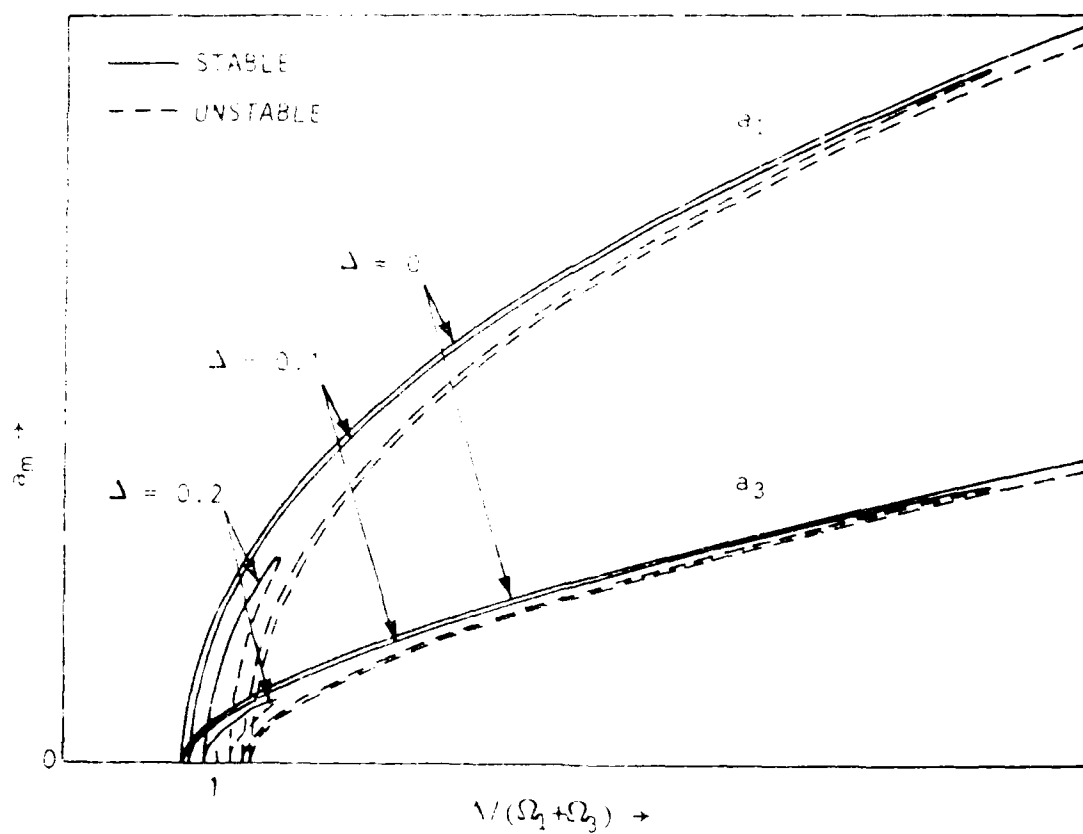


FIG. 5 Stationary response curves associated with a combination additive resonance

Typical stationary frequency-response curves associated with the specified combination resonance are illustrated in Fig. 5. All of the response curves exhibit a right-hand overhang which is typical of a "hard spring" effect. The results also indicate the domination of the lower mode over the stationary response when two mode shapes are involved in a combination additive resonance. Fig. 5 also shows the beneficial effect of linear viscous damping on the combination resonance response. An undamped system response exhibits neverending steady-state amplitudes. Nevertheless, an increase in linear damping narrows the instability zone and reduces the maximum values of the overhangs.

The frequency-response curves associated with the resonance $\Lambda = \Omega_1 + \Omega_3$ for two different values of the aspect ratio are shown in Fig. 6. The results illustrate once again the stabilizing influence of increasing R , as mentioned previously.

Figures 7 and 8 show the effects of varying the static and dynamic components of the in-plane load on the combination resonance response of a rectangular plate. It stands to reason that, for the system investigated an increase in N_{y0} or N_{yt} should always be destabilizing. This destabilizing effect manifests itself in two typically contrasting fashions. Firstly, an increase in N_{y0} moves the combination instability zone to lower load frequencies. Secondly, an amplitude increase of any component of the periodic in-plane load widens the combination instability zone and augments the maximum values of the corresponding overhangs.

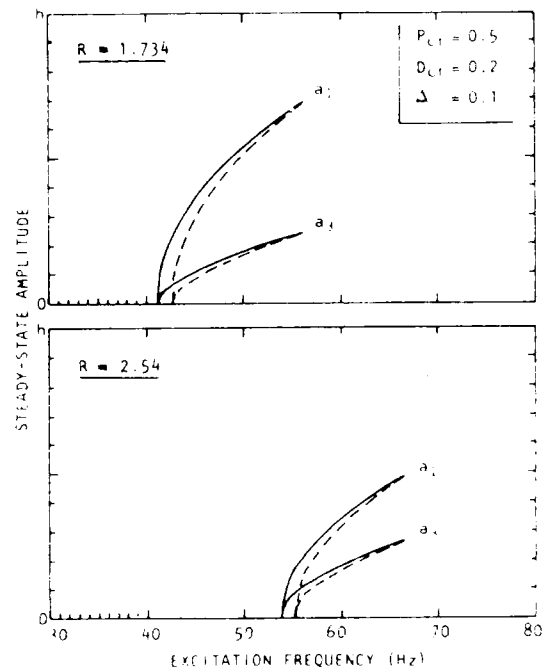


FIG. 6 Effect of varying the aspect ratio on the combination resonance response curves

7. CONCLUDING REMARKS

Rectangular plates subjected to the action of periodic in-plane forces uniformly distributed along two opposite edges are theoretically analyzed under the assumption that the two loaded edges of a plate are clamped and the other two unloaded edges are simply supported and stress-free. The solution for this kind of boundary conditions indicates, besides the possibility of principal parametric resonances and simultaneous resonances (external resonance coinciding with an internal resonance), the presence of parametric combination resonances. Moreover, only combination additive resonances involving either two odd or two even spatial modes of vibration are possible [5], a combination resonance involving the first and third mode shapes being considered in this work.

The results of the present investigation show that damping has a stabilizing influence on the system under a condition of combination resonance. An increase in the aspect ratio of the plate also has a somewhat stabilizing effect on the stability characteristics and system response. On the contrary, an increase of the static or dynamic component of the in-plane

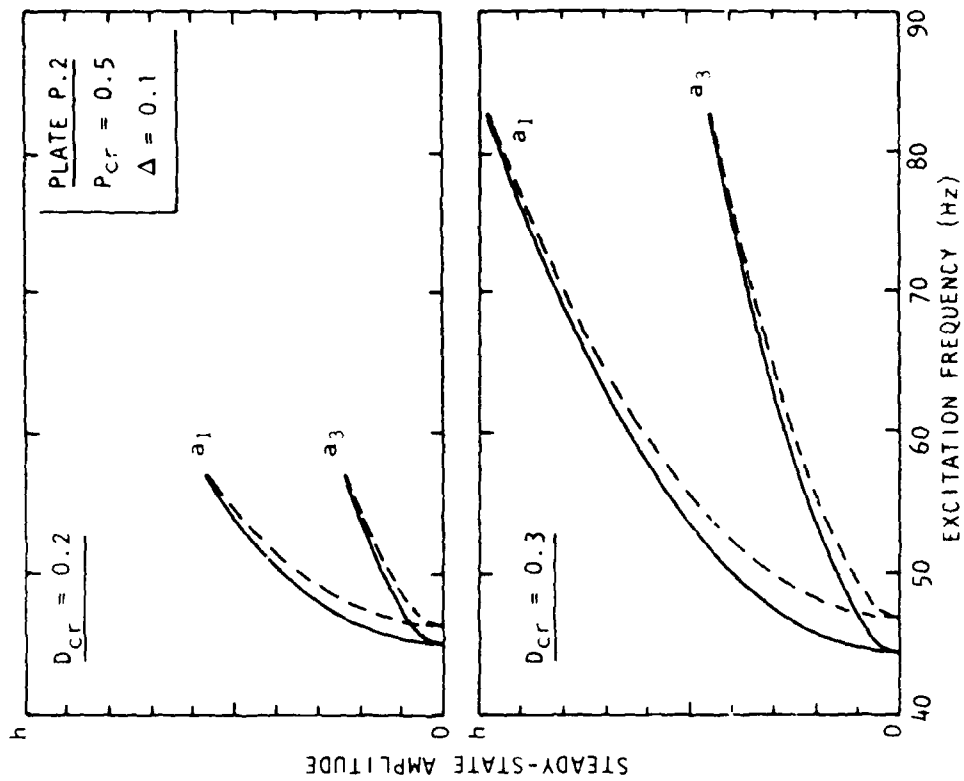


FIG. 8 Effect of varying dynamic in-plane load N_{yt} on the combination resonance response curves

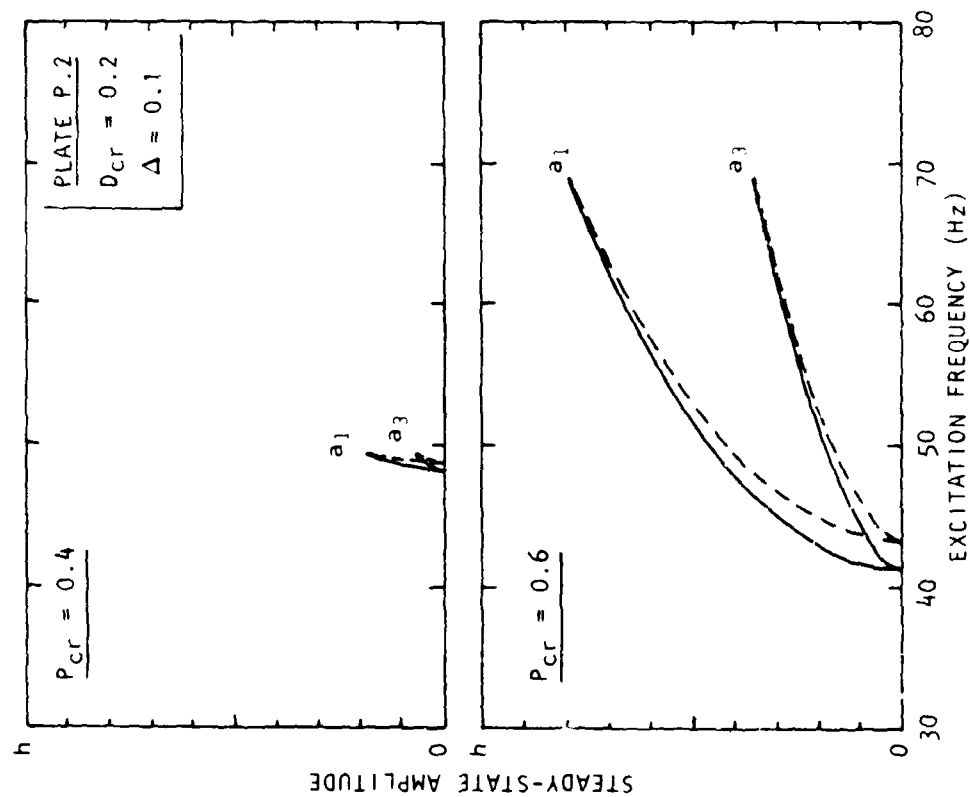


FIG. 7 Effect of varying static in-plane load N_{yo} on the combination resonance response curves

load is usually destabilizing for the system investigated. The graphical results also show that the response associated with the combination additive resonance under study exhibits small amplitudes of vibration where the lower mode shape dominates the response.

ACKNOWLEDGEMENTS

The study was sponsored in part by the National Sciences and Engineering Research Council of Canada (Grant A-4207), for which the authors express gratitude.

REFERENCES

1. V.V. BOLOTIN 1964 The Dynamic Stability of Elastic Systems. San Francisco: Holden-Day Inc.
2. R.M. EVAN-IWANOWSKI 1976 Resonance Oscillations in Mechanical Systems. New York: Elsevier/North-Holland Inc.
3. A.H. NAYFEH and D.T. MCCOOK 1979 Nonlinear Oscillations. New York: John Wiley & Sons.
4. G.L. OSTIGUY and H. NGUYEN 1986 Proceedings of the 1986 Pressure Vessels and Piping Conference, Design and Analysis of Plates and Shells, Vol.105, Chicago, Illinois, July 20-24, 1986, 127-135. Recent developments on the nonlinear parametric vibrations of rectangular plates.
5. H. NGUYEN 1987 Ph.D. Thesis, Ecole Polytechnique de Montreal. Effect of boundary conditions on the dynamic instability and responses of rectangular plates.
6. K.S. JAGADISH 1974 Ingenieur-Archiv 43, 240-246. The dynamic stability of degenerate systems under parametric excitation.
7. N. YAMAKI and K. NAGAI 1975 Tohoku University, Report No. 288 of the Institute of High Speed Mechanics 32, 103-127. Dynamic stability of rectangular plates under periodic compressive forces.
8. K. TAKAHASHI, M. TAGAWA and T. IKEDA 1985 University of Tokyo Proceedings of the 33rd Japan National Congress for Applied Mechanics 33, 311-318. Dynamic stability of a rectangular plate subjected to inplane moment.
9. P.R. DIXON and J.R. WRIGHT 1970 Aeronautical Research Council, A.R.C. 32670 Report No. 129. Parametric instability of flat plates.
10. C.Y. CHIA 1980 Nonlinear Analysis of Plates. New York: McGraw-Hill.
11. Yu.A. MITROPOLSKII 1965 Problems of the Asymptotic Theory of Nonstationary Vibrations. New York: D. Davey & Co., Inc.
12. B.N. AGRAWAL and R.M. EVAN-IWANOWSKI 1973 AIAA Journal 11(7), 907-912. Resonances in nonstationary, nonlinear, multidegree-of-freedom systems.

DEFINITION OF SYMBOLS

$R = b/a$: Plate aspect ratio

$P_{cr} = N_{y0}/N^*$: Ratio of static over critical loading

$D_{cr} = N_{yt}/N^*$: Ratio of dynamic over critical loading

N^* : Lowest critical load

11. STRUCTURAL/ ACOUSTIC INTERACTION

A. Frid

Division of Solid Mechanics
Chalmers University of Technology
S-41296 Gothenburg, Sweden

1. INTRODUCTION

Fluid vibrations in piping systems are often classified as being either transient or stationary. An important subgroup of the latter are the harmonic vibrations (forced and free). This paper presents a 'Structural Mechanics Approach' to the linear analysis of uniaxial vibrations of compressible fluids. All the categories mentioned above will be dealt with.

The present approach sets out from the differential equation for a bar in tensile vibration and ends with a systematized matrix method, suitable for computer implementation. The fluid motion in each pipe is assumed to be uniaxial and no fluid-structure interaction is considered except for a reduction in longitudinal wave speed as caused by the radial flexibility of pipe walls. Distributed damping is included.

A mobility matrix method is used in the study of harmonic vibration. It is analogous to the stiffness method in structural mechanics [1]. The behaviour of each member (finite element) is represented by an exact frequency-dependent 1×1 or 2×2 member mobility matrix (complex-valued). The member matrices are assembled into a structure mobility matrix following the standard assembly procedure of the stiffness method. Six types of members are incorporated as shown in Figure 1.

The 2×2 mobility matrix for the finite fluid column member is a reformulation of the well-known four pole matrix of the transfer matrix method, eg [2], used in the traditional 'Acoustical Approach' to harmonic vibration. The use of the transfer method is easy and straightforward for simple systems but is complicated for large systems containing several branches and loops. An analysis by the the mobility method, however, is practically insensitive to the system topology and thus should be especially attractive to use for complex piping systems.

In the mobility matrix formulation, undamped eigenfrequencies can be calculated by use of the algorithm of Wittrick and Williams [3].

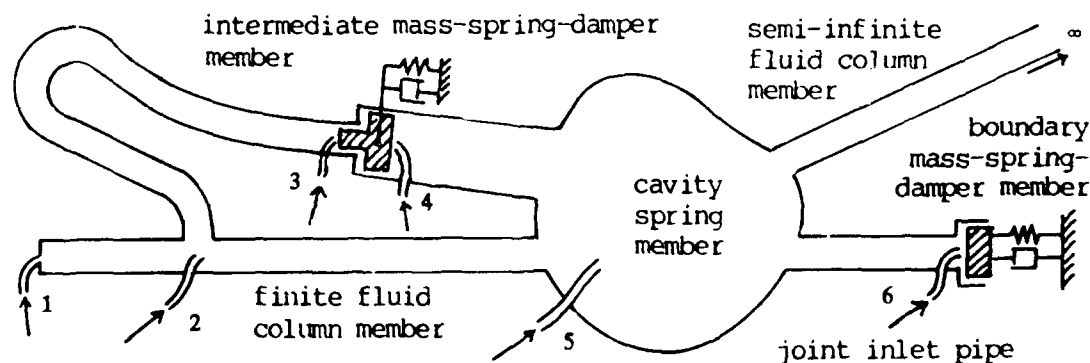


Figure 1. Piping system composed of $J=6$ joints and $K=9$ members. Relative size of cavity spring member has been exaggerated. No modal body is shown

When eigenfrequencies, eigenmodes and modal masses are known for a system, transient responses can be calculated by the method of modal superposition which is a standard technique in solid body structural mechanics. The total transient response is then formed as a weighted sum of contributions from eigenmodes. Applications of modal superposition have so far been rare in the field of fluid vibration. However, the bond graph technique was extended to modal analysis of piping systems by Lebrun [4]. Acoustical approaches, like the method of characteristics and similar wave propagation methods [5], eg Boucher and Kitsios [6], have been more common in the analysis of transient vibration.

At the end of this paper, the structural mechanics method will be applied to some simple piping geometries where the correctness of the results can be checked. The present method has been implemented in the computer program SFVIBAT-DAMP [7] which was used in the numerical examples.

2. NOMENCLATURE

Appropriate SI-units are given for the quantities. Some locally used symbols are explained where introduced and are not listed below.

A	Cross-sectional area of inlet pipes and fluid column members	m^2
a(t)	Inward inlet pipe fluid acceleration	m/s^2
c	Wave speed = $(K/\rho)^{1/2}$	m/s
c_n	Modal damping number n	Ns/m
i	Imaginary unit	-
K	Compressive stiffness of fluid (bulk modulus)	Pa
k_n	Modal stiffness number n	N/m
L	Length of member fluid column	m
m_n	Modal mass number n	kg
p^{e*}	Member (element) pressure amplitude column matrix (2x1)	Pa
P	Structure pressure amplitude column matrix (Jx1)	Pa
$q_n(t)$	Modal displacement number n	m
$Q_n(t)$	Modal load number n	N
s(t)	Inward inlet pipe fluid displacement	m
t	Time coordinate	s
v^{e*}	Member (element) volume velocity amplitude column matrix (2x1)	m^3/s
v^*	Structure volume velocity amplitude column matrix (Jx1)	m^3/s
x	Length coordinate	m
y^{e*}	Member (element) mobility matrix	$(m^3/s)/Pa = m^5/Ns$
Y	Structure mobility matrix (JxJ)	m^5/Ns
η	Dynamic viscosity of fluid	$Pa/(1/s) = Ns/m^2$
κ	Wave number = ω/c	$1/m$
ρ	Density of fluid	kg/m^3
ω	Radian frequency = $2\pi f$	$1/s$

Indices

j	Current index of structural joints ($j = 1, 2, \dots, J$)
k	Current index of members ($k = 1, 2, \dots, K$)
n	Current index of modes ($n = 1, 2, \dots, N$)
d	Subscript for damping
e	Superscript for member (element)
r	Subscript for reduced
() [*]	Superscript indicating complex quantity
()'	Derivative d/dx or $\partial/\partial x$
() [.]	Derivative d/dt or $\partial/\partial t$

3. MEMBER ANALYSIS

The member (or element) matrices $Y^e(\omega)$ will be given for the fluid members. These matrices relate end volume velocity amplitudes to end pressure amplitudes at a certain radian frequency ω . Generally, one has

$$Y^e p^e = v^e \quad (1)$$

No mean flow will be considered in the member analysis. For a nonzero mean velocity v_{mean} , this will be an acceptable approximation provided that $|v_{\text{mean}}|/c \ll 1$. The six types of members incorporated are introduced below.

3.1 Fluid Column Members

The uniform fluid columns 12 and 1 ∞ in Figure 2 perform uniaxial harmonic vibration at radian frequency ω . The member mobility matrices Y^e for these members are [8], respectively,

$$Y^e = (iA^e/\rho c^*) \begin{bmatrix} -1/\tan \kappa^* L & 1/\sin \kappa^* L \\ 1/\sin \kappa^* L & -1/\tan \kappa^* L \end{bmatrix} \quad Y_{11}^e = A^e/\rho c^* \quad (2a,b)$$

The so-called frequency parameter is $\kappa^* L = \omega/(K^*/\rho L^2)^{1/2}$. Radial flexibility of the pipe wall can be included through a reduced compressive stiffness K_r . For a circular pipe one has $K_r = K/(1+2Kr/Eh)$ where r is the inner radius, E the Young modulus and h the wall thickness. Damping is accounted for through the complex wave number $\kappa^* = \kappa - i\alpha$ where the attenuation constant α can be expressed as, eg [2], $\alpha = (\omega\eta/2\rho)^{1/2}/cr$.

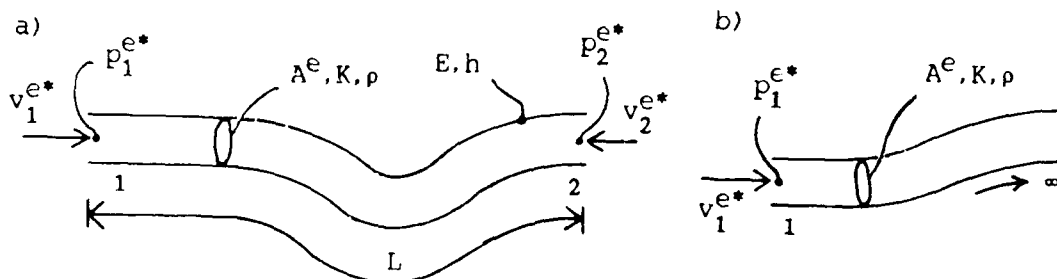


Figure 2. a) Finite uniform fluid column 12 of length L , cross-sectional area A^e , density ρ and compressive stiffness K (or K_r). b) Semi-infinite fluid column member 1 ∞ . Chosen positive directions for volume velocities

3.2 Discrete Mass-Spring-Damper Member

This member (abbreviated as msd-member) can be either one- or two-terminal as shown in Figure 3. The boundary msd-member can be seen as an intermediate msd-member having zero pressure on the outer piston face, thus reducing to a one-terminal member. The member mobility matrix for these two msd-members are [8]

$$Y^e = [1/(i\omega M_0 + C_0 + S_0/i\omega)] \begin{bmatrix} A_1^2 & -A_1 A_2 \\ -A_1 A_2 & A_2^2 \end{bmatrix} \quad (3a)$$

$$Y^e = [1/(i\omega M_0 + C_0 + S_0/i\omega)] A_1^2 \quad (3b)$$

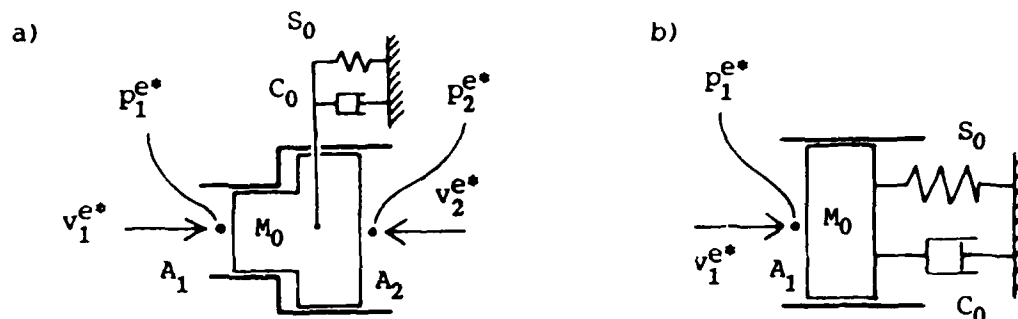


Figure 3. a) Intermediate msd-member with mass M_0 , stiffness S_0 , damping C_0 , and piston areas A_1 and A_2 . b) boundary msd-member with piston area A_1

3.3 Cavity Spring Member

The one-terminal cavity spring member represents a volume in which the pressure is equal at all positions. It thus acts as a pure spring stiffness (or capacitance). This approximation requires that the wavelength in the adjoining fluid columns is much greater than the diameters of the cavity. The member mobility matrix for a cavity spring member is [8]

$$Y_{11}^{e*} = i\omega V_0/K_0 \quad (4)$$

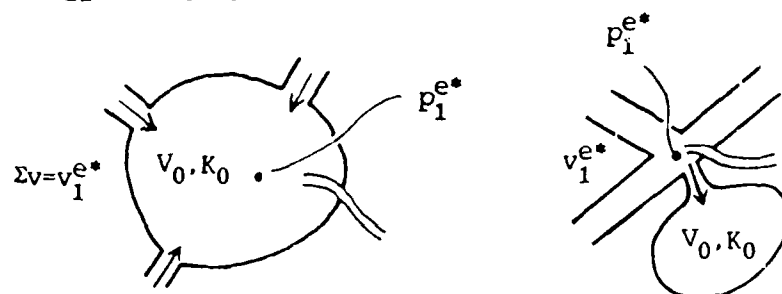


Figure 4. Two equivalent cavities at joint $j=1$ with volume V_0 and compressive stiffness K_0 (where K_0 may account for flexibility of cavity walls)

3.4 Modal Body Member

This multi-terminal member can be used to model a cavity when its diameters are not small as compared to the wavelengths considered. The modal properties (eigenfrequencies, modal masses and eigenmode displacements at connecting joints) of the cavity must then be known for all modes $n=1,2,\dots,N$ considered. The elements Y_{ij} in the member mobility matrix are [8]

$$Y_{ij}^{e*} = i\omega A_i A_j \sum_{n=1}^N p_i^{(n)} p_j^{(n)} / [m_n (\omega_n^2 - \omega^2)] \quad (5)$$

The modal parameters may have been found from a physical experiment or a separate standard finite element calculation (three-dimensional). Modal damping may be added in the denominators in (5).

4. STRUCTURE ANALYSIS

At each joint j ($j=1,2,\dots,J$) of the piping system, a so-called inlet pipe (see Figure 1) is connected where either pressure p_j^* or volume velocity v_j^* must be prescribed. These inlet pipes may not physically exist at all joints but are helpful in clarifying computational procedures. At an open inlet $p_j^*=0$, and at a closed inlet $v_j^*=0$. A harmonic excitation source can be located at the inlet pipe of a joint j by prescribing a nonzero value for either p_j^* or v_j^* .

The $J \times J$ structure mobility matrix $Y^*(\omega)$ is the coefficient matrix of a system of J scalar equations. It is formed by adding all member mobility matrices, equation (6b), into their correct positions.

$$Y^*(\omega)p^* = v^* \quad Y^* = \sum Y_k^{e*} \quad (6a,b)$$

The assembly of member matrices into a structure matrix is based on two assumptions: At each structural joint 1) the pressures are the same for all connecting member ends and 2) the sum of volume flows into the connecting member ends equals the applied volume flow through the joint inlet pipe. Since analogous conditions prevail at the joints of a beam structure, the assembly of the structure mobility matrix for fluid vibration in a piping system [8] is identical to the assembly of the stiffness matrix for a frame structure (a simplifying fact is that no coordinate transformations between the members and the structure are needed here since only scalar quantities are dealt with).

5. EIGENFREQUENCIES AND MODAL PROPERTIES

Eigenfrequencies ω_n and eigenmodes $p^{(n)}$ of an undamped piping system without mean flow satisfy the equation

$$Y^*(\omega)p^* = 0 \quad (7)$$

Here the matrix $Y^*(\omega)$ will be symmetric. For an undamped structure without semi-infinite members, every non-zero element in the structure mobility matrix $Y^*(\omega)$ is pure imaginary and real eigenvalues and eigenmodes are obtained. The mobility matrix can be condensed through deletion of the rows and columns belonging to joints having zero pressure. The eigenvalue problem then is to find the roots of the determinantal equation

$$|Y^{*cond}(\omega)/i| = 0 \quad (8)$$

For a structure including continuous members (as in our case) the equation is transcendental comprising trigonometric functions. The Wittrick-Williams algorithm [3], accounting also for dofs 'between joints', is preferably used for such systems. When an eigenfrequency ω_n has been determined, the associated eigenmode $p^{(n)}$ is obtained by solving (7) with $\omega=\omega_n$ inserted.

5.1 Resonance

Resonance of a harmonically excited undamped structure occurs when the forcing frequency ω is equal to (or close to) one of the eigenfrequencies ω_n given by (8). Since we are dealing with real amplitudes for the undamped case, asterisks (*) indicating complex quantities will be dropped in the following. When determining the relevant eigenfrequencies ω_n and

eigenmodes $p^{(n)}$, the appropriate boundary condition (either $p_j=0$ or $v_j=0$) to be used at the inlet pipe of a typical joint j depends on the type of excitation:

- o A joint j where a prescribed volume flow $v_j e^{i\omega t}$ acts should be closed ($v_j=0$) in the eigenvalue analysis. Resonance in eigenmode number n will then be excited at $\omega=\omega_n$ by $v_j \neq 0$ if $p_j^{(n)} \neq 0$.
- o A joint j where a prescribed pressure $p_j e^{i\omega t}$ acts should be open ($p_j=0$) in the eigenvalue analysis. Resonance in eigenmode number n will then be excited at $\omega=\omega_n$ by $p_j \neq 0$ if $v_j^{(n)} \neq 0$.

6. METHOD OF MODAL SUPERPOSITION

In the method of modal superposition, an N degree-of-freedom (N dof) system is decoupled into N single degree-of-freedom (1 dof) systems, from which the total response is superposed. Each of these 1 dof systems represents an eigenmode of the structure. For a continuous structure (infinitely many degrees-of-freedom), an infinite number of 1 dof-systems must be substituted in order to give an exact result. Practically, however, it is often sufficient to include relatively few modes and still get an accurate response.

For a piping system the modal parameters in Figure 5 are [1],[9]

$$m_n = \int A \rho [u^{(n)}(x')]^2 dx' + \Sigma M_0 [u^{(n)}(x_0)]^2 \quad k_n = m_n \omega_n^2 \quad (9a,b)$$

$$c_n = \zeta_n c_{n,crit} \quad c_{n,crit} = 2m_n \omega_n \quad (9c,d)$$

$$Q_n(t) = \int U(x',t) u^{(n)}(x') dx' + \Sigma F_0(t) u^{(n)}(x_0) \quad (9e)$$

In equations (9a-e), $u^{(n)}(x')$ is the particle displacement in eigenmode number n , M_0 the mass of a rigid body, $U(x',t)$ the distributed load along a member, and $F_0(t)$ the concentrated load at a joint.

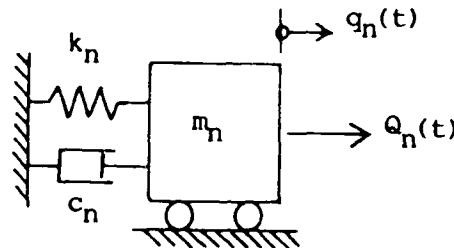


Figure 5. Single degree-of-freedom system representing eigenmode number n , characterized by modal mass m_n , modal stiffness k_n and modal damping c_n . System is subjected to a modal load $Q_n(t)$ causing a modal displacement $q_n(t)$

So-called proportional (or Rayleigh) damping has been assumed. The modal displacement $q_n(t)$ is calculated from the equation of motion for the 1 dof-system,

$$m_n \ddot{q}_n(t) + c_n \dot{q}_n(t) + k_n q_n(t) = Q_n(t) \quad (10)$$

Initial conditions on $q_n(t)$ are required and can be found in a standard way from the initial conditions on $u(x,t)$. Transient responses are superposed by contributions from each retained eigenmode,

$$p_j(t) = \sum q_n(t) p_j^{(n)} \quad p_1^e(t) = \sum q_n(t) p_1^{e(n)} \quad (11a,b)$$

$$s_j(t) = \sum q_n(t) s_j^{(n)} \quad s_1^e(t) = \sum q_n(t) s_1^{e(n)} \quad (12a,b)$$

$$v_j(t)/A_j = \sum \dot{q}_n(t) s_j^{(n)} \quad v_1^e(t)/A^e = \sum \dot{q}_n(t) s_1^{e(n)} \quad (13a,b)$$

$$a_j(t) = \sum \ddot{q}_n(t) s_j^{(n)} \quad a_1^e(t) = \sum \ddot{q}_n(t) s_1^{e(n)} \quad (14a,b)$$

6.1 Transient Force Excitation

Transient pressures may be applied to joints that were open ($p_j=0$) in the eigenvalue analysis of the structure. The modal load from a number of transient joint pressures is $Q_n(t) = \sum p_j(t) A_j s_j^{(n)}$. Eigemode displacements $q_n(t)$ as caused by $Q_n(t)$ are now calculable from equation (10).

6.2 Transient Volume Acceleration Excitation

No intermediate msd-members and no modal body members (see Figures 1 and 3a) are considered for the piping systems studied here (these members will call for a special formulation).

Transient volume accelerations may be applied to joints j that were closed ($v_j=0$) in the eigenvalue analysis of the structure. For excitation at a typical joint j , the solution now consists of contributions from two loading cases [9]:

1. Volume acceleration $A_j a_j(t)$ in inlet pipe number j as applied to an imagined massless structure (quasistatic part of solution).
2. Distributed 'inertia' loads $U(x,t)=-m(x)a(x,t)$ and concentrated inertia loads $F_0(t)=-M_0 a(x_0)$ as applied to a structure in which the inlet pipe at the excited joint is closed ($v_j=0$) and where the acceleration $a(x,t)$ along the fluid members and the acceleration $a(x_0)$ of each rigid body are determined from loading case 1. The part of the solution from this loading case 2 can be calculated by modal superposition.

If the system has two or more open joints in excess of the excited joint j , the quasistatic solution is not unique. The present study does not consider this case.

If the system has one such open joint, the fluid between the excited joint and the open joint performs a rigid body motion while the fluid and the boundary msd-members in all branches remain still. For 'moving' fluid members k , one has $a_k(x,t) = (1/A_k^e) A_j a_j(t)$ and for members k in the branches, one has $a_k(x,t)=0$. The pressure $p(x,t)$ is zero for all members.

If the system has no open joints in excess of the excited joint j , the pressure can be calculated from the compression of all fluid column members k , cavity spring members l , and boundary msd-members m ,

$$p(t) = A_j s_j(t) / \left[\sum_k (V_k^e/K_k) + \sum_l (V_0/K_0) + \sum_m (A_1^2/S_0) \right] \quad (15)$$

The quasistatic acceleration $a^e(t)$ is now calculable from the compression of each member starting with the members in the branches. One finds $\Delta V_k^e(t) = (V_k^e/K_k) p(t)$. The quasistatic acceleration along each member in this case varies linearly as $a(x,t) = a_1(t) - [a_1(t) + a_2(t)]x/L$.

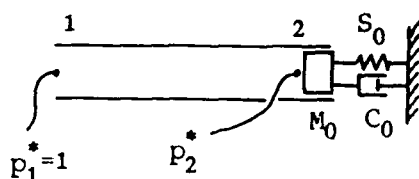
7. NUMERICAL EXAMPLES

Four numerical examples are studied below. The computer program SFVIBAT-DAMP [7] is applied.

7.1 Example 1 - Harmonic Pressure Excitation

The simple system in Figure 6 will be used to verify the correctness of the harmonic analysis. The pressure amplitude at joint 2 will be calculated for different values of S_0 , M_0 and C_0 when the pressure is prescribed at joint 1. The system consists of two structural joints ($j=1,2$) and one finite fluid column member with (see Figure 2) $L=1000$ m, $\rho=1000$ kg/m³, $K=1$ GPa, $A^E=0.03142$ m² (pipe radius 100 mm) and $\eta=10^{-6}$ Ns/m², and one msd-member with $A_1=0.03142$ m². Parameters S_0 and C_0 are varied.

a)



b) S_0 varied: c) C_0 varied:

closed end	100000 Ns/m
1000000 N/m	50000 Ns/m
100000 N/m	31420 Ns/m
10000 N/m	10000 Ns/m
	1000 Ns/m

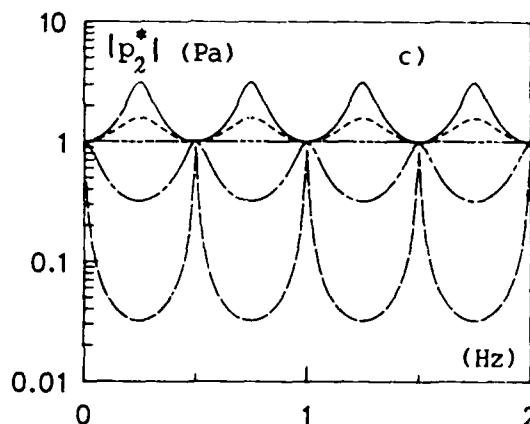
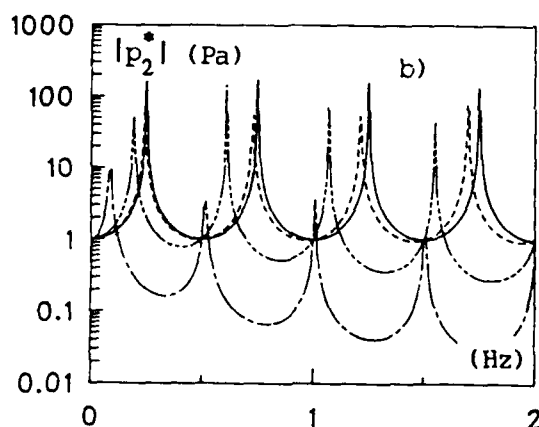


Figure 6. a) Piping system subjected to a harmonic unit pressure excitation ($p_1^*=1$). Calculated pressure amplitude at joint 2 when b) S_0 is varied while $M_0=0=C_0$, c) C_0 is varied while $S_0=0=M_0$

7.2 Example 2 - Eigenfrequencies

Eigenfrequencies are calculated for the system in Figure 7a for different values of M_0 . To [10] calculated resonance frequencies of the system in Figure 7 with $S_0 \rightarrow \infty$, i.e. a blocked end at joint 3. Figure 7b shows how the eigenfrequencies f_1 to f_3 are influenced by S_0 and how they ultimately approach To's values as S_0 goes to infinity. Fixed parameters for the system are $L_1=1.062$ m, $L_2=3.8327$ m, $L_3=0.2540$ m, $A^E=0.06998$ m², and $c=354.70$ m/s ($\rho=99.7$ kg/m³). No damping is considered.

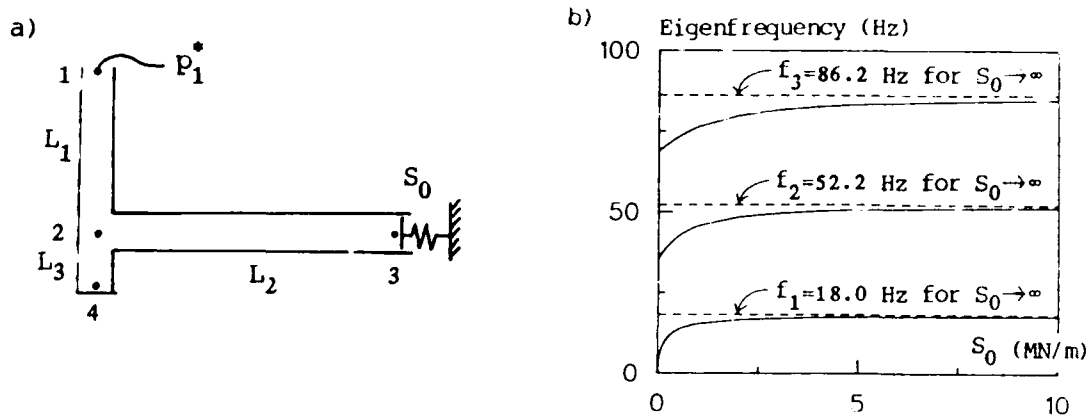


Figure 7. a) Branched system with four joints ($j=1,2,3,4$), three ffc-members and one msd-member (with $M_0=0$). b) Calculated lowest three eigenfrequencies as functions of spring stiffness S_0

7.3 Example 3 - Transient Pressure Excitation

The system in Figure 7a with a blocked end at joint 3 ($S_0 \rightarrow \infty$) will be studied. The pressure variation in Figure 8a may represent a sudden rupture at a joint in a pressurized system. An accurate representation of a propagating step pressure wave as in Figure 8 may demand contributions from relatively high-frequency modes. The highest mode ($N=60$) used in the present modal superposition has the period 0.456 ms.

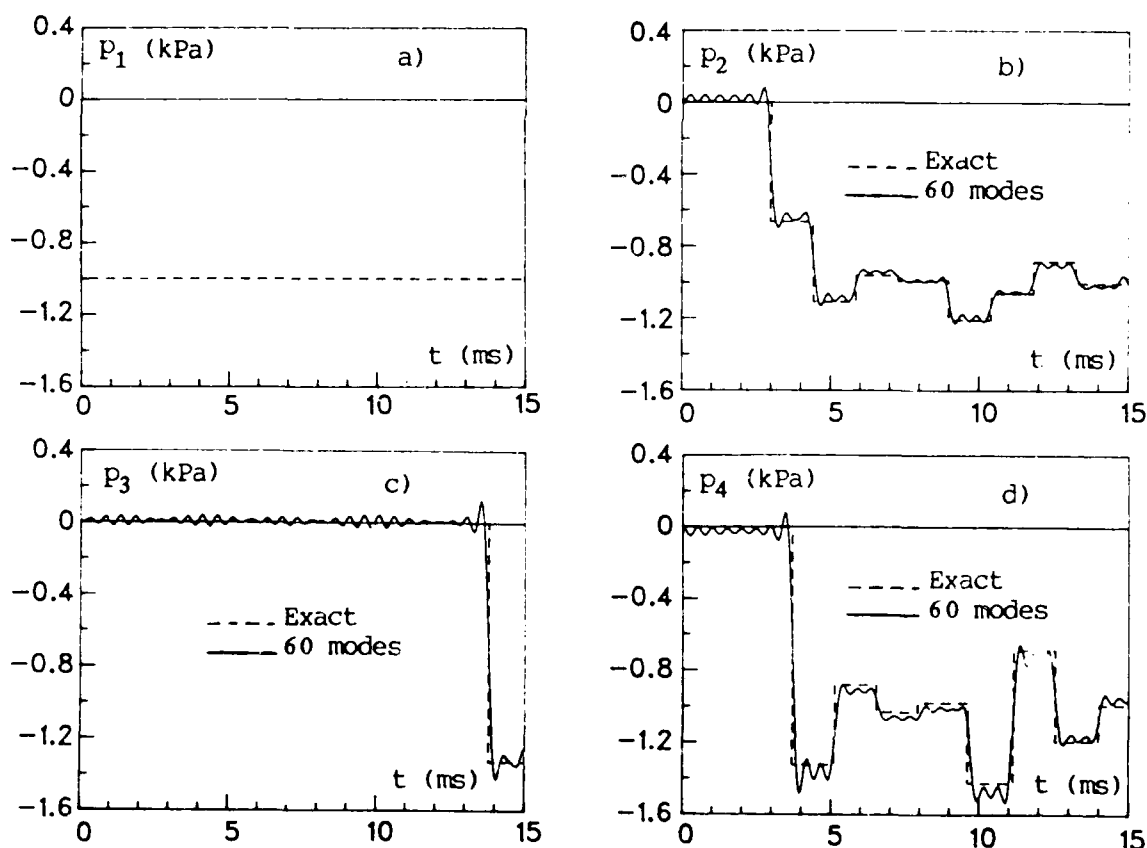


Figure 8. a) Applied transient step pressure of magnitude -1 kPa at time $t=0$ at joint 1 of system in Figure 7. Calculated pressure versus time at b) joint 2, c) joint 3, and d) joint 4

7.4 Example 4 - Transient Acceleration in Open System

The system in Figure 9 was analysed by Lebrun [4] who used the bond graph method to calculate transient pressures caused by valve operations. Parameters are $c=600$ m/s ($\rho=950$ kg/m³), $L_1=0.77$ m, $L_2=0.40$ m, $L_3=0.77$ m, $L_4=1.00$ m, $A_1^e=A_2^e=A_4^e=70.9$ mm², $A_3^e=491$ mm². Modal damping is considered. Fluid properties were omitted by Lebrun, so the present results cannot be compared with his results in detail. The valve opening is prescribed through the fluid acceleration (velocity change) at joint 1 shown in Figure 10a. The resulting pressure changes are plotted in Figure 10b.

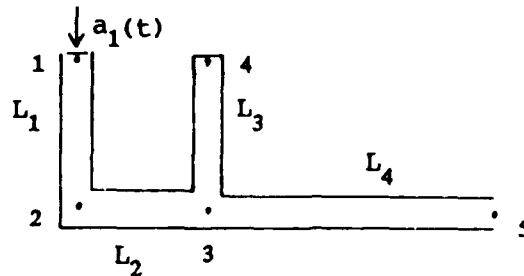


Figure 9. Piping system consisting of five joints and four ffc-members

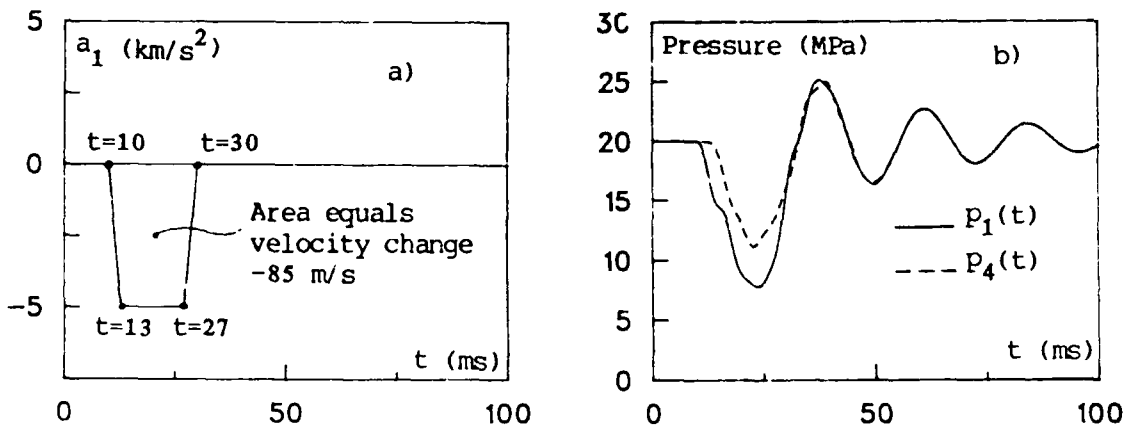


Figure 10. a) Transient acceleration applied at joint 1 of system in Figure 9. b) Calculated pressures at joints 1 and 2. Ten modes are considered, each with relative modal damping $\zeta_n=0.1$. Static pressure at time $t=0$ is 20 MPa

8. CONCLUDING REMARKS

A method suitable for a general and computerized analysis of linear uniaxial fluid vibration in piping systems has been developed. In both harmonic and transient vibration problems, the attractive features of this method become evident when large and complicated piping systems need be analysed. Branches and loops introduce no difficulties.

In harmonic vibration, the assembly of mobility matrices is by far a simpler procedure than the use of transfer matrices. Also eigenfrequencies (resonance frequencies) and eigenmodes of complicated systems are readily calculated when the present mobility matrix formulation is applied.

In transient vibration, the standard method of characteristics involves a time-stepping from the initial state, keeping track of transmitted and reflected waves. The present method of modal superposition calculates transient responses simply as weighted sums of contributions from a selected number of modes at any requested instant of time. Damping can easily be included.

One disadvantage of the present method (in contrast to time-stepping techniques) is that nonlinear members cannot be considered. Another disadvantage is that an accurate modal superposition may require a very large number of modes when the piping system is large and complicated and when the transient excitation is steep (loading of impulse and step types).

Further details and numerical examples are given in the full-length report [8].

9. ACKNOWLEDGMENT

This work was supervised by Professor Bengt A. Akesson, Division of Solid Mechanics, Chalmers University of Technology, Sweden.

10. REFERENCES

1. B. AKESSON 1976 International Journal for Numerical Methods in Engineering 10, 1221-1231. PFVIBAT - A computer program for plane frame vibration analysis by an exact method.
2. C.W.S. TO 1984 Journal of Sound and Vibration 96 (2), 175-194. The acoustic simulation and analysis of complicated reciprocating compressor piping systems. I: Analysis technique and parameter matrices of acoustic elements.
3. W.H. WITTRICK and F.W. WILLIAMS 1971 Quarterly Journal of Mechanics and Applied Mathematics 24, 263-284. A general algorithm for computing natural frequencies of elastic structures.
4. M. LEBRUN 1985 Journal of the Franklin Institute 319, 137-156. The use of modal analysis concepts in the simulation of pipeline transients.
5. E.B. WYLIE and V.L. STREETER 1983 (1978) Fluid Transients. New York: McGraw-Hill, 384 pp.
6. R.F. BOUCHER and E.E. KITCLOS 1986 Institution of Mechanical Engineers Proceedings, Part C: Mechanical Engineering Science 200, 21-29. Simulation of fluid network dynamics by transmission line modelling.
7. B. AKESSON, H. TACNIORS and R. LUNDEN 1980 Chalmers University of Technology, Division of Solid Mechanics, Publication No 29. SFVIBAT-DAMP - a computer program for damped space frame vibration analysis.
8. A. FRID 1987 Chalmers University of Technology, Division of Solid Mechanics, F104. Fluid vibration in piping systems - a structural mechanics approach, 49 pp.
9. B. AKESSON 1979 Chalmers University of Technology, Division of Solid Mechanics, F60. Modal analysis of transient vibration of continuous systems including rigid-body motion, 38 pp.
10. C.W.S. TO 1984 Journal of Sound and Vibration 96 (2), 195-205. The acoustic simulation and analysis of complicated reciprocating compressor piping systems. II: Program structure and applications.

APPLICATION OF STATISTICAL ENERGY ANALYSIS TO HELICOPTER CABIN TYPE STRUCTURES

J.S. Pollard *
Anthony Best Dynamics Ltd.

1. INTRODUCTION

Statistical Energy Analysis modelling is becoming more widely adopted in a number of acoustic fields for the analysis of structure borne noise paths. Helicopter cabin structures, with high modal densities and excited by mid frequency gear noise, are better suited to SEA modelling than its low frequency FEA counterpart. To assist the helicopter studies, a purpose built cabin box was developed at Westland Helicopters Ltd and subjected to experimental and theoretical modelling programmes.

The cabin box, of approximate dimensions 1.8m x 1.5m x 1.2m high, incorporated an aluminium framework and three alternative sets of typical helicopter panels (plain aluminium sheeting, stiffened skin/stringer aluminium panels and fibrelam composite panels) bolted externally to the framework. Excitation with known input force and power levels was applied via an electrodynamic shaker and drive rod to one bolted panel/frame member and resulting energy levels around the structure were measured (by WHL) with frame and panel accelerometers and cavity microphones.

This paper describes the results of firstly applying an SEA model to the box with only bending waves considered and with simple textbook formulae for the beam to beam coupling loss factors, etc. A more sophisticated model was then developed for the framework alone, with the panels removed. This incorporated additional effects of beam acoustic radiation, longitudinal and torsional wave transmission, and required assumptions regarding the suitability of literature coupling loss factor theory to junctions between L and T section cross section beams. With the 'beam only' model completed it was then only a short step to re-introduce the panels and complete the overall prediction model.

Although the three panel types were fitted to the box framework in turn, only the plain panel results are presented here for reasons of lack of space.

The study was intended mainly as a demonstration of the application of existing SEA knowledge to a cabin type structure rather than any fundamental development of new SEA theory. Nevertheless the investigation highlights the problem areas of tackling such a complicated structure and points the way forward for future work.

2. DAMPING DEFINITION

Panel damping in this paper refers to damping ratio (half loss factor) and the total damping of a panel is given by

$$\eta_{PT} = \eta_P + \eta_{PR}$$

where η_P = structural damping, η_{PR} = acoustic damping. Structural damping has been set at 1% damping ratio for both beams and panels with no frequency variation (in line with generally accepted literature values).

3. SIMPLIFIED BEAM AND PANEL MODEL

The cabin box structure (fig.1) was initially modelled with 22 beam elements, 6 panel elements and one cavity element (the SEA numbering system is shown in figure 1). The beams of L and T section cross section (fig.2) were modelled as rectangular beams and were assumed to act only as energy carriers rather than energy storage/dissipative elements. Hence beam structural and acoustic damping values were assumed to be zero. L, T and X junctions between beams (fig.3) were given simple text book coupling loss factor values of 1/2, 2/9 etc, independent of frequency. Beam to panel coupling loss factor theory, based on line junction excitation, was developed in a previous SEA study by WHL (1). Panel to panel coupling loss factors were given zero

* previously at Westland Helicopters Ltd

values, since the panels were structurally connected to the frames but not to each other, and panel to cavity coupling was obtained from known radiation efficiency values for the plain panels.

With only bending waves considered and with the input energy equally divided between beam 17 and panel 23 (see fig 1a), SEA predictions were performed for panel acceleration levels and cavity noise levels. A small selection of results corrected to 1 watt input power is shown in figure 4 (for panel elements 23, 24 and 25 and cavity element 29). At low and mid frequencies up to 1250 Hz the acceleration level agreement is good for all three panels, but at high frequencies the agreement deteriorates the further the panel is located away from the drive point. For example panel element 25 is 15 dB overpredicted at 3150 Hz. The noise level agreement is good throughout the frequency range.

Two aspects of the measured data to be noted and discussed later are the general decrease in acceleration levels away from the drive panel, particularly at high frequencies, and the characteristic frequency response trough at about 3.15 KHz on the panel data (and later beam data).

4. 'BEAM ONLY' MODEL

With the panels removed, the framework provided the opportunity to perform a 'beam only' SEA model and permit a closer assessment of beam acoustic radiation and beam to beam coupling loss factors. As shown in figure 2 the beams were constructed of single and double thickness L and T section with their principal axes XX and YY displaced. Likewise the beam junctions (fig.3) were complicated L, T and X constructions, making modelling extremely difficult.

As a starting point, however, the simplified SEA model was reconstituted with 22 beam elements, no panel elements, no beam acoustic radiation and only bending wave transmission. With 1% beam structural damping, the beam acceleration levels were overpredicted by 10-20 dB at this stage, and the shape of the curves, with a steadily rising frequency characteristic, was also incorrect. Modifications were, therefore, required.

4.1 Inclusion of Beam Acoustic Loss Factors

Johnston and Barr (2) initiated studies of beam acoustic radiation by measuring beam total damping in air and in vacuo, thereby separating out structural damping and acoustic radiation. They also modelled circular cross section beams as circular cylinders vibrating in flexural motion and rectangular beams as elliptical cylinders, giving good agreement with measured data (fig.5).

Richards et al (3) in a study of ringing noise from machinery components took Johnston's work a stage further by examining "the radiation efficiencies of a family of elliptical cylinders whose eccentricities are such as to allow them to represent a series of beams which, on the one hand, approximate to flat plates of finite width or, on the other hand, are circular or elliptical with major axis along the direction of vibration". They derived a series of curves of acoustic loss factor η_{rad} (versus semi axis wave number $k_d a$) for elliptical shaped pipes of varying aspect ratio a/b .

Jeyapalan and Richards (4) then generalised these curves by using the parameter $\eta_{rad}*(b/a)$, which is independent of ellipse eccentricity, and the acoustic path length given by the cross section circumference. The result was a universal curve of loss factor versus $k_d \times$ circumference ($k_d =$ modified wave number) reproduced in figure 6. The measured data relates to the experiments performed by Johnston and Barr (2). Reference 4 then proceeded to use this curve for beams of arbitrary cross sectional shape to determine the acoustic loss factor η_{rad} and the radiation efficiency of any vibrating beam in flexural motion.

The shape of this curve is similar to the results for thin plates but with the important difference that the peak occurs at a frequency well above the beam coincidence frequency and dependent on the number of wavelengths in the beam cross section circumference.

Richards et al applied the theory to I section beams by assuming that the I beam radiation efficiency is the same as that from a completely enclosed circular, square or elliptical beam, providing that the same bending wave speed and the same circumferential lengths are used. The elliptical models tended to give the best agreement with measured data.

Proceeding along the same lines, the cabin box L section beams were modelled by treating each leg of the beam by an elliptical model just enclosing the leg cross section and doubling the resulting acoustic loss factor to account for both legs. The bending wave speed was that of the whole beam, however, and the circumference related to the cross section of one leg. Similar procedures were adopted for the T section beams, with appropriate changes in bending wave speed etc.

The results of applying acoustic radiation to the beam model are shown in figure 7 (--- initial predictions, --- revised predictions). The mid and high frequency content of the beam acceleration levels are reduced, giving a much flatter frequency response curve, more akin to the measured data with a dip occurring at about 3.15 KHz. This point corresponds to maximum acoustic radiation and occurs when the wavelength of the radiated sound is one circumference of the L section leg and provides an explanation for the previously noted high frequency characteristics of the measured data. The coincidence frequency of the L section beam is about 185 Hz. For a beam damping of 1% the predictions are now about 5-10 dB adrift from the measured data.

4.2 Inclusion of Other Wave Types

Whilst bending waves are the prime source of acoustic radiation from the structure, longitudinal and torsional waves act as energy distributors as well and there will be cases where a longitudinal or torsional wave incident on a beam junction produces a flexural wave out of the junction and vice versa. Thus, in analysing the coupling loss factors at each beam junction, it is necessary to include all three wave types and both in-plane and out-of-plane bending motion.

Taking a simple L junction of two rectangular beams, Cremer (5) and Sablik (6 & 7) reduced the possible 36 wave combinations at the junction to 8 permitted combinations:-

<u>Incident wave</u>	<u>Transmitted wave</u>	<u>Transmission coeff:</u>
flexural in plane	flexural in plane	T _{FF}
flexural in plane	longitudinal	T _{FL}
longitudinal	flexural in plane	T _{LF}
longitudinal	longitudinal	T _{LL}
flexural out of plane	flexural out of plane	T _{ff}
flexural out of plane	torsional	T _{tt}
torsional	flexural out of plane	T _{tf}
torsional	torsional	T _{tt}

They then derived the respective transmission coefficients by solving the wave equations for the boundary conditions at the junctions. Cremer (5) covered the in-plane combinations and Sablik (6 & 7) the out-of-plane derivations. Each derivation involved 4-6 simultaneous complex numbered equations in 4-6 unknowns and can either be solved by lengthy algebra or numerically by matrix methods.

For example, in the case of torsional wave in beam 1 transformed to a flexural out of plane wave in beam 2, the six

equations are:-

$$\begin{array}{rcccccccc}
 r_F & + & r_{jF} & - & t_F & - & t_{jF} & + & 0 & + & 0 & = & 0 \\
 -ir_F & + & r_{jF} & + & 0 & + & 0 & - & \delta_{12} t_R & + & 0 & = & 0 \\
 0 & + & 0 & + & it_F & + & t_{jF} & + & 0 & + & \delta_{12} r_R & = & -\delta_{21} \\
 r_F & + & r_{jF} & + & 0 & + & 0 & + & i\alpha_{12} t_R & + & 0 & = & 0 \\
 0 & + & 0 & - & t_F & + & t_{jF} & + & 0 & - & i\alpha_{12} r_R & = & -i\alpha_{21} \\
 -ir_F & + & r_{jF} & - & i\beta t_F & + & \beta t_{jF} & + & 0 & + & 0 & = & 0
 \end{array}$$

where α, β, δ are beam parameters dependent on mass (m) bending stiffness (B), polar moment of inertia (H), wave number k etc. In this particular case the equations are solved to give t_F and the transmission coefficient is:-

$$T_{FF} = (2C_{B_2} m_2 / C_t H_1 K_1^2) |t_F|^2$$

for bending wave speed C_B and torsional wave speed C_t . Similar relationships are derived for other wave combinations. It is then a simple matter to convert the transmission coefficients to coupling loss factors using relationships of the form

$$\eta_{FF} = \frac{2C_{B_1} T_{FF}}{\omega L_1}, \quad \eta_{LL} = \frac{C_{L_1} T_{FL}}{\omega L_1} \text{ etc.}$$

The application of these L junction formulae to the cabin box becomes extremely complicated because the beams are L and T section cross section and not rectangular. For the L section, bending waves are no longer in plane or out of plane due to the positions of the principal axes XX and YY (fig.2) and the torsional wave axis runs parallel to the beam's lengthwise axis. In the absence of any theoretical models specifically developed for this situation and with the need to progress further with the SEA model, it was decided to assume that the rectangular cross section theory was applicable to the L section cross section and that the combinations of incident/transmitted waves occurring at an L junction of L section beams was the same as for an L junction of rectangular beams. It was, therefore, necessary to calculate the bending wave speeds and torsional wave speeds relative to the principal axes for an L cross section and apply them to the formulae discussed in the previous paragraphs for rectangular beams.

For the T section cross section beams the in-plane principal axes are perpendicular to the arms of the T (fig.2). These constitute the two bending wave axes with the torsional axis running along the beam. The analysis was, therefore, not quite so complicated as for an L section cross-section but it was still necessary to assume that the wave type transmission combinations to the next beam through an L-junction are the same as for a rectangular cross-section.

In the calculation of the bending wave speed C_B , 'thick beam' bending was allowed for, i.e. rather than assume that the bending wavelength was large compared to the dimensions of the beam, which is only true at low and mid frequencies, corrections were made at high frequencies to account for rotational motion and shear deformation of the beam during bending. In fact, the difference between thin and thick beam bending was found to be negligible in these beam studies.

The summarised transmission coefficients for an L junction of the two L section beams (fig.8) show very small contributions from the torsional waves, but large contributions from the bending waves and the longitudinal waves, particularly at high frequency. When these are converted to coupling loss factors, the presence of the frequency term in the formula reverses the dominance of the high frequency contribution (fig 9). In other words the beams only couple well at low frequencies, whereas at high frequencies the beams retain their energy. The longitudinal to flexural wave transmission dominates, throughout virtually the

whole frequency range. The two flexural to flexural wave transmissions are very similar whilst the torsional contribution is negligible in comparison. When, however, the modal densities of the different wave types are taken into account in the relationship $N(\omega) = N(\omega) \eta_i$ (for the other half of the SEA energy flow model) the dominance of the torsional wave modal density helps to offset its low coupling loss factor.

In order to proceed with the revised SEA model including the four different wave types, it was necessary to assume that each junction of the ship's box frame structure could be represented by L junctions. This is clearly not the case in practice as L, T and X junctions exist in different formats. The manner in which the beams were divided up for the SEA model, however, results in any two beams always being at right angles to each other (fig.1). For example, beam 1 was treated as one long beam and not split into three parts. Thus to simplify matters, each junction was represented by a set of L junctions joined together, with the L junction coupling loss factor used in the calculations. This approach introduces errors but cannot be avoided until good theoretical models have been developed for L and X junctions.

The result of including four different wave types was to increase the number of degrees of freedom from 12 to 36 and increase the matrix size from 22 x 22 to 36 x 36 (beams and cavity).

For the structural analysis it was assumed that (i) the damping term also was the same for all wave types and (ii) the coupling loss factors were the same for all wave types. Thus, for example, the coupling loss factor between wave type 1 and wave type 2 was the same as the coupling loss factor between wave type 1 and wave type 3. The drive point for the experiments was beam 17 at the junction to the external structure. As a starting point the energy was assumed to excite the three wave types (2 bending and 1 torsional) in equal amounts, i.e. 1/3 input power in each. The contribution of the longitudinal wave was not considered for the other input divisions were all assumed.

With regard to the structural analysis output, the energy level of each beam for each wave type was calculated. Consequently, for each structural analysis value in fig. 10, frequency, there were 36 level energy levels. This was necessary at this stage in order to separate energy levels, and hence the acceleration levels, for each resolved wave type.

The bending wave energy E is usually given by $E = \frac{1}{2} \rho A v^2$ where ρ is density, A is area, v is velocity and mass m is in terms of acceleration level. The bending wave contribution is given by $10 \log \omega^2 (1/\rho A)^2$. The torsional relationship was assumed for the longitudinal waves. For torsional waves, however, the energy level is $E = \frac{1}{2} I \omega^2$ where I is the area polar moment of inertia and ω is the angular velocity. To convert this to torsional wave contribution level an assumption was made for the measurement point. It was necessary to take into account the offset distance d of the measurement point from the centre of gravity of the beam cross section. The resulting acceleration level is then $10 \log \omega^2 (1/\rho A)^2 d^2$. For the beams there was no offset distance because the accelerometers were positioned at the apex of the beam. Consequently, for these beams there were no torsional wave contributions at the measurement points due to the offset distance being zero.

For comparison with the measured data, the bending wave contributions are assumed to be the most important. Since in the case of the L section cross section, both bending waves could contribute, it was assumed that the two waves were independent of each other and of random phase, this permitting their summation on a root mean square basis. It could be argued that for the section beams there may be a torsional wave contribution to the measured data, in addition to the two resolved bending waves. Such contributions were not considered however.

The predicted levels are compared with the measured data in fig. 10 for beams 1-4 and 5-8 respectively. Three prediction curves are shown on each figure consisting of two separate lines for the longitudinal and torsional waves and one line for the combined bending wave contributions.

The general shape of the predicted curves with frequency is rather disappointing. Whereas, previously, the inclusion of the beam acoustic radiation values had produced a dip at 3.15 kHz, this dip is now hardly noticeable and the predictions no longer follow the measured curves. It is not entirely clear why this change has occurred but it may be due to the fact that the increased structural damping of 1% to each wave type has swamped the acoustic damping term. Certainly the prediction is now lower in level than previously, which means that agreement with the measured data is better, but to the detriment of the general shape of the curves.

Taking the wave types in turn, the combined bending wave (which is the wave type most likely to be representative of the measured data) is showing good agreement throughout the frequency range for L section beams 1-4. Beams 5-8 show equally good agreement at low frequencies but are overpredicted at mid and high frequencies. Similar differences were obtained for the T section beams.

Surprisingly the longitudinal wave (in terms of junction transmission effects) produces the largest contribution of all the wave types and can certainly not be ignored in any SEA prediction model of this type of structure. The torsional wave contribution for the L section beams is generally 5-15 dB below the other two wave types but is still nevertheless an agent for transporting energy around the structure. Changing the distribution of input energy on the drive point beam 17 between the different wave types in the calculation procedure had only a marginal effect on the agreement with measured data.

One disconcerting factor of the whole prediction process, and the reason why the agreement with measured data at high frequencies is poor, is the similarity in predicted levels throughout the cabin box beam structure. In other words there is almost equipartition of energy across the structure according to the prediction model. This is not true in practice since the measured levels generally decrease with increasing distance from the drive point. In fact, across the whole structure there is a variation in measured level of 15 dB at low frequencies and 25 dB at high frequencies, compared with 5 dB and 10 dB respectively for the predicted bending waves. An increase in predicted structural damping level, particularly at high frequencies, would, however, improve the situation.

5. REVISED BEAM AND PANEL MODEL

The improved beam model was inserted back into the original SEA model to see what benefits might accrue to the predicted panel acceleration and cavity noise levels. This time, absorption effects of the cavity were included by modifying the cavity loss factor in accordance with measured reverberation time measurements. An extra element representing the external receiving space (reverberation room) was also inserted, making a 96 x 96 SEA matrix.

The results are presented in figure 11 for the same panel elements 23- 25 and cavity element 29 as before. Compared with the previous results of figure 4, the revised predictions surprisingly show no improvement in panel acceleration level agreement. Marginally better agreement for panel 23 is offset by a deterioration in high frequency agreement of panel 25. The cavity noise level is also slightly worse at mid frequencies. This is probably due to the inclusion of the beam acoustic radiation and a reduced contribution from this source in the predictions would improve matters. The cavity absorption effects have helped to reduce the high frequency discrepancies.

Similar results and conclusions were obtained for the sandwich panels (although not shown), but the equipartition of energy problem previously highlighted for the acceleration level distribution still exists, however, on both sets of panels.

6. CONCLUDING REMARKS

The development of an SEA model for a cabin box structure has given promising agreement with measured data for 1% structural damping particularly at low and mid frequencies. At high frequencies the agreement is poor with the model overpredicting by up to 10dB.

For a 'beam only' model it is necessary to allow for longitudinal and torsional wave transmission, and include beam acoustic radiation. Despite the assumptions made regarding beam junction modelling, the agreement on a flexural wave comparison is again quite good, particularly at low/mid frequencies and particularly for the outer lengthwise beam members.

It is questionable, however, whether the sophistication of accurately modelling beams and beam junctions etc. is necessary for large panelled structures since to a first approximation reasonable results have been obtained with simple beam junction models, particularly for the cavity noise level.

Unfortunately, the one area of disappointment is the inability for the predicted acceleration data to show almost equalisation of energy around the structure. The model is obviously not functioning correctly yet for either beam or panel vibration is an area requiring further research.

7. ACKNOWLEDGEMENTS

The author wishes to thank Westland Helicopters Ltd and the Ministry of Defence for permission to publish the information. It was obtained with financial support from MOD. In particular, Mr A. Rossall and Mr M. Reed of WHL and Dr K. Heron of Cranborough are acknowledged for their considerable participation in the study.

8. REFERENCES

1. J. HAWKINGS 1973 106 Meeting of Acoustical Society of America California. An application of SEA to Helicopter Structure Borne Noise.
2. A. J. E. WINSTON, A. J. S. BARR 1969 J. of Mechanical Engineering Science Vol 11, no 2. Acoustic and Internal Damping in Uniform Beams.
3. E. J. RICHARDS, M. E. WESTCOTT, R. K. JEYAPLAN 1979 J of S & V. 65 (1) 419-451. The Prediction of Impact Noise 11 Ringing Noise.
4. E. J. RICHARDS, E. J. RICHARDS 1979 J. of S & V 67 (1) 55-67 Radiation Efficiencies of Beams in Flexural Vibration.
5. M. CREMER, M. HECKL, E. E. UNGAR 1973 Springer Verlag. Structure Borne Sound.
6. N. J. SABLİK. 1982 J. Acoustic Soc. America 72.(4) October. Coupling Loss Factors at a Beam. L Joint Revisited.
7. N. J. SABLİK, R. E. BEISSNER, H. S. SILVUS, M. L. MILLER 1985 J. Acoustic Soc. America 77(3) March. Statistical Energy Analysis, Structural Resonances and Beam Networks.

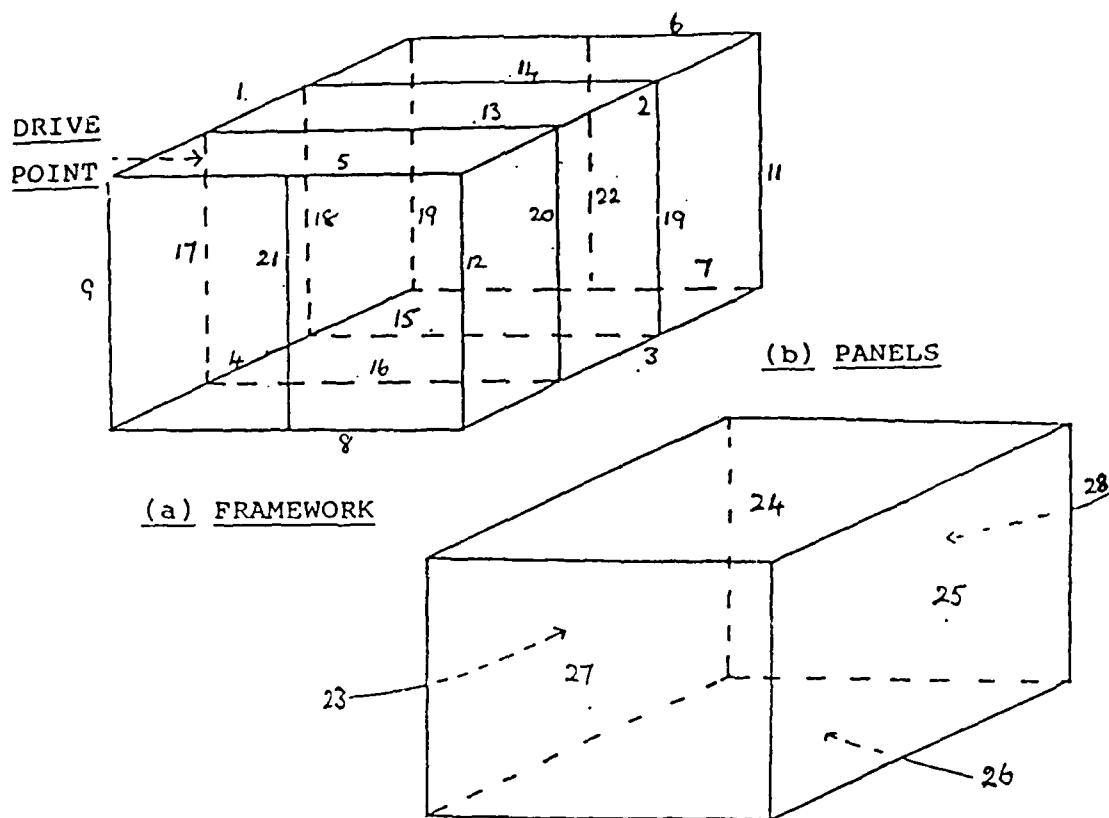


FIG 1. SEA ELEMENT NUMBERING SYSTEM

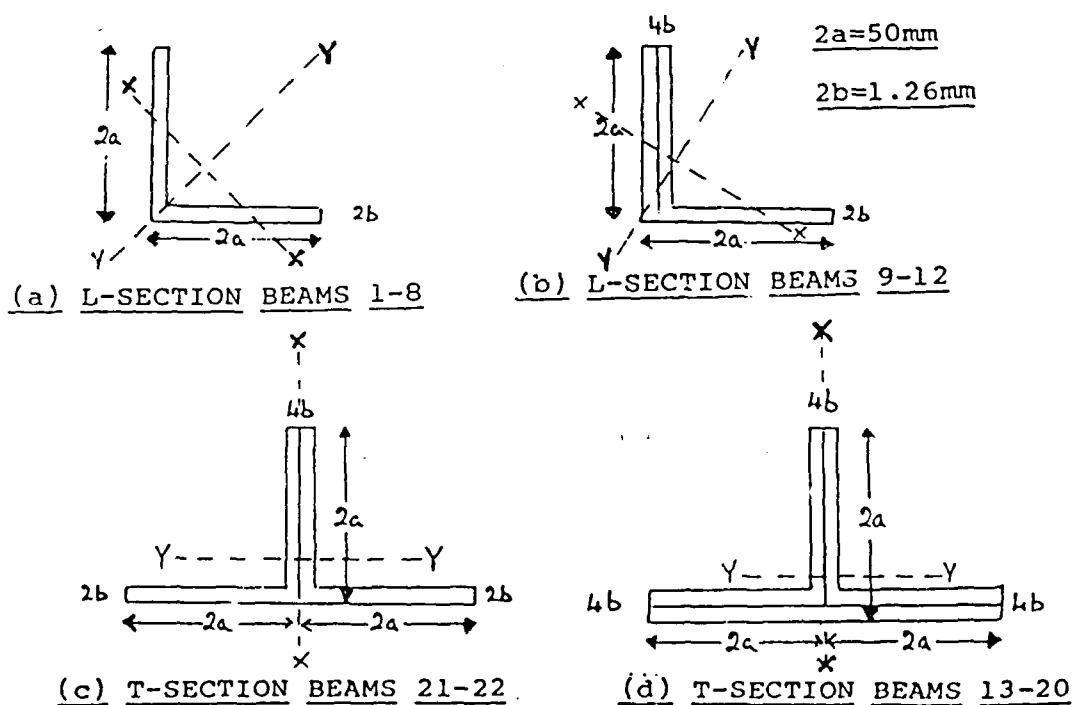


FIG 2 BEAM CROSS SECTIONS

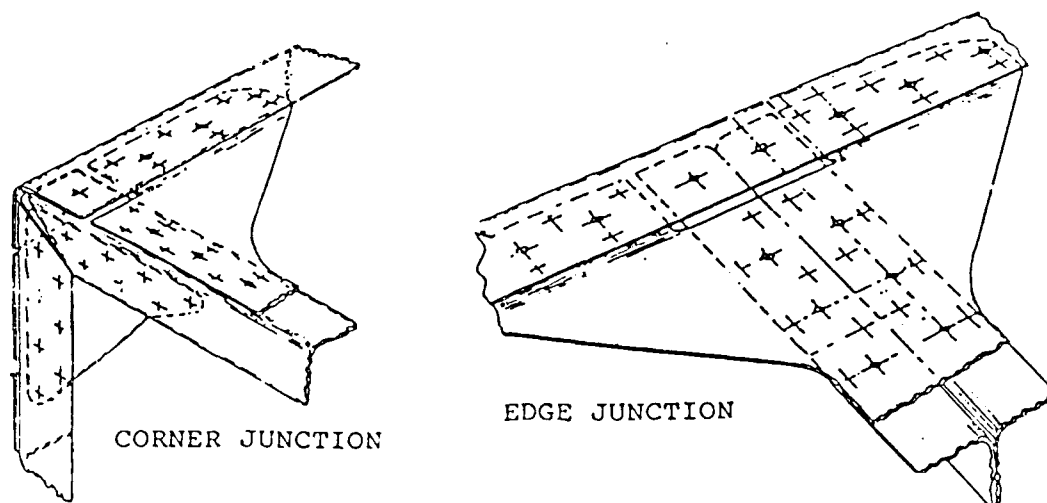


FIG 3 TYPICAL JUNCTIONS (REPRODUCED FROM WHL)

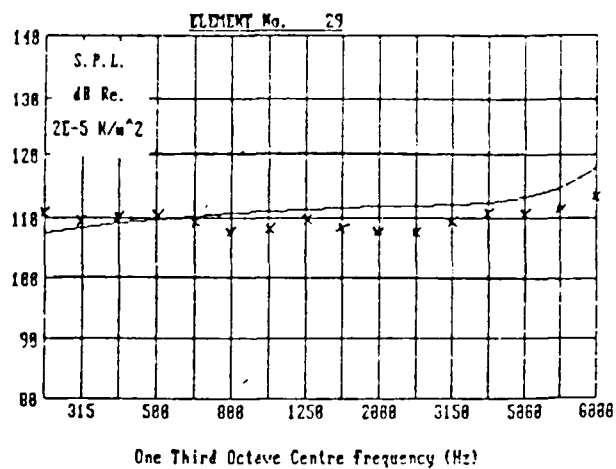
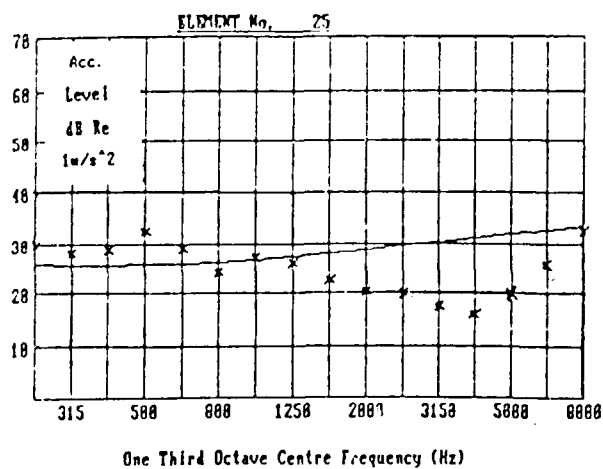
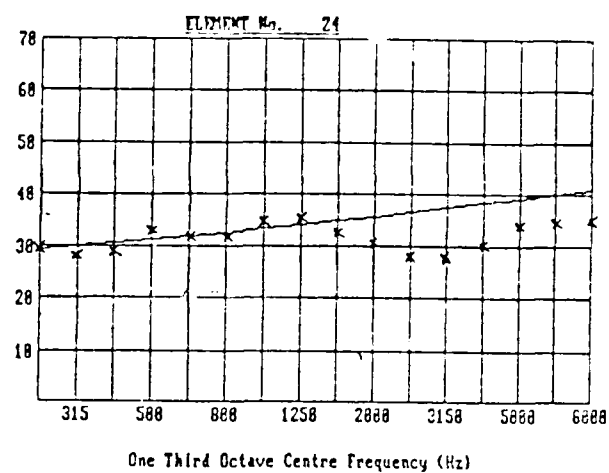
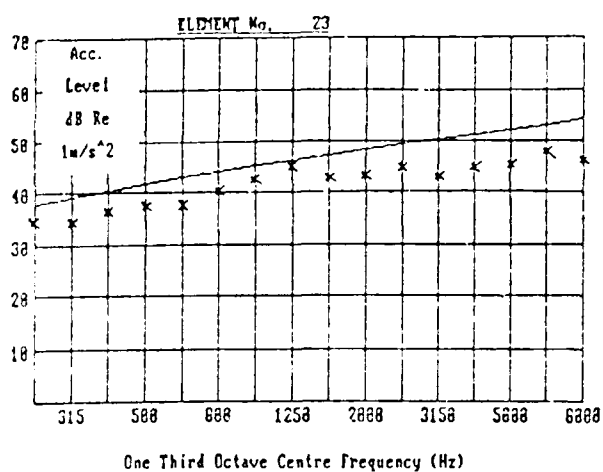


FIG 4. RESULTS FOR SIMPLIFIED MODEL

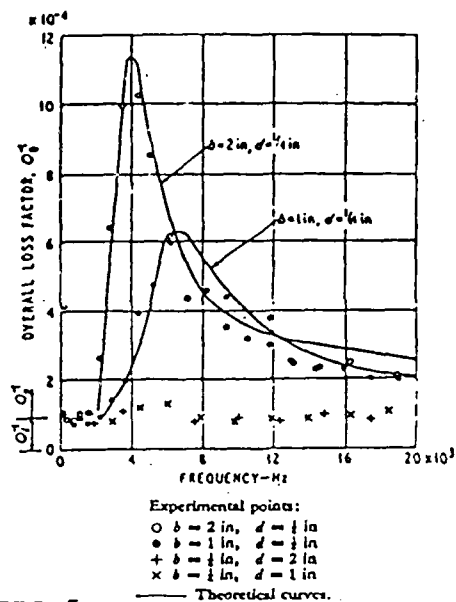


FIG 5.
OVERALL DAMPING OF RECTANGULAR
SECTION BEAMS (FROM REF 2.)

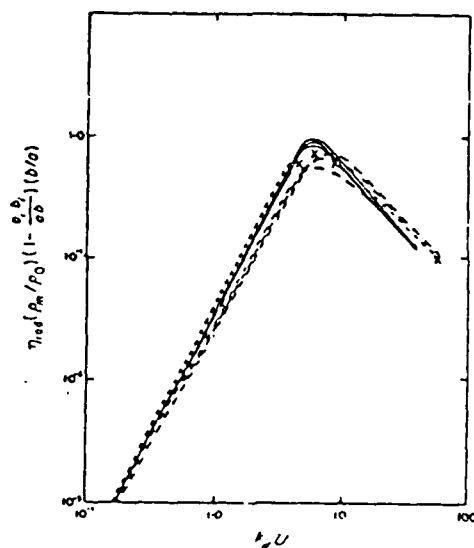


FIG 6 NORMALISED LOSS FACTORS FOR
ELLIPTICAL BEAMS
(FROM REF 4)

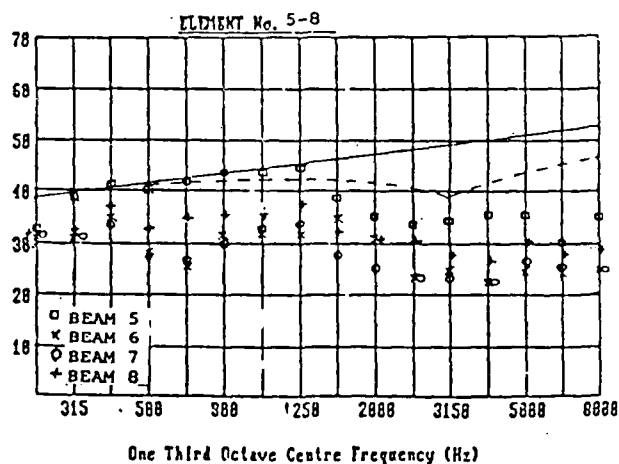
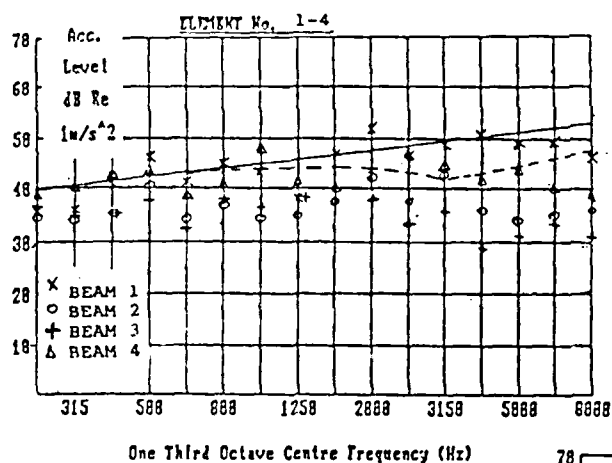
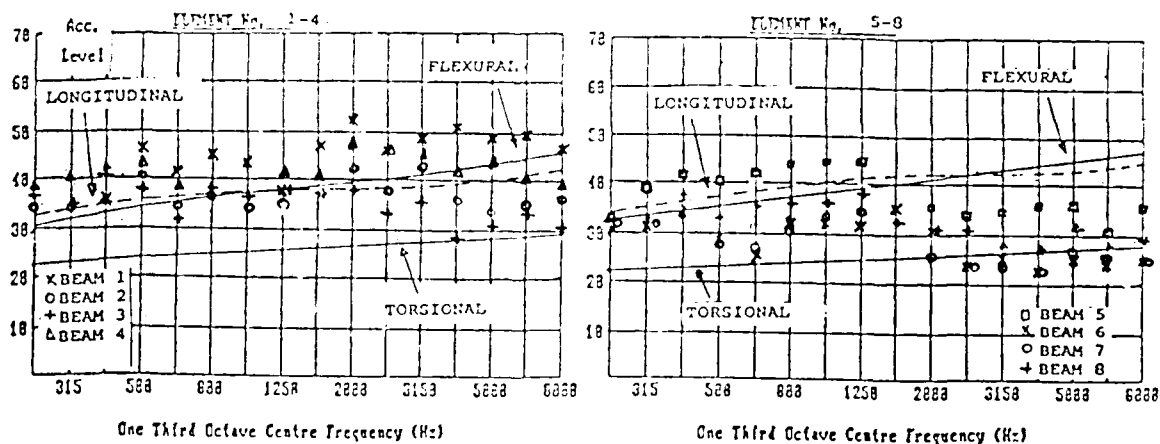
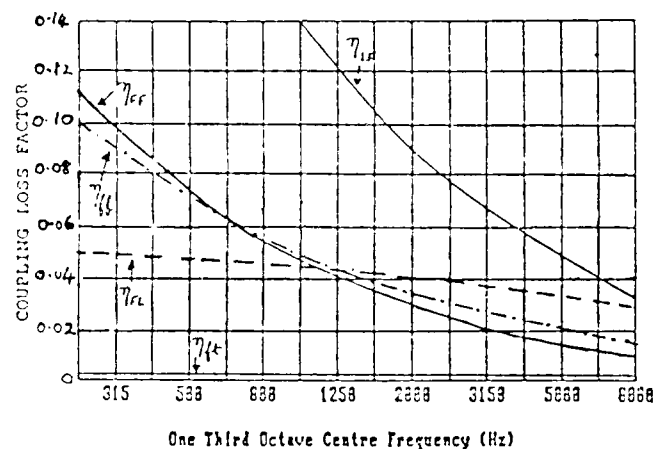
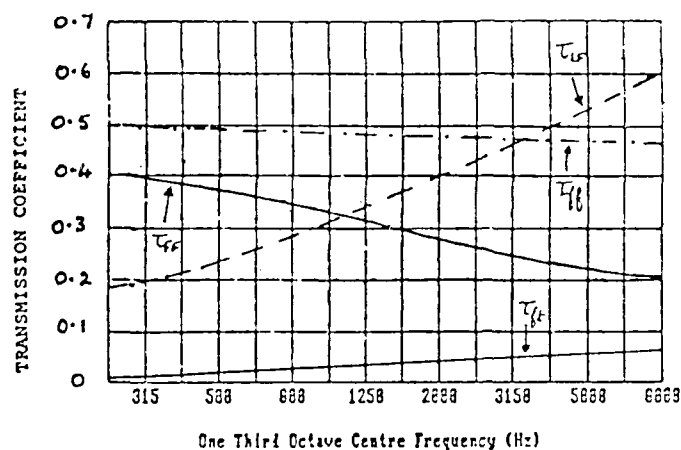


FIG 7 EFFECT OF BEAM ACOUSTIC RADIATION



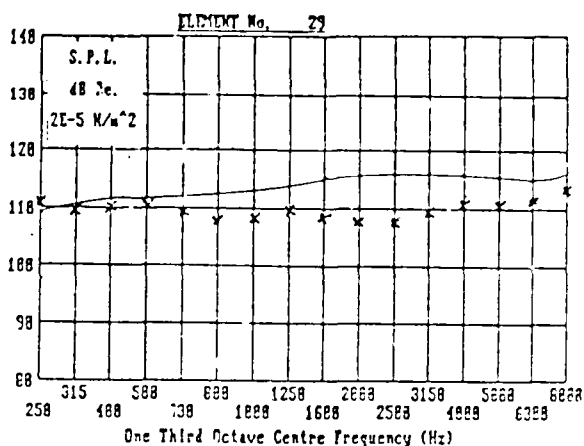
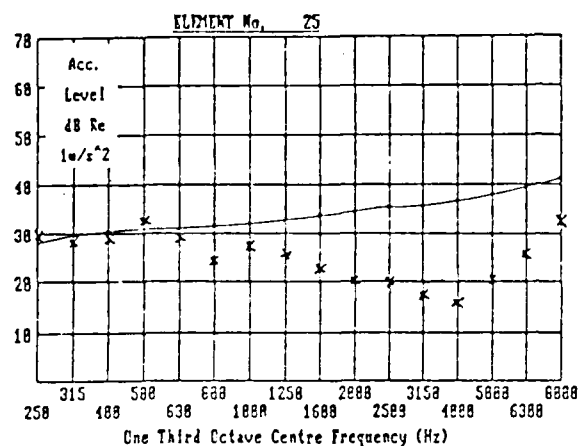
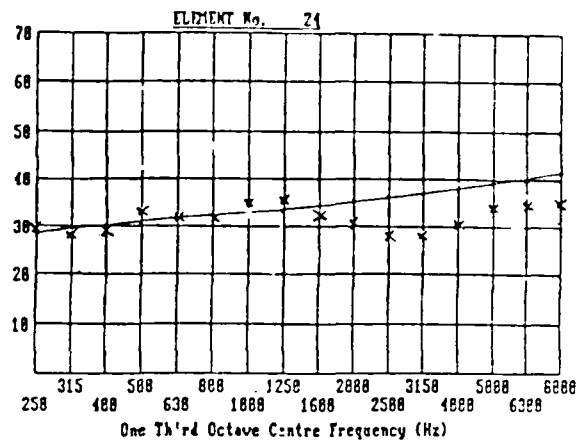
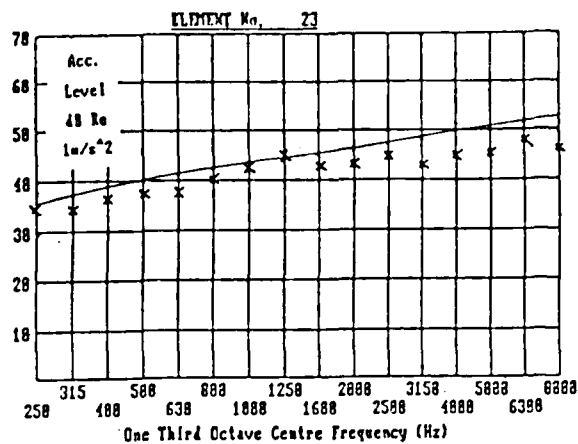


FIG 11. RESULTS FOR MODIFIED SEA MODEL

FINITE ELEMENT ANALYSIS OF STRUCTURE ACOUSTIC INTERACTION

Håkan Carlsson and Göran Sandberg
Division of Structural Mechanics
Lund Institute of Technology
Sweden

1. INTRODUCTION

The introduction of light-weight materials in automobiles and aircraft has created an interest in predicting sound pressure levels and displacement fields in these type of vehicles to ensure passenger comfort. For small fluid volumes, measured in acoustic wavelengths, enclosed in thin flexible structures the structure-acoustic interaction becomes significant and hence the two physically separated system has to be considered coupled in the analysis. Various methods are used to treat this problem such as the Green's Function Method, the Modal Analysis Approach, Statistical Energy Analysis, the Boundary Element Method (BEM) and the Finite Element Method (FEM).

This paper is concerned with the Finite Element Modelling of this coupled structure acoustic system under various types of loadings. The coupling between the structural motion and the fluid variable is done by direct integration on the element level. Special interest is put on different formulations of the coupled differential equations leading to a symmetrical or non-symmetrical set of discrete equations due to different choice of primary variables in the fluid domain. Although, the coupled system is physically conservative (ignoring fluid and structural damping) non-symmetrical systems of equations are achieved for certain choice of primary variables.

A symmetric formulation is preferable because symmetric equation solvers and eigenvalue solvers are more highly developed and also require less computer storage. A physical formulation introduced by Sandberg [1] based on the displacement potential function leading to symmetrical equations is presented.

Acoustic elements have been implemented for small amplitude coupled vibrations. Numerical results are given for harmonic and transient excitation of one- and two-dimensional models. Test runs are also made with commercial FE-codes employing acoustic elements like ABAQUS and ASKA.

A laboratory setup of a three dimensional idealized automobile compartment done by SAAB Car Industry is presented. Acoustic field and vibration characteristics of this structure-acoustic system received from measurements is planned to be available in March 1988 for comparison to numerical results.

Numerical calculations are carried out on an IBM 3090 vector computer and results visualized on a graphical device by the CAEDS software package. Great effort is done on working out routines for acoustic visualization of harmonic and transient loadings and example of this is shown on slides.

2. FINITE ELEMENT FORMULATION OF GOVERNING EQUATIONS

2.1 Mathematical description

The structural motion is governed by

$$L(u_s) = F_s(r, t) \quad (1)$$

where L is a partial differential operator with respect to time and space. u_s is the structural displacement field, which depend on the material point co-ordinate r and time t , and F_s is an external time dependent load. At the wet surface, i.e. the fluid-structure interface the boundary condition is described by

$$F_f(r, t) = p(r, t)n \quad (2)$$

where p is the ambient fluid pressure and n is the outward unit normal vector to the fluid domain.

The fluid is assumed to be compressible, but irrotational and inviscid. Further, we assume the fluid velocity to be considerably smaller than the speed of sound. Conservation of mass and linear momentum then yields

$$\dot{\rho} + \rho_s \nabla \cdot v = q \quad (3)$$

$$\rho_s \dot{v} + \nabla p = 0 \quad (4)$$

where ρ and ρ_s is the ambient and static fluid density respectively, v is the fluid velocity field, q is the added fluid mass per unit volume and time, \hat{p} is the total fluid pressure and ∇ is the del operator. (Partial time derivatives are denoted by dots).

Equations (3) and (4) together with the equation of state, assuming fluid motion to be independent of temperature,

$$\hat{p} = \hat{p}(\rho_s + \rho) \quad (5)$$

constitute a mathematical model for a linearized flow. The equation of state can be expressed as

$$\hat{p} = p_s + p \approx p_s + c^2 \rho \quad (6)$$

where p and p_s is the ambient and static fluid density respectively and c is the speed of sound.

By combining (3), (4) and (5) we can establish the wave equation with

source terms like

$$\ddot{\rho} = c^2 \nabla^2 \rho + \dot{q} \quad (7)$$

or in terms of pressure

$$\ddot{p} = c^2 \nabla^2 p + c^2 \dot{q} \quad (8)$$

Applying the gradient to (3) and the partial time derivative to (4) we get the wave equation in terms of the velocity field

$$\ddot{\mathbf{v}} = c^2 \nabla^2 \mathbf{v} - \frac{c^2}{\rho_s} \nabla q \quad (9)$$

Integrating (9) with respect to time gives in terms of the fluid displacement field \mathbf{u}_f

$$\ddot{\mathbf{u}}_f = c^2 \nabla^2 \mathbf{u}_f - \frac{c^2}{\rho_s} \nabla Q \quad (10)$$

$$\text{where } Q = \int_0^t q d\tau$$

Introducing the displacement potential ψ defined by

$$\mathbf{u}_f = \nabla \psi \quad (11)$$

we can rewrite (10) to

$$\ddot{\psi} = c^2 \nabla^2 \psi - \frac{c^2}{\rho_s} Q \quad (12)$$

Thus, we have derived five alternative formulations of the wave equation with respect to the choice of primary variable.

We treat the fluid close to the boundary as a continuum and assume that the displacement field at any time must be a continuous mapping of the initial state. Hereby, the displacement of the structure and the normal component of the fluid motion coincide

$$\mathbf{u}_s \cdot \mathbf{n} = \nabla \psi \cdot \mathbf{n} = \mathbf{u}_f \cdot \mathbf{n} = u_{sf} \quad (13)$$

where u_{sf} is the structural displacement component perpendicular to the fluid boundary. The fluid boundary condition is in this paper concerned about the fluid-structure interface even though other boundary conditions could be incorporated, see [1].

2.2 Finite Element Formulation

The aim of this section is to show how the choice of primary variable effects the symmetry of the discretized coupled system of equations. The

derivation of the finite element formulation in the fluid domain is based on the weak formulation of the governing equations and on the Galerkin procedure.

Choosing the pressure variable to be the independent variable, equation (8) can be rewritten by multiplication by a test function $w=w(r)$, integrated over the total fluid domain and using Green's first formula to get

$$\int_V w \ddot{p} dV + c^2 \int_V (\nabla w) \cdot (\nabla p) dV = c^2 \int_V w \dot{q} dV + c^2 \int_S w \nabla p \cdot n dS \quad (14)$$

where in the last term we can use (4) noting that $\hat{\nabla p} = \nabla p$ since $\nabla p_s = 0$ and the last equivalence in (13). The discretized form of (14) can be established by the expansion

$$p(r, t) = \sum_j N_f^j(r) P_j(t) \quad (15)$$

where N_f is the shape function in the fluid domain and $P_j(t)$ is the time-dependent pressure at the associated nodal point.

Using the standard Galerkin procedure and letting $w \in \{N_f\}$ we get

$$M_f \ddot{P} + K_f P = -L_s + L_q \quad (16)$$

where P is the unknown nodal pressure column matrix and

$$(M_f)_{ij} = \int_V N_f^i N_f^j dV \quad (17)$$

$$(K_f)_{ij} = c^2 \int_V (\nabla N_f^i) \cdot (\nabla N_f^j) dV \quad (18)$$

$$(L_s)_i = c^2 \rho_s \int_S N_f^i \ddot{u}_{sf} dS \quad (19)$$

$$(L_q)_i = c^2 \int_V N_f^i \dot{q} dV \quad (20)$$

A discretized formulation of the structure is based on the expansion of the structural displacement as

$$u_s = \sum_j N_s^j U_s^j \quad (21)$$

where U_s^j is the discrete value of the structural displacement at point j .

For an undamped structure, for short, we get

$$M_s \ddot{U}_s + K_s U_s = L_s^e + L_f \quad (22)$$

where M_s and K_s are the symmetric mass and stiffness matrices. L_s^e is the structural load vector due to the external loads and L_f is the fluid load vector due the coupling effects. Using the shape function set N_s in the structural domain gives

$$(L_f)_i = \int_S N_s \cdot n p \, dS \quad (23)$$

Thus, we have established two system of matrices (16) and (22), one for each domain, linked together by the coupling matrices L_s and L_f . Comparing (13), (19), (21) and (23), we may write

$$L_s = M_c \ddot{U}_s \quad (24)$$

where

$$(M_c)_{ij} = c^2 \rho_s \int_S N_s^i N_s^j \cdot n \, ds \quad (25)$$

and

$$L_f = K_c P \quad (26)$$

where

$$(K_c)_{ij} = \int_S N_s^i \cdot n N_f^j \, dS \quad (27)$$

Thus, shifting L_s and L_f to the left hand side, we finally get an unsymmetric system of equations of the form

$$\begin{bmatrix} M_s & 0 \\ M_c & M_f \end{bmatrix} \begin{bmatrix} \ddot{U}_s \\ \ddot{P} \end{bmatrix} + \begin{bmatrix} K_s & -K_c \\ 0 & K_f \end{bmatrix} \begin{bmatrix} U_s \\ P \end{bmatrix} = \begin{bmatrix} L_s^e \\ L_q \end{bmatrix} \quad (28)$$

This system can be rewritten to a symmetric form in the harmonic case since $M_c = c^2 \rho_s K_c^T$. This approach is used in ABAQUS Version 4.6 thus excluding the possibility of transient analysis.

Another choice of independent variable may be the displacement potential function ψ . Using the expansion

$$\psi(r, t) = \sum_j N_\psi^j(r) \psi_j(t) \quad (29)$$

the corresponding derivation from (12) will end up with the unsymmetric system

$$\begin{bmatrix} M_s & \frac{1}{c^2} M_c \\ 0 & M_f \end{bmatrix} \begin{bmatrix} \dot{U}_s \\ \ddot{\psi} \end{bmatrix} + \begin{bmatrix} K_s & 0 \\ -c^2 K_c^T & K_f \end{bmatrix} \begin{bmatrix} U_s \\ \psi \end{bmatrix} = \begin{bmatrix} L_s^e \\ L_q \end{bmatrix} \quad (30)$$

where M_c , K_f and K_c is defined above and

$$(L_q)_1 = c^2 \int_V N_f^1 \dot{q} dV \quad (31)$$

However, a symmetric formulation can be achieved by combining the pressure and the displacement potential formulation. To do this from a physical point of view we have to start from (3) and (4). We substitute (11) in (3) and (11) and (6) in (4) to get

$$\frac{1}{\rho_s c^2} \dot{p} + \nabla^2 \dot{\psi} = \frac{1}{\rho_s} \dot{q} \quad (32)$$

$$\nabla p + \rho_s \nabla \ddot{\psi} = 0 \quad (33)$$

Integration of (32) with respect to time, assuming the system to be initially at rest, and using w as a test function yields the following integral equation

$$\frac{1}{\rho_s c^2} \int_V w p dV - \int_V \nabla w \cdot \nabla \psi dV + \int_S w \nabla \psi \cdot n dS = \frac{1}{\rho_s} \int_V w q dV \quad (34)$$

By using ∇w as test function we find the weak form of (33) to be

$$\int_V \nabla w \cdot \nabla p dV + \rho_s \int_V \nabla w \cdot \nabla \ddot{\psi} dV = 0 \quad (35)$$

Expanding p and ψ in different shape functions set $\{N_p\}$ and $\{N_\psi\}$, and running w over $\{N_p\}$ in (34) and over $\{N_\psi\}$ in (35) results in

$$\frac{1}{\rho_s c^2} M_p P - B^T \Psi + M_c^T U_s = L_q \quad (36)$$

$$B P + \rho_s K_f \ddot{\Psi} = 0 \quad (37)$$

$$(M_f)_{ij} = \int_V N_p^i N_p^j dV \quad (38)$$

$$(K_f)_{ij} = \int_V \nabla N_\psi^i \cdot \nabla N_\psi^j dV \quad (39)$$

$$(M_c)_{cj} = \int_S N_s^i \cdot n N_p^j dS \quad (40)$$

$$(B)_{ij} = \int_V \nabla N_\psi^i \cdot \nabla N_p^j dV \quad (41)$$

$$(L_q)_i = \frac{1}{\rho_s} \int_V N_p^i Q dV \quad (42)$$

Finally, using (15) in (23) and shift the term L_f to the left hand side in (22) results in

$$M_s \ddot{U}_s + K_s U_s - M_c P = L_s^e \quad (43)$$

and the assembled symmetric system

$$\begin{bmatrix} M_s & 0 & 0 \\ 0 & \rho_s K_f & 0 \\ 0 & 0 & 0 \end{bmatrix} \begin{bmatrix} \ddot{U}_s \\ \ddot{\psi} \\ \ddot{P} \end{bmatrix} + \begin{bmatrix} K_s & 0 & -M_c \\ 0 & 0 & B \\ -M_c^T & B^T & -\frac{1}{\rho_s c^2} M_f \end{bmatrix} \begin{bmatrix} U_s \\ \psi \\ P \end{bmatrix} = \begin{bmatrix} L_s^e \\ 0 \\ -L_q \end{bmatrix} \quad (44)$$

where $K_f = B$ for $N_p = N_\psi$.

This formulation has been implemented as an optional program module DASVAP [2] to be linked to the commercial FE-code ASKA. Numerically, some considerations have to be made due to the zero entries on the diagonal in the mass and stiffness matrices respectively, see [3].

3. NUMERICAL EXAMPLES

3.1 One dimensional example with frequency separation

To illustrate a coupled problem where an exact analytical solution can be obtained we consider a tube of length L and unit cross sectional area A , terminated by a rigid, moveable plug of mass m and supported by a spring with stiffness k as shown in Fig. 3.1. The tube is filled with water.

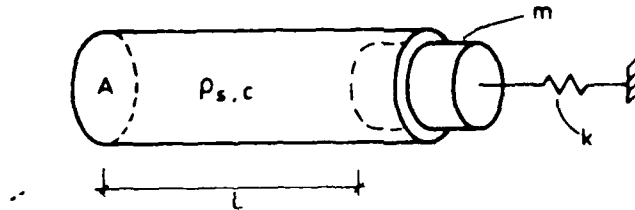


Fig. 3.1 Tube filled with water and with an elastically mounted termination plug. $c = 1500$ m/s, $\rho_s = 1000$ kg/m³, $L = 3$ m, $A = 1$ m², $m = 200$ kg, $k = 493.48$ MN/m

The eigenfrequencies of this system can be analytically determined by

$$\omega_n^2 - \left[\frac{\rho_s c}{m} \cot \left(\frac{\omega_n L}{c} \right) \right] \omega_n - \frac{k}{m} = 0 \quad (45)$$

with notations from Fig. 3.1

In the finite element analysis the fluid domain is discretized by three one-dimensional quadratic fluid elements and the result is shown in Table 3.1 for the three lowest modes.

	<u>Pipe</u>		<u>Mass-Spring</u>
<u>Analytical</u>			
Uncoupled	250.0	500.0	250.0
Coupled	144.0	362.4	594.1
<u>FE</u>			
Uncoupled	250.2	505.4	250.0
Coupled	143.2	363.5	601.8

Table 3.1 Uncoupled and coupled eigenfrequencies by use of three fluid elements

In Table 3.1 we see the result of a typical frequency-separation in a hard-coupled system. Further the agreement between the analytical and the finite element solution is good.

3.2 Two dimensional example of transient structural excitation

A two dimensional fluid domain enclosed by rigid walls and divided into two parts by a thin structural member is analyzed for a transient structural load. The model with the fluid element mesh indicated is shown in Fig. 3.2. Fluid element used is a four node quadrilateral element made up of four triangular elements where the midnode is regarded as a slave node. The structural member is simply supported at both ends and is modelled by two node beam elements having a third degree polynomial approximation.

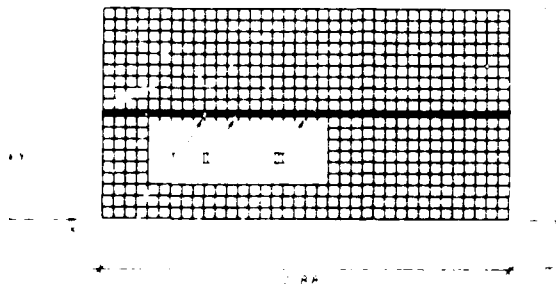


Fig. 3.2 The fluid mesh and the intersecting beam. The beam elements ($L = 24$ cm) are given data corresponding to a 2 mm steel sheet with $E = 200.0$ Gpa, $\nu = 0.0$, $\rho = 7830.0$ kg/m³.

This system is analyzed for two cases: a simple non-interacting structure, and the room filled with air ($\rho_s = 1.29$ kg/m³ and $c = 340$ m/s).

In each domain the numerical resolution is linked to the physical wavelength and since the coupling routines lock a certain number of structural elements to a certain number of fluid elements, it is only at a fixed frequency that the coupling routines produces numerical resolution of the same quality in both the structural and fluid domains. In harmonic analysis, the element size in the structural and fluid domains, can be adjusted to get the appropriate accuracy in the frequency range of interest. In a transient analysis, the element size puts a limit to the possibility of detecting the high frequency content, and because the decrease of wavelength in the fluid is faster than in the structure as the frequency increases, the fluid element size define this upper limit.

The element coupling and the corresponding shape functions at the fluid-structure interface used in this example are shown in Fig. 3.3. Thus, along the boundary of the flexible structure each beam element couples to three fluid elements.

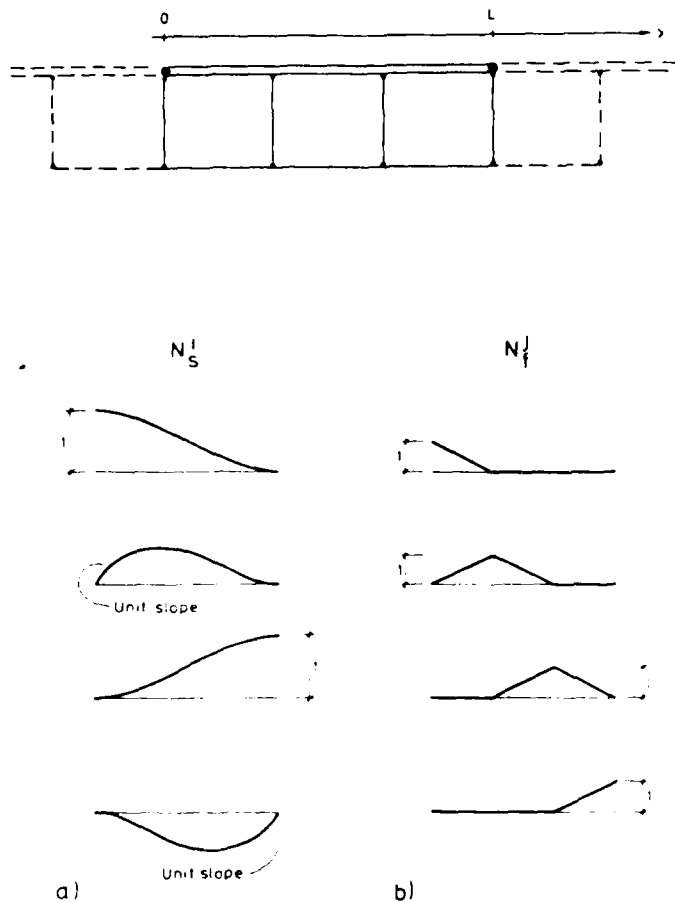


Fig. 3.3 The fluid-structure element coupling (top). Shape functions at the fluid-structure interface (bottom) for a) beam b) fluid.

A vertical transient point load is applied at the centre of the structure with the corresponding load vector

$$L_s^e = [0 \dots -1 \dots 0]^T f(t) \quad (46)$$

where

$$f(t) = \begin{cases} 2.0 t \text{ (kN)} & 0 < t < 1 \text{ ms} \\ 2.0 \text{ (kN)} & t \geq 1 \text{ ms} \end{cases}$$

The calculations were performed using a Newmark-type implicit algorithm, see [1]. The structural displacement at the locations I, II and III is shown in Fig. 3.4.

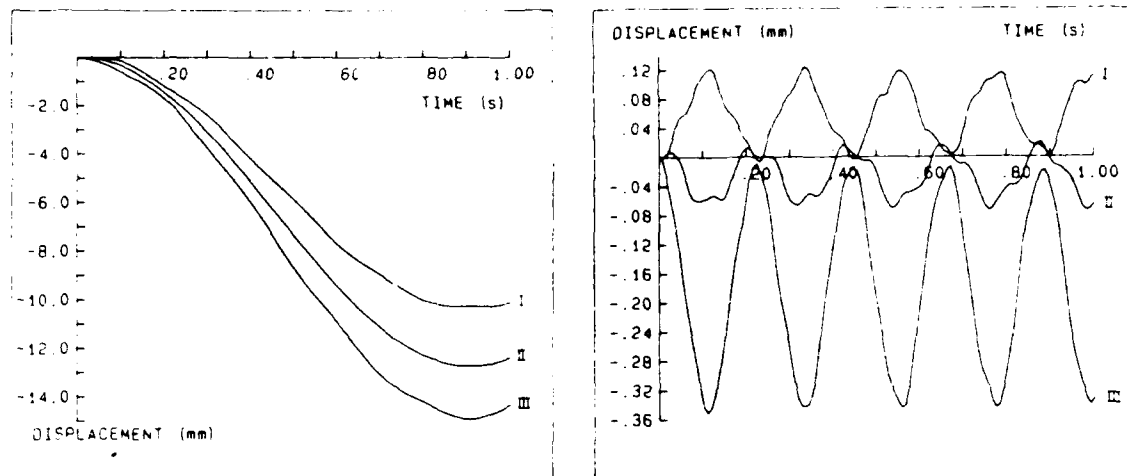


Fig. 3.4 The displacement time history for a non-interacting beam (left) and an interacting beam (right).

We note the dramatical decrease in the displacement amplitude due to the coupling effects. We may also note the high-frequency content in the solution for the interacting beam and that, while the centre node (III) vibrates below its unloaded position, node (I) vibrates above that position.

4. LABORATORY MODEL OF AN IDEALIZED AUTOMOBILE COMPARTMENT

A laboratory setup of an idealized automobile compartment is built by SAAB Car Industry. The shape of the car model is illustrated in Fig. 4.1 and its major dimensions are $3.0 \times 1.6 \times 1.0$ (m). All walls are made of 1 mm steel except the front and rear "windows" that are made of 2 mm steel. The two longer side walls and the roof are slightly curved while the other panels are flat. All edges are considered to be stiff.

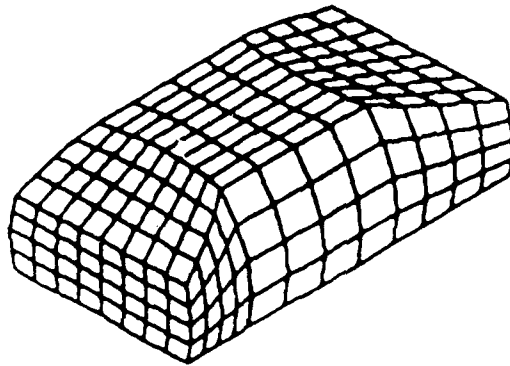


Fig. 4.1 Three dimensional idealized laboratory setup of an automobile compartment.

A numerical study of the uncoupled
of the cabin is followed
harmless

ANALYSIS OF THE TRANSMISSION OF SOUND INTO THE PASSENGER COMPARTMENT OF A PROPELLER AIRCRAFT USING THE FINITE ELEMENT METHOD

Peter Göransson

FFA, The Aeronautical Research Institute of Sweden

1. INTRODUCTION

The ever increasing interest in propeller driven aircraft poses difficult problems in the struggle to obtain sound pressure levels which compare favourably with those found in modern jet aircraft. Not only is the propeller a hardly understood source of noise, but its spectrum is of an extremely cumbersome nature. The distinct peaks at low frequencies, starting with the first blade passage frequency and continuing with the harmonics, forces the acoustician to control pure tones which have acoustic wave lengths in comparison with the dimensions of the aircraft itself. The response of the aircraft structure and interior is mainly governed by global modes, some of which couple the structure to the acoustic field strongly. In this state of complexity the finite element method has been used quite extensively resulting in a wider understanding of these difficult matters, [1].

In this paper, acoustic finite elements are used to analyse the transmission of sound through the double shell represented by the fuselage skin and the composite trim panels. In particular the scope is to show the relative effects of changes in the trim panels material data and installation. Similar work has been published recently by Pope et al [1]. In that paper an aircraft interior noise prediction model was discussed. The fundamental difference in approach between Ref. [1] and the current paper is that here the transmission analysis is based upon a coupled acoustic-structure FE formulation, [2], while in the former the uncoupled modes are used. Earlier analyses have shown that this coupling is sometimes very strong, thus causing large frequency shifts compared to the in vacuo resonance frequencies for the structure, [2, 3].

The analyses are performed with the FE system ASKA-Acoustics, [3], which is a joint development project between FFA and Saaba-Scania AB.

2. IDEALISATION OF AIRCRAFT FUSELAGE

In the analyses performed in this paper the behaviour of the fuselage wall and the trim panel is simplified to a plane, two dimensional dynamic fluid-structure model. The aircraft is modelled as a true double shell with isolated air cavities in the interior and in the double wall space. This is to some extent a crude model since in the aircraft the trim panels are mounted to the frames of the fuselage. Of course such a three dimensional attachment is not possible to cover in a plane model, but this will be simulated by means of mechanical connections between the fuselage and the trim panel.

The fuselage structure and the trim panel are modelled with beams which have been given section properties equivalent to a slice of the real aircraft. Hence, in, e.g., the moment of inertia of the fuselage beams, mass and stiffness from the skin and the longerons are included. For the trim panel the stiffness and the mass are given values according to manufacturers and measurements that have been performed.

The material data used for the beam section properties of the trim panel are shown in table 1, for the four different design cases studied in this paper. It should be pointed out that the mechanical connections are comparatively stiff and so are the floor part of the trim shell which supports seats, etc.

Case	Trim panel properties						Mechanical coupling
	wall			floor			
	E [N/m ²]	I [m ⁴]	ρ [kg/m ³]	E [N/m ²]	I [m ⁴]	ρ [kg/m ³]	
1	12·10 ⁹	1.9·10 ⁻⁹	767	7·10 ¹⁰	11·10 ⁻⁷	2800	yes
2	- " -	- " -	278	- " -	- " -	- " -	yes
3	- " -	- " -	767	- " -	- " -	- " -	no
4	- " -	- " -	278	- " -	- " -	- " -	no

Table 1. Properties for trim panel in the different cases studied

The first case, case 1, in the analysis is to be considered as the basic design. Here the fuselage and the trim panel are in mechanical contact and the density of the trim panel is high. This case will serve as the reference for comparisons. Case 2 is similar to case 1, the difference being a lighter trim panel. However, case 3 is of a quite different type since here the trim panels are uncoupled to the fuselage except for the fluid-structure interaction. This represents some kind of ideal mechanical vibration isolation and is of an extreme design. The last case, case 4, differs from case 3 in the density of the trim panel which is the same as in case 2.

These four cases were analysed for eigen frequencies and eigen modes, in the range 80-110 Hz. For the same cases a response calculation was performed with a pressure field having a maximum pressure of 130 dB SPL at 90 Hz, see figure 3a. This frequency corresponds to the fundamental tone of a four bladed propeller at cruising conditions. The pressure field is purely real, i.e., effects of propeller phasing are not included.

It is believed that this ideal model will serve as a reliable tool for the study of mechanisms and qualitative effects on the sound transmission at low frequencies.

3 EIGENVALUE ANALYSIS

The eigen frequencies for the four different cases in table 1 are shown in table 2.

Case	Eigen frequencies				
1	81	85	87	95	109
2	86	102	104		
3	92	94	105		
4	81	95	100		
without trim panel	38	110			

Table 2 Calculated eigen frequencies

In this table the results of an analysis of the fuselage without the trim panels are included for comparison. As may be seen there are more modes in the interesting region when the trim is taken into account. A change in the density of the trim panels shifts the frequencies of the modes dominated by the inner shell quite a lot as expected. The eigen modes around 90 Hz for the two extremes, i.e., case 1 and 4, are shown in figure 1 and 2 respectively. The lower frequencies, 87 Hz for case 1 and 81 Hz for case 4, have similarities in the pressure field while the structure in case 1 does not move as much as in case 4. However, for the frequencies above 90 Hz, i.e., 95 Hz for both cases the pressure patterns are different due to differences in vibration shapes of the trim panel. In fact, as may be seen in figures 1a and 2a, the air is vibrating in two different modes. The nodal line (zero pressure) goes from wall to wall in case 1 and from top to floor in case 4. Similar changes in modal patterns for the fluid due to changes in the coupling to the structure might also be observed for the other cases in table 2.

4 RESPONSE ANALYSIS FOR UNDAMPED AIRCRAFT

The pressure field discussed above was applied to the outside of the fuselage for the four different cases, without damping in the system. The primary objective is to study the transmission through the double wall system into the passenger compartment inside the trim panel. Hence, the results discussed in this chapter might be seen as effects of different approaches to the design problem. The focus will be on the obtained SPL in the interior and to some extent vibrations of the structures.

4.1 Case 1.

The maximum pressure level in the interior is about 122 dB and the pressure field resembles the modal pattern in figure 1b, as may be seen in figure 3a. The structural vibration, though seems to be a mix between the modes below and above 90 Hz. The fuselage has a smaller amplitude than the lighter, stiffer trim panel which excites the air.

4.2 Case 2

Decreasing the weight of the trim panel is advantageous as may be seen in figure 3b. The maximum pressure is 119 dB, a decrease mainly due to the shift in eigenfrequencies. The pressure pattern is very different in nature as compared to case 1.

4.3 Case 3

Removing the mechanical contact between the fuselage and the trim panel moves one eigen frequency closer to the excitation, see table 2. This results in an increase for the maximum pressure level up to 123 dB compared to case 1 where the maximum was 122 dB. Despite the prevention of transmission of energy through mechanical components the levels go up, a rather astonishing fact. In this case the trim panel is vibrating in a shape which is similar to the 92 Hz mode, and also the acoustic modal pattern at this frequency is seen, see figure 4a.

4.4 Case 4

A decrease in the density from the above case results in a drastic lowering of the maximum pressure level down to 117 dB. The vibration levels in this case are also small over a large portion of the trim panel. It is also interesting to see that the pressure pattern is different from the one observed in case 3. As may be seen from figure 4b, the nodal line is transverse from wall to wall and more complex in nature.

4.5 Discussion

Through a variation of mechanical contact conditions and the density of the trim panel, large changes in the SPL in the interior of the aircraft are seen from the calculations performed. The best configuration seems to be an ideally isolated trim panel with rather low density. Quite contrary to common practice the high density panel seems to be the worst of the studied cases. Of course the background of these results is found in the location of the eigen frequencies of the different cases that have been studied.

5. RESPONSE ANALYSIS INCLUDING THERMAL INSULATION

To investigate the effect, if any, of the thermal insulation, an analysis was performed for the best design, i.e., case 4. The space between the fuselage and the trim was filled with a porous absorbent, the effects of which, were included in the analysis. Previous calculations and experiments have shown the possible existence of low frequency resonance effects of a porous material, [3]. The effects, which are dependent on the mass density of the material, have a narrow bandwidth. This analysis was therefore intended to show whether there is any significant influence in such a complex situation as discussed in this paper. The material chosen have a mass density of 19 kg/m^3 and a flow resistance of $2 \cdot 10^4 \text{ Ns/m}^3$. The density have been chosen to provide an optimal effect at 90 Hz and from figure 5 it may be seen that indeed, the pressure levels are generally lower by about 3 dB. As may be seen from figure 5 the pattern of the pressure field has not changed as compared to figure 4b. The real and imaginary parts of the displacement are also shown in figure 5. Most of the structural response is in phase with the excitation.

6. CONCLUDING REMARKS

The analyses of an aircraft cross section discussed in this paper show that the transmission of low frequency sound is strongly dependent on the dynamics of the fuselage-air-trim-air system. The maximum SPL may vary from 123 down to 118 dB in the extreme cases where only attachment and density of the trim panel are changed. The results also show that a porous absorbent in the air space may give an additional decrease down to a maximum of 114 dB by carefully tuning the mass density of the porous material.

7 ACKNOWLEDGEMENTS

This work was sponsored by the Swedish Board for Technological Development. The author is indebted to Mr Urban Emborg, Saab-Scania Aircraft Division, for inspiring discussions about problems in double wall transmission.

8 REFERENCES

- [1] L.D. POPE, E.G. WILBY and J.F. WILBY 1987, J. Sound and Vibration 118(3), 449-467. Propeller aircraft interior noise model, Part I: Analytical model.
- [2] G. SANDBERG and P. GÖRANSSON 1988, To appear in J. Sound and Vibration. A symmetric finite element formulation for acoustic fluid-structure interaction analysis.
- [3] P. GÖRANSSON and P. DAVIDSSON 1986, The Aeronautical Research Institute of Sweden, FFA TN 1986-70. Eigenvalue analysis of 2D aircraft fuselage beam model and fuselage air cavity using a symmetric fluid-structure interaction finite element formulation.
- [4] P. GÖRANSSON 1986, Saab-Scania Aircraft Division, Sweden. TKH R-3608 ASKA-Acoustics. Overview of capabilities.
- [5] U. ENBORG 1987, Saab-Scania Aircraft Division, Sweden. TKME-87.49. Measurement of double wall transmission in Saab Car Division Acoustic Laboratory, (in Swedish).

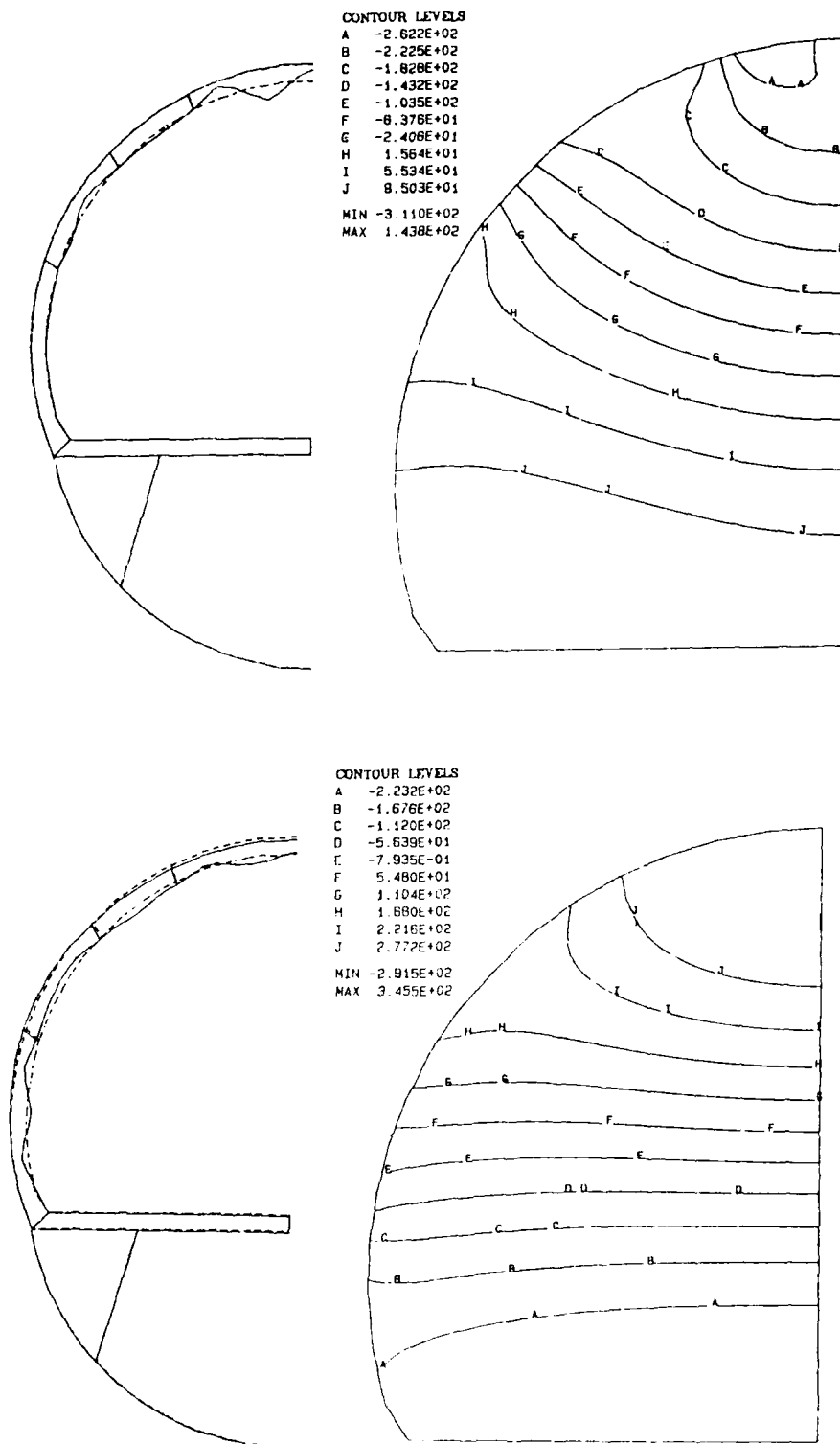


Figure 1. Eigen modes around 90 Hz for case 1.
a) 87 Hz, b) 95 Hz

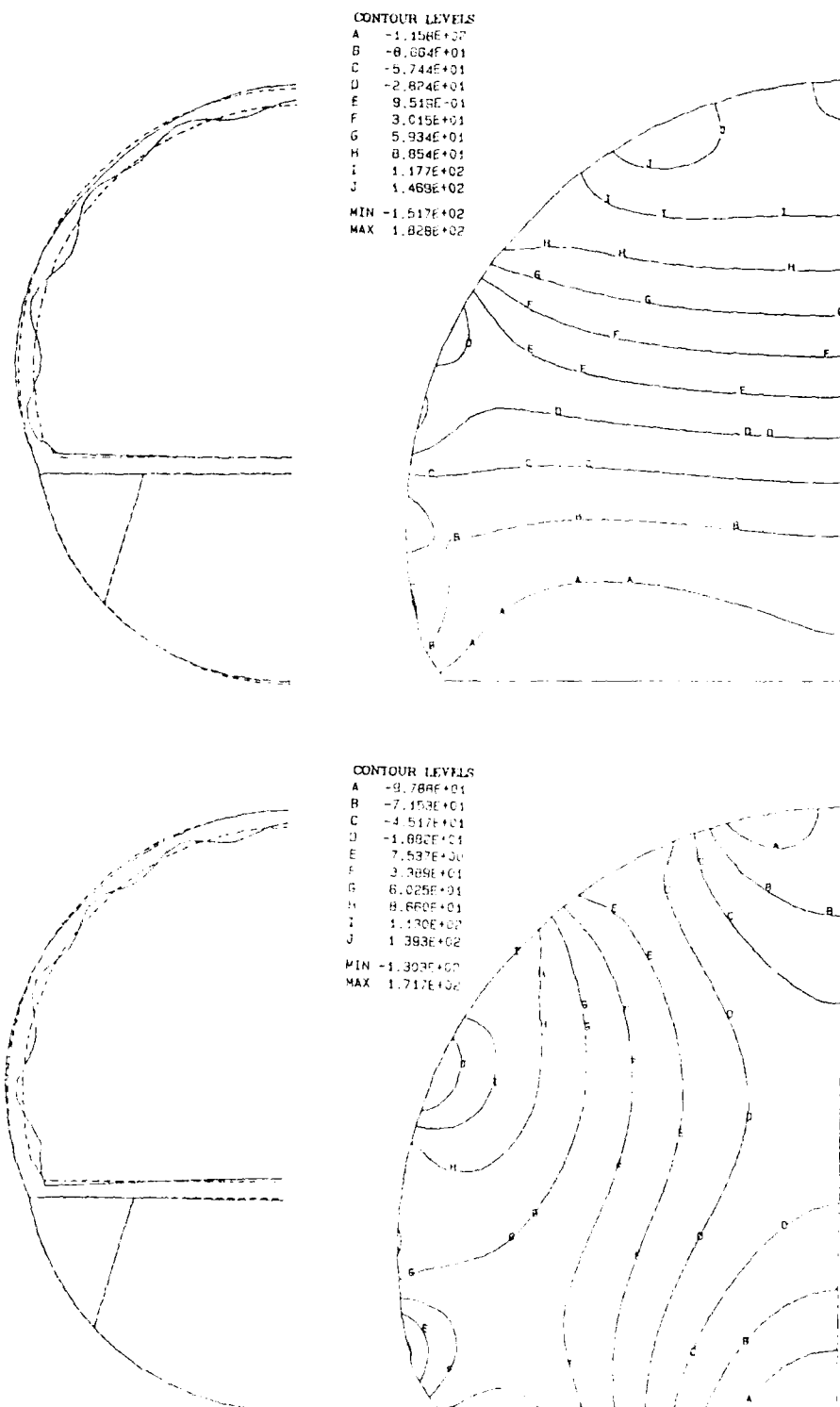
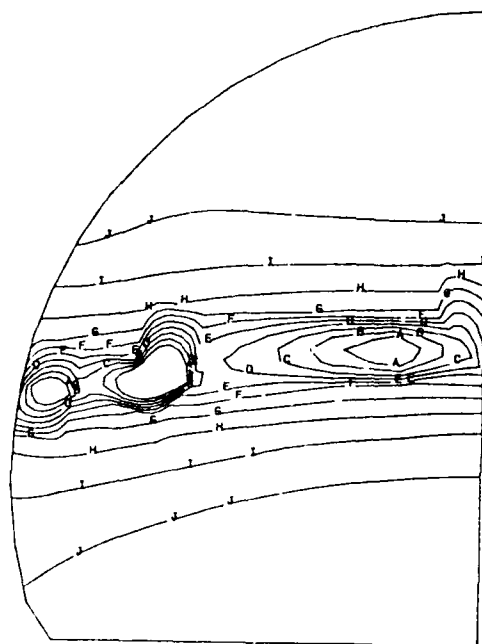
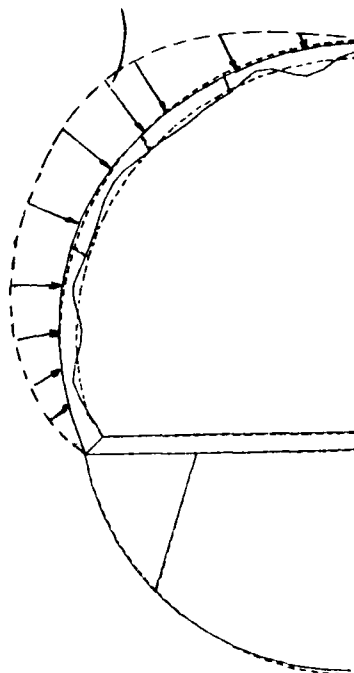


Figure 2. Eigen modes around 90 Hz for case 2.
a) 81 Hz, b) 95 Hz

a) 130 dB SPL

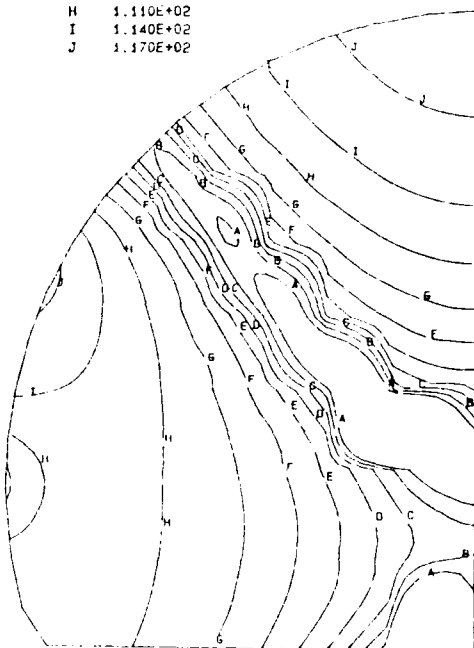
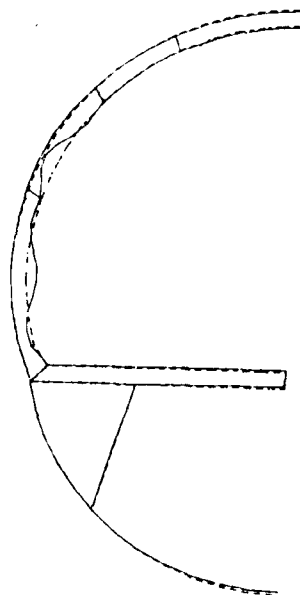


MAX 1.218E+02

CONTOUR LEVELS

A	9.000E+01
B	9.300E+01
C	9.600E+01
D	9.800E+01
E	1.020E+02
F	1.050E+02
G	1.080E+02
H	1.110E+02
I	1.140E+02
J	1.170E+02

b)



MAX 1.188E+02

Figure 3. Frequency response at 90 Hz. Loading in response cases
a) case 1, b) case 2

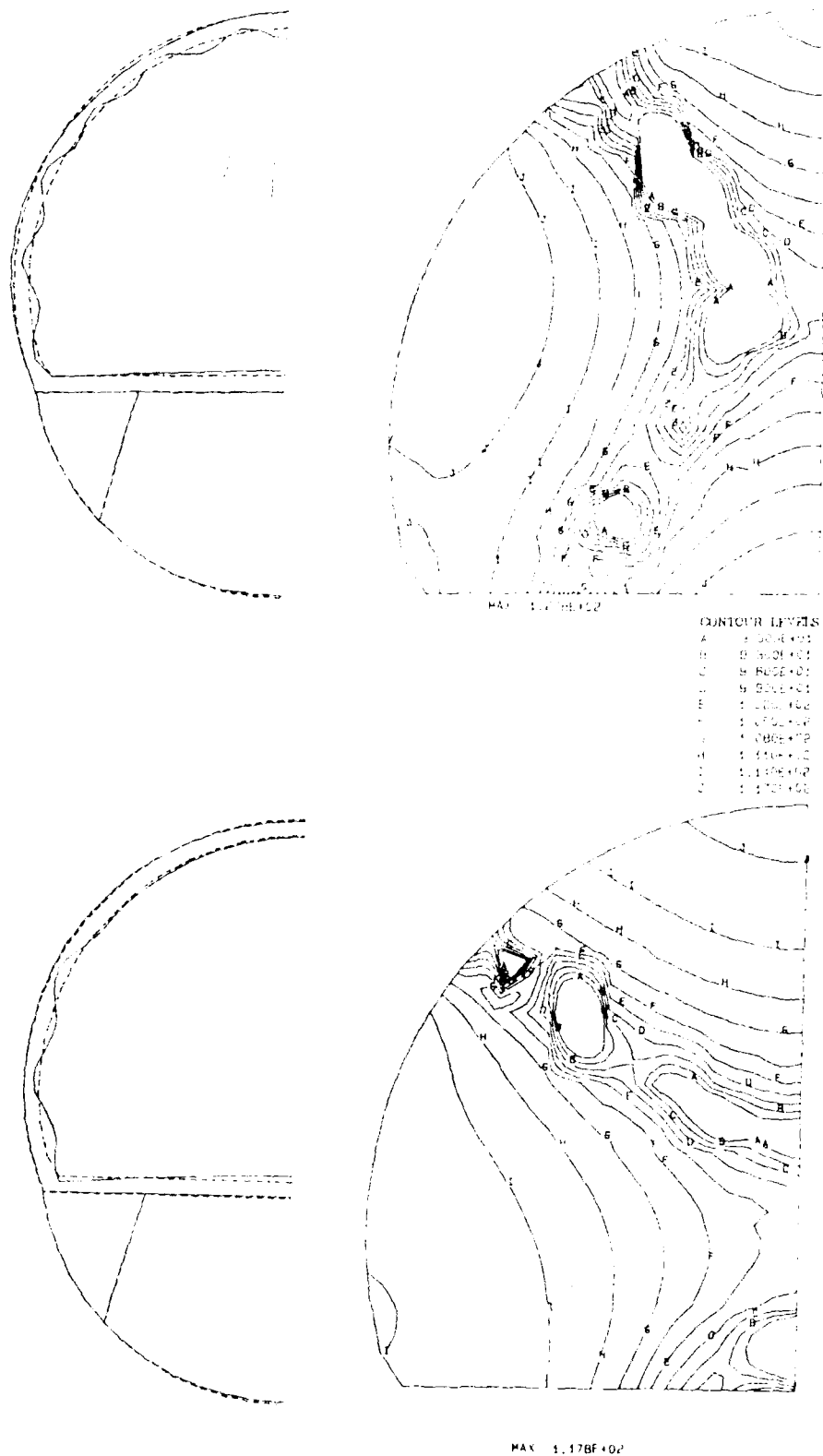
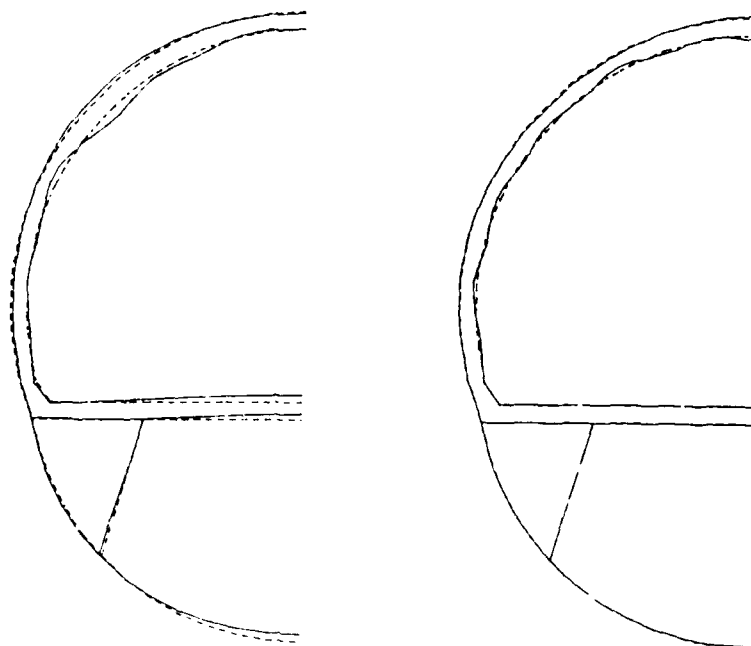


Figure 4. Frequency response at 90 Hz.
a) case 3, b) case 4



CONTOUR LEVELS	
A	9.000E+01
B	9.300E+01
C	9.600E+01
D	9.900E+01
E	1.020E+02
F	1.050E+02
G	1.080E+02
H	1.110E+02
I	1.140E+02

MAX 1.147E+02

Figure 5. Response at 90 Hz with thermal insulation

12. LARGE SPACE STRUCTURES

MODELING OF LATTICED STRUCTURES FOR DYNAMIC ANALYSES

Serge Abrate
Dept. of Mechanical & Aerospace Engineering
University of Missouri-Rolla
Rolla, MO 65401-0249

1. INTRODUCTION

The dynamic behavior of large periodic structures is often analyzed using finite element methods for a direct approach or by replacing the structure with an equivalent continuum in order to predict global effects with simple efficient models. By studying the propagation of harmonic waves, it is shown on an example, that the continuum models provide a low frequency - long wavelength approximation to the behavior of the structure. Discrete structures exhibit a filtering effect and expressions are given to determine the limits of the pass-band for each mode, long wavelength approximations to the dispersion curves are presented and matching long wavelength behavior of the equivalent model to that of the discrete structure provides expressions for the equivalent properties.

2. HARMONIC WAVE PROPAGATION IN PERIODIC STRUCTURES

Propagation of harmonic waves in periodic structures can be studied by studying a single cell [1]. A typical cell is isolated and its equations of motion are written as

$$M\ddot{q} + Kq = F \quad (1)$$

The displacement and force vectors are partitioned as

$$q = (q_L, q_i, q_R)^T$$

$$F = (F_L, F_i, F_R)^T \quad (2)$$

where the subscripts L, i, and R denote degrees of freedom to the left, inside, and to the right of the typical cell, respectively. The stiffness and mass matrices K and M are partitioned accordingly.

The dispersion relations are obtained by solving the eigenvalue problem

$$|K(\mu) - \omega^2 M(\mu)| = 0 \quad (3)$$

with

$$K(\mu) = \begin{bmatrix} K_{LL} + K_{RR} + e^{\mu}K_{LR} + e^{-\mu}K_{RL} & K_{Li} + e^{-\mu}K_{Ri} \\ K_{iL} + e^{\mu}K_{iR} & K_{ii} \end{bmatrix}$$

where $\mu = ikL$, $i^2 = -1$, k being the wave number ($2\pi/\text{wavelength}$) and L the length of the typical cell. The M matrix is evaluated in a similar fashion, the K is being replaced by M's in the expression for K.

Propagation of harmonic waves in the plane truss of Figure 1 can be studied using several finite element models. Each member is modeled by one element, motion is described by two degrees of freedom at each node. In every case K and M will be 4x4 matrices and solving the equation:

$$[(a - b)(d + e) + c^2] [(a + b)(d - e) + c^2] = 0 \quad (4)$$

the dispersion relations are obtained.

2.1 Discrete Model with Consistent Mass Matrices

Each member is modeled using one classical frame finite element with zero moment of inertia. Each element matrix will reduce to a 4 x 4, the stiffness matrix being to that of a 2D truss element, but the mass matrix now accounts for both axial and transverse inertias.

$$\begin{aligned} a &= k_L(1 - \cos kL) + k_d \frac{L^2}{D^2} - \omega^2 [M_L(2 + \cos kL) + \frac{78}{35} M_v + (2 + \frac{8}{35} \frac{H^2}{D^2}) M_d] \\ b &= -k_d \frac{L^2}{D^2} \cos kL - \omega^2 [\frac{27}{35} M_v + (1 - \frac{8}{35} \frac{H^2}{D^2}) M_d \cos kL] \\ c &= i \frac{LH}{D^2} [k_d - \omega^2 \frac{8}{35} M_d] \sin kL \\ d &= k_v + k_d \frac{H^2}{D^2} - \omega^2 [M_L \frac{78 + 27 \cos kL}{35} + 2 M_v + (2 + \frac{8}{35} \frac{L^2}{D^2}) M_d] \\ e &= -(k_v + k_d \frac{H^2}{D^2} \cos kL) - \omega^2 [M_v + (1 - \frac{8}{35} \frac{L^2}{D^2}) M_d \cos kL] \end{aligned} \quad (5)$$

where $k_L = EA_L/L$, $k_v = EA_v/2H$, $k_d = EA_d/D$, $M_L = \rho A_L L/6$, $M_v = \rho A_v H/12$, and $M_d = \rho A_d D/6$.

Since there are 4 degrees of freedom in this problem there will be 4 wavemodes and 4 dispersion curves as shown in Figure 1. Equation (4) can be written as

$$\alpha_1 \omega^4 + \alpha_2 \omega^2 + \alpha_3 = 0 \quad (6)$$

with coefficients of the form

$$\alpha_i = \alpha_{i1} + \alpha_{i2} \cos kL + \alpha_{i3} \cos^2 kL$$

The coefficients α_i are periodic with period $kL = 2\pi$, so it is sufficient to study a 2π interval. But since

$$\omega_i(kL) = \omega_i(-kL) \quad i = 1, 4 \quad (7)$$

only the $[0, \pi]$ interval needs to be considered. For the example considered the cross-section areas were taken as $A_L = 80 \times 10^{-6} \text{ m}^2$, $A_d = 40 \times 10^{-6} \text{ m}^2$,

$A_v = 60 \times 10^{-6} \text{ m}^2$, Young's Modulus $E = 7.17 \times 10^7 \text{ N/m}^2$ and the density $\rho = 2768 \text{ kg/m}^3$. The cell dimensions $L = 7.5 \text{ m}$ and $H = 5 \text{ m}$. The dispersion curves plotted in Figure 1 exhibit filtering effect, that is, for each mode, the wave can propagate only in a certain range of frequencies called a pass-band. For very long wavelengths ($k \rightarrow 0$) the structure behaves as a beam or a rod depending on the type of motion being considered. This is why equivalent continuum models have been developed and are used successfully for analyzing the static and dynamic behavior of latticed structures.

Using a Taylor series expansion for the sine and cosine functions in equation 5 we obtain the following long wavelength approximations

$$\omega_1^2 = \frac{\frac{1}{2} EA_\ell L^2}{2\rho A_\ell + \rho A_v \frac{H}{L} + 2\rho A_d \frac{D}{L}} k^4 [1 - \alpha k^2] \quad (8a)$$

$$\omega_2^2 = \frac{2 [EA_\ell + \frac{EA_d}{\beta} L^3/D^3]}{2\rho A_\ell + \rho A_v \frac{H}{L} + 2\rho A_d \frac{D}{L}} k^2 \quad (8b)$$

$$\omega_3^2 = \frac{2 EA_d LH^2/D^3}{H^2 [\frac{1}{2} \rho A_\ell + \frac{17}{140} \rho A_v \frac{H}{L} + \frac{1}{6} \rho A_d \frac{D}{L} (1 + \frac{16}{35} \frac{H^2}{D^2})]} [1 + \gamma k^2] \quad (8c)$$

$$\omega_4^2 = \frac{EA_v + 2EA_d H^3/D^3}{\frac{H^2}{12} [6 \rho A_\ell \frac{L}{H} + \rho A_v + 2\rho A_d \frac{D}{H} (1 + \frac{16}{35} \frac{L^2}{D^2})]} \quad (8d)$$

where $\beta = 1 + 2 \frac{EA_d H^3}{EA_v D^3}$ and the coefficients α and γ are not reproduced here for the sake of brevity.

The coefficients α and γ in equations (8a) and (8c) are different where as they are equal for a Timoshenko beam as we will show.

Figure 2 shows the 4 wavemodes for very long wavelengths and for the case when the wavelength is equal to the cell length.

For short wavelengths the behavior of the truss differs markedly from that of a continuum. For $kL = \pi$ we find

$$(\omega_1')^2 = \frac{12 EA_d H^3/D^3}{H^2 [\frac{51}{35} \rho A_\ell \frac{L}{H} + \frac{3}{2} \rho A_v + \frac{1}{6} \rho A_d \frac{D}{H} (1 + \frac{16}{35} \frac{L^2}{D^2})]} \quad (9a)$$

$$(\omega_2')^2 = \frac{6EA_v}{H[3\rho A_d D + \frac{1}{2}\rho A_v H + \frac{51}{35}\rho A_\ell L]} \quad (9b)$$

$$(\omega_3')^2 = \frac{12EA_\ell}{L^2[\rho A_\ell + \frac{51}{70}\rho A_v \frac{H}{L} + 3\rho A_d \frac{D}{L}]} \quad (9c)$$

$$(\omega_4')^2 = \frac{12(EA_L + EA_d L^3/D^3)}{L^2[\rho A_\ell + \frac{3}{2}\rho A_v \frac{H}{L} + \rho A_d \frac{D}{L}(1 + \frac{16}{35}\frac{H^2}{D^2})]} \quad (9d)$$

Equations 8, 9 allow to study the influence of the various parameters on the dynamic behavior of the structure. For example, when $A_v = 0$, $\omega_4' = 0$ and in this case a breathing mode can propagate at a low frequency. This situation, which cannot be handled by simple continuum models, was considered in [3].

2.2 Discrete Model with Lumped Mass Matrices

Using lumped mass matrices the global mass matrix becomes diagonal which results in substantial memory space savings. Here the element mass matrices are evaluated by assigning half the mass of each element to each node. For free harmonic wave propagation, the dispersion curves are obtained by solving Eq. (4) with

$$\begin{aligned} a &= k_L(1 - \cos kL) + k_d L^2/D^2 - 3\omega^2 (M_L + M_v + M_d) \\ b &= -k_d \frac{L^2}{D^2} \cos kL, \quad c = i k_d \frac{LH}{D^2} \sin kL \\ d &= k_v + k_d \frac{H^2}{D^2} - 3\omega^2 (M_L + M_v + M_d) \\ e &= -(k_d \frac{H^2}{D^2} \cos kL + k_v) \end{aligned} \quad (10)$$

Long wavelengths approximations to the dispersion relations for the lumped mass matrix model are

$$\omega_1^2 = \frac{\frac{1}{2}EA_\ell H^2}{2\rho A_\ell + \rho A_v \frac{H}{L} + 2\rho A_d \frac{D}{L}} k^4 [1 - (\frac{1}{6} + \frac{1}{4} \frac{EA_\ell D^3}{EA_d L^3}) k^2 L^2] \quad (11a)$$

$$\omega_2^2 = \frac{2EA_\ell + \frac{EA_d L^3}{D^3}}{2\rho A_\ell + \rho A_v \frac{H}{L} + 2\rho A_d \frac{D}{L}} k^2 \quad (11b)$$

$$\omega_3^2 = \frac{2 EA_d L^2 H / D^3}{\frac{H}{4} [2\rho A_\ell + \rho A_v \frac{H}{L} + 2\rho A_d \frac{D}{L}]} \left[1 + \frac{1}{4} \frac{EA_\ell D^3}{EA_d L} k^2 \right] \quad (11c)$$

$$\omega_4^2 = \frac{EA_v + 2 EA_d H^3 / D^3}{\frac{H}{4} [2\rho A_\ell + \rho A_v \frac{H}{L} + \rho A_d \frac{D}{L}]} \quad (11d)$$

When $kL = \pi$ the lumped mass model gives:

$$(\omega_1')^2 = \frac{8 EA_d H^3 / D^3}{HL(2\rho A_\ell + \rho A_v \frac{H}{L} + 2\rho A_d \frac{D}{L})} \quad (12a)$$

$$(\omega_2')^2 = \frac{4 EA_v}{HL(2\rho A_\ell + \rho A_v \frac{H}{L} + 2\rho A_d \frac{D}{L})} \quad (12b)$$

$$(\omega_3')^2 = \frac{8 EA_\ell}{L^2(2\rho A_\ell + \rho A_v \frac{H}{L} + 2\rho A_d \frac{D}{L})} \quad (12c)$$

$$(\omega_4')^2 = \frac{8(EA_\ell + EA_d L^3 / D^3)}{L^2(2\rho A_\ell + \rho A_v \frac{H}{L} + 2\rho A_d \frac{D}{L})} \quad (12d)$$

Comparison of results of the consistent and lumped mass matrices in Figure 1 indicates that for low frequencies and long wavelengths the lumped mass approximation is adequate for the axial and bending modes. For the thickness-shear and breathing modes the lumped mass model is inadequate even for very long wavelengths.

3. EQUIVALENT CONTINUUM MODELS

The analysis of large repetitive structures is simplified when the actual discrete structure is replaced by an equivalent continuum. This method has been used extensively because it allows to determine the overall behavior of the structure without considering its internal details. This results in substantial simplification, computer time and memory space savings. The behavior of the continuum model is expected to approximate behavior of the discrete structure at low frequencies.

For studying the bending of beam-like trusses and frames the Bernoulli-Euler and Timoshenko beams are commonly used as equivalent models. The Bernoulli-Euler beam model [2] leads to the dispersion relation

$$\omega = (EI/\rho A)^{1/2} k^2 \quad (13)$$

For the Timoshenko beam model, the dispersion relations are obtained by solving the equation

$$\omega^4(\rho A \cdot \rho I) - \omega^2[\rho I \cdot GA k^2 + (GA + k^2 EI)\rho A] + GA \cdot EI k^4 = 0 \quad (14)$$

For long wavelengths results from equation (14) can be approximated by

$$\omega_{\text{bending}}^2 = \frac{EI}{\rho A} k^4 \left[1 - \left(\frac{\rho I}{\rho A} + \frac{EI}{GA} \right) k^2 \right] \quad (15)$$

$$\text{and} \quad \omega_{\text{shear}}^2 = \frac{GA}{\rho I} \left[1 + \left(\frac{\rho I}{\rho A} + \frac{EI}{GA} \right) k^2 \right] \quad (16)$$

For small values of k , the Timoshenko beam solution tends to the Bernoulli-Euler beam solution.

For short wavelengths ($k \rightarrow \infty$),

$$\omega_{\text{bending}}^2 = (GA/\rho A)k^2 \quad \text{and} \quad \omega_{\text{shear}}^2 = (EI/\rho I)k^2 \quad (17)$$

which indicates that contrary to what happens with discrete structures, bending and shear waves can propagate freely in the continuum model at very high frequencies.

For axial deformation, the equation of motion for a rod is the classical wave equation and the dispersion relation is

$$\omega = (EA/\rho A)^{1/2} k \quad (18)$$

3.1 Equivalent Properties

Equivalent properties can be determined by comparing the dispersion relations for the discrete and continuum models. For example, comparing Eq. (8a) and (13) and noticing that the denominator in equation (8a) represents the mass of the truss per unit length, we obtain the equivalent properties

$$\overline{EI} = \frac{1}{2} EA_\ell H^2 \quad (19a)$$

$$\overline{\rho A} = 2\rho A_\ell + \rho A_v \frac{H}{L} + 2\rho A_d \frac{D}{L} \quad (19b)$$

Similar considerations for the axial and shear modes lead to

$$\overline{EA} = 2\left[\rho A_\ell + \frac{EA_d}{\beta} + L^3/D^3\right], \quad \text{with } \beta = 1 + 2 \frac{EA_d H^3}{EA_v D^3} \quad (19c)$$

$$\overline{GA} = 2 EA_d L H^2/D^3 \quad (19d)$$

$$\overline{\rho I} = h^2 \left[\frac{1}{2} \rho A_\ell + \frac{17}{170} \rho A_v \frac{H}{L} + \frac{1}{6} \rho A_d \frac{D}{L} \left(1 + \frac{16}{35} \frac{H^2}{D^2} \right) \right] \quad (19e)$$

where $\overline{\rho I}$ has been chosen so that the thickness-shear mode cut-off frequency of the equivalent Timoshenko beam will match that of the truss given by Eqn. (8c). The dispersion curves of the equivalent Timoshenko beam model are compared with those of the discrete structure in Figure 3. Figure 3 shows the variation of phase velocities with wavelength for all 4 models for bending waves.

3.2 Finite Element Modeling of the Equivalent Continuum

In many instances the equivalent model of a discrete structure is itself discretized using the Finite Element Method. With this approach complex systems and boundary conditions can be handled with a much smaller number of degrees of freedom than for the direct finite element analysis of the original structure. Then a practical question arises: what should be the ratio of the length of the equivalent finite element model to the length of one typical cell of the original structure.

For our example the equivalent continuum model is discretized using the classical 4 degrees of freedom cubic beam element. For this element we can show that the dispersion relations are obtained by solving the equation

$$a\omega^4 - b\omega^2 + c = 0 \quad (20)$$

where

$$\begin{aligned} a &= (\rho A \cdot l/420)^2 (455 - 252 \cos kl + 7 \cos^2 kl) \\ b &= (\rho A \cdot EI/420) (828 - 444 \cos kl - 12 \cos^2 kl) \\ c &= 12 (EI/l)^2 (1 - 2 \cos kl + \cos^2 kl) \end{aligned}$$

Using Taylor series expansion, the long wavelengths approximation for the bending mode is

$$\omega^2 = (EI/\rho A) k^4 + O(k^8) \quad (21)$$

The phase velocity varies almost linearly with the wave number k for values of kl between 0 and π . For $kl = \pi$, the maximum frequency at which a bending wave can propagate freely is

$$\omega_{\max} = (EI/\rho A)^{1/2} (\pi/l)^2 \quad (22)$$

So that the finite element model is valid for frequencies up to ω_{\max} . If it is determined that the Bernoulli-Euler beam model is valid up to a frequency ω^* , then the finite element discretization will not introduce additional errors provided that ω_{\max} remains larger than ω^* . Equation (22) indicates that if $l = nL$, then ω_{\max} is inversely proportional to the number of cells represented by the beam finite element. The maximum number of cells that can be accommodated using the finite element model of the equilibrium model is then equal to the ratio of the shorter wavelength allowable λ_{\min} to the cell length L . Further mesh refinement would not bring about improvement compared to the discrete structure model.

4 FREE VIBRATIONS

The first five natural frequencies of the 10 bay truss in Figure 1 were determined using 4 methods. For direct analysis using consistent and lumped mass matrices, the truss was modeled using the ADINA finite element program. The equivalent Bernoulli-Euler and Timoshenko beam models were also used. Huang's solution [4] for the cantilever Timoshenko beam was used. Equivalent properties were determined using Eqns. (19). Results in Table 1 show similar trends as in Figure 4.

5. CONCLUSION

Harmonic wave propagation analysis in a discrete periodic structure can be performed very simply by considering a simple typical cell. The basic dynamic behavior of the structure can then be considered irrespective of the number of cells and boundary conditions of a particular example as it is the case when studying natural vibrations.

The equivalent continuum models were shown to approximate the long wavelength behavior of the discrete structure. Approximate expressions are provided for the dispersion relations and equivalent properties are determined by matching dispersion curves for long wavelengths.

References

1. Mead, D. J., J. Sound & Vibration, 27(2), pp. 233-260, "A General Theory of Harmonic Wave Propagation in Linear Periodic System with Multiple Couplings."
2. Graff, K. F., Ohio State University Press, 1975, Wave Motion in Solids.
3. Engels, R. C., Meirovitch, L., J. Sound and Vibration (1978), 56(4), pp. 481-493, Response of Periodic Structures by Modal Analysis.
4. Huang, T. C., J. of Applied Mech., pp. 579-584, Dec. 1961, The Effect of Rotatory Inertia and of Shear Deformation in the Frequency and Normal Mode Equations of Uniform Beams with Simple End Conditions.

Table 1. Natural Frequencies for 10 Bay Cantilever Truss

Mode	Natural Frequencies (rad/s)			
	Consistent	Lumped	Timoshenko Beam Model	Bernoulli-Euler Beam Model
1	5.646	5.629	5.721	5.8459
2	32.05	31.46	32.04	36.636
3	79.92	76.80	78.42	102.58
4*	86.69	86.54	88.38	88.38
5	138.2	128.9	132.89	

* -axial mode

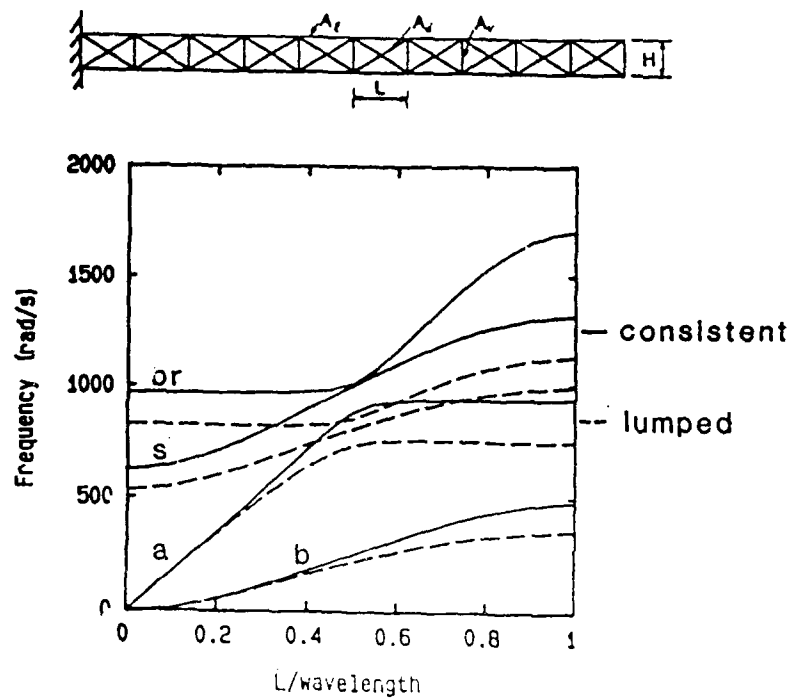


Figure 1 : Dispersion curves for plane truss

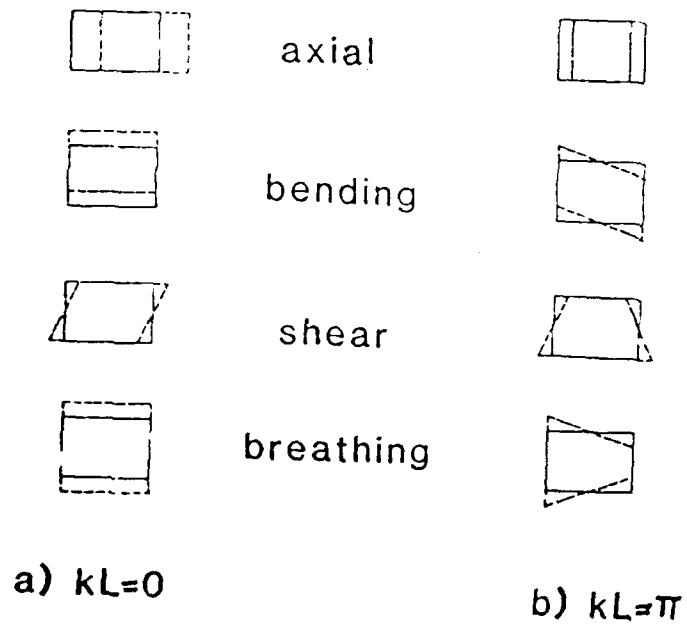


Figure 2 : Wavemodes for plane truss

— discrete --- equivalent model

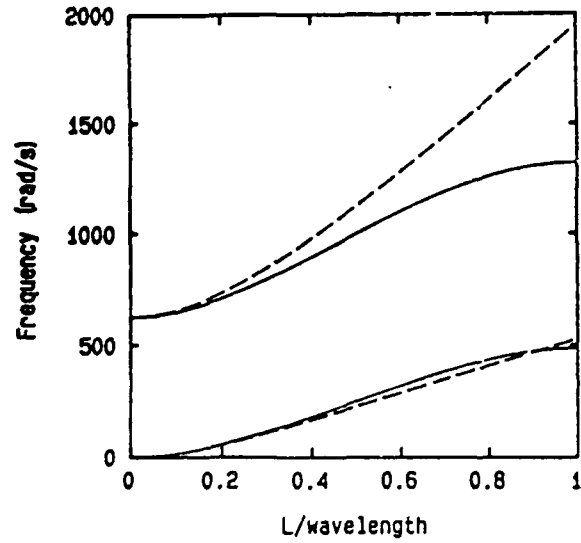


Figure 3 : Comparison of discrete and equivalent models

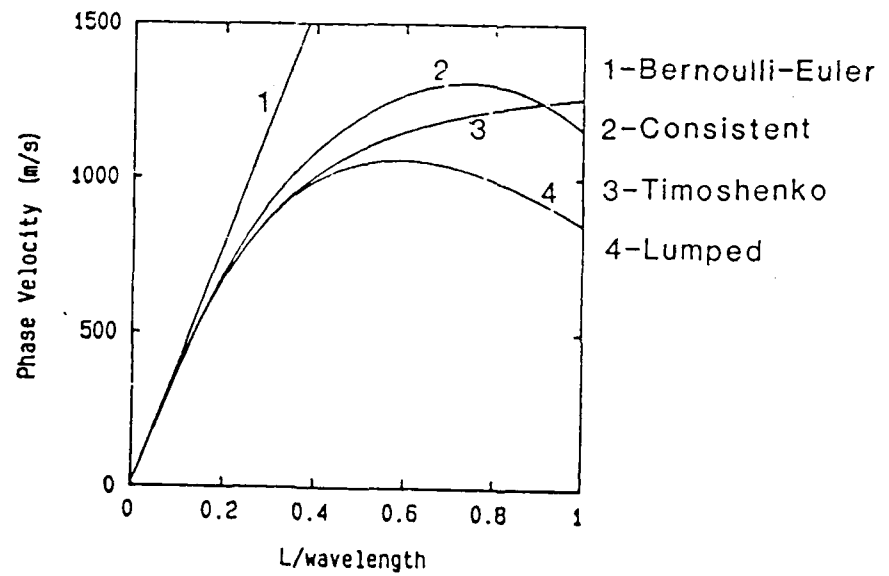


Figure 4 : Comparison of 4 models for bending waves

AN ASSESSMENT OF MODEL ORDER REDUCTION TECHNIQUES*

Hagop V. Panossian

Rockwell International/Rocketdyne Division
Canoga Park, California

1. INTRODUCTION

A central issue in the active control of complex systems such as large flexible space structures (LFSS) is the derivation of a "correct" mathematical model. Theoretically, there are infinitely many elastic modes or degrees of very low natural damping. Moreover, the flexible modes contribute to the actual deformation of the structure [1].

The development of a model of low-enough dimensional order that it can be utilized by the onboard controller, yet high enough dimensional order that it preserves the dynamic characteristics of the real system represented and controlled is a nontrivial task [2]. The motivations for such a reduction are either to reduce computations for analysis and practical control design or to simplify the control system structure [3].

The reduction or the condensation methods are based on transformations of the coordinates in the equations of motion that essentially maintain the invariance of the quadratic forms of the potential and kinetic energies. An important feature of these methods is that the reduced order model often loses the basic characteristics of the original system. Considerable progress was made by Likins, Ohkami, and Wong [4] in this respect. It has often been pointed out that such techniques generally constitute application of Rayleigh-Ritz/Galerkin optimization, and matrix transformation methods to the eigenvalue/eigenvector formulation for structural dynamic problems [5].

Reduced "balanced" models of linear time-invariant dynamical systems are obtained by deleting those states that contribute the least to the controllability and observability (or the impulse response) of the original system [6] and thus are optimal only in this sense.

A more recent approach to model reduction is proposed in Skelton's work [7], where each state of the system model is assigned a "cost" relative to a given basis, via a quadratic criterion, and the states with the least cost are deleted in a systematic manner.

The latest development in model order reduction techniques is the work by Hyland and Bernstein [8]. Herein first order necessary conditions for reduced order modeling of linear time-invariant systems are derived.

In the following pages, the various techniques in model order reduction will be presented and appropriately discussed. The advantages and disadvantages of each will be commented upon, and further requirements and trends will be briefly touched.

*This work was supported, in part, by the Air Force Wright Aeronautical Laboratories, Wright-Patterson, AFB, Structures and Dynamics Division, while the author was employed by HR-Textron, Valencia, California.

2. PROBLEM STATEMENT

The most general linear finite dimensional model of structures can be expressed as follows:

$$M \ddot{x}(t) + C \dot{x}(t) + K x(t) = F u(t) \quad (1)$$

where M , C , and K are termed the mass, the damping, and the stiffness matrices, respectively, and they could be functions of spacial variables. Appropriate transformations will change Eq. (1) into the state-space representation given by

$$\dot{y} = Ay + Bu \quad (2)$$

where

$$A = \begin{bmatrix} 0 & I \\ -M^{-1}K & -M^{-1}C \end{bmatrix} \text{ and } B = \begin{bmatrix} 0 \\ M^{-1}F \end{bmatrix}$$

3. CONDENSATION METHODS

During the 1950s, the classical approach to generating a reduced static model for a structural system was to use discrete masses associated with certain selected deflections. [9, 10] In the early 1960s, Guyan, [11] and Davison [12] introduced ad-hoc methods of model reduction that are commonly known by various names. These methods basically reduce the order of the original large dimensional linear model by discarding some of the modal deflections called "slave" DOF and retaining the remaining ones called "master" DOF. The choice relative to the master and slave DOF is made, based on engineering judgment, in such a way that the lower frequencies in the eigen-spectrum of the structure are preserved as much as possible [13].

3.1 Guyan Reduction

The underlying problem in model order reduction via reducing the mass and stiffness matrices can be expressed as a general algebraic eigenvalue problem.

$$Kx = \lambda Mx$$

where K , M are as before and λ are the eigenvalues of the system. In what is commonly called "Guyan reduction," the basis for the above order reduction is the elimination of coordinates at which there are no forces applied [11].

Thus, the abovementioned eigenvalue problem can be expressed as follows:

$$\begin{bmatrix} F_1 \\ F_2 \end{bmatrix} = \begin{bmatrix} K_{11} & K_{12} \\ K_{12} & K_{22} \end{bmatrix} \begin{bmatrix} x_1 \\ x_2 \end{bmatrix} = \lambda \begin{bmatrix} M_{11} & M_{12} \\ M_{21} & M_{22} \end{bmatrix} \begin{bmatrix} x_1 \\ x_2 \end{bmatrix} \quad (3)$$

where F_1 , F_2 are the components of forces, and F_2 is assumed to be zero. x_1 , x_2 are the corresponding component coordinates, M_{ii} and K_{ii} , $i = 1, 2$, are the mass and stiffness components. This amounts to a coordinate transformation of the forces: $x = Tx_1$. After more manipulations, it is found that the

stiffness matrix corresponding to the forces F_1 is given by

$$K_1 = K_{11} - K_{12} K_{22}^{-1} K_{21} \quad (4)$$

and the mass matrix corresponding to F_1 is

$$\begin{aligned} M_1 = & M_{11} - M_{12} K_{22}^{-1} K_{21} - K_{12} K_{22}^{-1} M_{21} \\ & + K_{12} K_{22}^{-1} M_{22} K_{22}^{-1} K_{21} \end{aligned} \quad (5)$$

As is mentioned in Ref. 11, this transformation creates some discrepancy in the eigenvalue eigenvector problem. For, from Eq. (3),

$$x_2 = [I - \lambda K_{22}^{-1} M_{22}]^{-1} K_{22}^{-1} [\lambda M_{21} - K_{21}] x_1 \quad (6)$$

and in expanded form,

$$x_2 = \left[I + \lambda K_{22}^{-1} M_{22} + \frac{\lambda^2}{2!} (K_{22}^{-1} M_{22})^2 + \dots \right] K_{22}^{-1} (\lambda M_{21} - K_{21}) x_1 \quad (7)$$

Thus, in the reduced matrices K_1 and M_1 , the higher order terms are eliminated resulting in changes in eigenvalues and eigenvectors of the original system. It has been established that the absolute values of the eigenvalues are always increased due to the reduction of a model order [14].

Alternate approaches to model truncation or reduction are proposed by several authors that are variations of the Guyan reduction. Wilson [15] showed the relationship between condensation and Gaussian elimination. Downs [16] attempts to address several issues of accuracy and detection of master DOF. The convergence of the approximations in Eq. (7) are functions of the choice of elements retained, and the process of back transformation could lead to erroneous results. Also, there seems to be some confusion in the number of retained DOF required for an accurate lower mode of vibration.

In many situations in structural analysis, the main reason for the derivation of the "exact" eigenvalues and eigenvectors is their use for the reduction of the order of the system model. Wilson, Yuan, and Dickens [17], and Arnold et al. [18] present an approach whereby an "accurate dynamic analysis" is obtained at a reduced computational expense. Paz [19], on the other hand, presents his "dynamic condensation" approach that starts by assigning to the eigenvalues an approximate or zero value for the first eigenvalue. It then proceeds by elementary operations to eliminate the undesired displacements. Sotiropoulos [20] points out methods that could lead to estimates of the error between the eigenvalues of the original and the reduced system.

3.2 Cost Decomposition Method

In applications of optimal control theory to linear quadratic Gaussian systems, the process model is often too complicated for techniques involving Riccati equation solutions. The traditional approach is to obtain a reduced order model, according to the control/observation and performance requirements, by some appropriate model reduction technique and then derive the optimal controller for the new system. However, it has been established that

the optimal model reduction can only be accomplished if the modeling and control problems are tackled in unison [21]. Component cost analysis was first considered by Skelton [22] as an attempt to arrive at the abovementioned unified approach. The derivation of an optimal control law of low-enough order n_c (for implementation purposes) from a reduced order model, n_r , entails (1) application of component cost analysis to the full order (n) open-loop system model in order to arrive at the reduced order (n_r) model; (2) solution of the optimal control problem for the n_r th order system; and (3) application of component cost analysis to reduce the order of the controller from n_r to n_c [23].

The requirement to determine the relative importance of modal vectors in a structural analysis and control design setting is apparent in various applications. A systematic approach to establish the contribution or "cost" of each component mode of a large-order system, based on a quadratic cost or performance index, and accordingly truncate those that have a minimal contribution is presented by Skelton [24]. This method can be considered a condensation method that addresses one of the important issues in model reduction, namely, the "best" choice of the retained modes.

Suppose Eq. (2) is of order n_r and is corrupted by additive white Gaussian noise. Also, suppose its corresponding measurement system and the performance functional are given. Thus,

$$\dot{y} = Ay + Bu + Dw \quad (8)$$

$$m = Cy \quad (9)$$

and

$$z = My + v \quad (10)$$

where m is the k -dimensional output vector that is used to measure the performance, z is the l -dimensional measurement vector, and w, v are zero-mean white Gaussian noise vectors with intensities of W and V , respectively. The matrices are of appropriate dimensions with $\{C, A\}$ and $\{M, A\}$ observable and $\{A, B\}$ and $\{A, D\}$ controllable. The cost functional of the system is then

$$J = E \left[\int_0^\infty (m^T Qm + u^T Ru) dt \right] \quad (11)$$

The n_r order feedback controller is

$$u = G\hat{y} \quad (12)$$

$$\dot{\hat{y}} = A_c \hat{y} + Fz \quad (13)$$

where $A_c = A + BG - FM$, $G = R^{-1}B^TK$, $F = PM^TV^{-1}$. And

$$KA + A^TK - KBR^{-1}B^TK + C^TQC = 0 \quad (14)$$

$$PA^T + AP - PM^TV^{-1}MP + DWDT = 0 \quad (15)$$

The underlying feature of component cost analysis is to evaluate numerically the significance of each "component" (states y) by assigning a metric called

"component cost" to each component; then a reduced order controller is derived by deleting those controller states y that have smallest component costs.

3.3 Balanced State-Space Representation

The model reduction problem relative to minimal realization theory was first introduced in control design by Moore [7]. His main idea was to be able to drive approximations to a given control system model that has a lower order and that has virtually the same impulse response matrix.

Moreover, the balanced coordinate procedure usually requires that the system be asymptotically stable such that the observability and controllability Grammians be finite.

These are the unique symmetric positive definite matrices satisfying the following Lyapunov equations:

$$AW_C + W_C A^T = -BB^T \text{ and } A^T W_0 + W_0 A = -C^T C, \text{ respectively.}$$

In the above equations, C is the matrix of the observation system of Eq. (9) and t_0 is the initial time. These are defined for continuous deterministic systems. The procedure used to generate a transformation T that simultaneously diagonalizes W_0 and W_C and sets them equal is the singular value decomposition. After equalization, the new coordinates (that are referred to as "balanced coordinates") are reduced by deleting the diagonal elements in $W_0 = W_C$ with smallest magnitudes and keeping the dominant components. It is shown in Ref. [25] that the reduced order models thus obtained are stable only if the original model is stable.

Let us define a coordinate transformation $\tilde{y}(t) = Py(t)$. Then, Eq. (2) and (9) reduce to

$$\dot{\tilde{y}} = \tilde{A}\tilde{y} + \tilde{B}u \quad (16)$$

$$\tilde{m} = \tilde{C}\tilde{y} \quad (17)$$

where

$$\tilde{A} = P^{-1}AP, \quad \tilde{B} = P^{-1}B, \quad \tilde{C} = CP$$

and

$$e^{\tilde{A}t}\tilde{B} = P^{-1}e^{At}B \text{ and } \tilde{C}e^{\tilde{A}t} = Ce^{At}P$$

Consider the response function to initial inputs

$$\begin{aligned} \int_0^T \tilde{m}^T(\tau) \tilde{m}(\tau) d\tau &= y^T(0) \int_0^T e^{A^T\tau} C^T C e^{A\tau} dt \tilde{y}(0) \\ &= \tilde{y}^T(0) W_0 \tilde{y}(0) \end{aligned} \quad (18)$$

Thus, W_0 provides a measure of the size of the response to an initial value of $\tilde{y}(0)$.

In the case when W_C and W_0 are diagonal and the performance index is

$$\int_0^{\infty} u^T u dt$$

then

$$\int_0^{\infty} u^T u dt = \sum_1^n \frac{x_{fi}^2}{\lambda_i} \quad (19)$$

where λ_i are the diagonal elements of W_C , and x_f is the final state. Clearly, if $\lambda_i > \lambda_j$, then it can be argued that less control effort is required to move from the origin to x_{fi} than to x_{fj} , hence is more controllable. A similar argument can be derived for more observable coordinates. Thus, a criteria for model reduction can be to retain those states that are highly excited by the input and which contribute strongly to the output. In this approach, the coordinates corresponding to small values of λ_i will be truncated. Even if W_C and W_0 are not diagonal, it is always possible to perform coordinate transformation to convert them into diagonal form. The system of coordinates emerging from such model reduction is referred to as "balanced."

All the various treatments based on balanced realizations involve systems theoretic arguments rather than optimality criteria. Moreover, Kabamba [26] has pointed out that in the L^2 space, the balancing method is not optimal, as can be expected.

3.4 Optimal Projection Methods

Optimal selection of reduced model coordinates was first treated by Wilson [27, 28] and Kabamba [29]. In this approach, the steady-state output error, that is quadratically weighted, is minimized when both the original system and the truncated model are affected by white-noise inputs. First order necessary conditions involving two Lyapunov equations, each of an order equal to the sum of the orders of the original model and the reduced model, are obtained via parameter optimization. The basic procedure generates optimal reduced order matrices in an iterative manner; however, the guarantee of convergence of the iteration has not been established.

Several papers appeared recently on optimal projection equations for model reduction [30, 31]. The main result concerns the derivation of necessary conditions (in the form of two modified Lyapunov equations and rank conditions with nonnegative definite solutions) for an optimal reduced order model to exist. Multiple solutions to these optimal projection equations may exist corresponding to various local extrema.

The main idea behind the optimal projection approach is to directly characterize the optimal reduced-order controller with a quadratic performance functional for a given large-order model. Specifically, the optimal projection equations comprise a system of four matrix Riccati and Lyapunov equations coupled with an oblique projection that determines the optimal control gains.

Consider the system in Eq. (8) through (10). Suppose we want to design a fixed reduced order dynamic compensator

$$\dot{y}_c = A_c y_c + B_c u \quad (20)$$

$$u = C_c y_c \quad (21)$$

which will minimize the following performance functional

$$J = \lim_{t \rightarrow \infty} E[y^T R_1 y + u^T R_2 u] \quad (22)$$

where

$$y_c \in R^{n_c}, \quad n_c \leq n,$$

R_1 is a symmetric nonnegative definite, and R_2 is a symmetric positive definite matrices of appropriate dimensions. The intensities of the w and v were given as W and V , respectively, and w and v are assumed uncorrelated. To guarantee the existence of a finite J that is independent of initial conditions, an admissible stabilizing compensator (such that the matrix

$$\begin{bmatrix} A & B C_c \\ B_c C & A_c \end{bmatrix}$$

is asymptotically stable) is only considered, where (A_c, B_c) is controllable and (C_c, A_c) is observable.

Define

$$\Sigma = B R_2^{-1} B^T \text{ and } \bar{\Sigma} = C^T V^{-1} C \quad (23)$$

It is shown in Ref. [30] that there exist $n \times n$ nonnegative definite matrices Q , P , \hat{Q} and \hat{P} such that

$$A_c = \Gamma(A - Q\bar{\Sigma} - \Sigma P) G^T \quad (24)$$

$$B_c = \Gamma Q C^T V^{-1} \quad (25)$$

$$C_c = -R_2^{-1} B^T P G^T \quad (26)$$

and where

$$\hat{Q}\hat{P} = G^T M \Gamma \quad (27)$$

$$\Gamma G^T = I_{n_c} \quad (28)$$

$$S = G^T \Gamma \quad (29)$$

and the following conditions are satisfied ($G, \Gamma \sim n_c \times n$):

$$0 = (A - SQ\bar{\Sigma})Q + Q(A - SQ\bar{\Sigma})^T + W + SQ\bar{\Sigma}QS^T \quad (30)$$

$$0 = (A - \Sigma PS)^T P + P(A - \Sigma PS) + R_1 + S^T P \Sigma PS \quad (31)$$

$$0 = S[(A - \Sigma P)\hat{Q} + \hat{Q}(A - \Sigma P)^T + Q\bar{\Sigma}Q] \quad (32)$$

$$0 = [(A - Q\bar{\Sigma})^T \hat{P} + \hat{P}(A - Q\bar{\Sigma}) + P\Sigma P]S \quad (33)$$

$$\text{rank } \hat{Q} = \text{rank } \hat{P} = \text{rank } \hat{Q}\hat{P} = n_c$$

The geometric structure of the reduced order compensator is entirely dictated by the projection S . Moreover, the above optimal projection can also be carried out by taking the output error between the initial and the reduced order outputs, such that

$$J = E[(m - m_c)^T R(m - m_c)] \quad (34)$$

The question of where the projection should take place is still unclear in this approach, and engineering insight and practical experience apparently has its place. Computationally, solving Riccati and Lyapunov equations is no minor task. However, for low-order systems, it is practical.

4. CONCLUSIONS

The above paragraphs have presented the model reduction problem; namely, generating reduced order models for large-scale systems based on an appropriate performance criterion. In the case of an optimal reduced order compensator, one could define the cost as an appropriate functional of the error between the reduced order-gain and the full order one. Similarly, estimator gains for a reduced order system can be derived. After completing the procedure of developing reduced order gains for the controller and the estimator, one can construct an approximate feedback compensator.

In the effort of reducing computational requirements as well as compensator complexity, there are two ways that one could follow. System model reduction (in which those elements of the system are kept that are "most important" by some criterion) and compensator simplification (in which the compensator order is reduced based on a given criterion). The methods discussed earlier are tools that can accomplish these tasks.

The ultimate aim of any model reduction method is to lend itself to simple numerical algorithms for obtaining optimal low order models for large-scale systems. The optimal projection method seems to have a great deal of potential in this aspect. Given the proper formulation with the right performance criterion, the methods reviewed herein can be utilized to the full advantage of the designer.

5. REFERENCES

1. N. K. GUPTA, M. G. LYONS, J. N. AUBRUN, and G. MARGULIES 1981 Modeling, Control and System Identification Methods for Flexible Structures, P. Ph. Vanden Block and S. Z. Szirmay, ed., in NATO AGARDOGRAPH 260, 12-1-12-41.
2. SHERMAN M. SELTZER, 1979 The Journal of the Astronautical Sciences, XXVII, No. 2, 95-101. Dynamics and control of large space structures: an overview.
3. NILS R. SANDELL JR., PRAVIN VARAYA, MICHAEL ATHANS, and MICHAEL G. SAFONOV 1978 IEEE Trans. A. Contr. AC-23, No. 2, 108-128. Survey of decentralized control methods for large scale systems.
4. B. IRONS, 1963 J. of the Royal Aero. Soc., 67, 526-528. Eigenvalue economizers in vibration problems.
5. P. LIKINS, Y. OHKAMI, and C. WONG, 1976 J. of Spacecraft and Rockets, 13, 611-617. Appendage model coordinate truncation, criteria in hybrid coordinate dynamic analysis.
6. B. C. MOORE, 1981 IEEE Trans. A. Contr. AC-26, 17-32. Principal component analysis in linear systems: controllability, observability, and model reduction.
7. R. E. SKELTON, 1980 Int. J. Contr. 32, 1031-1055. Cost decomposition of linear systems with application to model reduction.
8. DAVID C. HYLAND and DENNIS S. BERNSTEIN, 1985 IEEE Trans. A Contr. AC-30, No. 12, 1201-1211. The optimal projection equations for model reduction and the relationships among the methods of Wilson, Skelton, and Moore.
9. A. L. DORAN, 1987 Control and Dynamic Systems (C. T. Leondes ed.) Vol. 25, 309-356, Academic Press, NY. Coordinate selection issues in the order reduction of linear systems.
10. BRUCE IRONS 1965 AIAA Journal, 3, 961-962. Structural eigenvalue problems: elimination of unwanted variables.
11. ROBERT J. GUYAN 1965 AIAA Journal 3, No. 2, 380. Reduction of stiffness and mass matrices.
12. EDWARD J. DAVISON 1966 IEEE Trans. A. Contr. AC-11, No. 1, 92-101. A method for simplifying linear dynamic systems.
13. R. D. HENSHELL and J. H. ONG 1975 Earthquake Engr. and Struct. Dynamics 3, 375-383. Automatic masters for eigenvalue economization.
14. R. COURANT and P. HILBERT 1966 Methods of Mathematical Physics 1, Interscience, NY.
15. EDWARD L. WILSON 1974 Int. J. for Num. Meth. in Engr. 8, No. 1, 198-203. The static condensation algorithm.
16. B. DOWNS 1980 Trans. ASME 102, 412-416. Accurate reduction of stiffness and mass matrices for vibration analysis and rationale for selecting master degrees of freedom.

17. EDWARD L. WILSON, MING WU YUAN, and JOHN M. DICKENS 1982 Earthquake Engineering and Structural Dynamics 10, 813-821. Dynamic analysis by direct superposition of Ritz vectors.
18. R. R. ARNOLD, R. L. CITERLY, M. CHARGIN, and D. GALANT 1985 Comp. and Structures 21, No. 5, 901-907. Application of Ritz vectors for dynamic analysis of large structures.
19. MARIO PAZ, 1984 AIAA J. 22, No. 5, 724-727. Dynamic condensation.
21. GEORGE H. SOTIROPOULOS 1984 ASCE J. 110, No. 12, 3072-3073. Practical reduction of structural eigenproblems.
20. MASANAO AOKI 1968 IEEE Trans. A. Contr. AC-13, No. 3, 246-252. Control of large scale dynamic systems by aggregation.
21. G. S. NURRE, R. S. RYAN, H. N. SCOFIELD, and J. S. SIMS 1984 J. Guidance, Control, and Dynamics 7, No. 5 514-526. Dynamics and control of large space structures.
22. R. E. SKELTON and P. C. HUGHES 1980 J. of Dynamic Systems, Measurement, and Control 102, 151-158. Model cost analysis for linear matrix second order systems.
23. AJMAL YOUSUFF and ROBERT E. SKELTON 1984 IEEE Trans. A. Contr. AC-29, No. 6, 520-530. Controller reduction by component cost analysis.
24. ROBERT E. SKELTON, PETER C. HUGHES, and HARJ B. HABLANI 1982 J. Guidance Control and Dyn. 5, No. 6, 351. Order reduction for models of space structures using modal cost analysis.
25. L. PERNEBO and L. M. SILVERMAN 1982 IEEE Trans. A. Contr. AC-27, 382-387. Model reduction via balanced state space representation.
26. P. T. KABAMBA 1985 IEEE Trans. A. Contr. AC-30, No. 3 690-693. Balanced gains and their significance for H^2 model reduction.
27. D. A. WILSON 1970 Proc. IEE 117, 1161-1165. Optimum solution of model reduction problems.
28. D. A. WILSON 1974 Int. J. of Contr. 20, No. 1, 57-64. Model reduction for multivariable systems.
29. PIERRE T. KABAMBA, 1980 J. Guidance and Control, 3, No. 6, 555-562. Model reduction by Euclidean methods.
30. DAVID C. HYLAND and DENNIS S. BERNSTEIN 1984 IEEE Trans. A. Contr. AC-29, 1034-1037. The optimal projection equations for fixed order dynamic condensation.
31. DENNIS S. BERNSTEIN and DAVID C. HYLAND 1985 IEEE Trans. A. Contr. AC-30, 583-585. The optimal projection equations for reduced order state estimation.

ENERGY METHODS FOR MODEL REDUCTION IN THE DYNAMICS AND CONTROL OF LARGE STRUCTURAL SYSTEMS

G. A. Becus and C. W. Cheng
Department of Aerospace Engineering and Engineering Mechanics
University of Cincinnati, Cincinnati, OH 45221

ABSTRACT

This paper provides a theoretical justification for Energy Based Model Reduction [1-2]. This scheme is discussed in the context of vibration suppression for large space structures using linear quadratic regulator (LQR) theory. Following optimal projection conditions of Hyland [3-4], the controllability and observability gramians based on the modified dual Lyapunov equations are approximately diagonal. The optimal reduced-order model can be obtained by using orthogonal projection and truncating some insignificant modes. We express the Energy Based Model Reduction scheme as a suboptimal projection and explain the good performance of the method. Illustrative examples of two and three bay trusses are presented.

1. INTRODUCTION

Large structural systems in general and large space structures in particular present new challenges to the structural dynamicist and the control engineer as well. Indeed, such large systems may exhibit well over a thousand vibrational modes usually closely spaced and with little, if any, damping. Clearly, some sort of model reduction is in order. This model reduction is even more important to the control engineer who can only hope to actively control a few of the modes using system identification based on information from a limited number of sensors. The model reduction scheme chosen will to a large extent determine the amount of "control spillover" (in which the control inputs excite the neglected dynamics) and/or "observation spillover" (where neglected dynamics affect system identification).

In Venkayya's Energy Based Model Reduction scheme [1-2] one computes a performance index (J) for the reduced model which is in fact the total mechanical energy (kinetic, strain and potential energies) in the model. A mode is added to or subtracted from the model based on its contribution to J . The advantages of this method are clear. First, the value of J can be computed a priori using only initial state values; different reduced models can be compared directly by comparing their corresponding J without a need for J of the full unreduced model (which is often unknown). Finally, the same J can be used in an optimal control design for active control of the system using the reduced model and LQR synthesis. In this case control and potential energies coincide.

Following Hyland [3-4], we expressed this Energy Based Model Reduction scheme as an orthogonal projection and truncation with respect to an energy norm. This expression as a projection provides the theoretical justification sought for the method.

2. LITERATURE REVIEW

Various techniques to carry out model reduction have been proposed by several authors. Almost all are based on the same philosophy: only the modes which play a significant role are retained. They differ in the way the roles of the modes are quantified. Among these techniques we mention (see [4] for more references): (i) Modal Truncation where only low order modes are kept; (ii) Balanced Controller Reduction of Moore [5] (with later modifications by Yousuff and Skelton [6]); (iii) Component Cost Analysis of Yousuff and Skelton [7]; (iv) Optimal Projection Conditions of Hyland [3-4]; (v) Energy Based Model Reduction scheme of Venkayya (also referred to as Modal Performance Tracking [8]). While method (i) lacks any form of theoretical justification, methods (ii) through (iv) have been shown by Hyland [3-4] to be similar once expressed as projections on the full state space. Method (v) does not have a theoretical justification although the heuristic energy arguments used by its developers are quite convincing. Furthermore, its performance as compared with other methods and as reported by Parry and Venkayya [8] appears to be quite good. The main thrust of this paper is to provide a theoretical justification for method (v).

3. THE FINITE ELEMENT CONTROL MODEL

Consider a controlled structural system described by the finite element dynamical equations

$$M\ddot{r} + C\dot{r} + Kr = bu \quad (1)$$

where r is a vector of n physical displacements and the number of control inputs (forces) u is m . M , C and K are the mass, proportional damping and stiffness matrices of appropriate dimensions respectively. b is the $n \times m$ applied load distribution matrix. Assume that M and K are positive definite.

The change of variables

$$r = \phi\eta \quad (2)$$

where η is an $n \times 1$ vector of modal coordinates and ϕ is an $n \times n$ normal mode matrix obtained from the free undamped system and having been normalized such that

$$\phi^T M \phi = I \quad (3)$$

diagonalizes system (1).

A state space representation of the diagonalized system is

$$\dot{x} = Ax + Bu \quad (4)$$

where

$$x = [\dot{\eta}^T \quad \eta^T]^T \quad (5)$$

$$A = \left[\begin{array}{c|c} -2\zeta_i\omega_i & [-\omega_i^2] \\ \hline & \end{array} \right] \text{ and } B = \left[\begin{array}{c} T \\ \hline \end{array} \right] \quad (6)$$

where ζ_i are the damping ratios (For large space structures, the ζ_i are small, typically $\zeta_i \approx 0.001$). ω_i are the natural frequencies of the free system.

4. ENERGY BASED MODEL REDUCTION SCHEME

LQR synthesis determines a control u^* which minimizes the quadratic performance index J

$$J = \int_0^{\infty} [\theta_m \dot{r}^T M \dot{r} + \theta_k r^T K r + \theta_r u^T b^T K^{-1} b u] dt \quad (7)$$

or in the normal mode coordinates

$$J = \int_0^{\infty} [x^T Q x + u^T R u] dt \quad (8)$$

where $Q = \begin{bmatrix} \frac{\theta_m}{0} & \begin{bmatrix} 0 \\ \theta_k [\omega_i^2] \end{bmatrix} \end{bmatrix}$ and $R = [\theta_r b^T K^{-1} b]$ (9)

for nonnegative weighting parameters θ_m , θ_k and θ_r . In Eq. (7), J is the weighted sum of the kinetic, strain and potential energies. The optimal state feedback control is

$$u^* = -Gx \quad (10)$$

where $G = R^{-1} B^T P$ (11)

is the state feedback gain matrix. P is the symmetric positive definite matrix solution of the algebraic Riccati equation

$$A^T P + P B R^{-1} B^T P + P A + Q = 0 \quad (12)$$

The optimal control derived from this full order system gives the min J as follows

$$\text{Min } J = x_0^T P x_0 \quad (13)$$

where x_0 is initial state value.

We define :

regulation-cost $J_R = \int_0^{\infty} x^T Q x dt$ (14)

control-cost $J_C = \int_0^{\infty} u^{*T} R u^* dt$ (15)

total-cost $J_E = J_R + J_C$ (16)

Different parameters θ_m , θ_k and θ_r will reflect different J_R , J_C and J_E so that the use of Q and R provides a proper balance between J_C and J_E [1].

When using the Energy Based Model Reduction scheme, a mode is added to or subtracted from the model based on its contribution to the performance index J .

Consider a vector of initial displacements and assume for the sake of simplicity no initial velocities

$$r_o = \sum_{i=1}^n c_i \phi^{(i)} \quad (17)$$

Based on their contribution to the performance index, we choose p modes from the n system modes

$$r_o = \sum_{i=1}^p c_i \phi^{(i)} \quad (18)$$

and obtain the reduced model [2]:

$$\dot{x}_m = [\dot{\eta}^T \quad \eta^T]^T_{2p \times 1} \quad (19)$$

$$A_m = \begin{bmatrix} \frac{[-2\zeta_i \omega_i]}{I} & \frac{[-\omega_i^2]}{0} \end{bmatrix}_{2p \times 2p} \text{ and } B_m = \begin{bmatrix} \frac{\phi_m^T b}{0} \end{bmatrix}_{2p \times m} \quad (20)$$

where ϕ_m is a matrix with column vectors $\phi^{(i)}$, $i=1, \dots, p$. Solving the algebraic Riccati equation

$$A_m^T P_m + P_m B_m R^{-1} B_m^T P_m + P_m A_m + Q_m = 0 \quad (21)$$

We compute the total-cost of reduced model

$$J_{E_m} = x_o^T P_m x_o \quad (22)$$

Following Hyland [3] or Moore [5], define the positive definite controllability and observability gramians

$$W_c \triangleq \int_0^\infty e^{At} B B^T e^{A^T t} dt ; W_o \triangleq \int_0^\infty e^{A^T t} Q e^{At} dt \quad (23)$$

which satisfy the dual Lyapunov equations

$$0 = A W_c + W_c A^T + B B^T ; 0 = A^T W_o + W_o A + Q \quad (24)$$

In Hyland's optimal projection method, new state variables are introduced so that W_c, W_o and $W_c \cdot W_o$ are all diagonal. In this case, the projection is orthogonal and is simply a truncation; the n_m states being kept are those corresponding to the n largest eigenvalues of $W \cdot W$.

Solving equation (24) in model coordinates, we find

$$W_o = \left[\frac{[(\theta_m + \theta_k)/(4\zeta_i \omega_i)]}{[\theta_k \cdot 1/2]} \middle| \frac{[\theta_k \cdot 1/2]}{[(\theta_m + (1+4\zeta_i^2)\theta_k \omega_i)/(4\zeta_i)]} \right] \quad (25)$$

Since $1/(2\zeta_i \omega_i) \gg 1/2$ and $(1 + (1+4\zeta_i^2))\omega_i/(4\zeta_i) \gg 1/2$

$$W_o \approx \frac{(\theta_m + \theta_k)}{4} \left[\frac{[1/(2\zeta_i \omega_i)]}{0} \middle| \frac{0}{[\omega_i/\zeta_i]} \right] \quad (26)$$

As $\zeta_i \rightarrow 0$ and/or $\theta_k \rightarrow 0$, W_o becomes more and more nearly diagonal. Also

$$W_c = \left[\frac{[a_{ij}]}{[c_{ij}]} \middle| \frac{[b_{ij}]}{[d_{ij}]} \right] \quad (27)$$

where

$$a_{ij} = \frac{-\Phi(i,j)(2\zeta_i \omega_j^2 + 2\zeta_j \omega_i^2)}{-4(\zeta_i \omega_i + \zeta_j \omega_j)(\zeta_i \omega_j + \zeta_j \omega_i)\omega_i \omega_j - (\omega_j^2 - \omega_i^2)^2}, \quad (28)$$

$$b_{ij} = \frac{a_{ij}(\omega_i^2 \cdot \omega_j^2)}{2(\zeta_i \omega_j + \zeta_j \omega_i)\omega_i \omega_j} = -c_{ij}, \quad (29)$$

$$d_{ij} = (a_{ij} - 2\zeta_j \omega_j b_{ij})/\omega_j^2, \quad (30)$$

$$\Phi(i,j) = \phi^T b b^T \phi \quad (31)$$

and for simplicity we have set the weighting parameters equal to 1. By proper choice of actuator position, $\Phi(i,j)$ can be made nearly diagonal and as $\zeta_i = \zeta_j = \zeta \rightarrow 0$, we have

$$W_c \approx \left[\frac{[\Phi(i,i)/(4\zeta \omega_i)]}{0} \middle| \frac{0}{[\Phi(i,i)/(4\zeta \omega_i^3)]} \right] \quad (32)$$

Eq.(32) remains valid for weighting parameters different from 1. The product $W_c \cdot W_o$ is also nearly diagonal as shown below

$$W_c \cdot W_o \approx \frac{(\theta_m + \theta_k)}{16} \left[\frac{[\Phi(i,i)/\zeta_i^2 \omega_i^2]}{0} \middle| \frac{0}{[\Phi(i,i)/\zeta_i^2 \omega_i^2]} \right] \quad (33)$$

Based on Venkayya's energy methods, which use modal coordinates, $W_c \cdot W_o$ and $W_c \cdot W_o$ are nearly diagonal as shown in equations (25)-(33). Therefore, Venkayya's modal coordinate system is very close to Hyland's coordinate system and the truncation is also nearly the same, as ranking of states according to the eigenvalues of $W_c \cdot W_o$ and according to the energy costs are similar. Energy Based Model Reduction is not an

optimal projection but a suboptimal projection. It becomes closer to optimal when $\zeta \rightarrow 0$, $\theta_k \rightarrow 0$ and also Φ becomes closer to diagonal (position of actuators).

From Hyland [3] proposition 4.1 and Moore [5]

$$\epsilon(A_m, B_m, C_m) \triangleq \left[\int_0^\infty \|H_e\|^2 dt / \int_0^\infty \|H\|^2 dt \right]^{1/2} \quad (34)$$

where $H = [\text{tr}(W_c W_o A)]^{1/2}$, (35)

$$H_e = [\text{tr}(W_{c_m} W_{o_m} A_m)]^{1/2}, \quad (36)$$

also

$$\epsilon = (H - H_e) / H \quad (37)$$

where W_c, W_o are controllability and observability gramians respectively, W_{c_m}, W_{o_m} are reduced model controllability and observability respectively and ϵ is a relative model reduction error.

5. ILLUSTRATIVE EXAMPLES

The trusses shown in Fig. 1 and 2 were selected for studying the effects of modal reduction on the control design. The parameters θ_m, θ_k and θ_r are all set equal to 1. Both trusses are fixed at the base and free everywhere else. They are assumed to move only in plane, giving two degrees of freedom per node. A non-structural mass of 0.585 kg per node was assigned to all nodes except the two at the base. The trusses are all made of aluminum with $E=68.94 \times 10^9 \text{ N/m}^2$ and weight density $\rho=7.1635 \text{ kg/m}^3$, and all member areas are 0.645 cm^2 . The initial states were assumed to be static displacement vectors resulting from the application of a F force at each of the actuator locations and a zero velocity vector. Actuator forces are applied only in the transverse direction.

Example 1. Two Bay Truss (Ten bars shown in figure 1)

The total length of the truss is 254 cm. and it is divided into two bays of equal lengths. It is a cantilevered truss with depth 91.44 cm. at the base and 60.96 cm. at the tip. The truss has 8 degrees of freedom in the configuration displacement and 16 degrees of freedom in the state space (displacements and velocities).

Table 1. Characteristics of the Structure (F=4448.22 N)

No.	Initial State (cm)		Natural Frequencies (Hz)
	$\dot{\eta}_0$	η_0	
1	0	-6.7026	3.4500
2	0	6.7026	12.5040
3	0	-6.3726	15.0968
4	0	6.3726	26.6069
5	0	47.8973	36.2856
6	0	47.8973	37.9460
7	0	17.9301	39.3612
8	0	17.9301	43.8277

Table 2. Normalized Minimum J for the Initial State

Model Description	Full System	Reduced Order Models						
		Modes						
J_{EN}		1-2	1-3	1-4	1-5	1-6	1-7	1,2,4,5
	1.0000	0.9990	0.9990	0.9994	1.0000	1.0000	1.0000	1.0000

$$J_{EN} : \text{Normalize } J_E = \frac{\text{Actual Min } J}{J_E}$$

Table 3. By Using Orthogonal Projection

Full System H	Modes 1,2,4,5 H_e	Relative Error ϵ
3.5410	3.3137	0.0642

Example 2. Three Bay Truss (Fifteen Bars as shown in figure 2)

The total length of the truss is 381 cm. and it is divided into three equal bays. It is a cantilevered truss with depth 39.6 cm. at the base and 30.5 cm. at the tip. The truss has 12 degrees of freedom in the configuration displacement at 24 degrees of freedom in the state space (displacements and velocities).

Table 4. Characteristics of the Structure (F=444.82 N)

No.	Initial State (cm)		Natural Frequencies (Hz)
	$\dot{\eta}_0$	η_0	
1	0	-4.9485	0.8305
2	0	4.9485	4.1336
3	0	-4.9645	8.5219
4	0	4.9645	12.0328
5	0	-3.5722	27.7452
6	0	3.5722	33.8549
7	0	91.9202	38.1516
8	0	91.9202	39.2201
9	0	50.4890	48.9397
10	0	50.4890	52.8947
11	0	16.1535	55.0943
12	0	16.1535	57.5319

Table 5. Normalized Minimum J for che Initial State

Model Description	Full System	Reduced Order Models					1,2,3,5,7,8
		1-2	1-3	1-4	1-5	1-6	
J _{EN}	1.0000	0.9980	0.9999	0.9999	0.9999	0.9999	1.0000
		1-7	1-8	1-9	1-10	1-11	
		1.0000	1.0000	1.0000	1.0000	1.0000	

Table 6. By Using Orthogonal Projection

Full System H	Modes 1,2,3,5,7,8 H _e	Relative Error ε
6.0451	5.9514	0.0155

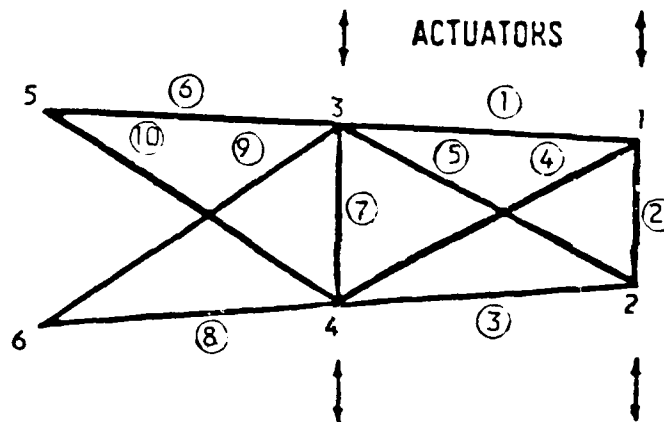


Figure 1. Two Bay Cantilevered Truss with 4 Actuators

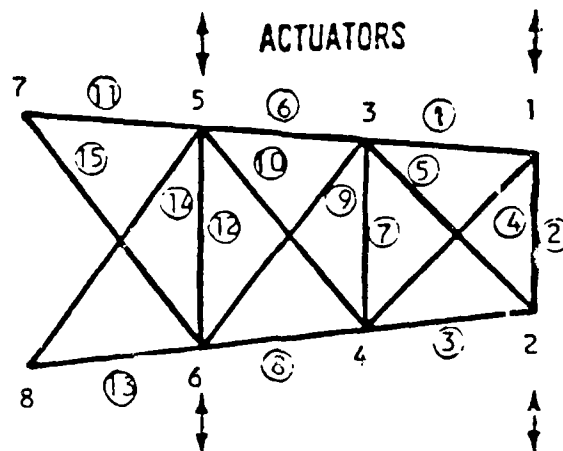


Figure 2. Three Bay Cantilevered Truss with 4 Actuators

6. DISCUSSIONS AND CONCLUSIONS

Both the structural and non-structural masses were considered in Examples 1 and 2. The natural frequencies of Table 1 are approximately the same as those of Ref. [2] Table 1 where the distributed mass was neglected, the structural mass is quite insignificant compared to the non-structural mass for large space structures.

From Table 2 we observe that the normalized performance index of modes 1 and 2 ($J_{EN_{1-2}}$) is equal to 0.9990. If mode 3 is added, the value

$J_{EN_{1-3}}$ does not change, which means that mode 3 has no contribution to the performance index J . If mode 4 is added, the value of $J_{EN_{1-4}}$ becomes

0.9994 and so on. Hence, the reduced model in Example 1 includes modes 1, 2, 4 and 5. The performance index of the reduced model is equal to that of the full system. In example 2, we find the largest eigenvalues of $W_c \cdot W_o$ correspond to states 1,2,3 and 5 (13,14,15 and 17). From table 5, we observe that the most significant modes are also 1,2,3 and 5, which shows that the reduced model of Hyland and Venkayya are nearly the same. Following Hyland and using suboptimal projection, the relative errors are 0.0642 and 0.0155 for the two and three bay trusses respectively, which shows the good performances of the energy method.

A theoretical justification for Energy Based Model Reduction scheme is proposed. In this scheme, a mode is added to or subtracted from the model based on its contribution to the J . The value of J can be computed a priori using only initial state values; different reduced models can be compared directly by comparing their corresponding J without a need for J of the full unreduced model. The advantages of this method are clear. For large space structures, damping is always very small; therefore, the energy method can be considered as an orthogonal projection on an energy norm which provides the theoretical justification.

REFERENCES

1. D.F. Miller, V.B. Venkayya and V.A. Tischler, "Integration of Structures and Controls - Some Computational Issues," Proceedings of 24th Conference on Decision and Control, Ft. Lauderdale, FL, Dec 1985.
2. V.B. Venkayya and V.A. Tischler, "Direct Output State Feedback Control of Large Order Systems," AIAA-85-0114-CP, AIAA 23rd Aerospace Sciences Meeting, Jan. 14-17, 1985.
3. D.C. Hyland and D.S. Bernstein, "The Optimal Projection Equations for Model Reduction and the Relationships Among the Methods of Wilson, Skelton, and Moore," IEEE Transactions on Automatic Control, Vol. AC-30, No. 12, Dec. 1985.
4. D.C. Hyland, "Comparison of Various Controller-Reduction Methods: Suboptimal versus Optimal Projections," AIAA Paper 84-1033, 1984.
5. B.C. Moore, "Principal Component Analysis in Linear Systems: Controllability, Observability, and Model Reduction," IEEE Transactions on Automatic Control, Vol. AC-26, No. 1, Feb. 1981.
6. A. Yousuff and R.E. Skelton, "A Note on Balanced Controller Reduction," IEEE Transactions on Automatic Control, Vol. AC-29, No. 3, Mar. 1984.
7. A. Yousuff and R.E. Skelton, "Controller Reduction by Component Cost Analysis," IEEE Transactions on Automatic Control, Vol. AC-29, No. 6, June, 1984.
8. C.O. Parry and V.B. Venkayya, "Issues of Order Reduction in Active Control System Design," AIAA Paper 86-2138, 1986.

STRUCTURAL DYNAMIC ANALYSIS AND TESTS OF A PLANAR LARGE SPACE TRUSS SUBCOMPONENT

S.E. Lamberson
Lab Director and Assistant Professor
Applied Mechanics Laboratory
United States Air Force Academy

C. A. Fisher
Professor and Department Head
Department of Engineering Mechanics
United States Air Force Academy

ABSTRACT

Experimental investigation in Large Space Structures to date has focused on simple beams and complex beam-like lattices. Little has been done in the area of dynamics and control experiments on planar scale models of generic trusses. At the United States Air Force Academy we are pursuing such an experimental program. We are examining the effects of scaling, boundary conditions, and joint type on the validity of various structural dynamic analysis techniques and automated feedback design methodologies using scale models of planar trusses. The methodology employed is to develop two structural dynamics models of the proposed thirty-bay truss. Several levels of detail are used in the Finite Element Models. In addition, the truss is modeled as an equivalent beam. These models are upgraded by building a six-bay portion of the truss and measuring the static and dynamic structural characteristics. The resulting models are used to correlate with measured natural frequencies and mode shapes of the structure.

1. INTRODUCTION

As the advent of large flexible structures in space approaches, accurately predicting the on-orbit dynamic performance of such structures is becoming increasingly important. Since high order control systems will generally be required to meet the stringent performance requirements of such structures, accurate structural response predictions become critical. Several methods of incorporating experimental data into these performance and response predictions are currently being examined. Since these structures are too flimsy to be built on the ground without a large number of supports, ground testing is generally limited to component, subcomponent and scale model testing.

The large flexible space truss effort at the United States Air Force Academy centers around a planar Warren truss supported in the horizontal plane on air tables (Fig 1). Since the motion of the structure is restricted to the horizontal plane, perpendicular to gravity, and the flotation of the feet attached to each joint of the structure is nearly frictionless, a very "spacelike" environment is obtained in two dimensions. This paper will examine results from the component and subcomponent tests performed on such a structure and the use of these results to calibrate a variety of analytical models. These analytical models are then used to predict the dynamic response of the full thirty-bay truss.

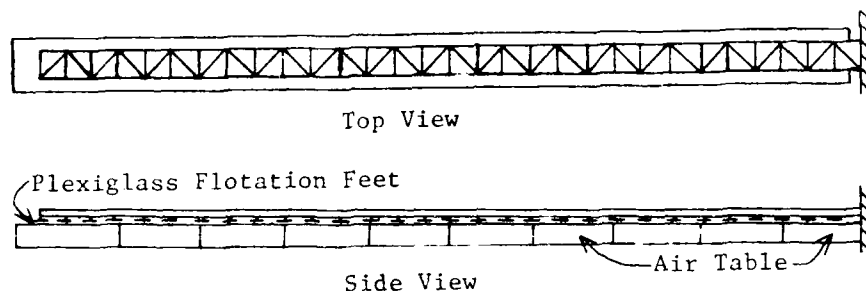


FIG 1 THIRTY-BAY LARGE SPACE TRUSS PLANAR SCALE MODEL

2. THIRTY BAY-TRUSS CONFIGURATION

Before discussing the various tests and analyses performed on components and subcomponents of the thirty-bay truss, a more detailed description of the truss configuration itself is in order. The main structural members (longitudinally, laterally and diagonally) are aluminum tubes. Each of the tubes has an aluminum insert which is drilled and tapped to take a 6.35 mm. machine screw. The insert is pressure fit and pinned into each end. The joints are each made from a steel pipe with slots cut as appropriate for installation of the aluminum tubes (Fig 2). The truss is assembled by installing the screws, nuts and washers into each end of the truss and preadjusting the total length of each member. Each truss member is then slipped into the appropriate slots in the joints and held in place with a nut. This truss design is more appropriate than others previously considered, since it resembles a widely used three dimensional joint design [1]. In this design, a composite tube with a metal insert in each end is connected to a metal joint with a solid metal member of much smaller diameter. In addition, any member can be removed, adjusted, replaced without disturbing any other member.

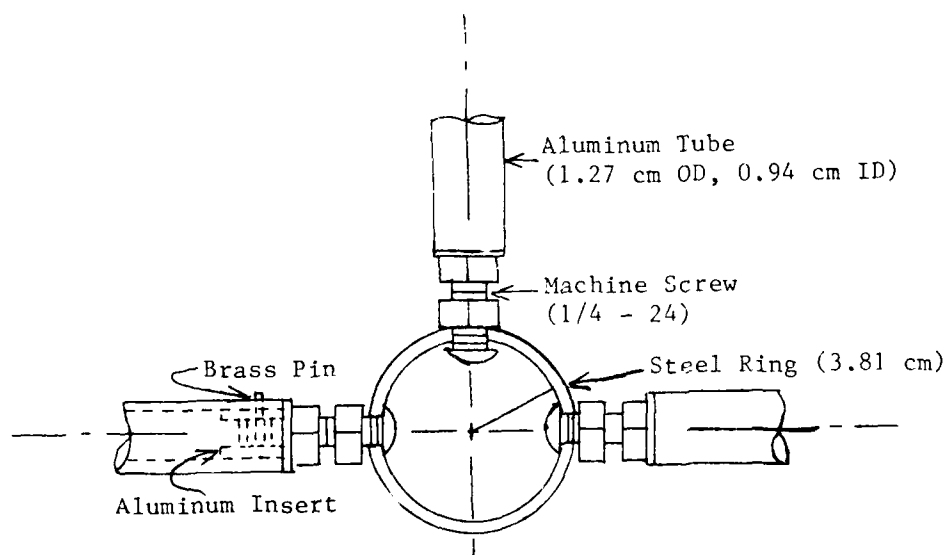


FIG 2 JOINT & MEMBER GEOMETRY

3. STATIC CALIBRATION

The truss consists of two major structural parts: the joint and the aluminum tube. The joint was tested by fastening one of the rings into a tensile test machine using screws 180° apart mounted as in the actual structure. A load-deflection curve was generated by gradually applying a tensile force and measuring the load with a loadcell and the displacement with an inductive proximity gauge. The measured diametrical stiffness was $175 \times 10^6 \text{ N/m} \pm 25\%$. One of the longitudinal aluminum tubes was tested in a similar manner and its stiffness was measured as $95,422 \text{ N/m} \pm 25\%$. The error bands indicate scatter in the data, not error in the measurements. This value is almost half the expected stiffness of $176,380 \text{ N/m}$ which was calculated using the measured area (A), modulus of elasticity (E) and length (L) of the member. This difference is probably due to the large local deformations near the brass pin which holds the inserts in place. The joint was modeled with quadrilateral shell finite elements (Fig 3). When a finite element analysis was performed using this model, a stiffness of $112,883 \text{ N/m}$ was predicted.

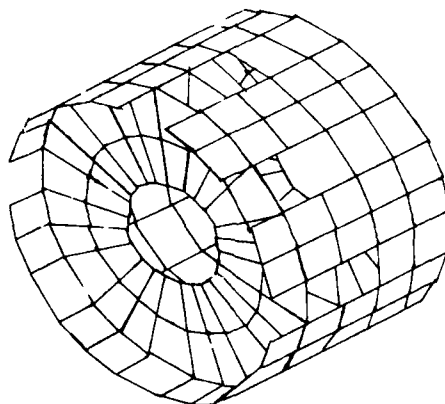


FIG 3 THREE DIMENSIONAL RING MODEL

4. SIX-BAY SUBCOMPONENT ANALYSES

A six-bay portion of the thirty-bay truss was analyzed for a transverse load applied at three different locations using three different models. A detailed model was developed using four beam elements to represent each truss member. A simple model was developed using a single element for each truss member. An equivalent beam model was developed in which the entire truss was modeled as an equivalent Timoshenko beam [2].

In the detailed model (Fig 4), a stiff beam was used to model the last 38.1 mm of each member. These stiff beams were intended to represent the joints which are much stiffer than the truss members. The remaining portion of the beam was modeled with elements having the modulus of elasticity (E) and moment of inertia (I) of the actual aluminum tube but an effective area which was reduced to account for the reduction in stiffness caused by the deformation of the brass pins. The diagonal members have a different effective area than the longitudinal and lateral members because the stiffness of the longer aluminum tube is less in comparison to the brass insert stiffness.

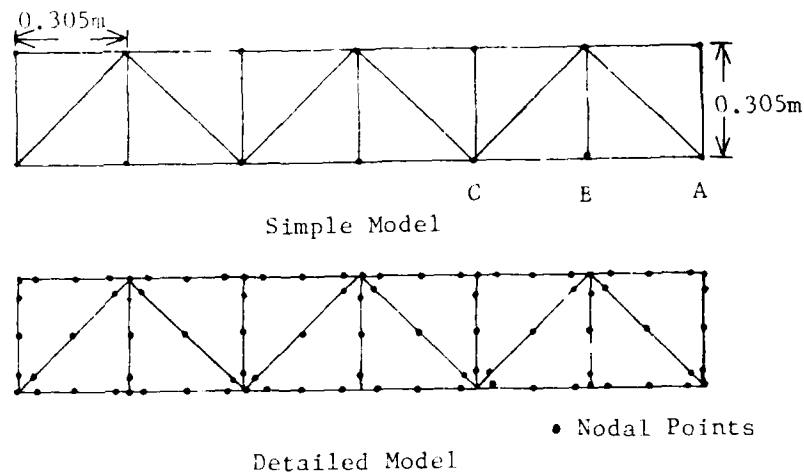


FIG 4 FINITE ELEMENT MODELS

Longitudinal and lateral members: $A_{eff} = K_m \cdot (0.229 \text{ m}) / E$

Diagonal members: $A_{eff} = (0.356 \text{ m}) / E (1/K_m + (0.178 \text{ m}) / AE)$

where: A is the actual area of the tube,

A_{eff} is the reduced effective area,

and K_m is the measured stiffness of a longitudinal tube.

The simple model (Fig 4) has a single beam element for each member of the truss. The modulus of elasticity and moment of inertia of the actual tube are used. Effective areas are lower than the detailed model since the members are longer but are calculated the same way. Both models are analyzed using the NASTRAN finite element code with the nodes at the ends of the left hand joints pinned and the motion of the truss restricted to the plane of the truss. The results are listed in Table 1.

Finally, the truss was modeled as an equivalent beam, including the effects of shear deformation. In order to determine the equivalent material constants from the truss to be used in the beam equations of motion, two bays of the detailed model were used for analysis. As shown in Figure 5, the static tests of the two-bay truss provide equivalent values [3] for the necessary material constants (AE, EI, kAG).

Rather than solve the coupled equations of motion using standard numerical techniques, an ANSYS finite element model of the equivalent Timoshenko beam was used as an efficient solution generator. The static analysis was accomplished using a 12 element finite element model of the six bay equivalent beam, with the results given in Table 1. As expected, the equivalent beam static model is in good agreement with the more complicated finite element models of the entire truss.

Static deflections on the actual six bay subcomponent test article were generated using loads applied with weights and the deflections were measured using inductive displacement sensors. The displacement as a function of load at each measured location was extremely linear. The loading point flexibilities are compared with the various analytical models in Table 1. As expected, all of the calibrated models are in close agreement with the measured values.

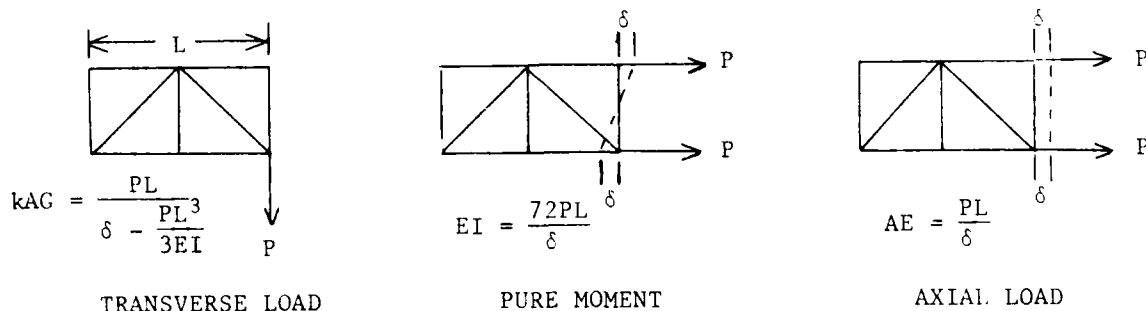


FIG 5 EQUIVALENT BEAM MODEL

TABLE 1

Subcomponent Static Deflection Test Results

Loading Pt Flexibility (mm/N) at Location

	A	B	C
Measured	17.29	10.77	6.24
Detailed Model	17.18	10.49	5.73
Simple Model	17.01	10.38	5.61
Equivalent Model	17.46	10.60	5.90
Uncalibrated Model*	12.59	7.60	4.25

*The simple model using the actual area of the aluminum tubes

5. DYNAMIC PREDICTIONS

The simple and detailed finite element models were used to predict the natural frequencies with lumped masses at the nodes to represent the total mass of the six bay truss subcomponent. All transverse deflections were retained as "dynamic" degrees of freedom. The principle difference in the predicted natural frequencies occurs at 283 Hz when the diagonal elements start vibrating as individual members. This phenomena is not predicted well by either the simple or equivalent model.

As before, the equivalent beam dynamic analysis was accomplished using the 2-D beam element of the ANSYS finite element program. A 20 element dynamic model was used, with 20 master or "dynamic" degrees of freedom specified for the structure. The ANSYS program uses the specified master degrees of freedom and a Guyan reduction procedure to reduce the number of unknowns prior to the modal analysis. The Guyan reduction procedure does not affect the potential energy of the system but slightly modifies the kinetic energy, thus modifying the reduced mass matrix without changing the reduced stiffness matrix. The natural frequencies predicted by the model are shown in Table 2, and compare favorably with the other more complex finite element models of the entire truss.

Table 2

Six Bay Subcomponent Natural Frequency Predictions (hz)

Mode	Detailed Model	Simple Model	Equivalent Model	Uncalibrated Model	Measured (Fig 8)
1st Bending	23.1	22.4	22.6	28.7	22
2nd Bending	98.4	96.5	94.8	123.7	116
3rd Bending	201.2	198.1	182.7	240.6	230
Complex*	283.3	279.1	244.3	253.3	-
"	320.2	323.4	286.0	266.2	-
"	325.5	333.8	312.9	278.9	-
"	337.1	342.2	331.2	280.6	-
"	359.6	357.1	343.7	284.6	-

* After the third bending mode the diagonals start vibrating in a local mode and the mode shapes become very complicated.

6. FREQUENCY RESPONSE PREDICTIONS

The frequency response of the acceleration at the tip due to a white noise input on the other side of the truss at the tip was calculated for each of the models using a viscous damping coefficient of 0.03.

$$H_{mk}(f) = \sum_{i=1}^n \left(\frac{f}{f_i} \right)^2 \frac{e_{mi} e_{ki}}{\left(1 - \left(\frac{f}{f_i} \right)^2 \right) - j(2\zeta \frac{f}{f_i})}$$

where $H_{mk}(f)$ is the frequency response of the tip acceleration

f_i is the natural frequency of the i^{th} mode

ζ is the viscous damping coefficient

e_{mi} is the eigenvector component at the loading point

e_{ki} is the eigenvector component at the output point

n is the number of modes

The magnitude of this function is plotted for each of the models in Fig 6. The models are in remarkable agreement over this frequency range which contains four modes of the structure. The two truss models are shown over an expanded frequency range (Fig 7) to highlight the effect of the local bending modes of the diagonals. The effect was minimal considering the large differences in the mode shapes predicted by the three models.

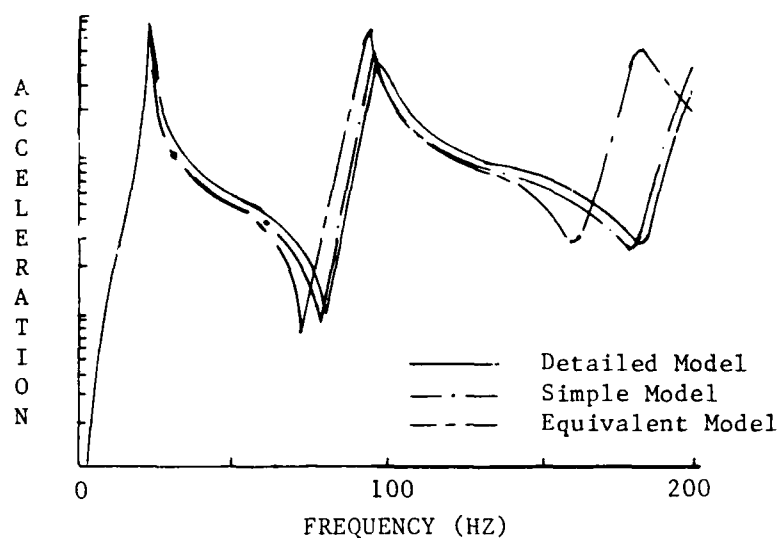


FIG 6 FREQUENCY RESPONSE PREDICTIONS

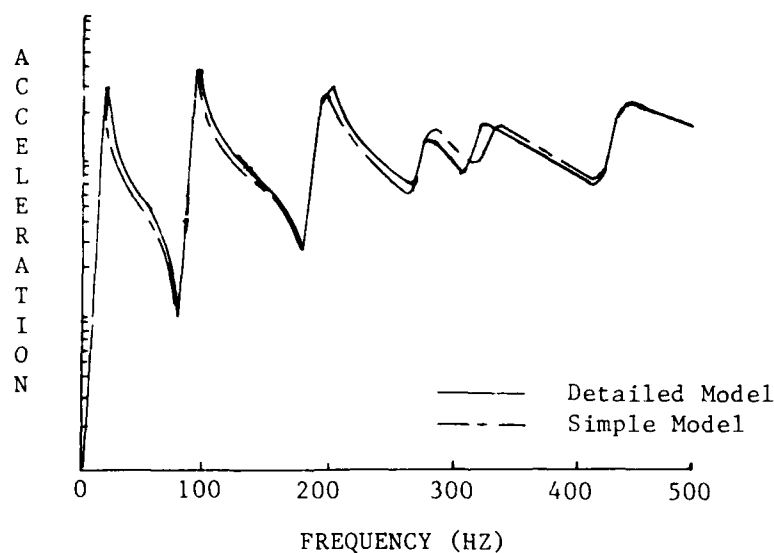


FIG 7 FINITE ELEMENT FREQUENCY RESPONSES

The frequency response was measured experimentally by driving the truss with a Modal 50 shaker and measuring the response with a PCB accelerometer. A Signology spectrum analyzer was used to calculate the measured frequency response (Fig 8). A comparison of Figures 7 and 8 indicates generally good agreement except for a low energy mode (near 60 hz) in the measured response. This extra mode was determined to be a vibration mode of the supporting structure. A model was developed which included this mode and the change in the other modes was insignificant.

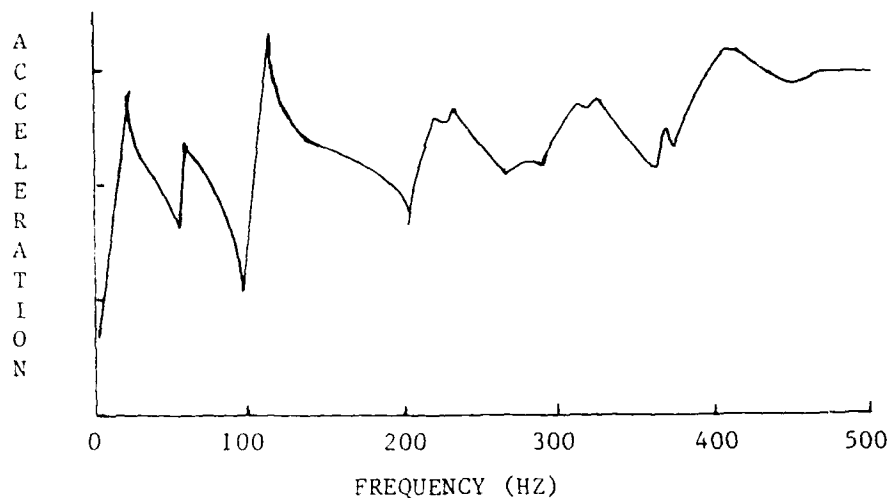


FIG 8 MEASURED FREQUENCY RESPONSE

7. THIRTY-FOOT PREDICTIONS

The various models developed were used to predict the natural frequencies of the thirty-bay truss. These are shown to agree well for all the calibrated models (Table 3). The uncalibrated model is considerably off and would be unusable for controller designs.

Table 3

Thirty Bay Natural Frequency Predictions (hz)

Mode #	Detailed Model	Simple Model	Equivalent Model	Uncalibrated Model
1	1.0	1.1	1.0	1.3
2	6.0	6.7	6.1	8.1
3	16.0	18.0	16.4	21.9
4	29.6	33.2	30.4	40.7
5	45.9	51.5	47.2	63.2
6	72.8	71.8	65.7	88.4
7	83.3	93.2	85.2	115.2
8	102.7	115.1	104.8	142.7
9	122.3	137.0	124.3	170.2
10	160.0	158.8	143.1	197.8

8. CONCLUSIONS

Component testing of Large Space Structures is critical to accurately predict their natural frequencies, mode shapes, frequency response and closed loop performance. Even simplified planar structures exhibit structural behavior substantially different from that predicted by simple models. Once calibrated with component test results, equivalent models and simple finite element models appear to predict the natural frequencies and mode shapes accurately until the frequency band in which local bending of the truss members occurs is reached. The frequency response of the structure is adequately represented by the simple model well into this region. The use of Air Tables as a supporting "spacelike" environment in two dimensions is very effective.

The authors would like to acknowledge the support of Dr. Hallauer, Major Ewing, and the Applied Mechanics Laboratory Technicians. This work was performed under a grant from the Office of Scientific Research sponsored by Dr. Salkind.

9. REFERENCES

1. HARRISON, JAMES K. and CRAMBLIT, DAVID C., 1982 "SADE-A Space Experiment to Demonstrate Structural Assembly," Large Space Antenna Systems Technology, NASA-CP-2269-Pt 2, 1029-1036.
2. TIMOSHENKO, S.P., Strength of Materials, 3rd Ed., Vol 1, p. 318.
3. SUN, C.T.; KIM, B.J., and BOGDANOFF, J.L., "On the Derivation of Equivalent Simple Models for Beam- and Plate-like Structures in Dynamic Analysis," AIAA Journal, AIAA-81-0624, p. 523-532.

THE EFFECTS OF CABLE SUSPENSION ON BENDING VIBRATION OF LARGE BEAMS

S. MAHANIAN

Mechanical Engineering Department
University of Puerto Rico

INTRODUCTION

Satellite antennas and space stations, extensively, use large truss-beam structures. Before these structures can be launched, proper structural ground tests are performed to ascertain among other things the vibrational characteristics of the structure. Efforts are made in these ground tests to simulate zero-gravity orbital environment and prevent any gravitational effects that can drastically alter the structural characteristics of the joints or other components through excessive deformation.

Cable suspension is one of the simple methods that has been frequently used in ground tests to counteract the force of gravity. However, cable suspension introduces errors in the measurement of natural frequencies of the structure by introducing pendulum motions that can couple with the flexible motion of the structure.

Herr [1] performed experimental investigations on the effects of cable suspension of the first flexural natural frequency of free-free uniform beams.

The present paper explores analytically, the effects of cable suspension on the transverse bending vibration of a 60 meter, cantilevered, uniform beam, with a fundamental natural frequency of about 0.32 Hz. This paper is based on a linear analysis of the transverse vibrations. The cables are assumed to be massless and unstretchable. Future papers by the author on this theme will consider the nonlinear effects of large amplitudes of oscillation as well as the mass and stiffness effects of the cables.

The analysis in this paper consists of three parts. In part one the pendulum motion is studied separately. Here the bending stiffness of the beam is not considered at all and the stiffness effect is solely due to the tensions in the cables. The inertia effect is provided by the mass and inertia properties of the beam. In part two, the bending vibration are considered without taking into account the pendulum actions. Finally, in part three the combined behavior of the beam-cable assembly is considered and the effects of cable suspension on bending vibration is discussed.

PART 1- PENDULUM MOTION

Fig.1a shows a beam consisting of n segments. Segment 1 is fixed at the left hand side to a stationary wall. The joints are connected one to the next by ball-and-socket connections without any stiffness at any of the joints.

Fig.1b shows a typical segment i whose orientation is described by two angles θ_i and ϕ_i . n_1^i, n_2^i , and n_3^i are mutually perpendicular unit vectors fixed to segment i . The angular velocity of segment i can be written as:

$$\omega_i = \dot{\theta}_i \sin \phi_i n_1^i + \dot{\theta}_i \cos \phi_i n_2^i + \dot{\phi}_i n_3^i \quad (1)$$

The velocity of center of mass of any segment i will be:

$$V^{i*} = \sum_{k=1}^{i-1} (b_k \dot{\phi}_k n_2^k - b_k \dot{\theta}_k \cos \phi_k n_3^k) + b_i^* \dot{\phi}_i n_2^i - b_i^* \dot{\theta}_i \cos \phi_i n_3^i \quad (2)$$

where b_k is the length of any segment k and b_i^* the distance from the left end of segment i to its center of mass. The linearized acceleration of the center of mass will be:

The support of NASA Langley Research Center in general and Mr. Brantley Hanks of the Structural Dynamics Division in particular is gratefully acknowledged. Furthermore, the invaluable help of Mr. Alfonso Hermida in generating the computer plots is sincerely appreciated.

$$\mathbf{a}^{is} = b_i^s \ddot{\phi}_i \mathbf{n}_2^i - b_i^s \ddot{\theta}_i \mathbf{n}_3^i + \sum_{k=1}^{i-1} (b_k \ddot{\phi}_k \mathbf{n}_2^k - b_k \ddot{\theta}_k \mathbf{n}_3^k) \quad (3)$$

Following Lagrangian-D'Alembert method of derivation of equations of motion developed by Kane [2], one proceeds to find partial velocities and partial angular velocities and subsequently generalized active and inertial forces. This hybrid method has advantages over the Lagrangian method, especially when numerous segments are involved and thus the formation of the kinetic energy expression and its subsequent differentiation can prove cumbersome.

In this method of derivation sum of the generalized active and inertial forces are set to zero, i.e.

$$F_r + F_r^* = 0 \quad (4)$$

where:

$$F_r^* = \sum_{i=1}^n (-m_i \mathbf{a}^{is} \cdot \mathbf{V}_{q_r}^{is} - \dot{\mathbf{H}}^i \cdot \boldsymbol{\omega}_{q_r}^i) \quad (5)$$

\dot{q}_r = time derivative of the r th generalized coordinate which can be either $\dot{\theta}_i$ or $\dot{\phi}_i$ for $i=1$ through n
 n = number of segments

m_i = mass of segment i

$\dot{\mathbf{H}}^i$ = time derivative of the angular momentum vector and for our case

$$\dot{\mathbf{H}}^i = I_i \ddot{\theta}_i \mathbf{n}_2^i + I_i \ddot{\phi}_i \mathbf{n}_3^i \quad (6)$$

I_i = transverse centroidal moment of inertia of segment i . $\mathbf{V}_{q_r}^{is}$ and $\boldsymbol{\omega}_{q_r}^i$ are the q_r coefficients in the \mathbf{V}^{is} and $\boldsymbol{\omega}^i$ expressions respectively

$$\mathbf{V}_{\theta_j}^{is} = \begin{cases} -b_j \mathbf{n}_3^j & \text{for } j < i \\ -b_j^s \mathbf{n}_3^j & \text{for } j = i \\ 0 & \text{for } j > i \end{cases} \quad (7)$$

$$\mathbf{V}_{\phi_j}^{is} = \begin{cases} -b_j \mathbf{n}_2^j & \text{for } j < i \\ -b_j^s \mathbf{n}_2^j & \text{for } j = i \\ 0 & \text{for } j > i \end{cases} \quad (8)$$

$$\boldsymbol{\omega}_{\theta_j}^i = \begin{cases} \mathbf{n}_2^j & \text{for } i = j \\ 0 & \text{for } i \neq j \end{cases} \quad (9)$$

$$\boldsymbol{\omega}_{\phi_j}^i = \begin{cases} \mathbf{n}_3^j & \text{for } i = j \\ 0 & \text{for } i \neq j \end{cases} \quad (10)$$

Therefore using (5), (6), (7), and (9) one can write

$$\begin{aligned} F_{\theta_j}^* = & -\ddot{\theta}_1 (m_j b_1 b_j^s + b_1 b_j \sum_{i=j+1}^n m_i) - \ddot{\theta}_2 (m_j b_2 b_j^s + b_2 b_j \sum_{i=j+1}^n m_i) \\ & - \ddot{\theta}_3 (m_j b_3 b_j^s + b_3 b_j \sum_{i=j+1}^n m_i) \dots - \ddot{\theta}_j (I_j + m_j b_j^{s2} + b_j^2 \sum_{i=j+1}^n m_i) \\ & - \ddot{\theta}_{j+1} (m_{j+1} b_j b_{j+1}^s + b_j b_{j+1} \sum_{i=j+2}^n m_i) \dots - \ddot{\theta}_n (m_n b_n^s b_j) \end{aligned} \quad (11)$$

Similarly using (5), (6), (8), and (10) one can write

$$\begin{aligned}
 F_{\theta_j}^* = & -\bar{\phi}_1(m_j b_1 b_j^* + b_1 b_j \sum_{i=j+1}^n m_i) - \bar{\phi}_2(m_j b_2 b_j^* + b_2 b_j \sum_{i=j+1}^n m_i) \\
 & - \bar{\phi}_3(m_j b_3 b_j^* + b_3 b_j \sum_{i=j+1}^n m_i) \dots - \bar{\phi}_j(I_j + m_j b_j^{*2} + b_j^2 \sum_{i=j+1}^n m_i) \\
 & - \bar{\phi}_{j+1}(m_{j+1} b_j b_{j+1}^* + b_j b_{j+1} \sum_{i=j+2}^n m_i) \dots - \bar{\phi}_n(m_n b_n^* b_j)
 \end{aligned} \quad (12)$$

The generalized active forces are formed as follows:

$$F_r = \sum_{i=1}^n \sum_{k=1}^m (F^{ki} \cdot V_{q_r}^{Ki} + M^i \cdot \omega_{q_r}^i) \quad (13)$$

where F^{ki} = a force acting on body i at point k

M^i = an external moment acting on body i

V^{Ki} = velocity of point K on body i

In our case, there are two points for every body where there is an acting force: One due to gravity, the other due to the tension in the cable and there are no external torques.

$$F_r = \sum_{i=1}^n -m_i g J \cdot V_{q_r}^{is} + T^{ei} \cdot V_{q_r}^{ei} \quad (14)$$

where T^{ei} = tension in the cable attached to the right of segment i $V_{q_r}^{ei}$ = the q_r coefficient in the expression for the velocity of the right end of segment i given by the following expressions

$$V_{\theta_j}^{ei} = \begin{cases} -b_j n_j^i & \text{for } j \leq i \\ 0 & \text{for } j > i \end{cases} \quad (15)$$

$$V_{\phi_j}^{ei} = \begin{cases} -b_j n_j^i & \text{for } j \leq i \\ 0 & \text{for } j > i \end{cases} \quad (16)$$

T^{ei} can be written as the product of its magnitude times its direction vector:

$$T^{ei} = \frac{T_i}{L} (-\sum_{k=1}^i b_k n_1^k + L J + \sum_{k=1}^i b_k I) \quad (17)$$

substituting equations (17) and (15) into (14) one can write

$$F_{\theta_j} = -\frac{b_j}{L} \sum_{i=j}^n T_i \sum_{k=1}^i b_k \theta_k \quad (18)$$

Similarly, substituting equations (17) and (16) into (14) one may show that:

$$F_{\phi_j} = b_j \sum_{i=j}^n T_i (1 - \sum_{k=1}^i \frac{b_k}{L} \phi_k) - (b_j^* m_j g + b_j \sum_{i=j+1}^n m_i g) \quad (19)$$

Now a constraint equation can be written if we assume that the length of each one of the n cables is to be constant as L

(i.e.)

$$\|LJ + \sum_{k=1}^i b_k(I - n_1^k)\| = L \quad \text{for } i=1 \text{ to } n \quad (20)$$

where

$$n_1^k = \cos \phi_k \cos \theta_k I + \sin \phi_k J - \cos \phi_k \sin \theta_k K \quad (21)$$

therefore

$$(L - \sum_{k=1}^i b_k \sin \phi_k)^2 + (\sum_{k=1}^i b_k (1 - \cos \phi_k \cos \theta_k))^2 + (\sum_{k=1}^i b_k \cos \phi_k \sin \theta_k)^2 = L^2$$

upon linearization, this will result to:

$$\phi_i = 0 \quad i=1, 2, \dots, n \quad (22)$$

(22) implies that $F_{\phi_j}^* = 0$ and $F_{\theta_j} = 0$ for $j = 1$ to n

$F_{\phi_j} = 0$ will yield an expression for T_i s in terms of the weights of the segments.

$$T_j = \frac{b_j^*}{b_j} m_j g + m_{j+1} g - \frac{b_{j+1}^*}{b_{j+1}} m_{j+1} g \quad (23)$$

Equation (4) implies:

$$F_{\phi_j} + F_{\theta_j}^* = 0 \quad \text{for } j=1 \text{ to } n \quad (24)$$

substituting (11), (18), and (23) into (24) one obtains an equation of the form:

$$[M_{ij}] [\bar{\theta}_j] + [K_{ij}] [\theta_j] = 0 \quad (25)$$

where $[M_{ij}]$ is an $n \times n$ symmetric inertia matrix whose diagonal elements are given by:

$$M_{ii} = I_i + m_i b_i^{*2} + b_i^2 \sum_{k=i+1}^n m_k \quad (26)$$

and the off diagonal elements are given by

$$M_{ij} = m_j b_j^* b_i + b_i b_j \sum_{k=j+1}^n m_k \quad (27)$$

Similarly $[K_{ij}]$ is an $n \times n$ symmetric stiffness matrix whose diagonal elements are given by:

$$K_{ii} = \frac{b_i^2}{L} \sum_{k=i}^n T_k = \frac{b_i}{L} (b_i^* m_i g + b_i \sum_{k=i+1}^n m_k g) \quad (28)$$

and whose off-diagonal elements are as follows:

$$K_{ij} = \frac{b_i b_j}{L} \sum_{k=j}^n T_k = \frac{b_i}{L} (b_j^* m_j g + b_j \sum_{k=j+1}^n m_k g) \quad (29)$$

The square root of the eigenvalues of (25) constitute the natural frequencies ω_n of the pendulum motion, and the eigen vectors $[x]$ the mode shapes.

$$[[K_{ij}] - \omega_n^2 [M_{ij}]] [x] = 0 \quad (30)$$

For illustration (25) is shown for a three-segment beam

$$\begin{bmatrix} I_1 + m_1 b_1^2 + m_2 b_1^2 + m_3 b_1^2 & m_2 b_1 b_2^* + m_3 b_1 b_2 & m_3 b_1 b_3^* \\ m_2 b_1 b_2^* + m_3 b_1 b_2 & I_2 + m_2 b_2^2 + m_3 b_2^2 & m_3 b_2 b_3^* \\ m_3 b_1 b_3^* & m_3 b_2 b_3^* & I_3 + m_3 b_3^2 \end{bmatrix} \begin{bmatrix} \bar{\theta}_1 \\ \bar{\theta}_2 \\ \bar{\theta}_3 \end{bmatrix} + \frac{g}{L} \begin{bmatrix} m_3 b_1^2 + m_2 b_1^2 + m_1 b_1 b_1^* & m_2 b_1 b_2^* + m_3 b_1 b_2 & m_3 b_1 b_3^* \\ m_2 b_1 b_2^* + m_3 b_1 b_2 & m_2 b_2 b_2^* + m_3 b_2^2 & m_3 b_2 b_3^* \\ m_3 b_1 b_3^* & m_3 b_2 b_3^* & m_3 b_3 b_3^* \end{bmatrix} \begin{bmatrix} \theta_1 \\ \theta_2 \\ \theta_3 \end{bmatrix} = 0 \quad (31)$$

For a uniform beam where

$$b_i = b \quad b_i^* = \frac{b}{2} \quad m_i = m \quad I_i = \frac{1}{12} m b^2 \quad (32)$$

(31) becomes independent of m and b.

$$\begin{bmatrix} \frac{7}{2} & \frac{3}{2} & \frac{1}{2} \\ \frac{3}{2} & \frac{4}{2} & \frac{1}{2} \\ \frac{1}{2} & \frac{1}{2} & \frac{1}{2} \end{bmatrix} \begin{bmatrix} \bar{\theta}_1 \\ \bar{\theta}_2 \\ \bar{\theta}_3 \end{bmatrix} + \frac{g}{L} \begin{bmatrix} \frac{5}{2} & \frac{3}{2} & \frac{1}{2} \\ \frac{3}{2} & \frac{4}{2} & \frac{1}{2} \\ \frac{1}{2} & \frac{1}{2} & \frac{1}{2} \end{bmatrix} \begin{bmatrix} \theta_1 \\ \theta_2 \\ \theta_3 \end{bmatrix} = 0 \quad (33)$$

which yield the following eigen values:

$$\omega_1^2 = 1.0467 g/L$$

$$\omega_2^2 = 1.5000 g/L$$

$$\omega_3^2 = 2.6456 g/L$$

Table 1 shows the non-dimensionalized eigen-values $\Omega^2 = \omega^2/(g/L)$ for increasing values of n = number of segments. Ω_F^2 , Ω_M^2 , and Ω_L^2 indicate the first, middle, and last non-dimensionalized eigen-value respectively.

TABLE 1- NONDIMENSIONALIZED PENDULUM FREQUENCIES

n	Ω_F^2	Ω_M^2	Ω_L^2
3	1.0467	1.5000	2.6456
5	1.0165	1.5000	2.8600
7	1.0084	1.5000	2.9266
9	1.0051	1.5000	2.9551
11	1.0034	1.5000	2.9698
15	1.0018	1.5000	2.9836

what is significant about table 1 is the following as n approaches large values

$$\text{as } n \rightarrow \infty \text{ then } \begin{cases} \Omega_F^2 \rightarrow 1.000 \\ \Omega_M^2 \rightarrow 1.500 \\ \Omega_L^2 \rightarrow 3.000 \end{cases} \quad (34)$$

therefore the natural frequencies are contained in the following band:

$$\text{for } i = 1 \text{ to } n \quad \sqrt{g/L} \leq \omega_i \leq \sqrt{3g/L} \quad (35)$$

The mode shapes are shown in Fig.(2)

The first mode shape is characterized by swinging motion and the higher modes are characterized by increasingly more rotational motion of the beam. This behavior is similar to the motion of a rigid beam suspended by two cables as shown in Fig.(3) where θ represents the swinging motion of the bar and ϕ the rotational motion. The natural frequency of the swinging motion $\omega_\theta = \sqrt{g/L}$ and that of the rotational motion $\omega_\phi = \sqrt{3g/L}$

PART II BEAM-BENDING MOTION

The transverse bending vibration of a uniform cantilevered beam has been amply discussed in classical textbooks. Meirovitch [3] is one example. The natural frequencies and mode shapes can be found by modeling the beam as a continuum; or they may be calculated by modeling the beam as a collection of finite rigid elements connected to each other by torsional springs. Fig. 4. As the number of elements increase naturally the calculated natural frequencies tend to approach the natural frequencies of the continuous beam.

This type of finite segment approximation lends itself very well to studying the effects of cable suspension on beam vibration.

In order for the continuous and discrete models to be equivalent i.e. give rise to approximately the same natural frequencies and mode shapes the mass and stiffness characteristics must be equivalent.

$$m_i = m \quad \text{for all } i \quad (36)$$

$$l_i = \frac{L}{n} = b \quad \text{for all } i \quad (37)$$

$$K_i = \frac{EI}{b} \quad \text{for } i = 2 \text{ to } n \quad (38)$$

$$K_1 = \frac{6n}{3n-1} \left(\frac{EI}{b} \right) \quad (39)$$

Equations (38) and (39) are obtained by applying a load P to the rightmost tip of both the continuous and discrete beam and requiring that the displacement of the n joints in the discrete and continuous model be equal. For large n , the stiffness of the first torsional spring is two times the stiffnesses of the other torsional springs.

The matrix equation of motion for this bending mode is the same as (25) i.e.

$$[M_{ij}] [\ddot{\theta}_j] + [K_{ij}] [\theta_j] = 0 \quad (40)$$

the elements of the inertia matrix are the same as those of (27) and (28). However, the stiffness matrix has different form given by the following:

$$K = \begin{bmatrix} k_1 + k_2 & -k_2 & 0 & 0 & \dots & 0 \\ -k_2 & k_2 + k_3 & -k_3 & 0 & \dots & 0 \\ 0 & -k_3 & k_3 + k_4 & -k_4 & \dots & 0 \\ 0 & 0 & -k_4 & k_4 + k_5 & -k_5 & 0 \\ \vdots & \vdots & \vdots & \vdots & \ddots & -k_{n-1} \\ 0 & 0 & 0 & 0 & -k_{n-1} & k_n \end{bmatrix} \quad (41)$$

where the k_i s are given by (38) and (39). To build confidence in the model its results are compared with the analytical solution given in [3] i.e.

$$\omega_i = z_i^2 \sqrt{\frac{EI}{mL^4}} \quad (42)$$

where z_i is the i th root of the following equation

$$\cos z \cosh z + 1 = 0 \quad (43)$$

let us use the following

$$EI = 26.7 \times 10^6 \text{ Nm}^2$$

$$L = 60 \text{ m}$$

$$m = 7.167 \text{ kg/m}$$

The discrete model has 30 elements and Fig. 5 displays the comparison of the natural frequencies of the discrete and continuous model.

It can be seen clearly that the discrete model produces very accurate results for the first 15 to 20 natural frequencies and then accuracy suffers gradually as one goes to higher modes. This is common knowledge among the finite element community that the number of elements one uses to model the modal dynamics of a continuum must be about 2 times the number of natural frequencies one seeks.

PART III BEAM BENDING PLUS PENDULUM MODES OF VIBRATION

Up to now the pendulum motion and the beam-bending motions have been each studied here separately. Now we combine the two to study the effect of the pendulum motion on the beam bending motion.

The equations of the combined motion are still of the type given by (31). The inertia matrix is as before given by (27) and (28). The stiffness matrix is the sum of the stiffness matrices associated with the pendulum motion and the beam bending motion respectively (i.e.)

$$[K]_{\text{Pendulum+Beam}} = [K]_{\text{Pendulum}} + [K]_{\text{beam}} \quad (44)$$

To develop the pendulum stiffness matrix one needs to know the tension in each cable for any arbitrary cable arrangement. Fig. 6 shows the nomenclature for the cable arrangements.

We assume the cables are unstretchable and thus the deflection δ_i at the point where the cable i is attached is zero i.e.

$$\delta_i = \int_0^L \frac{M}{EI} \frac{\partial M}{\partial T_i} dz = 0 \quad \text{for } i = 1 \text{ to } m \quad (45)$$

or

$$\sum_{k=1}^m \int_{x_i}^{x_{i+1}} (x - x_i) \left[-mg \frac{x^2}{2} + \sum_{j=1}^k T_j (x - x_j) \right] dz = 0 \quad \text{for } i = 1 \text{ to } m \quad (46)$$

(46) gives rise to m equations for the tensions in the m cables. (46) can be written in the matrix form as follows:

$$A_{ij} T_j = B_i \quad \text{for } i = 1 \text{ to } m \quad (47)$$

where

$$A_{ij} = \int_{\max(x_i, x_j)}^L (x - x_j)(x - x_i) dz \quad (48)$$

$$B_i = mg \int_{x_i}^L \frac{x^2}{2} (x - x_i) dz \quad (49)$$

and mg is the weight per unit length.

To summarize, the calculations necessary for calculating the natural frequencies and mode shapes of the combined beam-cable assembly are as follows. First, equations (47) are solved and tensions are substituted in equations (28) and (29) and the pendulum stiffness matrix is constructed. Third, the beam stiffness matrix is constructed by using (39), (40) and (41). The combined stiffness matrix is then constructed by using (44). Equations (26) and (27) will then provide the elements of the mass matrix. The eigenvalues and eigenvectors are subsequently calculated by solving equation (30). These calculations were performed by a fortran program called BEAMSUSP.FOR on a VAX computer.

RESULTS

To understand the effects of cable suspension on the natural frequency of a beam, we treat the following specific example where the 1st natural frequency of the beam is 0.3 Hz. and the length of the cables 2.5m. which correspond to the 1st pendulum natural frequency of 0.315 Hz. Table 2 shows the first five pendulum, beam and the combined beam-pendulum frequencies along with the resulting percentage errors.

TABLE 2- NATURAL FREQUENCIES (N.F.) IN HZ.

Mode	Pendulum N.F. ω_p	Beam N.F. ω_b	Beam Cable N.F. ω_{bp}	%Error $(\omega_{bp} - \omega_b)/(\omega_b)$
1	0.315	0.3	0.435	45.06%
2	0.316	1.878	1.904	1.4%
3	0.317	5.252	5.261	0.18%
4	0.319	10.279	10.284	0.05%
5	0.321	16.972	16.975	0.02%

This example is so designed that 1st N.F. of the beam approximately coincides with the 1st N.F. of the pendulum mode. Therefore the 1st N.F. of the beam-cable assembly differs rather substantially from the 1st N.F. of the beam and thus the error introduced by the cables is rather high 45.06%. However in the higher modes the errors introduced by the cables are low. In fact one can notice that the higher the mode the lower the errors. This is due to the fact that the higher pendulum frequencies are very closely spaced together and do not increase as rapidly as the higher beam frequencies. In such a manner that the higher modes become virtually unaffected by the pendulum modes.

Examination of the data in table 2 reveals the following relationship among ω_b , ω_p , and ω_{bp}

$$\omega_{bp,i}^2 = \omega_{b,i}^2 + \omega_{p,i}^2 \quad \text{for } i=1 \text{ to } n \quad (50)$$

The above relationship was also found by Herr [1] for the fundamental mode. As far as the mode shapes are concerned, no noticeable difference could be detected between the mode shapes of the beam and the mode shapes of the beam cable assembly. Fig. 7 and Fig. 8 display the first 6 mode shapes of the beam and beam-cable assembly respectively.

Table 3 shows the effects, or actually the lack of any significant effects, of number of cables and different cable arrangements on natural frequencies.

TABLE 3-EFFECTS OF CABLE ARRANGEMENTS
ON THE ERRORS IN NATURAL FREQUENCIES
PERCENT ERRORS IN N.F.

Num. of Cables	1st Mode	2nd Mode	3rd Mode	4th Mode
30	45.06%	1.4%	0.18%	0.05%
15	45.06%	1.4%	0.18%	0.05%
6	45.12%	1.43%	0.19%	0.06%
3	45.53%	1.74%	0.33%	0.03%
3 at the nodes of 4th mode	45.04%	1.41%	0.19%	0.01%
2 at the nodes of 3rd mode	44.74%	1.49%	0.00%	0.05%

In the first 4 cases the cables are placed at equally spaced intervals. In the last 2 cases, the cables are placed, strategically, at the nodes of the 4th and 3rd mode shape. This leads to relatively minor improvements.

Fig. 9 shows the influence of cable length on the percentage error introduced in the first N.F. (0.3 Hz) of the beam. The equation for this hyperbolic curve is derived from (50).

$$\% \text{Error} = \left[\sqrt{1 + \frac{\omega_{p1}^2}{\omega_{b1}^2}} - 1 \right] \times 100$$

where $\omega_{p1}^2 = g/L$.

Thus for example if the errors are to be less than 10% in the first N.F. of the beam (0.3 Hz) pendulum frequency must be less than 0.137 Hz or the cable length must be greater than 13 meter. This calls for relatively tall buildings for testing sites.

CONCLUSION

The pendulum frequencies are contained within a well defined band of $\sqrt{g/L}$ to $\sqrt{3g/L}$. The percentage errors in the natural frequencies can be accurately predicted by the following formula:

$$\% \text{Error} = \left[\sqrt{1 + \frac{\omega_{p1}^2}{\omega_{b1}^2}} - 1 \right] \times 100$$

where ω_{p1} = the 1st pendulum frequency and ω_{b1} the 1st beam frequency. For a beam whose first natural frequency is 0.3 Hz the cable length must be greater than 13 meters in order for the errors to be less than 10%. Only the 1st mode would be affected by errors, the higher modes would be well above the pendulum band and are unaffected by them. The number and arrangement of cables do not seem to affect the errors substantially. The mode shapes are also unaffected by the pendulum motion.

NEED FOR FURTHER RESEARCH

The depth and cross-sectional geometry of the beam need to be taken into account. They give rise to double pendulum action which can couple with the torsional and bending modes. Future research must address the effects of the mass and finite stiffness of the cables. The nonlinear motion of the beam-cable assembly as well as the nonlinear stiffening effects of the joints of a realistic truss-beam structure will be addressed in future publications.

REFERENCES

1. R. W. Herr, *Some Cable Suspension Systems And Their Effects On Flexural Frequencies Of Slender Aerospace Structures*, NASA TECHNICAL NOTE, NASA TN D-7693.
2. T. R. Kane and Levinson, "DYNAMICS: Theory and Applications," McGraw-Hill, New York, 1985.
3. L. Meirovitch, "Elements of Vibration Analysis," McGraw-Hill, New York, 1986.

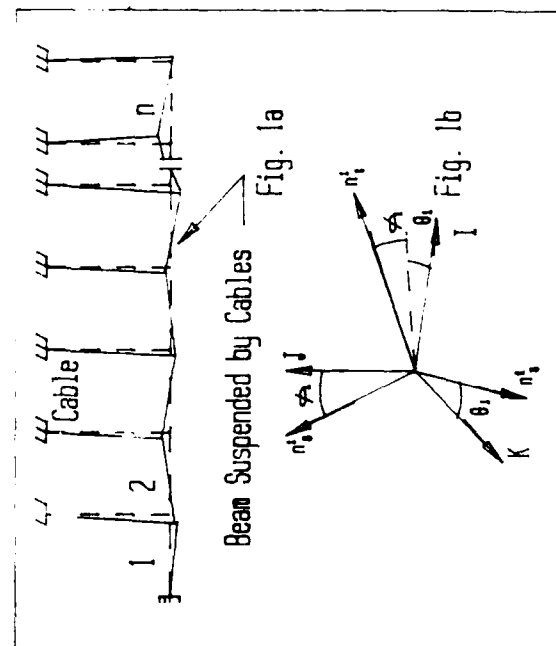


Fig. 1-Diagram of Beam-Cable Assembly and the Unit Vectors

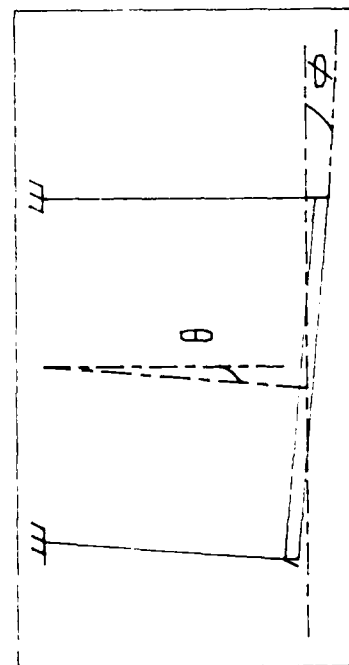


Fig. 3-Swing & Rotation Mode

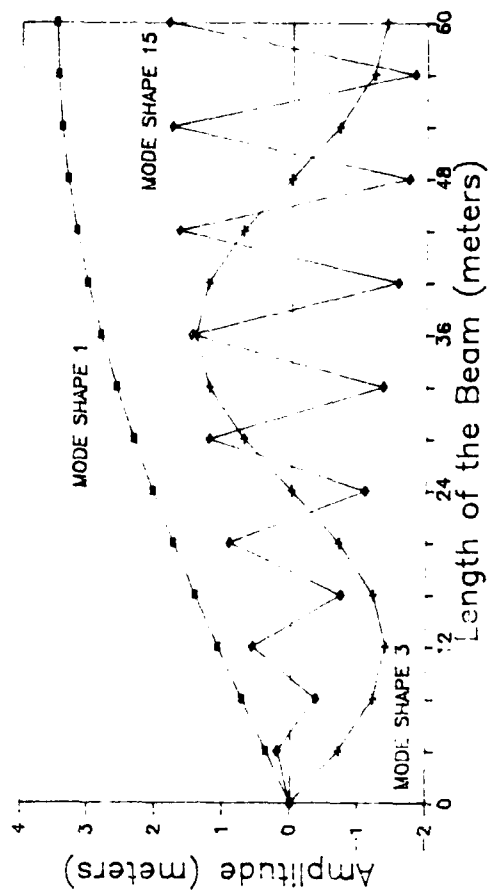


Fig. 2-Some Pendulum Mode Shapes

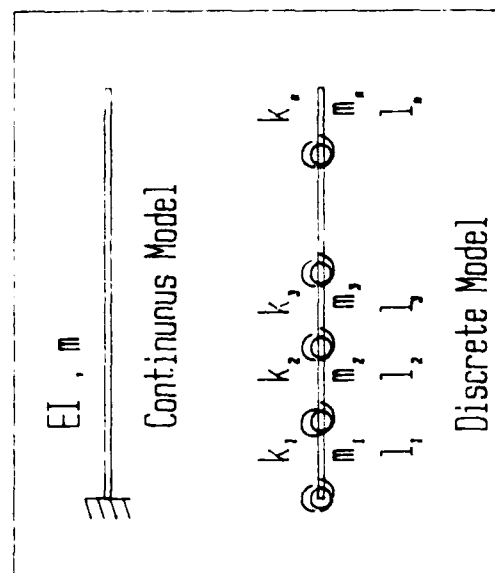


Fig. 4- Continuous vs. Discrete Model

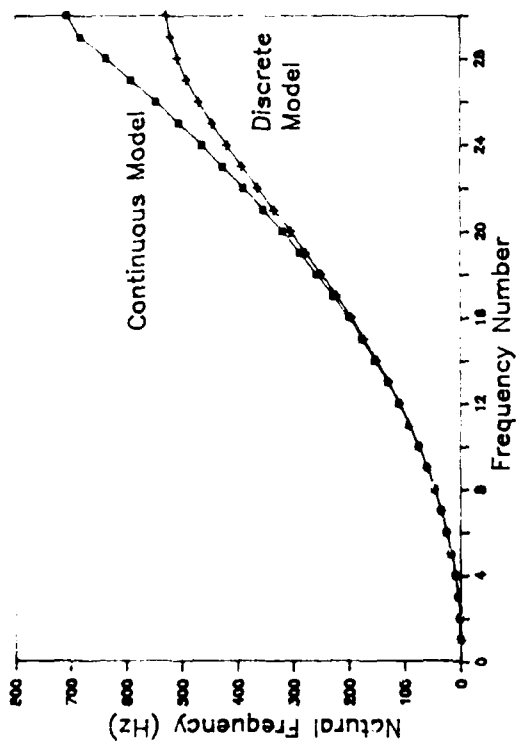


Fig. 5—Natural Frequencies for Continuous and Discrete Model

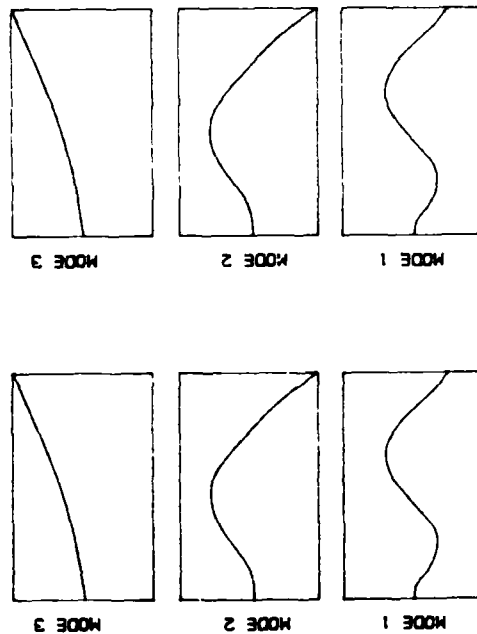


Fig. 7-Beam Mode Shapes

Fig. 8-Beam Plus Cable Mode Shapes

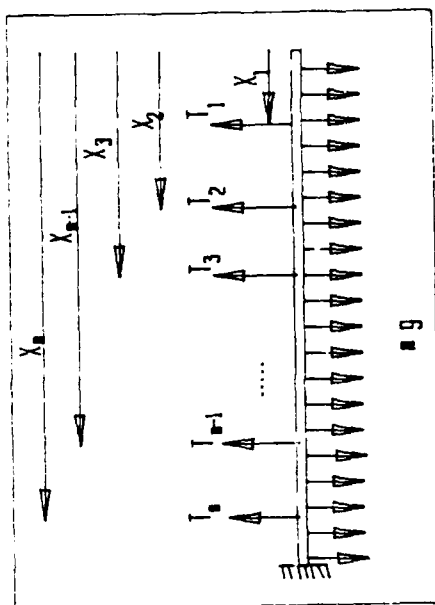


Fig. 6- Cable Arrangement

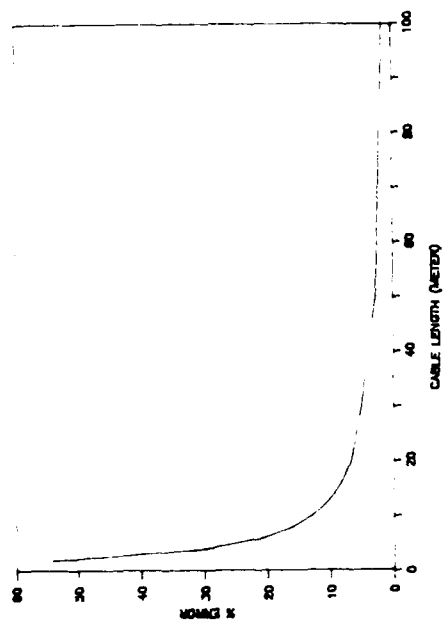


Fig. 9—The Effects of Cable Length on the First Natural Frequency Error

ROBUSTNESS AND POSITIVE REAL CONTROL DESIGN FOR LARGE SPACE STRUCTURES

G.L. Slater and M.D. McLaren
Department of Aerospace Engineering and Engineering Mechanics
University of Cincinnati, Cincinnati, Oh 45221

V.B. Venkayya and V.A. Tischler
Air Force Wright Aeronautical Laboratories
Wright-Patterson Air Force Base, OH 45433

1. INTRODUCTION

The design of controls for large space structures (LSS), flexible aircraft and other flexible systems is a difficult task due to the complexity of these dynamical systems. The structural model of these flexible bodies has a large number of vibration modes which are characterized by a generally very low inherent damping. Generally, the dynamic model is poorly defined leading to considerable uncertainty (especially in the higher modes) in the modal frequencies, damping and mode shapes. In addition, the control design model is usually based on a low order modal representation of the finite element model in order to reduce the complexity and sensitivity of the control design. This modal truncation leads to observation and control spillover which can destabilize one or more of the poorly damped modes.

The existing literature on the space structure control problem is extensive, see e.g. Refs. [1-4]. Numerous investigators have proposed techniques for dealing with the uncertainties inherent in the structure. A technique which can mathematically guarantee stability in the presence of significant modeling uncertainty is the "positive real" approach, [5, 6] which is based on the positive real property of the input-output relationship between collocated force actuator and velocity sensors. The positivity approach has been used to design stable controls for spacecraft models which give good transient performance, are robust to parameter variations in the spacecraft structural model and are insensitive to failures in multiple actuators and/or sensors [6].

A fundamental limitation remains however in the strictness of the positive real property, a mathematical condition which can be satisfied for ideal sensors and actuators, but which fails for real components due to phase lag, excessive high frequency attenuation and computational delays.

Our simulation experience for an aircraft flutter model [7] has shown that while reasonable models of the physical components violate the positive real condition and hence the sufficiency conditions of the positive real stability theorem, in practice high gain attenuation is often sufficient to maintain stability far beyond the conditions implied by the theorem. Currently in the controls field, the robustness of multivariable systems is one of the major research areas. The seminal article by Doyle and Stein [8] showed the importance of the singular values of the return difference matrix $\sigma(I+GH)$ for investigating robustness to various perturbative models. A succession of articles by Doyle and other researchers [9-12] has led to an abundance of information on structured and unstructured perturbations, stability analyses and even design procedures to ensure robustness.

Unfortunately the perturbation models for the conventional unstructured perturbation are inappropriate for the large space structure model and generally fail to give significant results. For example, in a

design for the DRAPER II space telescope, Kissel and Hegg [13] were unable to achieve desired stable performance due to the modal perturbations encountered. The essence of the problem lies in the nature of the assumed perturbations. The conventional singular value analysis is oriented toward high frequency unstructured perturbations in magnitude and phase. The modal control problem has high frequency uncertainties caused by the sensors and actuators, but the modal uncertainty is not of this form. Recourse must be made to structured perturbation models and in particular to real perturbations to capture this problem. Current work in this direction has been reported by Doyle [12], Jones [14] and Speyer [15] yet much remains to be done before a general theory is complete. Much of the difficulty encountered in the robustness research is caused by the generality of the systems which must be considered. By focusing on the structural control problem, we can take advantage of the special mathematical structure of this problem to yield important results.

For large space structures the dynamic model is characterized by a large number of 'significant' structural modes in a frequency range which is within the desired bandwidth of the system. These modes are characterized by a fairly low damping and the primary goal of the controller is to add damping to these modes. Mathematical models of these systems are generally constructed from a finite element representation or from a simplified continuum approach. In either case it has been common knowledge that while the first few low frequency modes can be predicted fairly well, higher frequency modes are extremely difficult to accurately predict. In addition these modes may be extremely sensitive to small parameter changes (e.g., stiffness, mass) which may be expected to occur over the life of the structure. Finally in terms of constructing a control design model, it is often not the lowest frequency modes which are of interest. E.g. for the Draper II space telescope model, Gregory [16] concluded that a five mode reduced order model must include the 17th (vibration) mode of the structure and can omit numerous lower frequency modes. These low frequency modes which are neglected may be associated with the vibration of appendages or other "local modes", or perhaps the mode shape of that vibration is either not easily excited by the perturbation model or is not a significant component in the controller cost function. While not contributing greatly to the overall system response, the maximum singular value of the perturbation matrix $\bar{\sigma}(L)$ will be quite large at the unmodeled modal frequency, warning of a potential stability problem. Mathematically this is correct - a small (unstructured) change in the system dynamics at this frequency could cause the system poles to go unstable. Nevertheless, since this mode is within the control system bandwidth, the conventional approach of reducing system gains at this frequency is not appropriate. Classically for a mode of this type a complex zero pair could be added to form a "notch filter". If however the modal frequency is uncertain, then the notch may be placed in the wrong location. Also, since there may be many modes of this type, we would need multiple notches, a solution which is generally neither desirable or practical.

Another source of modeling error is in the area of actuator dynamics. In most preliminary analyses, actuation dynamics are neglected. Tests of "proof mass" type of actuators indicate significant amounts of phase shift are often present as well as non-linear effects due to friction and hysteresis. Since this uncertainty is generally restricted to higher frequencies, then the unstructured singular value analysis can accommodate this error source.

For low frequency error sources, the primary conclusion to be drawn is that there must be additional information available regarding the

system if some stability robustness is to be ensured. Our work in the area of positive real controls indicates that this approach offers additional robustness criteria not available through unstructured singular value analysis. In this paper we outline the theory of positive real control (Section 2) and the standard robustness results (Section 3). Finally in Section 4 we propose a methodology to combine these analyses to produce meaningful stability results.

2. REVIEW OF POSITIVITY

A system with $m \times m$ transfer matrix $G(s)$ is positive real if for $\text{Re}(s) > 0$, then

$$[G(s) + G^*(s)] \geq 0 \quad (1)$$

where $()^*$ means conjugate transpose and the inequality in (1) means that the matrix on the left side of (1) is non-negative definite. Equivalent conditions to (1) are the conditions:

- (i) The elements of $G(s)$ have no poles in $\text{Re}(s) > 0$.
- (ii) Poles of $G(s)$ on the imaginary axis are simple and such that the residue matrix is non-negative definite Hermitian.
- (iii) For all real ω with $s = j\omega$ not a pole of an element of $G(s)$, then

$$[G(j\omega) + G^*(j\omega)] \geq 0$$

In network theory, positive realness is commonly related to a property of passive networks; viz. that the system is dissipative in that the (generalized) energy in the system at time t , minus the energy added to the system by the input function, is bounded (above) by the initial energy. Thus positive realness implies a rather strong type of stability.

The theory of positive systems was developed initially by Popov [17], who showed that for a conventional feedback system as shown in Figure 1 with forward transfer function G , and feedback function H , then if G and H are (strictly) positive real then the feedback system is guaranteed to be closed loop stable. The test for positive realness is seen to be fairly restrictive in terms of the type of transfer functions commonly encountered in engineering. For a scalar function to be positive real the Nyquist plot of $G(j\omega)$ must remain in the first and fourth quadrants, i.e., it must exhibit less than $\pm 90^\circ$ of phase shift, at all frequencies. Thus, e.g., the transfer functions $1/(s + p)$ and $s/(s^2 + \zeta\omega_n s + \omega_n^2)$ can easily be shown to be positive real. The transfer function $\omega_n^2/(s^2 + 2\zeta\omega_n s + \omega_n^2)$ is seen to be not positive real since it exhibits phase shift approaching -180° for large ω . The positivity tests on transfer matrices may be replaced with an equivalent criterion applicable to systems in state variable form [18].

Application to Structural Control

A flexible structure may be modeled as having a large (theoretically infinite) number of vibration modes which govern the motion of the structure. In practice only a few modes are modeled accurately; the remaining modes have uncertain frequency, damping and mode shape. The important fact to observe about the structure - control problem is the following: The transfer function matrix between colocated velocity sensor

- force actuator pairs is positive real. A proof of this can be found in Benhabib [5] and will not be repeated here. This implies that for ideal velocity sensors and force actuators, then any strictly positive real feedback function can stabilize the structure. This is independent of any knowledge or model of the flexible modes. In a realistic application we demand more than just stability, and for this an appropriate model is required. The important stability result however is that for a positive real control design then uncertainty in the positive real plant can not cause an instability with loop closure. The primary difficulty in applying this concept is the strict phase requirement of the positive real assumption. In reality no physical system can meet these requirements exactly and to actually guarantee stability we must consider the effect of deviations from the positive real assumption.

3. MODELING ERRORS

In this section we review the robustness results of Doyle et al [8-10] and show how these results can be integrated with the positivity concepts to yield strict stability results. The problem considered by Doyle is based on the Nyquist stability criteria which for single input-single output (SISO) systems, can be phrased in terms of encirclements of the origin by the return difference function $(1 + GH)$ evaluated along the $j\omega$ axis (ie. the Nyquist contour). To ascertain the stability in the presence of unmodeled changes in the system transfer matrix we consider a perturbed system where the transfer function model G of Figure 1 is replaced by

$$G_{act}(s) = (I + L(s))G(s) \quad (2)$$

The multiplicative perturbation $L(s)$ represents changes in magnitude and phase of the actual system from the nominal design model. A sufficient condition for the perturbed system to be stable is that the perturbation does not produce any change in encirclements of the origin. We may state this mathematically as

$$1 + (1 + \epsilon L)GH \neq 0 \quad \text{for all } 0 \leq \epsilon \leq 1 \quad (3)$$

For the multivariable case the condition for the perturbation "L" to produce instability is, in analogy with our SISO result

$$\det(I + (I + \epsilon L)GH) \neq 0 \quad \text{for all } 0 \leq \epsilon \leq 1 \quad (4)$$

to relate this easily to the size of "L" requires recourse to the singular values of the return difference matrix. Now for (4) to hold we can equivalently require that

$$\underline{\sigma}(I + (I + \epsilon L)GH) > 0 \quad (5)$$

where $\underline{\sigma}(\cdot)$ indicates the minimum singular value and as before $0 \leq \epsilon \leq 1$. Using a series of singular value inequalities (see [9]), the inequality (5) can be guaranteed to hold if

$$\underline{\sigma}[(I+GH)(GH)^{-1}] = \underline{\sigma}(I+(GH)^{-1}) > \bar{\sigma}(L) = L_m(\omega) \quad (6a)$$

or

$$\bar{\sigma}[GH(I+GH)^{-1}] < \frac{1}{L_m(\omega)} \quad (6b)$$

Equations (6) represent a fundamental bound on the size of perturbation allowed for the MIMO system to maintain stability. This last statement is

a precise quantification of a familiar SISO result, namely that the closed loop gain should be small if the perturbation in G is likely to be large. It is precisely this requirement that causes the conventional application of the singular value robustness result to structural controls to break down.

Application to Structural Controls

For large space structures the dynamic model is characterized by a large number of 'significant' structural modes in a frequency range which is within the desired bandwidth of the system. These modes are characterized by a fairly low damping and the primary goal of the controller is to add damping to these modes. Mathematical models of these systems are generally constructed from a finite element representation or from a simplified continuum approach. In either case the first few low frequency modes can be predicted fairly well while higher frequency modes are extremely difficult to accurately predict. In addition these modes may be extremely sensitive to small parameter changes (e.g., stiffness, mass) which may be expected to occur over the life of the structure.

Using the multiplicative perturbation approach, the maximum singular value of the perturbation matrix $\tilde{\sigma}(L)$ will have numerous peaks corresponding to these shifted modes. Because of the relatively low frequency of these perturbations, application of the singular value bound (6) to a modal uncertainty problem is useless. For example, a standard test model for flexible system control design is the tetrahedral truss model referred to as DRAPER I. The system possesses 12 degrees of freedom with six inputs and six sensors. The nominal frequencies range from about 1 - 10 rad/sec. Randomly perturbing the truss elements (areas and mass) by $\leq 5\%$ produces a different set of frequencies and mode shapes. The singular value plot $Lm(\omega)$ for one 'typical' perturbation is shown in Figure 2. (Note: We use the standard control systems terminology where the 'db' scale refers to $20\log(|*|)$.) Each double peak in this plot corresponds to a slightly displaced modal frequency. The classic singular value robustness requirement is that the closed loop transfer function must be below the inverse of this curve which is clearly inappropriate considering the frequencies and the height of these peaks. (Note we have arbitrarily assumed a nominal modal damping of 0.2% and have not perturbed this number). In spite of the inability to satisfy the singular value requirement, a positive real control design is guaranteed stable since even for the perturbed model, the positive real stability theorems are satisfied.

The primary stability question then comes when additional error sources are considered, in particular those modeling errors that invalidate the positive real assumption. Most commonly these may be attributed to actuator dynamics, although sensor dynamics may also be important in some problems. The key to considering the stability problem then is to evaluate the singular value bounds on the deviation from positivity - not on the deviation from an a priori model. Using this philosophy, extended stability results can be obtained for a class of realistic problems.

4. APPLICATION

To show an application of the singular value/positivity robustness consider the flutter example solved by Takahashi and Slater [7]. In this paper the nominal transfer function between sensor and control deflection was 'almost' positive real if actuator dynamics were neglected. The presence of the actuator added significant phase shift destroying the

positivity at the high frequency range (see Figure 3). Nevertheless, a positive real design (see Figure 4) which neglected the actuator was successful in controlling the structural oscillations. Considering the vehicle transfer function, a reasonable first assumption is to model the deviation from positivity strictly as a phase change, i.e.

$$1 + L = e^{j\phi} \quad (7)$$

hence

$$|L| = Lm(\omega) = 2 \left| \sin\left(\frac{\phi}{2}\right) \right| \quad (8)$$

which clearly is bounded by

$$\begin{aligned} Lm(\omega) &< 2 \\ &< 6 \text{ db} \end{aligned} \quad (9)$$

Note that inequality (9) is only applied for frequencies outside the positive real range, and that the more precise bound (8) may be applied if desired. Applying this criteria to the product GH (Figures 3,4) we can determine that (8) is in fact satisfied, giving a sufficiency condition that guarantees stability for this problem. This stability had previously been verified by a numerical procedure for the given modal data, but in fact this result guarantees stability for arbitrary modal variations from the base positive real model.

A second example involves the DRAPER I structural model previously mentioned. The singular value inequality bound (6) clearly can not be satisfied for the type of modal uncertainty depicted in Figure 2. Using a positive real control design we know however that such variations will not harm the closed loop stability of the nominal design. We have chosen a nominal design here from Ref. 6, and the singular value plot $\bar{\sigma}[GH(I+GH)^{-1}]$ is shown in Fig. 5. We may now use this plot to test stability due to a perturbation from a positive real model. For this control design we consider the effect of a second order actuator with a natural frequency of 30 rad/sec at each of the six inputs. For this set of actuator dynamics, inequality (6) is always satisfied, hence the positive real controller is guaranteed stable even for additional unmodeled modal variations. A representative time response is shown in Figure 6 which verifies the stability in the presence of actuator dynamics.

5. CONCLUSION

This paper shows that singular value robustness tests can be combined with a positive real control design to give guaranteed stability for systems with uncertainties in the modal parameters and in multiplicative uncertainties due to actuator and sensor dynamics. These results should be a valuable aid in control design for large space structures and other flexible systems with significant structure-control interaction.

ACKNOWLEDGEMENT

This work was supported by the Air Force Office of Sponsored research, Bolling AFB, DC, and by the Flight Dynamics Laboratory, Air Force Wright Aeronautical Laboratories, Wright Patterson AFB, Ohio.

REFERENCES

1. Arbel, A. and Gupta, N.K., "Robust Colocated Control for Large Flexible Space Structures", J. Guidance & Control, vol 4, #5, Sept-Oct 1981, pp 480-486
2. Hablani, H.B., "Stochastic Response Analysis, Order Reduction, and Output Feedback Controllers for Flexible Spacecraft", J. Guidance Control & Dynamics, vol 8, #1, Jan-Feb 1985, pp 94-103
3. Inman, D.J., "Modal Decoupling Conditions for Distributed Control of Flexible Structures", J. Guidance Control & Dynamics, Vol 7, #6, Nov-Dec 1984, pp 750-752
4. Venkayya, V.B., Tischler, V.A., Khot, N.S., "Dynamics and Control of Space Structures", Engineering Optimization, Vol. 11, 1987, pp 251-264.
5. Benhabib, R.J., Iwens, R.P. and Jackson, R.L., "Stability of LSS Control Systems Using Positivity Concepts", J. Guidance & Control, Vol 4, #5, Sept-Oct 1981, pp 487-494
6. McLaren, M., Slater, G.L., "Robust Multivariable Control of Large Space Structures Using Positivity", J. Guidance, Control, and Dynamics, vol. 10, #4, July-August 1987, pp 393-400.
7. Takahashi, M.D., Slater, G.L., "Design of a Flutter Mode Controller Using Positive Real Feedback" J. Guidance, Control. and Dynamics, vol. 9, #3, May-June 1986, pp 339-345.
8. Doyle, J.C., Stein, G., "Multivariable System Design: Concepts for a Classical/Modern Synthesis", IEEE Transactions on Auto. Control, vol. AC-26, #1, Feb. 1981, pp 4-16.
9. Doyle, J., "Multivariable Design Techniques Based on Singular Value Generalizations of Classical Control", AGARD Lecture Series 117 Multivariable Analysis and Design Techniques, Sept. 1981.
10. Safanov, M.G., Laub, A.J. and Hartmann, G.L., 'Feedback Properties of Multivariable Systems: The Role and Use of the Return Difference Matrix', IEEE Trans. on Auto. Control, Vol AC- 26, No 1, 1981, pp 57-65
11. Mukhopadhyay, V. and Newsom, J.R., 'Application of Matrix Singular Value Properties for Evaluating Gain and Phase Margins of Multiloop Systems', AIAA Guidance and Control Conference, San Diego Ca., Aug 9-11, 1982
12. Doyle, J. "Analysis of feedback systems with structured uncertainty", IEE Proc., vol. 129, Pt. D, #6, Nov. 1982, pp 242-250.
13. Kissel, G.J., Hegg, D.R., "Stability Enhancement for Control of Flexible Space Structures", IEEE Control Systems Magazine, Vol. 6, #3, June 1986, pp 19-26.
14. Jones, R.D. "Structured Singular Value Analysis for Real Parameter Variation", AIAA Paper 87-2589CP, Guidance and Control Meeting, Monterey, CA., August 1987.

15. Tahk, M., Speyer, J. "Modeling of Parameter Variations and Asymptotic LQG Synthesis", IEEE Trans. on Auto. Control, vol. AC-32, #9, Sept. 1987, pp 793-801.
16. Gregory, C.Z., "Reduction of Large Flexible Spacecraft Models Using Internal Balancing Theory", J. Guidance Control & Dynamics, Vol 7, #6, Nov-Dec 1984, pp 725-732
17. Popov, V.M., Hyperstability of Control Systems, Springer-Verlag, 1963.
18. Anderson, B.D.O., Vongpanitlerd, S., Network Analysis and Synthesis, Prentice-Hall,

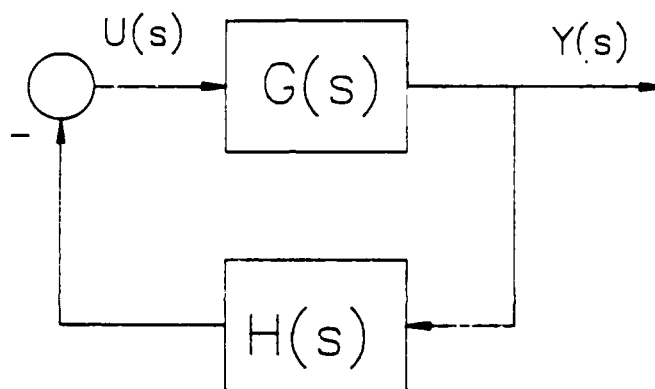


Figure 1 General Feedback Control Model

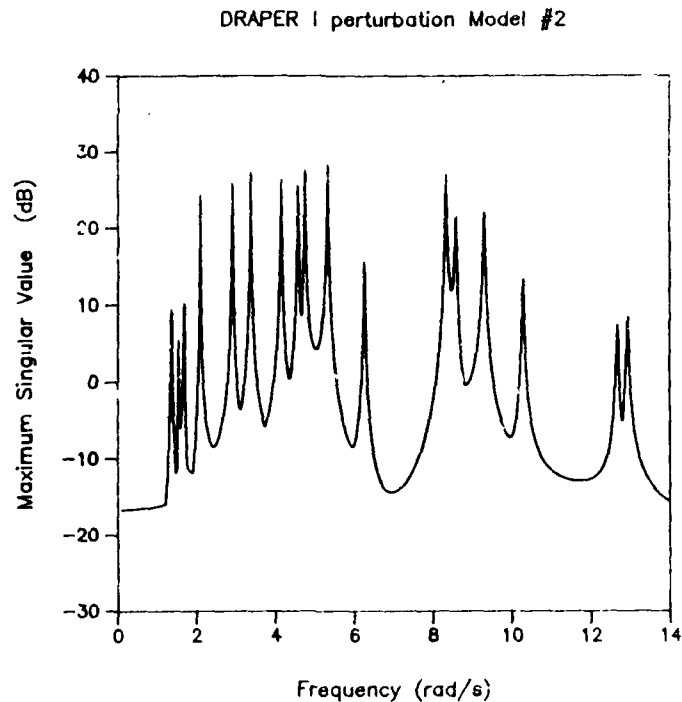


Figure 2 $L_m(\omega)$ for a Typical Perturbation of the Draper I Spacecraft Model

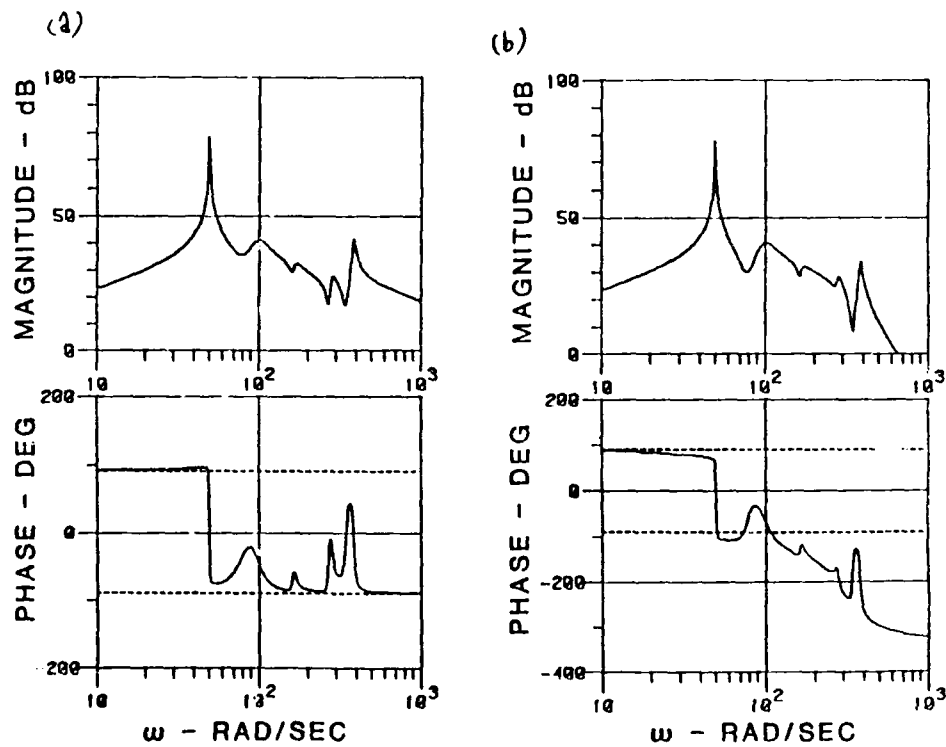


Figure 3 Transfer Function of Flexible Aircraft Model (a) Without, and (b) With Actuator Dynamics (from Ref. 7)

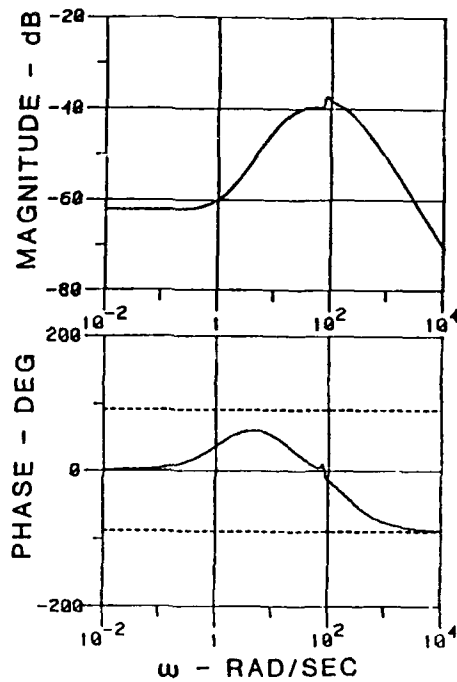


Figure 4 Positive Real Feedback Transfer Function for Control of Flexible Aircraft Model (from Ref. 7)

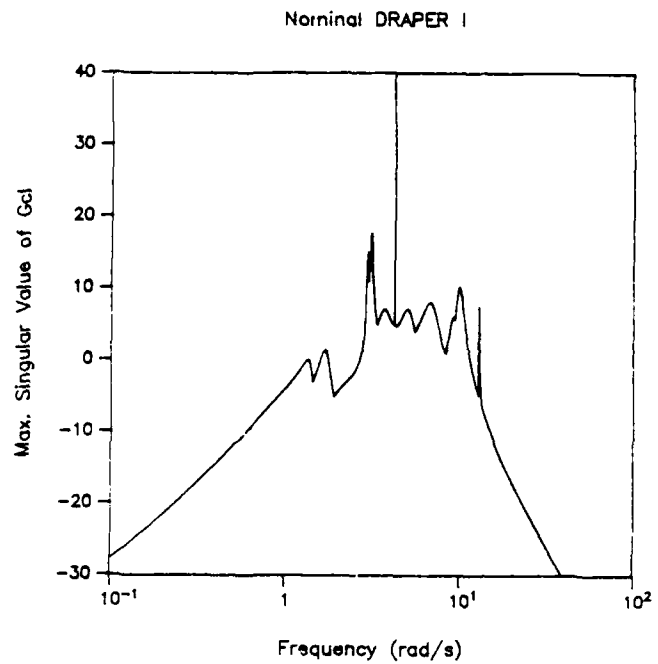


Figure 5 Singular Values for Draper I Nominal Closed Loop Design Model

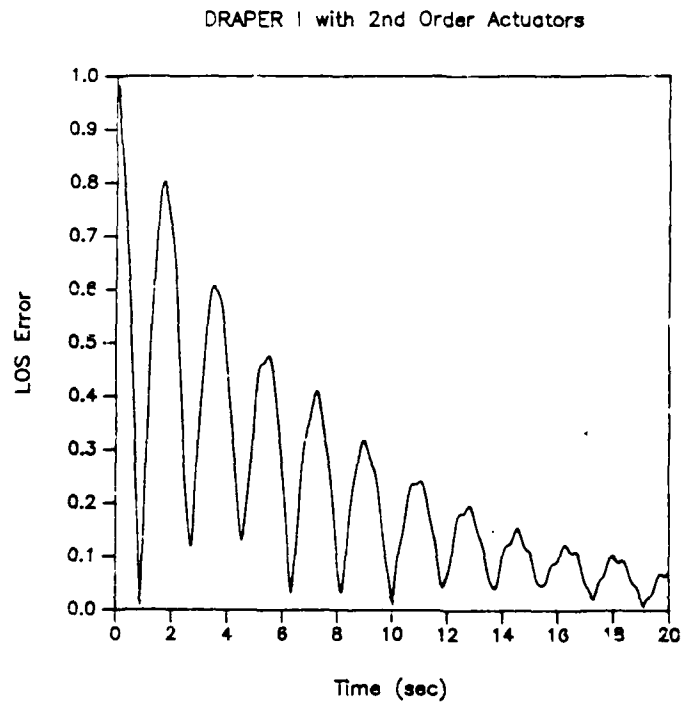


Figure 6 Time Response of Draper I Model Including a Second Order Actuator Showing Stable Response

13. CIVIL ENGINEERING

DYNAMICS OF BRIDGES

L. Frýba

Institute of Theoretical and Applied Mechanics
of the Czechoslovak Academy of Sciences
Prague, Czechoslovakia

1. INTRODUCTION

The new types of vehicles are characterized by increasing speeds and weights. As a result, the modern slender bridges, along which the vehicles are moving, have been subjected to vibrations and dynamic stresses far larger than before.

The history of the dynamics of bridges began in England at the first half of the 19-th century at the occasion of the construction of first railway bridges. The investigators R. Willis and G. G. Stokes tackled the problem as the first and since that time the dynamics of bridges has received a great deal of attention in the literature. The classical English book by C. E. Inglis [1] should be especially mentioned here while the history of the problem is described in [2] in details.

In the present paper, the main dynamic characteristics of bridges like natural frequencies and logarithmic decrements of damping are summarized. The modern stochastic approach to the dynamics of bridges has been developed and it has provided some characteristics which describe the vibration of bridges more truthfully than the dynamic impact factor.

The experimental data are coming mostly from railway bridges what corresponds to the specialization of the author.

2. NATURAL FREQUENCIES OF RAILWAY BRIDGES

We do not meet with difficulties in calculating the natural frequencies of bridges if a computer is at disposal. The suitable methods are described in textbooks on dynamics of structures, see e.g. [3]. The comparisons of theoretical and experimental results show, however, some divergences which may be explained by different modulus of elasticity, moment of inertia, mass per unit length, boundary conditions and/or length of the theoretical model and of the real bridge.

Therefore, natural frequencies of 113 railway bridges from Czechoslovakia and from other European railway administrations [4] were summarized and evaluated using statistical methods.

The set of experimental data was divided in 5 groups :

1. steel trusses with and without ballast,
2. steel plate girders with ballast,
3. steel plate girders without ballast,
4. concrete bridges with ballast,
5. concrete bridges without ballast.

It has shown that the first natural frequencies of railway bridges are the function of the span. Among four types of regressions (linear, exponential, logarithmic and power regression), the power regression answers well to the tests

$$f_1 = a l^b, \quad (1)$$

where

- f_1 - first natural frequency in Hertz,
 l - span of the bridge in meters,
 a, b - regression coefficients.

The Table 1 summarizes the results of statistical evaluation. There are given the regression coefficients a, b , the reliability bound s for the estimation of the lower and upper bound, respectively, with a 95 % reliability

$$f_1 = a l^b s^{-1}, \quad f_1 = a l^b s, \quad \text{respectively,} \quad (2)$$

correlation coefficients r showing how close are the experimental data to the equation (1) and the boundaries of applicability of the equation (1) in span, l_{\min} and l_{\max} .

The Figure 1 gives a survey of all experimental data plotted as a function of the span. There is also the mean value (solid line) in concordance with the equation (1) and the lower and upper bound, equation (2), for the 95 % reliability (dashed lines).

The rounded values from the Table 1 provide an empirical formula

$$f_1 = 133 l^{-0,9}, \quad s = 2,1, \quad (3)$$

which is valid for railway bridges of all types, materials and of usual static systems. The equation (3) may serve for the estimation of the first natural frequency of a railway bridge in the design stage.

A detailed analysis has shown a high reliability of the estimation of the first natural frequency for truss bridges

Table 1 First natural frequencies of railway bridges, power regression $f_1 = a f^b$

Railway bridges	Ballast with without -	No. of tested bridges n	Regression coefficients		Relia- bility bound s [1]	Correla- tion coeffi- cient r [1]	Boundary of applicability	
			a [m ^{-b} .s ⁻¹]	b [1]			f _{min} [m]	f _{max} [m]
steel trusses plate and box girders	+/-	27	306,754	-1,073	1,363	0,944	25	200
	+	23	59,477	-0,743	1,717	0,829	10	70
	-	36	208,039	-1,036	1,939	0,923	3	80
	+	23	190,415	-1,102	2,312	0,906	4	60
concrete	-	4	225,353	-1,191	1,424	0,995	5	20
all bridges	+/-	113	133,006	-0,911	2,080	0,899	3	200

because they are of uniform type. On the other hand, various types of bridges were included among steel plate girder bridges (e.g. box girders etc.) so that their reliability bounds are wider. There are only few results from concrete bridges without ballast, nevertheless, the regression coefficients for concrete bridges with and without ballast are close together. It justifies a conclusion that the ballast on concrete bridges affects their natural frequencies in a little way only (the mass ratio of the ballast and of a concrete bridge is small).

3. DAMPING OF RAILWAY BRIDGES

Damping is a favorable property of structural materials which diminishes the amplitudes of vibration in many cases. The physical reasons of damping are very complex and they may be distinguished in internal and external ones. The internal reasons of damping are : viscous and plastic internal friction of structural materials during their deformations, their non-homogenous properties, cracks etc. External reasons in railway bridges are : friction in supports and bearings, friction in ballast, in joints, aerodynamic resistance of the bridge (it is small with respect to the rigidity of usual railway bridges), viscoelastic properties of the soil and ground etc.

It is almost impossible to take into account all reasons of damping in engineering calculations. Therefore, the basic theoretical model in dynamics of bridges (i.e. a simple beam subjected to a force which moves with a constant velocity along the beam) was solved for several kinds of damping :

3.1 Viscous Damping Proportional to the Velocity of Vibration

The elementary hypothesis of viscous damping (Kelvin-Voigt) assumes that the external damping is proportional to the velocity of vibration of each element of the beam. Due to its simplicity, the hypothesis is widely spread, although it supposes that the damping depends on the frequency of vibration. This is in contradiction to some laboratory experiments. However, the global results correspond rather well to experiments carried out on large and complex structures as railway bridges in many cases.

The basic theoretical model mentioned above is covered for viscous damping by the differential equation

$$EI \frac{\partial^4 v(x,t)}{\partial x^4} + \mu \frac{\partial^2 v(x,t)}{\partial t^2} + 2\mu\omega_b \frac{\partial v(x,t)}{\partial t} = \delta(x-ct) F \quad (4)$$

where :

$v(x,t)$ - deflection of the beam,
 EI - constant bending rigidity of the beam,

- μ - mass per unit length of the beam,
- ω_b - constant of the viscous damping,
- $\delta(x)$ - Dirac delta function,
- c - velocity of the movement of the force,
- F - constant force.

The solution of the equation (4) is well known [2] and the damping diminishes the maximum dynamic deflection of the beam for subcritical speeds of the force.

If higher modes of vibration are damped with different coefficients ω_{bj} , the solution of the equation (4) remains formally the same with interchanging of ω_b by ω_{bj} .

An other hypothesis assumes that the damping is proportional to the velocity of stress variations and expresses the internal damping depending on stress. The pertinent differential equation of the basic theoretical model appears in the form

$$EI \frac{\partial^4 v(x,t)}{\partial x^4} + b EI \frac{\partial^5 v(x,t)}{\partial x^4 \partial t} + \mu \frac{\partial^2 v(x,t)}{\partial t^2} = \delta(x-ct) F \quad (5)$$

If the constant of this type of damping $b = 2 \omega_b / \omega_j^2$ the solution of (5) remains formally the same as that of the equation (4).

3.2 Dry Friction

The Coulomb hypothesis of dry friction supposes a constant force acting against the movement of each element of the beam so that the following equation is valid for our basic theoretical model

$$EI \frac{\partial^4 v(x,t)}{\partial x^4} + \mu \frac{\partial^2 v(x,t)}{\partial t^2} \pm b = \delta(x-ct) F \quad (6)$$

where the upper sign at the damping constant b is valid for $\dot{v}(x,t) > 0$ and the lower sign for $\dot{v}(x,t) < 0$, respectively.

The solution of the equation (6) is decomposed in three phases: $q(t) = 0$, $\dot{q}(t) > 0$, and $\dot{q}(t) < 0$, where $q(t)$ is the generalized deflection of the centre of the beam.

At the end of the movement, i.e. at $t = l/c$, where l is the span of the beam, a residual deflection v_r remains due to the presence of dry friction. After evaluating v_r , the particular constant b of dry friction may be obtained

$$b = \frac{\pi F}{2l[1 - 2\cos \pi/(2\alpha)]} \frac{v_r}{v_0} \quad (7)$$

where :

v_0 - the deflection of the centre of the beam due to the force F at the same place,

$$\alpha = \frac{c}{2 f_1 l} \quad (8)$$

is the dimensionless speed parameter,

f_1 - the first natural frequency of the beam.

An other dry friction may occur at bearings of bridges :

$$N(t) = \pm f (G/2 + F ct/l) \quad (9)$$

$N(t)$ is the horizontal longitudinal force according to the Coulomb's law which is proportional to the reaction force beneath the moving bearings,

f - coefficient of friction,

G - dead load of the bridge.

The upper sign of the force $N(t)$ (9) is valid for the movement of the moving bearing to the left hand side (the moving bearing is supposed on the right hand side of the beam) and vice versa.

The differential equation for this case takes the form

$$EI \frac{\partial^4 v(x,t)}{\partial x^4} + \mu \frac{\partial^2 v(x,t)}{\partial t^2} - N(t) \frac{\partial^2 v(x,t)}{\partial x^2} = \delta(x-ct) F \quad (10)$$

and leads to the Bessel functions [5].

3.3 Complex Theory of Internal Damping

The complex theory of internal damping assumes that the nonelastic deformation delays the elastic one so that the damping does not depend on the frequency [6].

The differential equation of our basic theoretical model may be written in the following form

$$(\beta_1 + i\beta_2) EI \frac{\partial^4 v^*(x,t)}{\partial x^4} + \mu \frac{\partial^2 v^*(x,t)}{\partial t^2} = \frac{2}{l} F (\sin \omega t - i \cos \omega t) \sin \pi x/l \quad (11)$$

where $\dot{v}^*(x,t)$ - complex deflection,

$$\beta_1 = \frac{1 - \gamma^2/4}{1 + \gamma^2/4}, \quad \beta_2 = \frac{\gamma}{1 + \gamma^2/4}$$

γ - coefficient of internal damping,
 $\omega = \pi c/l$,

and the real part of the right hand side corresponds to the right hand side of the equation (4).

The solution of the equation (11) is easy, however, it does not present any result much more different from the result of the Kelvin-Voigt theory. The forced vibration dominates over the free vibration in this transient case and the event lasts for a limited time only. Nevertheless, the complex theory enables to take into account nonlinear damping, e.g. damping proportional to the amplitude of vibration.

3.4 Experimental Results

In practice, the logarithmic decrement of damping δ is evaluated from the experimental deflection- or stress-time histories

$$\delta = \frac{1}{n} \lg \frac{a_0}{a_n} \quad (12)$$

where a_n is the amplitude after the n -th cycle of free damped vibration. Unfortunately, the past tests did not conserve the amplitudes appertaining to the particular cycles of vibration.

Therefore, only logarithmic decrements of damping were summarized from 73 railway bridges. The statistical analysis has provided the following conclusions :

- a very weak correlation of δ on span l and on the natural frequency f_1 ,
- a weak correlation on the presence of ballast for spans greater than 20 m,
- for spans less than 20 m, dry friction occurs and its effect grows with diminishing spans,
- logarithmic decrements of damping for concrete bridges are greater than that for steel bridges and, therefore, only these two types of bridges are statistically important,
- large dispersion of all test results.

Table 2 Logarithmic decrements of damping δ
of railway bridges

Characteristic	Symbol	Bound of applicability	Railway bridges	
			steel	concrete
No. of tested bridges	n	$f > 20 \text{ m}$	43	3
Mean value	δ		0,080	0,177
Standard deviation	s		0,041	0,073
Reliability for Gauss distribution	1,96 s		0,080	0,143
No. of tested bridges	n	$f < 20 \text{ m}$	16	11
Exponent in eqs. (14), (16)	a		1,494	0,918

The results of evaluation are plotted in Figures 2 and 3 where the mean values are given by solid lines while the statistical data together with 95 % reliability (1,96 s) are given in the Table 2.

The rounded values of Table 2 have supplied the empirical formulae of the logarithmic decrements of damping for railway bridges :

steel bridges

$$f \geq 20 \text{ m} \quad \delta = 0,08, \quad s = 0,04 \quad (13)$$

$$f < 20 \text{ m} \quad \delta = 0,08 \left(20/f \right)^{1,5} \quad (14)$$

concrete bridges

$$f \geq 20 \text{ m} \quad \delta = 0,18, \quad s = 0,07 \quad (15)$$

$$f < 20 \text{ m} \quad \delta = 0,18 \left(20/f \right)^{0,9} \quad (16)$$

where s is the standard deviation of the statistical set of data, see Table 2.

4. STOCHASTIC APPROACH

The dynamic impact factor has been used for the design of bridges in practice although it does not reflect the dynamic properties of the bridge and/or vehicles. According to most national standards for design of bridges it depends on the span of the bridge only and for bridges in traffic at most on the dimensionless speed parameter α (8).

The dynamic impact factor is verified by tests during which a certain vehicle is running along a bridge with various speeds. Then, the dynamic impact factor δ is evaluated from the relation

$$\delta = \frac{\max v_{\text{dyn}}(x, t)}{v_{\text{stat}}(x, t)} \quad (17)$$

where $\max v_{\text{dyn}}(x, t)$ is the maximum dynamic stress or deflection at x and $v_{\text{stat}}(x, t)$ is the corresponding static value at the same point under the action of a moving vehicle.

This approach is possible in special tests only using a particular vehicle. As the weight of the testing vehicle is in most cases much lower than the weight of the standard load, the dynamic impact factor (17) can hardly be applied as a multiplying factor together with the standard load.

Usual traffic on bridges is much more realistically idealized by a stochastic approach which was developed for short span bridges in [7] and [8] as a sequence of random forces moving along a bridge and for large span bridges in [9] as a moving continuous random load which is a random function both of time and of the length coordinate.

The stochastic analysis has presented the coefficient of variation s/\bar{v} with which a statistical dynamic coefficient may be suggested

$$\delta = 1 + k \frac{s}{\bar{v}} \quad (18)$$

where

s - standard deviation,
 \bar{v} - mean value,
 k - coefficient ascertaining the reliability that the peaks of vibration would not cross a certain threshold (e.g. $k = 1,65$ for the 95 % reliability of the one-sided Gauss process).

The coefficient of variation may also be obtained during experiments under traffic loads if the stress-time record is

divided in equidistances and such a set of test data is evaluated using statistical methods. The modern experimental devices and/or computers enable such a statistical evaluation.

The dynamic coefficient (18) may serve for strength calculations, however, it is not sufficient for fatigue which requires the knowledge of number and amplitudes of vibration. Therefore, the stress-time records are classified using e.g. "rain-flow" counting method [10] which classifies the stress ranges

$$\Delta\sigma = \sigma_{\max} - \sigma_{\min} \quad (19)$$

and assumes that the fatigue damage due to small stress ranges can be added to the damage due to large stress ranges.

The result of counting may be presented in the form of a stress spectrum, i.e. the probability density of stress ranges $\Delta\sigma_i$ in the i-th class. The stress spectra include both static and dynamic components of the response and possess a great number of small stress ranges while the great stress ranges are rare for bridges.

The statistical evaluation of stress spectra of railway and of highway bridges has presented an empirical formula

$$n_i = a T^b L^c \lambda_i^d e^{ks} \quad (20)$$

where :

n_i - number of stress ranges in the i-th class per year,
 T^i - mass of all trains on the given line per year for railway bridges (in million of tons), or

- mean value of heavy highway vehicles per 24 hours (divided by 500) for highway bridges,

L - length of influence line of the investigated bridge element (in metres),

$\lambda_i = \Delta\sigma_i / \Delta\sigma_s = 0,1; 0,2; \dots; 0,9; 1$ - dimensionless stress range,

$\Delta\sigma_s$ - stress range due to standard load multiplied by the standard dynamic impact factor,

s - standard deviation of measured data,

$k = 1,65$ - coefficient ascertaining the 95 % reliability,

a, b, c, d - regression coefficients according to our experiments :

	for railway bridges	for highway bridges	
a	17,74	13,10	
b	0,86	1,00	
c	- 0,35	- 0,46	(21)
d	- 4,46	- 5,21	
s	1,32	0,93	

The stress spectra enable to calculate the traffic load factor

$$\lambda_T = \left[\frac{1}{n_T} \sum_i n_i \lambda_i^m \right]^{1/m} \quad (22)$$

where

n_T is the number of vehicles per year,

$1/m$ denotes the slope of the particular Wöhler curve and other symbols come from the equation (20).

The traffic load factor λ_T serves for the design of bridges for fatigue [10] using the theory of limit state design or for the estimation of the fatigue life [11].

5. DYNAMIC MODELS

5.1 Vertical Forces

The dynamic models of bridges and vehicles have been elaborated in details for the investigation of vertical dynamic forces.

The beam, simple or continuous, is the most used model for a bridge [1], [2], [3]. The vehicle is idealized by a system of lumped masses or rigid desks connected by springs and dampers together. The lumped masses are also used for modelling the bridge if numerical methods and computers are used.

The system of differential equations describes the vertical movements of the bridge and of lumped masses and the rotation of rigid desks during the motion of the vehicle along the bridge. Various theoretical models were verified by experiments up to the speed of 250 km/h, [12], [2], and they show a satisfactory agreement between theory and tests.

Both theory [2] and experiments [12] have supplied the most significant information: the dynamic effects on bridges grow with increasing speed of the vehicle, and dimensionless speed parameter α (3) possesses a deciding significance. Other important parameters are: track irregularities, dynamic characteristics of the bridge and of the vehicle (frequencies, damping) etc.

5.2 Horizontal Longitudinal Forces

Horizontal longitudinal forces on bridges are caused by starting and braking vehicles. The starting force is growing from zero to a certain maximum and then it diminishes. The me-

ximum starting force occurs at a low speed of the vehicle. The maximum braking force appears just before stopping of the vehicle.

For these reasons, experiments [13] as well as the appropriate theory [14], [15] have shown that the tackled problem is of quasi-static character rather than dynamic one.

The starting and braking forces in bridges depend on the coefficient of adhesion, on the type of bearings and on the continuity of rails over the bridge ends in the case of railway bridges. The starting forces arise under the powered vehicles only, while the braking forces under all vehicles. Therefore, the length of the bridge with respect to the length of the train plays a certain part.

5.3 Horizontal Lateral Forces

Horizontal lateral forces are caused by horizontal track irregularities and by the "sinus" motion of rail vehicles. They induce horizontal and rotational vibration of the bridge.

The simplest model that could explain the coupled spacial vibration just mentioned is a thin-walled beam [16]. The stochastic approach gives a certain chance of solving the given problem.

6. CONCLUSIONS

Since the last century the dynamics of bridges has been elaborated in deep details and it presents the models and methods that could explain all events during the movement of vehicles along a bridge.

The basic dynamic characteristics of bridges, i.e. natural frequencies and logarithmic decrements of damping of railway bridges were collected from extensive tests so that we are able to estimate these values with a high reliability. The regression equation (1) estimates the first natural frequency as a function of the span where the appropriate constants are given in the Table 1 for the investigated types of bridges and/or in the equation (3) for all bridges.

Several theoretical models of damping exist and the simplest one (Kelvin-Voigt) corresponds well to experiments for large span bridges. The dry friction applies at short span bridges while the other models bring no important improvements.

The experimental data have shown that the material (steel or concrete) is statistically deciding parameter that gives the appropriate logarithmic decrement of damping for railway bridges (13) and (15). The correction for spans shorter than 20 m

implies the effect of dry friction due to the presence of ballast on the bridge or due to the friction in bearings (14), (16).

The stochastic approach to the dynamics of bridges has brought some possibilities how to calculate the bridges more realistically using the statistical dynamic coefficient (18) and the traffic load factor (22). The first one is suggested for strength calculations while the second one for the design of bridges for fatigue.

Various dynamic models of bridges and vehicles enable to idealize the movement of vehicles across the bridge. The speed of vehicles (8), track irregularities and dynamic characteristics both of bridge and vehicles are most important parameters for the investigation of bridges in vertical direction. Horizontal longitudinal forces cause quasi-static effects on bridges rather than dynamic ones while a stochastic spatial model of the bridge could explain the effect of horizontal lateral forces on railway bridges.

REFERENCES

1. C.E. INGLIS 1934 A Mathematical Treatise on Vibration in Railway Bridges. Cambridge: University Press
2. L. FRÝBA 1972 Vibration of Solids and Structures Under Moving Loads. Groningen: Noordhoff International Publishing
3. V. KOLOUŠEK 1973 Dynamics in Engineering Structures. London: Butterworths
4. ORE D 23 1955-1970 Determination of Dynamic Forces in Bridges. Utrecht, research reports No. 1-17
5. E. KAMKE 1956 Differentialgleichungen, Lösungsmethoden und Lösungen. I. Gewöhnliche Differentialgleichungen. 5. Auflage. Leipzig: Akademische Verlagsgesellschaft
6. E.S. SOROKIN 1960 To the Theory of Internal Friction in the Vibration of Elastic Systems. (in Russian). Moscow : Gosstrojizdat
7. L. FRÝBA 1976 Journal of Sound and Vibration 46, 323-338. Non-stationary response of a beam to a moving random force
8. R. IWANKIEWICZ and P. SNIADY 1984 Journal of Structural Mechanics 12, 13-26. Vibration of a beam under a random stream of moving forces
9. L. FRÝBA 1977 Acta Technica 22, 444-479. Stationary response of a beam to a moving continuous random load
10. L. FRÝBA 1980 Rail International 11, 573-598. Railway bridges subjected to traffic loads and their design for fatigue

11. L. FRYBA 1980 Journal of Sound and Vibration 70, 527-541. Estimation of fatigue life of railway bridges under traffic loads
12. ORE D 128 1973-1979 Statistical distribution of axle-loads and stresses in railway bridges. Utrecht, research reports No. 1-10
13. L. FRYBA 1974 Rail International 2, 698-716. Quasi-static distribution of braking and starting forces in rails and bridge
14. L. FRYBA 1973 Acta Technica 18, 54-68. Effect of a force moving at variable speed along a beam
15. L. FRYBA 1974 Acta Technica 19, 673-687. Response of a beam to a rolling mass in the presence of adhesion
16. V.Z. VLASOV 1959 Thin-Walled Elastic Beams (in Russian). 2-nd ed. Moscow: Fizmatgiz

TEXT TO FIGURES

Fig. 1 Natural frequency of railway bridges f_1 as a function of span l , mean value - solid line, f_1 95 % bounds of reliability - dashed lines

- 1 - steel truss bridges
- 2 - steel plate girder bridges with ballast
- 3 - steel plate girder bridges without ballast
- 4 - concrete bridges with ballast
- 5 - concrete bridges without ballast

Fig. 2 Logarithmic decrement of damping δ of steel railway bridges as a function of span l , mean value - solid line

- 1 - steel truss bridges
- 2 - steel plate bridges with ballast
- 3 - steel plate girder bridges without ballast

Fig. 3 Logarithmic decrement of damping δ of concrete railway bridges as a function of span l

- mean value - solid line
- 1 - concrete bridges with ballast
- 2 - concrete bridges without ballast

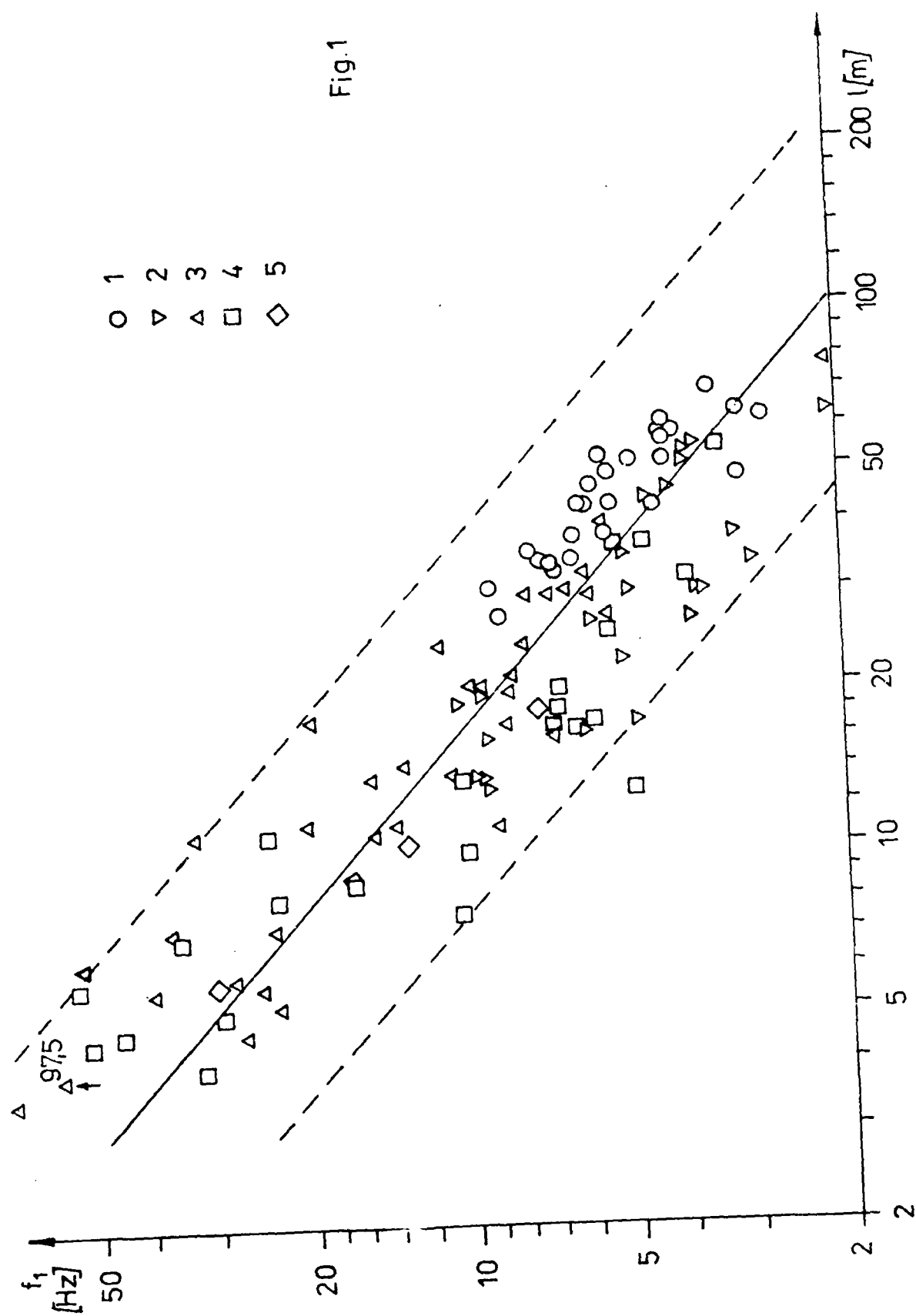


Fig.1

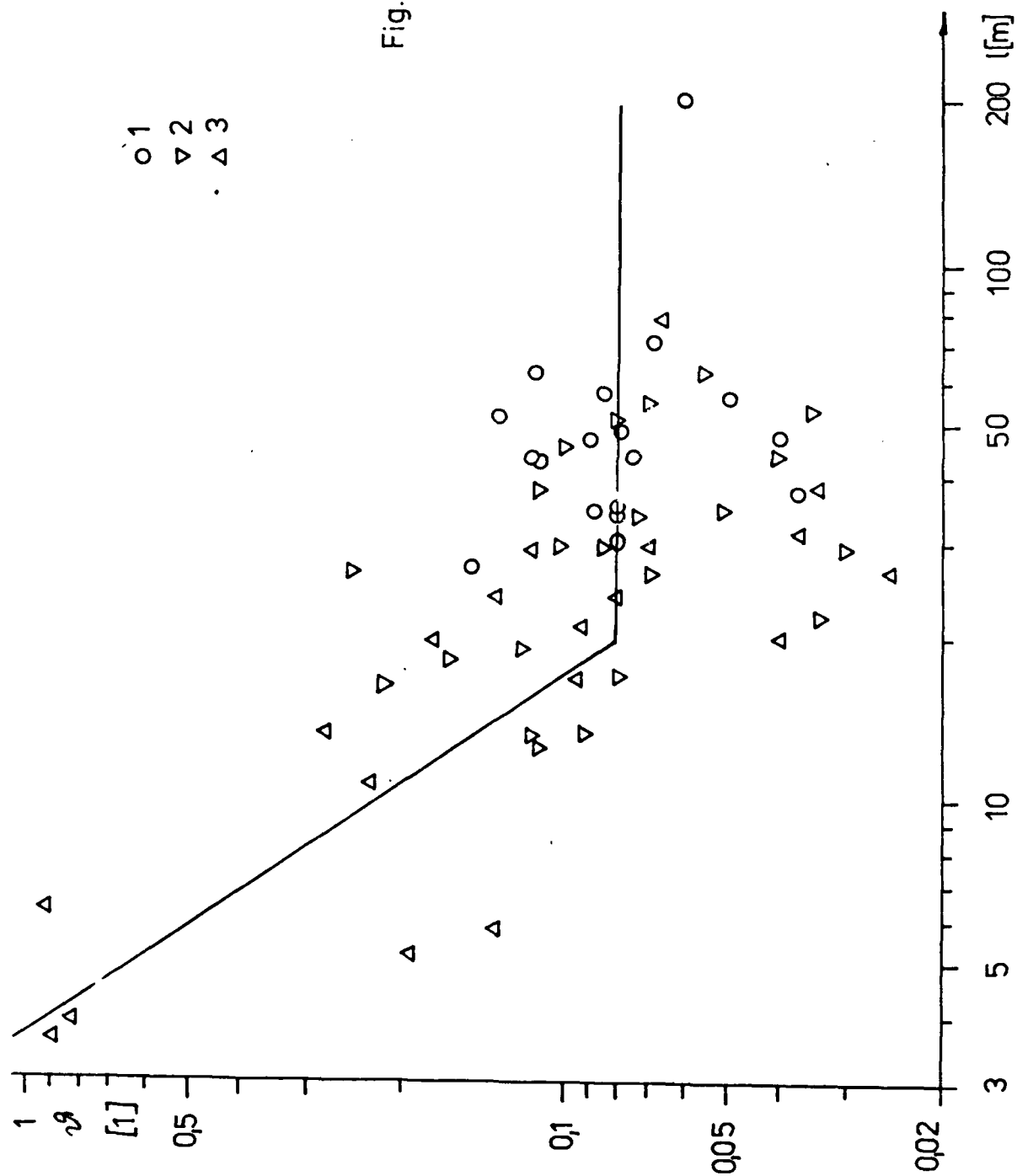


Fig.2

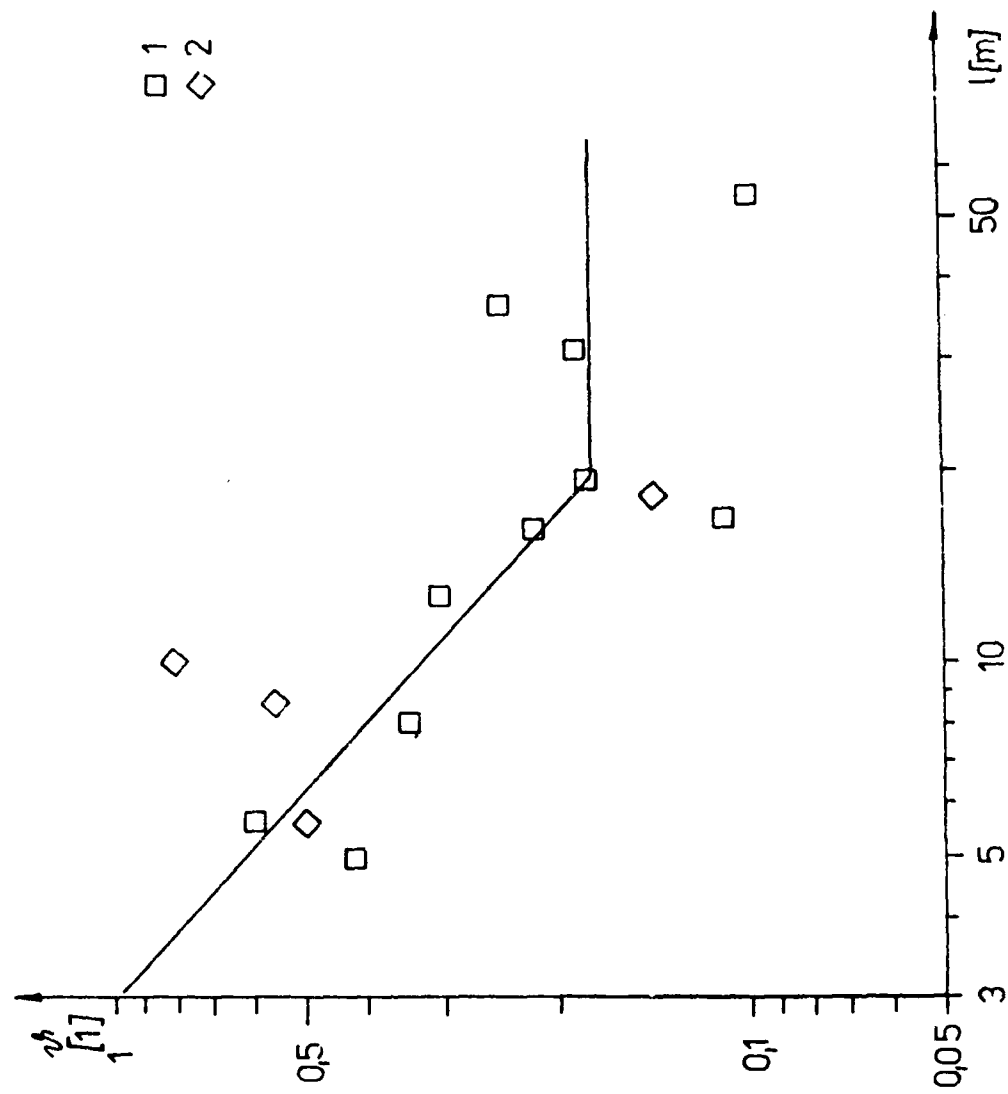


Fig. 3

DYNAMIC POST-BUCKLING BEHAVIOUR OF SLENDER WEBS

J. Ravinger

Institute of Building Constructions and Architecture
Slovak Academy of Sciences, 842 20 Bratislava, Czechoslovakia

1. INTRODUCTION

The slender web (thin plate) is the main construction element of a thin-walled structure. The detail knowledge of the behaviour of the slender web enables us to determine the load carrying capacity of the whole thin-walled structure more accurately. New computers give us a chance to solve theoretically more complicated problems. The geometrically non-linear theory is necessary to describe the post buckling behaviour of slender web. By including the inertia forces the problem can be extended into dynamics. The dynamic non-linear problems of the slender webs are well known in the aircraft constructions, but we can encounter them in other structures as well.

2. THEORETICAL ASSUMPTIONS

The total description /TLD/ is used, and according the von Kármán theory for the large deflections of the plates the strain vector is

$$\varepsilon = \begin{Bmatrix} u, x \\ v, y \\ u_y - v_x \end{Bmatrix} + \frac{1}{2} \begin{Bmatrix} w, x^2 \\ w, y^2 \\ 2w, x w, y \end{Bmatrix} - z \begin{Bmatrix} w, xx \\ w, yy \\ 2w, xy \end{Bmatrix} \quad (1)$$

where $u, v,$ are the functions of the in-plane displacements,
 w is the function of plate displacements.

In a harmony with the von Kármán theory (the plate displacements are much larger than in-plane displacements), we take into consideration the inertia forces acting only in the direction of the plate displacements. Then the inertia force per unit volume is

$$p_m = -\rho \frac{\partial^2 w}{\partial t^2} \quad (2)$$

where ρ is the mass per unit volume, t is the time.

2.1 SYSTEM OF CONDITIONAL EQUATIONS

Using the Hamilton's principle we have

$$-\int_{t_1}^{t_2} \delta(T - A + W) dt = 0. \quad (3)$$

The sum of the variations of the kinetic and potential energies and the variation of the non-conservative forces considered during any time interval t_1 to t_2 must be equal zero.

$$\begin{aligned}
T &= \frac{1}{2} \int_V \rho \dot{\underline{q}}^T \dot{\underline{q}} dV && \text{is the total kinetic energy of the system,} \\
A &= \frac{1}{2} \int_V (\underline{\varepsilon}^T - \underline{\varepsilon}_0^T) \underline{\sigma} dV && \text{is the potential energy of the system} \\
W &= \int_V (\underline{q}^T - \underline{q}_0^T) \underline{p} dV - \int_V c(\underline{q}^T - \underline{q}_0^T) \dot{\underline{q}} dV && \text{is the work of non-conservative forces,}
\end{aligned}$$

where

$$\begin{aligned}
\underline{q} &= \begin{Bmatrix} u \\ v \\ w \end{Bmatrix} && \text{are the functions of the displacements,} \\
\dot{\underline{q}} &&& \text{are the velocities of the displacements,} \\
\underline{p} &= \begin{Bmatrix} p_x \\ p_y \\ p_z \end{Bmatrix} && \text{are the external loads,}
\end{aligned}$$

$$\begin{aligned}
\underline{q}_0 &&& \text{are the functions of the initial displacements,} \\
\underline{\sigma} &&& \text{is the stress vector,} \\
V &&& \text{is the volume of the slender web,} \\
C &&& \text{is the damping coefficient,} \\
\underline{\varepsilon}_0 &&& \text{is the vector of initial strains.}
\end{aligned}$$

The variational assumptions for the displacements functions

$$\underline{q} = \begin{Bmatrix} u(x,y,t) \\ v(x,y,t) \\ w(x,y,t) \end{Bmatrix} = \begin{Bmatrix} q_S(x,y,t) \\ w(x,y,t) \end{Bmatrix} = \left[\frac{B_S(x,y)}{B_D(x,y)} \right] : \begin{Bmatrix} \alpha_S(t) \\ \alpha_D(t) \end{Bmatrix} \quad (4)$$

We suppose only the initial displacements in the directions of the plate displacements

$$\underline{q}_0 = \begin{Bmatrix} 0 \\ 0 \\ w_0 \end{Bmatrix} = B_D \underline{\alpha}_0$$

$$\begin{aligned}
B_D; B_S &&& \text{are the basic variational functions of the displacements;} \\
&&& \text{plate in-plane,} \\
\alpha_D; \alpha_S &&& \text{are the parameters of the displacements functions;} \\
&&& \text{plate, in-plane.}
\end{aligned}$$

Eq. (3) must be satisfy for time interval t_1 to t_2 and finally it leads to the system of conditional equations in the form

$$K_M \ddot{\underline{\alpha}}_D + K_C \dot{\underline{\alpha}}_D + (K_{LD} + K_{GD} + K_{GD0}) \underline{\alpha}_D + K_{DS} \underline{\alpha}_S = \underline{P}_D + \underline{P}_{D0} \quad (5a)$$

$$K_{SD} \underline{\alpha}_D + K_{LS} \underline{\alpha}_S = \underline{P}_S + \underline{P}_{S0} \quad (5b)$$

- K_M is the mass matrix,
 K_C is the damping matrix,
 K_{LD} is the linear stiffness matrix of the plate,
 K_{GD} is the geometrically non-linear stiffness matrix of the plate,
 K_{GDO} is the matrix of the increasing of the bending stiffness of the plate due to the initial displacements, non-linear part,
 K_{DS} is the non-linear stiffness matrix, the interaction between the plate and the in-plane displacements parameters,
 \underline{P}_D is the vector of the transform external load of the plate,
 \underline{P}_{DO} is the vector of the transform plate internal forces due to the initial displacements,
 K_{SD} is the non-linear stiffness matrix, the interaction between the in-plane and the plate displacements parameters,
 \underline{P}_S is the vector of the transform external load of the web /in-plane forces/,
 \underline{P}_{SO} is the vector of the transform in-plane internal due to the initial displacements.

The stiffness matrix of the web K_{LS} is linear and we can do the elimination of Eq. (5b).

$$\underline{\dot{\alpha}}_S = K_{LS}^{-1} (\underline{P}_S + \underline{P}_{SO} - K_{SD} \cdot \underline{\alpha}_D)$$

Putting this into Eq (5a) we have the final system of the conditional equations

$$\begin{aligned}
 K_{M-D} \ddot{\underline{\alpha}}_D + K_C \dot{\underline{\alpha}}_D + (K_{LD} + K_{GD} + K_{GDO} - K_{DS} \cdot K_{LS}^{-1} \cdot K_{SD}) \underline{\alpha}_D = \\
 = \underline{P}_D + \underline{P}_{DO} - K_{DS} \cdot K_{LS}^{-1} \cdot (\underline{P}_S + \underline{P}_{SO})
 \end{aligned} \quad (6)$$

This is the system of differential equations. The number of the differential equations is equal to the number of the plate displacements parameters.

3. NUMERICAL EXAMPLES

The rectangular slender web loaded in compression has been solved (Fig. 1). The combined Rayleigh-Ritz FEM has been used the - trigonometric functions for the approximation of the plate displacements; the rectangular elements with bicubical polynoms for the in-plane displacements.

The Newmark's method with the combination of Newton-Raphson iteration has been used for the solution of the differential equations Eq. (6).

3.1 THE LINEAR INCREASING IN LOAD IN TERMS OF TIME

We can introduce

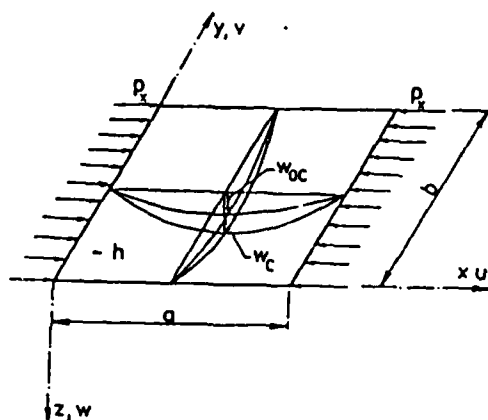
$$p_x = s \cdot t,$$

s is the velocity of the increase in the load,

$$S = p_{CR}^3 \left(\frac{\lambda \cdot c \cdot E \cdot h^3}{s \cdot b^4} \right)^2 \quad \text{is the parameter of the dynamic buckling of the slender web.} \quad (7)$$

$$c = \sqrt{\frac{E}{\rho}}; \quad \bar{a} = \frac{a}{h}; \quad \bar{a}_0 = \frac{a_0}{h}; \quad \lambda = \frac{a}{b}; \quad \bar{t} = \frac{s \cdot t}{P_{CR}}$$

$\bar{P}_{CR} = \frac{P_{CR}}{E} \left(\frac{b}{h}\right)^2$ is the elastic critical load of the slender web in compression.



$$\left(\frac{\partial u}{\partial y} = 0\right)_{x=0} \\ x=a$$

Fig. 1.
Slender web loaded
in compression

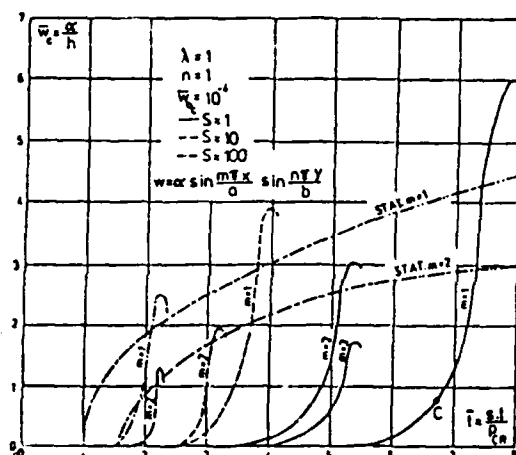


Fig. 2 Dynamic buckling of
slender web for different
forms of buckling surface

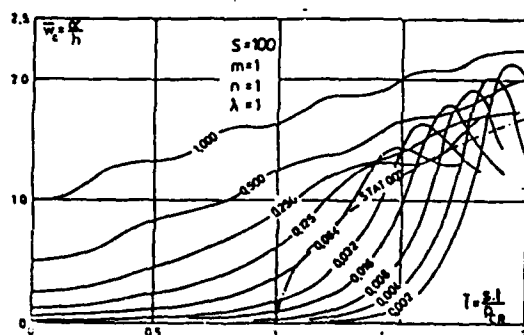


Fig. 3 Dynamic buckling of
slender web for different
values of initial displacements

Results in Figs. 2 and 3 enable us to do the following comments.

We can see that the slenderness ratio a/h or b/h , which is a suitable parameter for a description of the post-buckling behaviour of a slender web under a static load, is not sufficient in dynamic. As a suitable equivalent parameter we can take the parameter of dynamic buckling of a slender web

Eq.(7), but we can see that here Young's modulus, the dimensions of the slender web and the velocity of the increase in the load are introduced in a non-linear form.

Fig. 2 shows an interesting result in which, for a small value of the parameter of dynamic buckling and for a small value of the initial displacements, we see that buckling in the form of two or more waves occurs earlier than the trivial one-wave buckling associated with the static case.

One of the ways to investigate the dynamic buckling of a slender web is the introduction of "a dynamic critical load". For a web with a small initial displacement, we can observe that intensive buckling starts at a certain level of the load, (see point C in Fig. 2). This load is called "the dynamic critical load", and, dividing it by the elastic critical load, we get "the coefficient of dynamic critical load". The fact that the dynamic critical load is higher than the static one can be utilized only in some special structures or mechanisms, where the regime of the load and other circumstances are exactly defined. This is impossible to satisfy in such steel structures as bridges, towers and so on. Here, for example, if we have a high velocity of the increase in load, we are bound to suppose a slow velocity as well, and such a load would be worse in this "concept". It means that we must try to find some other way to study this problem. One detail can help us. If we evaluate the parameter of dynamic buckling (Eq.(7)) for a real variety of the properties and dimensions of steel structures, we can see that the values of this parameter are large in most cases more than 100. If moreover, we take in to consideration that ordinary steel structures always exhibit some initial imperfections (the influence of initial displacements is shown in Fig. 3), we can see that the dynamic post-buckling effect can be considerable only under rare conditions. But anyhow, the presented theory and results enable us to carry out a description of this problem and to find the conditions for a characterization of the "demarcation line" between the static and the dynamic buckling.

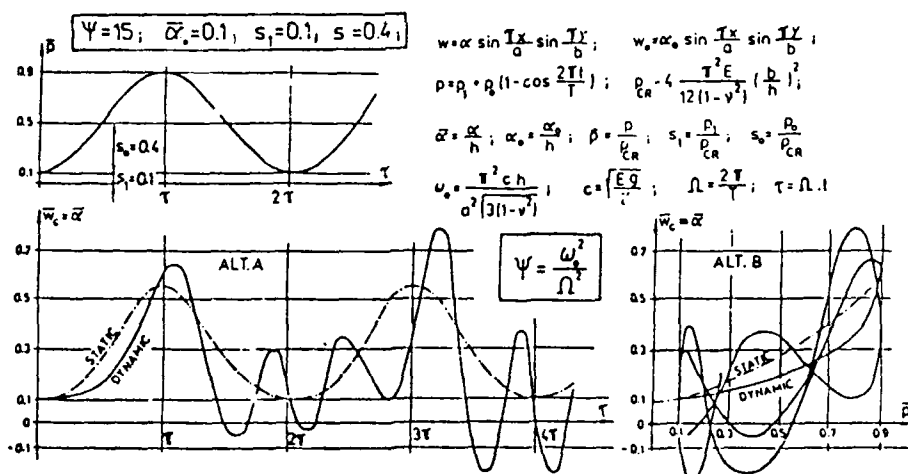


Fig. 4 Behaviour of slender web under harmonic load

3.2 THE HARMONIC LOAD

As the external load is supposed in the following form:

$$p_x = p_1 - p_0 (1 - \cos \Omega t)$$

$$\omega_0 = \frac{\pi^2 c h}{a^2 \sqrt{3(1 - \nu^2)}} \quad \text{is the circular frequency of free vibrations of a slender web,}$$

$$\psi = \frac{\omega_0^2}{\Omega^2} \quad \text{is the frequency ratio,}$$

$$\Omega = \frac{2\pi}{T} \quad \text{is the circular frequency of the applied load.}$$

If in the obtained equations the cubic term α^3 and the terms of the initial displacements are neglected we have the Mathieu differential equations; and in the Ince-Strutt diagram we can determinate the conditions for the parametric resonance.

Bolotin [5] and Volmir [6] determined the limits of the parametric resonance for the non-linear system (Eq.(6)), but without taking account of the initial displacement terms, and they showed that the amplitudes were limited even in the case of the parametric resonance.

We used the following way: Eq.(6) was solved with all terms. The initial conditions were given by zero acceleration and zero velocity. Fig. 4 shows two ways of expressing the results and also the notations of the parameters involved. For ordinary steel structures, similarly to the previous case of a linear increase in load in terms of time, an interesting problem is to follow the conditions for the origin of the non-linear dynamic effects. Accordingly, the alternative B is used to express the results. Here, the relationship between displacements and load is shown, as it is usual in the case of a static load. The dispersion around the lines characterize the dynamic effects.

The obtained results (Figs. 5-9) enable us to draw some conclusions.

The displacements in the dynamic solutions are highly influenced by the initial displacements.

As the main parameter, we can use the frequency ratio. For large values of this parameter, the dynamic solution converges to the static one.

When we change the frequency of the applied load through the limit points for the parametric resonance (from the Ince-Strutt diagram for the non-linear systems [5]), this does not display an increase in obtained amplitudes. This could mean that the full non-linear problem of the dynamic regime of the post buckling behaviour of the slender web studied does not lead to parametric resonance.

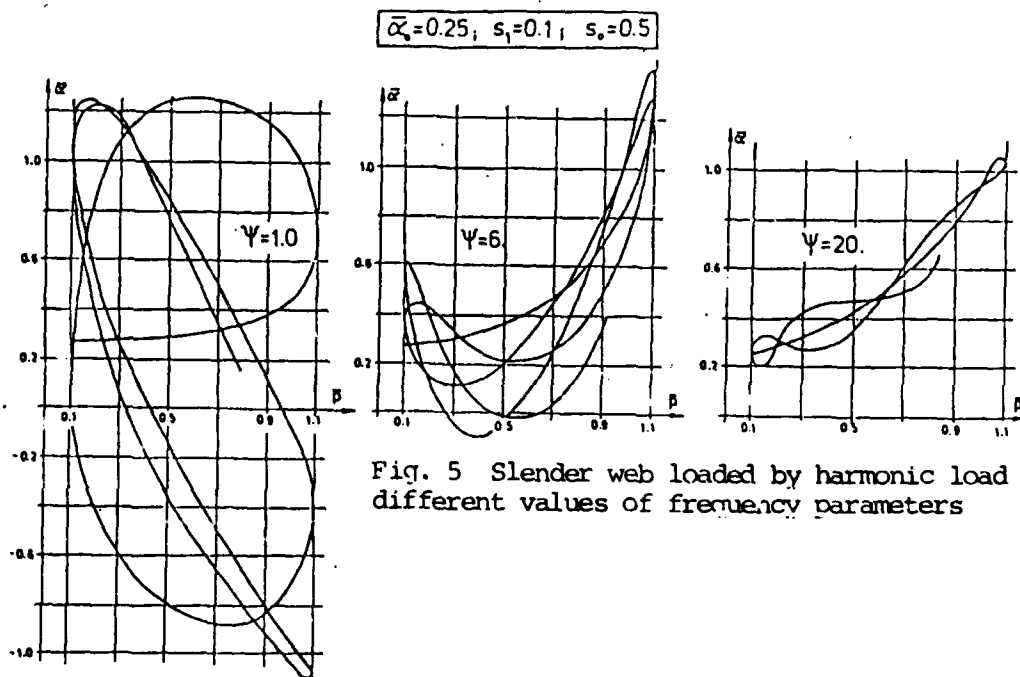
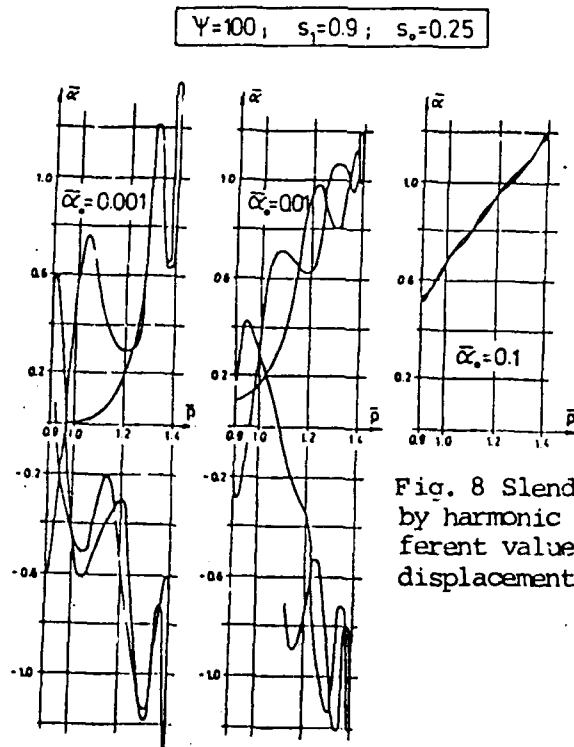
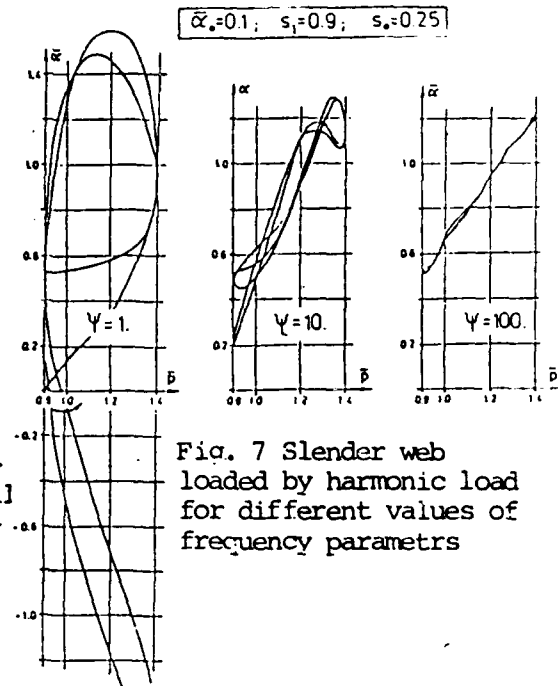
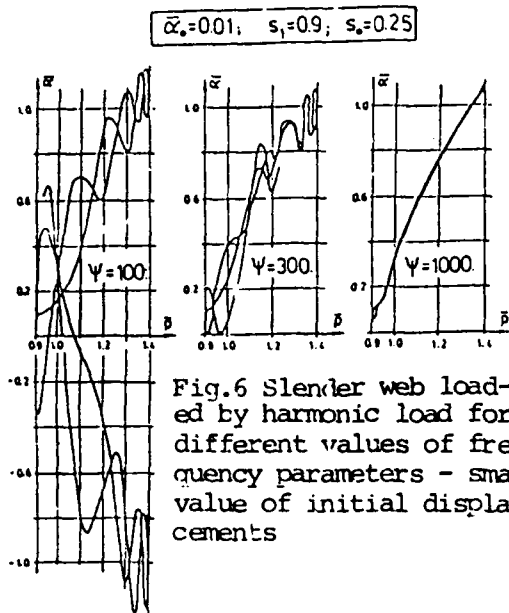


Fig. 5 Slender web loaded by harmonic load for different values of frequency parameters



Note: The linearized Mathieu equation was solved in the same way and the limits /areas/ of the parametric resonance according to the Ince-Strutt diagram were proved. This means that, for conditions where the parametric resonance was expected, the solutions gave, after some cycles of the applied load, amplitudes increasing very quickly to infinity while for conditions where the parametric resonance was not expected the amplitudes were settled.

The above interesting, but not surprising, results are shown in Figs. 6-8, where for small values of the initial displacements and after some applied load cycles, we can obtain dynamic deformations on the opposite side than is the case for the static solution.

The peculiarities of the non-linear problem of dynamic post-buckling behaviour can be demonstrated even through a simple comparison. For example, for a frequency ratio $\psi = 15$ and for a linear single degree of freedom, the dynamic magnification factor is $w_{\max}/w_{\text{STAT}} = \psi/(\psi - 1) = 1.07$. Fig. 4 shows that for the non-linear problem this value is much larger.

$$\Psi=10; \bar{\alpha}_0=0.25; s_1=0.1; s_0=0.5$$

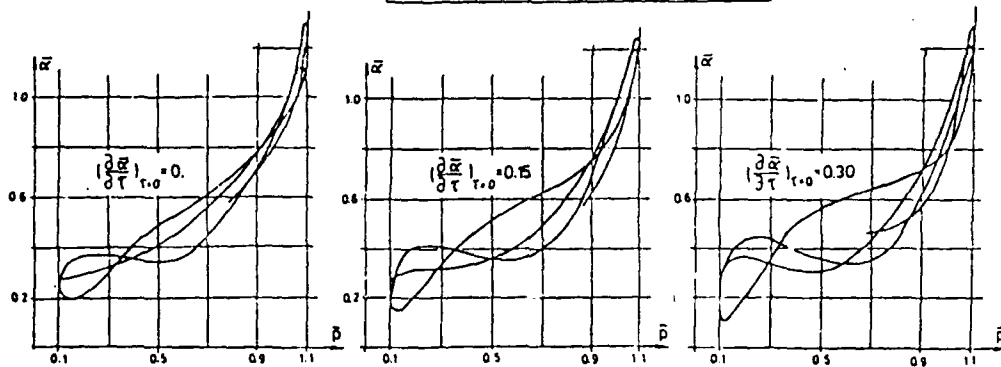


Fig. 9 Slender web loaded by harmonic load for different values of initial velocity

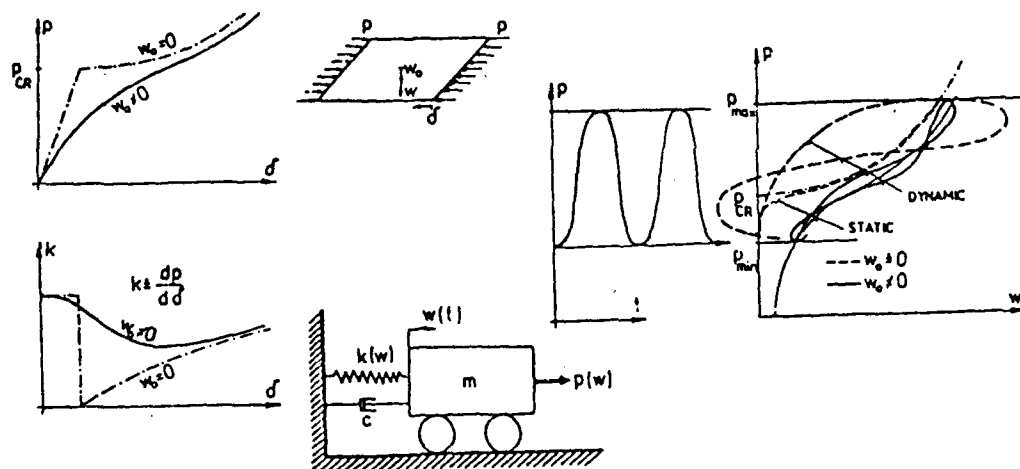


Fig. 10 Dynamic post-buckling of slender web as model of single degree of freedom

4. CONCLUSIONS

Fig. 10 shows the approximate explanation of the behaviour of the slender web under the dynamic load as the model of the single degree of freedom. We can see that the stiffness of the spring is highly influenced by the initial imperfection. The discontinuity in the stiffness of the spring for the ideal plate can arrange the conditions for an arise the high non-linear dynamic effects. It means that the slender web with the initial imperfection is less sensitive for non-linear dynamic effects as the ideal plate. The non-linear dynamics of slender webs are very extensive problems. This article deals only with one part of them. The present theory and the results show the main ideals about the baheviour of the slender webs under the dynamic load.

REFERENCES

1. J. RAVINGER, 1987 ACTA TECHNICA ČSAV No.1, 36-59. Dynamic Post-buckling Behaviour of Slender Webs.
2. J. RAVINGER, 1983 Journal of Constructional Steel Research, Vol.3, No.2, 14-22. Girders with Unstiffened Slender Webs.
3. R.M. CALLAGHER, 1970 Int. Journal Computer and Structures, Vol.3, The Finite Element Method in Shell Stability Analysis.
4. S. SYIGAL and T.Y. YANG, 1985 Int. Journal for Numerical Methods in Engineering, Vol.21, 1115-1128. Non-Linear Dynamic Analysis with 48 D.O.F Curved Thin Shell Element.
5. V.V. BOLOTIN, 1956 Dynamic Stability of Elastic Systems. Moskva: GITTL /in Russian/.
6. A.S. VOLMIR, 1972 Non-Linear Dynamic of Plates and Shells. Moskva, Nauka /in Russian/.
7. K.J. BATHE, 1982 Finite Element Procedure in Engineering Analysis. New Jersey: Prentice Hill.

Zhou Hong-jun Wang Fu-ming Li Qing-bin

Zhengzhou Institute of Technology, Zhengzhou P. R. China

ABSTRACT

Based on the theory of shells and variational principles, a semianalytic method which is used to analyse the dynamic characteristics of thin arch dams is developed in the paper. The form of the displacement function is given as a product of the cubic B-spline function and a series which is derived from the solution of the beam vibration differential equation and suitably transformed. The technique of calculating the total potential energy of each strip has been adopted when the energy theorem is applied.

The method retains to some extent the versatility of the finite element method. Compared with the finite element method and other numerical method, the computational effort and core requirement are drastically reduced. Since the order of the eigenvalue equations solved by this method is around 14, it can conveniently be carried out on a packet computer, such as PC-1500. Two examples are presented.

1. INTRODUCTION

The dynamic analysis and anti-earthquake design of arch dams is of great importance in hydro-electric engineering. However, for such irregular shells, the work is rather complicated and at present, it mainly relies on the finite element method with heavy computational work and expensive cost of solutions. In this paper, a simple method is developed, which is based on the spline finite point method and applicable to the dynamic analysis of thin arch dams. Since the order of the eigenvalue equations solved by the present method is only around 14, it can conveniently be carried out on a packet computer, such as PC 1500. But the order by finite element method is generally over 300. And, the results of examples obtained by both methods indicated desired agreement. Therefore the present method is evidently an alternative tool for the thin arch dams.

2. FUNDAMENTALS

In this present study for dynamic analysis the following assumption are used;

- (1) the body of arch dam is considered as a linear elastic material;
- (2) the foundation is treated as rigid body;
- (3) the vertical displacement $u=0$;
- (4) the effect of damping is not considered.

For free vibration, the displacement functions of the arch dam in the y and the Z directions can be written as,

$$\{\delta\}_t = \{\delta\} \cos(\omega t + \varphi) \quad (1)$$

$$\text{in which } \{\delta\} = [v \quad w]^T \quad (2)$$

$$V = \sum_{m=1}^M [\phi^T]_m Y_m(b) \quad (3)$$

$$W = \sum_{m=1}^M [\phi]_m Z_m(c) \quad (4)$$

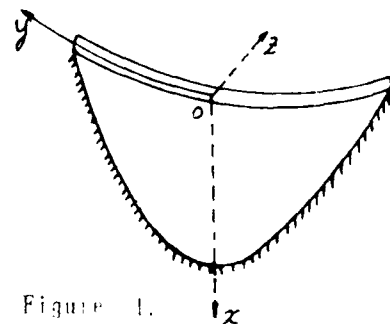


Figure 1.

$$\{\Phi\} = [\Phi_{-1}, \Phi_0, \Phi_1, \dots, \Phi_{N-1}]$$

$$\{b\} = [b_{-1}, b_0, b_1, \dots, b_{N-1}]^T$$

$$\{c\} = [c_{-1}, c_0, c_1, \dots, c_{N-1}]^T$$

where b_i, c_i are the parameters of the spline nodes.

$\Phi_i = \Phi_i(x)$ is the basic function of cubic B-spline with nodes at x_i for N equal division in the interval $[0, H]$.

$$0 = x_0 < x_1 < x_2 < \dots < x_N, \quad x_i = ih, \quad h = \frac{H}{N}$$

$$\Phi_{-1}(x) = \Phi_1\left(\frac{x}{h} + 1\right),$$

$$\Phi_0(x) = \Phi_1\left(\frac{x}{h}\right) - 4\Phi_1\left(\frac{x}{h} + 1\right),$$

$$\Phi_1(x) = \Phi_1\left(\frac{x}{h} + 1\right) - \frac{1}{2}\Phi_1\left(\frac{x}{h}\right) + \Phi_1\left(\frac{x}{h} - 1\right),$$

$$\Phi_2(x) = \Phi_1\left(\frac{x}{h} - 2\right),$$

.....

$$\Phi_i(x) = \Phi_1\left(\frac{x}{h} - i\right),$$

.....

$$\Phi_{N-2}(x) = \Phi_1\left(\frac{x}{h} - N + 2\right),$$

$$\Phi_{N-1}(x) = \Phi_1\left(\frac{x}{h} - N + 1\right) - \frac{1}{2}\Phi_1\left(\frac{x}{h} - n\right) + \Phi_1\left(\frac{x}{h} - N + 1\right),$$

The basic functions satisfy the following conditions,

$$x = H, \quad \Phi_i(x) = 0, \quad \Phi_i(x) = 0.$$

Y_m, Z_m are the following orthogonal functions,

$$Y_m = Y_m(y) = \begin{cases} \sin \frac{(m+1)\pi [y+b(k)]}{2b(k)} - \sin \frac{(m-1)\pi [y+b(k)]}{2b(k)}; & m=2, \\ \sin \frac{(m+1)\pi [y+b(k)]}{2b(k)}; & m=1, 2, 3, \dots, M. \end{cases} \quad (5)$$

$$Z_m = Z_m(y) = \sin \frac{\mu_m [y+b(k)]}{2b(k)} - \text{sh} \frac{\mu_m [y+b(k)]}{2b(k)} - \alpha_m \left(\cos \frac{\mu_m [y+b(k)]}{2b(k)} - \text{ch} \frac{\mu_m [y+b(k)]}{2b(k)} \right)$$

$$\alpha_m = \frac{\sin \mu_m - \text{sh} \mu_m}{\cos \mu_m - \text{ch} \mu_m}, \quad \mu_m = \frac{(2m+1)\pi}{2}, \quad m=1, 2, \dots, M. \quad (6)$$

If the foundation of the arch dam is supposed to be rigid, or the dam is somehow lengthened to consider the elasticity of the foundation, the displacement boundary conditions of the dam have been satisfied by (3) and (4). Furthermore, when m is equal to 1, 3, 5, and 2, 4, 6, the symmetrical and unsymmetrical modal shapes are expressed respectively.

3. DYNAMIC EQUATIONS

According to the theory of elastic thin shell, the total potential energy of the thin arch dam can be written as,

$$\Pi = \frac{\pi}{2\omega} \int_S \{ (\epsilon)^T [J] (\epsilon) + (x)^T [D] (x) - \bar{m} \omega^2 \{ \delta \}^T \{ \delta \} \} ds \quad (7)$$

where $\{ \epsilon \} = \{ \epsilon_x \quad \epsilon_y \quad \epsilon_{xy} \}^T$

$$(x) = \left[-\frac{\partial^2 w}{\partial x^2} \quad -\frac{\partial^2 w}{\partial y^2} \quad -2\frac{\partial^2 w}{\partial x \partial y} \right]^T$$

$$[J] = J \begin{bmatrix} 1 & \mu & 0 \\ \mu & 1 & 0 \\ 0 & 0 & 1-2(1-\mu) \end{bmatrix}, \quad J = \frac{Et}{1-\mu^2}$$

$$[D] = D \begin{bmatrix} 1 & \mu & 0 \\ \mu & 1 & 0 \\ 0 & 0 & 1-2(1-\mu) \end{bmatrix}, \quad D = \frac{Et^3}{12(1-\mu^2)}$$

J - area of middle surface of arch dam;

\bar{m} - mass per unit area arch dam;

ω - natural frequency of arch dam.

In order to simplify the calculation, we divide the dam into N strips at spline nodes, and calculate separately the total potential energy of each strip which is approximated by a rectangular strip with the average length $2b(k)$. Then, the total potential energy of the whole dam is given as the sum. Thus, for k th strip,

$$\Pi_k = \frac{\pi}{2\omega} \int_{(k-1)h}^{kh} \int_{-b(k)}^{b(k)} \{ (\epsilon)^T [J] (\epsilon) + (x)^T [D] (x) - \bar{m} \omega^2 \{ \delta \}^T \{ \delta \} \} dy dx \quad (8)$$

and for the whole dam,

$$\Pi = \sum_{k=1}^N \Pi_k = \frac{\pi}{2\omega} \sum_{k=1}^N \int_{(k-1)h}^{kh} \int_{-b(k)}^{b(k)} \{ (\epsilon)^T [J] (\epsilon) + (x)^T [D] (x) - \bar{m} \omega^2 \{ \delta \}^T \{ \delta \} \} dy dx \quad (9)$$

According to Hamilton's principle $\Pi=0$, we obtain the eigenvalue equations. Because of the orthogonal property of functions (5) and (6) each term of the series can be analysed separately. Thus the eigenvalue equations take the form of

$$[G]_m \{r\}_m = \omega^2 [M]_m \{r\}_m \quad m=1, 2, \dots, M \quad (10)$$

in which $\{r\}_m = \{ \{b\}_m^T \quad \{c\}_m^T \}^T$

$$[G]_m = \begin{bmatrix} [G]_{bh} & [G]_{bc} \\ [G]_{cb} & [G]_{cc} \end{bmatrix} \quad (11)$$

$$\begin{aligned}
[G]_{bb} &= J \sum_{k=1}^N (C_y^k [F_x^k] + \frac{1}{2} (1 - \mu) F_y^k [C_x^k]) \\
[G]_{bc} &= -J \sum_{k=1}^N (\mu K_1 + K_2) H_{zy}^k [F_x^k], \quad [G]_{cb} = [G]_{bc}^T \\
[G]_{cc} &= J \sum_{k=1}^N (K_1^2 + 2\mu K_1 K_2 + K_2^2) [F_x^k] + [G]_0 \\
[G]_0 &= D \sum_{k=1}^N \{ F_z^k [A_x^k] + \mu B_z^k ([B_x^k] + [B_x^k]^T) + 2(1-\mu) C_z^k [C_x^k] + A_z^k [F_x^k] \}
\end{aligned} \tag{12}$$

$$[M]_m = \begin{bmatrix} [M]_b & 0 \\ 0 & [M]_c \end{bmatrix} \tag{13}$$

$$\begin{aligned}
[M]_b &= \bar{m} \sum_{k=1}^N F_y^k [F_x^k] \\
[M]_c &= \bar{m} \sum_{k=1}^N F_z^k [F_x^k]
\end{aligned} \tag{14}$$

$[A_x^k]$, $[B_x^k]$, $[C_x^k]$, $[F_x^k]$ ($k=1, 2, \dots, N$) are the following matrices,

$$\begin{aligned}
[A_x^k] &= \int_{(k-1)h}^{kh} (\phi'')^T [\phi''] dx, & [B_x^k] &= \int_{(k-1)h}^{kh} [\phi']^T [\phi''] dx \\
[C_x^k] &= \int_{(k-1)h}^{kh} (\phi')^T [\phi'] dx, & [F_x^k] &= \int_{(k-1)h}^{kh} [\phi']^T [\phi] dx
\end{aligned} \tag{15}$$

In accordance with the compactness of spline function, each above matrices contains only a forth-order nonzero submatrix and the rest elements are equal to zero.

For application we have worked out the matrices $[A_x^k]$, $[B_x^k]$, $[C_x^k]$ and $[F_x^k]$.

$$\begin{aligned}
A_z^k &= \int_{-b(x)}^{\bar{b}(x)} Z''_m Z''_m dy & B_z^k &= \int_{-b(x)}^{\bar{b}(x)} Z''_m Z''_m dy \\
C_z^k &= \int_{-b(x)}^{\bar{b}(x)} Z'_m Z'_m dy & F_z^k &= \int_{-b(x)}^{\bar{b}(x)} Z'_m Z'_m dy \\
C_y^k &= \int_{-b(x)}^{\bar{b}(x)} Y'_m Y'_m dy & F_y^k &= \int_{-b(x)}^{\bar{b}(x)} Y'_m Y'_m dy \\
H_{zy}^k &= \int_{-b(x)}^{\bar{b}(x)} Z'_m Z'_m dy
\end{aligned} \tag{16}$$

The above coefficients can be found in refence.

K_1 and K_2 are the curvities of arch dam along the x-axis and y-axis. For cylindrical arch dam $K_1 = 0$, $K_2 = 1/R$. For the hyperbotical arch dam K_1 and K_2 are approximate to average curvities of each strip $K_1(x)$ and $K_2(x)$ respectively.

For the variable thickness arch dam, each striip is approximated by a constant thickness strip $\bar{t}(K)$, the striffness matrix $[G]$ and the mass matrix $[M]$ need to be managed appropriately, J , D and \bar{m} express in term of $\frac{E\bar{t}(k)}{1-\mu^2}$, $\frac{E\bar{t}(k)^3}{12(1-\mu)}$ and $\rho \bar{t}(k)$ separately.

When the eigenvaue equations (10) are sloved, the natural frequencies and modal shapes of the arch dam are obtained.

4. NUMERICAL EXAMPLES

Two thin arch dam have been analysed on the pocketcomputer PC 1500.

The first one is a cylindrical arch dam in Britain, as shown in Fig. 2. and its dynamic characteristic has been studied by a number of researchers. By the present method, the dam is divided into 6 and 10 strips, and the order of the eigenvalue equations is 14 and 22 respectively. The results are listed in Tab.1.

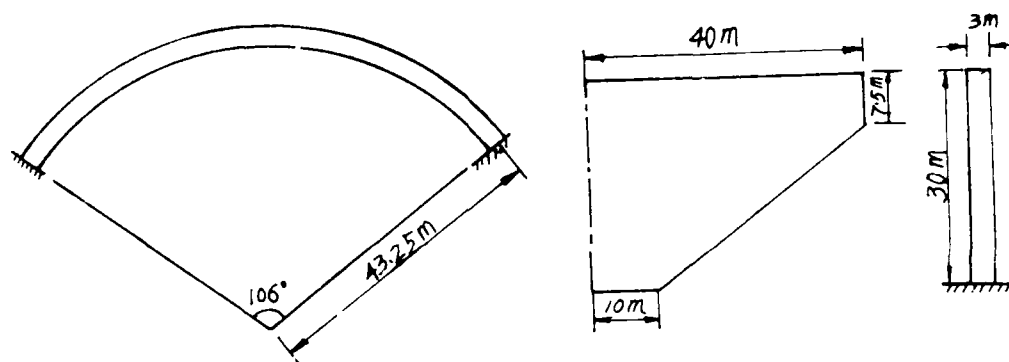


Figure 2.

Table 1. Natural frequencies of cylindrical arch dam with constant thickness

Modal number	1	2	3	4	5	6
Finite element method [3]	9.64	9.84*	14.05*	18.37*	18.56	24.81
Reference [4]	9.46	10.09*	13.42*	16.56	18.35*	21.95
Present method	N = 6	10.03	11.43*	14.88*	17.67	20.16
	N = 10	9.95	11.42*	14.80*	17.64*	20.10

Note, $E = 30000\text{MPa}$,

* -- Symmetric mode shapes.

The first six mode shapes of arch dam are plotted in Figure 3.

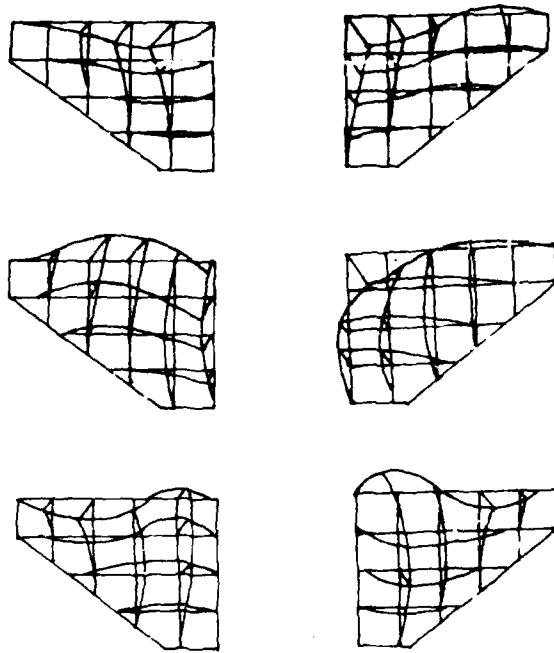


Figure 3.

The second example is a cylindrical arch dam with variable thickness. It is divided into 6 strips. The first six natural frequencies and modal shapes when compared with those obtained by the finite element analysis indicate excellent agreement. These results are tabulated in Table 2.

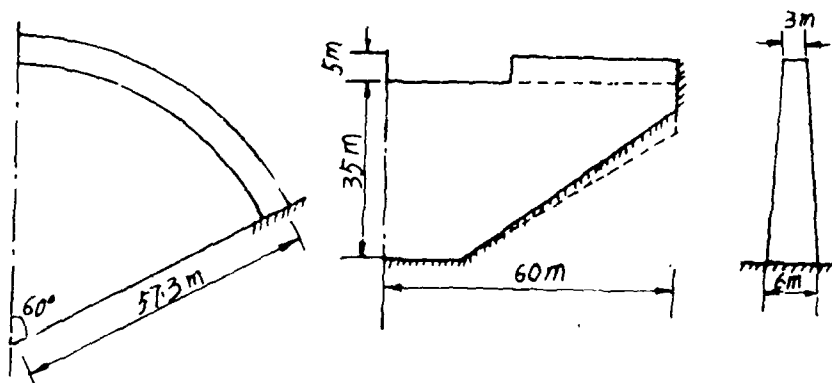


Figure 4.

Table 2. Natural frequencies of cylindrical arch dam with variable thickness.

Modal number	1	2	3	4	5
Mode shapes	AS	S	S	AS	S
Finite element method [5]	6.916	7.564	8.953	11.696	14.663
Present method ($N = 6$)	6.793	7.407	9.186	11.715	14.210

S -- Symmetric modes, AS -- antisymmetric.

5. CONCLUSION

The semi-analytic method applicable to the dynamic analysis of thin arch dams is developed in this paper. The computational effort and core requirement are rather small, and the results possess the ideal accuracy. Since it can be conveniently and economically carried out on a pocket computer, and a number of arch dams can be analysed in a short period, the method is evidently desirable for the systematic study of the dynamic characteristics of thin arch dams.

REFERENCES

1. QIN RONG 1982 Fundamentals and Applications of Spline Finite Point Method, Proceeding of the International Conference on Finite Element Method.
2. Y. K. CHEUNG 1976 Finite Strip Method in Structural Analysis, Pergamon Press.
3. DUNGAR, R., SEVERN, R.T., TAYLAR, P. 1967 Ninth international Congress on Large Dams.
4. LIN GAO, LOU MENG-LIN, SUN KE-MING 1983 Journal of Dalian Institute of Technology, No. 4. Dynamic Analysis of Arch Dams Through Mode Functions of Arch and Cantilever Elements.
5. LI ZHAN-MEI 1982 Design of Arch Dams, Water Resources and Electric Power Press, Beijing, China.

EFFECT OF THE GRADIENT OF ELASTIC ECCENTRICITY ON
THE LATERAL-TORSIONAL EFFECTIVE EARTHQUAKE
FORCES ON BUILDING SYSTEMS

L. A. de Béjar

Department of Civil Engineering
Louisiana State University
Baton Rouge, LA 70803, USA

1. INTRODUCTION

The results of a series of parametric studies on the variation of effective earthquake story lateral forces and story torques with the gradient of elastic eccentricity along building heights are described, suggesting the relevance of such consideration during the design phase of building systems.

This investigation leans on the efficiency of a previously developed simple mathematical model representing the full three-dimensional linear-elastic behavior of multistory building systems with rigid-body horizontal floors, being subjected to multicomponent earthquake excitations [2,3]. However, only the response of the lateral-torsional (L-T) elastic system of resistance is within the scope of the present report.

The model is believed to represent a notable improvement over other available idealizations [5] for the following reasons: (1) the centers of gravity of different story floors are not required to be aligned on a single vertical axis, (2) the principal directions of inertia of different story floors are not required to coincide, and (3) the lateral-torsional principal directions of rigidity of the various stories are not required to coincide. Thus, the resulting algorithm has a much wider range of applications.

The displacement response of the lateral-torsional system of the total building is described by a $3N$ -component vector. The first N components represent the first L-T principal rigidity coordinates of individual stories grouped together in sequence. The following N components represent the second L-T principal rigidity coordinates of individual stories grouped together in sequence. The last N components represent the torsional principal rigidity coordinates of individual stories grouped together in sequence, as well. The equations of motion of the building are referred to those coordinates. Therefore, the principal directions of inertia are determined for individual stories and the corresponding mass properties are transformed accordingly.

The structural dynamic characteristics are obtained by perturbing the eigenproblem of the corresponding two-fold symmetric building system. The procedure to generate building eigenproperties is simplified even further for an important class of buildings--those exhibiting stiffness similarity among stories.

Mathematical expressions for the dynamic natural properties of the structure are also derived with reference to the principal rigidity coordi-

nates. This formulation allows easy monitoring of the internal element force response during dynamic response.

2. SYSTEM STIFFNESS MATRIX

The system stiffness is given by the coefficient matrix in the analytical expression for the elastic resisting forces

$$\{F_s^{CR}\} = [K_{LT}] \{D^{CR}\} \quad (1)$$

with

$$[K_{LT}] = \begin{bmatrix} [K_{11}] & [K_{12}] & [K_{16}] \\ & [K_{22}] & [K_{26}] \\ \text{SYMM.} & & [K_{66}] \end{bmatrix} \quad (2)$$

where each matrix $[K_{ij}]$ is tridiagonal of order N . Mathematical closed-form expressions for these component matrices are derived elsewhere [2,3], and allow efficient completion of the analytical construction of the building stiffness matrix, without incurring the standard assembly process.

3. SYSTEM MASS MATRIX

The unassembled mass matrix for story (1), transformed into the story principal-rigidity-coordinate system of reference, has been derived in previous work [2]:

$$[M^{CR}]^{(1)} = m_1 [\tilde{M}_{LT}] \quad (3)$$

The building system mass matrix is synthesized by directly assembling the individual unassembled matrices of the different stories [1-4] to obtain

$$[M^{CR}] = \begin{bmatrix} [M_{11}] & [M_{12}] & [M_{16}] \\ & [M_{22}] & [M_{26}] \\ & & [M_{66}] \end{bmatrix} \quad (4)$$

where $[M_{ij}] = [M] \cdot [\tilde{M}_{ij}]$, $[M]$ is a diagonal matrix containing the lumped masses of individual stories: $m_1, m_2, m_3, \dots, m_N$; and, $[\tilde{M}_{ij}]$ are non-dimensional diagonal matrices.

4. EIGENPROBLEM

After the system eigenproblem is homogenized and normalized, it may be subjected to a perturbation technique, if the building constitutes a small deviation from the associated two-fold symmetric building system [2,3,5-7].

For the lateral-torsional system, the corresponding eigens may be expressed as

$$\lambda_L^K = \lambda_L^{*K} + \alpha_{KK} + \sum_{i \neq K} \frac{\alpha_{iK} \alpha_{Ki}}{(\lambda_L^{*K} - \lambda_L^{*i})} \quad (2nd \text{ order}) \quad (5)$$

$$\phi_{LK} = \phi_{LK}^* + \sum_{i \neq K} \frac{\alpha_{iK}}{(\lambda_L^{*K} - \lambda_L^{*i})} \cdot \phi_{Li}^* \quad (1st \text{ order}) \quad (6)$$

where

$$\alpha_{iK} = F_{\phi_{Lm}}^{*T} \cdot E_L^{pq} \cdot \phi_{Ln}^* \quad (7)$$

$$p = (i + N - 1) \text{ int } N \quad ; \quad q = (K + N - 1) \text{ int } N$$

$$m = [(i-1) \bmod N] + 1 \quad ; \quad n = [(K-1) \bmod N] + 1$$

$$\text{int} = \text{integer division} \quad ; \quad \text{mod: modulo arithmetic} \quad (8)$$

$$E_L^{pq} = \text{error matrix,}$$

and terms superscripted with the symbol * refer to the associated two-fold symmetric building.

Equation (6) can be transformed into [2,3,5,6]

$$\phi_{LK} = \begin{Bmatrix} \eta_1 \cdot \phi_{LK}^* \\ \eta_2 \cdot \phi_{LK}^* \\ \eta_6 \cdot \phi_{LK}^* \end{Bmatrix} \quad ; \quad K = 1 \dots N \text{ and } 3N \text{ sets of constants } \langle \eta_1, \eta_2, \eta_6 \rangle \quad (9)$$

and, for the particular class of buildings exhibiting geometric similarity among stories

$$\phi_{LK} = \begin{Bmatrix} \eta_1 \cdot \phi_{LK}^* \\ \eta_2 \cdot \phi_{LK}^* \\ \eta_6 \cdot \phi_{LK}^* \end{Bmatrix} \quad ; \quad K = 1 \dots N \text{ and } 3N \text{ sets of constants } \langle \eta_1, \eta_2, \eta_6 \rangle \quad (10)$$

Forcing a solution of this type, eq. (10) with $K = t$ into the original eigenproblem leads to a set of 3 vectorial equations of order N each. Premultiplying each equation by $\langle \phi_L^* \rangle_t$ leads to the following eigenproblem for the associated lateral-torsional single-story building:

$$([B_L'] - \lambda [I]) \cdot \{g\} = \{0\}_{(3 \times 1)} \quad (11)$$

where

$$[B'_L] = [L'] \cdot ([I] + [D']),$$

in which

$$[L'] = {}^1\lambda_L^*(t) \cdot [I],$$

$$[Z] = \begin{bmatrix} 1 \\ Z_2 \\ Z_6 \end{bmatrix}, \quad \text{and} \quad [D'] = \begin{bmatrix} \epsilon_{tt}^{61} & \epsilon_{tt}^{62} & \epsilon_{tt}^{66} \\ \epsilon_{tt}^{21} & \epsilon_{tt}^{22} & \epsilon_{tt}^{26} \\ \epsilon_{tt}^{61} & \epsilon_{tt}^{62} & \epsilon_{tt}^{66} \end{bmatrix},$$

in which

$$\epsilon_{tt}^{ij} = \langle {}^1\phi_L^* \rangle_t [E_L]^{ij} \{ {}^1\phi_L^* \}_t.$$

Eigenproblem (11) can easily be solved numerically. Thus, in the case of a particular class of buildings--those exhibiting "stiffness similarity"--only one symmetrical eigensolution is required to generate the homogenized eigenproperties of the whole building system.

5. EARTHQUAKE ANALYSIS

The equations of motion of the building system during earthquake response are given by

$$\underline{M}_L^{CR} \ddot{\underline{D}}_L^{CR} + \underline{C}_L^{CR} \dot{\underline{D}}_L^{CR} + \underline{K}_L^{CR} \underline{D}_L^{CR} = \underline{P}_{eff_L}^{CR}(t) \quad (12)$$

If the eigenvectors are normalized in such a way that

$$\underline{\psi}_L^T \underline{K}_L^{CR} \underline{\psi}_L = \begin{bmatrix} \underline{m} \\ \underline{m} \\ \underline{m} \end{bmatrix} \quad (13)$$

then, standard normal coordinate transformation [1] leads to the uncoupled equations

$$\ddot{q}_L + [2\xi_L \omega_L] \dot{q}_L + \frac{\lambda}{L} q_L = \underline{M}^{-1} \frac{\lambda}{L} \underline{\psi}_L^T \underline{P}_{eff_L}^{CR}(t) \quad (14)$$

The vector of effective earthquake forces on the right of eq. (14) is constructed by a standard assembly process [2,3].

Thus, the typical uncoupled equations of motion result in

$$\ddot{q}_{q_{Ln}} + p_{(2\xi\omega)} \dot{q}_{q_{Ln}} + p_{\lambda_{Ln}} q_{q_{Ln}} = \frac{1}{m_n} \cdot p_{\lambda_{Ln}} \cdot [p_{\psi_{Ln}}^T \cdot p_{eff_L}^{CR}] \quad (15)$$

where

$$p = (K + N - 1) \text{ int } N \quad ; \quad n = [(K - 1) \text{ mod } N] + 1,$$

with $K = 1 \dots (3N)$.

Eqs. (15) are solved using a closed-form algorithm for the solution of the corresponding differential equation for linear input forcing function. Once the normal coordinates are obtained, the determination of the time-histories of displacement response, of the effective earthquake forces, and, of element force response follows straightforward by a process of backsubstitution [1,4].

6. PARAMETRIC STUDY

Figure 1 shows the plan view of an 8-story building system. Each story is supported by 4 columns designed with lateral stiffnesses such as to reproduce the same structural properties as those presented in a similar example by Kan et al. [5]. The building is excited with the three translational components of the El Centro 1940 accelerogram, in such a way that the N-S component hits the structure along the global Y-Y axis.

Figures 3 and 4 are representative of typical results of the seismic analysis of the building. Figure 3 represents the time-history of the elastic force response at the lateral-torsional system of resistance of story 7, and Figure 4 shows the time-history of the internal force response of supporting element 3 at the same level.

Figure 5 depicts the peak values of the effective principal lateral forces on the various stories along the building height, and Figure 6 shows a similar description for the peak values of the story torques. Notice that the effective story torques at the lower levels (stories 2 and 3) adopt higher magnitudes than normally expected. This effect is due to the larger radii of gyration of the corresponding base floor-slabs, in this particular example.

A limited parametric study was conducted starting from this basic building model. Table 1 describes the variation of eccentricity ratio along the height of this basic building. To simplify the interpretation of results, all stories are assumed to exhibit elastic eccentricity along the global X axis only.

We now consider the effects on the basic building (with gradual variation of eccentricity ratio⁽¹⁾ along the height) of sudden discontinuities in the eccentricity ratio normal to the direction of the major component of input earthquake (N-S). Figure 2 shows the locations of the variations of eccentricity ratios for the 11 building models considered in this parametric analysis. Model (1) in the figure indicates the values of the eccentricity ratios for the basic building at the level of stories 4 and 8, whereas the arrows in the other models in the figure indicate whether the eccentricity ratio is increased (pointing to the right) or decreased

(1) By eccentricity ratio we mean the fraction e_x/r , where e_x is the X component of the elastic lateral-torsional eccentricity and r is the radius of gyration of the story floor-slab about its center of gravity.

(pointing to the left), by 50% at the corresponding location. Several possible combinations are analyzed including lumped variations at the top 3 stories (Models 10 and 11).

6.1 Analysis of Results

The effective earthquake lateral forces on the building in the direction of the strongest horizontal component of ground motion are affected in a localized manner by abrupt changes of eccentricity in the normal direction. The most important effect is noted at mid-level by the variation of eccentricity at the mid-height stories, regardless of the situation at the top stories (see Figure 7(a)).

Sudden changes of eccentricity at the top affect mostly the force on the story immediately under the discontinuity. Increasing eccentricity at the top story raises the lateral force on story 7, and increasing eccentricity at the top 3 stories raises the lateral force on story 5. The reverse effect takes place accordingly when the eccentricity is decreased. The most unfavorable combination can be expected when decreasing eccentricity at the top of the building and increasing it simultaneously in its mid-height region (see Figure 7(b)).

The effective earthquake torque at the lateral-torsional elastic centers of the various stories change dramatically with abrupt discontinuities of eccentricity. This effect is general along the height of the building, except at the very first or at the very top stories where no major effects were observed. The strongest variations in torque take place from the story with localized discontinuity of eccentricity towards the base of the building.

Abrupt discontinuity of any sign at the mid-height stories increases the effective torque in the same region; however, this effect is more powerful when the eccentricity decreases. The upper stories of the building are not affected by discontinuities at mid-level height (see Figure 8(a)). Increasing eccentricity in the upper stories increases the effective torque in general, but the most important effect is recorded at the top of the building. Accordingly, if the eccentricity decreases at the top stories, the effective torque goes down mostly at the top region (see Figure 8(b)).

Variations in the level of torque in the mid-lower portion of the building are caused much more strongly by the eccentricity discontinuities at mid-height of the building than by discontinuities at the top. The analyst may expect large effective torques if the combination of eccentricity increase at the top of the building and eccentricity decrease at the mid-height stories is given (i.e., a notable rate of variation of eccentricity along the building height, growing towards the top (Refer to Figure 8(c))).

7. CONCLUSIONS

A simple mathematical model for the three-dimensional linear elastic earthquake analysis of building systems was developed and implemented on a microcomputer.

An example problem illustrated a standard application of this capability. Based on this fundamental example, a limited program of parametric studies was conducted, leading to the following conclusions:

- (1) Abrupt variation in eccentricity along the height of the building did not affect significantly the displacement response. However,
- (2) the effective story torques, and the effective story lateral forces at elastic centers of resistance vary notably with the rate of variation of eccentricity normal to the direction of the input base motion.

The designer may expect large effective torques along the building height when the top stories show sudden increase of eccentricity and the midheight stories show sudden decrease of eccentricity; and, may expect large lateral earthquake forces in the direction of the applied input, when, conversely the top stories show sudden decrease of eccentricity and stories at midheight show sudden increase of eccentricity.

8. REFERENCES

1. R.W. CLOUGH and J. PENZIEN 1975 Dynamics of Structures. New York: McGraw-Hill.
2. L.A. de BÉJAR 1985 Ph.D. Thesis, Cornell University. Linear and nonlinear analysis of building systems subject to multicomponent Earthquake Excitations.
3. L.A. de BÉJAR and P. GERGELY 1984 XIII WCEE, 5, 219-226, San Francisco. Linear response of torsionally coupled buildings for multicomponent earthquake excitations.
4. P. GERGELY 1984 Class Notes at Cornell University, Dept. of Structural Engineering. Introduction to structural design for dynamic loads and earthquake engineering.
5. C.L. KAN and A.K. CHOPRA 1977. Earthquake Engineering and Structural Dynamics, 5, 395-412. Elastic earthquake analysis of torsionally coupled multistory buildings.
6. T.G. TSICNIAS and G.L. HUTCHINSON 1982 Earthquake Engineering and Structural Dynamics, 10, 171-174. "A note on the perturbation analysis of the mode shapes of torsionally coupled buildings.
7. J.H. WILKINSON 1965 The Algebraic Eigenvalue Problem. Oxford: Clarendon Press, 62-109. Perturbation theory.

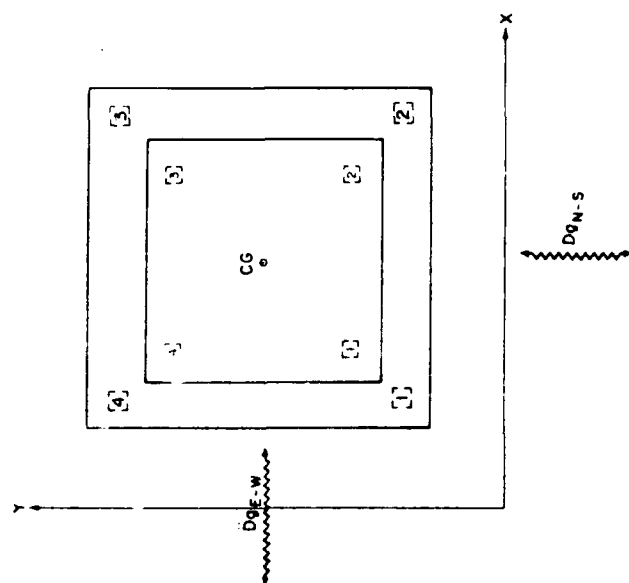


Figure 1. Application Example; Plan View of Multistory Building System

Table 1. Variation of eccentricity ratio along basic building height.

Floor	e_x/r
1	0.26
2	0.26
3	0.26
4	0.24
5	0.20
6	0.20
7	0.20
8	0.20

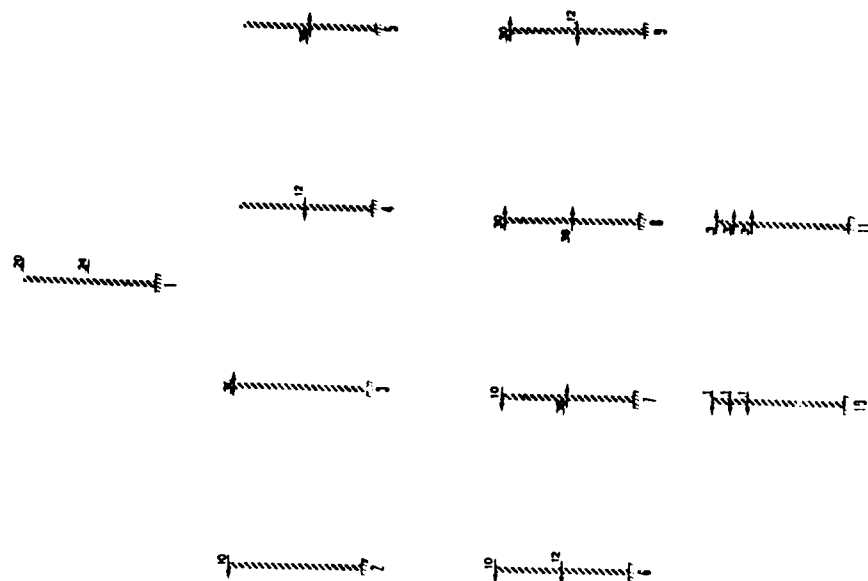


Figure 2. Parametric Study: Locations of Variations of Eccentricity Ratios for the Building Models Considered

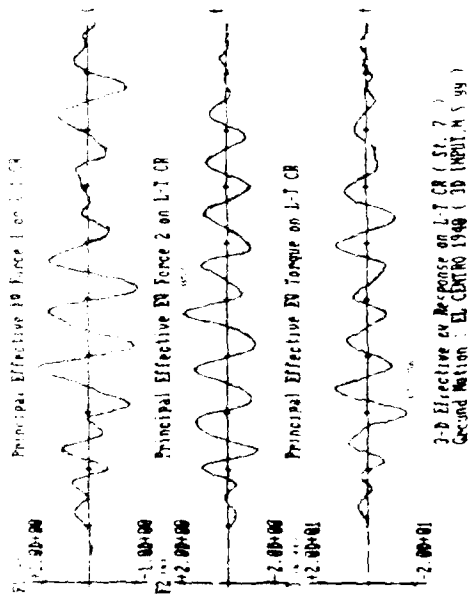


Figure 3. Effective Earthquake L-T Forces on Story 7

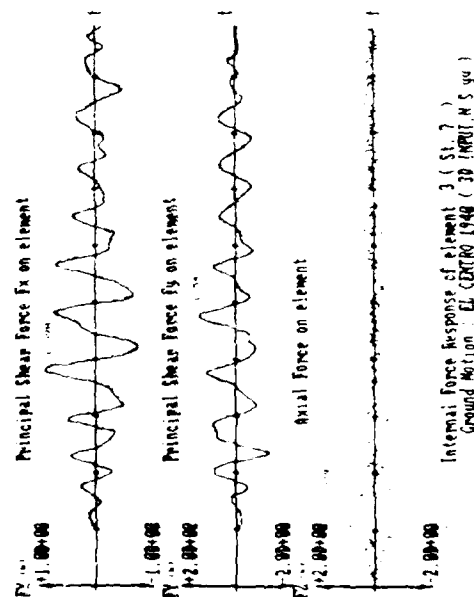


Figure 4. Internal Force Response of Element 7, Story 7

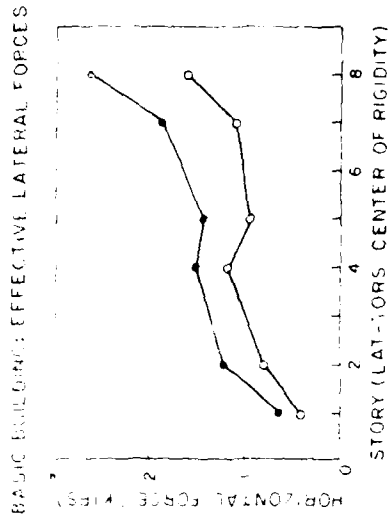


FIGURE 5. EFFECTIVE LATERAL FORCES ON BASIC EXAMPLE BUILDING

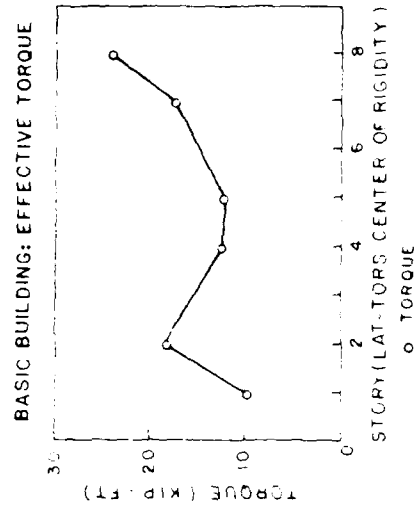


FIGURE 6. EFFECTIVE STORY TORQUES ON BASIC EXAMPLE BUILDING

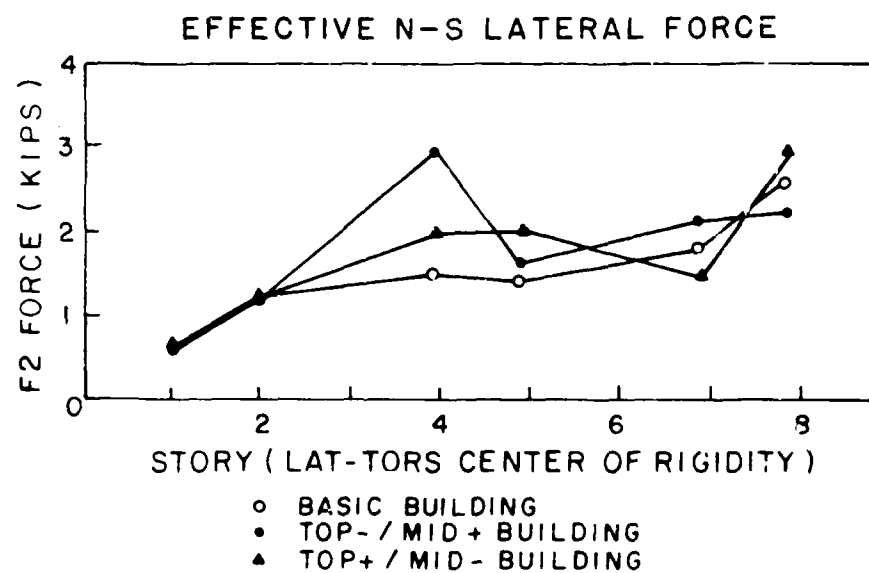
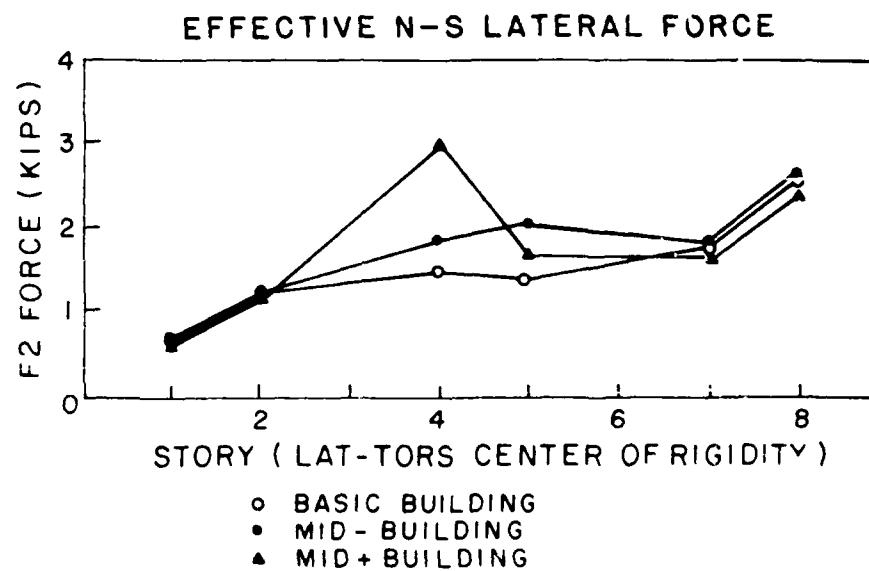


FIGURE 7. EFFECTIVE LATERAL FORCES ON BUILDING STORIES

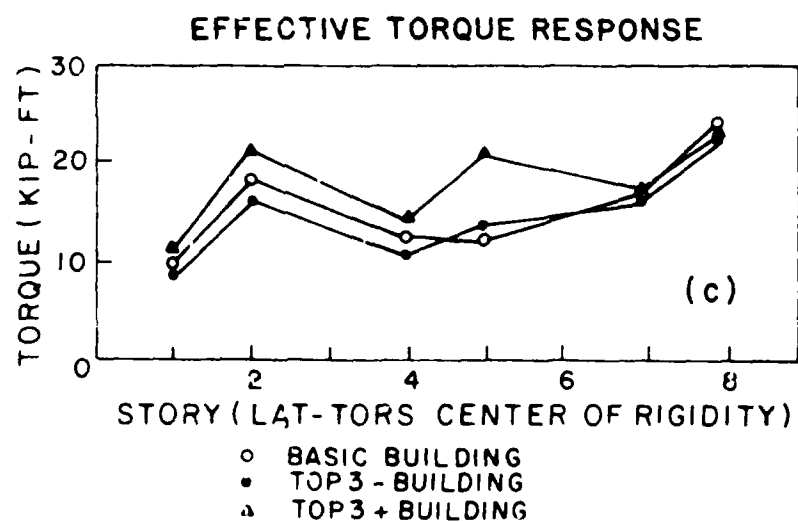
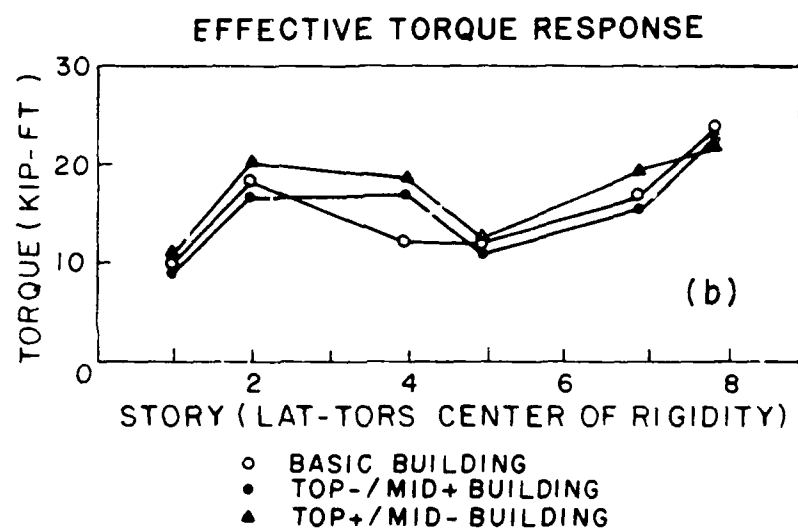
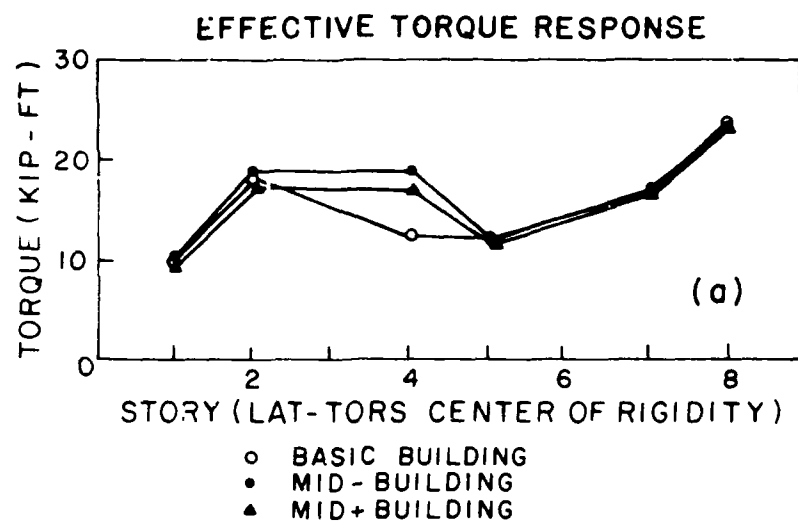


FIGURE 8. EFFECTIVE TORQUES ON BUILDING STORIES

TORSIONAL OSCILLATIONS OF FLEXIBLE INCLUSIONS IN A LAYERED ELASTIC HALF SPACE

R.K.N.D. Rajapakse and A.H. Shah

Department of Civil Engineering
University of Manitoba
Winnipeg, Canada R3T 2N2

1. INTRODUCTION

The study of harmonic axisymmetric torsional oscillations of partially embedded flexible inclusions in a layered elastic half space has useful applications in several branches of engineering. The flexible inclusion-layered half space system is used to model structural foundations in geomechanics, torque transfer problems encountered in aerospace engineering and biomechanics, and in-situ and non-destructive testing methods. The analytical study of torsion of inclusions which are partially embedded in a layered elastic half space has received limited attention in the past due to the complex nature of the associated mixed boundary-value problem. Existing solutions to this class of problems are mainly concerned with static loading [1-3]. An approximate analytical solution based on a two-dimensional representation of governing equations has been presented by Novak and Howell [4] to study the torsional oscillations of a long cylindrical elastic bar embedded in an elastic half space. In a recent study Rajapakse et al. [5] considered torsional oscillations of flexible objects partially embedded in an isotropic homogeneous elastic half space. The solution scheme presented in Ref. [5] is based on the decomposition used in Ref. [2] and subsequent application of Lagrange's equation of motion to the resulting system. It has been noted that with increasing frequency of vibration the solution may be distorted due to the inability of the algorithm to correctly incorporate the inertia effect.

A recent study by Rajapakse [6] demonstrated the application of a novel coupled boundary integral equation-variational formulation to study the elastostatic torque transfer from an elastic bar into a continuously nonhomogeneous elastic half space. In this paper an equivalent approach is developed to study the elastodynamic problems shown in Fig. 1. The analysis ensures displacement compatibility and traction continuity along the true contact surface and accurately treats inertia effects with increasing frequency of vibration.

2. GREEN'S FUNCTIONS

In an ensuing section dealing with the variational formulation of the system shown in Fig. 1, tractions acting on the inclusion-half space contact surface are determined through the application of indirect boundary integral equation method which is based on displacement and traction Green's functions of the surrounding undisturbed half space. In this section, the derivation of these Green's functions is discussed.

2.1 General Solution

The Fig. 2 shows the layered elastic half space with the cylindrical polar coordinate system (r, θ, z) . Due to the symmetry, the displacement and stress fields in the layer and the bottom half space are independent of circumferential coordinate θ and only the displacement $v(r, z, t)$ in θ -direction exists.

It is assumed that motion is time-harmonic so that $v_i(r, z, t) = v_i(r, z) e^{i\omega t}$, where ω is the circular frequency and the term $e^{i\omega t}$ is suppressed in the sequel. The subscript i ($i = 1$ for the layer and $i = 2$ for the half space) is used to denote quantities associated with the layer and the underlying half space. The general solution for displacement $v_i(r, z)$, ($i = 1, 2$) obtained through the application of Hankel integral transform techniques [7] can be expressed as

$$v_i(r, z) = \int_0^\infty (A_i e^{\beta_i z} + B_i e^{-\beta_i z}) J_1(\xi r) d\xi \quad (1)$$

$$\beta_i^2 = (\xi^2 - k_{si}^2)$$

$$k_{si}^2 = \omega^2 \rho_i / \mu_i$$

In Equation (1), J_1 is the Bessel function of the first kind of the first order, ξ is the Hankel transform parameter, and $A_i(\xi)$ and $B_i(\xi)$ are arbitrary functions associated with each domain to be determined from appropriate boundary and continuity conditions. In addition ρ_i and μ_i ($i = 1, 2$) denote the mass density and shear modulus respectively. At this stage it is convenient to nondimensionalise the problem by defining a , which denotes the radius of the embedded cylinder (or hemisphere), as a unit length.

2.2 Boundary-Value Problem

The boundary-value problem to be considered in the derivation of Green's function is depicted in Fig. 2. The layered elastic half space is subjected to a concentrated force in θ -direction along the circumference of a circle having radius s in the interior of the layered half space at $z = z'$. The explicit solution to this three domain boundary-value problem could be obtained by following a procedure identical to that used in Refs. [2] and [3] for the elastostatic problem.

3. VARIATIONAL FORMULATION OF INCLUSION-HALF SPACE SYSTEM

In this section the development of the coupled variational-integral equation solution scheme to analyse the system shown in Fig. 1 is presented.

3.1 Cylindrical Inclusion (Fig. 1a)

Consider the case of a cylindrical elastic bar of radius a and length h ($h/a \gg 1$) partially embedded in a layered elastic half space as shown in Fig. 1a. A cylindrical coordinate system (r, θ, z) is used in the analysis

with z-axis identical to the entroidal axis of the cylinder and normal to the stress-free surface of the half space. The shear modulus and mass density of bar are denoted by μ_b and ρ_b respectively. The bar is subjected to a time-harmonic torque $T_0 e^{i\omega t}$ at the top end ($z = 0$).

Following Rajapakse [6] the bar-half space system is decomposed into an elastic half space \bar{B} with a cylindrical cavity identical to the bar and the real bar B (Fig. 3). In the analysis \bar{B} and B are treated using three-dimensional and one-dimensional continuum theory respectively. The displacement in θ -direction of bar B denoted by v_b can be expressed in the admissible form

$$v_b(r, z, t) = \sum_{n=1}^N \alpha_n(t) r e^{-(n-1)z/h} \quad (2a)$$

$$\dot{v}_b(r, z, t) = \sum_{n=1}^N \dot{\alpha}_n(t) r e^{-(n-1)z/h} \quad (2b)$$

where $\alpha_1, \dots, \alpha_N$ can be viewed as generalised coordinates and superscript dot denotes differentiation with respect to time.

In view of Eqns. (2), the Lagrangian L_b of the bar B can be expressed as

$$L_b = \sum_{n=1}^N \sum_{m=1}^N [\dot{\alpha}_n \dot{\alpha}_m C_{mn} - \alpha_n \alpha_m D_{mn}] - \frac{1}{2} \int_S T_\theta \bar{v} dS + T_0 \sum_{n=1}^N \alpha_n \quad (3)$$

In Eqn. (3), S denotes the cylindrical cavity surface in \bar{B} ; \bar{v} and T_θ denote displacement and traction in θ -direction on S. Explicit representations for C_{mn} and D_{mn} are given in Ref. [5].

Since compatibility exists between B and \bar{B} the displacement in θ -direction on S is given by Eqn. (2a). The application of integral representation theorems [8] to B with respect to a set of nodal points on S leads to

$$\{T_\theta\} = [K]_\theta \{\bar{v}\} \quad (4)$$

where $\{\bar{v}\}$ and $\{T_\theta\}$ denote column vectors whose elements are displacements and tractions in θ -direction at nodal locations on S. An explicit representation for $[K]_\theta$ is determined in a subsequent section using the indirect boundary integral equation method.

Noting that

$$\bar{v} = \sum_{n=1}^N \alpha_n \bar{v}_n \quad (5a)$$

$$\text{where } \bar{v}_n = r e^{-(n-1)z/h} \quad (r, z) \in S \quad (5b)$$

the traction T_θ on S could be expressed as

$$T_\theta = \sum_{n=1}^N \alpha_n T_{\theta n} \quad (6)$$

where $T_{\theta n}$ denotes traction on S corresponding to \bar{v}_n given by Eqn. (5b).

In view of Eqn. (4)

$$\{T_{\theta n}\} = [K]_\theta \{\bar{v}_n\} \quad (7)$$

Substitution of Eqns. (2) and (4)-(7) in Eqn. (3) yields an expression for L_θ which is indeterminate with respect to generalised coordinates α_n ($n = 1, \dots, N$). These generalised coordinates are determined through the application of Lagrange's equation of motion [9] and this leads to the following equations of motion for the bar.

$$\sum_{n=1}^N \alpha_n [-2\omega^2 C_{ni} + 2D_{ni} + \sum_{j=1}^M (T_{\theta nj} \bar{v}_{ij} + T_{\theta ij} \bar{v}_{nj}) A_j / 2] = T_o \quad (i=1, 2, \dots, N) \quad (8)$$

$$\text{where } T_{\theta nj} = T_{\theta n}(r_j, z_j) \quad (r_j, z_j) \in S, j=1, \dots, M \quad (9)$$

$$\bar{v}_{nj} = \bar{v}_n(r_j, z_j) \quad (r_j, z_j) \in S, j=1, \dots, M \quad (10)$$

$$A_j = \text{tributary area of node } j \text{ on } S \quad (11)$$

and M in Eqn. (8) is the total number of nodes used to discretize S .

The numerical solution of Eqn. (8) result in values for α_i ($i = 1, \dots, N$). Thereafter bar displacements can be computed using Eqn. (2a) and the resultant torque acting on a bar cross-section is determined using Saint-Venant type torsion theory.

3.2 Explicit Representation for $[K]_\theta$

The explicit representation for $[K]_\theta$ that is necessary to compute vectors $\{T_{\theta n}\}$ whose elements appear in Eqn. (8) is discussed in this section. The study by Rajapakse [6] demonstrates the application of indirect boundary integral equation method to determine traction-displacement relationship along the surface of a cylindrical cavity created in an elastic half space. In this method a uniform half space S^* without a cavity is considered (Fig. 4). The contour S' representing the true contact surface is also defined in S^* . Interior to S' , an arbitrary surface S^* with geometry similar to S' is defined. Surfaces S' and S^* are discretized into M and M^* ring elements. A traction field τ_θ^* in θ -direction is applied on S^* such that

the displacement in θ -directions on S' are equal to that given by Eqn. (5b). Following Ref. [6] it can be shown that

$$[K]_{\theta} = [\bar{H}^{\theta\theta}] [\bar{G}^{\theta\theta}]^T [\bar{G}^{\theta\theta}]^{-1} [\bar{G}^{\theta\theta}]^T \quad (12)$$

The elements $\bar{H}_{ij}^{\theta\theta}$ and $\bar{G}_{ij}^{\theta\theta}$ of $[\bar{H}^{\theta\theta}]$ and $[\bar{G}^{\theta\theta}]$ are defined as

$$\bar{H}_{ij}^{\theta\theta} = H_{\theta\theta}(r_i, z_i; r_j^*, z_j^*) A_j^* \quad (13)$$

$$\bar{G}_{ij}^{\theta\theta} = G_{\theta\theta}(r_i, z_i; r_j^*, z_j^*) A_j^* \quad (14)$$

$$A_j^* = r_j^* dS_j^* \quad (15)$$

In Eqns. (13)-(15), $H_{\theta\theta}(r_i, z_i; r_j^*, z_j^*)$ and $G_{\theta\theta}(r_i, z_i; r_j^*, z_j^*)$ denote traction (on a plane with unit normal \bar{n}) and displacement in θ -direction respectively at point $(r_i, z_i) \in S'$ due to a unit time-harmonic ring load in θ -direction through point $(r_j^*, z_j^*) \in S^*$; dS^* , denotes the thickness of ring element j on S^* . $H_{\theta\theta}(r_i, z_i; r_j^*, z_j^*)$ could be derived from $G_{\theta\theta}(r_i, z_i; r_j^*, z_j^*)$ using basic relationships in elasticity. The order of $[\bar{H}^{\theta\theta}]$ and $[\bar{G}^{\theta\theta}]$ is $M \times M^*$.

3.3 Hemispherical Inclusion (Fig. 1b)

The Fig. 1b shows an elastic hemisphere of radius a embedded in a layered elastic half space. The hemisphere is assumed to be perfectly bonded to the surrounding layered half space along its contact surface. The shear modulus and mass density of the hemisphere are denoted by μ_h and ρ_h respectively. As in the case of a cylindrical elastic bar we can decompose the hemisphere - layered half space system into an elastic half space \bar{B} with a hemispherical cavity identical to the hemisphere and the real hemisphere B as shown in Figs. 3c and 3d. In the analysis, \bar{B} is treated using three-dimensional continuum theory and the deformation v_h of B in θ -direction is approximated by the following admissible form for frequencies within the low to medium range.

$$v_h(R, \phi) = \sum_{n=1}^N \alpha_n(t) R^n \sin n \phi \quad 0 < R < a, 0 < \phi < \pi/2 \quad (16)$$

Note that the displacement field given by Eqn. (16) includes the correct rigid body mode and satisfies zero-displacement along the z axis and results in non-singular stresses in its domain of definition. In addition, a conventional hemispherical coordinate system is used in Eqn. (16) to simplify the manipulations involved in the evaluation of strain and kinetic energies of B .

The method of analysis used to develop the equation of motion of

B is identical to that developed in the preceeding section for the cylindrical elastic bar.

4. DISCUSSION AND CONCLUSIONS

The numerical solution of equations of motion given by the Eqn. (8) for the cylindrical inclusion problem involves the computation of $[K]_0$ according to the Eqn. (12). This involves the computation of traction and displacement Green's functions with respect to contours S' and S^* . These Green's functions consist of complex-valued infinite integrals containing products of Bessel functions in the integrand. Furthermore the integrand contains several poles which correspond to Love waves in the layered system. In view of this numerical integration along a contour defined in the first quadrant of complex plane is used in the numerical evaluation of Green's functions.

The Figure 5 shows the variation of nondimensionalised torsional stiffness K_T [$K_T = 3T_0/16\mu_1 a^2 v_b(a,0)$] with bar flexibility ration $\bar{\mu}$ ($\bar{\mu} = \mu_b/\mu_1$), nondimensionalised frequency a_0 ($a_0 = ak_{s1}$) and ratio of shear moduli of layer and half space - α ($\alpha = \mu_2/\mu_1$). The real part of K_T decreases with increasing $\bar{\mu}$ and a_0 whereas the imaginary part shows an opposite trend. It can be concluded from Fig. 5b that as the underlying half space becomes stiffer lesser radiation damping occurs. The Fig. 6 shows the variation of nondimensionalised surface displacement $\bar{v}(r)$ [$\bar{v}(r) = v_h(r,0)\mu_1/qa_0$] with hemisphere flexibility ratio $\bar{\mu}$ ($\bar{\mu} = \mu_h/\mu_1$) and α . These results which correspond to $a_0 = 1.0$ indicate that as hemisphere becomes stiffer both real and imaginary components of surface displacement decrease in value. As in the case of cylindrical bar a stiffer underlying half space reduces the response of the hemisphere. Additional numerical results indicate that if $\bar{\mu} > 50$ the response of hemisphere is nearly identical to that of a rigid hemisphere. It is also noted that for both types of inclusion an increase in the mass density of the inclusion reduces the stiffness and increases the damping component. On the basis of comparison of selected numerical results presented herein and those in Ref. 5 corresponding to a homogenous half space it can be concluded that the presence of a layered system significantly influences the torsional response of a flexible inclusion.

5. ACKNOWLEDGEMENT

The work presented in this paper was supported by Grant A-6507 from the Natural Science and Engineering Research Council of Canada.

6. REFERENCES

1. H.G. POULOS 1975 Journal of Geotechnical Engineering Divisions, ASCE 101, 1019-1035. Torsional response of piles.
2. P. KARASUDHI, R.K.N.D. RAJAPAKSE and B.Y. HWANG 1984 International Journal of Solids and Structures 20, 1-11. Torsion of a long cylindrical

elastic bar partially embedded in a layered elastic half space.

3. A.P.S. SELVADURAI and R.K.N.D. RAJAPAKSE 1987 Journal of Engineering Mechanics, ASCE 113, 1534-1550. Variational scheme for analysis of torsion of embedded nonuniform elastic bars.
4. M. NOVAK and J.F. HOWELL 1978 Journal of Geotechnical Engineering Division, ASCE 104, 535-552. Dynamic response of pile foundations in torsion.
5. R.K.N.D. RAJAPAKSE, A.H. SHAH and S.K. DATTA 1987 Earthquake Engineering and Structural Dynamics 15, 279-297. Torsional vibrations of elastic foundations embedded in an elastic half-space.
6. R.K.N.D. RAJAPAKSE 1988 International Journal of Solids and Structures (in press). A torsion load transfer problem for a class of nonhomogeneous elastic solids.
7. I.N. SNEDDON 1951 Fourier Transforms New York: McGraw-Hill.
8. A.C. ERINGEN AND E.H. SUHUBI 1975 Elastodynamics 2 New York: Academic Press.
9. K. WASHIZU 1982 Variational Methods in Elasticity and Plasticity Oxford: Pergamon Press.

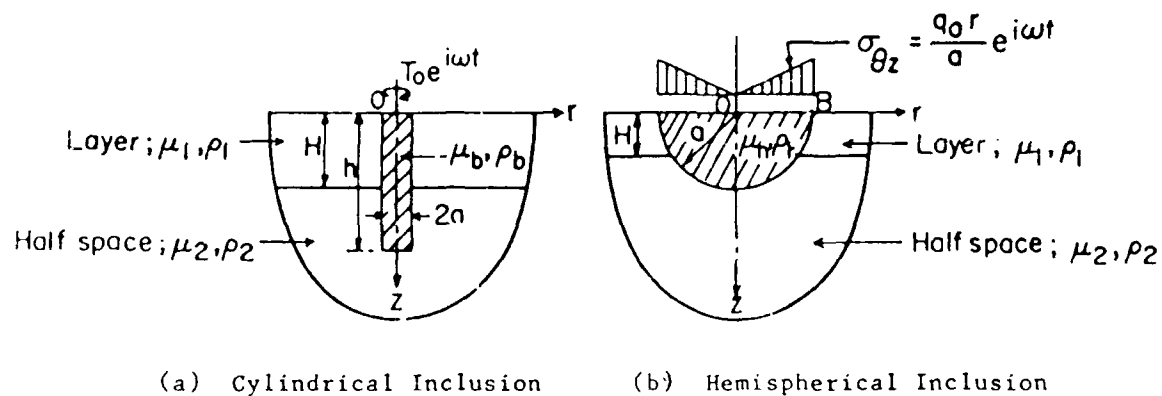


Fig. 1 Elastic inclusions embedded in layered half space

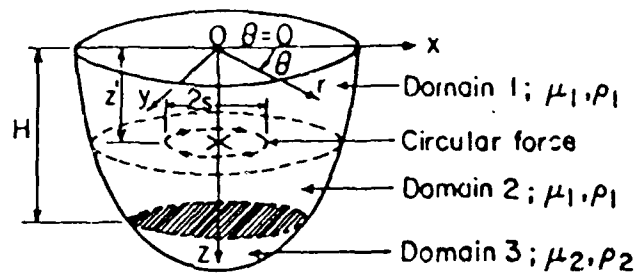


Fig. 2 System considered in the derivation of Green's functions

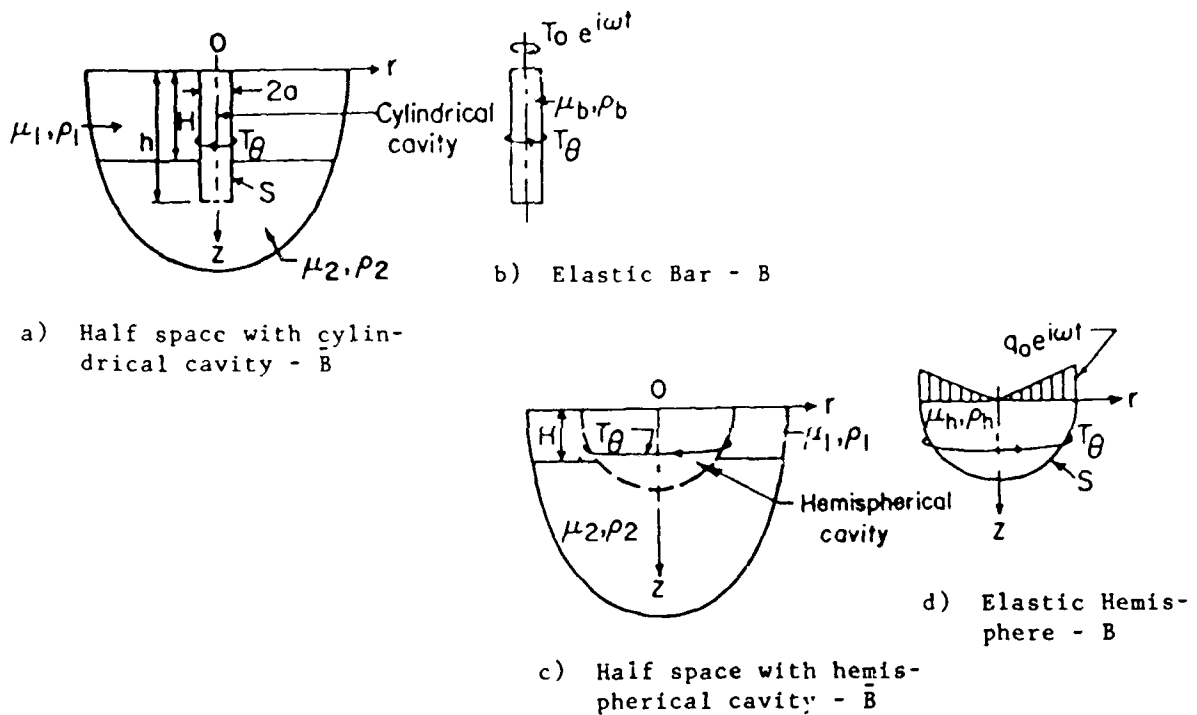


Fig. 3 Decomposition of inclusion-half space system

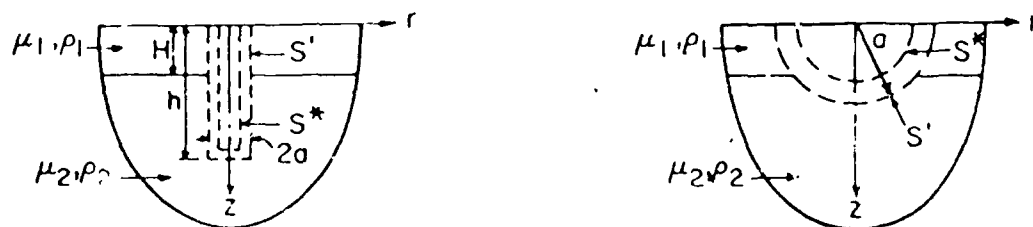
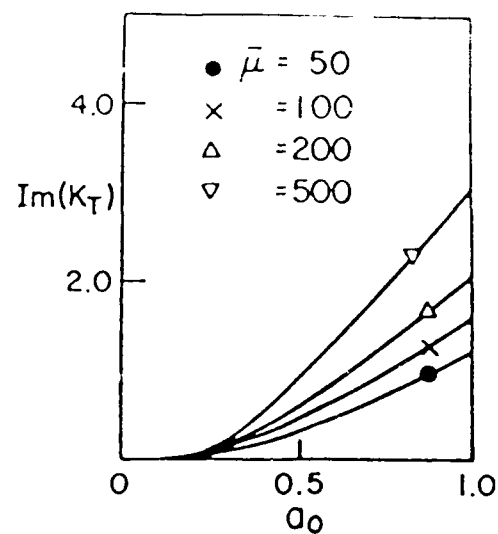
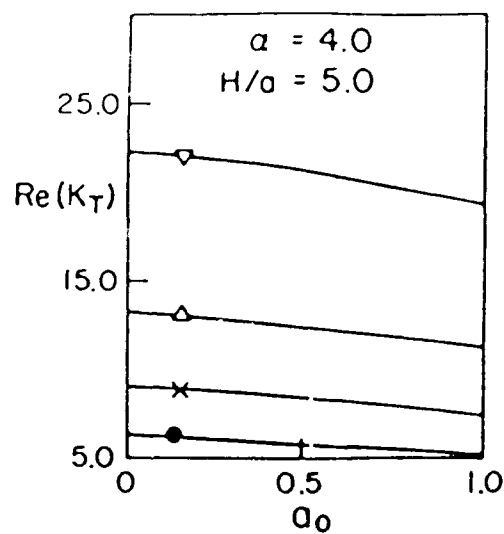
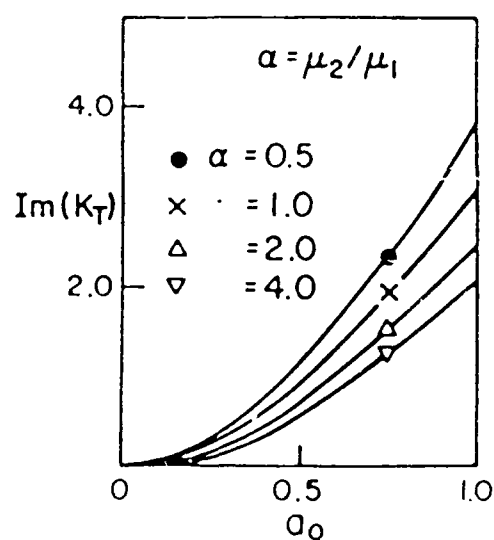
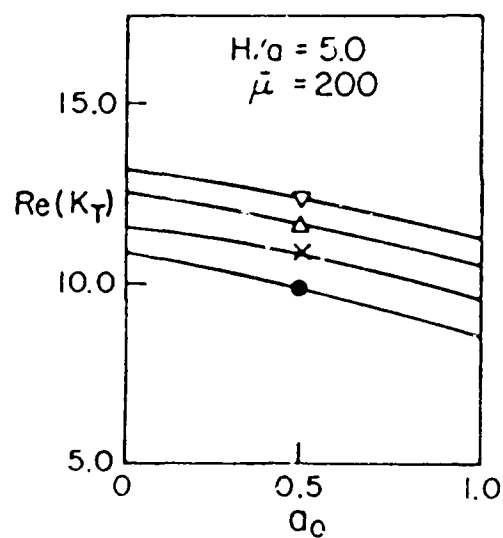


Fig. 4 Systems considered in the derivation of $[K]_{\theta}$

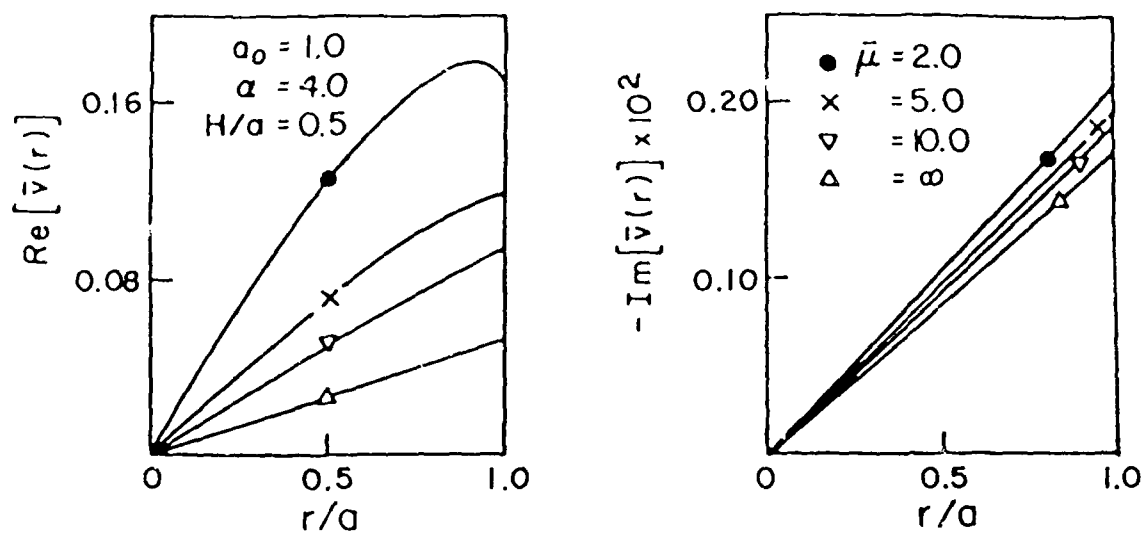


a) Variation of K_T with $\bar{\mu}$

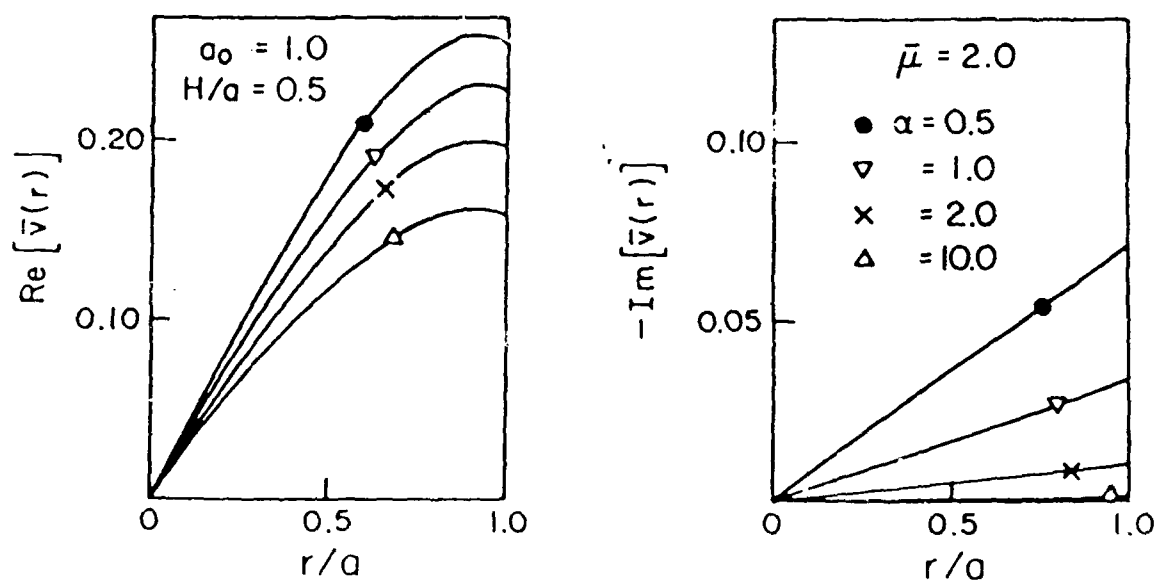


b) Variation of K_T with α

Fig. 5 Dependence of K_T on a_0 , $\bar{\mu}$ and α ; $h/a = 10$,
 $H/a = 5.0$, $\rho_b/\rho_1 = 1.5$, $\rho_2/\rho_1 = 1.0$



a) Variation of $\bar{v}(r)$ with $\bar{\mu}$



b) Variation of $\bar{v}(r)$ with α

Fig. 6 Dependence of $\bar{v}(r)$ on $\bar{\mu}$ and α ; $H/a = 0.5$,
 $\rho_b/\rho_1 = 1.0$, $\rho_2/\rho_1 = 1.0$, $a_0 = 1.0$

A FREQUENCY/DAMPING DATABASE FOR TALL CHIMNEYS

J.R. Maguire, B.Sc., Ph.D., C.Eng., M.I.C.E.

W.S. Atkins Engineering Sciences, Epsom, Surrey, England

1. INTRODUCTION

This technical note brings together diverse experimental data on the fundamental frequencies and damping values of eleven tall (height 126m-265m) chimneys, in order to form a database. The source data is referenced and a comparison is made with the Building Research Establishment (B.R.E.) recommendations for tall buildings. A recommendation is made that the damping value to be used in design should not exceed 0.5% of critical.

2. SOURCE DATA

References 1-7 at the end of this note detail the sources of the experimental data. The table below presents the fundamental frequency and damping values related to chimney height.

Ref No:	Chimney Name	Height in m.	Foundation Type	Fundamental Freq. (hz)	Damping (% critical)
1	Mount Isa	265	Not Stated	0.27	0.70
2	Drax	257	Piles to bedrock	0.25	0.80
3	Maysville	244	Piles	0.31	1.20
4	Pembroke	213	Slab on limestone	0.43	0.64
5	Eggborough	198	Slab on limestone	0.38	0.48
6	Kingsnorth	198	Slab	0.38	0.48
7	Didcot	198	Piles on clay	0.32	0.64
8	Fawley	198	Slab/piles in clay	0.46	0.48
9	Hirono	198	Slab on mudstone	0.48	0.50
10	Stigsnæs	150	Annular slab	0.65	1.19
11	Ferrybridge	126	Not Stated	0.61	0.95

3. BRIEF SUMMARY FOR EACH CHIMNEY

3.1 Mount Isa

- ° Reinforced concrete stack
- ° Outside diameter = 21.85m at base, 12.27m at tip
- ° Ambient wind (storm) vibration tests (windspeed 21m/s)
- ° Displacements at chimney tip = 116mm (max.)

3.2 Drax

- ° Reinforced concrete windshield, separated from flues by rubber
- ° Outside diameter = 26m (constant)
- ° Ambient wind vibration tests
- ° Accelerations at chimney tip = 0.0004g (displacements = 1.7mm)

3.3 Maysville

- ° Non uniformly tapered reinforced concrete column
- ° Outside diameter = 20.42m at base, 9.77m at tip
- ° Ambient wind vibration tests
- ° Accelerations at chimney tip = 0.005g (displacements = 13mm)

3.4 Pembroke

- ° Reinforced concrete cylindrical windshield (multiple flues supported on windshield)
- ° Outside diameter = 21m at base, 18m at tip
- ° Ambient wind vibration tests
- ° Accelerations at chimney tip = 0.0002 - 0.001g (displacements = 0.2 - 1mm)

3.5 Eggborough

- ° As for Pembroke (3.4)

3.6 Lawley

- ° As for Pembroke (3.4)

3.7 Kingsnorth

- Reinforced concrete cylindrical windshield (multiple free-standing flues)
- Outside diameter = 21m at base, 18m at tip
- Ambient wind vibration tests
- Accelerations at chimney tip = 0.0001 - 0.0002g (displacements = 0.1 - 0.4mm)

3.8 Didcot

- As for Kingsnorth (3.7)

3.9 Hirano

- Reinforced concrete chimney
- Outside diameter = 27m at base, 14.8m at tip
- Forced vibration/ambient (wind and earthquake) vibration tests
- Accelerations at chimney tip = 0.05g at wind speed of 34m/s
= 0.15g due to earthquake event

3.10 Stigsnaes

- Reinforced concrete tapered chimney (circular section)
- Outside diameter = 20.68m at base
- Ambient wind vibration tests (windspeed 20m/s)
- Neither accelerations nor displacements reported

3.11 Ferrybridge

- Reinforced concrete chimney stack
- Outside diameter = 7.3m at tip
- Rocket excitation tests
- Displacements at chimney tip = 14mm

4. COMPARISON WITH TALL BUILDINGS

Reference 8 at the end of this note summarises the BRE recommendations for tall buildings. Figures 1 and 2 present graphically the variation in fundamental frequency and damping against chimney height, with the BRE tall building recommendations superimposed. It may be seen from Figure 1 that the tall chimney data seems to follow a similar trend to the tall building data. The chimney trend line shown is $f = 50/(H-70)$ but this is not a design recommendation due to the sparsity of data. It may be seen from Figure 2 that the tall chimney damping data does not seem to have a distinct trend, but that generally it lies on the higher damping side of the conservative BRE tall building recommendation.

5. CONCLUSIONS

A frequency/damping database for tall chimneys has been established. Although small, the database provides a "starting point" for designers and other researchers. It is suggested that for design purposes tall chimneys (height 126m - 265m) should be conservatively designed with a damping value of not more than 0.5% of critical.

6. REFERENCES

1. W H MELBOURNE et al. November 1983 Proceedings of the ASCE, Vol. 109, No. ST11, pp. 2561-2577. Response to Wind Action of 265m. Mount Isa Stack.
2. R A WALLER February 1971 Proceedings of the ICE, Vol 48, pp. 303-323. The Design of Tall Structures with particular reference to Vibration.
3. K L BENUSKA et al. Jan 15-16 1981 Proceedings of the Second ASCE Speciality Conference, Eng. Mech. Div. Structural Characteristics of Concrete Chimneys.
4. A P JEARY 1974 Proceedings of the ICE, Vol. 57, pp. 321-329. Dynamic Measurements from the Dynamic Behaviour of Several Large Multi-flue Chimneys.
5. S SANADA and H KOSHIDA 6-8 April 1987 Joint I. Struct E/BRE Seminar on Structural Assessment, Paper 40 pp. 316-322. Full-Scale Measurements of Wind Force and Earthquake Ground Motion Acting on a 200m Concrete Chimney.
6. S C HANSEN 1981 Journal of Wind Eng. and Industrial Aerodyn., Vol. 8, pp. 145-155. Cross-Wind Vibration of a 130m tapered Concrete Chimney.
7. C SCRUTON and A R FLINT 1964 Proceedings of the ICE, Vol. 27, pp. 673-702. Wind-Excited Oscillations of Structures.
8. B R ELLIS and J D LITTLER 6-8 April 1987 Joint IStructE/BRE Seminar on Structural Assessment, Paper 8 pp. 63-70. Lessons from Dynamic Testing of Buildings.

FIGURE 1 - FUNDAMENTAL FREQUENCY (f) AGAINST HEIGHT (H)

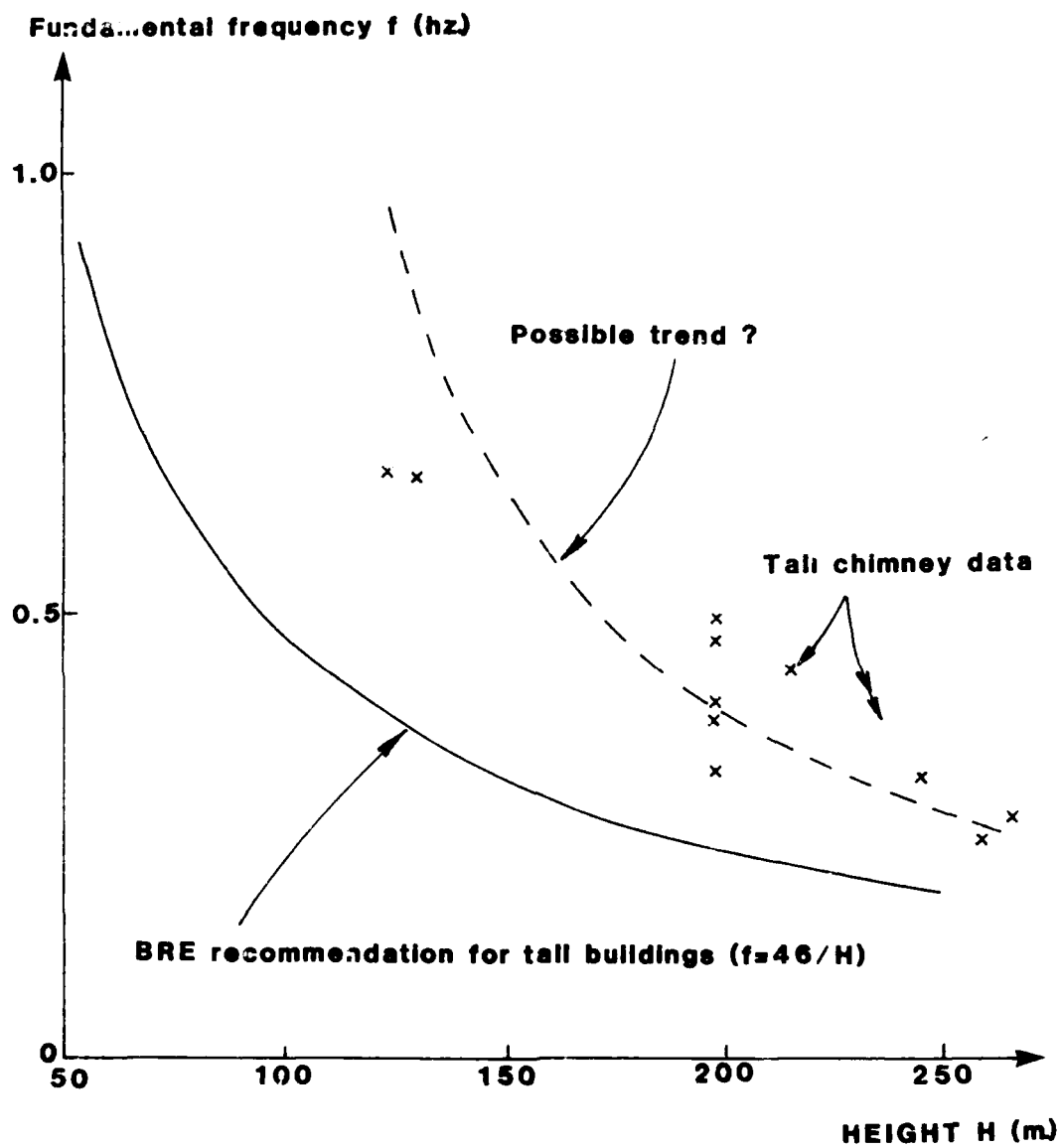
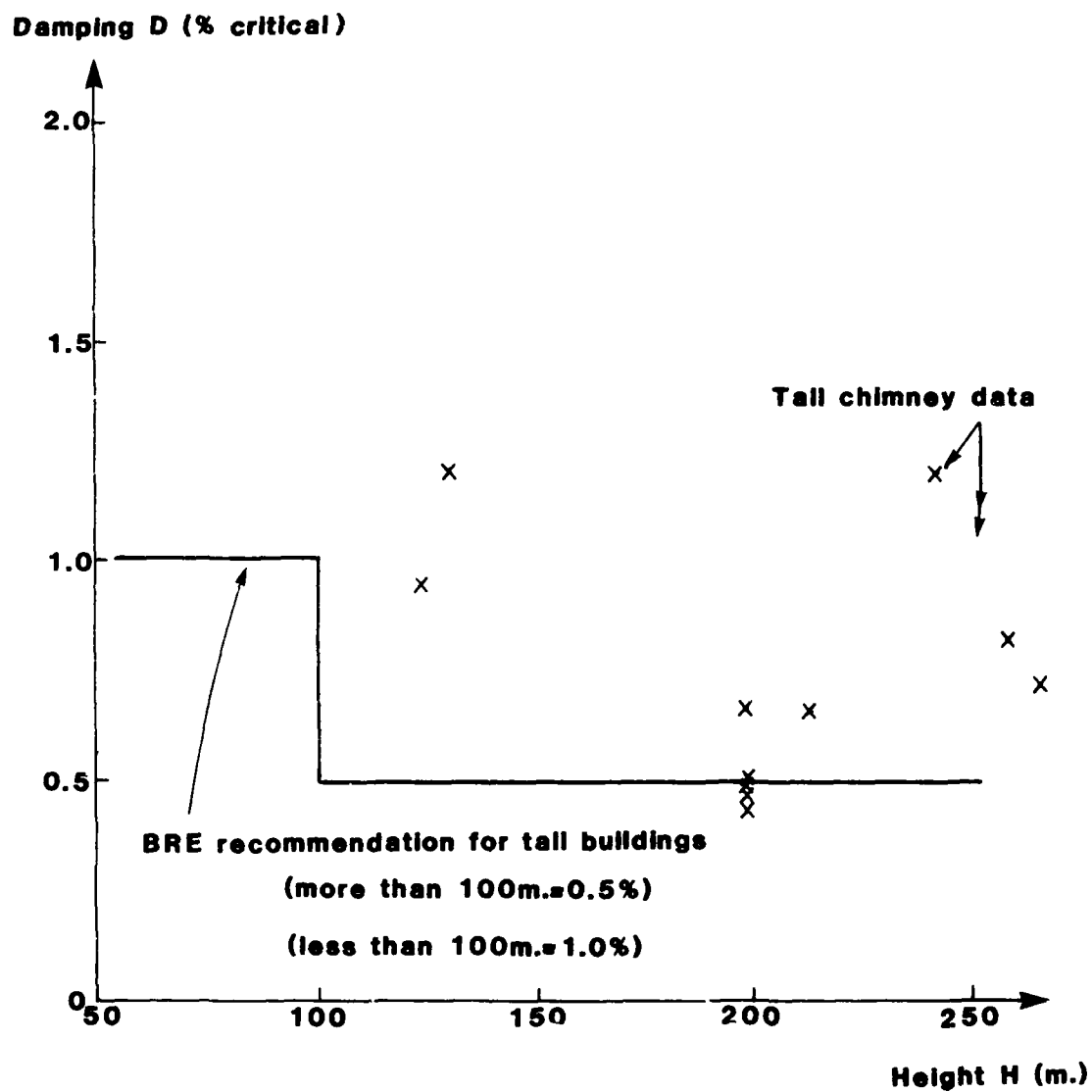


FIGURE 2 - DAMPING (D) AGAINST HEIGHT (H)



APPLICATION OF EXPERIMENTAL MODAL ANALYSIS TO FULL-SCALE CIVIL ENGINEERING STRUCTURES

W.F. Tsang, Royal Naval Engineering College, Plymouth
C. Williams, Department of Civil Engineering, Plymouth Polytechnic

1.0 INTRODUCTION

Recent advances in experimental modal testing and analysis (EMTA) have led to its application to a wide spectrum of engineering problems. This is because EMTA is a practical technique which allows an unknown system, whether it be structural or mechanical, to be identified. However, within civil engineering the technique is still not widely used but can be applied to determine a structure's vibrational properties.

The method is carried out in two overlapping phases. The first being the 'testing phase' in which the structure's response to a particular form of imposed excitation are measured. The second phase is analysis which involves the processing of the experimental data recorded. The data analyses are performed to extract the modal parameters from measured response characteristics. The aim is to construct a modal model from the modal parameters determined.

This paper describes the experience gained and application of EMTA to a reinforced concrete civil engineering structure. The successful implementation of the technique requires skill in a number of fields including full-scale testing, data measurement and analysis and application of engineering judgement.

2.0 METHODOLOGY

The process of reducing a physical system to a mathematical representation is a prevalent task mutual to all fields of analysis. This modelling exercise requires a realisation of the complex system to a simplified conceptual model. Young and On^[1] have given a detailed coverage of the general methodology of mathematical modelling via direct use of vibration data. The philosophy behind the testing technique is found in the theory of system modelling or system identification^[2].

In essence the method requires the system (the structure) to be subjected to known input excitations (the forces) and the responses (accelerations at measurement locations) to be measured. The excitation can be sinusoidal or random wide-band forces. The so called Frequency Response Functions (FRF) or Transfer Functions (TF) can be established which describe the input/output system characteristics.

The theoretical development of the modal testing theory is lengthy and interested readers are recommended to consult a useful reference by Ewins^[3]. However, the important equations in the relevant stages of development are detailed below.

The governing equations for the response of a structure subjected to imposed excitation are described by the equations of motion in matrix notations.

$$[M] \{\ddot{X}(t)\} + [K] \{X(t)\} + i [H] \{\dot{X}(t)\} = \{F(t)\} \quad (1)$$

where: $[M]$ is the system mass matrix;
 $[K]$ is the system stiffness matrix;
 $[H]$ is the system hysteretic damping matrix;
 $\{X(t)\}$, $\{\ddot{X}(t)\}$ are the displacement acceleration response vectors;
 $\{F(t)\}$ is the force vector.

This may be re-written using Fourier Transformations:

$$(-w^2[M] + [K] + i[H]) \{X^*(w)\} = \{F^*(w)\} \quad (2)$$

where: w is the angular frequency;
 $\{X^*(w)\}$ is the F.T. of $\{X(t)\}$ and is a function of w ;
 $\{F^*(w)\}$ is the F.T. of $\{F(t)\}$ and is a function of w .

If $\{X^*(w)\} = [\alpha] \{F^*(w)\}$
then $[\alpha] = (-w^2[M] + [K] + i[H])^{-1}$ (3)

where: $[\alpha]$ is the receptance or displacement F.R.F. matrix with α_{jk} the element on the j th row and k th column.

The series expansion of equation (3) gives:

$$\alpha_{jk}(w) = \frac{X_{jk}^*(w)}{F_k^*(w)} = \sum_{r=1}^N \frac{rA_{jk}}{(w_r^2 - w^2 + i\eta_r w_r^2)} \quad (4)$$

where: $\alpha_{jk}(w)$ is the receptance with displacement response at j and force at k ;
 rA_{jk} is the modal constant for the r th mode;
 w_r is the r th mode resonant frequency;
 η_r is the r th mode hysteretic damping loss factor;
 N is the total number of resonant modes.

Similarly the inertance matrix $[\gamma]$ can be defined such that:

$$\gamma_{jk}(w) = \frac{\ddot{X}_{jk}^*(w)}{F_k^*(w)}$$

The task for modal testing is therefore to measure the Transfer Functions (i.e. the receptances or inertance as depicted in these equations).

In the tests reported in this paper Transfer Functions were obtained from a large number of measurements at different locations. Processing of these data enabled the modal parameters of the structure being tested to be obtained.

3.0 INSTRUMENTATION

The quality of results in BMTA partly depends on the precision and capability of each item of instrumentation used in testing. In terms of functional classification the instrumentation required is:-

1. An excitation mechanism;
2. Force measurement transducers;
3. Vibration sensing transducers;
4. Signal conditioning and processing devices;
5. FFT analysis and recording system.

Full-scale testing of civil engineering structures requires that equipment be portable, robust and relatively quick to operate on site as working time is often limited.

3.1 The excitation method used in the tests was a purpose built linear motion hydraulic inertial exciter (Figure 1). A dead mass of up to 300kg, supported by linear bearings, was moved by a hydraulic actuator. The inertial reaction forces developed were transferred to the structure by securing it to a floor slab.

Eccentric rotating mass shakers have been used for some years to excite large civil engineering structures^[4]. The precision control of the exciter used in these tests and the ability to generate not only sinusoidal forces, but other complex wave forms give some advantages over the rotating mass shakers^[5].

3.2 The force input to the structure was measured by a load cell situated between the moving ram of the actuator and the 'dead mass'. Extensive laboratory calibration was carried out to correlate load measurement and shear force transferred at the base of the actuator which would be input to a structure under a test.

The movement of the building structure was captured by Schaevitz servo-drive accelerometers which operate down to d.c. Static as well as dynamic calibration was carried out. Signal conditioning units provided d.c. offset, filtering and amplification. The stability, accuracy, small size and low weight of these closed-loop, force balancing transducers make them particularly suitable for full-scale structural tests.

3.3 The signal processor used on site was an HP 3582A real time analyser with a 16 bit microprocessor which gives transformation of signals in the time domain into the frequency domain. The dual channel measurement mode gives the computation of transfer functions and coherence-spectra^[6].

Sinusoidal wave forms to drive the exciter on site were generated from a Philips PM 5130 programmable signal generator which could be controlled by a computer. The sinusoidal wave forms generated were based on digital algorithms rather than crystal oscillations as harmonic distortion had been encountered with the use of the actuator's own signal generator.

3.4 To meet the needs of digital data storage and fast operation on site an HP 86B computer was used. This was also interfaced with the signal generator and spectrum analyser so that tests were controlled from the computer, records kept, and on site analysis carried out. An in-house program was written to control the testing, set the analysis parameters and record the data. Having the data in a digital form allowed for subsequent further analysis in the laboratory and on the main frame computer.

4.0 FULL SCALE TESTS

The structure tested was a five storey fire drill tower at Camels Head Fire Station, Plymouth. Figure 2 shows the structure which is a reinforced concrete frame with openings and some brickwork infill panels.

The exciter was located at the top storey and could be operated in the direction of both principal plan axes. The structural response was monitored at four designated positions on each storey. Three accelerometers were positioned (two horizontal and one vertical) at each

location in turn. This arrangement enabled the spatial translation to be measured and was repeated at each story level including the ground, giving a total of twenty-four locations monitored.

Any full-scale in-situ testing is difficult due to the very nature of the large structure and testing away from the laboratory. In these tests the problems of getting heavy equipment to a high level was overcome with the use of a fire-fighting hydraulic platform.

5.0 MEASUREMENTS AND RESULTS

The results presented in this paper are the product of a lengthy process of analysis on an HP 86B and HP 9816 computer and the GINO-F package on a Prime main frame which was required for the second phase of the EMTA. Typical results are presented for one location only on the tower (South West column), but are for the force input in the two major axes.

Figures 3 and 4 show the amplitude receptance F.R.F. plots for the force input in the two directions respectively. The first two modes are distinctly excited while higher modes are shown to be coupled. For simplicity only the first three modes are reported here.

Figures 5 to 7 are examples of the circle-fitting on the Nyquist plots of raw inertance and receptance F.R.F. data. The numbers given on the plots are the designated 'frequency points' taken from the 128 points covering the range 0 to 25 Hz. The plots indicate sound data and that the result of the circle fitting process are much better for the receptance than the inertance data. This is because from theory only the Nyquist plot of receptance data for structures with hysteretic damping will trace an exact circle if the measurements have been free from experimental errors. The spacing of the 'frequency points' around the circles show that the frequency resolution in analysis needs to be finer for mode 1 than mode 3 (Figures 5 and 6).

The quality of the data can also be shown by plotting the real and imaginary part of the receptance F.R.F. data against frequency squared^[7]. In theory, error free data and the validity uni-modal response will give a sloping straight line in the real receptance against frequency squared plot and a horizontal line in the imaginary plot (Figures 8 and 9).

Table 1 gives a summary of the data analysis of the first 3 modes.

TABLE 1

SUMMARY OF MODAL ANALYSIS RESULTS OF TESTS ON FIRE STATION TOWER

MODE	FREQUENCY [Hz]	MODAL CONSTANT [1/kg]		DAMPING LOSS FACTOR	REMARKS
		REAL	IMAGINARY		
1	2.39	+2.20 E-03	+5.23 E-04	8.0 E-03	From measurement at S.W. Column N-S excitation
2	5.58	+1.90 E-03	-1.49 E-04	2.6 E-03	
3	10.39	+5.07 E-04	-3.56 E-05	2.9 E-03	
1	2.36	+2.57 E-03	+6.68 E-05	4.0 E-02	From measurement at S.W. Column E-W excitation
2	5.37	+3.91 E-04	-6.35 E-05	2.3 E-02	
3	10.32	+ 3.05 E-04	-5.86 E-05	3.3 E-02	

The modal constants are complex quantities with real and imaginary parts, and the unit is in Kg^{-1} . From theory the modal constant is the product of two mass-normalised mode shape coordinates. For instance:

if ϕ_{ir} is the modal coordinate of the r th mode at location i ;
 and rA_{ij} is the modal constant for the r th mode with response measurement at location i and excitation at j ;
 then $rA_{ij} = \phi_{ir} \phi_{jr}$.

The values of these modal constants have an implication on the "dynamic stiffness" of the respective modes concerned. At resonance the receptance is:

$$\alpha_{jk} = \frac{rA_{jk}}{i n_r \omega_r^2}$$

where: ω_r is the resonant frequency of the r th mode;
 n_r is the hysteretic damping of the r th mode;
 and i if $\sqrt{-1}$.

This is valid if the structure is free from modal coupling and the residual modes are negligible.

The determined resonant frequencies from the two sets of measurements are generally in agreement. The damping loss factors in the table are the ratios of the actual damping and the corresponding critical damping for the respective modes.

Discrepancies in these figures are much greater for the first two modes than those for the third mode. Figures 10 and 11 show the regeneration of the receptance F.R.F. curves for both measurements. In the regeneration process, residuals from rigid body modes and higher modes have been ignored. The plots have been generated based on the modal parameters determined as discussed earlier. In general, these plots show a good reproduction for the first three modes and considerable errors for the higher modes.

Figure 12 shows the spatial deformation shapes of the structure at the frequencies of excitations logged from data at the 128 frequency points. The spatial translation of each measurement location are shown with an arbitrary scale. Instead of conventional simple bending modes as would be expected, the deformation shapes reveal considerable variations with complexities such as floors warping and twisting. These plots are invaluable visual aids to determine the vibrational modes concerned.

6.0 CONCLUSIONS

The technique of EMTA is found to be applicable to large complex structures. The development of the linear motion hydraulic exciter has been found to be practical for exciting large structures. This exciter has extended the conventional excitation methods from sinusoidal testings to periodic random testings. In situations where time is strictly limited, the periodic random tests becomes more attractive. However the sinusoidal tests can generally provide better results.

In contrast to laboratory testing on scale models or components, in situ full-scale vibration testing suffers from several problems and limitations. Since there is no control of the test environment, the data obtained are generally not of as high quality as those obtained in

laboratory. In fact, full scale measurements on civil engineering structures are often corrupted with "noise" from wind, human movements, and traffic.

To realise the full potential of EMTA to civil engineering structures further work is required. EMTA can provide a set of modal parameters for the modes of interest within the frequency bands of testing and a modal model can be established. To establish spatial models of the tested structure would require a better quality of data from tests, more measurement locations and more modes to be determined.

The instrumentation system used in this research proved to be a relatively low cost solution. The computers provided a valuable tool in the experimentation as well as analysis of data.

7.0 ACKNOWLEDGEMENTS

The linear motion hydraulic exciter was developed with the aid of a Science and Engineering Research Council Grant (Grant No. GR/D/02119). The authors would also like to acknowledge the permission for testing and assistance given by the Devon Fire Brigade on the Fire Drill Tower, and the technician support of the Department of Civil Engineering, Plymouth Polytechnic. Support of the Royal Naval Engineering College, Manadon, Plymouth is gratefully acknowledged for use of software and facilities during the data analysis phase.

8.0 REFERENCES

1. J.P. YOUNG and F.J. ON 1969 Mathematical Modelling via Direct Use of Vibration Data. Society of Automotive Engineers, SAE Paper 690615.
2. G.A. BECKEY 1970 System Identification - An Introduction and a Survey. Simulation, Vol. 5, Pt. 4, pp151-166.
3. D.J. EWINS 1984 Modal Testing Theory and Practice, Research Studies, Press Ltd.
4. A.P. JEARY et al 1977 Some observation on the Sway Characteristics of Concrete Structures. Building Research Establishment Publication.
5. W.F. TSANG The Determination of Structural Parameters from Dynamic Testing. PhD Theses (to be published).
6. MANUAL HP 3582A, Operation Manual, Hewlett Packard.
7. B.J. DOBSON 1985 Modal Parameter Estimation using Difference Equations, Royal Naval Engineering College Internal Report No. RNEC-TR-85014.

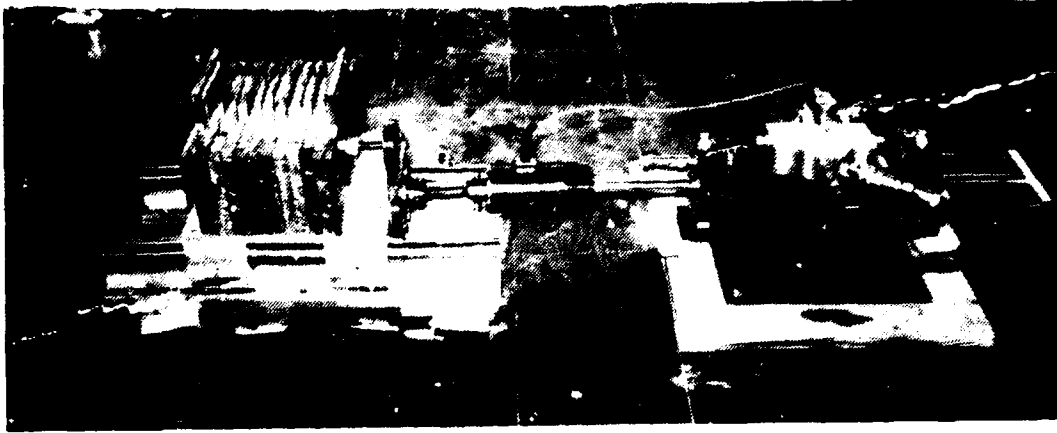


FIGURE 1 LINEAR MOTION HYDRAULIC EXCITER

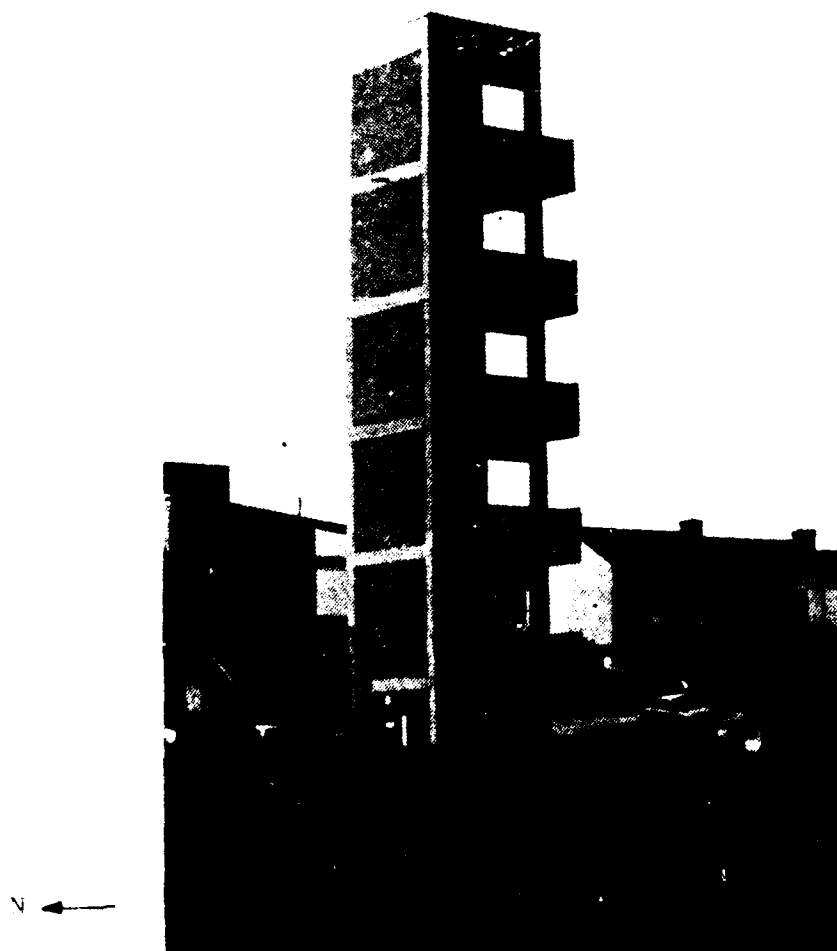


FIGURE 2 FIRE STATION DRILL TOWER

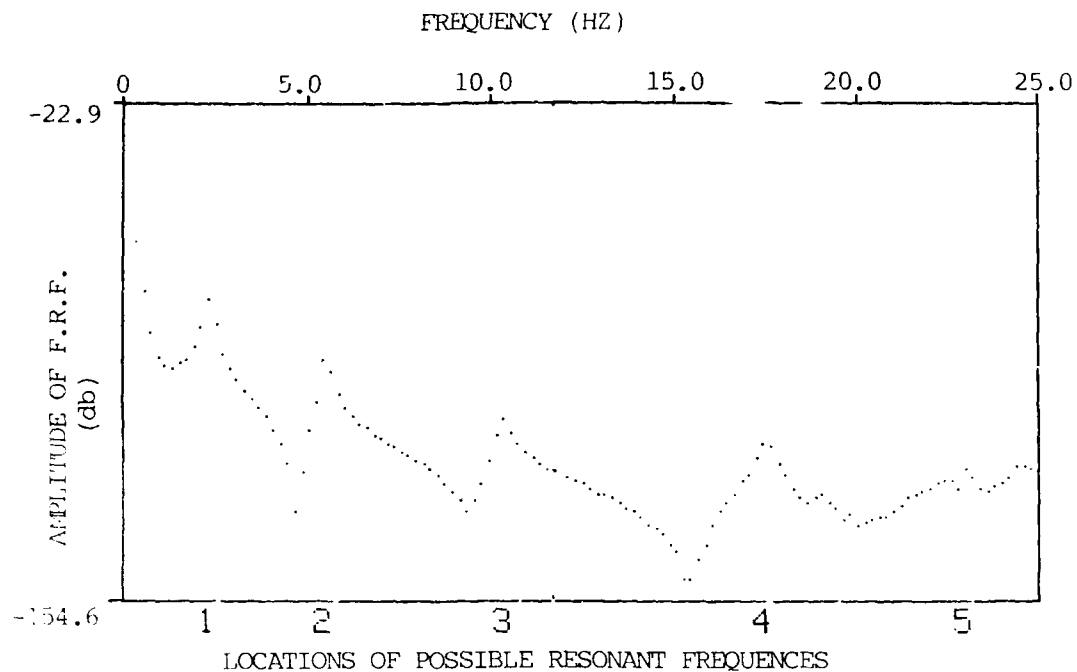


FIGURE 3 AMPLITUDE RECEPTANCE F.R.F. PLOT
(LOCATION S.W. COLUMN, EXCITATION E-W)

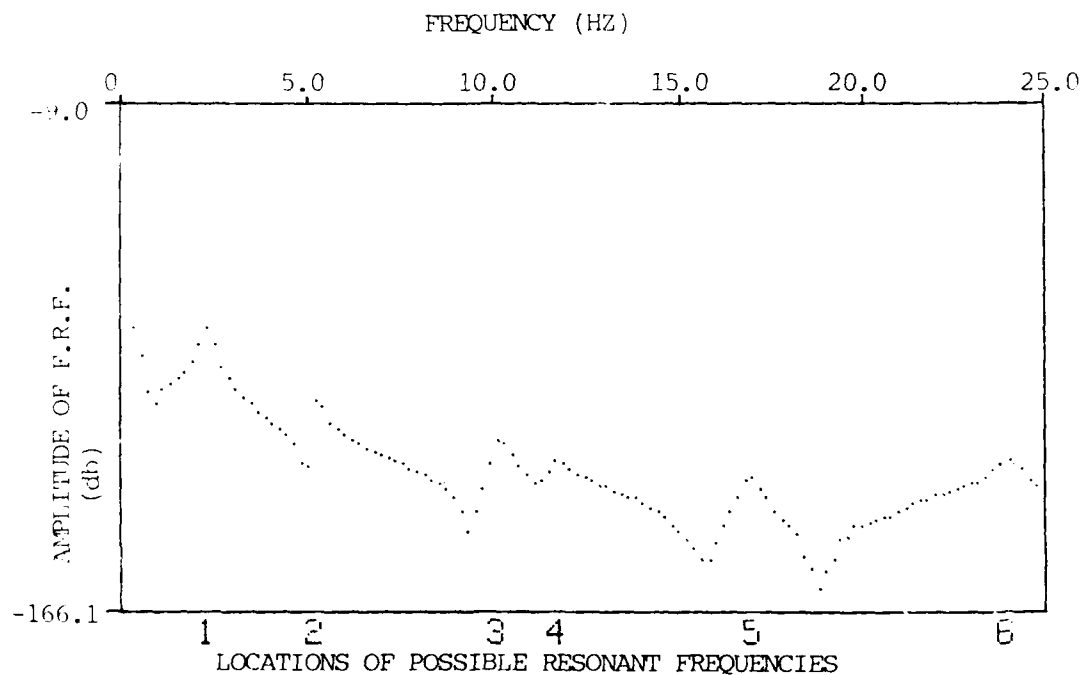


FIGURE 4 AMPLITUDE RECEPTANCE F.R.F. PLOT
(LOCATION S.W. COLUMN, EXCITATION N-S)

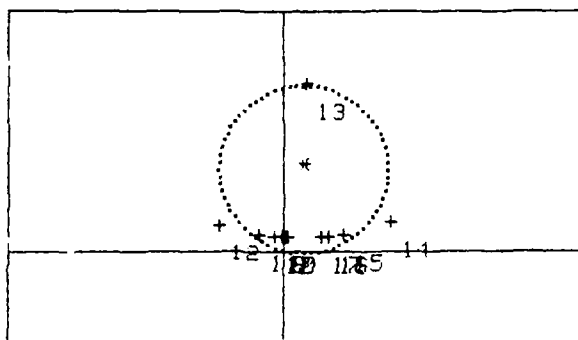


FIGURE 5 CIRCLE-FIT OF RAW INERTANCE F.R.F. DATA
MODE 1
(LOCATION S.W. COLUMN, EXCITATION N-S)

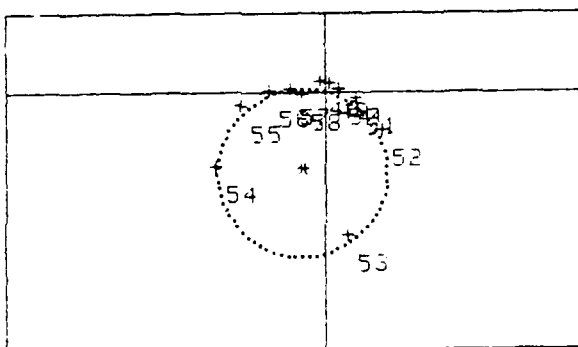


FIGURE 6 CIRCLE-FIT OF RAW RECEPTANCE F.R.F. DATA
MODE 2
(LOCATION S.W. COLUMN, EXCITATION N-S)

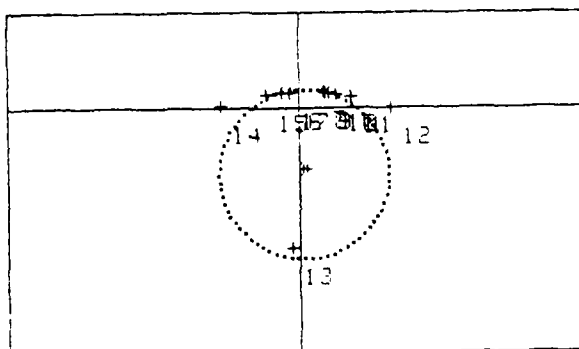


FIGURE 7 CIRCLE-FIT OF RAW RECEPTANCE F.R.F. DATA
MODE 1
(LOCATION S.W. COLUMN, EXCITATION N-S)

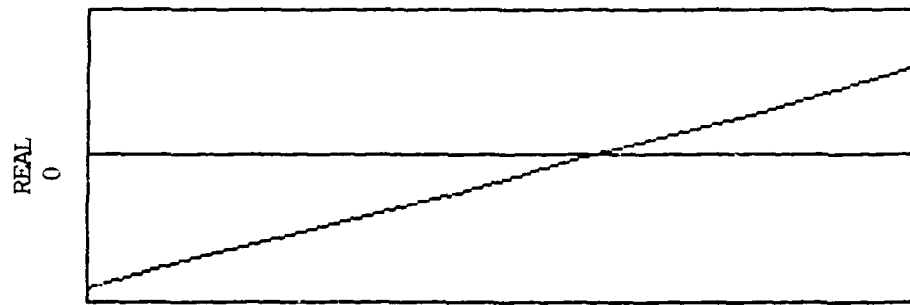


FIGURE 8 PLOT OF REAL PART OF RECEPTANCE F.R.F. AGAINST FREQUENCY SQUARED, MODE 3

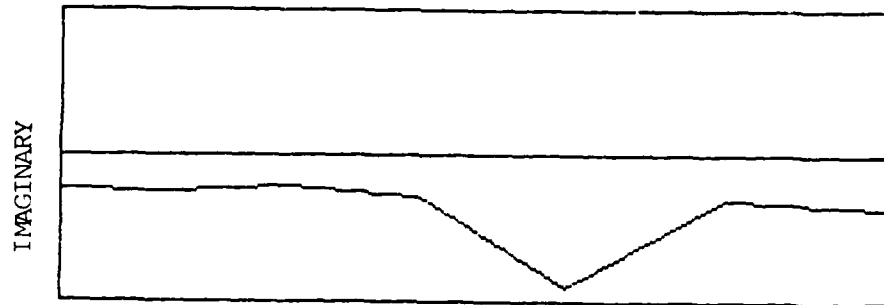


FIGURE 9 PLOT OF IMAGINARY PART OF RECEPTANCE F.R.F. AGAINST FREQUENCY SQUARED, MODE 3

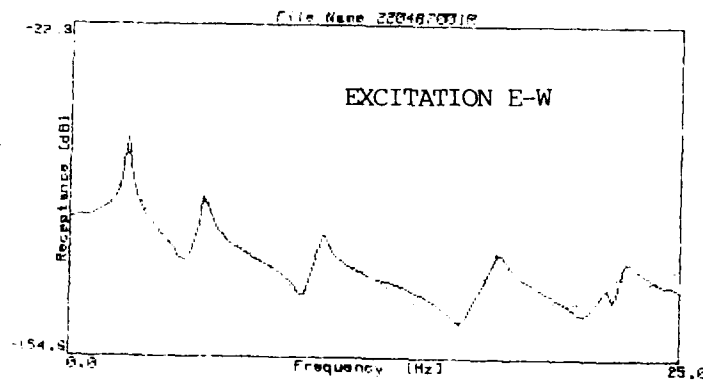
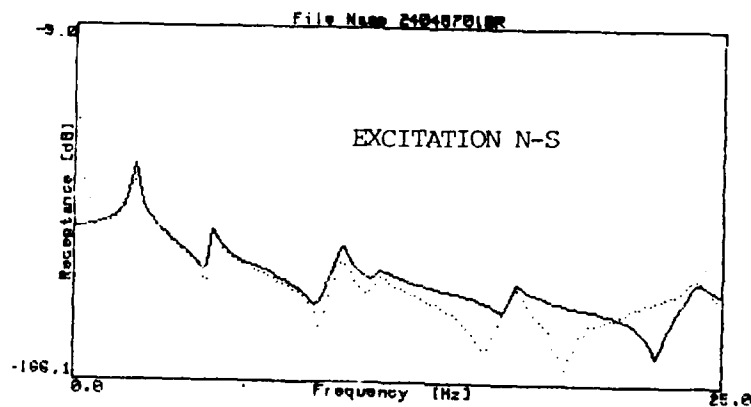


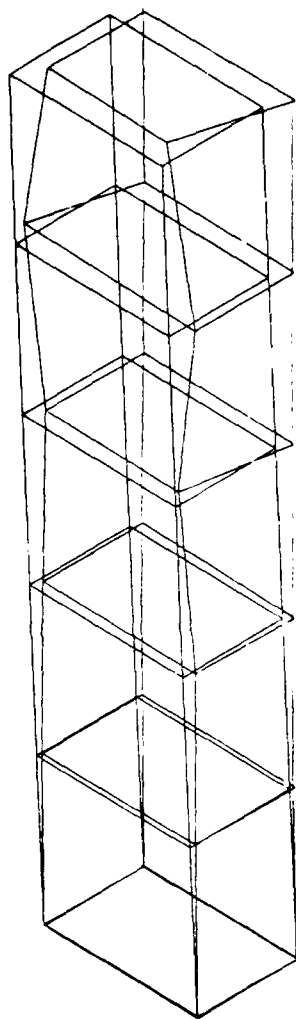
FIGURE 10

REGENERATION OF
RECEPTANCE F.R.F.
FROM DETERMINED
MODAL PARAMETERS
(LOCATION SW COLUMN)

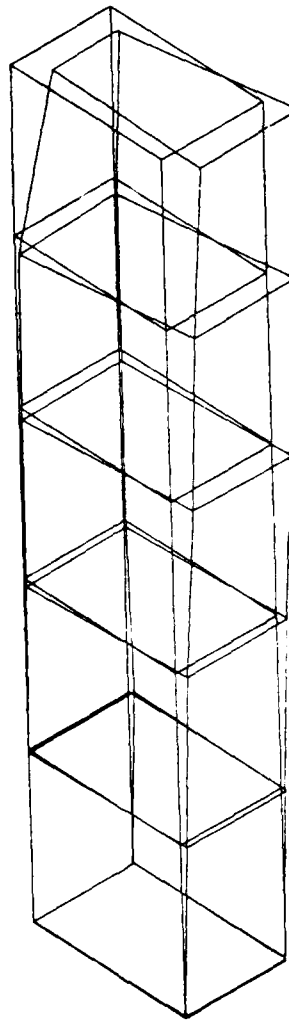


.... EXPERIMENTAL
DATA
— PREDICTED
DATA

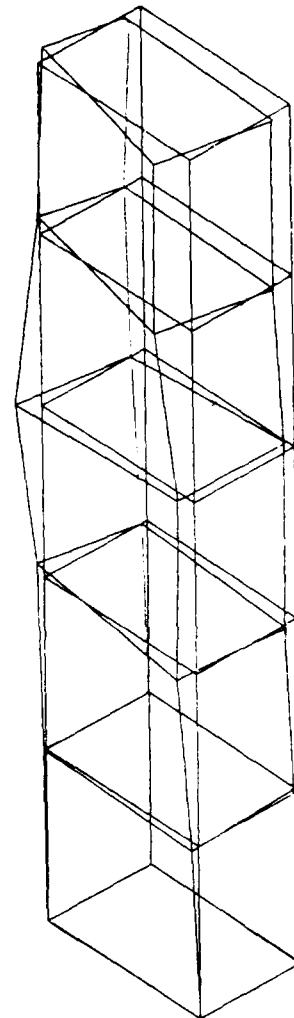
FIGURE 11



2.34HZ



2.36HZ



10.34HZ

FIGURE 12 THE SPATIAL DEFORMATION SHAPES OF THE
TOWER FROM EXPERIMENTAL DATA

SOURCE-TO-SITE SEISMIC MODELS IN STRUCTURAL DYNAMICS

L. Faravelli

Dept. of Structural Mechanics
University of Pavia - Italy

SUMMARY - When the uncertainty of the input of a dynamic structural problem is described by a stochastic process, structural analysis can be performed either by using stochastic dynamics results or by numerical integration of the equations of motion under simulated time histories.

Attention is focused here on the seismic excitation. Two aspects of its stochastic idealization are considered: to include non-stationarity in time and frequency and to allow for seismological schemes. The resulting evolutionary model leads to modifications in the structural analysis process which are discussed in detail.

1. INTRODUCTION

In a recent report, prepared for the Commission of the European Communities [1], it is expressed the "feeling" that there will soon be available numerical methods to compute the input-output relationships of linear multidegree of freedom systems subject to evolutionary excitation. This is due to the fact that "good evolutionary representations of the ground motion are possible".

In earthquake engineering, several stochastic models were proposed, discussed and analysed from the basic paper by Y.K. Lin [2]. Stationary models [3] (generally filtered white-noise), as Kanai-Tajimi idealization [4] [5], became popular due to both the simple way in which their parameters can be found [6] [7] and the advantages they offer in stochastic dynamic analyses [8] [9] [10]. Signal processing theory, then, has provided the tools for a deeper analysis of recorded accelerograms leading to evolutionary models in frequency [11] and time [12] domain.

The previous approach, however, ignores any suggestion from seismology, where the single time history is related to some basic parameters as magnitude, epicentral distance and soil properties. Although the general theory has still to be included in engineer practice, a simplified seismological idealization taking into account source mechanism and wave propagation was recently proposed by Boore [13] [14] and extended by the author to the evolutionary case [15].

This paper emphasizes the implications of the adoption of such a seismological model in structural dynamic analysis. The numerical example discusses the details of how evolutionarity can be introduced with reference to the Southern Italy earthquake of 1980.

2. BOORE'S SEISMOLOGICAL MODEL

The one-sided power spectral density function $G(\omega)$ of the stationary stochastic model proposed by Boore as a synthesis of seismological properties is written [13] [14]:

$$G(\omega) = [C A_1(\omega) A_2(\omega) A_3(\omega)]^2 / [\pi T_r] \quad (1)$$

The meaning of the notations is the following: ω = circular frequency; C = scaling factor; $A_1(\omega)$ = source factor; $A_2(\omega)$ = amplification factor; $A_3(\omega)$ = distance diminution factor; T_r = rupture duration.

Further details of the model must be added in order to clarify its seismological nature:

i) the scaling factor C can be expressed as the product of the radiation pattern R_p , by a first factor F which accounts for the free surface effects (usually $F = 2$.) and a second factor V (usually $V = 1/\sqrt{2}$) considering the partition of energy into horizontal components. The result of this product has then to be divided by 4π times the product of the density ρ by the cube of the shear velocity β in the source region. Finally, dividing by the hypocentral distance r , one finds:

$$C = R_p F V / [(4\pi \rho \beta^3) r] \quad (2)$$

ii) the source factor comes from seismological considerations on the source spectrum and can be expressed as

$$A_1(\omega) = [M_0 / (1 + (\omega_0/\omega)^2)] \cdot \omega_0^2 \quad (3)$$

where M_0 is the seismic moment and ω_0 is the corner frequency. Since Eq.(3) does not present any predominant frequency, for European and Russian earthquake [16] [17] it may be appropriate to write $A_1(\omega)$ as the product

$$A_1(\omega) = A_{1l}(\omega) \cdot A_{1h}(\omega) \quad (4)$$

with $A_{1l}(\omega)$ given by the r.h.s of Eq.(3) and

$$A_{1h}(\omega) = \zeta / (1 + (\omega/\omega_1)^2)^{1/2} \quad (5)$$

In Eq.(5), ζ is a normalization factor (~ 1.15) and ω_1 is a second corner frequency (≈ 2 Hz in [16]).

The scaling law, i.e. the relation between the corner frequency ω_0 and the seismic moment M_0 , is proposed by Boore [13] to have the form:

$$\omega_0 / (2\pi) = 4.9 \cdot 10^6 \beta (\Delta\sigma / M_0)^{1/3} \quad (6)$$

where $\Delta\sigma$ denotes a scaling parameter with dimension of stress ($\Delta\sigma = 100$ bar was originally assumed: European earthquakes however needs the introduction of higher values if Eq.(6) is adopted).

iii) the amplification factor should take into account both the amplification due to strong impedance contrast of soil layers

and the one in wave amplitude due to conservation energy for waves travelling through materials with decreasing velocities as the earth surface is approached. The latter term is tabulated in Refs. [17] and [14], while the author gave it an analytical form holding for $\omega > .32 \cdot 2\pi$ rad/s [15]:

$$A_2(\omega) = 2./[1 + ((.32 \cdot 2\pi)/\omega)^2] \quad (7)$$

iv) the distance diminution factor has been selected by Boore as:

$$A_3(\omega) = \exp(-\omega r / (2 Q(\omega) \beta) \cdot (1 + (\omega/\omega_m)^8)^{1/2} \quad (8)$$

where $Q(\omega)$ is the frequency dependent attenuation function. The second factor in the r.h.s. of Eq.(8) is a high-cut filter with corner frequency ω_m which is assumed to be independent of the seismic moment, its value being only a site effect.

Eq. (1) represents a stationary stochastic process: in Ref. [18] non-stationarity in time was included by the classical scheme making use of a deterministic function of time by which the stationary process is modulated.

3. NON-STATIONARY STOCHASTIC MODEL

The author has already emphasized in Ref.[15] that Boore's model can become very fascinating from a stochastic dynamics point of view. In fact, if one accepts that the high-cut filter in Eq. (8) is substituted with the smoothing of high frequencies of the additional source term $A_{1h}(\omega)$, the distance diminution factor reduces to:

$$A_3(\omega) = \exp(-\omega r / (2 Q(\omega) \beta)) \quad (9)$$

Moreover, Q can be assumed to be proportional to the frequency ($Q = Q_0 \omega / (2\pi)$) [16] and, hence, Eq. (9) simplifies into

$$A_3(\omega) = \exp(-\pi r / (Q_0 \beta)) = \text{const.} \quad (10)$$

Being constant with ω , it can be included into the scaling factor to form

$$C' = C \cdot A_3(\omega) \quad (11)$$

Eq. (01) can therefore be written

$$G(\omega) = [C'^2 / (\pi T_R)] \cdot [A_1(\omega) A_2(\omega)]^2 = C'' \{ [(M_0 \omega_0^2) / (1 + (\omega_0/\omega)^2)] \cdot [\zeta / (1 + (\omega/\omega_1)^2)^{1/2}] \cdot [2 / (1 + (.32(2\pi)/\omega)^2)] \}^2 \quad (12)$$

where $C'' = [C'^2 / (\pi T_R)]$. The corresponding stochastic process is a white-noise $w(t)$ of power spectral density function

$$G_0 = 4C'' \cdot M_0^2 \cdot \zeta^2 \cdot \omega_0^4 \cdot \omega_1^2 \quad (13)$$

filtered through:

1) the first order differential equation

$$\dot{s} + \omega_1 s = w(t) \quad (14)$$

for which the square modulus of the transfer function $H_1(\omega) = [(1/\omega_1)/(1+i(\omega/\omega_1))]$ is $[A_{1h}(\omega)]^2/(\omega_1^2 \zeta^2)$;

2) the second order differential equation

$$\ddot{u} + 2\omega_2 \dot{u} + \omega_2^2 u = -s \quad (15)$$

which is a spring-dashpot linear system with damping ratio 1. The square modulus of the transfer function for the acceleration $H_2(\omega) = \{(\omega^2/\omega_2^2)/[(1-(\omega^2/\omega_2^2))+2i\omega\omega_2]\}$, in fact, coincides with $[A_2(\omega)]^2/4$ for $\omega_2 = 0.32 \cdot (2\pi)$ rad/s;

3) the second order differential equation

$$\ddot{z} + 2\omega_0 \dot{z} + \omega_0^2 z = -u \quad (16)$$

which is again a spring-dashpot linear system with damping ratio 1. The square modulus of the transfer function for the acceleration $H_3(\omega) = \{(\omega^2/\omega_0^2)/[(1-(\omega^2/\omega_0^2))+2i\omega\omega_0]\}$, in fact, coincides with $[A_1(\omega)]^2/(\omega_0^4 M_0^2)$.

It follows that:

$$\begin{aligned} G(\omega) &= G_0 \cdot [(A_{1h}(\omega))^2/\zeta^2] \cdot [(A_2(\omega))^2/4] \cdot [(A_{1z}(\omega))^2/(M_0^2 \omega_0^4)] = \\ &= G_0 \cdot |H_1(\omega)|^2 \cdot |H_2(\omega)|^2 \cdot |H_3(\omega)|^2 \end{aligned} \quad (17)$$

Therefore, in the presence of a dynamical system with n degrees of freedom, the derivative d^2z/dt^2 in Eq. (16) denotes the ground acceleration, i.e. the external action. Since n degrees of freedom means a system of $2n$ first order differential equations, the global idealization consists of $(2n+5)$ first order differential equations driven by a white-noise. Note that the high frequency cut-off filter of Eq. (8) should be introduced for structural systems with significant frequencies larger than 10 Hz.

Such a model has been made nonstationary by the author in Ref. [15]. Essentially one introduces a evolutionary power spectral density function of the type:

$$G_e(\omega, t) = G(\omega) \cdot |g(\omega, t)|^2 \quad (18)$$

where $g(\omega, t)$ is a function to be determined on experimental basis which relates to the time the intensity $W(t)$ and, hence, the corner frequency $\omega_W(W(t))$ or viceversa. Given Eq. (17), $g(\omega, t)$ has been suggested to have the form:

$$|g(\omega, t)|^2 = K(\omega) [M_0^2/A_{11}(\omega)]^2 \cdot (\omega_W^4(t) W^2(t)) / [1 + (\omega_W(t)/\omega)^2]^2 \quad (19)$$

where K is a normalization term such that:

$$\int_0^\infty g(\omega, t) dt = 1/K(\omega) \quad (20)$$

For instance, one can assume according to Eq. (06)

$$\omega_W(t)/(2\pi) = 4.9 \cdot 10^6 \beta (\Delta\sigma/M_0 W(t))^{1/3} \quad t < t_p \quad (21)$$

$$\omega_W(t)/(2\pi) = 4.9 \cdot 10^6 \beta (\Delta\sigma W(t)/M_0)^{1/3} \quad t > t_p \quad (22)$$

t_p being the time at which $W(t)$ is maximum. It is well known in seismology, in fact, that primary waves have significant frequencies higher (1.5 to 2 times) than the ones of the secondary waves. Moreover, the latter waves are characterized by frequencies higher than the ones of the surface waves coming at the end of the record.

Although Eq.(22) needs further investigation, together with Eq. (21) it reduces the description of the model to the definition of $W(t)$. In Ref. [15] this was made by using the classical compound intensity function [9]. The next section is devoted to verify it on experimental bases.

From the point of view of structural analysis, it is worth noting that the response of a linear system can then be expressed in the same form of Eq. (18) with $g(\omega, t)$ replaced by $b(\omega, t)$ [19] with

$$b(\omega, t) = \int_{-\infty}^{+\infty} h_s(\tau) g(\omega, t-\tau) e^{-i\tau\omega} d\tau \quad (23)$$

where $h_s(\tau)$ is the impulse response function of the linear system. In the frequency domain this input-output relationship consists of a convolution, instead of a product as in the stationary case. The convolution can then be calculated by using the FFT algorithm [1].

For non-linear systems, time histories can be simulated from the proposed model or stochastic equivalent linearization [10] can be adopted.

4. EXPERIMENTAL TIME-DEPENDENCE OF THE CORNER FREQUENCY

The frequency content of the single wave type is not clearly emphasized by studies [20] using the physical spectrum [12], since the effects of the strong motion are always present during tail analysis. In this paper, therefore, the evolutionary response spectrum has been preferred. It is built, according to Ref.[11], for some accelerograms recorded during the Southern Italy earthquake of November 1980. The values of its main parameters are: $\rho = 2.6 \text{ g/cm}^3$, $\beta = 3.5 \text{ Km/s}$, $T_r = 6 \text{ s}$, $M_0 = 6.10^{25} \text{ dyn}\cdot\text{cm}$, $Q_0 = 40 \text{ s}$. Moreover for R_p one takes the average on the focal sphere 0.63.

Figure 1 summarizes the results obtained for the accelerogram A621EW recorded at Bagnoli Irpino, on stiff soil, at hypocentral distance $r = 28 \text{ Km}$. Figure 2 shows the characteristics of the relevant NS component. Finally, Figure 3 shows the characteristics of the record A629EW of the same event obtained in Sturmo, on stiff soil, at $r = 37.6 \text{ Km}$. Figure 4 provides perspective views of the estimates of $G_e(\omega, t)$.

The following remarks come out from the analysis of these figures: i) a non-stationary model making use of the superposition of three (or more) stationary processes with different frequency bands and with different modulating functions could be appropriate; ii) having in mind that the equivalent stationary duration d_0 is for the three records 6.1, 11.9 and 7.1 sec, respectively, the evolutionary power spectral density function $G_e(\omega, t)$ is nearly zero before and after the strong part occurs: the shift t_1 between primary and secondary waves is approximately 3.8 sec. for A621 and 5.37 sec. for A629; iii) the time dependence of the corner frequency (i.e. of the band where the frequency content concentrates) is not a function of the intensity $W(t)$, since it varies also during the strong part where $W(t)$ can be assumed nearly constant.

One has now the elements for updating Eqs. (21) and (22), remembering that ω_0 was estimated [15] in the range (1.01, 1.7 rad/sec). The corner frequency $\omega_W(0)$ is derived from the maximum ω (ω_{max}) for which significant $G_e(\omega, t)$ are computed (generally just after t_1); Eq. (21) provides then $W(0)$ and the model is maintained stationary till t_1 . Analogously, Eq. (22) is used for deriving from the minimum ω (ω_{min}) $\omega_W(t_1+d_0)$ and $W(t_1+d_0)$, and the model remains stationary after t_1+d_0 . In the middle $\omega_W(t)$ varies according to the exponential law:

$$\omega_W(t) = \omega_W(0) \exp[-B(t-t_1)^k] \quad (24)$$

with $B = (1/d_0)^k \ln(\omega_W(0)/\omega_W(t_1+d_0))$ and k an appropriate exponent. However, the intensity $W(t)$ must be determined in such a way that the maximum of $G_e(\omega, t)$, for different t , does not change even if the abscissa decreases in time.

In conclusion, evolutionary models of the seismic action can be easily built, but, since the strong part changes its frequency content as the motion progresses, significant consequences on the structural response can be expected.

ACKNOWLEDGEMENT - The financial support from the Ministry of Public Education (MPI) is here acknowledged.

REFERENCES

1. A. PREUMONT 1986 Belgonucleaire BN 8607-06, CEE Contract RAP-086-B(S). Application of the Random Vibration Approach in the Seismic Analysis of LMFBR Structures.
2. Y.K.LIN 1964 J. of Acoust. Soc. of America, 36, 1, 82-84. Nonstationary Shot-Noise
3. L.FARAVELLI 1988 accepted for publication in Probabilistic Engineering Mechanics. Stochastic Modeling of the Seismic Excitation for Structural Dynamics Purposes.
4. K.KANAI 1957 Bull. Earth. Research Inst., Univ. of Tokyo, 35, 309-325. Semi-Empirical Formula for Seismic Characterization of the Ground.
5. H. TAJIMI 1960 Proc. 2nd WCEE, Tokyo. Statistical Method for Determining the Maximum Response of a Building Structure During an Earthquake.

6. P.RUIZ and J.PENZEIN 1969 EERC Report, Univ. of California Berkeley. Probabilistic Study for the Behaviour of Structures during Earthquakes.
7. E. VANMARCKE and S.P.LAI 1980 Bull. of the Seismological Soc. of America, 70, 4, 1293-1307. Strong Motion Duration and RMS Amplitude of Earthquake Records.
8. Y.K. LIN 1976 R.E.Krieger Publ. Comp., Huntington. Probabilistic Theory of Structural Dynamics.
9. G. AUGUSTI, A. BARATTA and F.CASCIATI 1984 Chapman & Hall, London, Probabilistic Methods in Structural Engineering.
10. F. CASCIATI and L. FARAVELLI 1988 Research Studies Press, Letchworth. Fragility Analysis of Complex Structural Systems.
11. H.KAMEDA 1975 J. of Eng. Mechanics, Proc.ASCE, 101,6, 787-801. Evolutionary Spectra of Seismogram by Multifilter.
12. M.B. PRIESTLEY 1981 Academic Press. Spectral Analysis and Time Series.
13. D.M. BOORE 1986 Proc. NATO Adv. St. Inst. on Strong Motion. Seismology, Ankara. The Prediction of Strong Ground Motion.
14. D.M. BOORE 1986 Bull. of Seismological Society of America, 76, 1, 43-64. Short Period P and S-Wave Radiation from Large Earthquakes: Implication for Spectral Scaling Relations.
15. L. FARAVELLI 1987 Proc. ICASP5, Vancouver, Modeling the Seismic Input for a Stochastic Dynamic Structural Problem.
16. E. FACCIOLI, A. ROVELLI and R. FREGONESE 1984 Proc. 8th WCEE, S.Francisco, 361-368. A Study of the Special Characteristics of Accelerogram from Recent Earthquakes in Italy and Near Regions.
17. A.A. GUSEV 1983 Geophys. J. R. Astr. Soc., 74, 787-808, Descriptive Statistical Model of Earthquake Source Radiation and its Application to an Estimation of Short-Period Strong Motion.
18. E. SAFAK and D.M. BOORE 1986 Proc. 3rd US Nat. Conf. on Earth. Eng., Charleston, I, 137-148, On Non-Stationary Stochastic Models for Earthquakes.
19. Y.K. LIN and Y. YONG 1986 Florida Atlantic Univ., Report CAS-86-7. Evolutionary Kanai-Tajimi Type Earthquake Models.
20. F. SABETTA, R. MASIANI and A.GIUFFRE' 1986 Proc. 8th ECEE, Lisbon, 3.2.25. Frequency Non Stationarity in Italian Strong Motion Accelerograms.

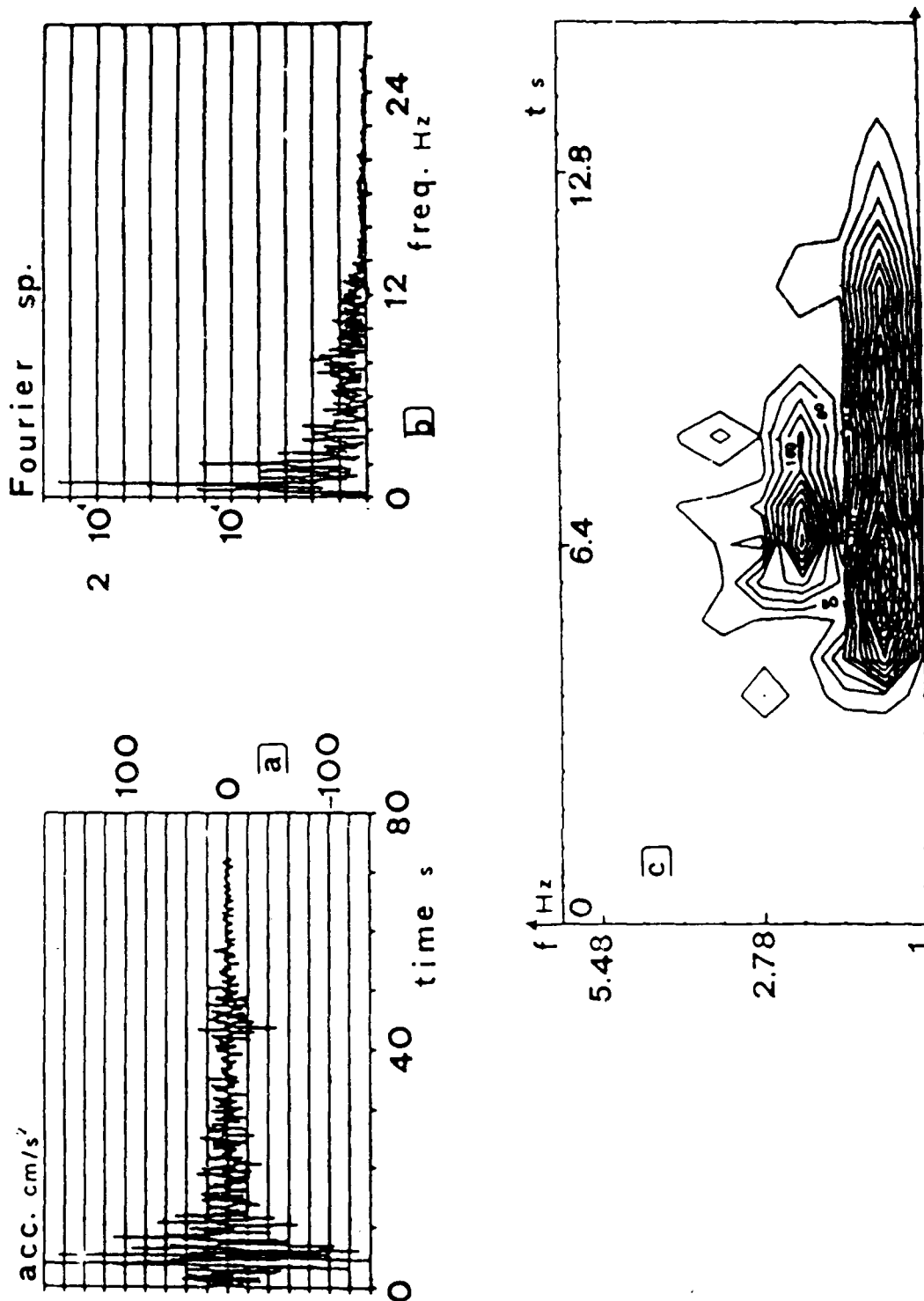


Figure 1 - a) Accelerogram A621EW after processing; b) Fourier spectrum of the accel. in a); c) evolutionary power spectral density function

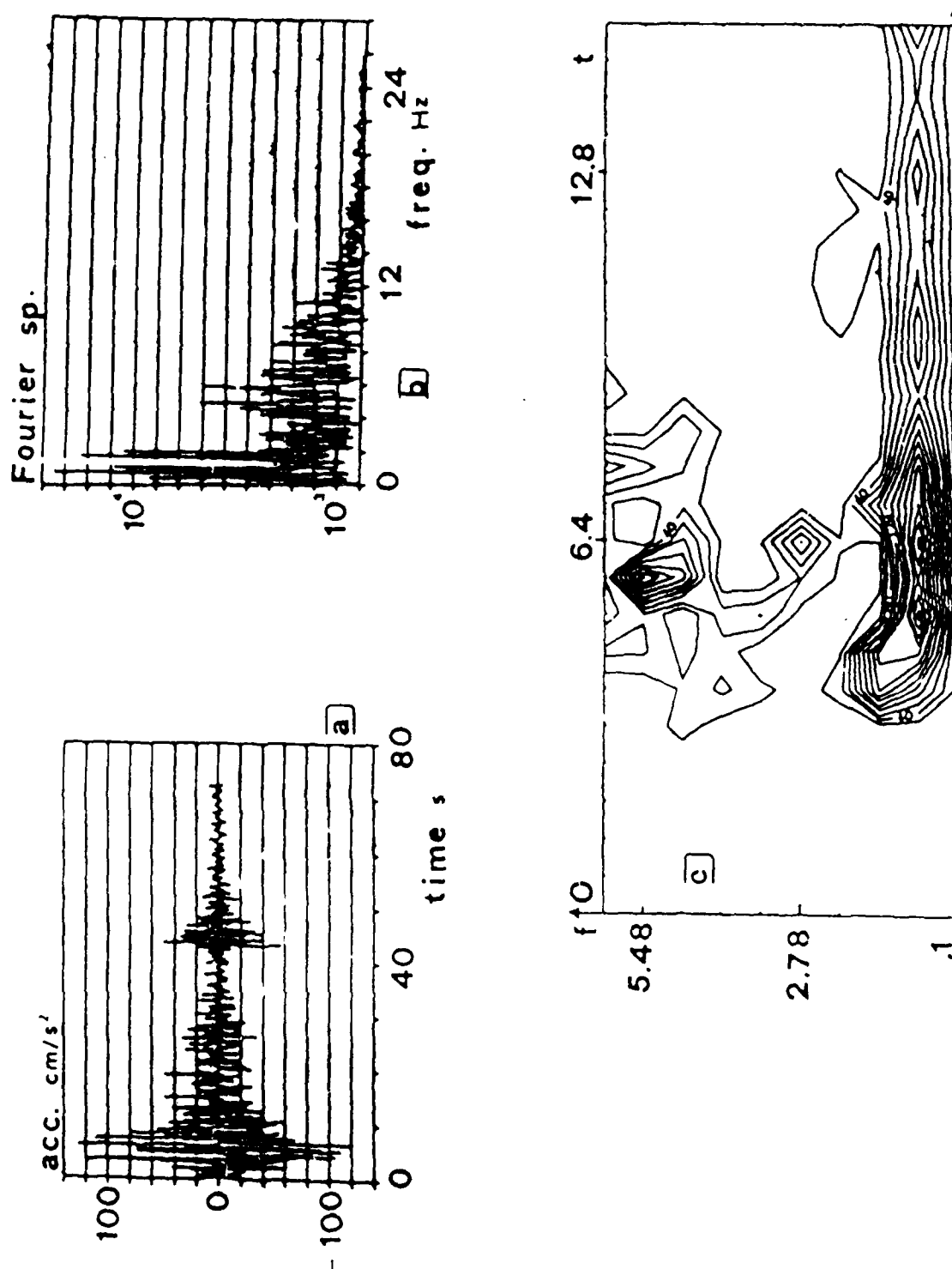


Figure 2 - a) Accelerogram A621NS after processing; b) Fourier spectrum of the accel. in a); c) evolutionary power spectral density function

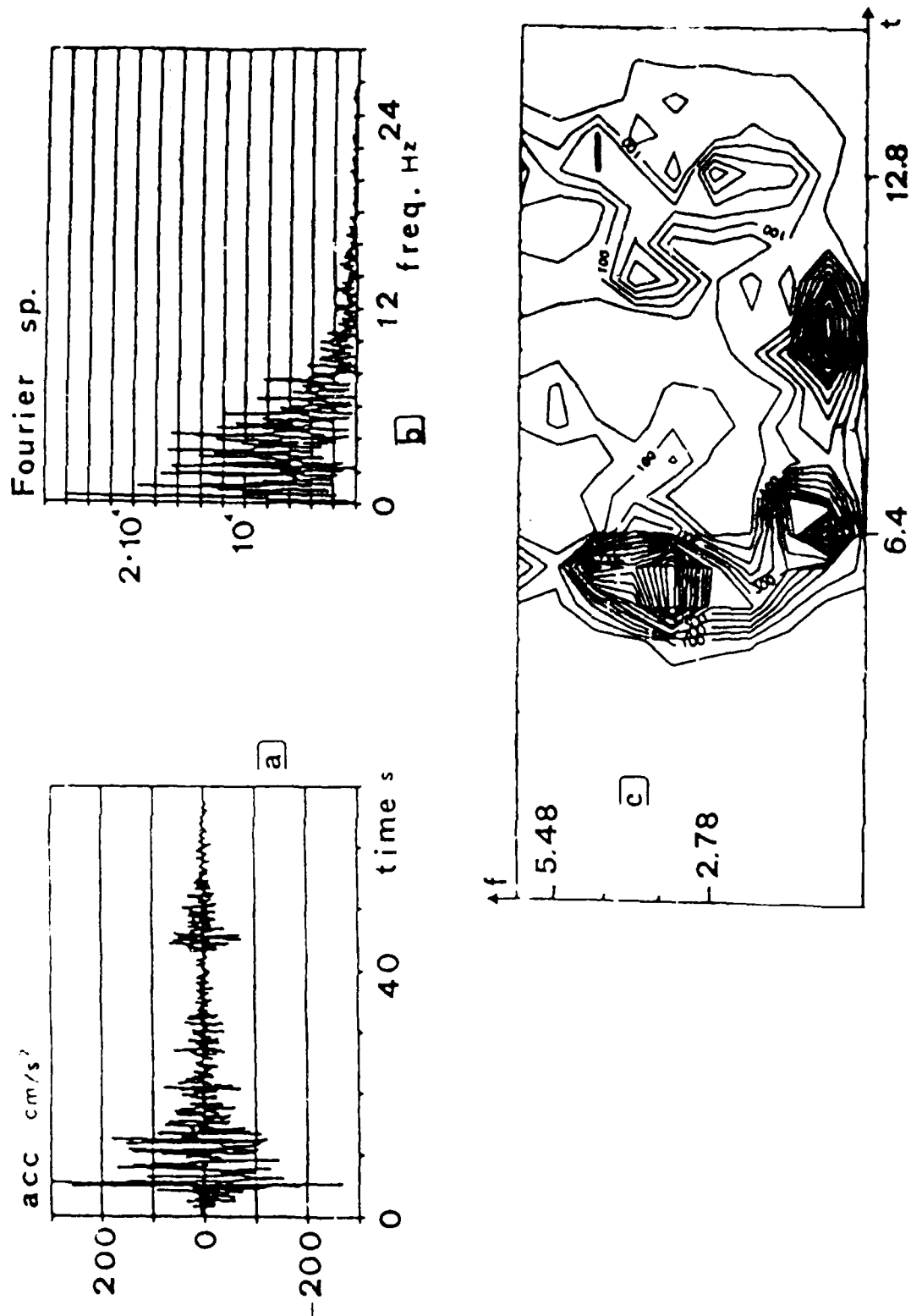


Figure 3 - a) Accelerogram A629EW after processing; b) Fourier spectrum of the accel. in a); c) evolutionary power spectral density function

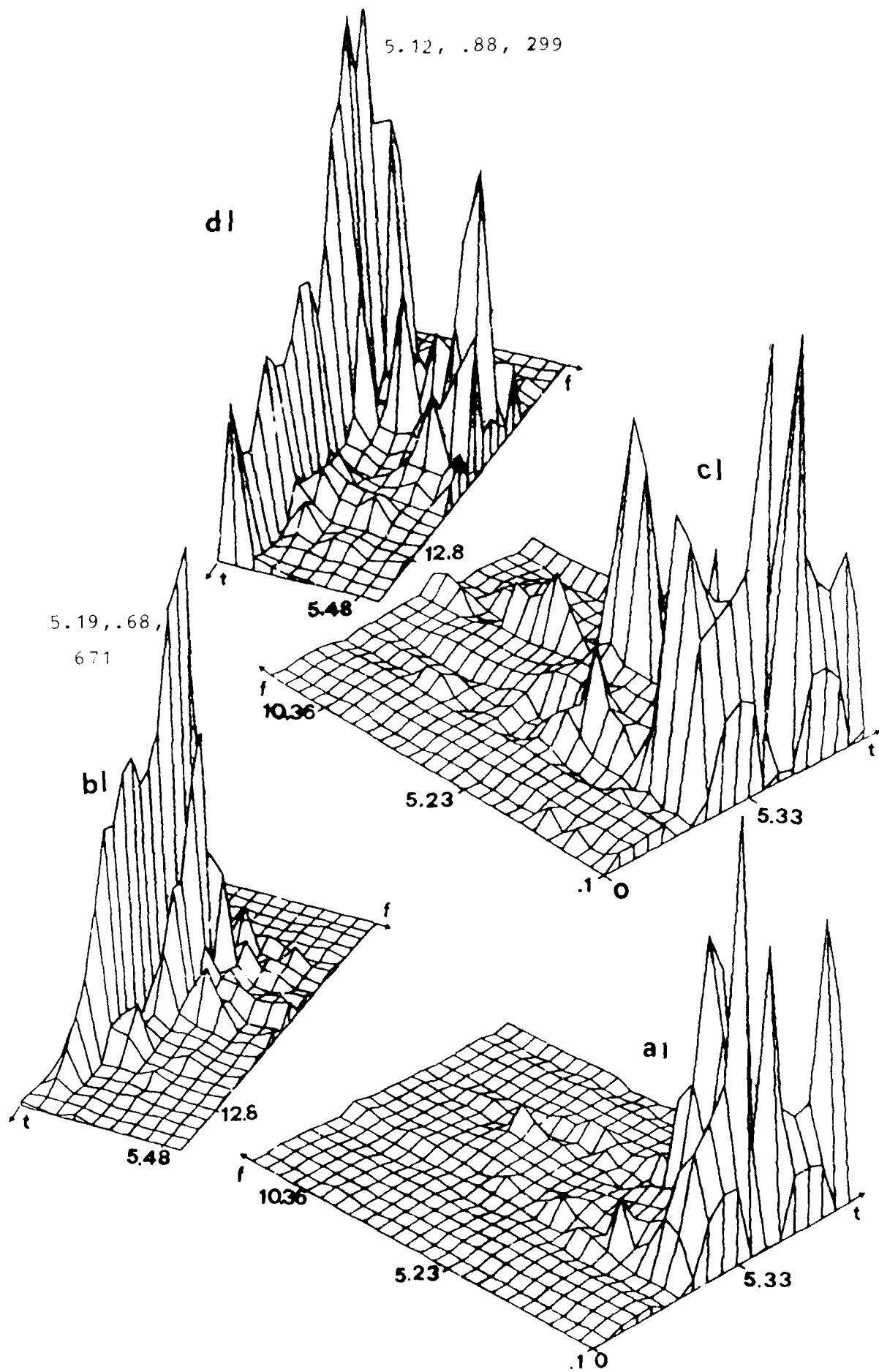
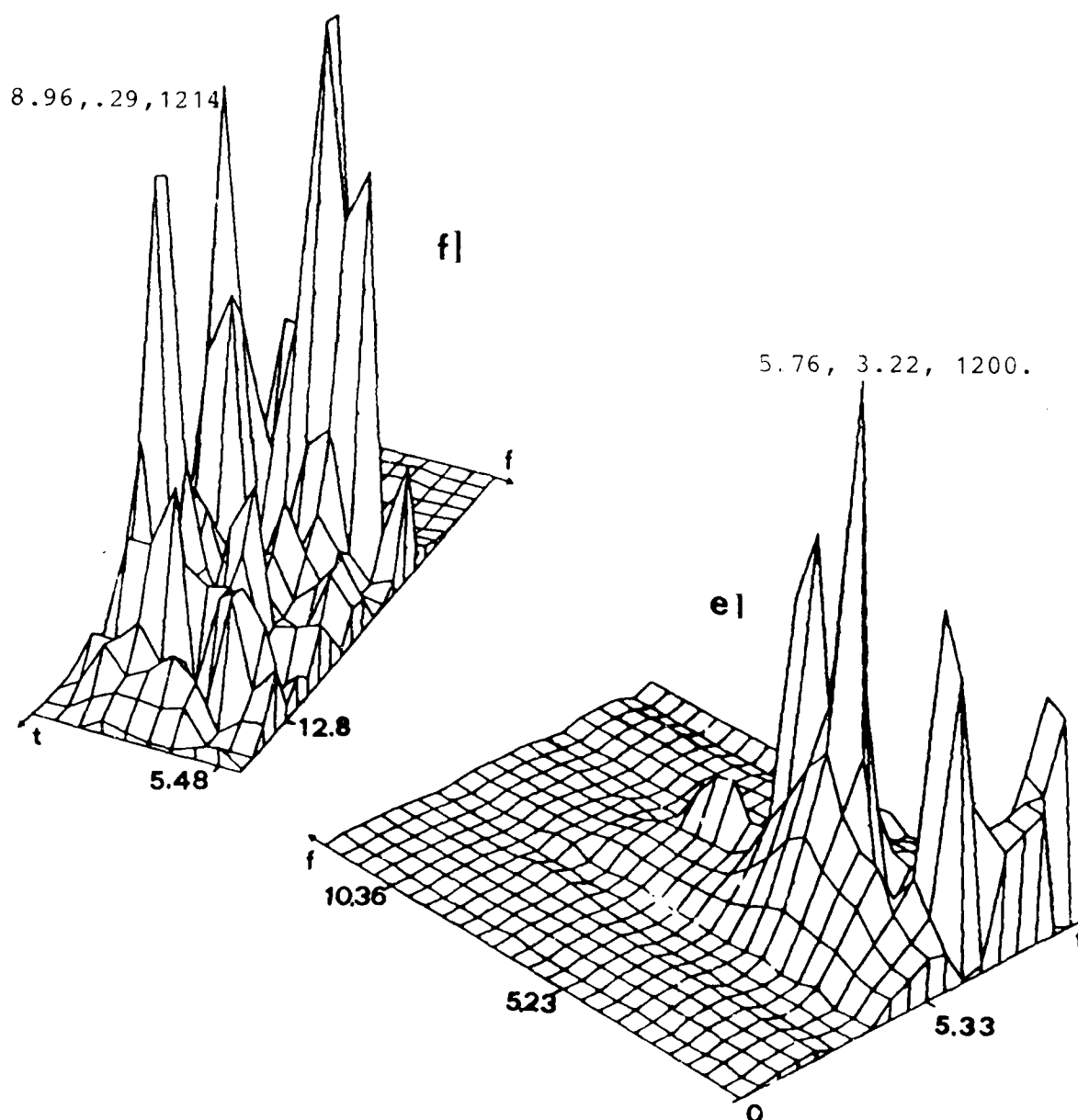


Figure 4 - a) A621EW: evol. power spectral dens. function over the domain $[(0, 15.36 \text{ s}), (.1, 6.15 \text{ Hz})]$; b) as in a) but over $((0, 9.6 \text{ s}), (.1, 12.4 \text{ Hz}))$; c) A621NS: evol. power spectral dens. function over the domain $[(0, 15.36 \text{ s}), (.1, 6.15 \text{ Hz})]$; d) as in c) but over $((0, 9.6 \text{ s}), (.1, 12.4 \text{ Hz}))$; e) A629EW: evol. power spectral dens. function over the domain $[(0, 15.36 \text{ s}), (.1, 6.15 \text{ Hz})]$; f) as in d) but over $((0, 9.6), (.1, 12.4 \text{ Hz}))$.



AN ASSESSMENT OF DIGITAL ACTIVE TENDON CONTROL OF BUILDING STRUCTURES

F. López-Almansa(*), J. Rodellar(**), A.H. Barbat(**) and J.A. Canas(**)

* School of Architecture, Technical University of Catalonia, Barcelona (Spain)

** School of Civil Engineering, Technical University of Catalonia, Barcelona (Spain)

SUMMARY: In this paper a control system by active tendons is proposed and its effectiveness to reduce the dynamic response of building structures with a reasonable cost of energy is tested by means of numerical experiments considering two 23-story buildings (called B_1 and B_2) subjected to seismic and wind excitations. Building B_1 has a stiff steel resistant structure and building B_2 has a vertical rigid centric nucleus having the rest of its structure no influence in the horizontal stiffness. The dynamic behaviours of buildings B_1 and B_2 are representative of those of the different types of structures most commonly used in buildings of about this number of floors. The results of the numerical experiments allow to conclude that active cables are useful for control of tall buildings and that they are more effective in buildings with a dynamic behaviour similar to the one of building B_2 .

1. INTRODUCTION

An active structural control system tries to minimize the response of structures subjected to dynamic excitations and is essentially based on the closed-loop scheme of Figure 1.

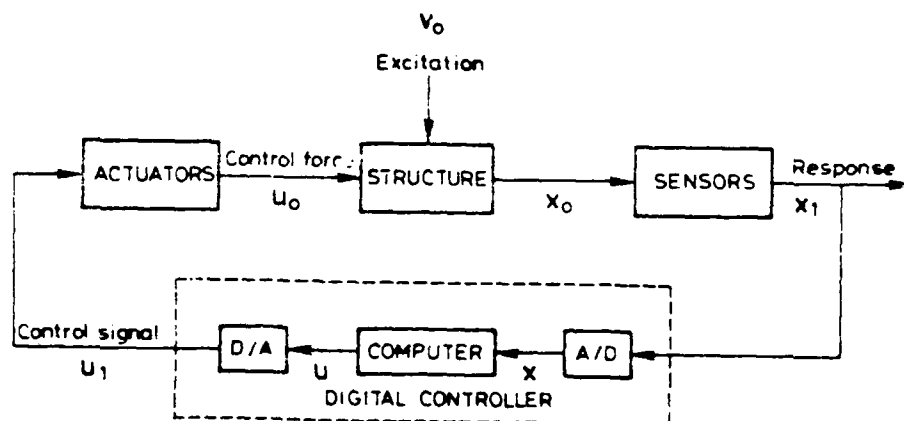


Figure 1 Block diagram of a digital active control system

The sensors measure continuously the structural response \mathbf{x}_0 and converts it in an analog electrical signal \mathbf{x}_1 which is transformed in a discrete-time sequence \mathbf{x} by the analog-digital converter. The digital computer calculates the discrete-time control signal \mathbf{u} by using a control algorithm. The digital control signal \mathbf{u} is transformed in a continuous-time signal \mathbf{u}_1 by the digital-analog converter and in the control forces \mathbf{u}_0 by the mechanical actuators.

In order to control the horizontal vibrations of tall buildings, actuators composed by active tendons have been proposed [1-4]. In [1] the ability of an active tendon control system to reduce the along-wind motion of a 40-story building is numerically tested and in [2] the same process is performed in a 8-story seismic excited building. In [1] and [2] the control law is based on a classical feedback scheme. In [3] another building's control system by active cables is proposed, its effectiveness to reduce the wind response being numerically tested. In [4] an experimental model of a 3-story building controlled by active cables is described and some seismic experiments showing the usefulness of the control system are presented. In [3] and [4] optimal control is considered as control algorithm.

In this paper, a more general control system by active cables for tall buildings is proposed and some numerical experiments of digital active control are presented to assess the effectiveness of the active tendons in seismic and wind excitation. In the numerical experiments two 23-story buildings are considered which are called, respectively, B_1 and B_2 [5]. The resistant structure of building B_1 is an orthogonal steel framework with rigid nodes while building B_2 has a vertical rigid centric nucleus having the rest of the structure no influence on its horizontal stiffness. The dynamic behaviours of buildings B_1 and B_2 are representative of those of the different types of structures most commonly used in buildings of about this number of floors: the horizontal deformation of building B_1 is firstly caused by the shear force while the one of building B_2 is firstly caused by the bending moment. The digital closed-loop control shown in Figure 1 is simulated in discrete time [6] and a predictive control algorithm [7] is considered taking into account the time delay in the actuators [8]. In the numerical experiments the physical features of the devices which constitutes the control system have been taken into account in order to compute the forces in the cables and its displacements and velocities to evaluate the feasibility of the active cables to perform a real control system.

2. ACTIVE TENDON CONTROL SYSTEM DESIGN

The horizontal active control forces \mathbf{u}_0 are applied on the building structure by a number m of mechanical actuators every one of them being composed by cables whose tension is quickly modified by hydraulic cylinders whose motion is governed by servovalves. The actuators are placed in such a way that the control forces are applied on the building at different floors. Every actuator i generates a control force u_{0i} from the control signal u_{1i} . Figure 2 shows two possible schemes of an actuator i ($i = 1, \dots, m$) [5].

In every one of the two schemes shown in Figure 2 two cables are braced to the frame of a floor by one of their ends while the other ends are connected to the embolus of a hydraulic cylinder placed on a lower floor. The movement of the cylinder is governed by a servovalve as a function of the component $u_{1i}(t)$ of the control signal. This movement results in two horizontal forces $f_{hi}(t)$ on the floors. The dynamics between these forces and the signal to the servovalve can be described by

$$f_{hi}(t) = C_{ai} u_{1i}(t - \tau_{ai}) \quad i = 1, \dots, m \quad (1)$$

where C_{ai} is a constant depending on factors such as the stiffness of the cables, the angle of the bracing and the servovalve calibration and τ_{ai} is the time delay caused by the inertia of the actuators. Assuming that τ_{ai} takes the same value τ_a for the m actuators, the expression (1) can be written in matrix form:

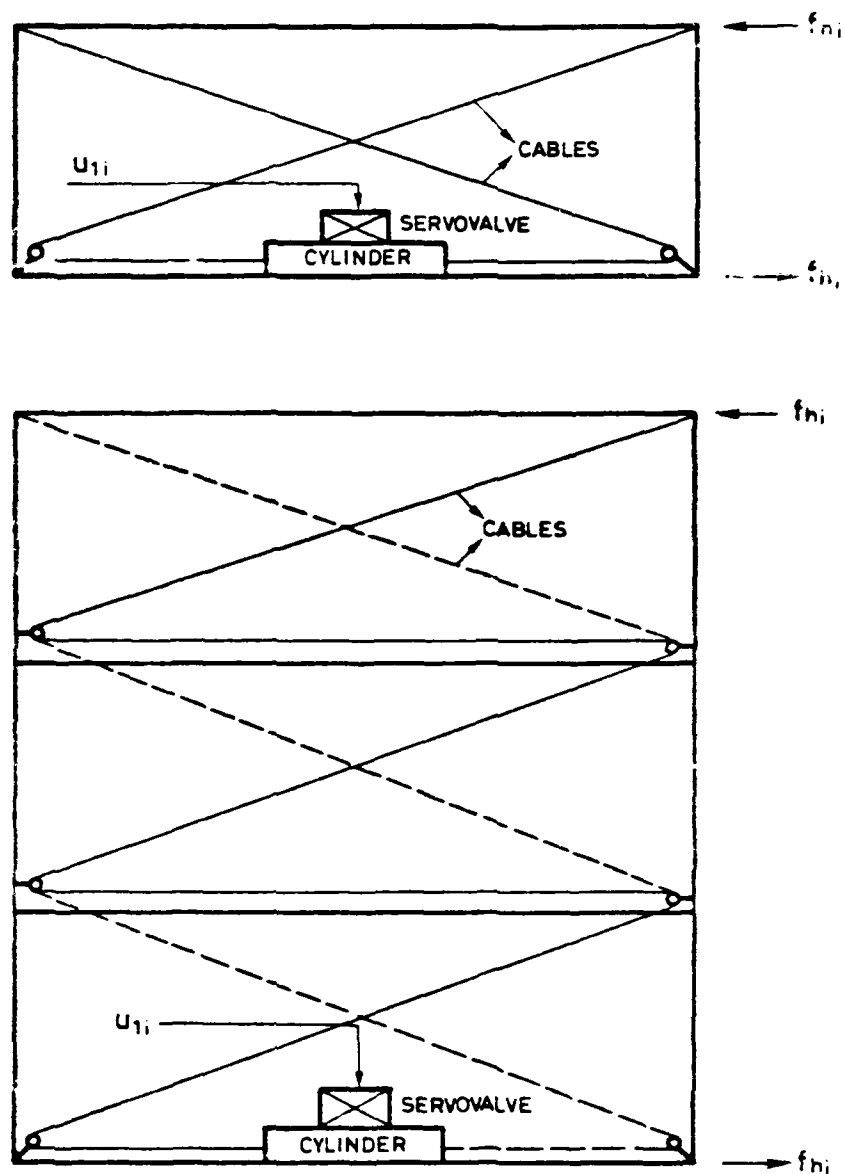


Figure 2 Cable control actuator.

$$f_h(t) = C_a u_1(t - \tau_a) \quad (2)$$

Every actuator is placed consecutively between each one of the m floors where the forces are wanted to be applied. Figure 3 illustrates a possible distribution of the cables.

The control forces $u_{0i}(t)$ are the resultings of the horizontal forces f_{hi} supplied by the cables. Thus one can write

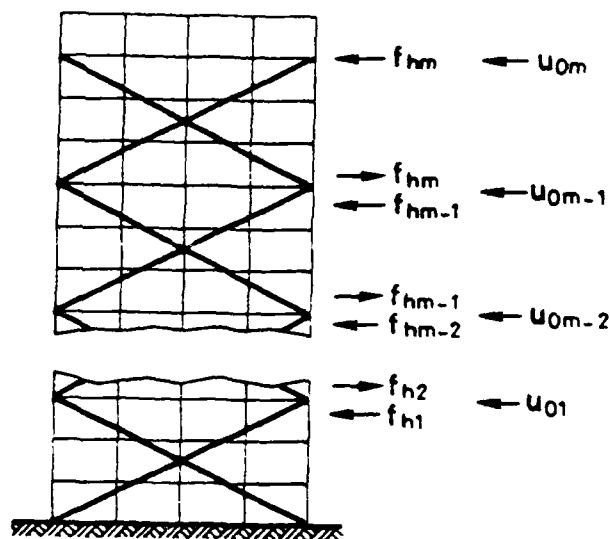


Figure 3 Actuators distribution.

$$u_0(t) = H f_h(t) \quad (3)$$

where

$$u_0 = \begin{pmatrix} u_{01} \\ \vdots \\ u_{0m} \end{pmatrix} \quad f_h = \begin{pmatrix} f_{h1} \\ \vdots \\ f_{hm} \end{pmatrix} \quad H = \begin{pmatrix} 1 & -1 & 0 & \dots & 0 & 0 \\ 0 & 1 & -1 & \dots & 0 & 0 \\ 0 & 0 & 0 & \dots & 1 & -1 \\ 0 & 0 & 0 & \dots & 0 & 1 \end{pmatrix} \quad (4)$$

From (2) and (3) one finally obtains the following model to describe the effect of the actuators

$$u_0(t) = K_a u_1(t - \tau_a) \quad (5)$$

where

$$K_a = H C_a \quad (6)$$

Since matrix K_a is not singular, expression (5) shows that with this arrangement of the cables it is possible to generate the control signal u_1 which produces an arbitrary value of the control forces u_0 .

3. SIMULATION OF CONTROL EXPERIMENTS

Different numerical tests are performed consisting of subjecting one building to a dynamic excitation in the presence of a number of horizontal control forces which changes between 1 (a force acting in the top of the building) and 23 (a force in every floor).

The operations involved in the closed-loop control are simulated in a digital computer by a discrete-time scheme which takes into account all the elements in the process shown in Figure 1 [6]. This scheme has proved its feasibility through comparisons with experimental results [8]. The motion of the building is simulated by a linear model with 23 degrees-of-freedom [5].

The results of every test are summarized in 6 indices which are called, respectively, $\Gamma_1, \dots, \Gamma_6$. The index Γ_1 represents the root mean square of the maximum values of the horizontal relative displacements between adjacent floors. Indices Γ_2 and Γ_3 correspond, respectively, to the r.m.s. of the maximum control forces u_0 , and the horizontal forces f_h , in the cables. Index Γ_4 represents the r.m.s. of the maximum undesired vertical forces introduced in the structure by the active cables. Indices Γ_5 and Γ_6 are, respectively, the r.m.s. of the maximum displacement and velocity of the embolus of the hydraulic cylinder.

4. CONTROL ALGORITHM

To generate the discrete-time sequence of control signals u , a control algorithm which is based on a predictive strategy is considered [7]. Taking into account the time delay, the expression which relates the control signal with the response of the structure x is

$$u(k) = -Dx(k) + \sum_{i=1}^d M_i u(k-i) \quad (7)$$

where k denotes the sampling instant, d is a number related to the time delay and D and M_i ($i = 1, \dots, d$) are constant matrices.

5. CONTROL OF THE SEISMIC RESPONSE

The seismic effectiveness of the active tendons is tested subjecting buildings B_1 and B_2 to sinusoidal ground excitations with different frequencies varying in the range $1 - 21 \text{ rad/s}$ and constant amplitude $0.1 g$. The values of indices $\Gamma_1, \dots, \Gamma_6$ are plotted as a function of the frequency of the excitation, the resulting diagrams being the controlled response spectra.

In Figure 4 one can see the comparison between the values of index Γ_1 for buildings B_1 and B_2 in the uncontrolled case.

Figure 4 shows that building B_1 is more stiff than building B_2 and in the dynamic response of building B_2 only the first mode has a significant importance while in the one of building B_1 the three first modes are important.

Figures 5, 6 and 7 show, respectively, the values of indices Γ_1 , Γ_3 and Γ_5 for buildings B_1 and B_2 and different values of the number of control forces.

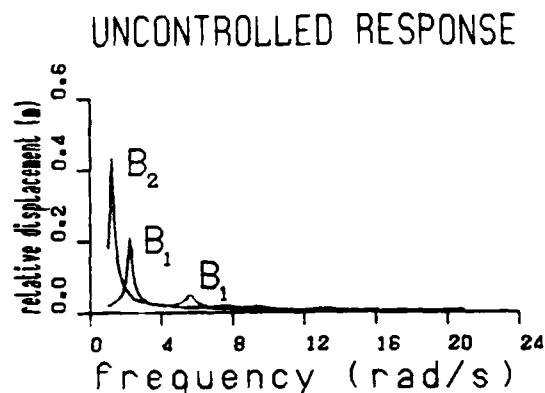


Figure 4 Values of Γ_1 in the uncontrolled seismic response.

By comparing Figure 4 with Figure 5 it can be noted that the control action generated by the active tendons produces a very important increase of the stiffness and the damping of the structure which results in an increase of the natural frequencies and a reduction of the response. These effects are more important as the number of control forces grows and, when 23 control forces are considered, the response is reduced in a percentage of about 0.1 % and the natural frequencies are fully out of the considered range. The reduction of the response and the increase of the natural frequencies are more important in building B_2 than in building B_1 the difference between the two cases being smaller when 23 control forces are considered.

Figure 6 shows that the reduction of the response of the structure is reached with a reasonable amount of energy and with forces which can be supported by the cables and Figure 7 shows that the maximum displacement of the embolus is not greater than 0.40 m in all the cases.

6. CONTROL OF THE RESPONSE TO WIND GUSTS

To simulate the dynamic behaviour of controlled buildings B_1 and B_2 subjected to the excitation of the wind, different numerical experiments have been carried out by considering the following expression for the force f_w due to the wind

$$f_w(t) = \kappa [3 \sin(\omega t) + 7 \sin(2\omega t) + 5 \sin(3\omega t) + 4 \sin(4\omega t)] \quad (7)$$

where κ depends on the speed of the wind and the height over the ground. Numerical experiment when the frequency ω varies between 0.5 and 7.5 rad/s are shown in [5].

These results confirm in the wind excitation case the features observed in the seismic case.

7. CONCLUSIONS

From Figures 4-7 and the results of the other numerical experiments two conclusions can be pointed out about the features of the active tendon control of buildings B_1 and B_2 :

- Generally, the control action produces an important reduction of the response with reasonable dimensions of the cables and the rest of the elements.

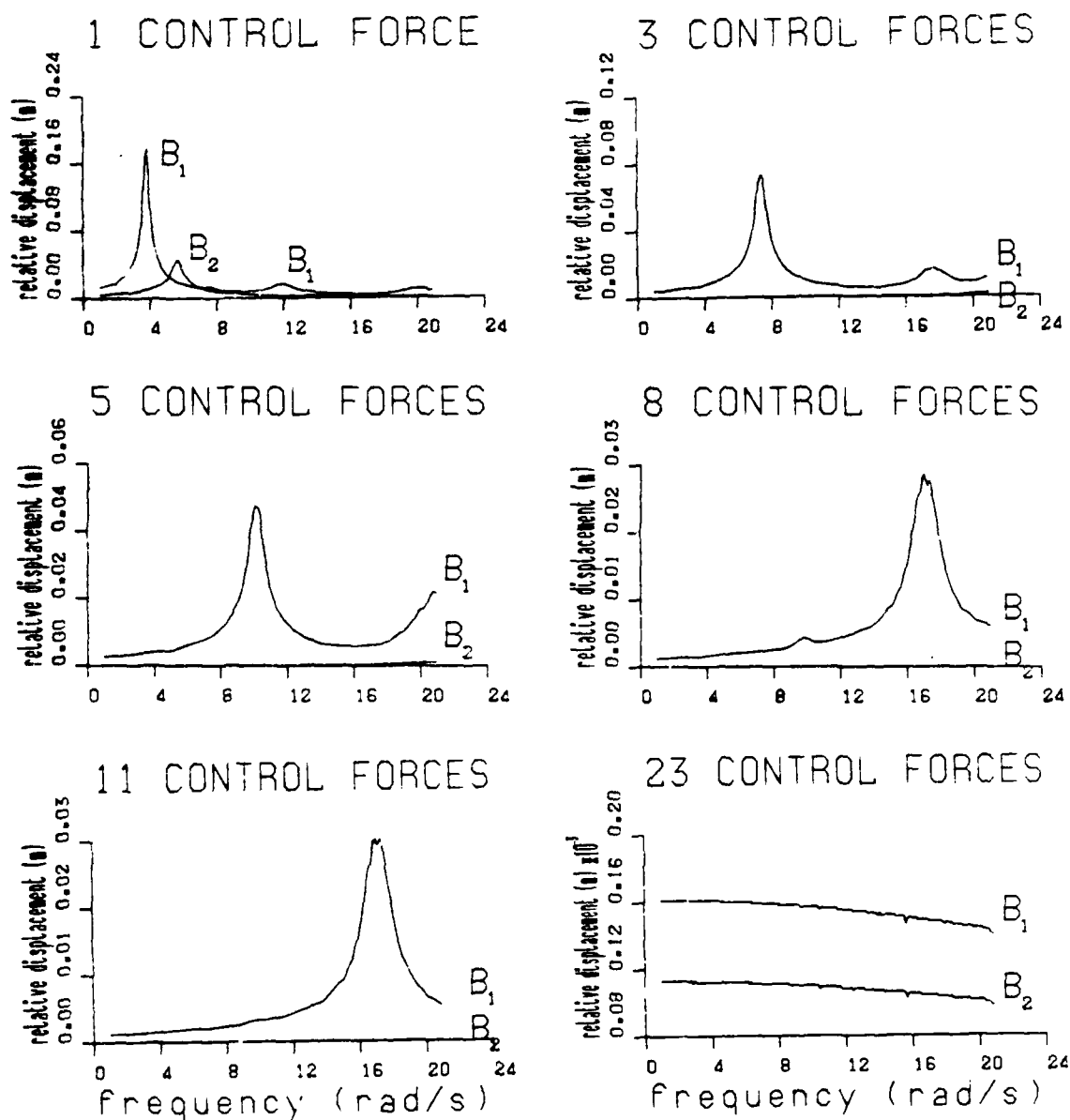


Figure 5 Values of Γ_1 in the controlled seismic response.

- In building B_1 a number of modes have a significant influence in its response while in building B_2 the first mode is almost the only one that has a significant influence. Consequently, it is possible to control the horizontal vibrations of building B_2 with a smaller number of cables. It is shown that with one control force acting in the top of building B_2 a satisfactory reduction of its response is achieved when the excitation is due to the ground acceleration or to the wind.

Some of the last conclusions about buildings B_1 and B_2 can be generalized for a wide class of tall buildings, in the following sense: if the horizontal dynamic behaviour is similar to the one of a portal

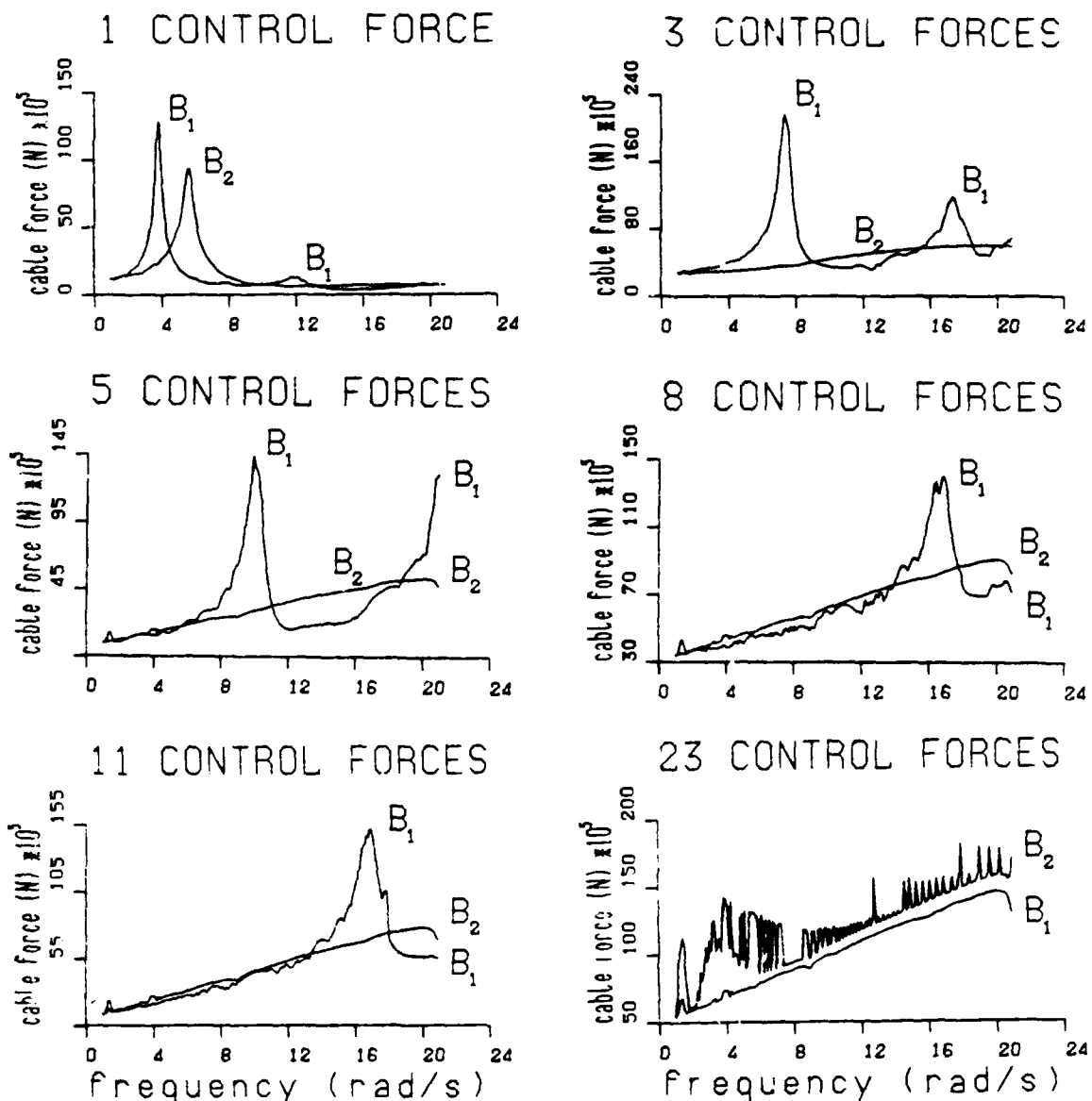


Figure 6 Values of Γ_3 in the controlled seismic response.

structure (as in buildings B_1), a considerable number of control forces (and consequently active cables) is required to reduce effectively the response. But, if the behaviour is similar to the one of a shear-wall (as in building B_2), an important reduction of the response can be achieved with a smaller number of cables.

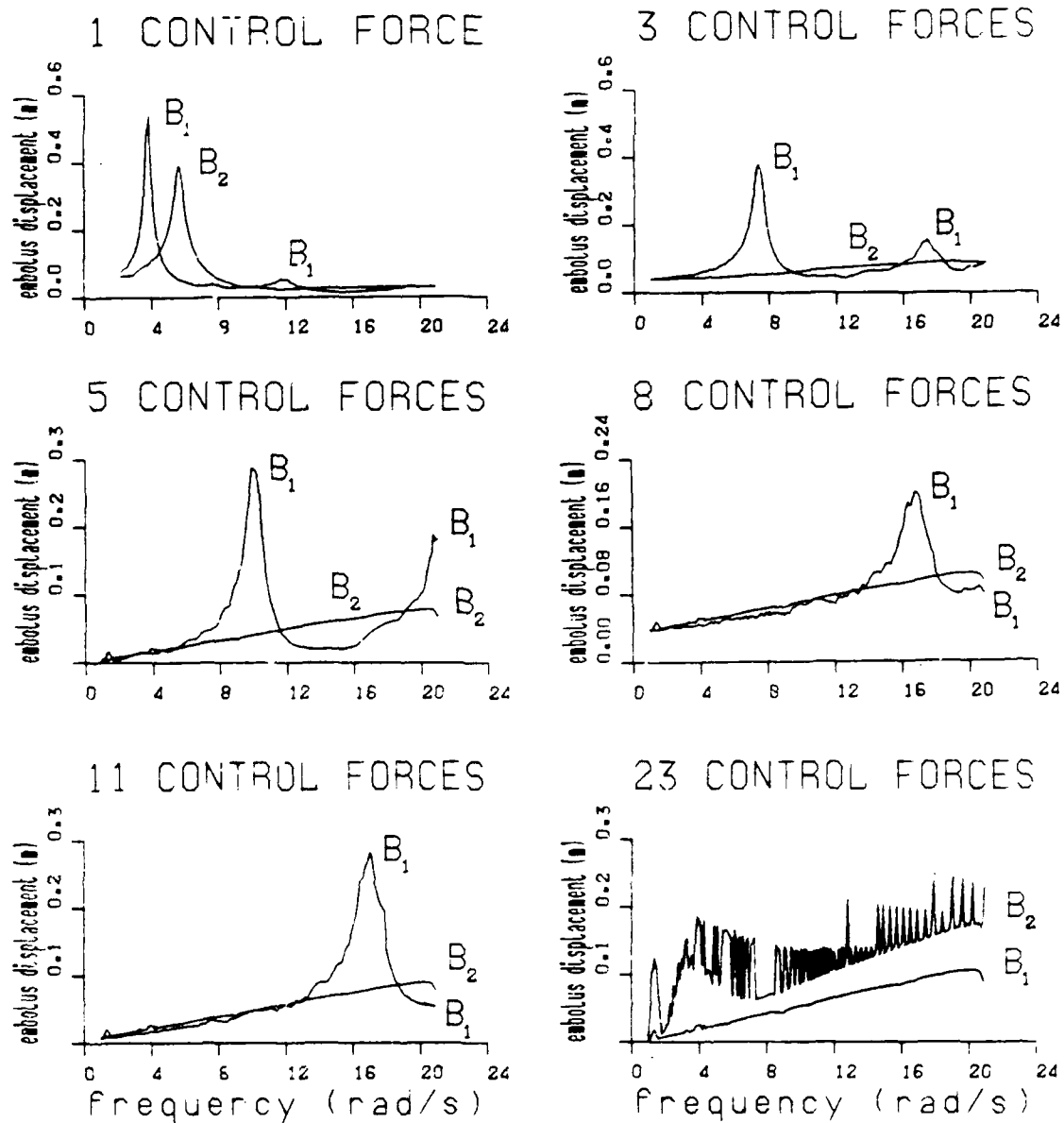


Figure 7 Values of Γ_2 in the controlled seismic response.

REFERENCES

1. J.N. YANG and B. SAMALI 1983 *Journal Structural Engineering Division ASCE*, 109 (EM1), 50-68. "Control of tall buildings in along-wind motion"
2. B. SAMALI, J.N. YANG and S.C. LIU 1985 *Journal Structural Engineering Division ASCE*, 111 (10), 2165-2180. "Active control of seismic-excited buildings".

3. H.H.E. LEIPHOLZ and M. ABDEL-ROHMAN 1985 *Structural Control*, "Control of structures", H.H.E. Leipholz, Editor, Martinus Nijhoff Publishers, Dordrecht, The Netherlands.
4. L.L. CHUNG, A.M. REINHORN and T.T. SOONG 1988 *Journal Engineering Mechanics Division ASCE*, (in print). "Experiments on active control of seismic structures".
5. F. LOPEZ-ALMANSA 1988 Ph.D. Thesis, Technical University of Catalonia. "Contribution to the development of control systems of building structures by active tendons" (in Spanish).
6. F. LOPEZ-ALMANSA, J. RODELLAR and A.H. BARBAT 1987 *Proc. of NUMETA87 Conference*, Swansea, Wales, U.K., Martinus Nijhoff Publ. Dordrecht, The Netherlands, Vol. 2, T29. "A simulation scheme for numerical analysis of active control systems for tall buildings".
7. J. RODELLAR, A.H. BARBAT and J.M. MARTIN SÁNCHEZ 1987 *Journal Engineering Mechanics Division ASCE* 113 (6), 797-812. "Predictive control of structures".
8. J. RODELLAR, L.L. CHUNG, T.T. SOONG and A.M. REINHORN 1987 *Proceedings of the Conference on Mechanical Vibrations and Noise*, ASME, Boston, September 27-30. "Experimental digital predictive control of structures".

SEMI-ACTIVE CONTROL OF EARTHQUAKE INDUCED OSCILLATIONS IN STRUCTURES
- MECHANICAL QUALIFICATIONS BY MEANS OF SAMSON-SHAKING TABLE -

G. Hirsch

Institut für Leichtbau, RWTH Aachen, Germany

and

A. Kleine-Tebbe

HRB Hochtemperatur Reaktorbau GmbH, Jülich, Germany

1. INTRODUCTION

Structural Control has recently become an important topic of research in Civil Engineering [1]. It has an essential influence on the design of modern high rise buildings, specially with respect to their resistance to wind forces and strong earthquake motions. Passive vibration control techniques have been found effective to reduce the wind induced response of tall buildings [2] and tower shaped structures [3]. In opposition to that passive control devices are not successful in like manner for reducing the maximum seismic response of tall buildings.

In this paper, a control system will be presented that operates on pure information (sensor and logic) and minimal energy (power) inputs, and thus it can be classified as semi-active. The earthquake induced vibrational energy will be dissipated through the use of Tuned Mass Damper System (TMD) in combination with a latch-release-mechanism intending for an optimum earthquake-response-shooting.

The new method of earthquake-response-control will be mechanical realized by means of the SAMSON-shaking table. In conclusion and originated by the test results recommendations will be made from engineer point of view to improve the resistance of civil engineering structures against seismic attacks.

2. PASSIVE AND ACTIVE STRUCTURAL CONTROL

In order to limit structural response under environmental actions, such as earthquake, within acceptable ranges, two main control ways can be considered: the passive control, where the dissipation of vibrational energy is the aim and the active structural control, which generates counteracting forces by external means.

2.1 Passive control

As pointed out by Yao [4] in a critical review, several passive control techniques can be effective in improving the safety measure of seismic structures. Later, these possibilities were summarized in a paper by Wirshing and Yao [5] ranking the effectiveness of following devices in decreasing order without economical considerations: base isolation, base isolation and absorber, and tuned mass damper system attached to the roof.

It was found that the base isolation was extremely effective in redu-

cing the structural response. The concept is to be seen in Figure 1 in that the superstructure is effectively insulated from the ground motion. Vibration isolation of nuclear reactor buildings by means of spring-dashpot system have been reported by Tezcan and Civi [6]. Figure 2 shows the acceleration response at roof to El Centro earthquake, with fixed base and rubber base.

In conclusion, the results of the studies show that with base isolation there are significant gains due to the reduction of acceleration responses and their shift out of the range of the frequencies which effect most the systems and the components.

When helical springs and viscodampers are used in the base isolation engineering, both the vertical and horizontal acceleration response is significantly reduced [7].

Pocanshi and Berg [8] have discussed intuitively the problem of decreasing the effects of strong seismic motions on buildings and have presented some techniques of dissipative connections, which are suited for this purpose.

Finally, references to the long-standing research work at the University of California, Berkeley, may appropriate. Kelley reported with regard to control devices for earthquake resistant structural design [9].

The tuned mass dampers have been found effective to reduce wind induced vibrations of buildings and structures. Recently Chowdhury, Iwuchukwu and Garske [10] studied linear elastic parameters on effectiveness of TMD considering higher modes.

In conclusion, the authors showed that a TMD tuned to the fundamental frequency of primary structure is less effective in reducing the response at higher modes, the higher modes response will increase in fact.

Sladek and Klingner have investigated TMD to reduce seismic response and have reported in conclusion [11] that the TMD did not reduce the prototype maximum seismic response. Figure 3 compares the tip displacement response for the linear elastic multi degrees of freedom model, with and without an optimum Den Hartog TMD. This figure shows the TMD to have no effect on the buildings maximum response. This findings have been contradicted by other authors [12]. The divergence of views is understandable since in case of white noise ground acceleration the TMD is more effective than in transient excitation. With regard to an improvement of the vibration control the paper deals with the semi-active TMD with the aim of a transient counteraction.

2.2 Active control

An investigation of the possible application of both the active tendon and active mass damper control systems to buildings excited by strong earthquakes is made by Samali, Yang and Liu [13]. The problem is formulated theoretically using the transfer matrices approach and a closed-loop control law. Unfortunately, the effectiveness of the control systems illustrated analytically by the authors will be demonstrated experimentally in the future. Because of the high costs involved in such experimental investigations, it has been difficult for these and other researchers to obtain adequate funding to fully develop and utilize their capabilities. As discussed by Yao and Soong [14] much more experimental work needs to be done before the concept of structural control can be accepted by the structural engineering profession and the general public. Consequently, the purpose of this paper is to investigate the effectiveness of the control technique experimentally by means of

the test facility SAMSON.

3. SEMI-ACTIVE STRUCTURAL CONTROL - EXPERIMENTALLY INVESTIGATION

In order to validate the semi-active control of earthquake induced transient vibrations of structures experimental investigations have been carried out on the shaking table SAMSON.

3.1 Test specimen

Figure 4 shows the drawing of the test specimen, a steel-frame structure with three floors. The weights of the floors are (without the additional tuned mass damper system) 19, 18 and 18 kg from the bottom to the top. The model structure weights 68 kg and is 1170 mm high and 750 mm by 600 mm in plan dimension. Figure 5 shows the photograph of the test specimen on the shaking table and Figure 6 shows details of the tuned mass damper system (pendulum-type).

The mass of the auxiliary system is 6.5 kg and the damping is viscously realized by the equipment as shown in Figure 7. According to [15] viscous damping will be obtained by means of a roller-brake and a light weight brake-clamp, as shown in the figure. If the shaft speed is relative high in comparison to the oscillation-velocity the damping force $P(t)$ is proportional \dot{w} and consequently viscous.

The tuned mass damper is in an eccentric position to the normal due to electromagnetic force, released by electric signal, if the seismic induced motion of the test structure is in the best possible position to counteract that motion.

3.2 Mechanical qualification of the vibration control technique

The mechanical qualification of vibration control system can be performed by uniaxial tests of a single component on a hydraulic or electrodynamic shaker and the subsequent calculation of the behaviour of assemblages of components or a complete structure. This procedure will be sufficient to predict the vibrational responses of systems with linear stress-strain relationships.

However, the codes available require a significant amount of idealization, especially in more complicated structures in combination with nonlinear mechanical behaviour. Improved testing techniques have been developed to enable the demonstration of the operability of equipment during seismic excitation (p.e. physical testing of scale models), the verification of the accuracy of analytical models and the development of new structural configuration.

For this purpose the large vibration test facility SAMSON has been designed in the laboratories of the Hochtemperatur Reaktorbau GmbH, Jülich, Germany [16]. Figure 8 shows a sectional view on the test facility. Its main feature is the vibration test platform - a welded steel, box-like structure measuring 5 x 5 x 1.2 m, which is designed for testing items weighing up to 25 t mass.

The platform has tapped holes (M24) at a pitch of 350 mm for fixing the test items, as shown in Figure 9. Four hydraulic actuators move the plat-

form in both horizontal axes, while a main actuator in the centre provides the dynamic forces required for the vertical motion of the platform. Four additional vertical actuators at the platform corners counteract the pitch motion occurring, when the centre of gravity is relatively high and the test object is arranged off-centre.

With this design it is possible to reproduce simultaneous and independent motions with three degrees of freedom. There exists also the possibility of extending the capacity of the facility to six degrees of freedom, thus enabling rotational movements to be generated. Two precision gimbals are used to fit each actuator to the platform and the foundation block.

The test facility is controlled in the frequency range up to 100 Hz by an analog system and a computer-based digital system, either of which can be used independently. The three axes in which the vibration platform can be moved can be controlled individually or simultaneously. The types of excitation desired, for example sinusoidal waveforms, seismic time-history functions, shock functions, etc., can be entered using the function generator, magnetic type or computer system.

An important aspect of the control system is the dynamic frequency compensator, which calculates for each axis, with the aid of acceleration feedback, the natural-frequency behaviour of a test item in a preliminary test at reduced power. This compensator modifies the platform movement during the subsequent vibration test to ensure a specific displacement-time characteristic for any particular part of the test item.

Figure 10 shows an example, which demonstrates the performance of the control system to keep the platform response at constant acceleration level over the whole frequency range. Time-history excitation can be performed with a high level of accuracy, as shown in Figure 11, an important point in testing technique for seismic qualification of structures. More details about control system and operating experience of SAMSON are reported in [17].

3.3 Performed test program

In order to cover all tasks of study objectives a test program has been set up as described briefly in the following points: (1) Earthquake simulation (safety earthquake time-history) and structure response without control. The natural frequency of the structural fundamental mode is 2.36 Hz, verified by means of SAMSON sine sweep test. (2) Recording the TMD passive controlled structure. The natural frequency of the TMD (uncoupled) has been 2.3 Hz, i.e. optimum tuning with regard to optimum passive control of transient inputs. (3) Recording the semi-active controlled structural response, i.e. transient counter-attack. The electronic control circuit will be presented in a separate publication by E. Schäfer (Institut für Leichtbau, RWTH Aachen, Germany). (4) Recording the structural response regarding the semi-active control turned the wrong way. (5) Recording the response due to excitation of the released TMD.

4.1 Test results

Figure 12 compares the acceleration response at the top level of the test-structure with and without the optimum TMD and additionally with semi-active control. It is clear that the TMD alter the response of the prototype building to the given earthquake record moderately. With the mass ratio .096 (with reference to the total mass of the test structure) a reduction in peak

response of 79 % (rest.) was realized. The structural peak response without control has been 50 % gravity. The improvement by semi-active control is approximately 40 % referring to TMD passive control. The response reduction effect is obviously and beyond that an improvement of the semi-active control by changing the set up time may be possible.

As shown in Figure 13, the new approach takes advantage of the fact that the time-history response of the structure is approximately the same in cases of earthquake excitation and also of TMD-releasing influence. Its the aim of the paper to demonstrate that fact.

In order to increase the control effect, installations of more than one TMD are possible. The different floors of the building can be carried out as TMDs with different tuning also with regard to the natural frequency of the higher structural modes of vibration. Basis of a new aseismic design will be a structural optimization including elastic supported floors, optimum tuned and damped to reduce the response by means of a semi-active control technique in the demonstrated way.

Figure 14 shows the drawing of an elastic supported floor (test laboratory of the Institut für Leichtbau, RWTH Aachen), designed by GERB Company, Essen, Germany.

Finally, it should be mentioned that the investigations, especially with special damping devices, and the optimum design of base-isolation and the optimum tuned floors are in progress.

4. CONCLUDING REMARKS

The intention of the presented paper is to suggest some semi-active control techniques for structures constructed most usually: low rise and medium rise buildings subjected to seismic loads.

The use of semi-active control with adaptable parameters of TMD systems (floors, etc.) is, in fact, a way to shooting the seismic response of structures.

The authors are hopeful that the presentation and the mechanical qualification of the semi-active control technique may give offence to a new understanding to aseismic design of civil engineering structures.

5. ACKNOWLEDGEMENTS

The authors acknowledge with thanks G. Schmidt and H. Jakobs for SAMSON tests assistance as also J. Gruß for performance of tests at the laboratory of Institut für Leichtbau, RWTH Aachen.

6. REFERENCES

1. H.H.E. LEIPHOLZ, editor 1987 Structural Control. Martinus Nijhoff Publishers, Dordrecht-Boston-Lancaster.
2. R.J. McNAMARA, 1977 Journal of the Structural Division ASCE 103 (1985-1998). Tuned Mass Dampers for Buildings.

3. G. HIRSCH, 1987 Structural Control (in [1]) 278-296. Practical Experiences in Passive Vibration Control of Chimneys - Conclusions from Wind Tunnel and Full Scale Tests.
4. J.T.P. YAO, 1979 Preprint 3460 Boston Convention ASCE. Passive and Active Control of Civil Engineering Structures.
5. P.R. WIRSHING and J.T.P. YAO, 1973 Computer and Structures 3, 809-826. Safety Design Concepts for Seismic Structures.
6. S. TEZCAN and A. CIVI, 1985 Transactions of 8th Conference on Structure Mechanics in Reactor Technology CEC Vol. K 491-496. Vibration Isolation of Nuclear Reactor Buildings by Means of Spring-Dashpot System.
7. G. HÜFFMANN, 1984 Internal report GERB GmbH Berlin, Germany. Shaking Table Tests of a 5-Storey Steel Frame.
8. A. POCANSCHI and D. v. BERG, 1986 Proceedings 8th ECEE Lisboa 8. 5-9. Some Types of Dissipative Connections for Earthquake Resistant Structures.
9. J.M. KELLEY, 1978 Structural Control. North-Holland Publishers. 391-413. Control Devices for Earthquake-Resistant Structural Design.
10. A.H. CHOWDHURY, M.D. IWUCHUKWU and J.J. GARSKE, 1987 Structural Control ([1]) 105-127. The Past and Future of Seismic Effectiveness of Tuned Mass Dampers.
11. J.R. SLADEK and R.E. KLINGER, 1983 Journal of the Structural Division ASCE (109), 2004-2009. Effect of Tuned Mass Dampers on Seismic Response.
12. P.H. WIRSHING and G.W. CAMPBELL, 1974 Earthquake Engineering and Structural Dynamics. New York: John Wiley & Sons. 303-312. Minimal Structural Response Under Random Excitation Using the Vibrations Absorber.
13. F. SANALI, J.N. YANG and S.C. LIU, 1985 Journal of the Structural Engineering (111), 2165-2179. Active Control of Seismic-Excited Buildings.
14. J.T.P. YANG and T.T. SOONG, 1984 ASCE Atlanta Convention Preprint 84-010. Importance of Experimental Studies in Structural Control.
15. H. ÖRY and G. HIRSCH, 1987 Proceedings of 4th Umbrella-Symposium Technion Haifa - RWTH Aachen - KFA Jülich. Earthquake Dynamics of Tall Buildings How to Alleviate?
16. A. KLEINE-TEBBE and H. JAKBOS, 1985 Transactions of the 8th International Conference on Structural Mechanics in Reactor Technology, Vol. K 491-496. Practical Experience During Installation of the Large Multi-Axes Vibration Test Facility SAMSON.
17. A. KLEINE-TEBBE, 1983 Proceedings of IASTED International Symposium on Applied Control and Identification ACI 83. A New Vibration Test Facility for Simulating Multi-Axes Dynamic Motion with Direct Frequency Control.

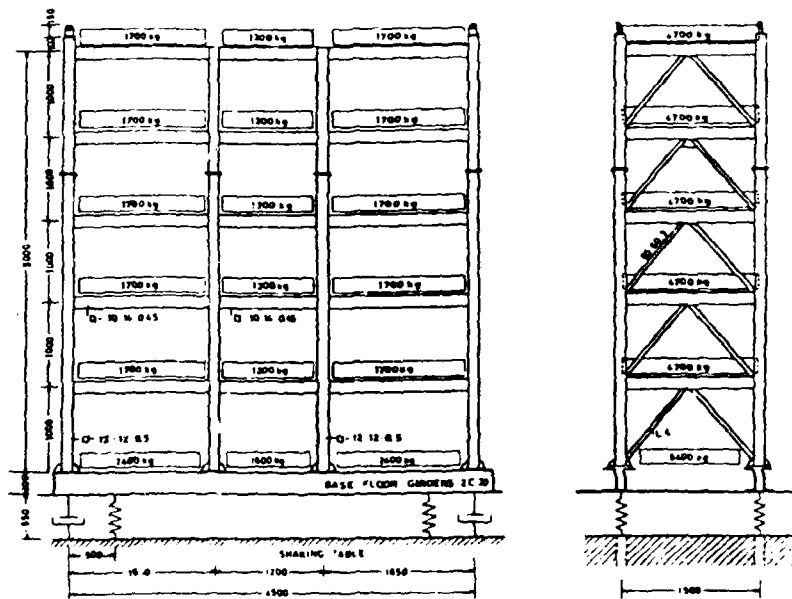


Figure 1. Base-isolation of a five-storey building [6]

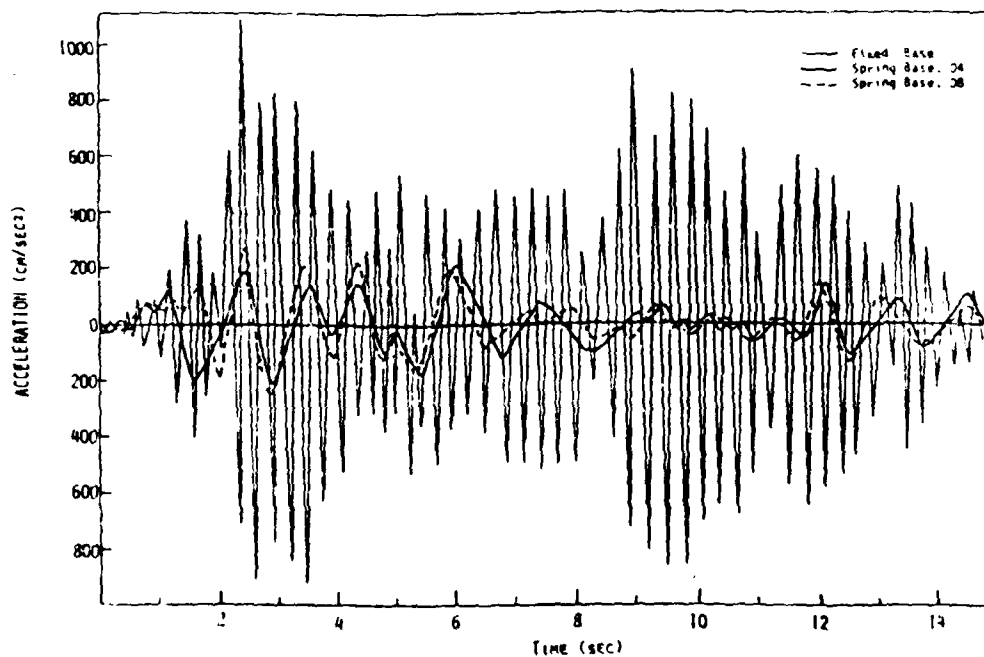


Figure 2. Acceleration-response of the base-isolated building. Fixed base and spring base with 4 (D4) and 8 (D8) dashpots

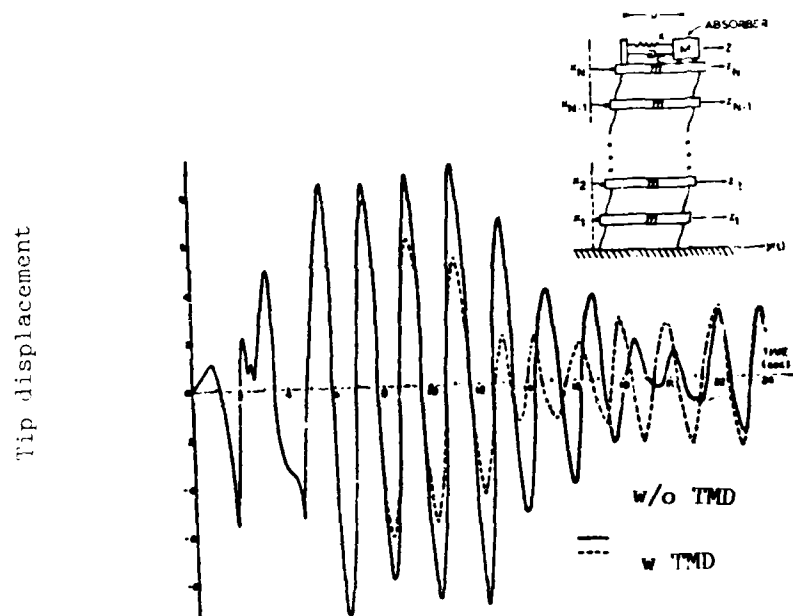


Figure 3. Tip displacement response of linear elastic multi degrees of freedom model with and without TMD

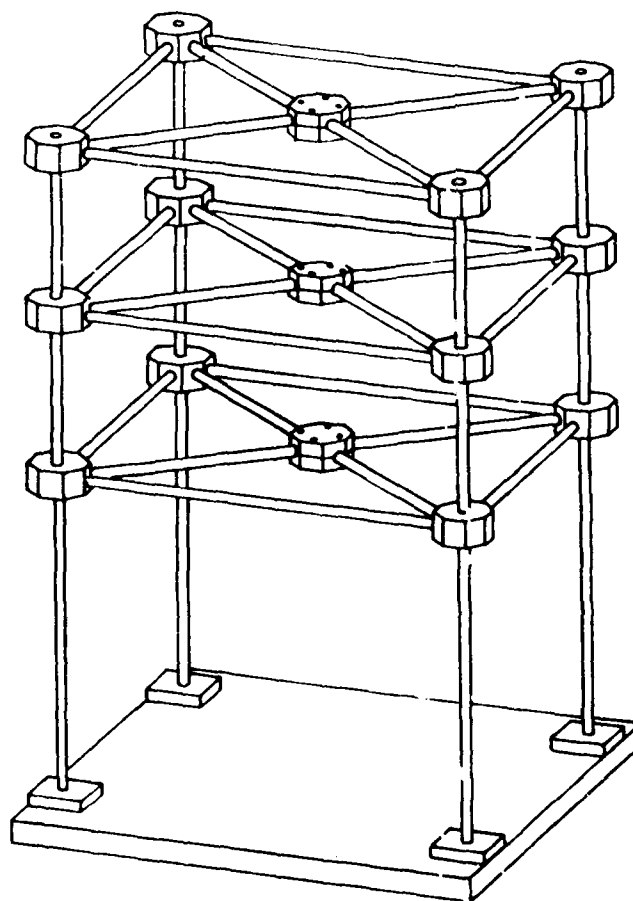


Figure 4. Test specimen 1170 mm high and 750 mm by 600 mm in plan dimension

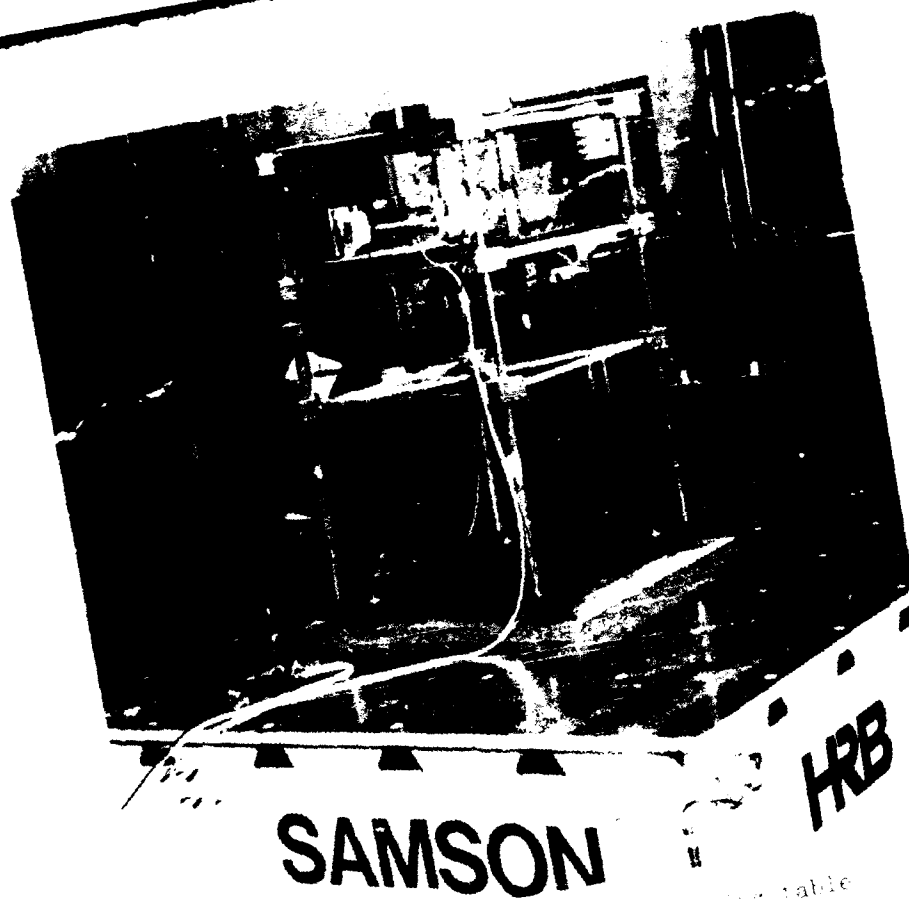


Figure 5. Test rig for SAMSON transfer table

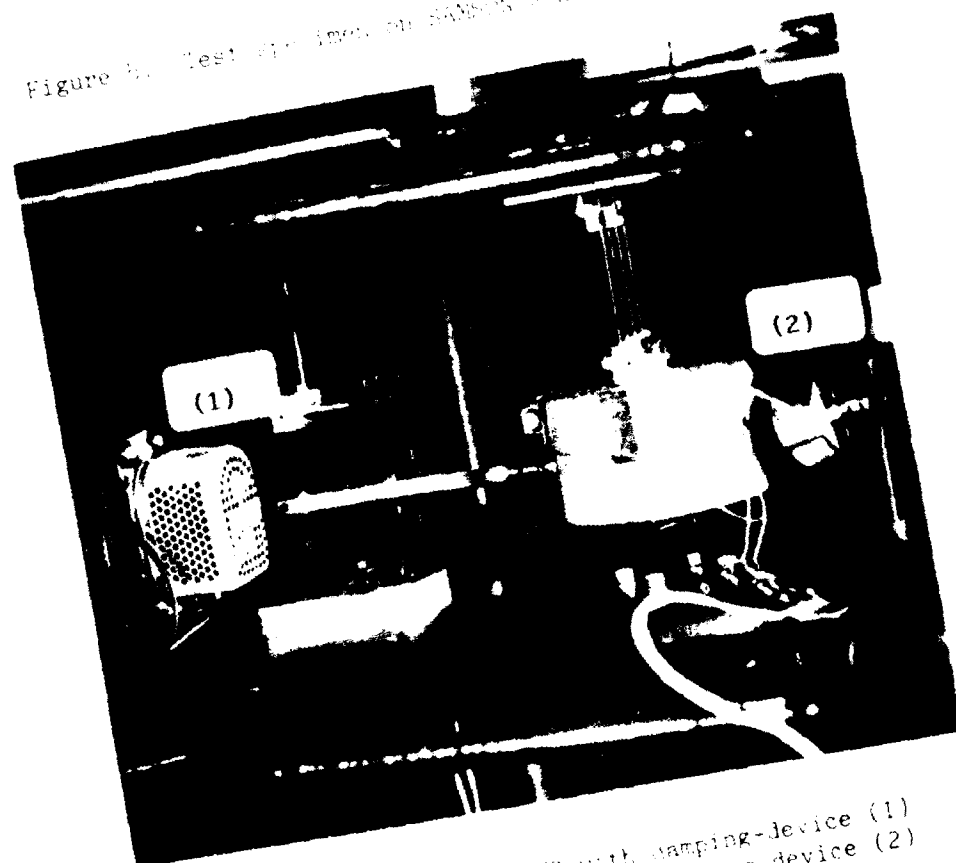


Figure 6. Pendulum-type PND with damping-device (1) and electromagnet releasing device (2)

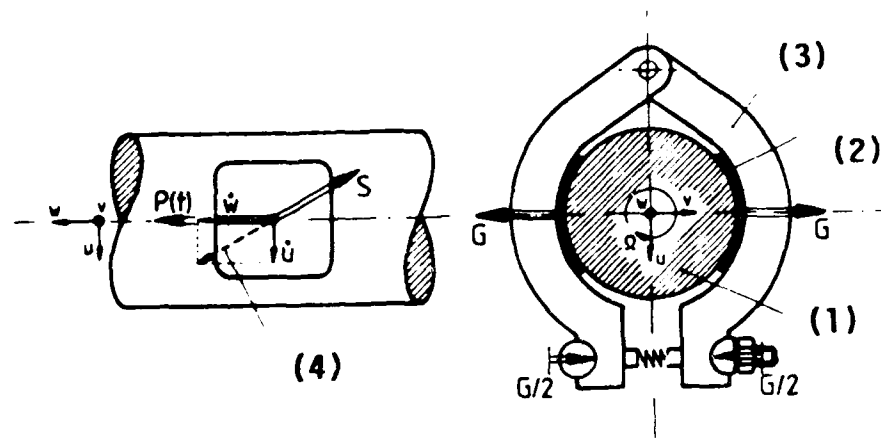


Figure 7. Viscously damping-device, (1) rotating shaft, (2) rubbing element, (3) roller-brake, (4) velocities and damping-force $P(t)$ prop. \dot{w}

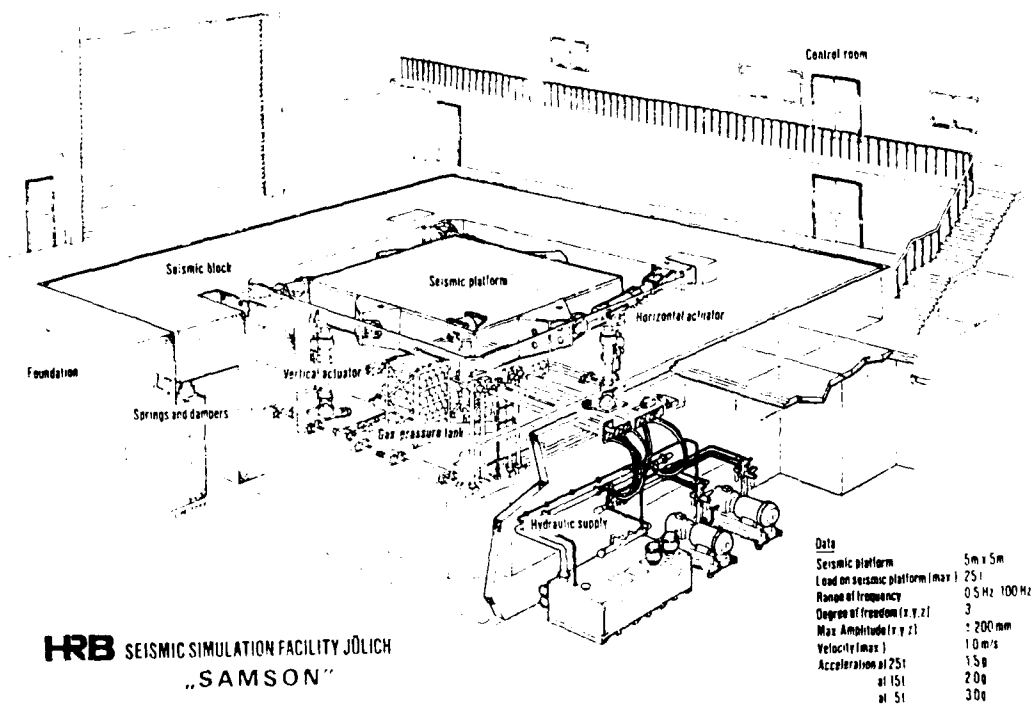


Figure 8.

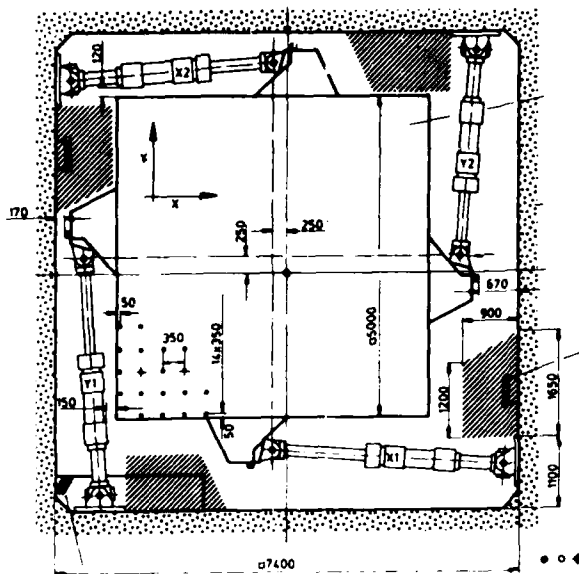


Figure 9. Platform of SAMSON shaking table

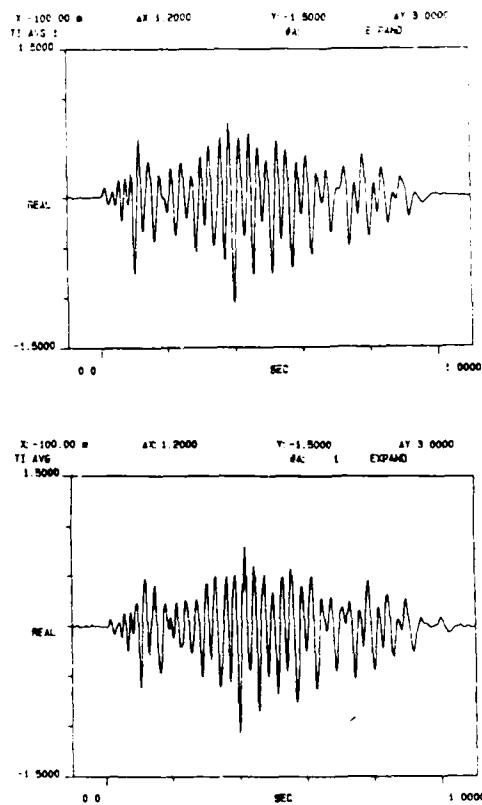


Figure 11. Comparison of time-history command signal (above) and platform response (below)

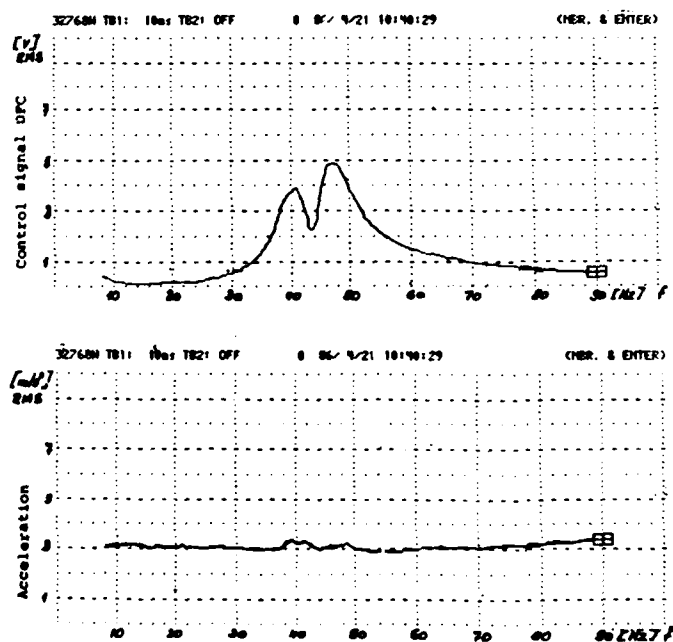


Figure 10. DFC-control signal (above) and platform response (below)

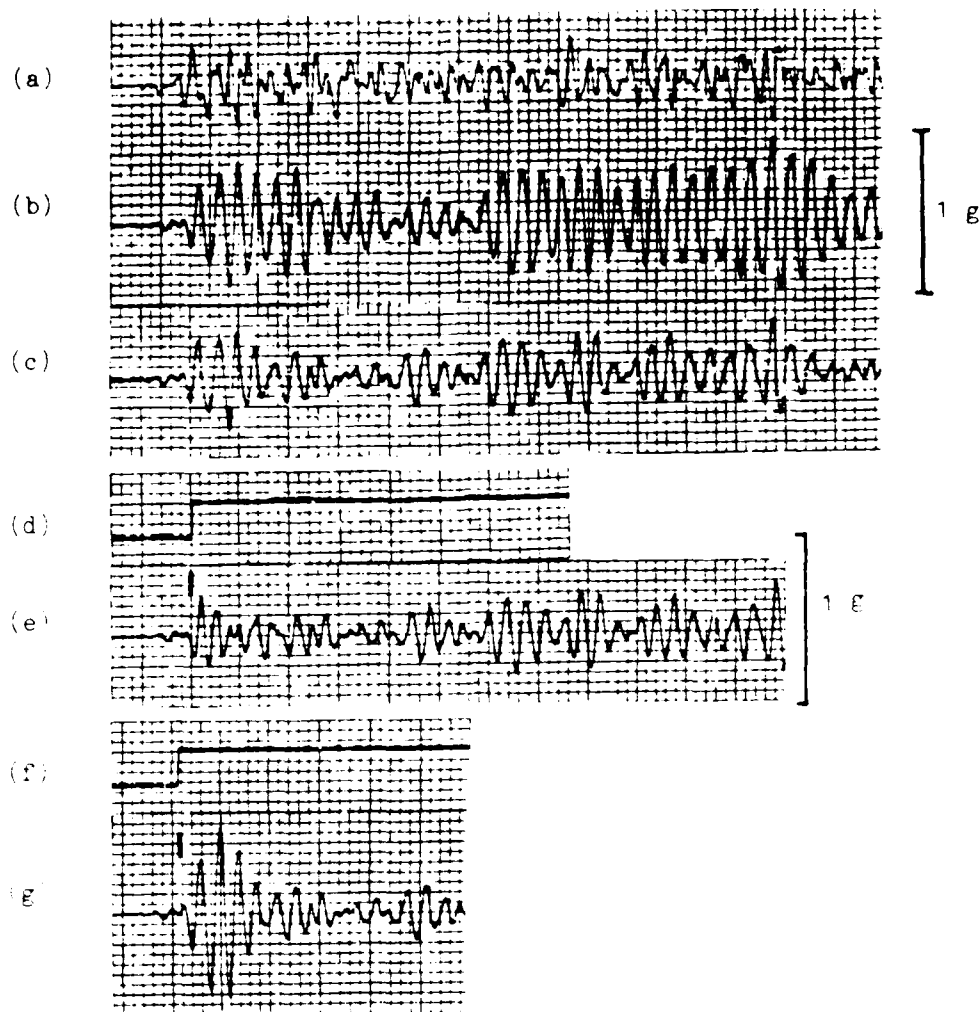


Figure 12. Acceleration recordings, (a) platform movement, (b) tip response without control, (c) response with TMD, (d) electric signal (releasing step), (e) response with semi-active control (transient counteracting), (f) analog (d), (g) uncorrect semi-active regulating

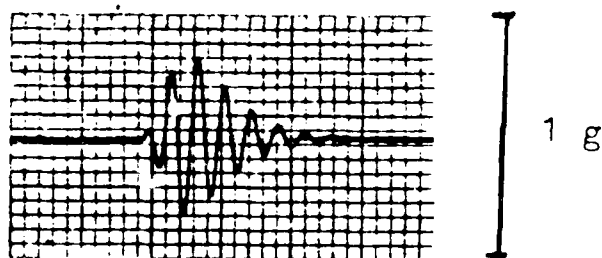


Figure 13. Structural response, excited by TMD-decay

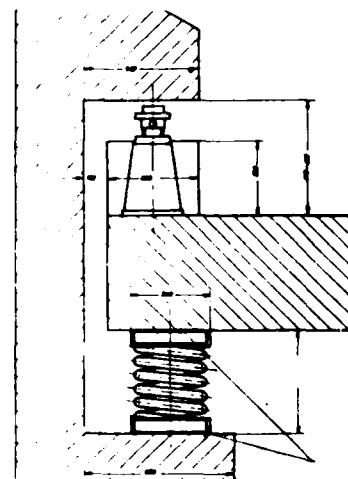


Figure 14. Elastic supported floor (sector)